ORNL/HTSPC-16

ORNL Superconducting Technology Program for Electric Power Systems

Annual Report for FY 2004

SUPERCONDUCTIVITY
FOR ELECTRIC SYSTEMS

DOCUMENT AVAILABILITY

Reports produced after January 1, 1996, are generally available free via the U.S. Department of Energy (DOE) Information Bridge:

Web site: http://www.osti.gov/bridge

Reports produced before January 1, 1996, may be purchased by members of the public from the following source:

National Technical Information Service
5285 Port Royal Road
Springfield, VA 22161
Telephone: 703-605-6000 (1-800-553-6847)
TDD: 703-487-4639
Fax: 703-605-6900
E-mail: info@ntis.fedworld.gov
Web site: http://www.ntis.gov/support/ordernowabout.htm

Reports are available to DOE employees, DOE contractors, Energy Technology Data Exchange (ETDE) representatives, and International Nuclear Information System (INIS) representatives from the following source:

Office of Scientific and Technical Information
P.O. Box 62
Oak Ridge, TN 37831
Telephone: 865-576-8401
Fax: 865-576-5728
E-mail: reports@adonis.osti.gov
Web site: http://www.osti.gov/contact.html

This report was prepared as an account of work sponsored by an agency of the United States government. Neither the United States government nor any agency thereof, nor any of their employees, makes any warranty, express or implied, or assumes any legal liability or responsibility for the accuracy, completeness, or usefulness of any information, apparatus, product, or process disclosed, or represents that its use would not infringe privately owned rights. Reference herein to any specific commercial product, process, or service by trade name, trademark, manufacturer, or otherwise, does not necessarily constitute or imply its endorsement, recommendation, or favoring by the United States government or any agency thereof. The views and opinions of authors expressed herein do not necessarily state or reflect those of the United States government or any agency thereof.

ORNL/HTSPC-16

ORNL SUPERCONDUCTING TECHNOLOGY PROGRAM FOR ELECTRIC POWER SYSTEMS

ANNUAL REPORT FOR FY 2004

Compiled by
R. A. Hawsey
A. W. Murphy

Edited by
W. S. Koncinski
D. M. Kroeger

Manuscript Completed: April 2005
Date Published: July 2005

Prepared for the
Office of Electricity Delivery and Energy Reliability
U.S. DEPARTMENT OF ENERGY
(TD 5001)

Prepared by the
OAK RIDGE NATIONAL LABORATORY
P. O. Box 2008
Oak Ridge, Tennessee 37831-6285
Managed by
UT-Battelle, LLC
for the
U. S. DEPARTMENT OF ENERGY
Under contract DE-AC05-00OR22725

Contributors

Left to right: S. Kang, A. A. Gapud, C. Cantoni, F. A. List III, S. W. Schwenterly, L. Heatherly, Jr., H. M. Christen, A. W. Murphy, M. P. Paranthaman, T. Aytug, D. F. Lee, C. M. Rey, M. J. Gouge, D. K. Christen, R. A. Hawsey, P. M. Martin, E. D. Specht, R. C. Duckworth, R. Feenstra, S. Sathyamurthy, Y. Zhang, D. R. James, A. Goyal, and J. A. Demko

Not pictured: D. B. Beach, S. W. Cook, A. R. Ellis, B. W. McConnell, I. Sauers, and J. R. Thompson

Contents

Contributors iii

List of Figures ix

List of Tables xxi

Abbreviated Terms xxiii

Executive Summary xxvii

1. Technical Progress in Applications Development 1-1

1.1 Ultera/ORNL HTS Cable Superconductivity Partnership with Industry (SPI).................... 1-1

1.2 Waukesha Electric Systems (WES)/SuperPower/ORNL 5/10 MVA HTS Transformer SPI 1-9

1.3 SuperPower Matrix Fault Current Limiter CRADA 1-14

1.4 General Electric Co. HTS Generator SPI 1-17

1.5 Conductor Engineering: Overcurrent Studies in HTS Tapes 1-22

1.6 Conductor Engineering: On the Effect of NiW on the Inductance and AC Loss of HTS Cables 1-25

1.7 Conductor Engineering: AC Losses in YBCO Tapes 1-27

1.8 Dielectric Materials R&D 1-28

1.9 Cryogenics Initiative 1-29

1.10 SPI Oversight/Readiness Reviews 1-29

1.11 2003 IEEE Conference on Electrical Insulation and Dielectric Phenomena 1-31

1.12 References 1-31

2. Technical Progress in Wire Development 2-1

2.1 High-Performance YBCO Coated Superconductor Wires 2-1

2.2 Oxidation of Carbon on Nickel-Based Metallic Substrates Implications for HTS Coated Conductors 2-7

2.3 Identification of a Self-Limiting Reaction Layer in Ni-3at%W Rolling-Assisted Biaxially Textured Substrates 2-14

2.4 Perovskite-Type Buffers for YBCO Coated Conductors 2-23

2.5 Growth of Lanthanum Manganate Buffer Layers for Coated Conductors via a Metal-Organic Decomposition Process 2-27

2.6 Epitaxial Growth of Eu_3NbO_7 Buffer Layers on Biaxially Textured Ni-W Substrates 2-31

2.7 Alternate Buffer Architectures for Improved YBCO Coated Conductors 2-35

2.8 Chemical Solution Deposition of Lanthanum Zirconate Barrier Layers Applied to Low-Cost Coated Conductor Fabrication 2-38

2.9 Detection of Interfacial Strain and Phase Separation in $MBa_2Cu_3O_{7-x}$ Thin Films by Raman Spectroscopy and X-Ray Diffraction Space Mapping 2-42
2.10 Investigation of TiN Seed Layers for RABiTS™ Architecture with Single-Crystal-Like Out-of-Plane Texture... 2-56
2.11 Growth of YBCO Films on MgO-Based RABiTS™ Templates.. 2-60
2.12 Faster Conversion Process Produces ex situ YBCO Coated Conductors with Critical Currents Greater than 350 A/cm-width at 77 K... 2-65
2.13 Low-Pressure Conversion Studies for YBCO Precursors Derived by PVD and MOD Methods 2-71
2.14 Growth of YBCO Films with High Critical Current at Reduced Pressures by the BaF_2 ex situ Process 2-75
2.15 Comparison of $YBa_2Cu_3O_{7-\delta}$ Precursors Made by TFA-MOD and BaF_2 ex situ Processes and their Post-Deposition Processing under Low Pressure Conditions............... 2-78
2.16 Growth of Epitaxial TiN Thin Films on Biaxially Textured NiW Substrates by rf Sputtering 2-81
2.17 Preparation of YBCO Films on CeO_2-Buffered (001) YSZ Substrates by a Non-Fluorine MOD Method 2-86
2.18 Non-Fluorine-Based Bulk Solution Techniques to Grow Superconducting $YBa_2Cu_3O_{7-\delta}$ Films—A Review... 2-93
2.19 Epitaxial Growth of Solution-Based Rare Earth Niobate, RE_3NbO_7 Films on Biaxially Textured Ni-W Substrates 2-106
2.20 Pulsed Electron Deposition of YBCO Precursors.. 2-109
2.21 An Approach for Electrical Self-Stabilization of HTS Wires for Power Applications......... 2-113
2.22 Characterization of Suitable Buffer Layers on Cu and Cu-Alloy Metal Substrates for Development of Coated Conductors 2-116
2.23 Electrical and Magnetic Properties of Conductive Cu-Based Coated Conductors 2-120
2.24 Simultaneous Inductive Determination of Grain and Intergrain Critical Current Densities of YBCO Coated Conductors.. 2-124
2.25 Magnetism and Ferromagnetic Loss in Ni-W Textured Substrates for Coated Conductors 2-127
2.26 Improvement of In-Field Transport Critical Currents in $(Y_2BaCuO_5/YBa_2Cu_3O_{7-x})xN$ Multilayer Films on Ni-Based Textured Substrates.. 2-133
2.27 Modeling Current Flow in Granular Superconductors and Implications for Potential Applications... 2-137
3. Summary of Technology Partnership Activities.. 3-1
3.1 Background 3-1
3.2 Relationship to the DOE Mission 3-1
3.3 Funding 3-1

3.4 Technology Partnership Approach... 3-1
3.5 Program inventions 3-2

4. Events, Honors, and Awards... 4-1
4.1 Mike Gouge Named Editorial Board Member for the *Journal of Superconductivity: Incorporating Novel Magnetism* 4-1
4.2 ORNL Showcases Superconducting Wire Technology at “Superconductivity Day on the Hill”... 4-1
4.3 Goyal Co-Edits Book on High-Temperature Superconductivity 4-1
4.4 ORNL’s Superconductivity Project Inventors named Patent Award Recipients at May 25 Ceremony.. 4-2
4.5 ORNL Superconductivity Researchers Partnered with North Carolina S&T State University to win $1.4 million NSF Grant.. 4-2
4.6 Paranthaman named an Associate Editor of the Journal of the American Ceramic Society 4-2
4.7 ORNL participates in Superconducting Cable Kick-off Event on Capitol Hill.................... 4-2
4.8 ORNL Team Leader Co-Edits an issue in *MRS Bulletin* 4-3
4.9 Amit Goyal named to Executive Editorial Board for the *Encyclopedia of Superconductivity*.. 4-3
4.10 Day of Science—November 17, 2003 4-3
4.11 The 2004 Summer Intern Program.. 4-4

5. Presentations/Publications 5-1

List of Figures

Figure *Page*

1.1. Electric and calorimetric measurements of ac losses compared with losses calculated by using the monoblock model 1-1

1.2. A 7-kA overcurrent pulse voltage response of the HTS cable 1-2

1.3. A 10-kA overcurrent pulse voltage response of the HTS cable 1-2

1.4. Comparison of the voltage-current characteristics before and after the overcurrent tests for the HTS cable 1-2

1.5. Parallel resistance approach to the flux flow model 1-3

1.6. Voltages for the cable calculated by using the flux flow model 1-3

1.7. Calculated fraction of current in the superconductor based on the flux flow model 1-3

1.8. Estimated laminated HTS tape heat capacity 1-4

1.9. Simulated thermal response of the cable for the 10-kA pulse 1-4

1.10. Comparison of the measured temperature response at 3 kA_{rms} for the damaged and undamaged cable 1-5

1.11. AC losses normalized to a per-phase basis for the 3-m cable 1-5

1.12. Partial discharge inception strength as a function of electrode gap and stressed volume 1-5

1.13. Partial discharge inception strength as a function of stressed volume for Stycast 2850 KT 1-6

1.14. Triaxial cable three-phase termination 1-6

1.15. Fault current and induced shield current from a single line-to-ground fault on phase C 1-7

1.16. Measured voltages across the phase 1 main conductor of data taken in June 2000 compared with measurements taken in June 2004 1-8

1.17. Measured voltages across the phase 1 shield conductor taken in June 2000 compared with data taken in June 2004 1-8

1.18. The 5/10-MVA transformer being lifted off its trailer at the WES main plant 1-9

1.19. The 5/10-MVA transformer leaves the WES Progress II building 1-10

1.20 Phase A diode comparison 1-11

1.21. Vacuum and cryocooler temperatures during warmup, 1/22/04 1-11

1.22. Crack between high-voltage terminals (HV-II on left) on the A-phase 1-14

1.23. Close-up of the inner diameter of the ceramic electrical break 1-14

1.24. Cryostat used for preliminary MFCL cooling tests 1-15

1.25. Layout of temperature sensors 1-15

1.26 Temperature profiles at various locations 1-16
1.27. Assembly of 52-kV, 250-kV BIL bushing into the high-pressure cryostat 1-16
1.28. Influence of water contamination on silver emissivity at 33 K 1-17
1.29. Influence of air contamination on silver emissivity at 32 K 1-18
1.30. Emissivity degradation comparison between pure water contamination and water vapor in air contamination experiments at different levels of assumed humidity 1-18
1.31. Comparison of absolute emissivity degradation of silver-plated copper samples due to direct water contamination 1-18
1.32. Comparison of relative emissivity degradation with respect to the room-temperature value of silver-plated copper samples due to direct water contamination 1-18
1.33. Emissivity degradation of a silver-plated copper sample due to the presence of G10 in the vacuum space 1-19
1.34. Comparison of water degradation of emissivity for silver-plated copper samples with different room-temperature emissivities 1-19
1.35. Typical negative impulse voltage waveform 1-20
1.36. Typical negative impulse breakdown voltage waveform 1-20
1.37. Schematic diagram of experimental setup for accelerated aging tests 1-20
1.38. Phase-resolved PD pattern for a selected composite sample obtained for the 60-s data scan duration 1-21
1.39. Three-dimensional PD plot for a selected composite sample obtained for the 60-s data-scan duration 1-21
1.40. Copper-laminated YBCO tape resistivity increase during a 1.36-kA pulse (top) and voltage-current curve measured after the shot compared with the initial curve (bottom) 1-23
1.41. Resistivity change of the copper-plated BSCCO sample during a 450-A, 320-ms overcurrent pulse 1-24
1.42. Copper-laminated YBCO tape resistivity increase from a 200-ms pulse (top) and a 330-ms pulse (bottom) 1-24
1.43. The addition of a strip of copper raised the peak achievable current while it decreased the resistivity increase of the copper-laminated YBCO sample 1-25
1.44. Diagram of inductance measurement setup of HTS cables with respect to 76.2-mm copper pipe ground 1-26
1.45. Measured ac loss as a function of peak current ratio compared with equivalent ferromagnetic loss for the Ni-10%Cr-2%W substrate, the Norris elliptical model, and the thin strip model for (left) the 1-cm YBCO conductor and (right) the 4-mm YBCO conductor 1-27
1.46. Normalized ac losses for 1-cm and 4-mm YBCO on Ni-10%Cr-2%W substrates 1-28
1.47. PD inception for three types of Material 1 samples at room temperature and in liquid nitrogen 1-28

1.48. Schematic of Material 2 cylinder showing electrode geometry and puncture location 1-29
1.49. The decrease in puncture strength of Material 2 with cylinder thickness 1-30

2.1. Schematics of HTS superconducting architectures 2-2
2.2. Schematics of the IBAD process wire architectures 2-2
2.3. Schematic of the RABiTS™ process. 2-3
2.4. Electrical performance for world's second generation HTS wire 2-5
2.5. Thermal desorption spectra for a bare Ni/3at%W tape heated sequentially to 1000°C in 2×10^{-6} Torr of first hydrogen, then water, and finally oxygen 2-9
2.6. CO desorption spectra for a Ni/3at%W tape heated to 800°C for a range of oxygen partial pressures 2-10
2.7. CO desorption spectra for a bare Ni/3at%W tape heated in an oxygen partial pressure of 5×10^{-6} Torr for a range of temperature 2-10
2.8. Integrated area beneath CO desorption spectra in Fig. 2.6(a) 2-10
2.9. CO desorption spectra measured experimentally at 800°C compared with those obtained via a diffusion model 2-11
2.10. Carbon remaining in the substrate as a function of heat-treatment time at 800°C 2-12
2.11. Properties of a 240-cm length of bare Ni/3%W tape processed continuously at ~850°C in an oxygen partial pressure of 5×10^{-6} Torr 2-12
2.12. HTS tape for a Ni/3at%W substrate containing 52 at. ppm C showing severe film detachment 2-13
2.13. Schematic representation of a 1-D diffusion model that describes carbon removal from HTS coated conductor substrates 2-14
2.14. Composite cross-sectional image of a 6.4-μm-thick YBCO film deposited by PLD on Ni-W RABiTS2 material 2-16
2.15. Cross-sectional images of the interface area located between the seed layer and metal substrate 2-17
2.16. High-resolution EDS line scan taken in cross section across the interface between the Y_2O_3 seed layer and metal substrate, showing the presence of the $NiWO_4$ phase 2-18
2.17. Selected area electron diffraction patterns taken of the reaction layers within the Ni-W RABiTS2, revealing the (100)$NiWO_4$ // (001)Ni-W orientation relationship 2-18
2.18. High-resolution images of the RABiTS2 samples comparing the thickness of the $NiWO_4$ and NiO layers 2-19
2.19. Standard free energy change for the formation of select Ni and W oxides vs temperature 2-20
2.20. The ideal ABO_3 perovskite structure 2-23

2.21. Field dependence of the transport critical current density, *J*_c, for a 200-nm-thick PLD YBCO film on sputtered $SrRuO_3$/$LaNiO_3$ multilayers on biaxially textured Ni substrates 2-25

2.22. Temperature dependence of the net resistivity for YBCO/$SrRuO_3$/$LaNiO_3$/ Ni tape 2-25

2.23. Field dependence of the transport critical current density, J_c, for A 200 nm-thick PLD YBCO film on sputtered $La_{0.7}Sr_{0.3}MnO_3$/Ni multilayers on biaxially textured Cu substrates 2-25

2.24. Temperature dependence of the net resistivity for the YBCO/$La_{0.7}Sr_{0.3}MnO_3$/Ni/Cu tape 2-25

2.25. Field dependence of the transport critical current density, J_c, for a 200-nm-thick PLD YBCO film on sputtered $La_{0.7}Sr_{0.3}MnO_3$/Ir multi-layers on biaxially textured Ni-W substrates 2-26

2.26. Temperature-dependence of the net resistivity for two YBCO/$La_{0.7}Sr_{0.3}MnO_3$/Ir/Ni-W tapes 2-26

2.27. Cross-sectional TEM bright-field image of the 200-nm-thick YBCO film on $La_{0.7}Sr_{0.3}MnO_3$/Ir buffered Ni-W tape 2-27

2.28. XRD patterns after firing at 900^{o}C with different water vapor partial pressures 2-29

2.29. XRD patterns of products after firing at 1100°C with various water vapor partial pressures 2-29

2.30. XRD patterns of products after firing at various temperatures with 2 Torr H_2O 2-29

2.31. Secondary electron image of the surface of the film after firing at 1100°C with (a) 2 Torr H_2O and (b) 3 Torr H_2O 2-30

2.32. Backscattered electron image of the surface of the film after firing at 1100°C with (a) 2 Torr H_2O and (b) 3 Torr H_2O 2-30

2.33. (002) LMO pole figure showing cube-on-cube epitaxy of the LMO film 2-30

2.34. High-temperature XRD setup with linear detector (upper right) and sample-heating strip (lower right) 2-33

2.35. Typical θ–2θ scan obtained for a 20-nm-thick Eu_3NbO_7 buffered Ni–W substrate heat-treated at various temperatures in a high-temperature in situ XRD 2-33

2.36. Typical room-temperature θ-2θ scan obtained for a 20-nm-thick Eu_3NbO_7 buffered Ni-W substrate 2-34

2.37. Typical Eu_3NbO_7 (222) pole figure obtained for a 20-nm-thick film grown on the textured Ni-W substrate 2-34

2.38. Phi and omega scans obtained for a 20-nm-thick Eu_3NbO_7 film grown on the textured Ni-W substrate 2-34

2.39. SEM micrograph of the film surface deposited on Ni-W 2-35

2.40. A typical θ-2θ scan for a 40-nm-thick LZO film grown on biaxially textured Ni-W substrates by metal-organic deposition 2-36

2.41. AFM scan of the surface of an 80-nm-thick LZO film (two coats) grown on a biaxially textured Ni-W substrate 2-37

2.42. Superconducting properties of a 0.8-μm-thick MOD-YBCO film grown on CeO_2 (sputtered)/YSZ (sputtered)/MOD-LZO (80 nm) buffered Ni-W substrates 2-37

2.43. A typical θ-2θ scan for a 0.8-μm-thick MOD-YBCO film grown on MOD-CeO_2 (60 nm)/MOD-LZO (120 nm) buffered Ni-W substrates 2-37

2.44. Superconducting properties of a 0.8-μm-thick MOD-YBCO film grown on MOD-CeO_2 (60 nm)/MOD-LZO (120 nm) buffered Ni-W substrates 2-37

2.45. XRD patterns of multiple coats of LZO showing proportional increase in the (004) peak intensity with the number of coats with no detectable amount of the (222) peak 2-40

2.46. RHEED patterns of LZO multiple coats of LZO showing good surface crystallinity of the sol-gel derived films 2-40

2.47. A typical θ–2θ scan obtained for a 20-nm-thick LZO film on Ni-W substrates in a high-temperature in situ XRD showing nucleation of LZO during the heatup to the process temperature 2-41

2.48. High-resolution cross-section TEM of LZO film on Ni-W substrate 2-41

2.49. Comparison of critical current density-B performance of solution-deposited LZO as a seed layer and as a barrier layer with a traditional all-vacuum buffered Ni-W substrate using PLD-YBCO 2-42

2.50. Raman Cu(2) mode band with fitted curve and component bands of (a) Y-123/STO, (b) Eu-123/STO, and (c) Eu-123/Er-123/STO 2-46

2.51. Texture maps 2-47

2.52. (005) diffraction space maps 2-48

2.53. (006) diffraction space maps 2-48

2.54. (104)/(014) diffraction space maps 2-51

2.55. (200) diffraction space map of STO 2-54

2.56. FWHMs of the TiN (002) rocking curves vs corresponding FWHMs of the (002) substrate rocking curve for TiN films on differently textured substrates 2-58

2.57. EBKP maps showing grain boundaries larger than 3° of a TiN film on Cu (left), and the underlying Cu substrate (right) 2-58

2.58. Comparison of the J_c(H) curves for four samples having different out-of-plane texture but similar in-plane texture 2-59

2.59. A typical θ-2θ scan for a 30-nm-thick MgO film on textured Ni substrate 2-61

2.60. The ω and ϕ scans obtained for a 30-nm-thick e-beam MgO film grown on textured Ni substrate 2-61

2.61. Typical MgO (220) pole figure obtained on a 30-nm-thick e-beam MgO film grown on textured Ni substrate 2-62

2.62. SEM micrograph obtained on (a) crack-free 30- and (b) cracked 300-nm-thick MgO surface 2-62

2.63. AFM images obtained on both 60- and 300-nm-thick MgO surface 2-62

2.64. A typical θ-2θ scan for a 50-nm-thick MgO film on textured Ni-W substrate 2-63

2.65. Typical θ-2θ scan for a 60-nm-thick sputtered $LaMnO_3$ film on e-beam MgO-buffered Ni substrate 2-63

2.66. The ω and ϕ scans obtained for a sputtered 60-nm-thick $LaMnO_3$ film on e-beam MgO buffered Ni substrate 2-63

2.67. A typical θ-2θ scan for a 200 nm thick PLD-YBCO film on sputtered $LaMnO_3$-buffered MgO/Ni substrate 2-63

2.68. Field dependence critical current density for a 200-nm-thick PLD-YBCO film on sputtered $LaMnO_3$-buffered MgO/Ni substrate 2-63

2.69. Schematic temperature-time diagram of the “fast” conversion process (solid) and the “baseline” process (dashed) in the standard 1-atm furnace system 2-67

2.70. Time-dependent variations of the peak intensities of BaF_2 (111) (open symbols, left axis) and YBCO (002) (closed symbols, right axis) reflections during fast (samples A, B) and baseline (sample C) conversion processes 2-67

2.71. Variation of the critical current normalized to 1-cm width with layer thickness *d* of ex situ processed YBCO coatings on RABiTS™ templates 2-69

2.72. XRD results during a slow conversion of a 0.3-μm-thick PVD precursor 2-72

2.73. XRD results during a slow conversion of a 0.23-μm-thick MOD precursor 2-73

2.74. XRD results during a fast conversion of a 0.3-nm-thick PVD precursor 2-74

2.75. XRD results during a fast conversion of a 0.23-nm-thick MOD precursor 2-74

2.76. G_p vs $P(H_2O)$ for thin PVD and MOD precursors 2-74

2.77. Schematic diagram of the reduced-pressure conversion chamber 2-75

2.78. Critical-current field dependency of several high critical-current samples processed in a similar fashion 2-76

2.79. Temperature dependence of resistivity for samples JY12_1 and JY12_7 2-76

2.80. SEM micrographs of sample JY12_1 2-77

2.81. SEM micrographs of sample JY12_7 2-77

2.82 XRD θ-2θ scans and YBCO(113) pole figures for samples JY12_1 and JY12_7 2-77

2.83. Atomic-force microscope images of the MOD-TFA precursor (a) and the BaF_2 precursor (b) 2-79

2.84. A mixed *c*- & *a/b*-axis-oriented YBCO film produced from a MOD-TFA precursor annealed at 780ºC, $P(O_2)$ = 200 mTorr, and $P(H_2O)$ = 12 mTorr 2-80

2.85. Magnetic field dependence of critical current density at 77 K of YBCO films 2-80

2.86. XRD θ-2θ scan patterns of MOD-TFA and e-beam BaF_2 precursors at as-deposited and quenched states 2-80

2.87. XPS spectra for as-deposited and quenched precursors indicating the difference in chemical states of F, Cu, and Ba 2-81

2.88. XRD θ-2θ scans for TiN films deposited at a substrate temperature of 650ºC and at an rf sputtering power of 100 W in a N_2:Ar mixture gas (0, 7, 15, 50%, and only N_2 gas) 2-83

2.89. XRD (111) pole figure of TiN films deposited at substrate temperatures of (a) 550, (b) 600, (c) 700, and (d) 780ºC in a 15% N_2:Ar mixture gas and at an rf sputtering power of 100 W 2-83

2.90. XRD θ-2θ scans for the TiN films deposited substrate temperatures of 600, 650, and 700ºC in a 7% N_2:Ar gas mixture 2-84

2.91. XRD θ-2θ scans for the TiN films deposited at substrate temperatures of 650, 700, and 780ºC in a 50% N_2:Ar gas mixture and an rf sputtering power of 100 W 2-84

2.92 XRD θ-2θ scans for the TiN films deposited at a substrate temperature of 650ºC in a 15% N_2:Ar gas mixture and rf sputtering powers of 80, 100, 120, 150, and 200 W 2-85

2.93 Transition critical current density with different humidity-to-dry ratio values and with magnetic field for samples annealed at 740°C in 180-ppm oxygen pressure for 30 min wet and 30 min dry 2-87

2.94. Four-probe-method critical transition temperature for samples annealed at 740°C in 180-ppm oxygen pressure with different humidity-to-dry ratio values 2-88

2.95 The θ-2θ XRD patterns of films annealed at 740°C in 180-ppm oxygen pressure with different humid-to-dry ratio values 2-88

2.96. The X-ray θ-2θ scan pattern for a sample annealed at 740°C in 180-ppm oxygen pressure for 30 min wet and 30 min dry 2-88

2.97. The X-ray ω-scans of the YBCO (005) plane for samples annealed at 740°C in 180-ppm oxygen pressure with different humid-to-dry ratio values 2-89

2.98 The X-ray ϕ-scans of YBCO (113) plane for samples annealed at 740°C in 180-ppm oxygen pressure with different humid-to-dry ratio values 2-89

2.99 Pole figures of YBCO (113) plane for films annealed at 740°C in 180-ppm oxygen pressure with different humid-to-dry ratio values 2-89

2.100. RBS spectra of a thin film of YBCO on YSZ buffered with CeO_2 2-89

2.101. SEM micrograph of 200-nm-thick TMAP-derived films annealed at 740°C in 180-ppm oxygen pressure with different humid-to-dry ratio values 2-90

2.102. Diagram of the oxygen partial pressure vs temperature for $YBa_2Cu_3O_{7-x}$ material 2-91

2.103 Oxygen partial pressure vs temperature diagram showing liquid-phase boundaries, stability of YBCO, tetragonal-to-orthorhombic transition line, and lines of constant oxygen stoichiometry of $YBa_2Cu_3O_{7-x}$ 2-94

2.104. Schematic diagram of reel-to-reel continuous dip-coating unit 2-96

2.105. The typical microstructure of 20-nm-thick Gd_2O_3 seed layer on Ni-W substrate 2-96

2.106. AFM scan of the 20-nm-thick Gd_2O_3 seed layer on Ni-W substrate 2-97

2.107. The various architectures developed by using solution seed layers 2-97

2.108. The field dependence of critical current density for YBCO films grown on various seed layers 2-97

2.109. Critical-current-density data on the 0.8-m solution seed ORNL RABiTS™ 2-98

2.110. Temperature dependence of resistivity for YBCO film on STO (100) single-crystal substrates grown from iodide precursors 2-100

2.111. Scanning electron micrograph of YBCO film on STO (100) single-crystal substrates grown from iodide precursors 2-100

2112. Magnetic field dependence of the transport J_c of $YbBa_2Cu_3O_{7-y}$ film deposited by solution process (solid circle) compared with YBCO film deposited by ex situ BaF_2 process (open circle) on STO (100) single-crystal substrates 2-101

2.113. A typical θ-2θ scan for a 20-nm-thick RE_3NbO_7 (RE = Y, Gd, Eu) film grown on biaxially textured Ni-W substrates by MOD. RE_3NbO_7 film has a preferred *c*-axis orientation 2-107

2.114. The ω and ϕ scans for a 20-nm-thick Gd_3NbO_7 film grown on biaxially textured Ni-W substrates by MOD 2-107

2.115. The (111) pole figure for 20-nm-thick (a) Y_3NbO_7, (b) Eu_3NbO_7, and (c) Gd_3NbO_7 2-108

2.116. SEM micrograph for a 20-nm-thick (a) Y_3NbO_7, (b) Eu_3NbO_7, and (c) Gd_3NbO_7 film surface 2-108

2.117. A typical θ-2θ scan for a 200-nm-thick YBCO film grown on three coats of 60-nm-thick Gd_3NbO_7 buffered Ni-W substrates by PLD 2-108

2.118. Superconducting properties of a 200-nm-thick YBCO film grown on Gd_3NbO_7 buffered Ni-W substrates by PLD 2-108

2.119. Schematic representation of the pulsed electron deposition apparatus 2-109

2.120. Photograph of the PED reel-to-reel deposition system 2-110

2.121. Spatial variation of the deposited material, determined from profilometry and a fit to Gaussian profiles 2-110

2.122. Composition (determined by ICP-MS) for films deposited at various background pressures and using a target of composition $(YF_3)(BaF_2)_2(CuO)_3$ 2-111

2.123. Composition of the deposited material as a function of process time 2-111

2.124. The typical trace (voltage as function of time, with the PED trigger signal defining the zero of time) can be fitted well with an exponentially modified Gaussian 2-112

2.125. Integrated area of ion probe traces (from least-square fits to a exponentially modified Gaussian curve) as a function of chamber pressure 2-112

2.126. Correlation between deposition rate and ion probe peak signal for two types of targets 2-112

2.127. Various target mounting approaches used for the study of growth rate deterioration 2-113

2.128. Growth rate as function of process time for the various target-mounting approaches 2-113

2.129. Ion probe peak voltage as function of process time for the various target mounting approaches 2-113

2.130. X-ray diffraction θ-2θ pattern of a 1-µm YBCO film on conductive LSMO(40 nm)/Ir(400 nm) buffered, biaxially textured Ni-W substrate.............................. 2-115

2.131. Cross-section TEM bright-field image of the 0.2-µm-thick YBCO/LSMO/Ir/Ni(W) composite structure showing well-defined interfaces between the layers.. 2-115

2.132. Temperature-dependent net resistivity measurements for 0.2 and 0.7-µm thick YBCO samples grown on conductive LSMO/Ir/Ni-W substrates 2-115

2.133. The *I-V* curves obtained from the 0.2-µm-thick YBCO on conductive LSMO/Ir/Ni-W in a field of 1 Tesla and for the bare Ni-W substrate 2-116

2.134. RHEED patterns of an epitaxial TiN film on (001) Cu (left) as deposited in a vacuum background and when exposed to an oxygen partial pressure of 8×10^{-6} Torr at a temperature of 600° (right).. 2-118

2.135. Critical current density vs applied magnetic field for a YBCO film deposited on MO/MgO/TiN/Cu/MgO(crystal) (black line and dots), and a typical YBCO films deposited on single crystal STO (gray line).. 2-118

2.136. STEM image of a YBCO/LMO/MgO/TiN/Cu multilayer structure on MgO single crystal acquired with high-angle annular dark field detector.. 2-119

2.137. High-resolution STEM micrograph of the LMO/MgO interface.. 2-119

2.138. θ–2θ XRD scan of a YBCO/LMO/MgO/TIN/CuNiAl sample 2-120

2.139. Magnetic field dependence of critical-current-density curves measured at 65 and 77 K, for a YBCO film on the conducting buffer structure of LSMO/Ni/Cu 2-121

2.140. Ideal current vs electric field characteristics for a model conductor architecture................ 2-122

2.141. The *I-V* curves obtained from the actual sample in a field of 1 Tesla................................. 2-122

2.142. Ferromagnetic hysteretic loss, *W*, due to the Ni layer in YBCO/LSMO/Ni/Cu 2-123

2.143. Magnetic hysteresis loops at 50 K 2-124

2.144. Numerically calculated dimensionless factors *g* and *x* as a function of *a*/*L*......................... 2-125

2.145. Temperature dependence of J_c^{GB} (closed symbols) and J_c^{G} (open symbols) for IBAD-a (♦), RABiTS™-a (★), and RABiTS™-b (●)... 2-126

2.146. Magnetization *M* vs applied magnetic field *H* for all samples studied 2-128

2.147. Variation of saturation magnetization of $Ni_{1-x}W_x$ alloys with W-content *x*......................... 2-129

2.148. A plot of M^3 vs temperature *T* for Ni-5at.%W and Ni-6at.%W.. 2-129

2.149. Dependence of Curie temperature of $Ni_{1-x}W_x$ alloys on W-content *x*, with present results and those of Marian 2-129

2.150. The magnetization *M* vs *H* for lossy, electroplated Ni at a temperature of 120 K............... 2-130

2.151. Hysteretic loss per cycle *W* as a function of field excursion H_{max}, for undeformed Ni, Ni-6at.%W and Ni-5at.%W samples (prepared by vacuum casting (AMSC, ORNL, and Oxford) or powder metallurgy methods (ORNL).............................. 2-130

2.152. Histogram showing maximum hysteretic loss *W* of samples studied 2-130

2.153 Hysteretic loss per cycle for Ni-3at.%W and Ni-5at.%W as a function of number of half-cycles of deformation 2-131

2.154. Hysteretic loss for undeformed Ni-5at.%W vs dc bias field at temperature of 77 K and a fixed ac field of 5 Oe 2-132

2.155. Ferromagnetic loss as a function of applied ac frequency for two different fixed values of ac field 2-132

2.156. Critical current density of two films with 211 nanoparticles (filled symbols) compared to PLD film without (open symbols), in applied field $H \parallel c$ at the temperatures shown 2-134

2.157. Log-log plot of two films with 211 nanoparticles compared to PLD film without in applied field $H \parallel c$ at the temperatures shown, indicating the estimates of α (dotted lines) for the power-law regime between 0.1 and 1 T where $J_c \sim H^{-\alpha}$ 2-135

2.158. Critical current density vs angle between the applied magnetic field and *c* direction, at 1 T for 77 K, at 1 T and 2 T for 65 K, and at 2 T for 40 K 2-135

2.159. Attempt to fit mass-anisotropy curve to data at 65 K, 1 T, using $J_c[H\varepsilon(\theta)] = J_c[1\text{ T}*\varepsilon(\theta)]^{-0.5}$ 2-136

2.160. Different ways in which a 4×4 array of hexagonal grains can be arranged 2-138

2.161. Schematic showing the relationship between critical current and boundary angle, with plateaus at (a) 4° and (b) 1.8° due to granular dissipation 2-140

2.162. Illustration of the algorithm for finding the minimum current sum across the tape width 2-140

2.163. The center pixel has an energy of (a) 5, (b) 4, or (c) 7, depending on which grain it is in 2-142

2.164 Grain structures generated by the model on a 300 × 300 pixel grid with MCS numbers of (a) 10, (b) 100, and (c) 1000 2-142

2.165. Definition of the total number of pixels (P), the average number of pixels per grain (p), and the number of grains in the width (N_w) and length (N_l) directions 2-142

2.166. Indexing of cells, edges and vertices in the square pixel model for a conductor C columns long and R rows wide 2-143

2.167. Plot showing grain growth rate in the Anderson model 2-144

2.168. (a) Histogram showing the distribution of absolute grain sizes for MCS = 3 ($p = 1.9$) and MCS = 30 ($p = 4.7$) and (b) the normalized distribution which for high values of p lie on a single curve 2-145

2.169. Modeled samples for which $N_l = 25$ and $N_w = 10$ 2-145

2.170. (a) The dependence of the calculated sample critical current density on the value of p ($N_l = 200$, $N_w = 20$) and (b) comparison of p=1 and p=5 for various conductor lengths ($N_w = 40$) 2-146

2.171. Dependence of calculated critical current density on grain size for two different conductor shapes, a 10 × 10 mm square and a 3 × 30 mm rectangle ($p = 5$) 2-146

2.172. Log-log plots of critical current density vs length for various conductor widths for a FWHM of 10° with (a) $p = 1$ and (b) $p = 5$ 2-147

2.173. Plots demonstrating the relationship between critical current density and sample width and length for a FWHM of 10° with (a) $p = 1$ and $p = 5$ 2-147

2.174. Graph showing how the critical current is reduced as the FWHM increases, and how it depends on the current carried by the grains 2-148

2.175. The effect of the FWHM and the intra-granular critical current density (represented by ε, the equivalent angle) on critical current density as predicted by the model 2-149

2.176. Graph showing regimes of dominance of grain boundary dissipation (GB), intragranular dissipation (IG) and the combination of the two (mixed)............................... 2-149

4.1. Attendees at the Superconductivity Day on the Hill, sponsored by the Coalition for the Commercial Application of Superconductors, February 26, 2004....................................... 4-1

4.2. *MRS Bulletin* special issue, August 2004.. 4-3

4.3. Parans Paranthaman with students at the 2003 ORNL Day of Science 4-3

4.4. Summer interns from North Carolina A&T University with mentors 4-4

4.5. Interns Jennifer Williams, a teacher from Carter High School in Knoxville, and Nicolas Cunningham, from Middle Tennessee State University, with ORNL mentor Patrick Martin 4-4

4.6. Interns Erin Stuart, from Indiana University of Pennsylvania, and Nicolas Cunningham, from Middle Tennessee State University, with ORNL mentor, Patrick Martin 4-5

4.7. Alex Thorn (left), intern from Princeton University. Kartik Venkataraman, visiting researcher from the University of Wisconsin... 4-5

List of Tables

Table *Page*

1.1. Fault currents applied 1-2

1.2. Results of fault simulations 1-7

1.3. Samples tested for overcurrent limitations 1-23

1.4. Radial dimensions and winding directions for cables A and B 1-26

1.5 Measured room-temperature (295 K) inductances of cables A and B compared with numerical and analytical values 1-26

1.6. Impulse breakdown of the Material 2 cylindrical tube 1-29

2.1. Considerations involved in developing the second generation of HTS wires by 2010 2-6

2.2. Measured electrical and texture properties of thick YBCO films on the RABiTS1 material (YBCO/CeO_2/YSZ/CeO_2/Ni substrate) 2-15

2.3. Measured electrical and texture properties of thick YBCO films on the RABiTS2 material (YBCO/CeO_2/YSZ/Y_2O_3/Ni-W substrate) 2-15

2.4. Texture data on various seed layers 2-37

2.5. Literature values for lattice parameters of tetragonal and orthorhombic M-123 materials 2-44

2.6. Band-fitting results for Raman spectra of M-123/STO specimens. 2-47

2.7. Buffer layer architecture and FWHM for ω and ϕ scans for YBCO samples 1, 2, 3, and 4 2-59

2.8. Processing parameters and electrical properties of YBCO films derived from TMAP approach 2-88

2.9 Summary of the growth of YBCO films 2-99

2.10. Magnetic properties of Ni-W alloys 2-129

2.11. A summary of the values of α for measurements on [001] tilt boundaries in thin film YBCO in self-field at 77 K 2-139

2.12. Values of α and β used in percolation models 2-140

3.1. Superconductivity Program summary of cooperative agreements as of September 30, 3004 3-3

3.2. Invention disclosures during FY 2004 3-4

3.3. Patents issued in FY 2004 3-4

3.4. Cumulative listing of patents 3-5

4.1 2004 Summer Intern Program Information 4-4

Abbreviated Terms

NOMENCLATURE

$\Delta\phi$	in-plane texture
$\Delta\omega$	out-of-plane texture
ρ	normal-state resistivity
σ	standard deviation
B_{irr}	irreversibility field
$c\ (2 \times 2)$	centered (2×2) superstructure
G_{P}	precursor growth rate
H	magnetic field
H_{max}	maximum magnetic field
I_{c}	critical current
I_{p}	peak current
I_{mp}	propagation current
I_{rms}	root mean square cable current
J_{c}	critical current density
$J_{\mathrm{c}}^{\mathrm{GB}}$	intergrain critical current density
$J_{\mathrm{c}}^{\mathrm{G}}$	intragrain critical current density
J_{E}	engineering critical current density
K_{c}	critical current per unit width of conductor
langmuir	10^{-6} Torr/s
ML	surface adsorbate atoms per surface substrate atoms
M_{sat}	saturation magnetization
Pa.s	pascal.second
P_{base}	base pressure
P(CO_2)	CO_2 partial pressure
P(CO)	CO partial pressure
P(H_2O)	water vapor partial pressure
P(O_2)	oxygen partial pressure
T	tesla
T_{c}	critical temperature/transition temperature
t	thickness

ACRONYMS AND INITIALISMS

ac	alternating current
acac	acetylacetonate
AEP	American Electric Power
AFM	atomic force microscopy
AMSC	American Superconductor Corporation
ANL	Argonne National Laboratory
APS	Advanced Photon source
ASTM	American Society for Testing and Materials
BIL	basic impulse level
BSCCO	Bi-Sr-Ca-Cu-O

CCAS	Coalition for the Commercial Application of Superconductors
CCVD	combustion chemical vapor deposition
CEIDP	Conference on Electrical Insulation and Dielectric Phenomena
CRADA	cooperative research and development agreement
CSD	chemical solution deposition
CTFE	chlorotrifluoroethylene
dc	direct current
DMF	dimethyl formamide
DOE	U.S. Department of Energy
DOE-HQ	DOE Headquarters
DSM	diffraction space mapping
e-beam	electron beam
EBKP	electon backscattering Kikuchi pattern
EBSD	electron backscatter diffraction
EDS	energy-dispersive spectroscopy
EDX	energy-dispersive X-ray diffraction
fcc	face-centered cubic lattice
FM	ferromagnetism
FWHM	full width at half maximum
GBMD	grain-boundary misorientation distribution
GE	General Electric
GM	Gifford-McMahon
GZO	gadolinium zirconium oxide
HR-PLD	high-rate pulsed-laser deposition
HTS	high-temperature superconductivity/superconductor/superconducting
IBAD	ion-beam-assisted deposition
ICP-MS	inductively coupled plasma mass spectroscopy
IEEE	Institute of Electrical and Electronics Engineers, Inc.
ISD	inclined substrate deposition
ISTEC	International Superconductivity Technology Center
LANL	Los Alamos National Laboratory
LMO	$LaMnO_3$
LNO	$LaNiO_3$
LPE	liquid-phase epitaxy
LSMO	$La_{0.7}Sr_{0.3}MnO_3$
LZO	lanthanum zirconium oxide ($La_2Zr_2O_7$)
MFCL	matrix fault current limiter
MgO	magnesium oxide
MLI	multiple-layer insulation
MOCVD	metal-organic chemical vapor deposition
MOD	metal organic decomposition
MRCAT	Materials Research Collaborative Access Team
MRS	Materials Research Society
ORNL	Oak Ridge National Laboratory
PD	partial discharge
PDIV	partial discharge inception voltage
PED	pulsed-electron deposition
PLD	pulsed-laser deposition

PSD	position-sensitive detector
PTFE	polytetrafluoroethylene
PVC	polyvinyl chloride
PVD	physical vapor deposition
R&D	research and development
RABiTS™	Rolling-Assisted Biaxially Textured Substrate
RBS	Rutherford backscattering spectroscopy/spectrum
rf	radio frequency
RHEED	reflection high-energy electron diffraction
rms	root mean square
SAD	select area diffraction
SCE	standard calomel electrode
SD	standard deviation
SEM	scanning electron microscopy
SIMS	secondary ion mass spectrometer
SPI	Superconductivity Partnership with Industry
SQUID	superconductivity quantum interference device
SRO	$SrRuO_3$
STEM	scanning transmission electron micoscope
STO	$SrTiO_3$
TBAP	tetrabutylammonium perchlorate
TEM	transmission electron microscopy
TFA	trifluoroacetate
TMAP	trimethyl acetate salts and proponic acid
WES	Waukesha Electric Systems
XPS	X-ray photoelectron spectroscopy
XRD	X-ray diffraction
YBCO	yttrium barium copper oxide ($YBa_2Cu_3O_{7-d}$)
YNO	Y_3NbO_7
YSZ	yttria-stabilized zirconia
Z-STEM	Z-contrast scanning transmission electron microscopy

Executive Summary

This report presents the results of projects conducted by Oak Ridge National Laboratory (ORNL) and its industry and university partners working in the U.S. Department of Energy's (DOE's) Superconducting Technology Research Program for Electric Systems. Funded primarily by DOE's Office of Electricity Delivery and Energy Reliability, ORNL projects include research and development toward second-generation high-temperature superconducting (HTS) wires, the Superconductivity Partnerships with Industry, and strategic research in materials and process development. Many of the articles in this report are adapted from papers submitted for open-literature publication; presentations at the annual DOE Peer Review in July 2004; and presentations given at the Applied Superconductivity Conference, Materials Research Society meetings, and other conferences and workshops held during FY 2004.

Among the Superconductivity Partnerships projects included in this report is the HTS cable project with long-time partner Southwire Company. Progress is reported toward development of a triaxial cable and terminations. For this, all three phases of the cable are concentric with one another, and the outer shield layer can be made of nonsuperconducting metal such as copper. This cable has the potential to revolutionize the development of distribution-voltage cables, as it uses half the superconducting wire of competing technologies and is the most compact cable technology in development. A new project with SuperPower involving extensive development and testing of high-voltage bushings and other materials for the Matrix Fault Current Limiter project is also described.

Progress is also reported in second-generation wire development in more than two dozen articles. Short samples of 2G wires based on the rolling-assisted, biaxially textured substrate (RABiTS™) exceeded 400 amperes per centimeter width in FY 2004. There were dramatic increases in conversion rate of precursors deposited ex situ on RABiTS™. Along with these results came an increased understanding of the role of carbon impurities in substrate and buffer layer performance, the first all-solution buffered substrate with a critical current in excess of 100 amperes per centimeter width, and development of improved understanding and new models of current flow in superconducting materials on textured templates.

1. Technical Progress in Applications Development

1.1. Ultera/ORNL HTS Cable Superconductivity Partnership with Industry (SPI)

J. A. Demko, R. C. Duckworth, A. R. Ellis, P. W. Fisher, M. J. Gouge, D. R. James, J. W. Lue, I. Sauers, and M. Young

1.1.1 Testing of a 1.5-m, Single-Phase Cable Made with Copper-Laminated HTS Tapes

1.1.1.1 Cable Description

Two layers of Bi-Sr-Ca-Cu-O (BSCCO) high-temperature superconducting (HTS) tape with 50-µm-thick copper laminations made by American Superconductor Corp. were wound into a 1.5-m nominal length cable. Cryoflex^{TM} dielectric was wound over the HTS layers to simulate the build of a triaxial HTS cable. The sample was instrumented with three thermometers at the center of the cable at different radial positions in the Cryoflex^{TM} layers. A heater was wound just outside the HTS tapes to provide for calibrating measurements of ac loss by the calorimetric method. Voltage taps were spaced 1.37 m apart on the HTS conductor. The former was filled with Araldite epoxy to prevent cooling by liquid nitrogen on the inside of the cable. The cable dc critical current at the 1-µV/cm criterion was measured in a liquid nitrogen bath to be 4750 A.

1.1.1.2 AC Losses

The ac losses were measured electrically by using a lock-in amplifier and a calibrated Rogowski coil. The Rogowski coil has an amplifier on the output signal that introduces a phase error in the measured current. A calibration of the phase error was made by using a coil that is purely inductive. The measured phase error was in agreement with the manufacturer's specifications for the device. The ac losses were also measured calorimetrically by comparing the temperature rise from the application of an ac current with the temperature rise measured by using the calibration dc heater. All of these results, along with the ac losses calculated with the monoblock model, are shown in Fig. 1.1. The monoblock model provides an upper bound to the ac losses and is about twice the value of the electrical measurements. The calorimetric measurements are somewhat higher than the electrical measurements but are less than the monoblock model calculations.

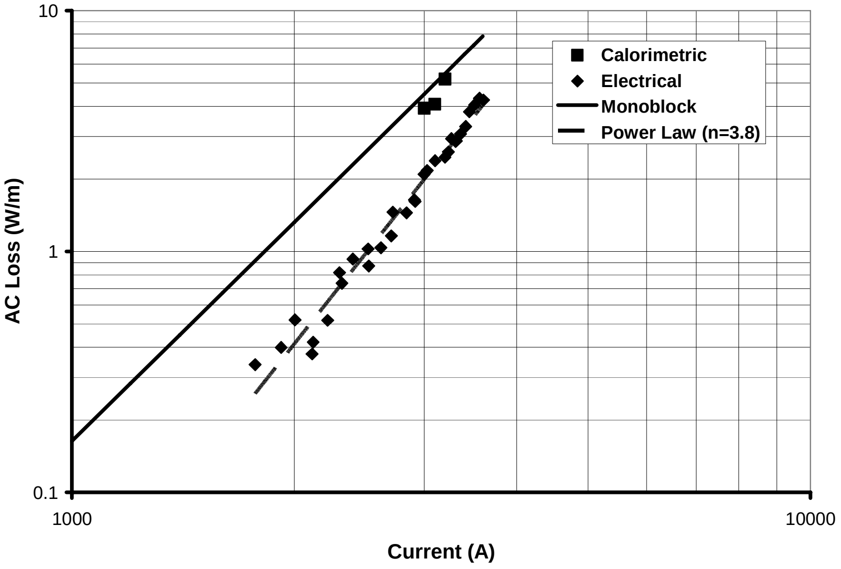

Fig. 1.1. Electric and calorimetric measurements of ac losses compared with losses calculated by using the monoblock model.

1.1.1.3 DC Overcurrents

The copper-laminated HTS cable was subjected to dc overcurrents to simulate faults that would be experienced in a utility setting. The series of dc overcurrent pulses ranged from 6 kA to 10 kA for the durations shown in Table 1.1. The energy input into the cable was calculated by numerically integrating the product of the measured current, I, and measured voltage, V, over the duration of the pulse, t, and dividing by the length, L, according to Eq. (1).

$$E = \frac{1}{L}\int_{\tau=0}^{\tau=t} VId\tau \tag{1}$$

Figure 1.2 shows a 7-kA pulse. At that current, the voltage drops over the pulse, indicating a possible redistribution of current within the HTS cable. Figure 1.3 shows a 10-kA fault with a drop to 1 kA after the fault. The voltage across the cable continuously rises during the fault, an indication of heating of the conductor. At the end of the fault, the cable voltage drops to a small value when 1 kA is applied, indicating that the cable has not heated up enough to significantly degrade the performance as a superconductor.

The dc voltage-current characteristics were measured before the fault current testing and after the application of some of the faults. The VI curves before and after the completion of the fault current testing are shown in Fig. 1.4. The measurements are the same, indicating no degradation of the conductor due to the application of these faults. This demonstrates that this conductor is suitable for this level of fault condition.

Table 1.1. Fault currents applied

Current (A)	Duration (s)	Energy (J/m)
6,000	1.1333	7.8
6,400	0.9	19.4
7,000	0.9	52.8
8,000	0.8	221.5
9,000	0.7	360.0
10,000	0.6	647.3

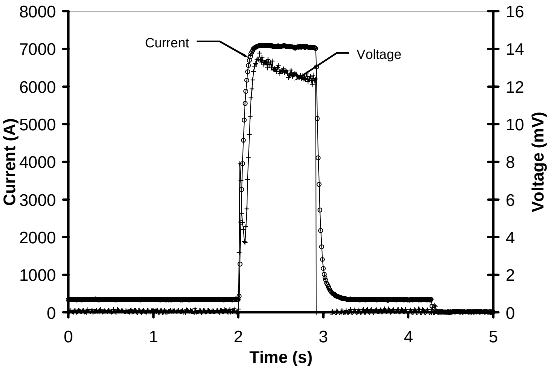

Fig. 1.2. A 7-kA overcurrent pulse voltage response of the HTS cable.

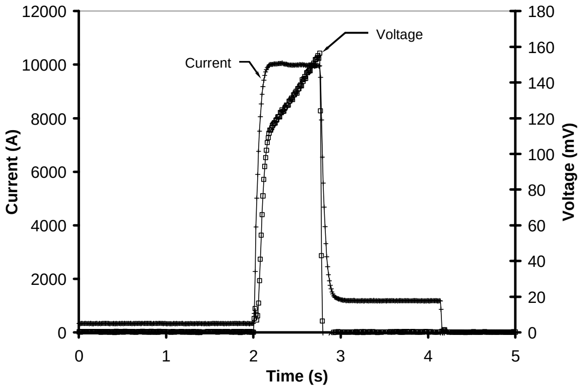

Fig. 1.3. A 10-kA overcurrent pulse voltage response of the HTS cable.

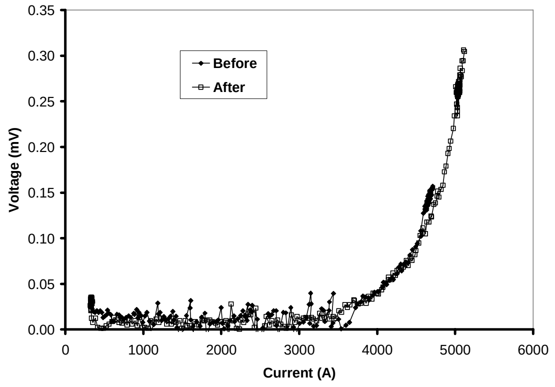

Fig. 1.4. Comparison of the voltage-current characteristics before and after the overcurrent tests for the HTS cable.

1.1.1.4 Flux Flow Analysis

When the HTS tape is operated at currents above the critical current, the voltage drop along the superconductor becomes high enough that current is shared by the matrix and the conductive lamination. This can be represented by three parallel resistances as shown in Fig. 1.5, which is analyzed by the flux flow method [1].

The normal metal resistance data for this tape was measured as a function of temperature, *T,* and includes the silver alloy matrix and the lamination materials. It is expressed in units of ohms per meter and calculated by a linear fit of the data [Eq. (2)]:

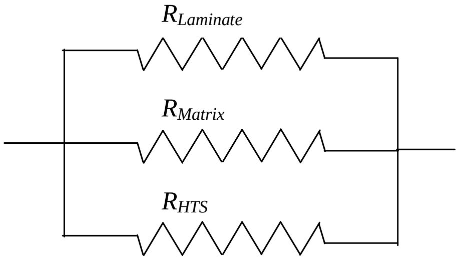

Fig. 1.5. Parallel resistance approach to the flux flow model.

$$\frac{R}{L} = 1.11\times10^{-3}\,\mathrm{T} - 3.10\times10^{-2}\,. \tag{2}$$

Two approximations were assumed in the implementation of the flux flow calculations. First, the critical current (I_c) was assumed to vary linearly with temperature and is zero at 104 K. Second, it was assumed that the *n* value is constant. The HTS material follows the power law relation given by Eq. (3). The values needed for this characterization are obtained from the measured dc V-I characteristics. The constant *C* is determined from the 1 μV/cm criterion for critical current.

$$V = C\left(\frac{I_{HTS}}{I_c}\right)^n \tag{3}$$

Figure 1.6 shows the nonlinear voltage dependence of the cable with temperature for different operating currents above the critical current. The measured voltages across the cable from the application of overcurrent pulses are indicated in Fig. 1.6 by the open symbols. From these voltages, the temperature of the cable during a pulse is seen to fall between 82 K and 84 K. These temperatures could not be confirmed with measurements because the thermometers response times are too slow. Even so, the estimated temperatures indicate that the HTS tapes heated about 2 K for the 10-kA overcurrent pulse. Figure 1.7 shows the calculated fraction of the current carried by the superconductor as a function of temperature for the range of overcurrents applied.

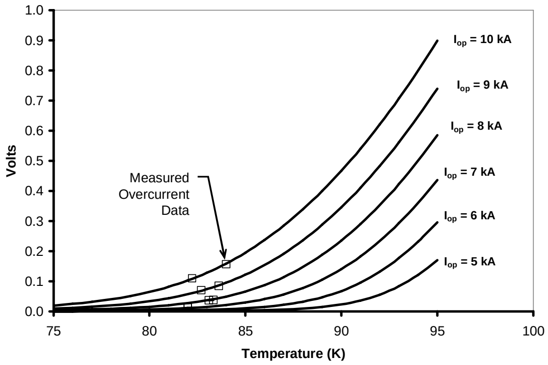

Fig. 1.6. Voltages for the cable calculated by using the flux flow model.

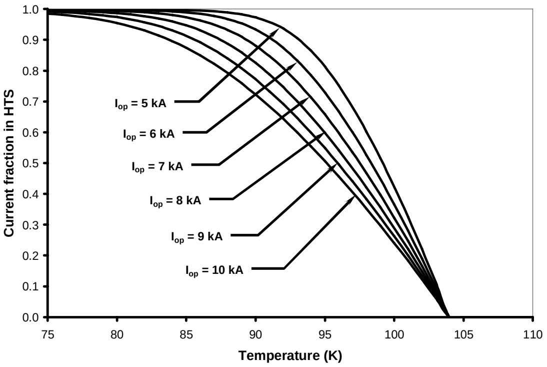

Fig. 1.7. Calculated fraction of current in the superconductor based on the flux flow model.

1.1.1.5 Fault Current Thermal Analysis

The overcurrents were simulated using a composite tape specific heat shown in Fig. 1.8. The adiabatic temperature rise based on these specific heats for the energy input into the cable is less than 3.7 K. The calculated response for the 10-kA pulse at different times is shown in Fig. 1.9. The calculated temperature increase of 1.8 K is consistent with the observed fact that the cable remained superconducting after the overcurrent application.

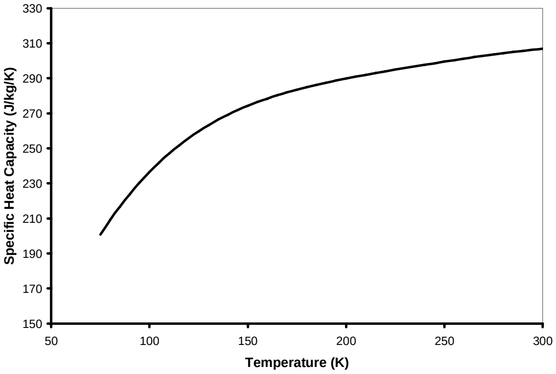

Fig. 1.8. Estimated laminated HTS tape heat capacity.

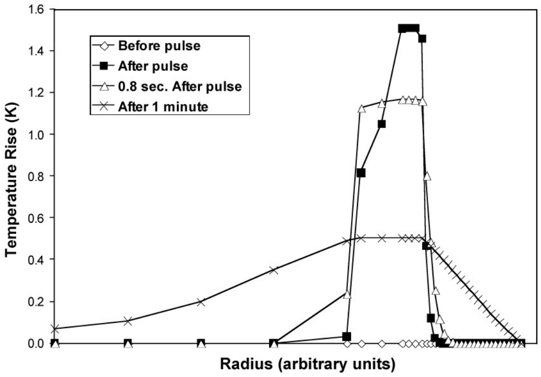

Fig. 1.9. Simulated thermal response of the cable for the 10-kA pulse.

1.1.1.6 Performance of a Damaged Cable

A few tapes were purposely cut to simulate minor damage to a HTS cable and to measure the degradation of the cable performance. The damage resulted in a decrease of the critical current to 4360 A. Figure 1.10 shows the measured temperature rise at 3000 A_{rms} before and after damage of the cable. Even though the critical current is degraded, the cable reaches a stable operating temperature but at a higher value with the damage. The ac loss at 3000 A_{rms} is 4.8 W/m in the damaged condition. The current was switched off at 400 min.

1.1.2 Tests of 3-m Triaxial Cable at NKT

A 3-m-long, triaxial cable was designed, fabricated, and tested to quantify ac losses at phase currents up to 3.4 kA. The HTS BSSCO conductor was stabilized with normal conductors to accommodate fault currents in a utility application. The 3-m cable was cooled down to liquid nitrogen temperatures, and the total ac loss was measured at 3-kA phase current (at 60 Hz) to be much lower, about 5 W/m at an average cable temperature of 77 K and a pressure of 3 bar. To verify the order of magnitude of the three-phase measurements, supplemental measurements were made on the three single phases. In Fig. 1.11, the single-phase ac losses (measured with both an electric and thermal technique) are shown along with the total three-phase loss (measured with a thermal technique) normalized to a per-phase loss basis. As noted in earlier triaxial cable experiments, the accumulated single-phase losses are larger than the corresponding three-phase loss. The nature of the ac losses were investigated in similar experiments conducted at a lower temperature (72.5 K) and a lower frequency (40 Hz). Both experiments indicate that the nature of the observed ac loss is indeed hysteretic.

In separate experiments, stability was demonstrated by operation for 2.5 h at the design current of 3 kA rms and at a temperature of 80 K. A second operation point was verified by stable conditions for 3 h at 3.4 kA rms current and a temperature of 76 to 77 K.

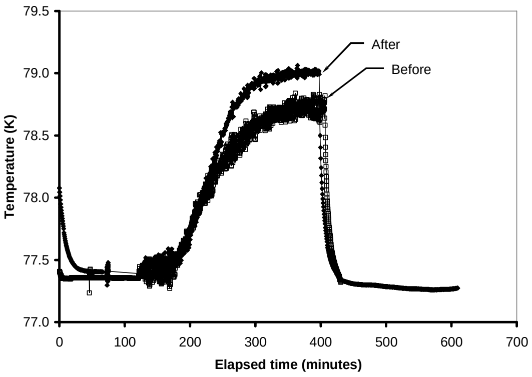

Fig. 1.10. Comparison of the measured temperature response at 3 kA_{rms} for the damaged and undamaged cable.

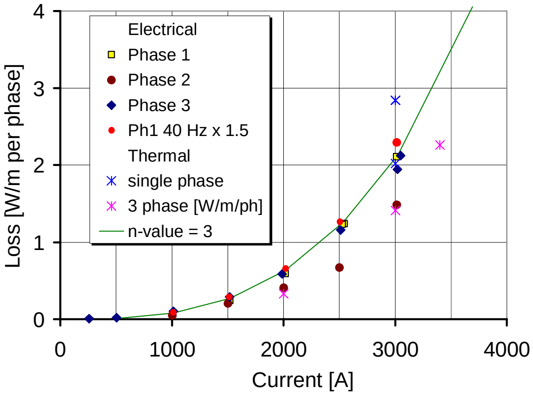

Fig. 1.11. AC losses normalized to a per-phase basis for the 3-m cable.

1.1.3 Triaxial Cable Termination R&D

Testing of filled (for enhanced thermal conductivity) and unfilled epoxy composite materials continued in a small-scale flat electrode configuration, medium-scale "baton" samples, and full-scale "barbell" sized samples. The latter two have a cylindrical electrode geometry. Improvements in curing have led to good, void-free samples in the flat and baton geometries but not in the larger barbells. Sufficient data have now been accumulated to assess the volume effect, which leads to a reduction in partial discharge (PD) inception voltage with increased stressed volume, as shown in Fig. 1.12. For comparison, Fig. 1.13 shows a similar plot of PD inception voltage for a reference epoxy (Stycast 2850 KT). The Stycast KT does not meet the design dielectric requirement at large volumes. The epoxy composite in Fig. 1.12 barely meets the design requirements if it is completely free of voids. Because of the marginal performance in attaining an absence of defects and the difficulty in ensuring that the full-scale application could be made

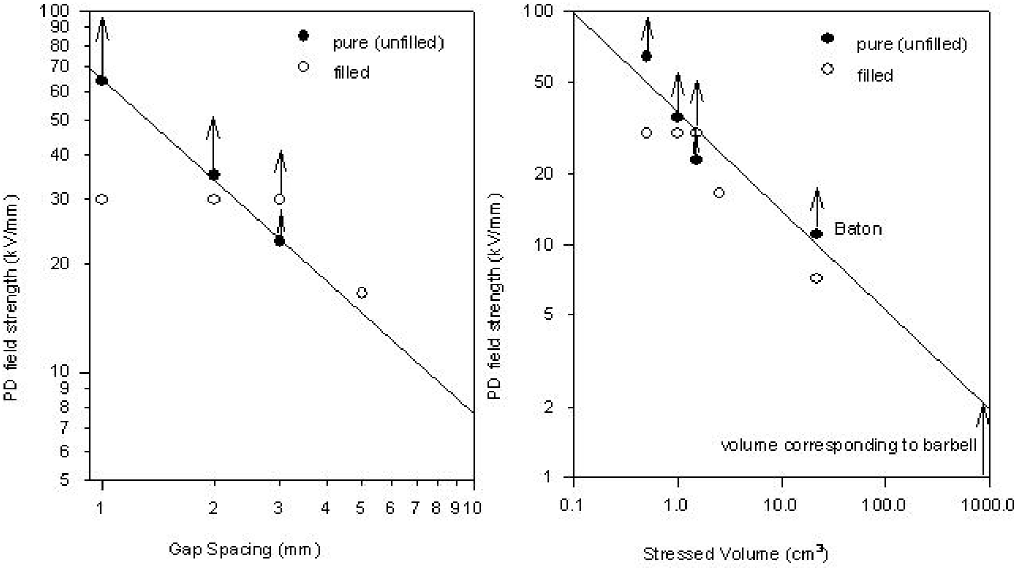

Fig. 1.12. Partial discharge inception strength as a function of electrode gap and stressed volume.

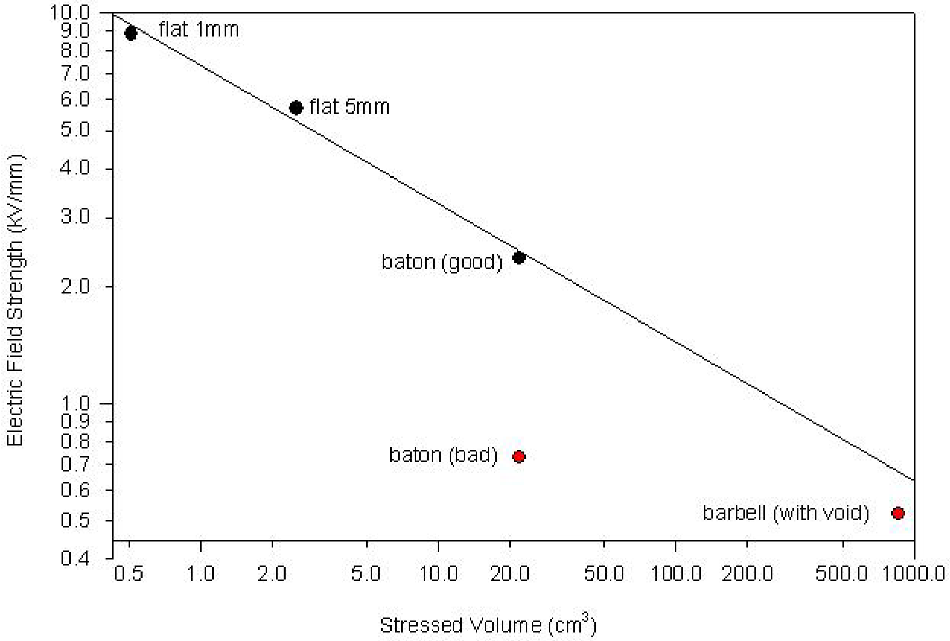

Fig. 1.13. Partial discharge inception strength as a function of stressed volume for Stycast 2850 KT.

free of defects (voids), use of the material in a cable termination is problematic. It could be acceptable in applications with smaller stressed volumes.

To be successful the concentric triaxial cable termination requires a high-thermal-conductivity dielectric material for insulation between phases. Tests on the candidate dielectric base and filler materials showed that their properties were not going to scale to the size necessary for the full-scale 3000-A_{rms} termination. Thus work related to their development was terminated. A design study based on utilizing the concentric design with available dielectrics with lower thermal conductivity showed that they would only work with addition of internal cooling to the termination.

Space and surface-area limitations inside the internal phase in the termination made this additional cooling requirement unachievable. Therefore, alternate termination designs have been explored with the objective of developing a design that utilizes available dielectrics within their normal stress limits. To this end, designs were evaluated that separated the triaxial phases while cold, thus eliminating the need for high-thermal-conductivity dielectric materials. A termination design has been developed and modeled that meets the 3,000-A, 110-kV basic impulse level (BIL), and fault overcurrent requirements of the AEP Bixby project (see Fig. 1.14). Materials and shop orders were placed to fabricate a full-scale test dielectric system with liquid nitrogen cooling at atmospheric pressure. In parallel with this, a half-scale model of the dielectric

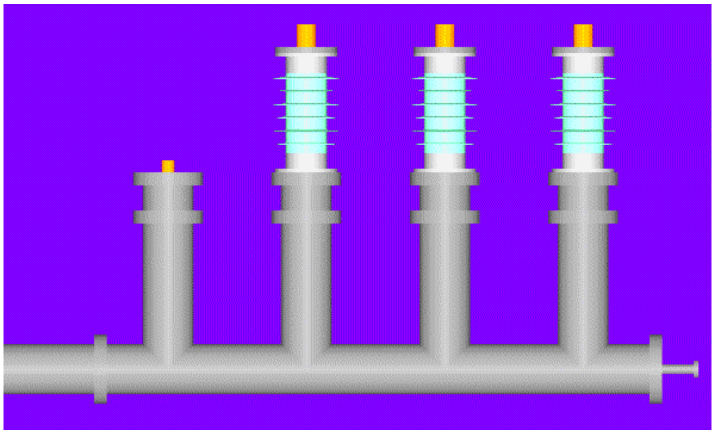

Fig. 1.14. Triaxial cable three-phase termination.

system has been fabricated. Testing with pressurized (up to 6-bar) liquid nitrogen cooling in an existing cryogenic pressure vessel was initiated at the end of the reporting period.

1.1.4 An Investigation of the Current Distribution in the Triaxial Cable and its Operational Impacts on a Power System

An investigation of the current distribution in a three-phase triaxial superconducting cable is under way to study phase imbalances under steady-state operation and to assist in the construction of a transient model to study operational impacts of the cable in a power grid. The triaxial cable consists of three superconducting concentric phases inside a copper shield. Each phase is composed of multiple layers of BSCCO tape wound helically in opposite directions. Current distribution within the cable is determined by using an electric circuit model containing the self and mutual inductances resulting from both axial and tangential fields. An ac loss term is also included in the model. Building on the electric circuit model, a lumped cable model is used to investigate the effects of the triaxial cable on a power grid when faults are applied to the system. Cable lengths practical for future applications (~10 km) are considered.

Fault currents were observed through simulation of an electric circuit model for a 16-km-long triaxial cable. The dynamic resistance of each phase was modeled by nonlinear resistance elements in the Alternative Transients Program to account for normal-state cable operation. An equivalent source impedance was included that represented the short-circuit impedance of the generator and the short-circuit capacity of the transformer. The prefault operating condition of the cable was obtained in the same manner as the steady-state operation, by using a purely resistive load. After one 60-Hz cycle, a single line-to-ground fault was applied to phase C at the load end so that the calculated fault current and induced shield current could be observed (see Fig. 1.15). Other fault types were conducted, including a double line-to-ground fault between phases A and C and a three-phase fault. Peak phase and shield currents for each case are presented in Table 1.2. Results from Table 1.2 show that currents are induced in the shield and unperturbed phases when a fault occurs, although the induced phase currents are small compared with that of the shield. Of the three fault types considered in this study, the three-phase fault resulted in the lowest shield current.

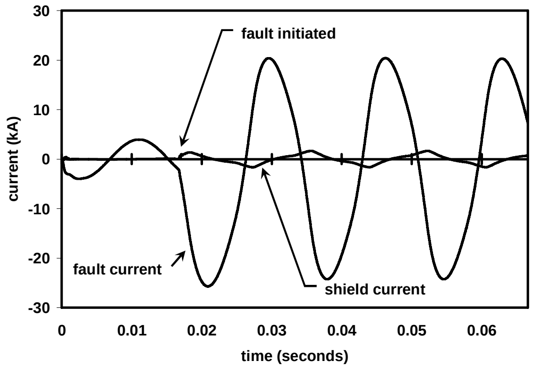

Fig. 1.15. Fault current and induced shield current from a single line-to-ground fault on phase C.

Table 1.2. Results of fault simulations

Condition	I_{inner} (kA$_{\text{peak}}$)	I_{middle} (kA$_{\text{peak}}$)	I_{outer} (kA$_{\text{peak}}$)	I_{shield} (kA$_{\text{peak}}$)
Prefault	3.51	3.80	3.96	0.07
Single line to ground	4.07	4.04	20.1	1.65
Double line to ground	26.0	4.21	28.8	1.10
3-phase	22.0	19.2	21.6	0.85

1.1.5 DC Critical Current Measurement of a 30-Meter Cable

The Southwire Company’s 30-m HTS cable system has been running at the Carrollton, Georgia, facility since 2000. As part of the operational data collected from this system, the dc critical current has been measured annually to demonstrate the continuing good performance of the HTS tapes. The connections, made on the external bus, include a significant resistive component in the measurement. The results for the phase 1 main conductor are shown in Fig. 1.16; results for the phase 1 shield conductor are shown in Fig. 1.17. As in the past measurements, the main conductor has a critical current greater than the

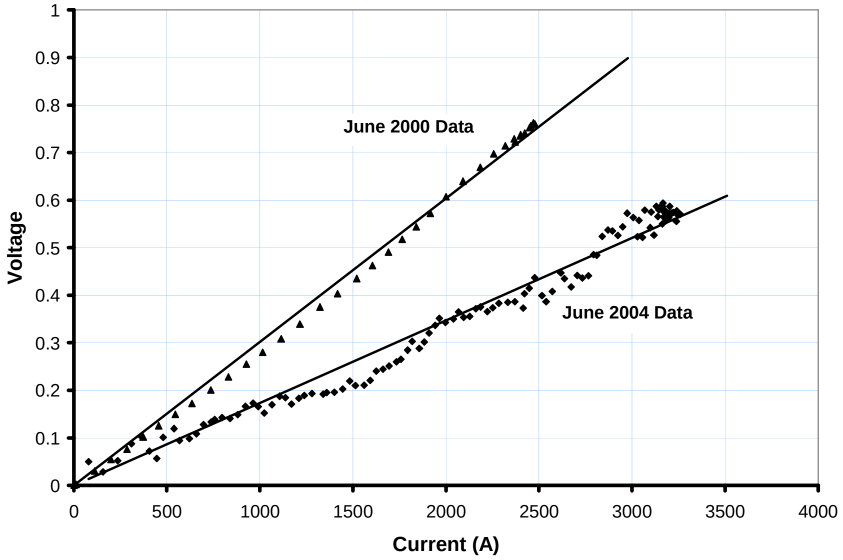

Fig. 1.16. Measured voltages across the phase 1 main conductor of data taken in June 2000 compared with measurements taken in June 2004.

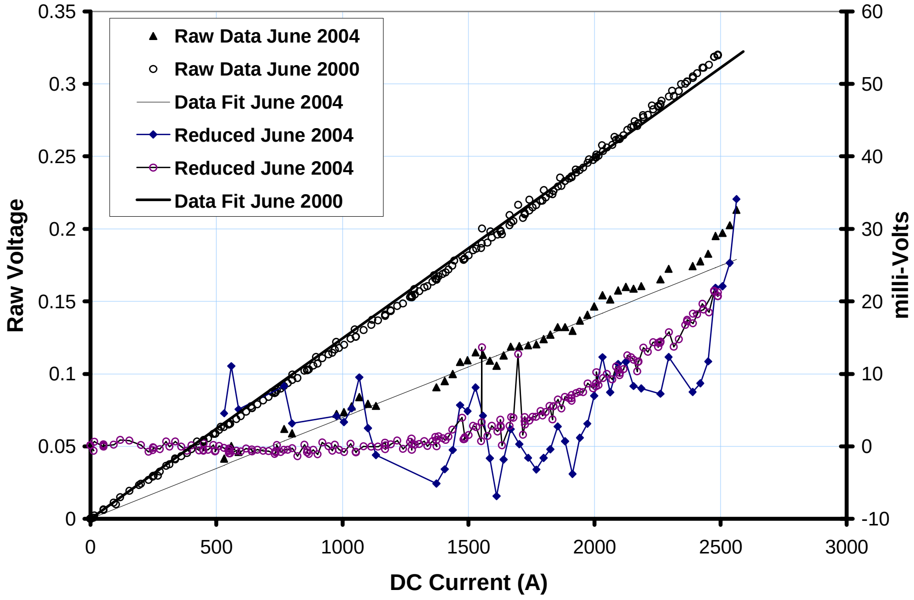

Fig. 1.17. Measured voltages across the phase 1 shield conductor taken in June 2000 compared with data taken in June 2004.

maximum current of the dc power supply (3000 A). Thus the results for the main conductor show a linear resistive relationship due to the copper bus work. (The different slopes are due to variations in external connections.)

For the shield, the dc critical current is lower and the raw voltage exhibits a nonlinear deviation from a straight line at higher currents. When the linear portion is subtracted out, the typical voltage-current characteristics of HTS materials are exhibited as shown in Fig. 1.17. The results from June 2000 and June 2004 are the same, indicating no degradation in critical current.

1.1.6 Modifications to the HTS Cable Test Facility Cryogenic System

It was determined from the results of earlier testing of the triaxial cable that modifications were necessary to the subcooler vacuum pump system in order to reach the desired operating temperatures for the HTS cable heat load. An analysis of the flows in the subcooler piping has been performed to understand the limitations of the existing system. It was decided that to achieve the required vapor flow from the subcooler, a larger vacuum pump and corresponding heater (vaporizer) would be necessary. These items were received in the first quarter of FY 2004 and were installed into the cable cryogenic cooling system in the second quarter.

1.2 Waukesha Electric Systems (WES)/SuperPower/ORNL 5/10 MVA HTS Transformer SPI

S. W. Schwenterly, J. A. Demko, A. R. Ellis, D. R. James, and I. Sauers

During the last quarter of FY 2003, the transformer was removed from its vacuum tank and inspected. Several leaks were found in the liquid nitrogen system and were repaired with Stycast epoxy. Helium leak checks on individual joints after the repairs indicated a leak rate of at most 10^{-8} atm-cc/s. The short circuit around the C-phase core was found to result from contact between the inner liquid nitrogen shield and the inner bore of the HTS coil set. It was eliminated by wedging the shield inward slightly and inserting a strip of insulation. A new compact turbopump vacuum system was installed (see Fig. 1.18).

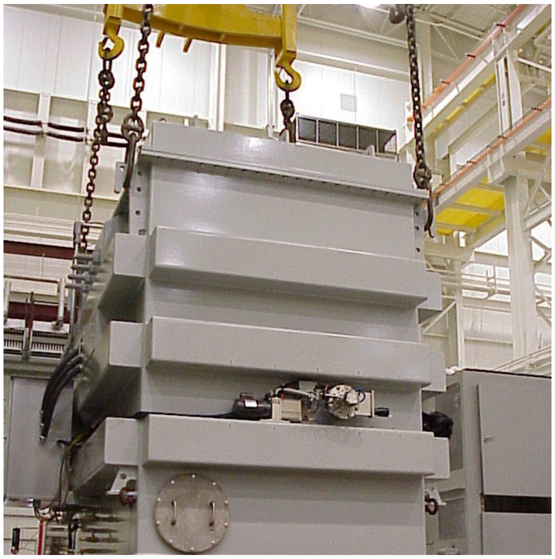

Fig. 1.18. The 5/10-MVA transformer being lifted off its trailer at the WES main plant. The new compact turbopump vacuum system can be seen.

In October 2003, the transformer was reassembled, and the tank was pumped down below 3×10^{-4} torr. Global leak checks were performed on each system by pressurizing it to 1 atm with helium and reading leakage into the evacuated tank. The indicated values were 3×10^{-7} atm-cc/s for the helium and liquid nitrogen systems and 2.4×10^{-7} atm-cc/s for the core cooling system, which were improvements over the values for the first cooldown in June 2003. All room-temperature electrical tests were at nominal values, and there was no sign of the C-phase short circuit. The transformer was cooled down below 30 K during 10 days in late October and early November. The process was very smooth with no technical problems.

During November, the transformer was disconnected from all its utilities, loaded onto a flatbed truck, and transported while still cold about two blocks to the WES main plant for installation on their test floor (see Figs. 1.18 and 1.19). The operation went well, and normal temperatures and vacuum were quickly established at the new site. Preliminary electrical tests showed that no damage had occurred.

Testing on the transformer resumed in December with three-phase high-current, low-voltage tests. The tests done on June 23, 2003, were repeated on December 16, 2003, with 116 A, 80 A, and 60 A on the high-voltage windings. A comparison of the temperature curves for the inner and outer cooling shells on Phase A is shown in Fig. 1.20. In both tests, the tank vacuum started in the mid-10^{-5} torr range and rose above 10^{-4} torr by the time the current was reduced to 60 A. The tank vacuum level corresponds closely to the vapor pressure of solid nitrogen at the temperature of the cryocooler heat exchangers, which generally run about 2 K colder than the coils. Vacuum performance should be improved by warming the transformer above 60 K to remove cryopumped residual air and nitrogen from the heat exchangers. The coil temperature curves for June 23 and December 16 show very similar behavior, indicating that the short circuit around Phase C was evidently not the source of the excess heating.

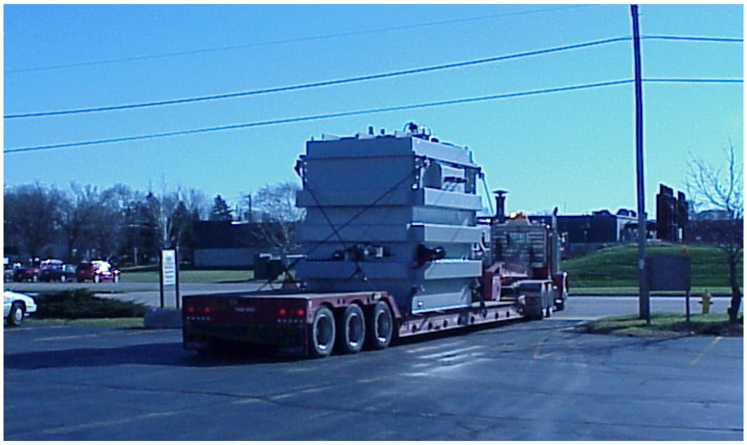

Fig. 1.19. The 5/10-MVA transformer leaves the WES Progress II building.

The maximum high-voltage winding line current that could be applied without excessive heating of the coils was less than the rated current of 116 A. Phase A was heating much faster than the other phases, but flowmeter measurements indicated that the flow was dividing evenly between the phases. This finding may indicate a problem in the A-phase conductor. The tank vacuum levels in these tests corresponded closely to the vapor pressure of solid nitrogen at the temperature of the cryocooler heat exchangers, which generally run about 2 K colder than the coils. It was theorized that vacuum performance could be improved and heat loads reduced by warming the transformer above 60 K to remove cryopumped residual nitrogen from the heat exchangers. This was done in late January 2004. The two coil cryocoolers were cycled on and off to control the warming rate. The tank pressure peaked at about 4 torr with the coils at 55 K and heat exchangers at 70 K (see Fig. 1.21). The whole system was allowed to warm to about 90 K while the tank was pumped down to the low 10^{-3} torr range. The liquid nitrogen cooler and one coil cooler were then restarted to recool the system. Thereafter the coils were always kept at about 50 K by only one cooler during standby periods to prevent excessive cryopumping of leaking nitrogen.

During January it was difficult to get access to the WES ac power test equipment because of the demands of their heavy production schedule. It was clear that an independent source of low-voltage, high-current ac power was needed. A large, three-phase variac bank that had been used to power a heater in the ORNL Large Coil Test Facility was loaned to WES in February. The heater was connected to the 5/10-MVA transformer through a voltage step-down transformer, allowing the full rated current to be applied in short-circuit mode. In March, the low-voltage, high-current tests were continued with this setup. The second cryocooler was started, and the coils were cooled below 40 K. With no burden of condensed nitrogen, the A-Phase coils still warmed rapidly with the maximum expected load of the WES plant if the transformer were installed in the substation. However, when the current was reduced, stable temperatures were maintained for 16 h. All the coil-cooling shells were at 42 to 43 K except for the Phase A inner shell, which was at 47 K. The vacuum was better than those in previous runs, at 3×10^{-4} torr. However, this vacuum level is still high enough to add roughly an extra 100 W of heat load due to molecular flow heat transfer. The initial heating rates of the coils observed when current was applied can be used to estimate the total ac losses, using the known heat capacities of the coils. This calculation gives much higher losses than the losses that were estimated in the design calculations. This excessive ac loss in combination with high heat loads from poor vacuum resulted in an overload of the cryocooler cooling capacity at currents below the rated operating current.

Having established that stable operation was possible, an attempt was made to operate at up to twice the rated operating current. Additional cooling was provided by circulating liquid helium through the auxiliary circuits on the coil cooling shells for these tests. Stable operation at the rated current of 116 A was achieved on the first day of tests before the helium dewar ran out. On the second day, another dewar

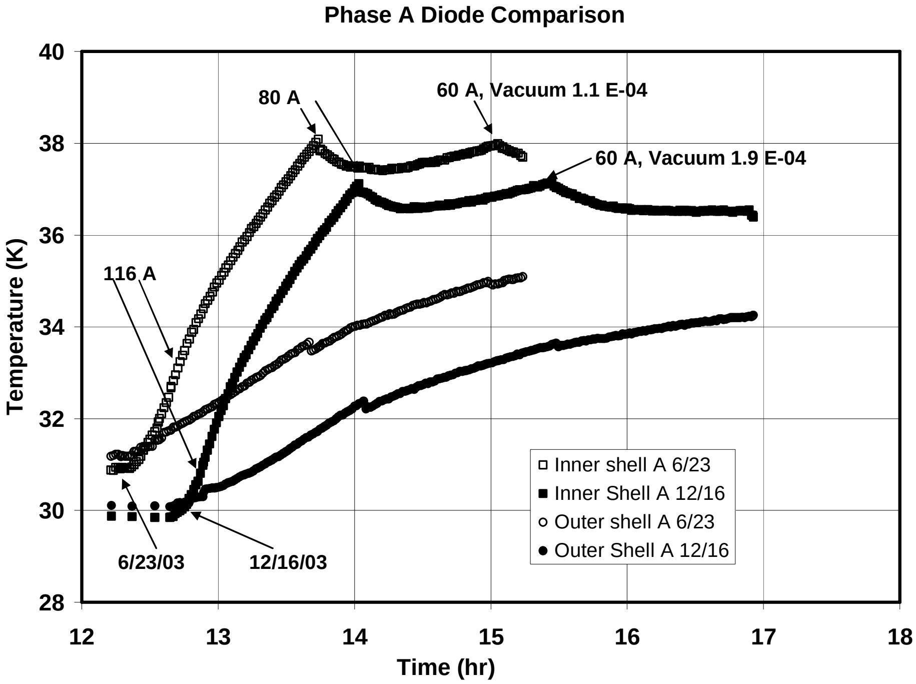

Fig. 1.20. Phase A diode comparison.

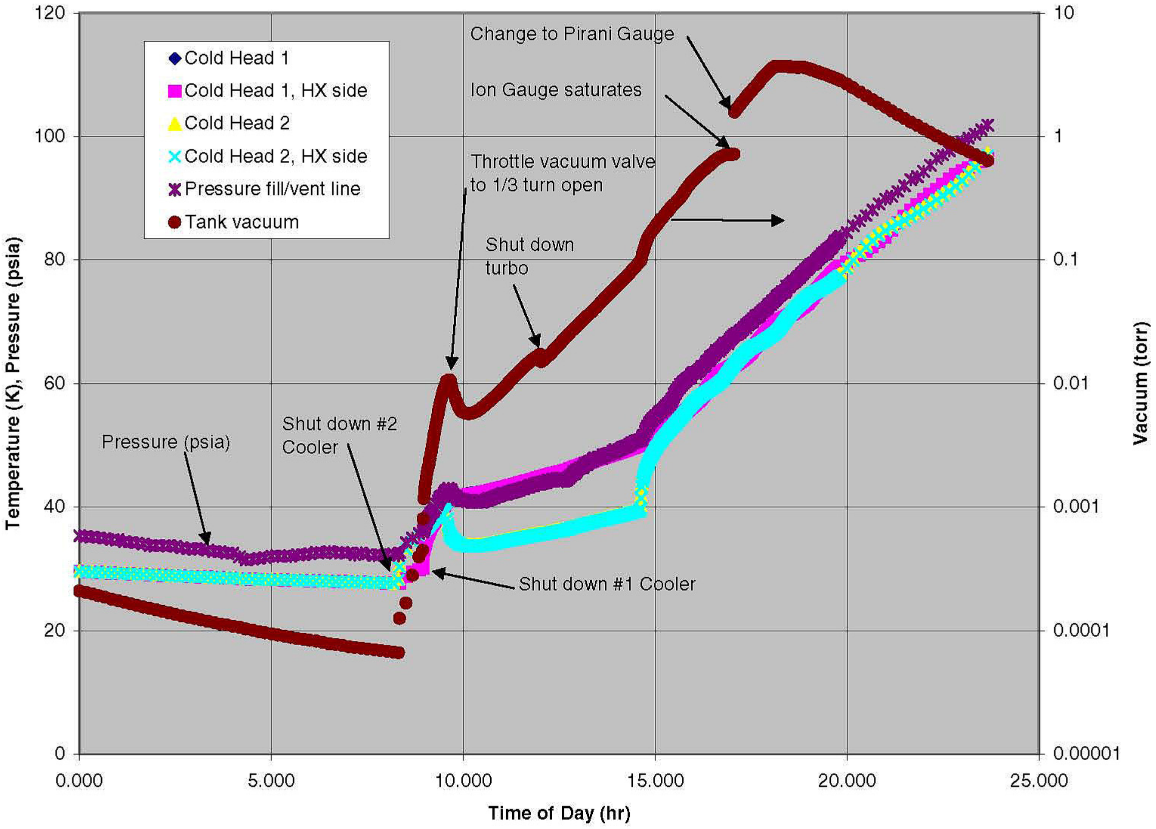

Fig. 1.21. Vacuum and cryocooler temperatures during warmup, 1/22/04.

was connected for overcurrent testing. The current was held for an hour at values up to 127 A with stable conditions. However, the HTS leads were approaching their maximum safe temperatures. The current was raised to 200 A for about 15 min and then to 230 A. After about 3 min at 230 A, the coil temperatures started running away, even with maximum helium flow, and the power was shut off. The coils still operated properly at 60 A the next day with normal cooling, indicating that no damage had occurred from the overcurrent tests.

In late March, open-circuit high-voltage tests were attempted. A three-phase, 4.4-kV transformer was connected to the low-voltage winding of the 5/10-MVA unit. The high-voltage winding of the unit was open-circuited. The 480-V primary of the supply transformer was energized by the ORNL variac to provide a variable ac voltage source. The variac voltage was raised in steps of 50 V, corresponding to steps of 460 V on the 5/10-MVA unit. The voltage was held for 5 min at each step. After about 2 min on the third step, with 1368 V on the low-voltage side and 8.2 kV on the high-voltage side, a snap was heard and the voltage collapsed. All the fuses on the ORNL variac that supplied Phases B and C of the 5/10-MVA unit were blown. A spike in the tank vacuum was seen. The ratio tester was connected, and it was found that Phase B had high excitation current. Megger tests at 500 V showed only 1 MΩ between the low-voltage and high-voltage windings but showed a high value of 500 to 1000 MΩ between both windings and ground. However, low-voltage resistance tests with a digital voltmeter showed infinite resistance. This voltage dependence of the insulation resistance usually indicates an external carbon track. Capacitance tests showed high dissipation factors, particularly between the low-voltage windings and ground. However, dc resistance measurements on all windings showed no changes from previous values, indicating that the conductor had not been damaged.

In early April, single-phase short-circuit tests confirmed that Phase B was drawing full rated current at only 25% of the voltage of the other two phases, indicating a section of shorted turns. A single-phase high-voltage test was carried out with both sides of Phase B shorted, Phase A low-voltage winding open, Phase C low-voltage winding energized, and Phases A and C high-voltage windings open. Another breakdown occurred with 13 kV across the high-voltage phases. After that, there was only 22-Ω of resistance between the high-voltage and low-voltage windings. At that point, it was impossible to carry out further testing, and the transformer was warmed to room temperature for disassembly and inspection.

When the tank was vented to the atmosphere and opened, a strong, ozone-like odor was noted. The four low-voltage leads (designated X0 through X3) were brought out through the top multiple-layer-insulation (MLI) blankets through sections of polyvinyl chloride (PVC) pipe. The pipe sections extended several inches beyond the MLI blankets and helped support the leads above them. The insulation was burned off the lead from the low-voltage “Y” connection to the X0 bushing. The pipe segment that held the X0 lead had partially melted, and the lead had drooped down and melted a large groove in the outer MLI blanket. A hole, which appeared to be arc damage, was found in the insulation on the Phase A low-voltage lead X1 at the X1 bushing. A similar hole was found in the insulation on the Phase C low-voltage lead X3 where it entered its PVC support tube through the MLI.

A multimeter showed that the top of the melted MLI was in electrical contact with the liquid nitrogen plumbing before the MLI was moved. That contact was broken when the C-phase low-voltage-side top MLI was peeled back. A “rainbow” pattern on the tank wall was also visible on the core clamp, the tank cover, and the top of the MLI. The pattern is indicative of an evaporative deposition and is spread uniformly around the spot where all the MLI had melted. There do not seem to have been two separate depositions, based on the uniformity of the rings.

The working assumption is that all the melting damage occurred during the single-phase short-circuit testing that was done after the 2× rated current tests. A thermocouple on the X0 lead reached as high as 480 K during the last single-phase short circuit tests. The thermocouple is located on the X0 lead, just inside the bushing. The test was done after the 2× current test and after the initial failure of B-phase during voltage testing. The damage to the X3 lead may have been a flashover to the now bare X0 lead, but there is no direct evidence of that. It is possible that a flashover between the two leads occurred earlier; the melting of the insulation on X0 lead would have masked any damage. There is no evidence of a corresponding point to the flashover from X1 lead. There is no line of sight between the flashover mark on X1 and the mark on X3.

When the MLI over the low-voltage leads was removed, it was found that the low-voltage neutral interconnects between A-phase and B-phase and between B-phase and C-phase had suffered serious overheating. The insulation wrapping had been carbonized, and the PVC tube that served as electrical isolation where the interconnect passed through the tight space under the support and over the top panels/frame was melted. The insulation materials have melting points in the range of 250 to 400°C (525 to 675 K). PVC melt temperature is on the order of 200^{o}C (475 K). The burn temperature would be higher than that. All indicators are that the temperature of the low-voltage neutral leads would have had to exceed 500 K to cause the damage shown.

Also visible was a pattern of brown deposition on the low-voltage top panels. A comparable deposition was seen on the bottom of the MLI blankets. Under the support, the deposition was thick and crumbly. Elsewhere, where the deposition was darkest, it was slightly sticky to the touch. The deposition was also evident on the plumbing and the ceramic breaks. All deposits were removable with acetone.

The most likely time when the damage occurred is during the 2× rated current test. During that test, even in the phase set that heated up the most, the temperatures at the top of the low-voltage leads did not rise more than 10°. However, the temperature of the low-voltage-side top liquid nitrogen shield panels on A-phase and B-phase rose more than 60°. These two panels lie just below the low-voltage interconnect leads. This test was done before any of the voltage tests. There was no visible evidence of a voltage flashover, although the dusty nature of the remaining insulation could easily hide a flashover. There was no visible damage to the fine copper wires of either of the interconnect cables in the examinable area or the interconnects outside the melted PVC sections. Even with damaged insulation, a breakdown from the interconnects to the liquid nitrogen panels would have been unlikely because they stay near ground potential during a three-phase high-voltage test.

A finite-element calculation was performed at ORNL to estimate the heating in the X0 lead and low-voltage neutral interconnections. It showed that the leads were indeed undersized in relation to their lengths. A single 4/0 cable was used for each neutral interconnection, and two #6 wires in parallel were used in the X0 lead. With the ends of the neutral interconnections perfectly heat-sunk at 80 K, the calculation showed that the center of each lead reached over 450 K at low-voltage currents of 700 A, corresponding to 1× operation. At 2× operation, the leads are unstable and heat up continuously, which explains the burned insulation. Three 4/0 cables would be needed in each interconnection for proper 2× operation. For the X0 lead, the calculation shows a peak temperature near 1000 K at 1× operation. Three such cables would also be needed for proper operation at that current. The X0 lead was sized for only 0.1× operation because single-phase tests were not originally anticipated.

In the coils, a fine powder deposit was observed on every inner and outer copper cooling shell. It is possible that the powder is a residue from the evaporated insulating material or the MLI, although it seemed to be evenly dispersed across the surfaces of all copper cooling shells, starting a few inches from the bottoms and tops. There was no evidence of surface arcing anywhere on the coils.

Surface cracks were found in the epoxy between the high-voltage leads on A-phase and C-phase, but not on B-phase. The crack on A-phase, measured with the feeler gauge, was approximately 22 mm deep. The crack on C-phase measured approximately 15 mm deep. The cracks in A-phase extended from HV-II toward HV-I (Fig. 1.22), and the same or another crack continues on until it disappears under the clamp. The bore scope was not able to get a clear view on the other side of the clamp to either confirm or deny the continuation of the crack. No visible cracks were seen in the epoxy on the low-voltage side of any phases. No additional cracks were found in C-phase when examined with the bore scope.

During voltage testing, it was discovered that the ceramic electrical break between LV-II and the liquid nitrogen plumbing on A-phase was only loosely resting in the corona ring. A slight tap caused the failure seen in Fig. 1.23. The ceramic break was the one that evidenced a substantial leak during the initial assembly of the transformer. It was repaired with black Stycast. During repairs after the first tests in 2003,

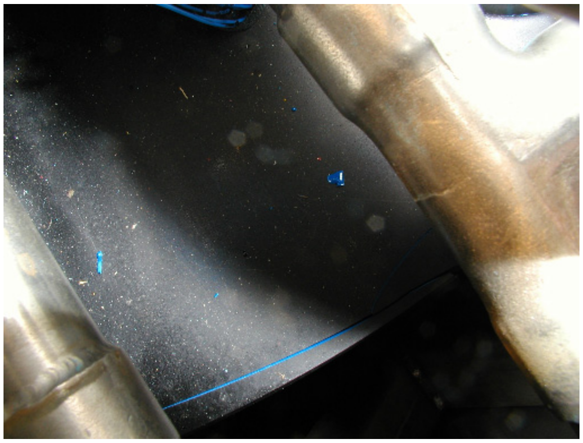

Fig, 1.22. Crack between high-voltage terminals (HV-II on left) on the A-phase.

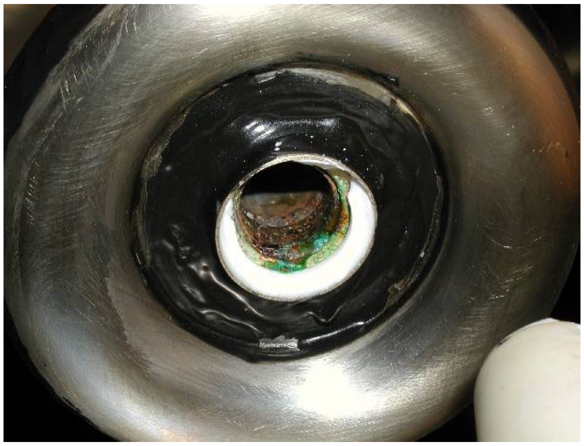

Fig. 1.23. Close-up of the inner diameter of the ceramic electrical break.

there was no confirmed evidence of a crack at that location, although there was a low-level leak at the top of A-phase that was never specifically identified. This ceramic break was probably the source of the liquid nitrogen system leakage in the final series of tests.

A look at the inner diameter of the remaining pieces revealed that the ceramic break was not properly cleaned after being welded on the corona shield. Clearly visible is the green residue typical of flux left in a metal tube. Also visible is substantial corrosion back into the pipe. Nothing of interest was found in the ceramic side.

After the interconnections were removed from all the coils, it was possible to make individual insulation resistance measurements on them. Phase A had a short of about 361 Ω from the high-voltage to low-voltage winding, and Phase B had a short of only 16 Ω from high voltage to low voltage. Phase C still had high high-voltage–low-voltage insulation resistance, and all the coils had good insulation resistance from the windings to the grounded cooling shells.

In the fourth quarter, the top yoke was removed from the transformer core by WES, and the coils were lifted out and shipped back to SuperPower. At the SuperPower facility, several shorts were found between the parallel HTS tapes in the low-voltage windings, particularly on Phase B. Phase A was cooled down with liquid nitrogen for critical current and impedance tests, but the results were inconclusive because problems with the plant liquid nitrogen supply prevented bringing the whole coil to 77 K. Further tests are planned. SuperPower is now conducting a root-cause analysis of the high-voltage failures in collaboration with Prof. Robert Degeneff at Rensselaer. Both nondestructive and destructive inspection methods for inspection and analysis are being considered. Because cutting a coil open will be a difficult and expensive process, a preliminary nondestructive inspection (e.g., X ray) is needed to determine the best places for the cuts. A paper on the final series of test results was presented at the 2004 Applied Superconductivity Conference in October 2004. Also, a complete chronicle of the entire HTS transformer development and testing program has been written and submitted to DOE.

1.3 SuperPower Matrix Fault Current Limiter CRADA

S. W. Schwenterly, A. R. Ellis, D. R. James, and I. Sauers

ORNL is collaborating with SuperPower, Inc. to develop their new concept for a matrix fault current limiter (MFCL), which consists of an array of HTS elements arranged to go normal simultaneously in a fault. The fault current is shunted to a parallel array of normal reactive elements that effectively limits the maximum current in the fault and allows downstream breakers to open. After the fault clears and the breakers close again, the HTS elements quickly return to the superconducting state and restore normal operation.

A cryogenic cooling test cryostat was described in the 2003 annual report. While it is being designed and built, preliminary cooling tests are being performed in an existing cryostat, shown in Fig. 1.24. Liquid nitrogen at 77 K is circulated through the coil of copper tubing at the lower end, which is immersed in pressurized supercritical nitrogen. This coil simulates the cooling ring that is attached to the cryocooler in Superpower's design. The foam discs above the coil simulate the vacuum above the pressurized tank that would surround the MFCL array. A disc heater mounted below the coil simulates the array heat load. Two temperature sensors are mounted above and below the G-10 plate that is on top of the coil. Initial tests at 3 atm and 5 atm supercritical nitrogen pressure indicate that the lower sensor (which is closer to the heater) stays about 2 K warmer than the one above the plate for power inputs up to 300 W. Good temperature stability was obtained.

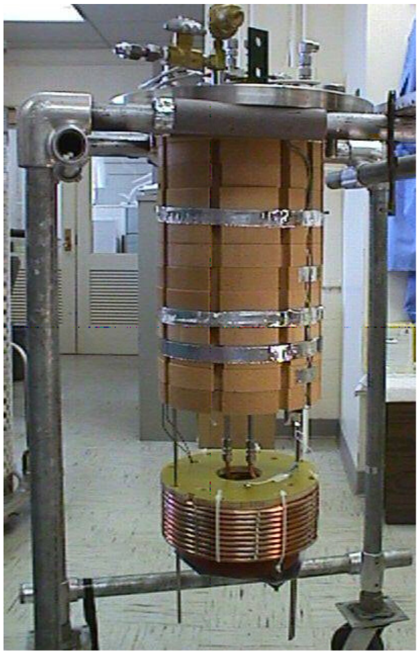

Fig. 1.24. Cryostat used for preliminary MFCL cooling tests.

Next, the temperature was measured at various locations for different heater power levels. The basic setup was modified to increase the temperature sensors from 2 to 12, as shown in Fig. 1.25. The G-10 plate that was just above the cooling coil in the earlier experiment was also replaced with a copper plate. The results show that the temperature profiles are relatively independent of heater power. Because the cryostat has no high-current bushing to provide a heat load, the liquid level tends to rise within 20 cm of the top plate, as can be seen by the sharp temperature increase that occurs at that location (see Fig. 1.26). Below the liquid level, there was very little temperature difference between the two radial sensor locations. The dip in temperature at the position of the copper plate is probably an artifact due to a difference in sensor calibration because the sensors came from a different manufacturer.

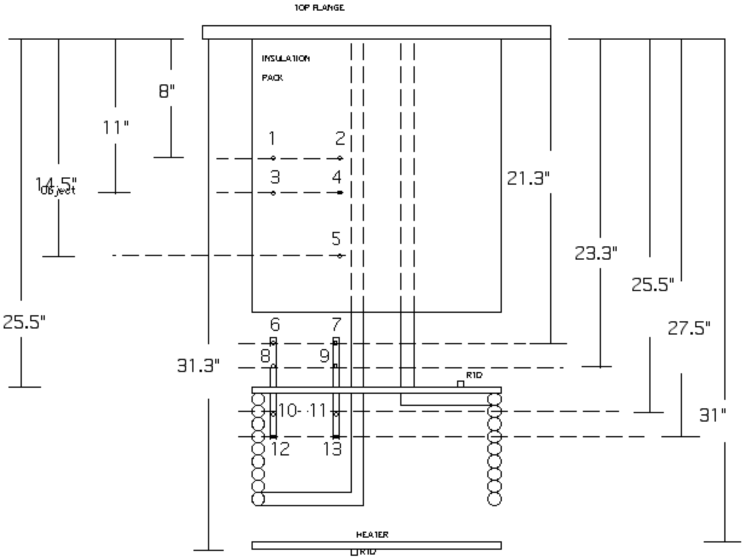

Fig. 1.25. Layout of temperature sensors.

Design of a new top flange to be fitted with a 50-kV high-voltage bushing was completed, and the flange was fabricated at a local machine shop. ORNL participated in the Technical Advisory Board meeting at SuperPower on May 4, where data were reviewed from the second round of testing at the Florida State University Center for Advanced Power Systems. An R&D cooperative research and development agreement (CRADA) between ORNL and SuperPower was approved in late June 2004.

Dielectric testing in support of the MCFL SPI program commenced in August 2004. From August 9 to 13, technical staff from SuperPower visited ORNL for safety training and indoctrination, badging, and initial high-voltage experiments on candidate MFCL dielectric materials. Testing continued during a

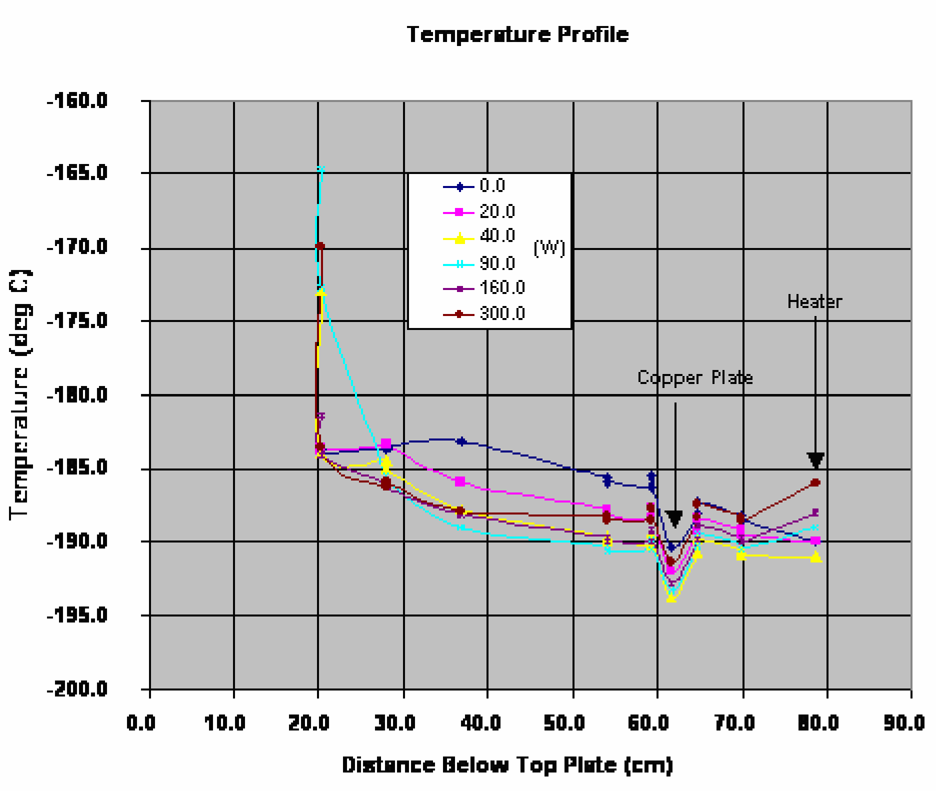

Fig. 1.26. Temperature profiles at various locations.

second round of experiments from September 13 to September 23. Extensive high-voltage testing was carried out on a prototype 52-kV, 250-kV BIL high-voltage bushing/lead assembly for the MFCL. Breakdown tests using various electrode geometries relevant to the MFCL design were also carried out in liquid nitrogen. During the first series of tests on the bushing/lead assembly (see Fig. 1.27), negative impulse tests resulted in breakdowns in the range of 63 to 80 kV in 3-atm, 300-K nitrogen gas and 2.2-atm, 77-K nitrogen gas. Tracking was found on a Teflon sleeve around the high-voltage lead. After the thickness and length of the sleeve were increased, no further tracking was observed at the test voltages. Another large series of ac and impulse breakdown tests was carried out in an open bath of liquid nitrogen in which sphere-plane and coaxial electrode sets were used.

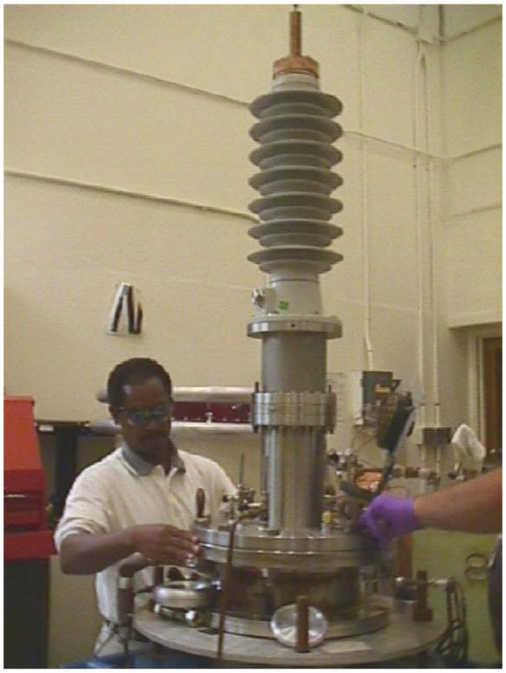

Fig. 1.27. Assembly of 52-kV, 250-kV BIL bushing into the high-pressure cryostat.

1.4 General Electric Co. HTS Generator SPI

R. C. Duckworth, A. R. Ellis, M. J. Gouge, R. Grabovickic, D. R. James, and I. Sauers

1.4.1 Emissivity Experiment

General Electric has tasked ORNL to evaluate the emissivity of candidate cold surfaces with and without contamination because radiation is a major heat load on cold HTS rotor components. Water contamination studies have been carried out on a silver-plated copper sample at temperatures of 33 to 35 K. From the baseline measurement, degradation occurred when water vapor was added to the system; emissivity increased from a steady-state value of 0.028 to 0.051 when 0.420 mg of water was added to the system. The emissivity caused by contamination was higher than the room-temperature measurement of 0.045.

Figure 1.28 shows the influence of water contamination mass on the emissivity of a silver-plated copper sample. The sample was a 17.8 × 38.1 cm (7 × 15 in.) thin rectangle plated with silver on both sides. The water leak entered through a ½-in. stainless steel tube pointed directly at one side of the sample at a rate of 1.25×10^{-7} g/s. The slow temperature decrease that was observed in the shield and the lack of any appreciable change in the vacuum pressure (8×10^{-7} torr) during and immediately following the water injection indicated that the change in the heat load was largely due to radiation effects.

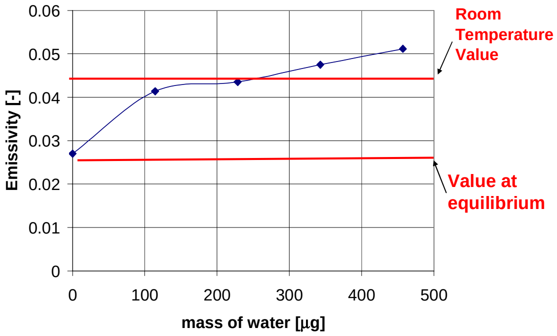

Fig. 1.28. Influence of water contamination on silver emissivity at 33 K.

Figure 1.29 shows the degradation of the emissivity due to air contamination. Air contamination was introduced after the experiment was shut down, and sufficient time was given to pump out the water contamination. The air leak entered through the same ½-in. stainless steel tube from the room-temperature environment at a rate of 1.27×10^{-6} g/s. Equation (4) was used to calculate the amount of water vapor so that the water contamination results could be compared with the air contamination results:

$$\omega = 0.622 \frac{p_v}{p - p_v} \tag{4}$$

where p_v is the vapor pressure of water at a given humidity.

Humidity of 50% provides good agreement between the contamination surfaces (Fig. 1.30).

Measurements of the emissivity degradation that is associated with direct water contamination were carried out on a replated silver-plated copper sample at temperatures of 30 to 32 K. The measurements were taken to see if the absolute value of emissivity at room temperature had any effect on the emissivity at 30 K and the degradation of emissivity due to water contamination. This sample initially had a room-temperature emissivity of 0.045 at 300 K, but the emissivity decreased to 0.038 after the sample was replated. Figure 1.31 shows the emissivity degradation due to water contamination for the silver-plated copper sample before and after replating. It is clear that the replating had an effect on the absolute value of the emissivity; however, when the relative changes of emissivity with respect to their corresponding room temperature values are compared, there is a fair amount of consistency between the two samples (Fig. 1.32).

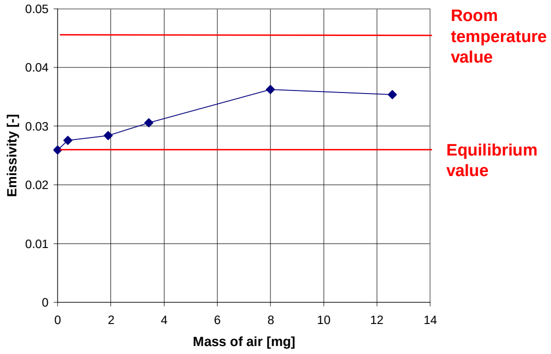

Fig. 1.29. Influence of air contamination on silver emissivity at 32 K.

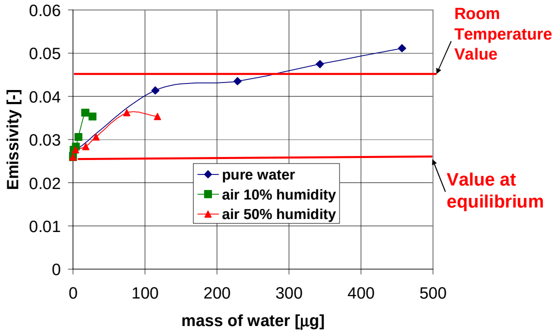

Fig. 1.30. Emissivity degradation comparison between pure water contamination and water vapor in air contamination experiments at different levels of assumed humidity.

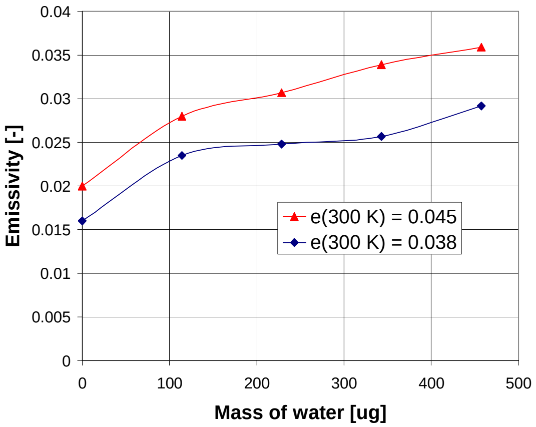

Fig, 1.31. Comparison of absolute emissivity degradation of silver-plated copper samples due to direct water contamination. The values of emissivity at room temperature of 0.045 and 0.038 represent the same sample before and after it was replated.

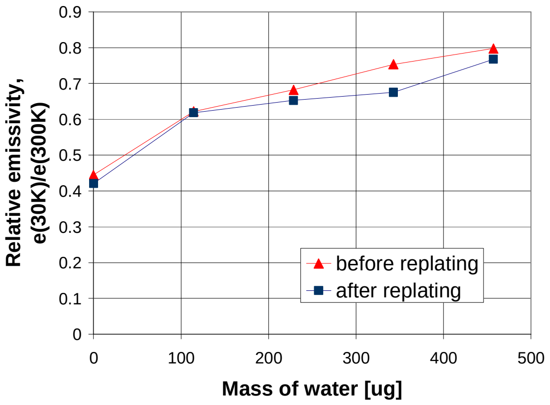

Fig. 1.32. Comparison of relative emissivity degradation with respect to the room-temperature value of silver-plated copper samples due to direct water contamination. The values of emissivity at room temperature of 0.045 and 0.038 represent the same sample before and after it was replated.

In addition to water contamination, preliminary measurements have been made of the emissivity degradation due to the presence of G10 within the vacuum space. Figure 1.33 shows the emissivity as a function of time for the test setup with and without G10 and shows the net change in emissivity due to G10. However after examination of the background measurements and the measurement of the leak rate of the system with and without G10, further refinement of the experimental system is needed to distinguish between the outgassing of the G10 and a variation in the o-ring seals of the system.

Preliminary measurements have been made of the emissivity at 30 K and the degradation of emissivity due to water on a new silver-plated copper sample. The sample had a lower emissivity at room temperature (0.021 +/- 0.002), which resulted in a lower emissivity at 30 K (0.010 +/- 0.001). The previous sample with the lowest emissivity had a room-temperature emissivity of 0.038 and an emissivity of 0.014 at 30 K. While the relative change for the new sample was smaller than previous sample, the initial emissivity was significantly smaller. Figure 1.34 shows the degradation of the emissivity as a function of water mass. Each mass point is a stepwise introduction of 110 µg of water onto the sliver-plated copper surface. The

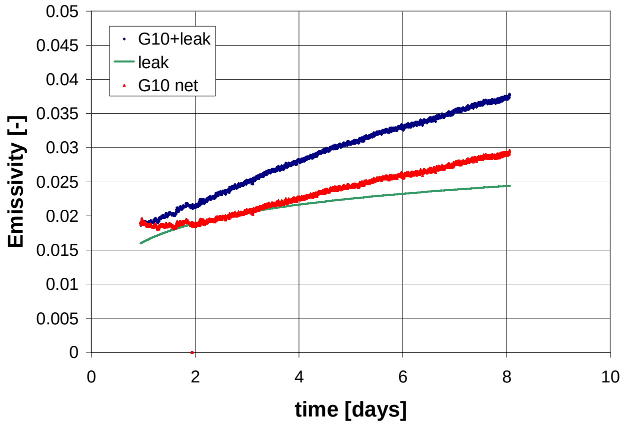

Fig. 1.33. Emissivity degradation of a silver-plated copper sample due to the presence of G10 in the vacuum space. The net G10 effect was found by subtracting the relative change in the silver emissivity due to the background effects from the change in emissivity as a function of time for the composite test system with G10 present.

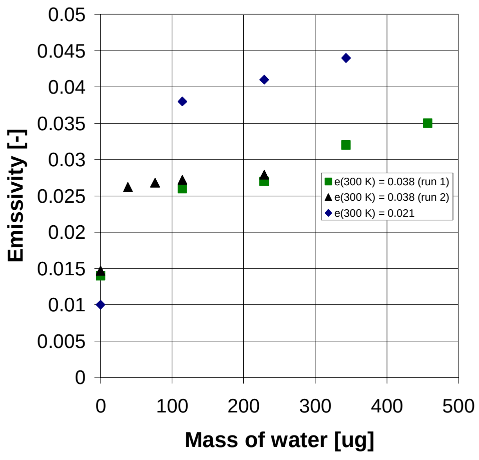

Fig. 1.34. Comparison of water degradation of emissivity for silver-plated copper samples with different room-temperature emissivities.

emissivity data for the new sample were significantly higher than the previous data, but the data for the old sample took into account a level of background contamination that was due to leaks in the cryostat at the time that may account for some discrepancy between the two samples. The initial measurement of the emissivity at 30 K is repeatable (meaning that an emissivity of 0.01 was measured on successive measurements after the water vapor was removed), and a repeat of the emissivity degradation will be done to confirm these findings.

While this wide data range could have an impact on the design allowance of the refrigeration system for the 100-MVA demonstration generator, the real-life case occurs when the emissivity degrades due to outgassing water vapor from G10 onto the silver-plated copper surface. Preliminary measurements have been made of this effect, but further testing is needed to verify the one-to-one correspondence on the direct water contamination and the indirect water contamination from the G10. The effect of baking the G10 and the relative thickness of the G10 are other issues that will be examined.

1.4.2 High-Voltage Ramp to Failure and Impulse Breakdown Tests on HTS Wire Insulation

One-layer and turn-to-turn dielectric strengths were measured for two types of superconducting wire insulation. Both insulations were tested for ac ramp to failure and impulse breakdown voltage at room temperature. The ac ramp-to-failure voltage tests on both types of insulation with one layer were performed according to the American Society for Testing and Materials standard ASTM D-3353-98. Impulse breakdown tests were performed by exposing the turn-to-turn insulation to a series of three 1.2/50-µs negative impulse voltage waves of equal peak value. Figure 1.35 shows typical negative impulse voltage waveform recorded on a Tektronix TDS 380 scope.

The peak value of successive three-voltage wave sets was increased until breakdown of the insulation occurred. Figure 1.36 shows a typical negative impulse breakdown waveform with a voltage collapse captured by the scope.

Measurements of the turn-to-turn dielectric strength with respect to the impulse breakdown voltage were completed for two candidate types of superconducting wire insulation at room temperature and at liquid nitrogen temperature. A relatively large number of samples (more than 45) were prepared and tested. The turn-to-turn tests were performed on HTS tapes with the insulation applied. The statistical distribution

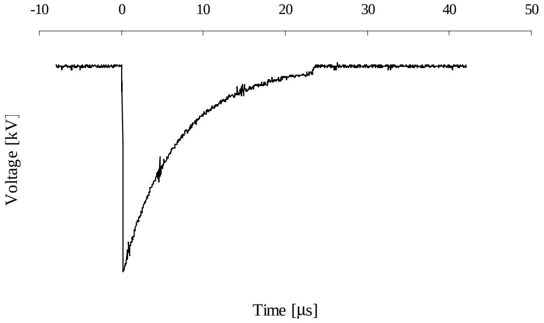

Fig. 1.35. Typical negative impulse voltage waveform.

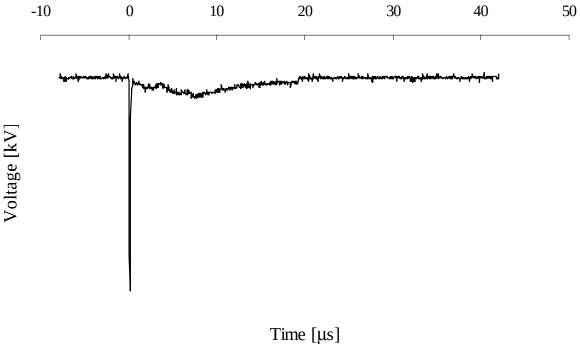

Fig. 1.36. Typical negative impulse breakdown voltage waveform.

of the measured impulse breakdown data (1.2/50-μs rise/fall) was presented in the form of Weibull plots, which indicate the insulation failure probability at a given voltage. For both insulation systems being considered, the impulse breakdown voltage increased going from 295 to 77 K. One type of wire insulation failed to meet General Electric requirements and was excluded from future accelerated aging tests.

1.4.3 Accelerated Pulsed Aging and Partial Discharge Inception Voltage Tests on HTS Tape Insulation

Accelerated aging tests for HTS tape insulation were initiated. The experimental setup for these tests was assembled as shown in Fig. 1.37.

In accelerated aging tests, the turn-to-turn insulation is exposed to elevated electrical stress conditions. Measurements are performed at several voltage levels with several samples at each voltage level so that the statistical distribution of insulation aging data can be obtained. The accelerated aging tests provide the insulation *n* value, which is required to estimate the insulation lifetime under normal service conditions.

Accelerated pulsed-aging and partial discharge inception voltage (PDIV) tests on the selected insulation between two adjacent superconducting tapes were completed at ambient temperature and were initiated at liquid nitrogen temperature. In the pulsed-aging tests, the turn-to-turn insulation was caused to

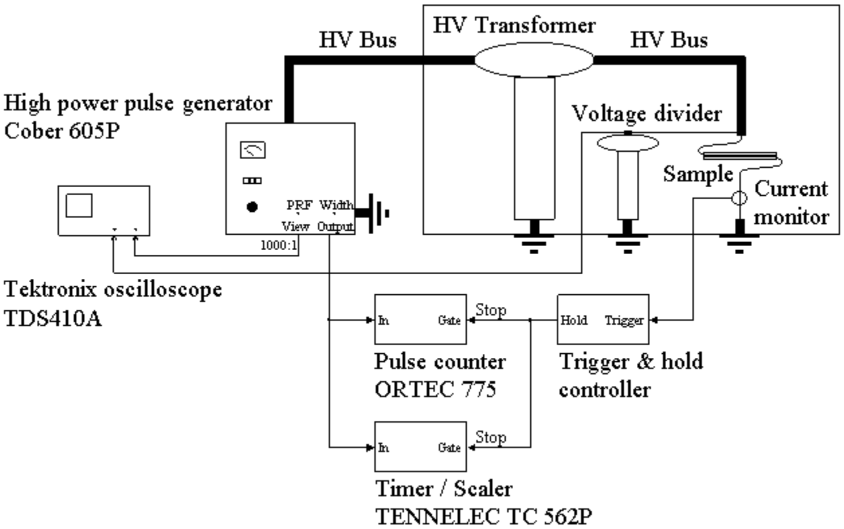
HV Bus
HV Transformer
HV Bus
High power pulse generator
Cober 605P
Voltage divider
Sample
Current
monitor
PRF Width
View Output
1000:1
Tektronix oscilloscope
TDS410A
In
Gate
Stop
Hold
Trigger
Pulse counter
ORTEC 775
Trigger & hold
controller
In
Gate
Stop
Timer / Scaler
TENNELEC TC 562P

Fig. 1.37. Schematic diagram of experimental setup for accelerated aging tests.

fail by a series of positive polarity high-voltage pulses with the specified magnitude (above the PDIV), width, and repetition rate. The time to breakdown and the total number of pulses at a given aging voltage were measured by a timer and a digital pulse counter, respectively. Aging experiments were performed on five samples at each voltage level so that the statistical distribution of the time to breakdown could be obtained. The two-parameter Weibull distribution function was used to calculate the time to breakdown with a cumulative failure probability of 63.2%. The applied voltage vs the thus-obtained time to breakdown was presented on a log-log plot with the linear regression fit. The slope of the linear regression fit was used to determine the insulation *n* value and to estimate the insulation lifetime under normal service conditions. At ambient temperature the slope of the lifetime aging curve was found to decrease at a lower voltage, which indicates a change in the aging mechanism(s). Future pulsed-aging tests will determine whether different aging mechanisms are also found for the case of cryogenic temperatures and whether the rate of aging decreases significantly when the tape samples are cooled to liquid nitrogen temperature.

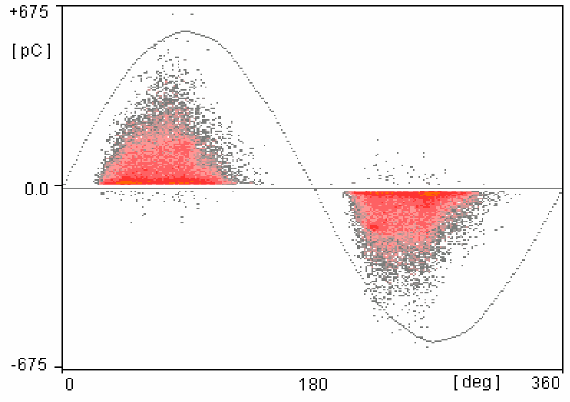

Fig. 1.38. Phase-resolved PD pattern for a selected composite sample obtained for the 60-s data scan duration.

In PD tests, the selected composite samples with lapped tape insulation between two superconducting tapes were exposed to a series of ac voltages of equal duration and increasing magnitude until PD initiation was observed on the insulation condition monitor digital PD system. The measured PDIV for all composite samples tested at room temperature compared favorably with the corresponding air Paschen curve value. A typical phase-resolved PD pattern with the occurrence of PD pulses superimposed on the applied voltage waveform for a selected composite sample is shown in Fig. 1.38. The corresponding three-dimensional plot with the number of PD pulses as a function of charge amplitude and phase angle is shown in Fig. 1.39.

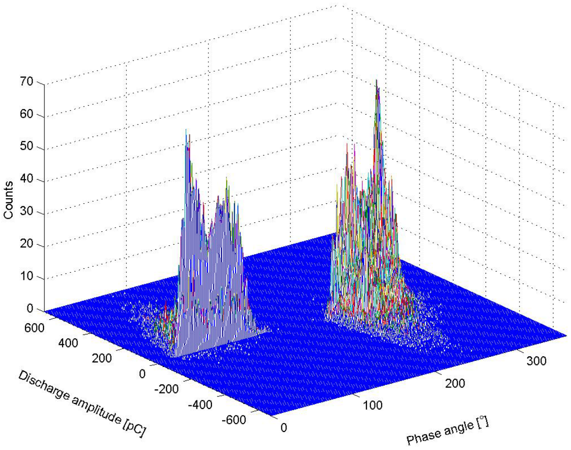

Fig. 1.39. Three-dimensional PD plot for a selected composite sample obtained for the 60-s data-scan duration.

1.4.4 Panel Discussion at IEEE Summit Power Meeting

ORNL was invited to participate in a panel session on Advances in Superconducting Machinery at the 2004 IEEE Summer Power Meeting (June 6–10, Denver, Colorado). The panel was sponsored by the Synchronous Machinery Subcommittee of the Electric Machinery Committee. The session chair was Konrad Weeber of GE. An overview of the material presented was submitted as a brief paper, entitled “Electrical Insulation Materials for Superconducting Coil Application,” by D. Randy James and Isidor Sauers. ORNL also presented a panel paper on cryogenic cooling of HTS electrical machines.

1.4.5 Measurements of Temperature Dependence of Partial Discharge in Air Gaps between Insulated BSCCO Tapes

PD in air-filled gaps trapped between two adjacent insulated BSCCO HTS tapes was investigated experimentally [2]. PD measurements were performed at several temperatures, ranging from 295 to 41 K. At each temperature a series of ac voltages of equal duration and increasing magnitude was applied to the inter-turn insulation until PD was initiated and observed on the insulation condition monitor digital PD system. The PD data were presented in the form of phase- and amplitude-resolved PD patterns. The PD initiation voltage and PD extinction voltage observed at a particular temperature were measured on an oscilloscope. Experimentally obtained values for initiation and extinction were compared with the Paschen curve values for air, and the effect of temperature on PDIV was documented.

1.4.6 Partial Discharge and Accelerated Pulsed Aging of Insulation between Parallel Plane-Plane Stainless Steel Electrodes and between BSCCO Tapes at Room Temperature

PD and pulsed aging were measured at room temperature for chlorotrifluoroethylene (CTFE) thin films between two parallel plane-plane stainless steel electrodes and for polytetrafluoroethylene (PTFE) lapped tapes between two adjacent BSCCO HTS tapes [3].

In the PD experiments, selected samples of PTFE and CTFE insulation were exposed to a series of ac voltages of equal duration and increasing magnitude until PD was initiated and observed on the insulation condition monitor digital PD system. The measured PDIV was comparable to the air Paschen curve value for each sample. Typical PD data were presented in a phase-resolved PD pattern and a three-dimensional plot.

In the pulsed-aging experiments, the samples were caused to fail by a series of positive-polarity high-voltage pulses with a specified magnitude (above the PDIV), width, and repetition rate. The time to breakdown and the total number of pulses at a given aging voltage were measured by a timer and a digital pulse counter, respectively. The aging data were presented in the form of a log-log plot of applied voltage vs time to breakdown to determine the n values for the lifetime performance of CTFE thin films and PTFE lapped tapes when used in the above configurations.

1.4.7 Quench Detection and Protection

A trip to General Electric was conducted on August 3, 2004, to informally review HTS generator rotor coil R&D and a proposed quench protection scheme.

1.5 Conductor Engineering: Overcurrent Studies in HTS Tapes

J. W. Lue, M. J. Gouge, and R. C. Duckworth

1.5.1 Experimental Procedure

A series of experiments with overcurrent pulses were performed on BSCCO and YBCO tapes. Each of the 20-cm-long HTS tapes was laid straight on a G-10 cylinder, covered with layers of Cryoflex^{TM} dielectric tapes to simulate an HTS cable construction, and tested in an open liquid nitrogen bath. The effect of reducing the peak conductor temperatures via electrical and thermal stabilizers was also tested by laying an extra copper strip (3.05 × 0.25 mm) on top of the HTS tape. Table 1.3 shows the seven different sample configurations tested in the experiments. Sample 1, made by American Superconductor Corporation, has a 15-μm-thick layer of copper plated around it. Sample 3, also made by American Superconductor, is composed of two 25-μm-thick layers of stainless steel laminated on both sides of a silver-alloy BSCCO tape. Sample 5, also made by American Superconductor, is composed of a 50-μm-thick layer of copper laminated on the HTS side of a YBCO tape. Sample 7 consists of two strips of copper and was used to verify and calibrate the temperature measurements and thermal analysis procedures.

Table 1.3 Samples tested for overcurrent limitations

Sample	Configuration	Dimensions (mm)	I_c (A)
1	Cu-plated BSCCO	4.27 × 0.25	117
2	Cu-plated BSCCO + Cu		114
3	Stainless steel laminated	4.75 × 0.345	126
4	ss-BSCCO + Cu strip		129
5	Cu-laminated YBCO	10 × 0.149	161
6	Cu-laminated YBCO +		148
7	2 strips of Cu	3.05 × 0.25	–

A 3-kA, 30-V dc power supply was used for both the voltage and current measurement of the HTS conductors and for supplying the overcurrent pulses. A thin-film resistance temperature detector was laid under the HTS tape or between the HTS tape and the copper strip at the center of the conductor to measure the temperature of the conductor. The voltage of the middle 10 cm of the conductor (i.e., the span between the 5- and 15-cm points on a 20-cm-long tape) was monitored to find the voltage excursion of the conductor during the current pulse. First, the voltage-current curve of the sample was measured. Then a short overcurrent pulse was applied to the conductor. The voltage-current curve was measured again to see whether there was any degradation to the HTS tape. This process continued until the HTS tape was damaged or the power supply reached its limit. The second series of tests on a given sample configuration was to set the overcurrent level somewhat lower than the electromechanical or power supply limit and to increase the pulse length to increase the heating to the conductor. A thermal limitation was found for each of the HTS samples.

1.5.2 Electromechanical Limitation of HTS Tapes

The power supply was remotely controlled by a square-wave voltage pulse to supply a pulsed current to the sample. The shortest pulse length that could be obtained with an appreciable flat top was about 35 ms. In a series of tests to find the electromechanical limitation of HTS tapes, the pulse length was set from 35 to 60 ms. For samples 1 and 3 (BSCCO tapes plated with copper and laminated with stainless steel, respectively), the maximum peak current obtained was ~1 kA. After this high-current pulse, the voltage-current curve was found to be the same as the initial curve. Thus, it is seen that BSCCO tapes having a critical current of about 115 to 130 A can take a short overcurrent pulse to at least 1 kA without being electromechanically damaged. For sample 5 (a copper-laminated YBCO tape), there was no change in the voltage-current curve after being pulsed to 1.23 kA. Figure 1.40 (top plot) shows the resistivity increase of the conductor when the peak current was increased to 1.36 kA and the voltage-current curve was measured after the pulse shot as compared to the initial curve (bottom plot). There was a slight degradation; the critical current decreased from 161 to 157 A. The resistivity increase indicates that the YBCO tape was heated to an average temperature of 370 K. At the same time, the electromechanical load on the YBCO tape produced a buckling compressive stress of 0.38 MPa (56 psi). A thermal limitation test indicated that the small degradation was more likely from the electromechanical load.

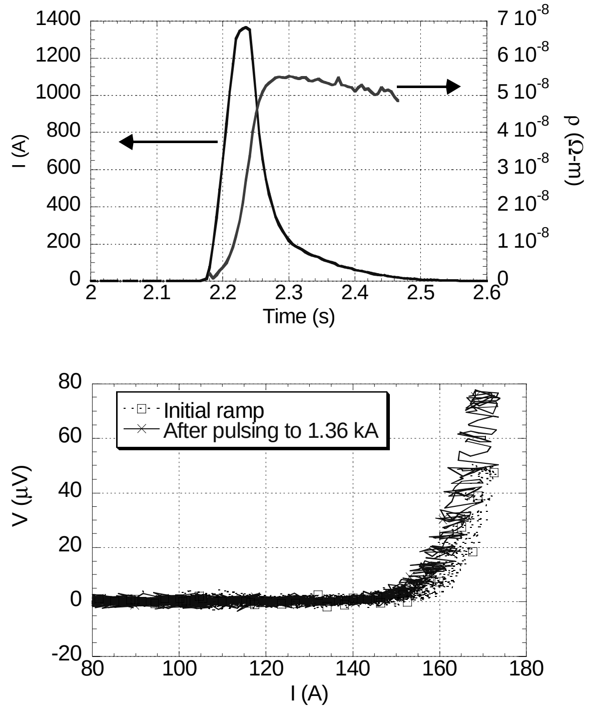

Fig. 1.40. Copper-laminated YBCO tape resistivity increase during a 1.36-kA pulse (top) and voltage-current curve measured after the shot compared with the initial curve (bottom).

1.5.3 Thermal Limitation of HTS Tapes

The resistivities of the copper-plated BSCCO, the stainless steel laminated BSCCO, and the copper-laminated YBCO tapes were all measured from room temperature to about 70 K with a Gifford-McMahon (GM) cryocooler. Superconducting transition temperatures of 109 K were found for the BSCCO tapes and 91 K for the YBCO tape. The resistivity above the superconducting transition can be fitted quite well with linear functions of temperature. These linear temperature dependences were extrapolated above 300 K in the present experiment to determine the average temperature reached in the conductors. The pulse-heating limits on the HTS samples were found by applying pulse currents between 450 and 750 A and by increasing the pulse duration in successive shots to increase the Joule heating in the conductor. Figure 1.41 shows a 450-A, 320-ms pulse shot for sample 1 (the copper-plated BSCCO tape). The resistivity of the tape increased sharply during the pulse and reached a peak of 7.6×10^{-8} Ω-m, which corresponds to a temperature of 725 K. The subsequent voltage-current measurement showed no difference from the initial measurements. The next shot at 450 A for 330 ms raised the peak temperature to about 800 K. The tape was significantly degraded; the critical current dropped from 119 A to below 50 A. For sample 5 (the copper-laminated YBCO tape), a shot of 675 A for 200 ms that raised the average tape temperature to 370 K (Fig. 1.42). After that shot, there was no change in the voltage-current characteristics. The next shot of 330 ms increased the peak temperature to 670 K. After that, the critical current of the YBCO tape dropped from 160 A to 90 A, a large degradation.

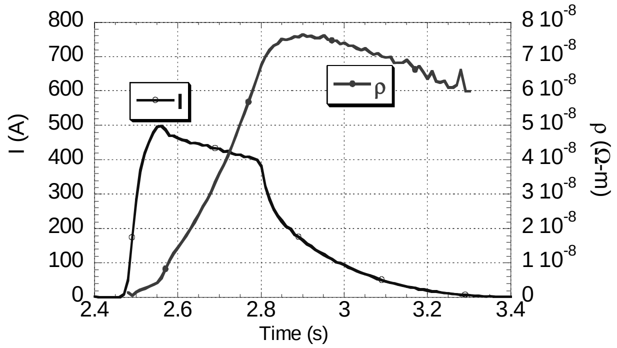

Fig. 1.41. Resistivity change of the copper-plated BSCCO sample during a 450-A, 320-ms overcurrent pulse.

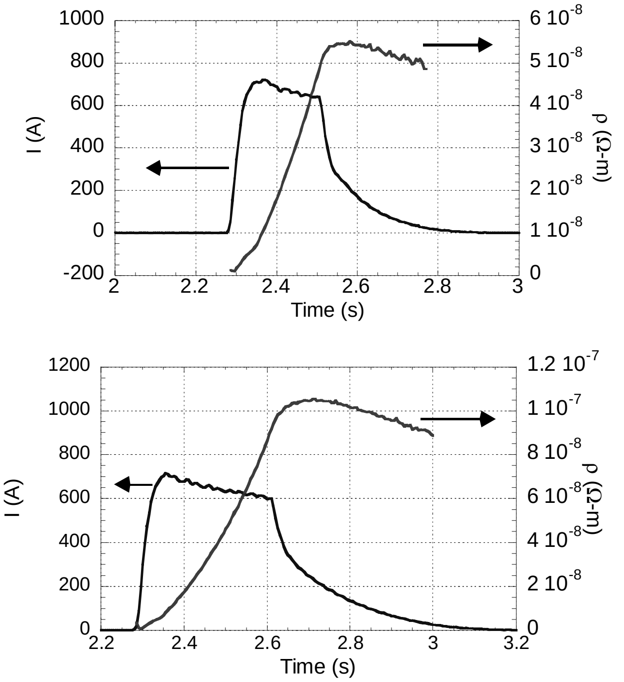

Fig. 1.42. Copper-laminated YBCO tape resistivity increase from a 200-ms pulse (top) and a 330-ms pulse (bottom).

1.5.4 The Effect of an Additional Strip of Copper

Higher peak currents can be drawn from the power supply when a strip of copper with a comparable cross section to that of the HTS tape is added in parallel to the HTS tape. For example, in samples 2, 4, and 6, the peak current reached about 2 kA. However, about 60% of the total current flows through the copper strip during the overcurrent pulse. Therefore, the peak current in the HTS tape was actually lower than it was during the tests of the HTS tape alone. Figure 1.43 shows that the peak current obtained for sample 6 went to 2 kA as compared to the 1.36 kA shown in Fig. 1.42. The conductor temperature only reached 230 K as compared to 370 K without the added copper strip. Thus, the shunting function of the additional copper increases the electromechanical limitation by about a factor of two.

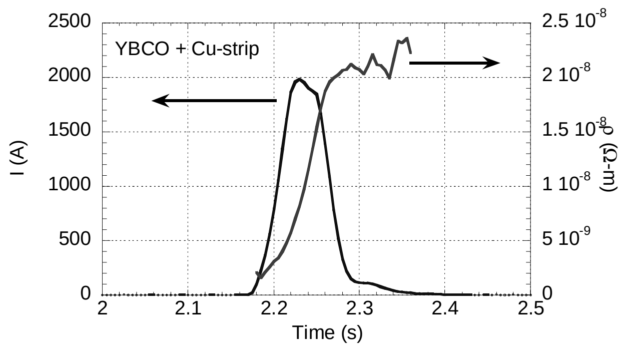

Fig. 1.43. The addition of a strip of copper raised the peak achievable current while it decreased the resistivity increase of the copper-laminated YBCO sample.

Longer pulse lengths can also be tolerated without overheating the HTS tape. In sample 2, the pulse length at a current of 710 A was extended to 600 ms (as compared to sample 1 of 450 A for 320 ms) without degrading the BSCCO tape. In sample 6, the pulse length at 845-A current was extended to 640 ms (as compared to sample 5 of 655 A for 330 ms) with only a small degradation in critical current, from 148 to 142 A in the YBCO tape.

1.5.5 Conclusion

Electromechanical and thermal limitations of overcurrent pulses were measured on BSCCO and YBCO tapes. With pulse lengths as short as 35 ms, the BSCCO tape with a critical current of about 115 to 130 A and the YBCO tape with a critical current of about 150 to 160 A can be pulsed to at least the 1-kA range without electromechanical damage. Longer pulses at moderate overcurrents indicated that both HTS tapes can be heated to over 400 K without suffering degradation. However, heating accelerates as the temperature and the resistivity of the tape gets higher. Thus, a prudent design peak temperature of the HTS tape for short-circuit, overcurrent faults would be 200 to 300 K. Other considerations with regard to the HTS cable, such as nitrogen pressure surge or vapor generation and thus high-voltage breakdown, may further limit the design temperature. When an additional copper strip of about the same cross section as the HTS tape was added, both the overcurrent magnitude and duration limitations about doubled, apparently because of the shunting function and the added heat capacity of the copper strip.

1.6 Conductor Engineering: On the Effect of NiW on the Inductance and AC Loss of HTS Cables

R. C. Duckworth, M. J. Gouge, J. Caughman, J. W. Lue, and J. A. Demko (ORNL); J. Tolbert (Ultera); and C. L. H. Thieme and D. T. Verebelyi (AMSC)

The impact of Ni-5at%W substrates on ac loss and inductance of HTS cables was examined. Two 1.2-m prototype cables were made with stainless steel laminated BSCCO tapes and were wound on a 25.4-mm-diam former. Each cable consisted of two layers of 15 BSCCO tapes wound at opposite lay angles and had an estimated critical current of 3000 A at 77 K. One cable had four additional layers of 4.8-mm-wide Ni-5at%W tape co-wound with the BSCCO tapes to simulate a commercial second-generation HTS cable. The Ni-5at%W tapes had the same width as the BSCCO tapes and a thickness of 50 μm. Through the use of a coaxial copper ground, the cable inductance was measured at room temperature and at liquid nitrogen temperature (77 K); high-frequency rf measurement techniques were used. Experimental results for the cable inductance and ac loss were compared with the results of numerical calculations to determine the significance of the Ni-5at%W substrate contribution.

Table 1.4 summarizes the dimensions of each 1.2-m cable. For the purposes of our discussion, “cable A” refers to the prototype cable without Ni-5at%W tapes; “cable B” refers to the prototype cable with Ni-5at%W tapes. With respect to the materials used in these cables, the HTS tape was 4.8-mm-wide stainless steel laminated BSCCO tape and the Ni-5at%W tape was 4.8-mm-wide and 50 μm thick. For cable B, the sequence of Ni-5at%W and HTS tape is equivalent to a four-layer YBCO cable in which two tapes in a given layer would be connected with the stabilization layers in contact with one another and the Ni-5at%W substrates opposite each other (“face-to-face architecture”).

Table 1.4. Radial dimensions and winding directions for cables A and B

Material	Diameter (mm)	Lay angle (degrees)
Cable A		
Former + bedding	26.42	
15 HTS	27.18	+20
15 HTS	28.19	–20
Cable B		
Former + bedding	26.42	
15 Ni-W	26.54	+20
15 HTS	27.43	+20
15 Ni-W	27.56	+20
15 Ni-W	27.68	–20
15 HTS	28.57	–20
Ni-W	28.70	–20

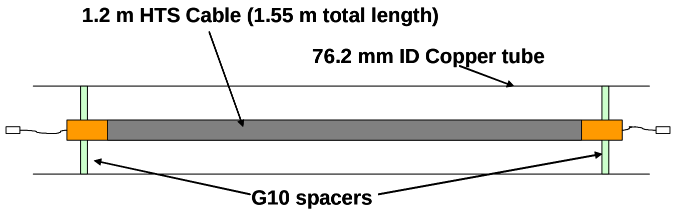

Fig. 1.44. Diagram of inductance measurement setup of HTS cables with respect to 76.2-mm copper pipe ground.

For the inductance measurements of cables A and B, a Sencore LC103 Capacitance and Inductor Analyzer was used to measure the inductance of the cable with respect to a 76.2-mm-diam copper tube grounded to the instrumentation, as shown in Fig. 1.44. Two G10 plates were placed on each copper end plug to isolate the cable from the copper ground and to center the cable inside the copper ground. For the inductance measurement, a wire was used to short the copper end plug to the copper shield at one end; the other end had the ground and copper end plug connected to the probe assembly of the LC103. A small current ramp (< 1 A) with a frequency of 1 MHz was introduced, and the inductance was found from the ratio of the measured electromotive force to the rate of current change over several cycles. This measurement was carried out at room temperature and at 77 K. The measured room-temperature inductances for cables A and B are compared with theoretical and numerical values in Table 1.5.

The increase in the inductance by 25% in cable B (see Table 1.5) was attributed to the Ni-5at%W tapes because, according to analytical coaxial inductance expressions, the inductance of cable B was supposed to decrease because of the increase in the radial build of cable B with respect to the fixed ground. With respect to temperature effects, the inductances of cable A and B did not change when the cable temperature was lowered to 77 K. The inductance for cable B at 77 K was 0.25 µH/m. There is a large difference between the numerical results for cable A and B because the stored energy in the ferromagnetic substrate does not behave as I^2 and because the inductance was calculated at a low current. The inductance decreases quickly to a value of 0.23 µH/m at a current of 1 kA and approaches an asymptotic value of 0.218 µH/m at higher currents due to the saturation of the Ni-5at%W. According to the numerical model, replacement of the Ni-5at%W tape with a nonferromagnetic tape would result in an inductance closer to that predicted by the analytical model.

As determined from the experimental results and analysis, Ni-5at%W tapes influence both the inductance and ac losses in single-phase prototype cables. A 25% increase in inductance from 0.20 µH/m to 0.25 µH/m was observed when the Ni-5at%W tapes were co-wound with stainless steel BSCCO tapes. With respect to ac loss, the addition of the Ni-5at%W substrate produced a ferromagnetic loss contribution of 25% to the ac loss such that $I_{peak}/I_c = 0.7$. The ferromagnetic loss was 0.25 W/m of a total ac loss of 1.05 W/m. To minimize the contribution of the Ni-5at%W tapes to the inductance and ac loss leads,

Table 1.5. Measured room-temperature (295 K) inductances of cables A and B compared with numerical and analytical values

Cable	Inductance (µH/m)		
	Measured	Analytical formulation	Numerical calculation[a,b]
A	0.20	0.204	0.209
B	0.25	0.201	0.339 (0.206)

[a] Stored energy calculated with FlexPDE.

[b] The value for the cable inductance when cable B has nonferromagnetic substrates but the same radial build is given in parentheses.

one can pursue several technical options. One option is to move from a four-layer cable to a two-layer cable. Another is to reduce the amount of Ni-5at%W substrate exposed to the magnetic field produced by the cable. It was shown that by changing from a four-layer to a two-layer cable by increasing the YBCO conductor performance to 300 A/cm-width, the ferromagnetic loss can be reduced from 0.25 W/m to 0.07 W/m. Another approach is to reduce the thickness of the Ni-5at%W from 75 µm to 50 µm where possible. This would further reduce the ferromagnetic loss in a two-layer cable to 0.045 W/m. These techniques would allow the fabrication of HTS cables with YBCO on Ni-5at%W substrates while the development of nonferromagnetic substrates such as Ni-9at%W takes place.

1.7 Conductor Engineering: AC Losses in YBCO Tapes

R. C. Duckworth, J. A. Demko, M. J. Gouge, and J. W. Lue

Electrical measurements of the ac losses at 77 K due to applied ac currents have been examined for 1-cm-wide and 4-mm-wide YBCO coated conductors on Ni-10%Cr-2%W substrates. Each sample was nominally 15 cm long with a conductor architecture of Ni-10%W-2%Cr/Ni/Y203/YSZ/CeO2/1 µm YBCO/3 µm Ag. The critical currents were nominally 100 A/cm-width; the 1-cm sample had a measured critical current of 98 A, and the 4-mm sample had a measured critical current of 40 A. Figure 1.45 shows the losses as a function of current for the 1-cm and 4-mm samples, respectively, in addition to showing the equivalent Norris elliptical and thin strip models.

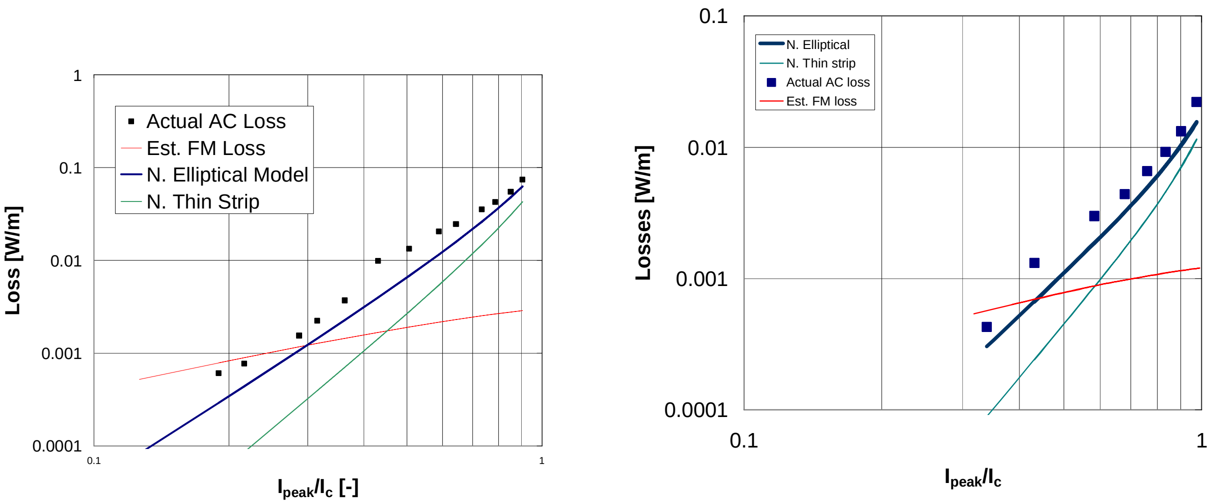

Fig. 1.45. Measured ac loss as a function of peak current ratio compared with equivalent ferromagnetic loss for the Ni-10%Cr-2%W substrate, the Norris elliptical model, and the thin strip model for (left) the 1-cm YBCO conductor and (right) the 4-mm YBCO conductor.

Two conclusions may be drawn from these results: (1) the ferromagnetic loss is significantly lower than that observed with previously measured Ni-5at%W substrates, and (2) both samples have a slightly higher loss when compared with the Norris elliptical model. Because the ferromagnetic loss is significantly lower, the ac loss data can be reduced further by dividing by the square of the critical current of the sample. As shown in Fig. 1.46, the transport losses have a width dependence, but it is really a dependence on the critical current because the critical current per unit width between the samples are nearly the same. If the critical currents of the 4-mm sample were increased, their losses would be lower.

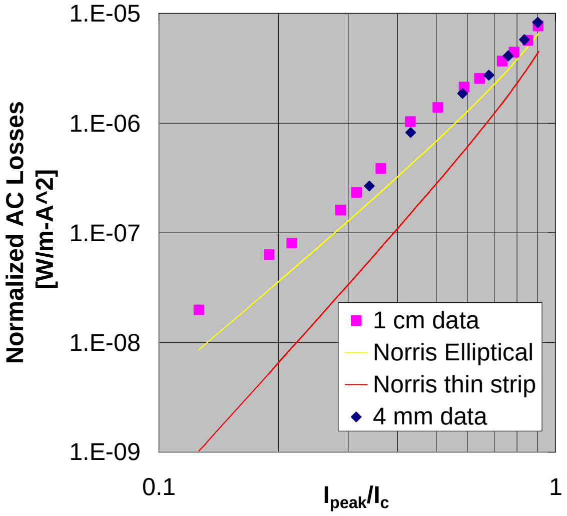

Fig. 1.46. Normalized ac losses for 1-cm and 4-mm YBCO on Ni-10%Cr-2%W substrates.

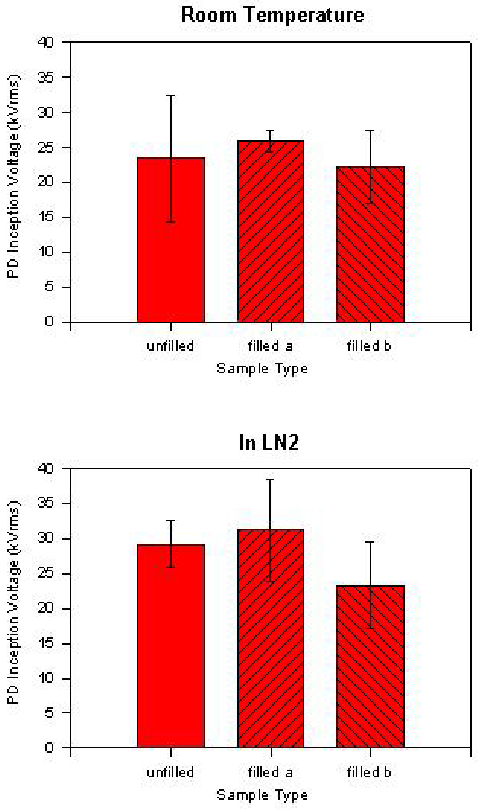

Fig. 1.47. PD inception for three types of Material 1 samples at room temperature and in liquid nitrogen. Error bars indicate the standard deviation of all measurements for the given sample type.

1.8 Dielectric Materials R&D

A. R. Ellis, R. Grabovickic, D. R. James, and I. Sauers

1.8.1 Partial-Discharge Data

Sample disks of three types of a commercial plastic (referred to here as Material 1, 1a, and 1b) were tested for PD. One type of Material 1 is unfilled while the other two (a and b) are filled materials with 30% and 40% filler, respectively. The disks were 4 in. in diameter and 3 mm thick. The electrodes were 3.5 in. in diameter, leaving about a 0.25-in. ring of sample outside the electrode. The room-temperature data were taken with the samples immersed in oil. For each sample type, two or more disks were tested, and for each disk there were two to four independent runs. The results at room temperature and in liquid nitrogen are shown in Fig. 1.47.

The PD inception voltage was operationally defined as the voltage at which the average charge of all PD pulses accumulated over 60 s was 5 pC. There was considerable variation in PD inception voltages from sample to sample of the same sample type and even from run to run on the same sample disk. The reason for the variation is not known at present. Because of the scatter in the data (as indicated by the error bars, which give the standard deviation for each sample type), there is no significant difference between the unfilled and the two filled sample types.

The three sample types showed a small increase in PD inception going from room temperature to liquid nitrogen. It is somewhat surprising that the filled samples did not show a more significant decrease in PD inception than the unfilled samples. It is possible that the PD may be coming from the triple junction where the electrode, sample, and oil (or liquid nitrogen) come together, which could explain why the PD inception appears to be independent of the sample type. On the other hand, the liquid nitrogen data indicate that the PD inception increases despite the lower dielectric constant of the liquid nitrogen over that in oil, which would have the tendency to reduce the strength, implying that the material property Material 1 is playing a role in the PD inception voltage. The lowest PD inception strength for all sample types and temperatures, approximately 15 kV/mm, provides at least a lower bound for these materials.

1.8.2 Flashover and Puncture Strength of Solid Cylinders

Cylinders of a commercial material (designated Material 2) were tested for puncture and flashover strength by negative polarity lightning impulse (1.2 × 50 μs) voltages at room temperature and in liquid nitrogen. The liquid nitrogen tests were performed in an open bath at 1 bar and in a high-voltage cryostat at elevated pressure. Figure 1.48 shows a schematic of a cylinder and electrode arrangement. The breakdown results are summarized in Table 1.6. A log-log plot of the puncture strength as a function of cylinder thickness is shown in Fig. 1.49. Based on the four data points obtained thus far, a minimum cylinder thickness of 6 mm is predicted to meet a 200-kV BIL.

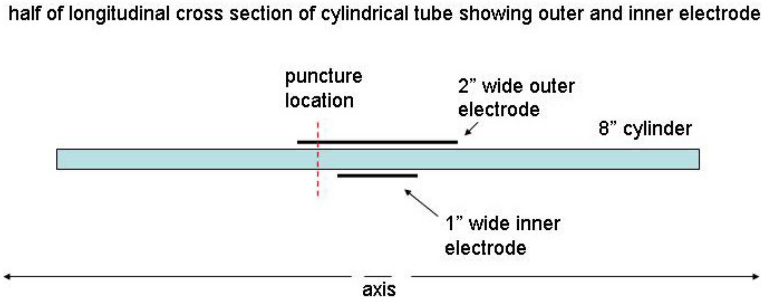
half of longitudinal cross section of cylindrical tube showing outer and inner electrode
puncture location
2" wide outer electrode
8" cylinder
1" wide inner electrode
axis

Fig. 1.48. Schematic of Material 2 cylinder showing electrode geometry and puncture location.

Table 1.6 Impulse breakdown of the Material 2 cylindrical tube
Dimensions: 8 in. (203 mm) long, 3.5 in. (89 mm) diam

Thickness, in. (mm)	Air (1 atm)		Liquid nitrogen	
1/16 (1.6)	250 V/mm	Flashover	47.9 kv/mm	Puncture (1 bar)
1/16 (1.6)	–	–	48.5 kv/mm	Puncture (1 bar)
1/8 (3.2)	–	–	40.0 kv/mm	Puncture (high pressure)
1/2 (12.7)	–	–	25.4 kv/mm	Flashover (high pressure)

1.9 Cryogenics Initiative

M. J. Gouge and J. A. Demko

Kick-off visits were conducted in early November 2003 to Praxair and Cryomech to review the technical approach that the contractors specified in their respective proposals and the cryogenic R&D infrastructure at the vendor locations to conduct the 3-year R&D program. No funds were provided for the Praxair and Cryomech Cryogenics Initiative subcontracts in FY 2004 due to budget reductions by the DOE Office of Electric Transmission and Distribution. The intent is to shift the 3-year work scope 1 year forward to FY 2005–2007.

1.10 SPI Oversight/Readiness Reviews

M. J. Gouge and S. W. Schwenterly (ORNL); S. Ashworth (LANL)

This was an active year for the SPI Readiness Review Program. The Matrix Fault Current Limiter (MFCL) Review on October 14 and 15, 2003, included a report on design progress since the conceptual design review in June, the AEP Sporn substation study update, cryostat tests and overcurrent (low-voltage)

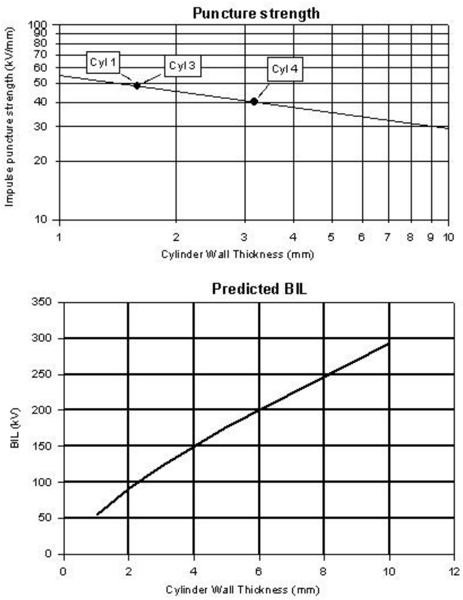

Fig. 1.49. The decrease in puncture strength of Material 2 with cylinder thickness (upper). The BIL voltage based on the straight line fit to the log-log plot in the upper graph (lower).

testing of the MFCL tubes at Nexans, and matrix mock-up modules in the test cryostat at the Florida State University Center for Advanced Power Systems.

A review of the Flywheel Project was conducted at the Boeing facilities in Seattle on October 21 and 22. Boeing presented a comprehensive overview of its program, including the work that has been accomplished over the past several years and the future direction of the program. Much of the focus was on reviewing the 3-kW/10-kWh system, for which component testing resulted in a flywheel failure during a spin test.

The Open Magnetic Resonance Imaging System being developed at Oxford Superconducting Technology was reviewed on November 14, and Oxford staff provided an update on their tradeoff evaluation between bare and sheathed BSCCO 2212 tape conductors. Additionally, a team led by Steve Ashworth, of Los Alamos National Laboratory (LANL) reviewed the Long Island Power Authority (AMSC/Nexans) and Albany (SuperPower/SEI) HTS cable projects during November and December.

A three-person team again led by Steve Ashworth, reviewed the Ultera (Southwire/NKT/ORNL) HTS cable project on February 10 and 11, 2004, at Southwire Company, Carrollton, Georgia.

M. J. Gouge conducted an informal progress review of the 100-MVA HTS Generator Rotor Project at GE, Schenectady, New York, on May 3, 2004. The following day he participated in a Technical Advisory Board Meeting for the SuperPower MFCL Project in Schenectady.

A readiness review of the Rockwell HTS motor project was conducted on August 19, 2004. Reviewers were Paul Bakke (DOE-Golden), Mike Gouge (ORNL), and Bill Schwenterly (ORNL). Participants from Rockwell included Rich Schiferl, D. Panda, Joe Zevchek, and Boris Shoykhet. The format included presentations by Rockwell, technical discussions, and a laboratory hardware tour, which included components from the previous 1000-HP HTS motor demonstration and the present R&D focus areas. A readiness review report was prepared and sent to Rockwell management and DOE-HQ.

The R&D focus areas for this project are as follows:

- motor-drive interaction,
- eddy-current heating in end regions,
- alternate (second-generation) HTS wire,
- alternate HTS motor topologies,
- on-board refrigeration,
- cryogenic persistent switch,
- composite torque tube creep and fatigue, and
- coil quench protection.

1.11 2003 IEEE Conference on Electrical Insulation and Dielectric Phenomena

Isidor Sauers and D. Randy James attended the 2003 IEEE Conference on Electrical Insulation and Dielectric Phenomena (CEIDP) held in Albuquerque, New Mexico, October 19–22, 2003 [4]. Two poster papers were presented and published in the annual report of the CEIDP. All major topics of electrical insulation were covered, including material characteristics, aging, space charge, breakdown and flashover, outdoor insulation, gases, modeling, PD, treeing, electrohydrodynamics, and biodielectrics. Many of the papers deal with topics and mechanisms relevant to cryogenic insulation. Of particular interest was PD in voids, which is a common problem for epoxy insulation. Cryogenic insulation papers included electrification of liquid nitrogen in polymeric pipes and breakdown associated with bubble formation in liquid nitrogen. Several discussions were held with attendees on how voids in epoxy are formed and how they can be mitigated

1.12 References

1. M. A. Young et al., “Burn-Out Tests of 1st and 2nd Generation HTS Tapes in Liquid Nitrogen Bath Cooling,” *Advances in Cryogenic Engineering Materials*, **50B**, 860 (2004).
2. R. Grabovickic et al., “Measurements of Temperature Dependence of Partial Discharge in Air Gaps between Insulated BSCCO Tapes,” in 2004 Conference on Electric Insulation and Dielectric Phenomena (CEIDP), Boulder, Colorado, October 17–20.
3. R. Grabovickic et al., “Partial Discharge and Accelerated Pulsed Aging of Insulation between Parallel Plane-Plane Stainless Steel Electrodes and between Bi-Sr-Ca-Cu-O Tapes at Room Temperature,” pp. in 2004 Conference on Electric Insulation and Dielectric Phenomena (CEIDP), Boulder, Colorado, October 17–20.
4. IEEE Conference on Electrical Insulation and Dielectric Phenomena (CEIDP), Albuquerque, New Mexico, October 19–22, 2003.

2. Technical Progress in Wire Development

2.1 High-Performance YBCO Coated Superconductor Wires*

M. P. Paranthaman (ORNL) and T. Izumi (ISTEC-SRL)

2.1.1 Introduction

Since the discovery of high-temperature superconductors, notably bismuth strontium calcium copper oxide (BSCCO) and $YBa_2Cu_3O_{7-x}$ (YBCO), researchers all around the world have searched for ways to produce affordable flexible wires with high current density. The potential use of high-temperature superconductor (HTS) wires for electric power applications include underground transmission cables, oil-free transformers, superconducting magnetic-energy storage units, fault current limiters, high-efficiency motors, and compact generators. Much progress has already been made, from the near-term commercialization of the first-generation BSCCO superconductor tapes to the continuing advancement of second-generation YBCO coated conductors.

Potentially lower manufacturing cost and improved properties in magnetic fields at liquid nitrogen temperatures are some of the advantages of YBCO coated conductor composites over BSCCO multifilament composites. BSCCO wire is formed by essentially surrounding a powder with a silver tube followed by deformation and heat treatments to produce a narrow tape. The YBCO coated conductor technology is a fundamentally different approach, based on producing an epitaxial thin film on a flexible metal substrate.

The U.S. Department of Energy's (DOE's) target price for the conductor is close to the current copper wire cost of $10/kA-meter. The strategic goal is to achieve HTS wire with a current capacity 100 times that of copper. Robust, high-performance HTS wire will certainly revolutionize the electric power grid and other electric power equipment as well.

American Superconductor Corporation (AMSC) has been widely recognized as one of the world leaders in using the oxide-powder-in-tube process to manufacture first-generation HTS wires based on BSCCO materials. AMSC has achieved electrical critical currents of more than 125 A in piece lengths of several hundreds of meters, and a champion current of 170 A at 77 K and self-field at the standard 4.1 mm width and 210 μm thickness [1]. However, due to the higher cost of first-generation wire, the researchers shifted their research toward the development of a second generation of wires based on YBCO. One of the main obstacles to the manufacture of commercial lengths of YBCO wire has been the phenomenon of weak links (i.e., grain boundaries formed by the misalignment of neighboring YBCO grains) that are obstacles to current flow. Careful alignment of the grains can produce low angle boundaries between superconducting YBCO grains, thus allowing more current to flow. In fact, below a critical misalignment angle of 4°, the critical current density approaches that of YBCO films grown on single crystals [2]. The other important advantages of second-generation wires over first-generation wires are that YBCO has better in-field electrical performance at higher temperatures, potentially lower cost to process, and low ac losses. Schematics of first- and second-generation HTS wire architectures are shown in Fig. 2.1.

Several methods have been developed to obtain biaxially textured substrates suitable for high-performance YBCO films, including ion-beam-assisted deposition (IBAD), Rolling-Assisted Biaxially Textured Substrates (RABiTS™), and inclined substrate deposition (ISD). The industry standard for characterizing the second-generation wire is to divide the current by the width of the wire. With either a 3-μm-thick YBCO layer carrying a critical current density of 1 MA/cm^2 or a 1-μm-thick YBCO layer carrying a critical current density of 3 MA/cm^2, the electrical performance would jump to 300 A/cm-width. Conversion of these numbers to the industry standard of 0.4-cm-wide HTS wire would correspond to 120 A, which is comparable to that of the commercial first-generation wire manufactured by AMSC.

---

*Adapted from M. P. Paranthaman and T. Izumi, "High-Performance YBCO Coated Superconductor Wires," *MRS Bulletin* **29** (8), 533 (2004).

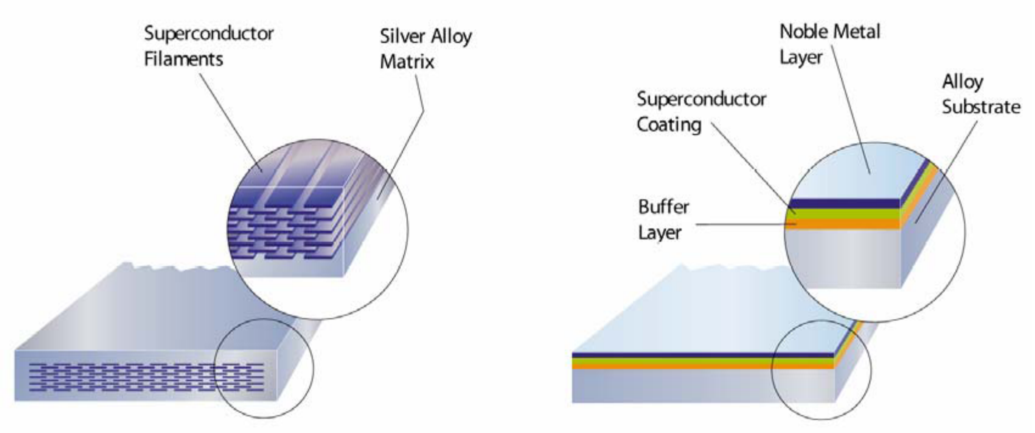

Fig. 2.1. Schematics of HTS superconducting architectures. Left: first-generation BSCCO multifilamentary wire composite. Right: second-generation YBCO coated conductor composite.

Further increasing the thickness or finding a way to incorporate two layers of YBCO (either a double-sided coating or joining two YBCO tapes face to face) in a single wire architecture would then give performance exceeding first-generation tapes (i.e., high overall engineering critical current density at 77 K).

In the IBAD process, an ion beam is used to grow textured buffer layers onto a flexible but untextured metal, typically a nickel alloy. After the initial announcement of an IBAD process that uses yttria-stabilized zirconia (YSZ) by Iijima et al. [3], researchers at Los Alamos National Laboratory (LANL) perfected the process and achieved high-performance YBCO films on IBAD-YSZ templates [4]. To date, YSZ, gadolinium zirconium oxide (GZO) or magnesium oxide (MgO) IBAD templates have been used to make YBCO tapes. The schematics of the IBAD architectures are shown in Fig. 2.2. The RABiTS™ process, developed at ORNL, utilizes thermomechanical processing to obtain flexible, biaxially oriented nickel or nickel-alloy substrates [5]. Both buffers and YBCO superconductors are then deposited epitaxially on the textured nickel alloy substrates. The starting substrate serves as a structural template for the YBCO layer, which has substantially fewer weak links. For comparison, first-generation wires made by the oxide-powder-in-tube process are expensive because the primary component is high-purity silver. However, in the RABiTS™ process, the silver is replaced by a low cost-nickel or nickel alloy, which allows for fabrication of less expensive HTS wires. A schematic of the RABiTS™ process is shown in Fig. 2.3.

During the RABiTS™ process, an untextured metal alloy is rolled to produce a particular desired rolling texture, which, upon annealing results in a sharp cube texture. Epitaxial buffer layers (generally, a

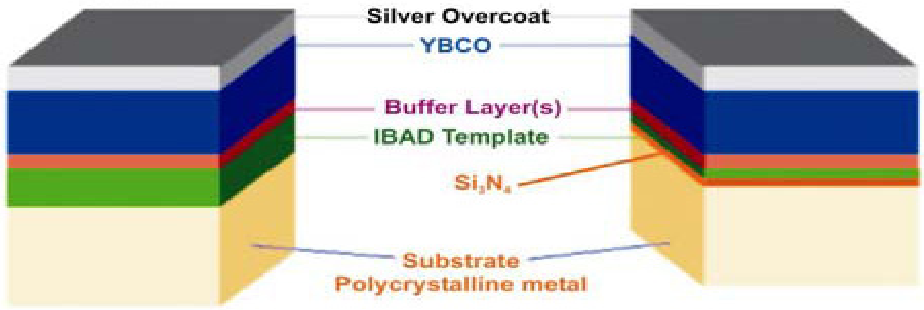

Fig. 2.2. Schematics of the IBAD process wire architectures. Left: YSZ/$Gd_2Zr_2O_7$ (GZO) template. Right: MgO template.

seed layer, a barrier layer, and a cap layer) are deposited epitaxially on the cube-textured substrate. Epitaxial superconductors such as YBCO are then deposited onto the RABiTS™ surface.

In the ISD process, the textured buffer layers are produced by vacuum-depositing material at a particular angle on an untextured nickel alloy substrate. After the discovery of ISD-YSZ process by Hasegawa et al. in 1996 [6], both Argonne National Laboratory (ANL) [7] and THEVA/Technical University of Munich, Germany [8], perfected reel-to-reel MgO buffer layer ISD texturing on Hastelloy tape. Ma et al. [7] have used pulsed laser deposition (PLD) to grow YBCO with a critical current density of 1.2 MA/cm^2 at 77 K and self-field on short ISD-MgO templates with YSZ/CeO$_2$ buffers. Recently, the THEVA group in Germany [8] has achieved grain alignment of 7 to 8° in MgO-ISD tapes. By using in situ electron beam co-evaporation to grow DyBa$_2$Cu$_3$O$_7$ films, they have achieved an improvement of 1 to 2° in the MgO layer. The typical HTS coating thickness is between 1.5 and 2.0 μm. THEVA has also reported a critical current density of 2.3 MA/cm^2 in 20-cm-long tapes with a critical current of more than 400 A/cm-width. Several meter-long tapes exhibited critical current densities of 1.4 to 1.5 MA/cm^2 at 77 K and self-field.

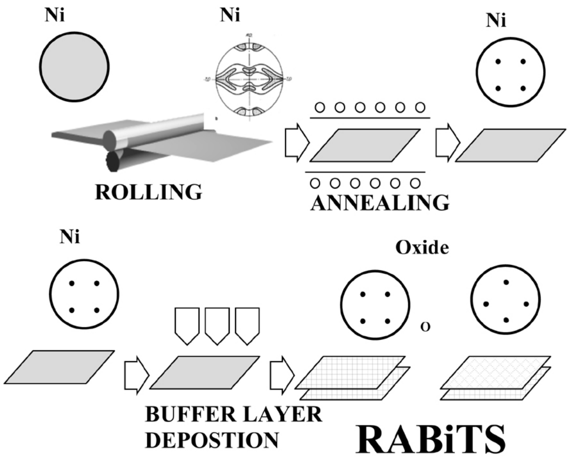

Fig. 2.3. Schematic of the RABiTS™ process.

2.1.2 The State of the Art

Recently, several industries have demonstrated that they can produce second-generation wires in 10- to 100-m lengths with critical currents ranging from 50 to 300 A/cm-width. For example, methods have been developed to produce oriented templates for growing high-performance YBCO coated conductor wires. This includes IBAD-MgO [9], ISD-MgO [8], RABiTS™ [10], and IBAD-GZO [11] templates. High-rate YBCO deposition processes, including trifluoroacetate-based metal-organic deposition (TFA-MOD) [12], metal-organic chemical vapor deposition (MOCVD) [13], and high-rate pulsed laser deposition (HR-PLD) [14], have also been developed. These developments represent the current status and future prospects for methods to produce YBCO coated conductor composite wire.

2.1.2.1 High-Performance Templates

The requirement for a thick YSZ buffer layer (~1.0 μm) to achieve proper texture such that the subsequent YBCO films have high critical current densities may limit the economical fabrication of long-length coated conductors. However, the IBAD-MgO exhibits good texture soon after the nucleation, and only about 10-nm-thick MgO films are needed to optimize the texture [9]. The texture development in an IBAD-MgO template depends strongly on the smoothness of the starting nickel alloy tapes. In collaboration with SuperPower, LANL has already optimized the reel-to-reel electropolishing of Ni alloy substrates and has achieved substrates with a surface roughness of less than 1 nm.

Perovskite buffers such as LaMnO$_3$, SrTiO$_3$, and SrRuO$_3$ have been found to be compatible with IBAD-MgO substrates. In a typical IBAD-MgO template, a total of five buffer layers are involved: (1) an Al$_2$O$_3$ barrier, (2) an amorphous Y$_2$O$_3$ as the nucleation layer, (3) an IBAD-MgO layer, (4) a homo-MgO layer, and (5) a layer of either SrTiO$_3$ or LaMnO$_3$. On IBAD-MgO templates, 1.4-μm-thick YBCO films with a critical current of 109 A (in a 3.8-m length) and 144 A (in a 1.6-m length) have been achieved.

The most commonly used RABiTS™ architecture by AMSC consists of a starting template of biaxially textured Ni-W (3 or 5%) with a seed layer of 75-nm-thick Y$_2$O$_3$, a barrier layer of 75 nm YSZ, and a cap layer of 75-nm-thick CeO$_2$ [10]. In that architecture, all the buffers have been deposited by using all physical vapor deposition (PVD) processes. However, efforts are being made to replace these layers with alternative architectures and multifunctional buffers deposited by industrially scalable thin-film deposition methods. Recently, AMSC has achieved a high critical current of 250 to 270 A/cm-width with a standard deviation of 2.0 to 4.0%. For certain applications, it is necessary to start with completely nonmagnetic substrates such as Ni-W 9% or Ni-Cr-W substrates. Efforts are under way to address these issues.

For deposition of YSZ, pyrochlore-based GZO has rather higher optimized temperatures (~200°C) than room temperature, which are difficult to maintain during deposition because of the indirect heating from the source [11]. In addition, better in-plane textures were observed in GZO within a shorter time (being as much as half that for YSZ). Fujikura has produced 100-m lengths of YBCO tape by PLD on GZO templates with an average in-plane texture ($\Delta\Phi$) of 10° and a tape moving speed of 0.5 m/h. In addition, self-epitaxial CeO_2 caps produced by PLD on IBAD-GZO templates had much improved texture ($\Delta\Phi$ of ~3°) in a very short time. Furthermore, no cracks were observed in the CeO_2 layers. High-critical-current YBCO films were grown on CeO_2/IBAD-GZO templates by using both PLD and TFA-MOD. High critical currents were realized by the multiple-coating method, especially by TFA-MOD.

Very recently, THEVA group reported the growth of $DyBa_2Cu_3O_7$ films with critical currents of 122 A/cm over 10-m-long ISD-MgO by using electron beam evaporation [15].

2.1.2.2 High-Performance Coatings

The MOD process involves three steps: coating, decomposition, and reaction [12]. AMSC has used MOD YBCO and RABiTS™ templates to produce high-performance YBCO coated conductors. The most commonly used MOD process involves the use of yttrium, barium, and copper TFAs in methanol. The decomposition step involves the slow (10-h) burn-out step to reduce volatility.

The YBCO film thickness is limited to less than 0.5 µm. Therefore, new copper precursors have been developed at various places to reduce the volatility of the copper and the fluorine content in the precursors, to increase the thickness of the films to more than 0.5 µm, and to shorten the YBCO processing time. The YBCO growth rates have been increased up to 10 nm/s for processing the YBCO films under reduced pressures. The MOD YBCO films have a laminar microstructure, unlike the columnar microstructure for PLD YBCO films. AMSC routinely uses 0.8-µm-thick MOD YBCO on RABiTS™ templates to produce 10 m ×1 cm lengths of second-generation wires. However, it is a big challenge is to produce ~1.5-µm-thick YBCO films in a single coat. The incorporation of dispersed "nanodots" (nanoparticles) in the YBCO matrix has been shown to enhance critical current retention in magnetic fields. Enhancement of flux pinning in YBCO/REBCO films is currently of great interest in the HTS community.

The MOCVD process has been widely recognized as a viable high-throughput method [13]. However, the cost of the precursors could still be an important deterrent to its use. SuperPower has produced 18-m lengths of YBCO tapes with an end-to-end critical current exceeding 100 A on IBAD templates and high deposition rates (12 nm/s) with critical current levels of 230 A/cm-width in short lengths.

The incorporation of rare-earth elements has been evaluated as a method to improve flux pinning in HTS conductors. Samarium-doped (10%) YBCO films exhibit a critical current density of 230 A/cm. In comparison, undoped YBCO films exhibit a critical current of 193 A/cm. The observed *c*-axis peak at 77 K and 1 Tesla (applied magnetic field) is also higher and broader for the doped sample than for the undoped sample. SuperPower is aggressively pursuing this MOCVD process for commercial manufacturing of coated conductors. Recently, SuperPower has also achieved world record performance of 6000 A-m in a 57-m HTS YBCO wire, 60% greater than the previous world record, which Fujikura announced last year. In that case, PLD was used to deposit the YBCO.

The HR-PLD method has been used on IBAD-YSZ templates to produce YBCO films with a critical current of 480 A/cm in short lengths and 360 A/cm in 6-m tapes [14]. Recently, it has been shown that HR-PLD has increased film deposition speed to 60 nm m^2/h. Further increase of deposition speed, to

140 nm m^2/h, is possible. It is still a big challenge is to use the PLD process to fabricate lower-cost YBCO coated conductors. We have to wait and see how this process comes out in the future.

2.1.3 Summary

The electrical performance for the world's second-generation HTS wires is shown in Fig. 2.4. Design engineering and performance considerations regarding conductor geometry for power applications in 2010 are summarized in Table 2.1 [16].

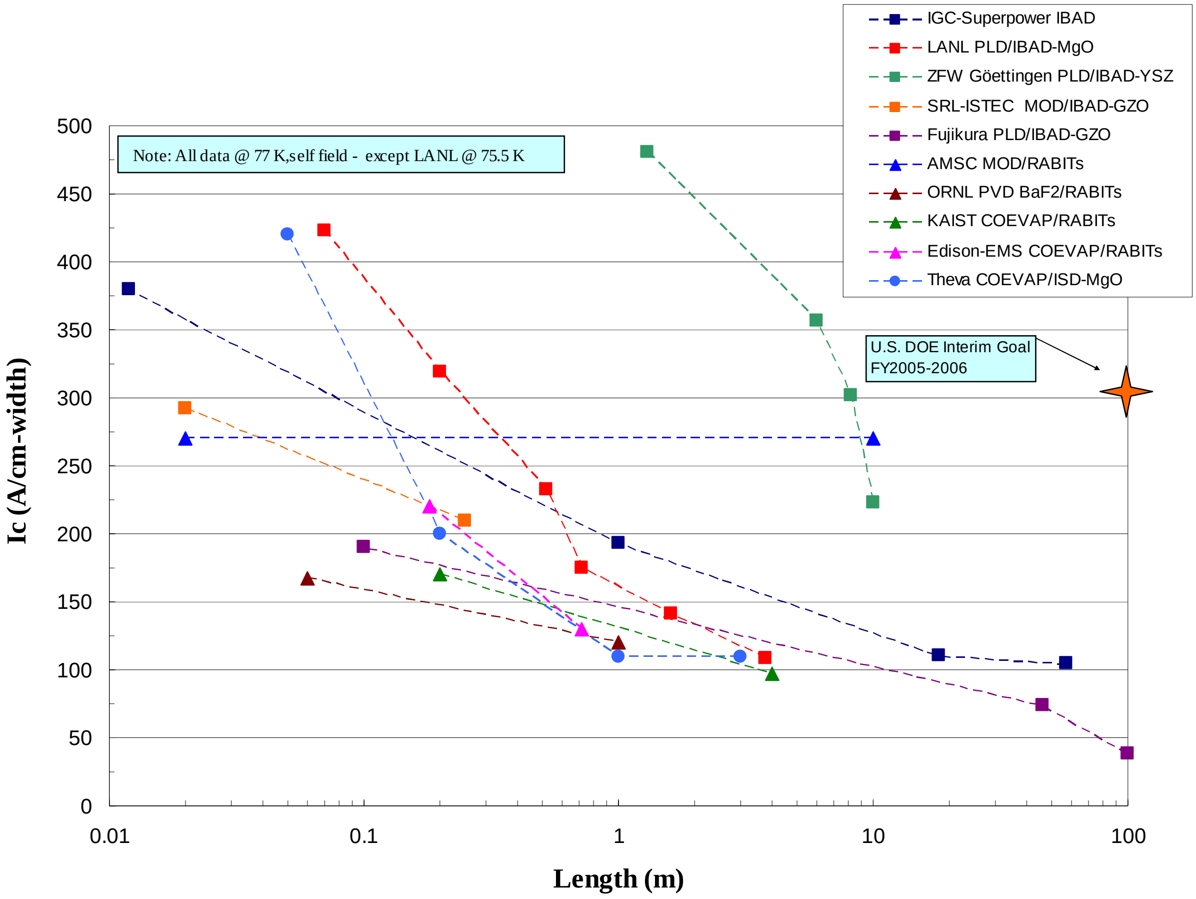

Fig. 2.4. Electrical performance for world's second generation HTS wire.
Source: P.N. Arendt, private communication.
Abbreviations:
IGC: Intermagnetics General Corporation
LANL: Los Alamos National Laboratory
ZFW: Zentrum fuer Funktionswerkstoffe gGmbH Windausweg (Germany)
SRL-ISTEC: Superconductivity Research Laboratory International Superconductivity Technology Center (Japan)
Fujikura Ltd. (Japan)
AMSC: American Superconductor Corporation
ORNL: Oak Ridge National Laboratory
KAIST: Korean Advanced Institute of Science and Technology
Edison-EMS (Spain)
THEVA (Germany)

Table 2.1. Considerations involved in developing the second generation of HTS wires by 2010[a]

Design and engineering considerations	Performance and operating specifications
Face-to-face	J_E = 10–20 kA/cm^2 at 30 to 65 K and 3 T
Neutral axis	I_c = 100–200 A at operating conditions
Alternate conductor designs	I_c = 1000 A/cm-width @ 77 K and self-field
Conducting substrates	Stabilizer design
Two-sided coating	Stress = 200 MPa (300 MPa) @ 77 K
Current carrying capacity of stabilizer	Irreversible strain limit = 0.4–0.6 % tension
Low ac loss	Compression for magnets = 0.3–1 %
Length: 100–1000 m	bend diameter = 2 to 3.5 cm
Width:≤ 4.1 mm	ac loss = 0.25 W/kA-meter
High-volume price: ~$10/kA-m	*n* value ≥ 14

[a] Compiled at the Coated Conductor Development Roadmapping Workshop II (U.S. DOE, Washington, D.C., July 28–29, 2003).

In summary, several templates comprising of IBAD-YSZ, IBAD-GZO, IBAD-MgO, ISD-MgO, and RABiTS™ have been developed, and superconductivity companies around the world are in the process of taking the technology to the pilot scale to produce commercially acceptable 100-m lengths. In addition, three different methods (MOD, MOCVD, and HR-PLD) have been used to demonstrate high critical currents in YBCO coated conductors exceeding 10 m in length.

2.1.4 References

1. L. Masur et al., *Proceedings of the EUCAS Conference*, Sorrento, Italy, Sept. 15–18, 2003 (in press).
2. D. Dimos, P. Chaudhari, and J. Mannhart, "Superconducting Transport Properties of Grain Boundaries in $YBa_2Cu_3O_7$ Bicrystals," *Phys. Rev. B* **41** (7), 4038–49 (1990).
3. Y. Iijima et al., "In-Plane Aligned $YBa_2Cu_3O_{7-x}$ Thin Films Deposited on Polycrystalline Metallic Substrates," *Appl. Phys. Lett.* **60** (6), 769–71 (1992).
4. X.D. Wu et al., "Properties of $YBa_2Cu_3O_{7-\gamma}$ Thick Films on Flexible Buffered Metallic Substrates," *Appl. Phys. Lett.* **67** (16)**,** 2397–99 (1995).
5. A. Goyal et al., "High Critical Current Density Superconducting Tapes by Epitaxial Deposition of $YBa_2Cu_3O_x$ Thick Films on Biaxially Textured Metals," *Appl. Phys. Lett.* **69** (12) 1795–97 (1996).
6. K. Hasegawa et al., pp. 745–48 in *Advances in Superconductivity IX, Proc. of the 9th Intl. Symp. on Superconductivity (ISS '96)*, ed. S. Nakajima and M. Murakami, Sapporo, Japan (1996).
7. B. Ma et al., "High Critical Current Density of YBCO Coated Conductors Fabricated by Inclined Substrate Deposition," *Physica C* **403** (3), 183–90 (2004).
8. W. Prusseit et al., "Evaporation—The Way to Commercial Coated Conductor Fabrication," *Physica C* **392–396** (2), 801–805(2003).
9. P. N. Arendt and S. R. Foltyn, "Biaxially Textured IBAD-MgO Templates for YBCO-Coated Conductors," *MRS Bulletin* **29** (8), 543 (2004).
10. A. Goyal, M. Paranthaman, and U. Schoop, "The RABiTS Approach: Using Rolling-Assisted Biaxially Textured Substrates for High-Performance YBCO Superconductors," *MRS Bulletin* **29** (8), 543 (2004).
11. Y. Iijima et al., "Research and Development of Biaxially Textured IBAD-GZO Templates for Coated Superconductors," *MRS Bulletin* **29** (8), 552 (2004).
12. M. W. Rupich et al., "Metalorganic Deposition of YBCO Films for Second-Generation High-Temperature Superconductor Wires," *MRS Bulletin* **29** (8), 564 (2004).
13. V. Selvamanickam et al., "MOCVD-Based YBCO-Coated Conductors," *MRS Bulletin* **29** (8), 579 (2004).
14. A. Usoskin and H. C. Freyhardt, "YBCO-Coated Conductors Manufactured by High-Rate Pulsed Laser Deposition," *MRS Bulletin* **29** (8), 583 (2004).

15. W. Prusseit et al., International workshop on coated conductors (CCA 2004), Kanagawa, Japan, November 19, 2004.
16. Proceedings of the Coated Conductor Roadmapping Workshop II, Washington DC, July 28–29, 2003, Prepared by Energetics, Inc., Superconductivity for Electric Systems Program, Office of Electric Transmission and Distribution, U.S. DOE, DOE/EE-000820404-CD.

2.2 Oxidation of Carbon on Nickel-Based Metallic Substrates: Implications for HTS Coated Conductors

F. A. List, L. Heatherly, D. F. Lee, K. J. Leonard, and A. Goyal

2.2.1 Introduction

For the past decade, the development of HTS coated conductors has relied predominantly on nominally pure nickel and nickel-based alloy substrates. These substrates (generally ~50–100 μm thick) provide a strong, flexible support for an epitaxial multilayer structure consisting of a variety of oxide buffers (~0.1–0.5 μm thick) and superconductors (~0.3–3 μm thick) [1–4]. Nickel and nickel-based alloy substrates can also provide a potentially significant and unintended source of carbon—carbon initially in the form of a substrate impurity. The role that the carbon can play in conductor fabrication is addressed in this paper.

One of the challenges for successful fabrication of HTS coated conductors is to maintain mechanical integrity of the multilayer structure throughout all processing steps. Detachment of the buffer layers from the substrate is occasionally observed during processing and leads to a catastrophic degradation of conductor performance. In order to reduce the tendency for buffer layers to detach, the factors contributing to detachment must be identified, understood, and controlled. Clearly, many factors can contribute to buffer layer detachment including (a) film stress (both thermally and growth induced), (b) film porosity and morphology (leading to enhanced diffusion and interface reactions), and (c) interfacial segregation of impurities. In this study, we attempt to demonstrate that the oxidation of carbon impurities to form CO can be a significant factor contributing to buffer layer detachment and that a simple heat treatment of the substrate in oxygen can effectively eliminate detachment caused by CO formation.

The oxidation of carbon impurities to form CO on refractory metal surfaces has been known for some time and has in some cases been used to measure the bulk diffusivity of carbon [5,6]. Similarly, studies of CO desorption from oxygen-covered nickel surfaces [7–10] have led to a fairly detailed understanding of underlying reaction mechanisms for CO desorption. Using Auger electron spectroscopy and temperature-programmed desorption, List and Blakely [10] identified three distinct CO peaks for nickel surfaces exposed to oxygen at room temperature. The lowest temperature peak (75–275°C) was associated with desorption of molecularly adsorbed CO from the background gas. The next peak (275–475°C) was related to a reaction between adsorbed oxygen and carbon bond to surface defects. The third peak (325–925°C), which was generally the most intense peak, was associated with a surface reaction involving adsorbed oxygen and carbon that had diffused from within the nickel. A carbon oxidation reaction similar to that associated with this third peak is believed to result in CO formation at the oxide/metal interface of HTS coated conductors.

The minimum level of interfacial CO that might be expected to lead to buffer layer detachment is perhaps ~1 monolayer (one CO molecule for each surface substrate atom). A simple calculation shows that in order to generate ~1 monolayer of interfacial CO on each side of a nickel-based, 50-μm-thick substrate, a carbon impurity level in the substrate of only ~7 at. ppm is required. Carbon impurity levels for commercially available nickel and nickel-based alloys range from ~100 at. ppm (for Ni-270) to >2000 at. ppm [11]. These levels of carbon clearly suggest the potential for commercially available substrates to produce substantial amounts of interfacial CO (~14 to >286 monolayers).

The degree to which interfacial CO contributes to buffer layer detachment of HTS coated conductors depends in part on how much CO is actually formed. The maximum amount of CO that a substrate can generate per unit area is determined by the substrate's thickness and carbon impurity level. The actual amount of CO generated during a particular processing step depends also on the rate of CO formation and the duration of that processing step. Typical processing steps for HTS coated conductor fabrication involve elevated temperatures (650–1250°C), oxygen partial pressures [$P(O)_2$] in the range 10^{-6} to 10^{-1} Torr, and durations from 15 to 100 min. If the rate of CO formation is assumed to be determined by the lesser of (a) the rate at which carbon diffuses to the interface or (b) the rate at which oxygen impinges on the surface, then the actual amount of CO generated during a particular processing step can be estimated.

The characteristic carbon diffusion time, τ, for a substrate of thickness, d, is given by $(d/2)^2/D$, where D is the bulk diffusivity of carbon in the substrate. If D is taken to be that reported for carbon in nickel ($D_o = 0.1$ cm^2/s, $E_d = 33$ kcal/mole) [12], then for a 50-µm-thick substrate, τ ranges from ~68 min for 650°C to ~3 s for 1250°C. The impingement rate of oxygen is proportional to $P(O)_2$ [13] and is roughly equal to 1 monolayer/s for $P(O)_2 = 10^{-6}$ Torr. Considering a 650°C processing step for a 15-min duration and $P(O)_2 = 10^{-6}$ Torr (the typical processing step producing the least CO), the amount of CO generated is roughly 22% ($15/\tau$) of that possible based on the carbon supply. For a high-purity Ni-270 substrate (~100 at. ppm C), oxidation of carbon for this processing step would not be limited by oxygen supply and could result in the formation of as much as ~3 monolayers of interfacial CO. Higher temperature, longer time, and higher carbon impurity would lead to the production of even more interfacial CO. Clearly, both the potential supply of carbon and the kinetics of carbon oxidation are sufficient during typical HTS processing to produce CO in adequate quantities to contribute to buffer layer detachment.

2.2.2 Experimental

The nickel-based metallic samples used for this study were cut from the same alloy tape as that used for substrates for HTS conductor fabrication. The tape was prepared from a 2.5-mm-thick coil (Ametek Specialty Metal Products) with a nominal composition Ni/3at%W. The coil, derived by powder metallurgical methods, was rolled at room temperature to a thickness of 50 µm and then slit to a final width of 1.0 cm (Hamilton Precision Metals). The resulting tape was then continuously cleaned ultrasonically in Micro solution (Cole-Parmer Instrument Co.) and distilled water for 30 min each and finally steam-cleaned in a ~250°C distilled-water steam jet. Carbon analysis of the cleaned, as-rolled tape by LECO Corp. revealed a carbon impurity level of 581 ± 5 at. ppm (~111 wt. ppm).

Temperature-programmed desorption was accomplished in a sealed, all-metal, hydrocarbon-free vacuum chamber. A base pressure of $\sim 5 \times 10^{-7}$ Torr was attained after a pumpdown of ~2 h. The major component of the residual gas was water vapor. Each stationary sample (~30 cm long) was suspended between two water-cooled copper electrodes. Tension was applied to the sample with counterweights (~170 g) attached to each end. A new, 75-µm-diam type K thermocouple pair was spot welded to the edge of each sample to monitor temperature. Resistive heating of the metallic sample was accomplished with a zero-crossing, phase-angle-fired, 60-Hz current controller, which limited thermocouple offset and noise. The sample was heated up to a reaction temperature (750 to 1000°C) at a rate of ~100°C/s. The temperature stability at the reaction temperature was ~±0.5°C, and the average quench rate following reaction was ~75°C/s to below 300°C.

The vacuum chamber was equipped with manual precision leak valves attached to sources of hydrogen (H_2 99.9999%), oxygen ($^{16}O_2$ 99.998%), isotopically pure oxygen-18 ($^{18}O_2$ 99%), and isotopically pure water ($H_2{}^{16}O$ 99.99%). Before the sample was heated to the reaction temperature, the partial pressures of the reactant gases were set by using a differentially pumped quadrupole mass spectrometer (SRS RGA 200) and the manual precision leak valves. To reduce the sensitivity of the mass spectrometer to desorption from surfaces other than the sample's, a probe tube (attached to the mass spectrometer) was positioned to within 1 mm of the sample's surface. During the temperature-programmed desorption, the sample temperature and the partial pressures of the reactant gas and potential product gases (e.g., CO, CH_3, H_2O, CO_2) were all recorded digitally every 2 s.

Meter lengths of the thermally processed tape were prepared in a second vacuum chamber. The all-metal sealed chamber was equipped with a reel-to-reel tape-handling system and had a base pressure of ~5 × 10^{-8} Torr. Moving tapes were heated radiantly by a pair of parallel, resistively heated Inconel sheets. An optical pyrometer was used to determine the temperature of the Inconel. The length of the hot zone in the chamber was ~5 cm. Oxygen was introduced into the chamber by a precision leak valve and was set and controlled by a quadrupole mass spectrometer. During the course of heat treatment, tape position, tape speed, heater current, and the partial pressures of oxygen and carbon monoxide were recorded digitally as a function of time.

2.2.3 Results and Discussion

The evolution of vapor-phase products was monitored during thermal treatment of bare Ni/3at%W substrate so that reactions that might contribute to the detachment of epitaxial oxides from nickel-based metallic substrates could be identified. Gases that are present during typical processing of HTS conductor include hydrogen, water, and oxygen. Shown in Fig. 2.5 are the thermal desorption spectra obtained for a cleaned, as-rolled Ni/3at%W sample that was sequentially exposed to 2 × 10^{-6} Torr of hydrogen, water, and oxygen ($^{16}O_2$). For both hydrogen and water, little change in the partial pressures of O_2, CH_3, and CO was observed during thermal treatment at 1000°C. The small feature in the CO desorption spectra observed during heat-up for both hydrogen and water exposure is likely from room-temperature molecular CO adsorption on the bare metallic substrate [10]. Observation of the CH_3 species is an indication of the formation of volatile hydrocarbon compounds.

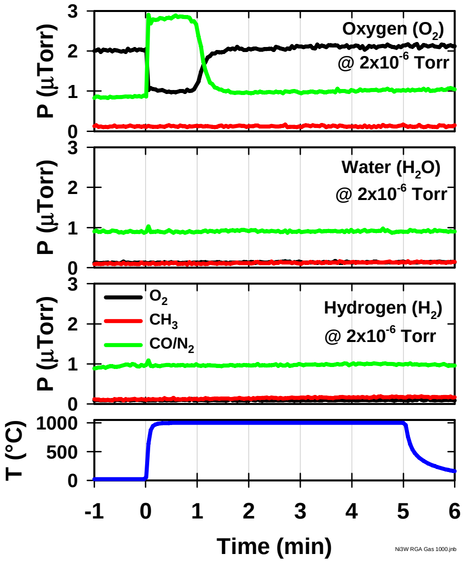

Fig. 2.5. Thermal desorption spectra for a bare Ni/3at%W tape heated sequentially to 1000°C in 2 × 10^{-6} Torr of first hydrogen, then water, and finally oxygen.

For oxygen exposure, a dramatically different desorption spectrum is observed (see Fig. 2.5). The partial pressure of oxygen dropped to ~1 × 10^{-6} Torr during heat-up and remained at that level for ~1 min before returning to 2 × 10^{-6} Torr. The CO partial pressure rose from ~1 × 10^{-6} to ~3 × 10^{-6} Torr during heat-up and remained at that level for ~1 min before returning to ~1 × 10^{-6} Torr. No change in P(CO_2) was observed during this thermal treatment. When the sample was heated a second time in oxygen, the desorption spectrum (not shown in Fig. 2.5) indicated constant P(CO) and P(O_2) during the entire heat treatment to 1000°C. These results suggest that the reaction to form volatile CO involves (a) oxygen in the vapor phase and (b) a depletable source of carbon.

Data for desorption of CO were gathered on bare Ni / 3at%W substrate for a range of P$(O)_2$ and temperature so that a better understanding could be obtained of the reaction mechanism and the reaction kinetics underlying the formation of CO. Isotopically pure oxygen-18 ($^{18}O_2$ 99%) was used for oxidation to differentiate CO desorption ($^{12}C^{18}O$; amu = 30) from N_2 and CO background ($^{14}N_2$ and $^{12}C^{16}O$; amu = 28). Figure 2.6 shows the results for heating to 800°C for a range of P(O_2). Similarly, Fig. 2.7 shows the results for heating in 5 × 10^{-6} Torr P(O_2) for a range of temperature. Interesting trends in the data in these two figures include (a) the complementary behavior of P(O_2) and P(CO) throughout the heat treatment, (b) the saturation of the reaction ("flat-topping") that occurs at low P(O_2) or high temperature, and (c) the relative constancy of the integrated CO partial pressure (see Fig. 2.8).

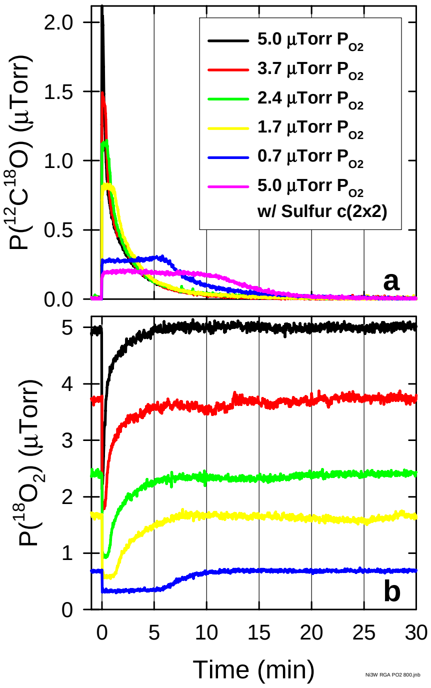

Fig. 2.6. CO desorption spectra for a Ni/3at%W tape heated to 800°C for a range of oxygen partial pressures. (a) CO partial pressure. (b) O_2 partial pressure.

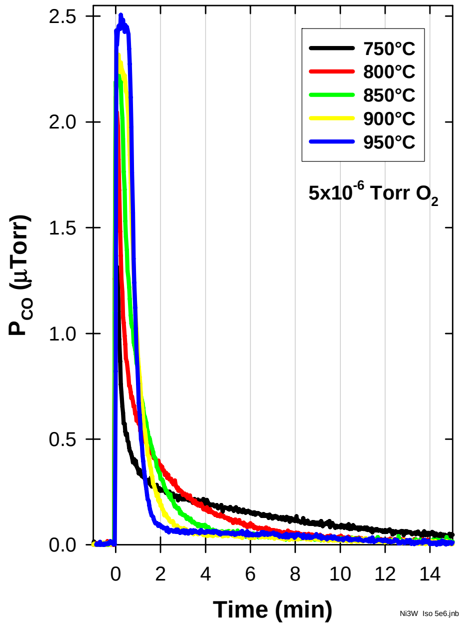

Fig. 2.7. CO desorption spectra for a bare Ni/3at%W tape heated in an oxygen partial pressure of 5 × 10^{-6} Torr for a range of temperature.

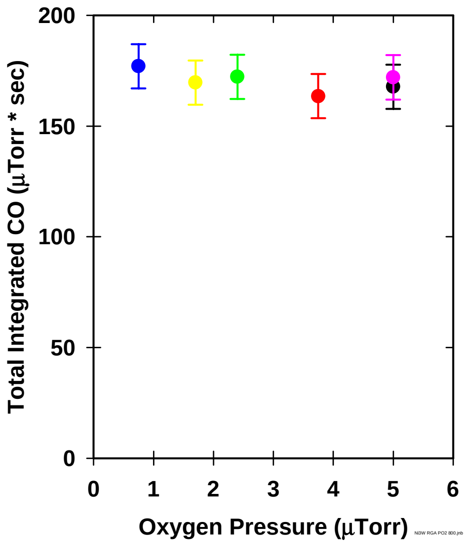

Fig. 2.8. Integrated area beneath CO desorption spectra in Fig. 2.6(a). Ramp rate = 100°C/s, Temperature = 800°C**.**

A simple model to describe the observed behavior is based on the following surface oxidation reaction:

$$2C + O_2 \Rightarrow 2CO\uparrow \qquad (5)$$

Carbon from within the sample reacts with oxygen from the gas to form carbon monoxide, which desorbs and is pumped away. For each molecule of oxygen consumed, two molecules of carbon monoxide are produced.

The rate at which the surface reaction in Eq. (5) proceeds is a directly measurable quantity [i.e., P(CO) vs time] and depends on a number of factors. Among these factors are the rate at which atomic carbon is supplied from the substrate to the surface and the rate at which molecular oxygen is supplied from the vapor to the surface. The supply of carbon to the surface is assumed to be governed by the following one-dimensional diffusion equations:

$$\frac{\partial c}{\partial t} = D\frac{\partial^2 c}{\partial t^2} \qquad (6)$$

and

$$J_c = -D \frac{\partial c}{\partial x} \tag{7}$$

where c, D, and J_c represent the concentration, diffusivity, and flux of carbon in the substrate, respectively. The supply of oxygen to the surface is assumed to be proportional to the partial pressure of oxygen:

$$J_o = \alpha \, P_{O_2} \tag{8}$$

where J_o represents the flux of adsorbed oxygen at the substrate surface and α is a proportionality factor the includes the sticking coefficient of oxygen to the surface.

A numerical solution of Eq. (6) and Eq. (7) can be easily obtained by using an appropriate choice of boundary conditions, including Eq. (8), and a single adjustable parameter, α. The results of this solution are plotted in Fig. 2.9 for the case of heating to 800°C for a range of P(O_2). Similarly good agreement between experiment and model is obtained for heating in 5×10^{-6} Torr P(O_2) for a range of temperature. The model clearly reflects all major trends observed in the data and thereby helps validate the assumptions on which the model is based.

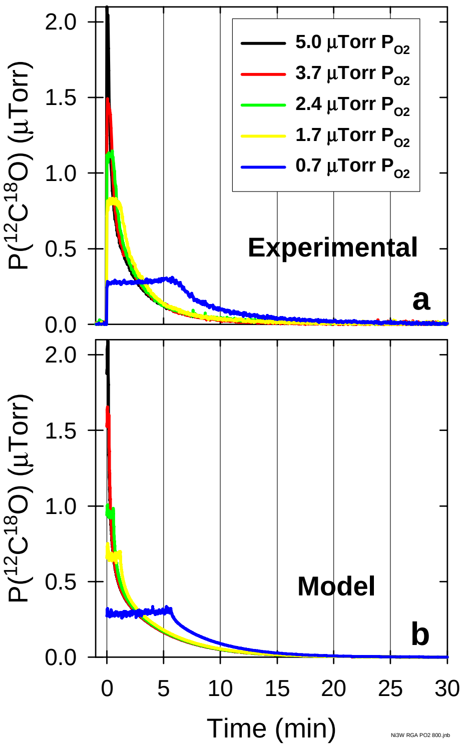

Fig. 2.9. CO desorption spectra measured experimentally at 800°C compared with those obtained via a diffusion model.

The model suggests that the flat-topping of the CO desorption observed at low P(O_2) or high temperature is associated with a reaction regime in which the supply of oxygen to the surface is rate limiting. To test that idea, the surface of a clean, as-rolled sample was first covered with an adsorbed ordered sulfur overlayer (c(2×2), ~0.5 monolayer coverage) [14], and then the sample was heat-treated at 800°C in 5×10^{-6} Torr P(O_2). The CO desorption results for this sulfur-covered sample are also shown in Fig. 2.10. Compared with the CO desorption for an initially clean surface, the CO desorption for a sulfur-covered surface is substantially more sluggish at 800°C and 5×10^{-6} Torr P(O_2). The value of α required to fit the model to the sulfur-covered data is ~9 % of that required to fit the clean surface data. These results are consistent with the notion that adsorbed sulfur occupies some of the surface sites on which oxygen adsorbs or carbon and oxygen react and thus reduces the rate of CO desorption. A similar reduction in the rate of CO desorption may be expected for a substrate covered with a dense, crack-free, epitaxial oxide.

The model also suggests that the time integral of P(CO) is a quantity proportional to the amount of carbon removed from the sample. To obtain the constant of proportionality requires knowledge of the carbon content of a sample for two different times. LECO carbon analysis was conducted for samples both before and after a 30-min heat treatment at 800°C in 5×10^{-6} Torr P(O_2). This oxygen treatment reduced the carbon content from 580 to 21 at. ppm. Approximately half of the 21 at. ppm C determined after heat treatment can be attributed to room-temperature CO adsorption that followed the heat treatment and preceded the carbon analysis. Based on these measurements, a value of ~3.35 ppm/µTorr/s is obtained for the proportionality constant relating the time integral of P(CO) to the carbon content for this particular vacuum system and sample size.

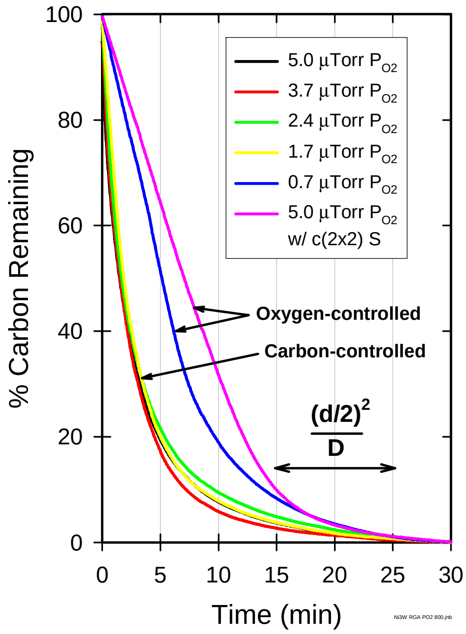

Fig. 2.10. Carbon remaining in the substrate as a function of heat-treatment time at 800°C.

Figure 2.10 shows the accumulative time integral of the P(CO) data in Fig. 2.6 expressed in terms of the percentage carbon remaining after a given time of treatment. Figure 2.6 is useful for determining the effect of oxygen heat treatment conditions (time and oxygen partial pressure) on carbon content at 800°C. The transition for carbon removal from carbon controlled to oxygen controlled is evident in Fig. 2.9. For high P(O_2), where little or no CO desorption flat-topping is observed, the rate of carbon removal is determined predominately by carbon diffusion in the substrate. For comparison to the observed carbon decay for high P(O_2), the characteristic carbon diffusion time at 800°C, $\tau = (d/2)^2/D$, is shown in Fig. 2.10.

For low P(O_2) (0.7×10^{-6} Torr), or for conditions where the surface reaction sites are blocked (e.g., an S-covered surface), the initial rate of carbon removal in Fig. 2.10 is determined by the effective supply of oxygen to the substrate surface. In this regime, the initial rate is reduced with respect to that observed for high P(O_2), and the initial slope for carbon removal is proportional to an effective partial pressure of oxygen. For processing conditions where extremely low P(O_2) is encountered, such as during substrate annealing in vacuum at 1250°C with a tantalum getter, where the equilibrium P(O_2) is approximately ~10^{-16} Torr [15], essentially no carbon is removed and no CO is formed. Interestingly, this low- P(O_2) vacuum annealing of the substrate is associated with especially frequent detachment of buffer layers during subsequent processing.

Lengths of Ni/3at%W substrate were prepared with different amounts of carbon removed by oxygen treatment so that the effect of carbon oxidation on buffer layer detachment could be assessed. The results in Fig. 2.10 provided the basis for selecting processing conditions for removal of carbon. Figure 2.11 shows results for a 240-cm length of substrate that was continuously processed at ~850°C in 5×10^{-6} Torr P$(O)_2$ for different times in the reel-to-reel vacuum system. Different processing times were achieved by varying the tape speed through the fixed-length (~5 cm) furnace [Fig. 2.11(e)]. During processing, P(CO) was continuously monitored with a mass spectrometer [Fig. 2.11(d)]. Higher P(CO) was observed for higher tape speed. This observation is consistent with the expectation that a higher delivery rate of a carbon-containing substrate to the furnace leads to higher rates of carbon oxidation and CO desorption.

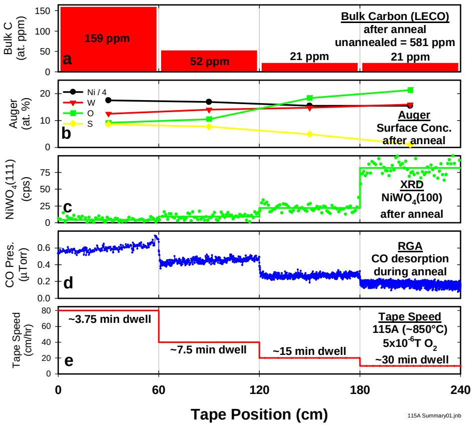

Fig. 2.11. Properties of a 240-cm length of bare Ni/3%W tape processed continuously at ~850°C in an oxygen partial pressure of 5×10^{-6} Torr.

After being thermally processed in oxygen, the 240-cm length of substrate was characterized in a reel-to-reel X-ray diffractometer [16]. Shown in Fig. 2.11(c) is the θ-2θ intensity for the NiWO$_4$(100) diffraction peak—the only peak in the θ-2θ spectrum not associated with the metallic substrate. The X-ray intensity of this crystalline oxide is significantly greater for the lower tape speeds. This may be the result of competition for oxygen between carbon and the metal. As carbon levels are reduced, more oxygen is available for metal oxidation. The $NiWO_4$ formed during the thermal processing in oxygen was absent after vacuum annealing at 1250°C for 15 min, which is the next step commonly included in conductor fabrication.

Auger electron spectroscopy was also used to examine the surface composition for regions of the 240-cm length of substrate treated for different dwell times [Fig. 2.11(b)]. Longer dwell times are associated with higher surface concentrations of W and O and lower surface concentrations of Ni and S. This result is consistent with the X-ray result shown in Fig. 2.11(c).

Sections of the 240-cm length of substrate were analyzed for carbon content by LECO Corporation so that the effectiveness of the oxygen treatment for carbon removal could be established. The levels of carbon [Fig. 2.11(a)] determined for these sections annealed for different times at ~850°C in 5×10^{-6} Torr $P(O_2)$ are in good agreement with those estimated from CO desorption at 800°C in the same $P(O_2)$ (Fig. 2.10).

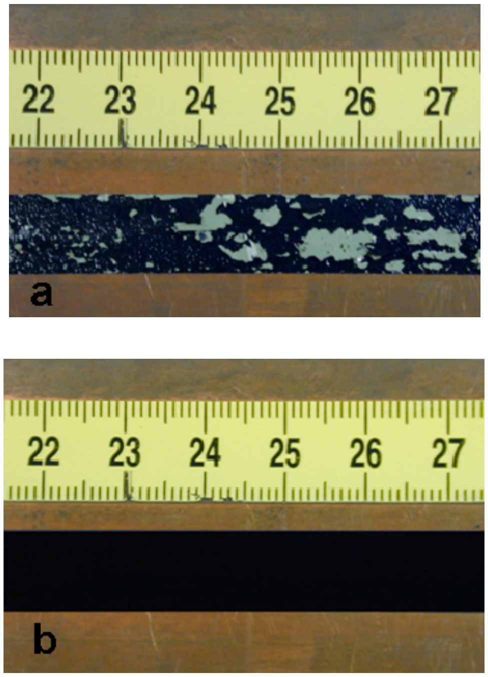

Fig. 2.12. (a) HTS tape for a Ni/3at%W substrate containing 52 at. ppm C showing severe film detachment. (b) HTS tape for a Ni/3at%W substrate containing minimal carbon (~21 at. ppm) showing no film detachment.

One goal of this study is to demonstrate a relationship between CO formation and detachment of the epitaxial oxide buffer layers of HTS coated conductors. In pursuit of this goal, portions of the 240-cm length of oxygen-treated substrate, as well as portions of untreated substrate, were further processed to prepare coated conductors by standard methods. For both the untreated substrate (581 ppm C) and the treated substrate (159 ppm C), extensive detachment of the buffer layers was observed during or immediately following their deposition. For the treated substrate containing 52 ppm C, detachment was not observed during buffer layer deposition but was first observed during processing of the superconducting layer [Fig. 2.12(a)]. For the treated substrates containing minimal carbon (~21 ppm C), no detachment was observed throughout the entire conductor fabrication process [Fig. 2.12(b)]. Moreover, high critical current densities (>1 MA/cm^2, 77K, self-field) were measured for them and for similarly processed, carbon-depleted substrates. These results clearly indicate that a relationship exists between oxygen treatment and buffer layer detachment and suggest that CO formation at the oxide-metal interface may contributed to this detachment.

2.2.4 Conclusions

Carbon impurities in substrates commonly used for HTS coated conductors can contribute to the detachment of buffer layers. Thermal treatments in reduced pressures of high-purity hydrogen or water vapor do not appear to remove significant amounts of carbon from the substrate. A similar treatment in a reduced pressure of oxygen dramatically reduces the level of carbon. The kinetics of carbon removal in the form of CO can be understood in terms of a simple diffusion model (Fig. 2.13). Based on these results, procedures have developed that effectively remove carbon and eliminate buffer layer detachment from lengths of continuously processed substrate.

2.2.5 References

1. M. P. Paranthaman and T. Izumi, “High-Performance YBCO-Coated Superconductor Wire,” MRS Bulletin 29, 533 (2004).
2. P. N. Arendt and S. R. Foltyn, “Biaxially Textured IBAD-MgO Templates for YBCO-Coated Conductors,” MRS Bulletin 29, 543 (2004).

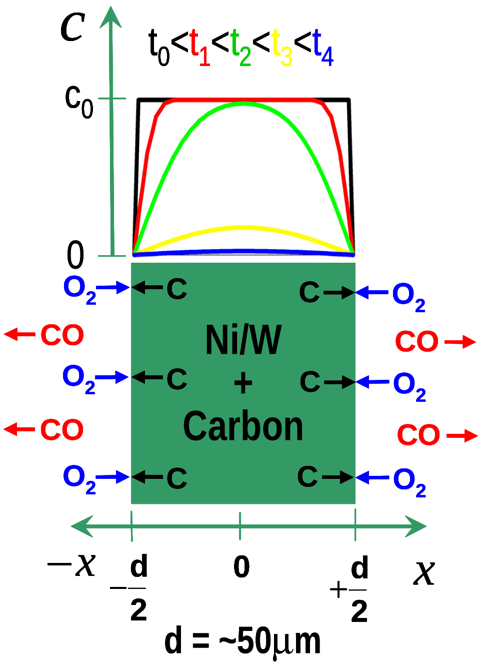

Fig. 2.13 Schematic representation of a 1-D diffusion model that describes carbon removal from HTS coated conductor substrates.

3. A. Goyal, M. P. Paranthaman, and U. Schoop, "The RABiTS Approach: Using Rolling-Assisted Biaxially Textured Substrates for High Performance YBCO Superconductors," *MRS Bulletin* **29**, 552 (2004).
4. Y. Iijima et al., "Research and Development of Biaxially Textured IBAD-GZO Templates for Coated Superconductors," *MRS Bulletin* **29**, 564 (2004).
5. J. A. Becker, E. J. Becker, and R. G. Brandes, "Reactions of Oxygen with Pure Tungsten and Tungsten Containing Carbon" *J. Appl. Phys.* **32**, 411 (1961).
6. M. P. Lopez Sancho and J. M. Lopez Sancho, "ESD Study of the Interaction of Oxygen with Tungsten Containing Carbon," *Appl. Surf. Sci.* **6**, 82 (1980).
7. J. W. McAllister and J. M. White, "The Oxidation of Carbon at the Surface of Nickel," *J. Phys. Chem.* **76**, 968 (1972).
8. H. Conrad et al., "Adsorption of CO on Clean and Oxygen Covered Ni(111) Surfaces," *Surf. Sci.* **57**, 475 (1976).
9. F. A. List and J. M. Blakely, "Oxidation of Carbon on Vicinal Surfaces of Nickel," *J. Vac. Sci. Technol.* **20**, 838 (1982).
10. F. A. List and J. M. Blakely, "Kinetics of CO Formation on Singular and Stepped Nickel Surfaces.," *Surf. Sci.* **152–153**, 463 (1985).
11. W. F. Smith, *Structural Properties of Engineering Alloys*, McGraw-Hill Publishing Co., New York, (1981).
12. P. L. Gruzin, Y. A. Polickarpov, and G. B. Federov, "Determining Carbon Diffusion in Nickel and Its Alloys by Means of Carbon-14," *Fiz. Metal. Metalloved.* **4**, 94 (1957).
13. F. Reif, pp. 269–73 in *Fundamentals of Statistical and Thermal Physics*, McGraw-Hill Book Co., New York (1965).
14. C. Cantoni et al., "Quantification and Control of the Sulfur c(2×2) Superstructure on {100}(100) Ni for Optimization of YSZ, CeO_2, and $SrTiO_3$ Seed Layer Texture," *J. Mater. Res.* **17**, 2549 (2002).
15. Thermo-Calc TCC Software, ver. 8.12, Thermo-Calc Software, Stockholm (2004).
16. E. D. Specht et al., "Uniform Texture in Meter-Long $YBa_2Cu_3O_7$ Tape," *Physica C* **382**, 342 (2002).

2.3 Identification of a Self-Limiting Reaction Layer in Ni-3at%W Rolling-Assisted Biaxially Textured Substrates

K. J. Leonard, A. Goyal, S. Kang, K. A. Yarborough, and D. M. Kroeger

2.3.1 Introduction

The development of rolling-assisted biaxially textured substrates (RABiTS™) for the growth of epitaxially aligned $YBa_2Cu_3O_{7-\delta}$ (YBCO) films as a cost-effective approach to the fabrication of coated-conductor tapes has progressively matured. RABiTS™ consists of layers of metal oxide buffers epitaxially deposited with either a cube-on-cube or rotated cube-on-cube orientation on {100} <100> textured Ni or dilute Ni-alloy substrates [1–3]. The buffer layers provide a barrier to Ni diffusion from the metal substrate into the superconductor during deposition or ex situ processing of the YBCO layer, while providing a template of reduced lattice mismatch between YBCO and substrate for *c*-axis-aligned epitaxial growth. Numerous RABiTS™ architectures, along with different deposition methods for producing biaxially textured buffer layers that have been investigated, have successfully yielded high-quality YBCO films [1–5]. Understandably, emphasis has been placed on the development of fewer, more cost-effective layers that can provide a stable template for YBCO deposition.

Recently, two bodies of work examining the thickness dependence of the critical current density on YBCO microstructure were reported on [6,7]. These experiments involved the pulsed laser deposition (PLD) of YBCO films up to 6.4 μm thick under the same conditions on two different RABiTS™ architectures. The first, RABiTS1, consisted of a 12-nm-thick CeO_2 seed layer deposited on textured Ni, with additional 300-nm-thick yttria-stabilized zirconia (YSZ) and 20-nm CeO_2 buffer layers grown on top. The second substrate, RABiTS2, consisted of a 150-nm Y_2O_3 seed layer deposited on Ni-3at%W (Ni-W) substrate, with 150-nm YSZ and 20-nm CeO_2 buffer layers. The critical current densities of the thick YBCO films and the film texture determined through X-ray diffraction (XRD) are listed in Tables 2.2 and 2.3 for RABiTS1 and RABiTS2, respectively. The critical-current-density values were calculated from the four-point probe measurements of critical current conducted at 77 K in self-field without micro-bridge patterning. Limitations in characterizing the films to 120 A prevented the full determination of critical current in films thicker than 1.0 μm of the RABiTS2 materials under self-field. For those films, a zero-field critical current density was calculated from in-field measurements at 0.5 Tesla, assuming that a factor of 4 to 5 drop in critical current density occurs from self-field to that of 0.5 Tesla [7]. Thus a range of calculated values are presented for the 2.9- and 4.3-μm-thick films in Table 2.3. During measurement of the 6.4-μm-thick film on RABiTS2, a crack was generated across the sample upon reaching 60 A. It is believed to have been the result of sample heating.

Table 2.2. Measured electrical and texture properties of thick YBCO films on the RABiTS1 material (YBCO/CeO_2/YSZ/CeO_2/Ni substrate)

YBCO thickness (μm)	J_c (MA/cm^2)	$\Delta\phi^a$	$\Delta\omega^b$	*a*-axis fraction $Ia_\perp(200)/I_{c\perp}(002)$	% Cube
0.19	2.6	1.07	0.73	0.0	98.8
0.43	1.4	1.04	0.70	0.0	90.4
1.6	0.59	1.03	0.76	0.03	89.7
3.0	0.45	1.08	0.73	0.05	79.9

Source: B. W. Kang, A. Goyal, D. F. Lee, J. E. Mathis, E. D. Specht, P. M. Martin, D. M. Kroeger, M. Paranthaman, and S. Sathyamurthy, J. Mater. Res., 17, 7, 1750 (2002).

[a] Change of in-plane texture between YBCO and Ni substrate calculated as the ratio of the FWHM of X-ray intensities of (113)YBCO to (111)Ni.

[b] Change of out-of-plane texture between YBCO and Ni substrate calculated as the ratio of (005)YBCO to (200)Ni/Ni-W.

Table 2.3. Measured electrical and texture properties of thick YBCO films on the RABiTS2 material (YBCO/CeO_2/YSZ/Y_2O_3/Ni-W substrate)

YBCO thickness (μm)	J_c (MA/cm^2)	$\Delta\phi$	$\Delta\omega$	*a*-axis fraction $Ia_\perp(200)/Ic_\perp(002)$	% Cube
1.0	1.18	0.90	0.79	0.0	92.5
2.9	0.9 - 1.1	1.03	0.78	0.1	93.5
4.3	0.65 - 0.81	1.09	0.89	0.2	87.9
6.4	-	0.96	0.91	0.1	95.8

Source: S. Kang, et al., *J. Mater. Res.*, in review (2003).

The use of Ni-W for the roll-textured substrates has been a recent development in RABiTS™ materials [8]. These substrates possess a sharper texture over earlier pure Ni tapes, with in-plane and out-of-plane textures of Δϕ = 7° and Δω = 5–6°, respectively, as compared with Δϕ = 9–10° and Δω = 7–8° of the Ni substrates [6]. The use of a Y_2O_3 seed layer in RABiTS2 instead of CeO_2 is another upgrade. Cracks appeared within the CeO_2 seed layer, possibly the result of volumetric changes between CeO_2 and Ce_2O_3 forms that occurred during subsequent processing of the tapes under varying oxygen partial pressures. Seed layer cracking as a result of structural changes, thermal expansion mismatch, or epitaxial strain can provide an easy pathway for base metal oxidation and the initiation of uncontrolled NiO growth from the base metal into the upper layers of the coated conductor. NiO growth into the YBCO layer as a result of buffer layer crack formation has a detrimental effect on both the physical properties of the films as well as their mechanical durability. (It has never been detailed in literature.)

Dramatic improvements in electrical properties and YBCO film quality have been observed for the Ni-W substrates as compared with earlier Ni tapes (see Tables 2.2 and 2.3). The microstructures of the YBCO layers for both the RABiTS1and 2 films have been characterized by cross-sectional transmission electron microscopy (TEM) [9,10]. As shown in Fig. 2.14, exceptional quality was observed within the 6.4-μm-thick YBCO film deposited on RABiTS2 throughout its thickness and across the film over a considerable distance. (Optimization of the processing conditions and determining the thickness of the Y_2O_3 layer required to produce a suitable seed layer are being investigated in a separate study.)

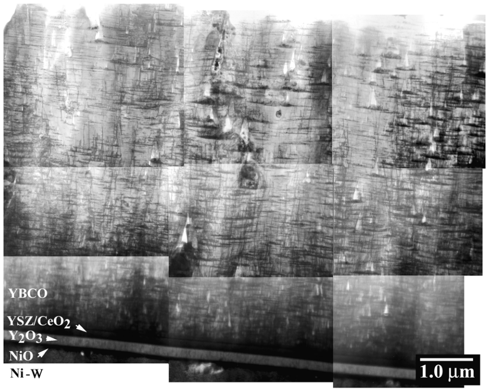

Fig. 2.14. Composite cross-sectional image of a 6.4-μm-thick YBCO film deposited by PLD on Ni-W RABiTS2 material.

The improvements to the film properties of the RABiTS2 samples were felt to outweigh the additional gains posed solely by the tighter texture of the Ni-W tapes and that of a nonoptimized buffer layer. Therefore, a closer investigation of the multilayered films deposited on Ni-W was performed. It was observed in the study, that the growth of the NiO layer was limited by the formation of a second reaction layer (a layer of $NiWO_4$) at the substrate interface. The following text identifies and characterizes the $NiWO_4$ layer, in addition to illustrating its dramatic effect of limiting NiO growth.

2.3.2 Experimental

The deposition of the buffer layers was conducted under a low water partial pressure to prevent NiO formation prior to YBCO film deposition. A XeCl excimer laser (λ = 308 nm) was used to deposit YBCO films ranging in thickness from 1.0 to 6.4 μm on 2.5 × 0.5 cm samples. A deposition rate of 5 to 13Å/s was conducted at 790ºC under an oxygen partial pressure of 120 mTorr. Following deposition, the films were cooled to room temperature at a rate of 5ºC/min under an oxygen partial pressure of 550 Torr. The thickness of the YBCO films was verified during cross-sectional TEM examination. (For descriptions of the development of biaxially textured Ni-W substrates and the conditions used for deposition of the buffer layers, see Ref. 8.)

Prior to preparing cross-sectional samples for TEM examination, an additional 1.0-μm-thick Ag layer was deposited by rf magnetron sputtering on top of the YBCO film to preserve the integrity of the coated conductor from damage incurred through sample preparation. An annealing treatment in O_2 was required to adhere the Ag layer to the sample: 10ºC/min ramp to 500ºC, 1-h hold, 5ºC/min cool to 350ºC, then furnace cooled. The samples were cleaned, cut in two, and glued silver-sides-together with M-bond 610. Additional pieces of YSZ single crystals were glued onto the sides of the sample stack to thicken the cross section for support. The sample stack was cured at 115ºC for 1 h while held under pressure in Teflon-jawed vise at 2 lb-in. of torque to ensure a uniformly thin glue line. Samples were then cut with a diamond wafering blade into approximately 1.0 × 1.0 mm square samples of 0.5 mm thickness.

The samples were set within the centers of 3-mm-diam graphite rings and were held in place with two-part epoxy (Gatan 601-07-001). Following drying overnight, the epoxy was cured for 1 h at 115ºC. The 3-mm-diam samples were mechanically ground to a 90-μm thickness with a 3-μm surface polish prior to milling in a Gatan Model 691 precision ion polisher. Milling was done with a 5-keV beam at an angle of incidence of 8º with the dual guns impinging from both top and bottom of the sample at a direction perpendicular to the glue line. Beam energies and angles of incidence were reduced in the later stages of sample polishing to prevent excessive ion damage. At no time were the samples exposed to water.

Philips Tecnai 20 (LaB_6, 200kV) and CM200 (FEG, 200-kV) transmission electron microscopes equipped with energy dispersive spectrometry (EDS) units were used to examine the cross-sectioned samples. The CM200 microscope was used in both conventional and high-resolution scanning modes.

2.3.3 Results

The overall quality of the YBCO films deposited on the Ni-W RABiTS2 substrate is best exemplified by the cross-sectional view of the microstructure of the 6.4-µm-thick YBCO sample, shown in Fig. 2.14. The thick film shows long, columnar *c*-axis-oriented grains throughout the thickness; no randomly oriented grain formations were observed within the sample. The deposition of such a thick of a film without the formation of so-called “dead zones” is encouraging in the development of high-current-carrying superconducting films. (For further in-depth analysis of the YBCO microstructure, see Ref. 10.)

When the cross section over a lateral distance beyond the 8 µm shown within the composite image of Fig. 2.14 was viewed, no NiO formation into the upper layers of the conductor was observed. The NiO layer present along the interface of the buffer and substrate was found to be very uniform and relatively thin. This finding was different from that observed within the RABiTS1 substrate, as shown within the cross-section image of the 3-µm-thick YBCO film in Fig. 2.15(a). In the thickest of YBCO films deposited on the RABiTS1 substrate, the NiO reaction layer was found to be well in excess of 100 nm thick and very irregular. For comparison, the 2.9-µm-thick YBCO film deposited on RABiTS2 is shown in Fig. 2.15(b). The development of NiO within both sets of RABiTS™ substrates occurred during the YBCO deposition process and not during buffer layer deposition. The thinner NiO layer within the RABiTS2 samples, which also showed a greater uniformity over distance, was separated from the Ni-W substrate by an additional layer.

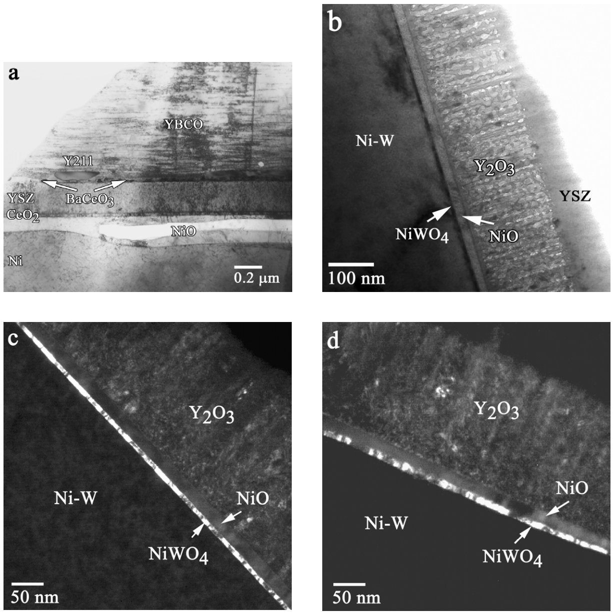

Fig. 2.15. Cross-sectional images of the interface area located between the seed layer and metal substrate. (a) Thick and irregular NiO produced within the 3.0-µm-thick YBCO film deposited on RABiTS1. The hole within the NiO layer is a milling artifact. (b) Bright-field image of NiO and $NiWO_4$ layers developed within the 2.9-µm-thick YBCO film on RABiTS2. (c and d) Dark-field images of the $NiWO_4$ layer using the (100) reflections within the 2.9- and 6.4-µm-thick YBCO films, respectively, on RABiTS2.

The layer of material between the Ni-W substrate and the NiO was identified by EDS during high-resolution scanning TEM analysis as consisting of Ni-W-O species and was later identified as $NiWO_4$ through diffraction. The EDS line scan generated by a 1.4-nm-diam electron beam probe scanned 100 nm across the interfaces from the Y_2O_3 seed layer into the Ni-W substrate is shown in Fig. 2.16. The line scan was conducted with the beam direction parallel to the Ni-W[100] and Y_2O_3[110] zone axis directions. Although not conducted under ideal kinematical conditions, the scan allowed the interfaces to remain parallel to the beam due to the biaxial texturing of the films. No distinct tungsten oxide phase was observed through EDS analysis, or as will be shown later, through electron diffraction or high-resolution imaging. The $NiWO_4$ phase was determined to range in thickness between 5 and 8 nm for all the RABiTS2 samples regardless of the YBCO film thickness. The uniformity in

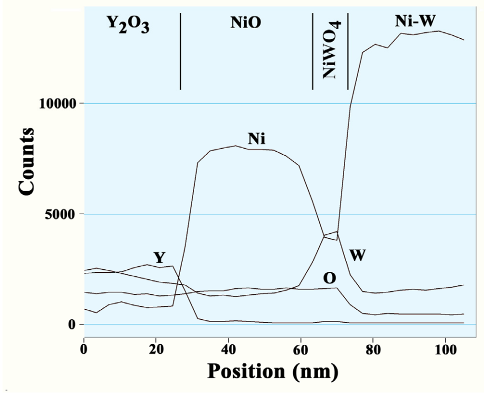

Fig. 2.16. High-resolution EDS line scan taken in cross section across the interface between the Y_2O_3 seed layer and metal substrate, showing the presence of the $NiWO_4$ phase.

thickness and coverage of the $NiWO_4$ layer between the NiO and Ni-W substrate is further illustrated in the dark field images of the 2.9- and 6.4-µm-thick YBCO samples in Figs. 2.15(c) and (d), respectively.

The precise identification of the Ni-W-O phase measured by EDS and its relationship to the Ni-W substrate and NiO layer was determined through select area diffraction (SAD) analysis about the Ni-W[010] and [110] zone axis (Fig. 2.17). The Ni-W[010] // Y_2O_3[110] epitaxial relationship between the buffer layer and substrate is illustrated in the SAD pattern shown in Fig. 2.17(a). Present within the diffraction pattern are the (111) and (100) reflections from the NiO and $NiWO_4$ phases, respectively. The (100) reflection of the $NiWO_4$ phase is observed at a slightly smaller d-spacing than (002) Y_2O_3. In a section of the sample where the Y_2O_3 layer was milled away but where the underlying NiO and $NiWO_4$ layers were left intact, the SAD pattern along the Ni-W[010] direction revealed the additional {111}$NiWO_4$ reflections not seen due to the Y_2O_3{222} intensities [see Fig. 2.17(b)]. The $NiWO_4$ intensities produced a pattern that is close to, but tilted from, the [011] zone axis, as the {011} reflections are missing. What is observed from the patterns in Figs. 2.17(a) and (b) is that the (h00) planes of the monoclinic $NiWO_4$ phase are parallel to the (200) planes of the cubic Ni-W substrate. When the sample was tilted along the <100> direction within these two phases to the [110] zone of the Ni-W phase, two well-defined patterns clearly emerged and identified the $NiWO_4$ phase.

In one location within the sample tilted to the [110]Ni-W zone, the $NiWO_4$ phase showed a [001] orientation relative to the Ni-W [Fig. 2.17(c)]. Although the NiO (111) reflections are still present, no NiO zone axis was aligned within that section of the film. In an adjacent region within the sample, diffraction patterns of both the NiO[110] and $NiWO_4$[010] were observed to be in relationship to the Ni-W[110] zone. The $NiWO_4$ (100) planes were found to be parallel to the (200) Ni-W planes, although multiple variants of the $NiWO_4$ phase are possible for a given Ni-W direction. This is particularly evident in the high-magnification image of Fig. 2.18(a), which shows the $NiWO_4$ layer within the 1.0-µm thick YBCO sample taken when the beam direction was parallel to the [010] zone axis of Ni-W. Within the layer of the $NiWO_4$ phase, two lattice image contrasts were

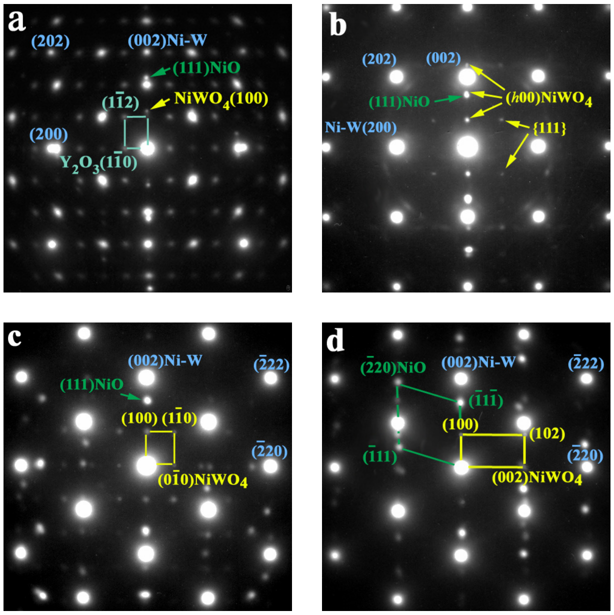

Fig. 2.17. Selected area electron diffraction patterns taken of the reaction layers within the Ni-W RABiTS2, revealing the (100)$NiWO_4$ // (001)Ni-W orientation relationship. (a) The Ni-W[010] zone axis illustrating the rotated cube-on-cube texture with the Y_2O_3[110] pattern along with the (111) NiO and (100) $NiWO_4$ reflections. (b) Ni-W[010] zone axis in a section of the sample with the Y_2O_3 buffer milled off, revealing the {100} and {111}$NiWO_4$ intensities. (c) The Ni-W[110] zone axis with [001]$NiWO_4$ pattern, and from an adjacent location under the same tilt conditions. (d) the $NiWO_4$[010] and NiO[110] zone axis patterns.

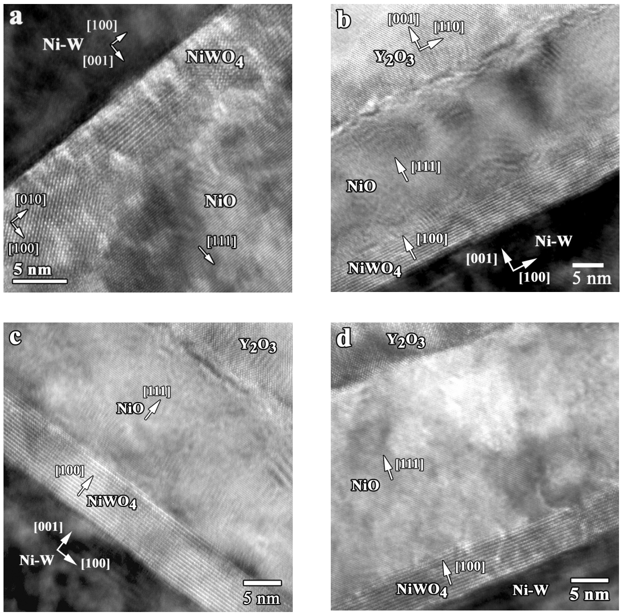

Fig. 2.18. High-resolution images of the RABiTS2 samples comparing the thickness of the NiWO$_4$ and NiO layers. Taken in cross section with the beam direction parallel to the Ni-W[010], YBCO thickness within the samples are (a) 1.0 μm, (b) 2.9 μm, (c) 4.3 μm and (d) 6.4 μm.

observed for a given tilt condition. The first, imaged as lines representing the {h00} planes observed in the upper right portion within the figure, is oriented with its zone axis tilted relative to the [010] Ni-W. In the lower left corner of the figure, a precise lattice image of the [001] zone axis is observed within the NiWO$_4$ film. Although a curvature in the sample may result in localized tilting of the NiWO$_4$ zone axis into alignment, and although the sample is relatively thick at that location, making it difficult to see a clean break in orientation between adjacent grains, variations in orientation relative to the substrate were nonetheless observed through diffraction.

The images within Fig. 2.18 give a comparison of the changes in NiO thickness occurring within the films for an increasing time at YBCO deposition conditions, or increasing YBCO film thickness. The images were all taken with the beam direction parallel to Ni-W[010]. Therefore, the images were taken precisely in cross section to show the true thickness of the NiO and NiWO$_4$ layers. The NiWO$_4$ thickness showed little or no change between the samples held for the minimum and maximum YBCO deposition times. The 5- to 8-nm-thick NiWO$_4$ layer showed very smooth interfaces to both the Ni-W substrate and the NiO layer. The NiO layers within the four samples examined also showed little change. Thickness of the NiO layer within the 1.0-, 2.9- and 4.3-μm-thick YBCO films was approximately 20 nm; the 6.4-μm-thick YBCO film had a NiO layer of approximately 25 nm. In comparison with the 3.0-μm-thick YBCO film deposited on the RABiTS1 substrate [Fig. 2.15(a)], the development of NiWO$_4$ clearly has a limiting effect on the growth of the NiO phase. More importantly, the barrier it creates to Ni diffusion reduces the development of NiO and its penetration through cracks within the buffer layers. Such penetration would produce either spallation or cracking within the YBCO film.

2.3.4 Discussion

The conditions and mechanisms through which the NiWO$_4$ phase develops within the substrates is not fully understood at this time and is currently being investigated. Even within the thinnest of the YBCO samples deposited on the RABiTS2 material, a continuous NiWO$_4$ layer had already been fully developed and shows no difference to that contained within the samples held more than six times as long under YBCO deposition conditions. There are two plausible routes of NiWO$_4$ formation within these materials (based on thermodynamics of the phases involved, observations made in this work, and from information culled from literature).

When considering the development of the phases produced at the buffer-substrate interface, one must look at both the PLD procedure in developing YBCO films and the thermodynamic properties of the phases involved. The buffered substrates are initially heated to 790ºC under a vacuum of 1×10^{-6} Torr, after which deposition of the YBCO occurs under an O_2 partial pressure of 120 mTorr followed by a 5ºC/min cooling under a 550 Torr O_2 environment. Based on the results of a galvanic-cell study of the phases within the Ni-W-O system [11], on established thermodynamic reference data [12], and by following the work of Jackson and coworkers [13], the standard molar Gibbs free energies of formation for $NiWO_4$, WO_3, and WO_2 are substantially greater than that of NiO for a given amount of O_2 (Fig. 2.19 left). Therefore, the formation of a tungsten oxide is very favorable within the Ni-W substrates. During initial heating of the buffered substrate to the deposition temperature or during YBCO deposition, the low partial pressure of O_2 within the chamber and consequently even lower pressure at the interface between the substrate and the buffer may be below the stability range of NiO but not that of the ternary and binary tungsten oxides (Fig. 2.19 right). Therefore, it is possible that the formation of the tungsten oxides occurs at that stage. Although it is possible that a reduction of the buffers may occur during the heating of the sample to the deposition temperature because of the minimal presence of hydrogen in the high-vacuum PLD chamber, the free energy of formation of tungsten oxides is not as great as that of the individual phases consisting of the buffer layers [13], and it is unlikely that tungsten oxides will form during sample heating.

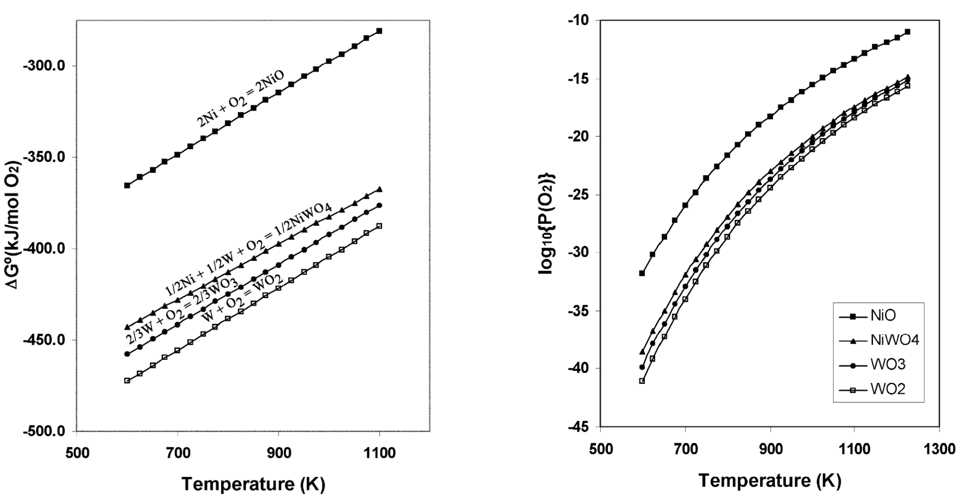

Fig. 2.19. Left: Standard free energy change for the formation of select Ni and W oxides vs temperature. Right: Equilibrium oxygen pressures for the dissociation of select Ni and W oxides vs temperature. Data plotted according to calculations reported in R.E. Aune, S. Sridhar and D. Sichen, *J. Chem. Thermodynamics* 26, 493 (1994) and comparable to those found in M.W. Chase, *NIST-JANAF Thermochemical Tables*, fourth edition, American Chemical Society (1998).

Assuming that tungsten oxide forms during the YBCO deposition portion of the PLD process, the exact form of tungsten oxide can only be speculated on at this point. However, WO_2 can be ruled out due to its high vapor pressure, which could lead to spalling of the upper buffer and film layers. Although WO_3 does not appear within the final fabricated samples of this study, it is thermodynamically possible to develop a $NiWO_4$ layer at its expense when NiO is present, as shown in the following reaction:

$$NiO + WO_3 = NiWO_4 \tag{9}$$

The development of $NiWO_4$ through the reaction in Eq. (9) has been reported on by El-Dahshan et al. [14] and C. Louro et al. [15] in the oxidation of nickel-tungsten alloys. In addition to the thermodynamic considerations of WO_3 formation, it may also be more kinetically feasible due to its cubic crystal structure (bcc, a_o = 7.521Å), in which low lattice mismatches between the WO_3 and Y_2O_3 phases are calculable.

The formation of $NiWO_4$ at the interface first cannot be entirely ruled out, however, because many variables and unknowns exist for the kinetics of the oxidation reaction. The formation of $NiWO_4$ from the interface may have been aided by the presence of sulfur, intentionally added to the surface of Ni-W during the annealing processes to aid the epitaxial growth of the seed layers by producing an ordered surface structure within the metal [16]. Similarly, in a study by Atanasova and Halachev [17], the development of $NiWO_4$ instead of WO_3 within Ni-W/Al_2O_3 catalysts was induced when phosphorus concentrations at the interface exceeded 1 at/nm^2. In samples with higher W concentrations, however, WO_3 was present regardless of phosphorus content. The presence of either sulfur or phosphorus may locally order the dilute Ni alloy at the surface, allowing for an easier nucleation of a ternary compound.

With the development of either WO_3 or $NiWO_4$ occurring first at the substrate–seed layer interface, a depletion of W at the interface would promote the development of NiO. Examination of the films through EDS revealed a slight depletion of W within the metal substrate and no measurable level within the NiO layer. The further growth of the NiO layer at the interface in this case is governed by the diffusion of Ni through the NiO layer forming and by the tungsten oxide layer. Similar results were reported on by Strawbridge et al. [18] on the oxidation of dilute nickel alloys at 1200ºC. In their work, NiO scale formation in a binary alloy containing 4 wt. % W was substantially less than that of a 5% Cr alloy, and internal oxidation occurred in $NiWO_4$ particles that were not fully incorporated into the NiO scale. Had NiO formed first within the Ni-W RABiTS™, then the rejection of W ahead of the growing front could have produced a boundary layer of $NiWO_4$ or WO_3. The development of an NiO reaction layer prior to the formation of $NiWO_4$ may initially favor the explanation of the relatively unchanged NiO thickness between samples seeing ever-increasing hold times at 790ºC under an oxygen partial pressure of 120 mTorr. It is possible that either an $NiWO_4$ or a WO_3 layer had developed primarily in this regime and that the NiO layer formed during the slow cooling after YBCO deposition under the higher oxygen partial pressure of 550 Torr. In support of this, the NiO layer within two 0.2-µm-thick YBCO samples deposited on pure Ni RABiTS1 from an earlier investigation [9] were examined. Both samples were deposited under the conditions described within this paper, but one sample was held at 790ºC at an oxygen partial pressure of 120 mTorr for 20 min longer (simulating a 1-µm-thick deposition requirement) prior to cooling under the same conditions as the other sample. Although changes in the YBCO microstructure were observed between the two samples, the thickness of the NiO layer was unchanged.

While an 800ºC isotherm calculated by Aune et al. [11] illustrated that an Ni-3at%W alloy would be within the Ni-NiO-$NiWO_4$ phase field, confirming the lack of WO_x phases present in the examined RABiTS™ samples, these materials are far from equilibrium conditions. If WO_3 forms initially during YBCO deposition and begins to be consumed by $NiWO_4$ once NiO begins to form in the higher oxygen environment of the cooling stage in PLD, the decreasing temperatures may result in a change in kinetics, making WO_3 harder to form. As temperature decreases, so must the diffusion rate of oxygen to the substrate interface. Based on the following equations for the same amount of oxide formation, the development of NiO would require less oxygen than would the development of WO_3:

$$Ni + 1/2O_2 = NiO \tag{10}$$

$$W + 3/2O_2 = WO_3 \tag{11}$$

This, in association with the further development of $NiWO_4$, would account for its removal in observed samples.

The uncontrolled growth of NiO is not observed in the Ni-W RABiTS™ and is attributed to the complex formation of a tungsten-based oxide. This in part played an important role in the improved physical and microstructural properties of the YBCO films. Because the samples in the PLD chamber are secured to a heat block during deposition, the uniform and minimal reaction layers produced in the Ni-W RABiTS™ may have aided in the uniformity of heat transfer to the YBCO at all stages of processing to yield an improved film. As previously reported, the YBCO films on the RABiTS2 substrates did not have randomly oriented grain formations within the upper portion of the film as were observed in the RABiTS1 materials and originally attributed to film surface cooling during deposition of the YBCO.

As the deposition of buffer and YBCO layers require a higher oxygenated environment to produce stable and stoichiometric layers [13], the development of a self-passivating or limiting reaction layer within Ni-based substrates is of great interest. In addition, this may allow for the reduction in number or specific requirements of the buffer layers needed between the Ni substrates and YBCO. Currently, work is being conducted on understanding the conditions and mechanisms of $NiWO_4$ development within Ni-W RABiTS™ and the ways in which it can be used to improve coated conductor technology for long-length tapes.

2.3.5 Conclusions

The development of a self-limiting reaction layer within Ni-W rolling-assisted biaxially textured substrates was investigated. The formation of a 5- to 8-nm-thick layer of $NiWO_4$ identified through cross-sectional TEM analysis was found to restrict the growth of NiO to between 25 and 30 nm. The $NiWO_4$ layer was found to be oriented with a (100) // {100}Ni-W orientation relationship; however, $NiWO_4$ growth directions of [001] and [010] to the <100>Ni-W were observed. The restricted growth of the NiO layer was believed to have been partially responsible for the dramatic improvement observed in the properties and quality of PLD YBCO films on the Ni-W substrates when compared with earlier pure Ni tapes.

2.3.6 References

1. A. Goyal et al., "High Critical Current Density Superconducting Tapes by Epitaxial Deposition of $YBa_2Cu_3O_x$ Thick Films on Biaxially Textured Metals," *Appl. Phys. Lett.* **69**(12), 1795 (1996).
2. A. Goyal et al., U.S. Patents 5,739,086; 5,741,377; 5,846,912; 5,898,020; 5,964,966; 5,958,599; 5,968,877.
3. A. Goyal et al., "Conductors with Controlled Grain Boundaries: An Approach to the Next Generation, High-Temperature Superconducting Wire," *J. Mater. Res.* **12**, 2924 (1997).
4. M. P. Paranthaman et al., **"**Bulk Solution Techniques to Fabricate High J_c YBCO Coated Conductors," *Physica C* **378–381**, 1009 (2002).
5. T. Aytug et al., "Reel-to-Reel Continuous Chemical Solution Deposition of Epitaxial Gd_2O_3 Buffer Layers on Biaxially Textured Metal Tapes for the Fabrication of $YBa_2Cu_3O_{7-\delta}$Coated Conductors," *J. Amer. Ceramic Soc.* **86(**2), 257 (2003).
6. B. W. Kang et al., **"**Comparative Study of Thickness Dependence of Critical Current Density of $YBa_2Cu_3O_{7-d}$ on (100) $SrTiO_3$ and on Rolling-Assisted Biaxially Textured Substrates," *J. Mater. Res*, **17**(7), 1750 (2002).
7. S. Kang et al., *J. Amer. Ceram. Soc.* (2005), in press.
8. A. Goyal et al. **"**Strengthened, Biaxially Textured Ni Substrate with Small Alloying Additions for Coated Conductor Applications," *Physica C* **382**, 251 (2002).
9. K. J. Leonard et al., "Microstructure Characterization of the Thickness Dependence of Critical Current Density of $YBa_2Cu_3O_{7-\delta}$ on Rolling-Assisted Biaxially Textured Substrates," *J. Mat. Res.* **18**(5), 1109 (2003).
10. K. J. Leonard et al., **"**Microstructural Characterization of Thick $YBa_2Cu_3O_{7-\delta}$ Films on Improved Rolling-Assisted Biaxially Textured Substrates," *J. Mat. Res.* **18**(7), 1723 (2003).
11. R. E. Aune, S. Sridhar, and D. Sichen, "A Galvanic-Cell Study of (Nickel + Tungsten + Oxygen) in the Temperature Range 1034 K to 1317 K," *J. Chem. Thermodynamics* **26**, 493 (1994).
12. M.W. Chase, *NIST-JANAF Thermochemical Tables*, fourth edition, American Chemical Society (1998).
13. T. J. Jackson, B. A. Glowacki, and J.E. Evetts, **"**Oxidation Thermodynamics of Metal Substrates during the Deposition of Buffer Layer Oxides**,"** *Physica C* **296**, 215 (1998).
14. M. E. El-Dahshan, D. P. Whittle, and J. Stringer, "The Oxidation of Nickel-Tungsten Alloys," *Corrosion Science* **16**, 83 (1976).
15. C. Louro and A. Cavaleiro, *Surface and Coatings Technology,* **116–119**, 121 (1999).
16. C. Cantoni et al., "Deposition and Characterization of $YBa_2Cu_3O_{7-\delta}$/$LaMnO_3$/MgO/TiN Heterostructures on Cu Metal Substrates for Development of Coated Conductors," *J. Mater. Res.* **18**(10), 2387 (2003).
17. P. Atanasova and T. Halachev, *Applied Catalysis A* **108**, 123 (1994).

18. A. Strawbridge, F. H. Stott, and G. C. Wood, "The Formation and Incorporation into the Scale of Internal Oxides Developed during the High-Temperature Oxidation of Dilute Nickel-Base Alloys," *Corrosion Science* **35**(5), 855 (1993).

2.4 Perovskite-Type Buffers for YBCO Coated Conductors

M. P. Paranthaman, T. Aytug, H. Y. Zhai, A. A. Gapud, P. M. Martin, K. J. Leonard, A. Goyal, and D. K. Christen

2.4.1 Introduction

The RABiTS™ and IBAD approaches have been identified as the leading techniques to fabricate long lengths of high-performance YBCO coated conductors[1–3]. In the standard RABiTS™ approach, a three-layer buffer architecture of $CeO_2/YSZ/Y_2O_3$ is used to fabricate long lengths of buffered tapes by epitaxial deposition on thermomechanically textured Ni alloy substrates. Such a structure would need at least a 50-μm layer of Cu stabilizers to stabilize the superconductor during an overcurrent situation. On the other hand, the use of Cu substrates with fully conductive architectures would be desirable because they would enable reduced ferromagnetism, higher electrical conductivity, higher thermal conductivity, and lower cost compared with Ni and Ni- alloys. Hence, it is essential to develop a superconductor with a fully conducting laminate structure having a nonoxidizing protective buffer layer to prevent substrate oxidation and diffusion of substrate components into the other buffers and/or superconductors and to stabilize the superconductor during an overcurrent situation. It would also eliminate the need for the Cu stabilizer layer on top of the superconductor and would result in an increase in the overall engineering current density.

Perovskite-based oxide buffers play an important role in second-generation YBCO coated conductors. The ideal ABO_3 perovskite structure is shown in Fig. 2.20. In addition, the list of perovskite-type oxides that have been developed for YBCO is also shown in Fig. 2.20. The material properties vary from insulators to semiconductors to metals. Conducting buffers such as $LaNiO_3$ (LNO), $SrRuO_3$ (SRO), and $La_{0.7}Sr_{0.3}MnO_3$ (LSMO) have been explored as potential candidates for this study. Sputtering was used to develop several conductive multilayer architectures. Here we report our successful demonstration of the fully conductive architectures for YBCO coated conductors.

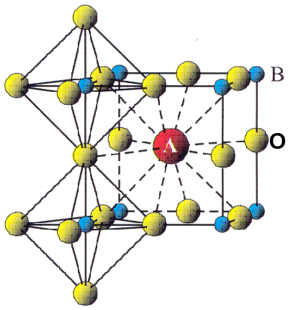

Ideal ABO_3 Perovskite Structure showing the Octahedral and 12-fold co-ordination of B and A-site cations

Material	Lattice parameter (pseudo cubic) Å	% lattice mismatch vs. YBCO	% lattice mismatch vs. Ni	Property
$BaCeO_3$	4.377	13.55	21.59	Insulator
$BaZrO_3$	4.193	9.27	17.34	Insulator
$SrRuO_3$	3.941	3.08	11.17	Metal
$SrTiO_3$	3.905	2.16	10.26	Insulator
$SrTi(Nb)O_3$	3.905	2.16	10.26	Semiconductor
$LaMnO_3$	3.880	1.60	9.70	Insulator
$(LaSr)MnO_3$	3.860	0.98	9.07	Metal
$LaNiO_3$	3.859	0.98	9.07	Metal
$NdGaO_3$	3.841	0.51	8.61	Insulator
$LaAlO_3$	3.793	-0.75	7.35	Insulator

Fig. 2.20. The ideal ABO_3 perovskite structure. The table provides the list of oxide buffers developed for YBCO coated conductors.

2.4.2 Experimental Procedure

Radio-frequency sputtering was used to grow SRO/LNO multilayers on biaxially textured Ni substrates. The sputter targets used for these experiments were made by lightly packing single-phase SRO and LNO powders into a 4-in. copper tray. LNO layers were deposited at temperatures ranging from 450 to 500°C in the presence of Ar/H_2 4% gas mixtures. The deposition rate was approximately 0.042 nm/s, and the resulting thickness was 300 nm. The details of the experimental conditions were published earlier [4,5]. Subsequent growth of SRO layers on LNO-buffered Ni substrates was performed at temperatures ranging from 600 to 650°C under 10-mTorr argon. The deposition rate for SRO was 0.048 nm/s, and the resulting thickness was 400 nm.

The LSMO/Ni multilayers were grown on biaxially textured Cu substrates. To minimize the Cu diffusion and also to reduce the oxidation rate of the substrate, a protective 1.6-µm-thick Ni overlayer was deposited by dc sputtering at a temperature of 600°C in a reducing atmosphere of forming gas (Ar/H_2 4%). Subsequent growth of the LSMO layers on Ni-buffered Cu substrates was performed at a temperature of 550 to 625°C by rf sputtering in a mixture of forming gas and 2×10^{-5} Torr of H_2O. The typical LSMO thickness is around 300 nm. The details of the experimental conditions were published earlier [6].

The LSMO/Ir multilayers were grown on biaxially textured Ni-W 3 at.% substrates. Ir metal is identified as having excellent oxidation and corrosion resistance among platinum group elements. In addition, its native oxide, IrO_2 is also a conducting layer with low oxygen diffusivity. These properties make Ir a unique candidate for this study. Ir thin films were deposited on Ni-W substrates by dc sputtering at a temperature of 550 to 650°C in the presence of $Ar\text{-}H_2$ 4%. Subsequent LSMO deposition was performed at 625 to 700°C in the presence of forming gas and 5×10^{-5} Torr H_2O. The details were published earlier.[7].

YBCO films were deposited on the three multilayers by PLD at 780°C in 120 mTorr oxygen with an average laser energy of 400 to 410 mJ. A stoichiometric YBCO target was used. Deposition was followed by annealing under 550 Torr oxygen during cooldown. Typical YBCO thickness varied from 200 to 700 nm. The crystalline structure of the films was analyzed by XRD techniques. Scanning electron microscopy (SEM) micrographs were taken with a Hitachi S-4100 field emission microscope. Cross-section examination of the samples were conducted with a high-resolution TEM equipped with an energy-dispersive spectrometry (EDS) unit. The films were then prepared for current density measurements by depositing silver current and voltage leads, followed by oxygen annealing at 500°C for 1 h. A standard four-point probe technique with a voltage criterion of 1 µV/cm was used to measure the transport critical current density.

2.4.3 Results and Discussion

LNO buffers were grown epitaxially on biaxially textured Ni substrates by sputtering. YBCO films grown on LNO-buffered Ni had a reduced transition temperature and poor superconducting properties, mainly due to the diffusion of Ni from the substrate into the superconductor. SRO buffers were also grown untextured on Ni substrates. Highly textured SRO layers were grown on LNO-buffered Ni substrates. YBCO films with a critical current density of 1.3 MA/cm^2 for a thickness of 200 nm have been achieved on conducting architecture of SRO/LNO/Ni substrates. The field-dependent critical current density for the tape is shown in Fig. 2.21. The irreversibility field for this tape is 7.5 T. The temperature-dependent net resistivity for YBCO/SRO/LNO/Ni conducting structure is shown in Fig. 2.22. YBCO film showed a metallic behavior from room temperature down to the transition temperature of 91 K. The measured room-temperature net resistivity was around 15 µΩ-cm. This indicates that there was some contact barrier between the superconductor and Ni substrate through SRO/LNO. Secondary ion mass spectrometry (SIMS), SEM, and X-ray analysis indicated the presence of nonconducting impurities at the buffer-Ni interface. However, NiO impurities were not observed before the YBCO deposition. As can be seen from Fig. 2.22, the SRO/LNO layers were fully connected to the underlying Ni substrate.

Sputtering was used to grow Ni overlayers epitaxially on biaxially textured Cu substrates. Highly textured LSMO layers were then grown on Ni-buffered Cu substrates. YBCO films with a high critical current density of 2.3 MA/cm^2 were grown on conductive LSMO/Ni/Cu structures. The field-dependent critical current density is shown in Fig. 2.23. The measured irreversibility for the tape is around 7.5 T. The temperature-dependent resistivity for YBCO/LSMO/Ni/Cu tape is shown in Fig. 2.24. The room-temperature resistivity for this tape is around 6 µΩ-cm; the measured transition temperature is 90.4 K. SIMS analyses indicated that the LSMO layer is a good Ni diffusion layer. However NiO impurity was

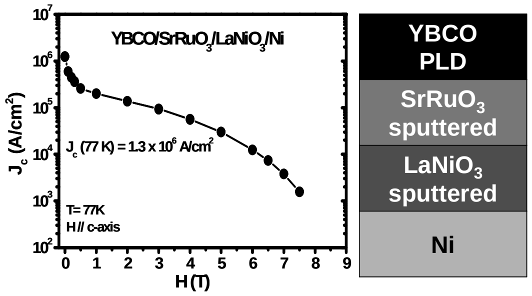

Fig. 2.21. Field dependence of the transport critical current density, J_c, for a 200-nm-thick PLD YBCO film on sputtered $SrRuO_3$/$LaNiO_3$ multilayers on biaxially textured Ni substrates.

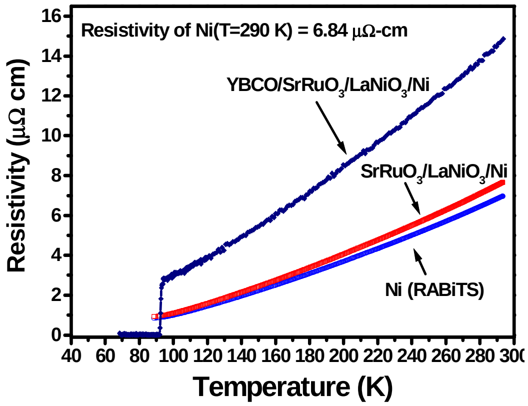

Fig. 2.22. Temperature dependence of the net resistivity for YBCO/$SrRuO_3$/$LaNiO_3$/Ni tape. Also shown for comparison are the ρ_{net}-T data for an as-grown $SrRuO_3$/$LaNiO_3$/Ni tape and for a biaxially textured Ni substrate.

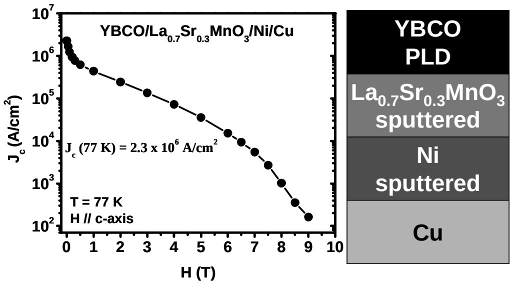

Fig. 2.23. Field dependence of the transport critical current density, J_c, for a 200 nm-thick PLD YBCO film on sputtered $La_{0.7}Sr_{0.3}MnO_3$/Ni multilayers on biaxially textured Cu substrates.

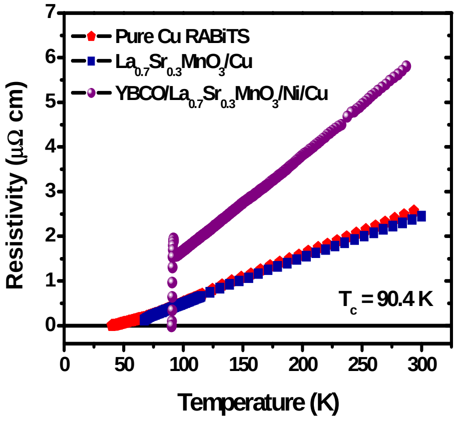

Fig. 2.24. Temperature dependence of the net resistivity for the YBCO/$La_{0.7}Sr_{0.3}MnO_3$/Ni/Cu tape. Also shown for comparison are the ρ_{net}-T data for an as-grown $La_{0.7}Sr_{0.3}MnO_3$/Cu tape and for a biaxially textured Cu substrate.

also observed at the Ni/LSMO interface. Also, Cu and Ni layers are completely miscible, and Cu/Ni interdiffusion depends mainly on the YBCO process temperatures. That is why thick Ni overlayers were deposited. However, the presence of thick Ni overlayer contributes to the ferromagnetism in the tape. Hence, there is a need to develop a fully conductive architecture based on nonmagnetic overlayers. For comparison, resistivity data for both LSMO/Cu and Cu tapes are also plotted in Fig. 2.24.

Ir buffers were grown epitaxially on biaxially textured Ni-W substrates. LSMO buffers were then grown on Ir-buffered Ni-W substrates. YBCO films with a critical current density of 2.2 MA/cm^2 (for a 200-nm thickness) and a critical current density of 1.3 MA/cm^2 (for a 700-nm thickness) were grown on conductive LSMO/Ir/Ni-W tapes. The field-dependent critical current density is shown in Fig. 2.25. The irreversibility field is 6.8 T for a 200-nm-thick YBCO film and 5.8 T for a 700-nm-thick YBCO film. Their temperature-dependent resistivities are shown in Fig. 2.26. Resistivity data for Ni-W and LSMO/Ir/Ni-W tapes are also shown for comparison. These resistivity data indicate that YBCO films are completely connected to the underlying Ni-W substrate. This is the first demonstration of the fully conductive architectures developed for second-generation YBCO coated conductors. Their observed transition temperature is 88–89 K. The cross-sectional TEM bright field image for 200-nm-thick YBCO film on fully conductive LSMO/Ir/Ni-W substrates is shown in Fig. 2.27. All the interfaces are clean, and there is no formation of oxide impurities at the substrate-buffer interface. The selected area diffraction data taken at all the interfaces indicate that YBCO, LSMO, and Ir films are cube-on-cube oriented. Ni-W and Ir also interdiffuse under certain conditions. Details are currently under investigation. Efforts are being made to grow conductive LSMO/Ir buffers on textured Cu substrates. The results will be published later.

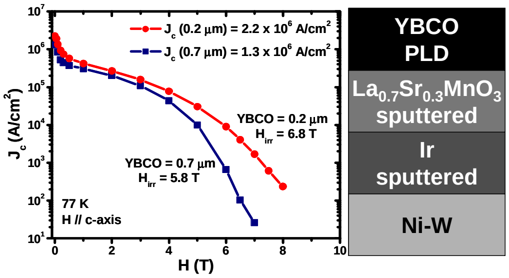

Fig. 2.25. Field dependence of the transport critical current density, J_c, for a 200-nm-thick PLD YBCO film on sputtered $La_{0.7}Sr_{0.3}MnO_3$/Ir multi-layers on biaxially textured Ni-W substrates.

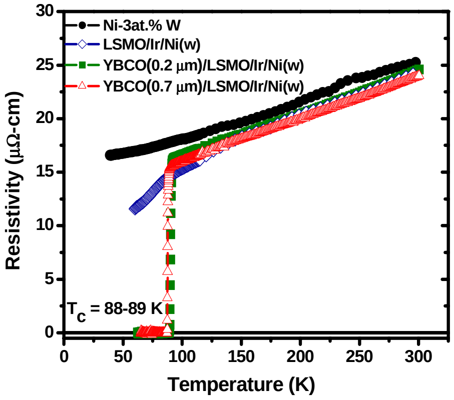

Fig. 2.26. Temperature dependence of the net resistivity for two YBCO/$La_{0.7}Sr_{0.3}MnO_3$/Ir/Ni-W tapes. Also shown for comparison are the ρ_{net}-T data for an as-grown $La_{0.7}Sr_{0.3}MnO_3$/Ir/Ni-W tape and for a biaxially textured Ni-W substrate.

2.4.4 Summary

We have developed three conductive architectures of YBCO/SRO/LNO/Ni; YBCO/LSMO/Ni/Cu; and YBCO/LSMO/Ir/Ni-W for second-generation YBCO coated conductors. Detailed temperature-dependent resistivity data indicate that fully conductive architectures were observed for YBCO/LSMO /Ir/Ni-W tapes. A self-field critical current density of 2.2 MA/cm^2 was observed for it. These results demonstrate that fully conductive architectures of YBCO/LSMO/Ir may be suitable for biaxially textured Cu or Cu-alloy substrates.

2.4.5 References

1. A. Usoskin et al., "Large Area YBCO-Coated Stainless Steel Tapes with High Critical Currents," *IEEE Trans on Appl. Supercond.* **13**, 2452 (2003).
2. Y. Iijima, K. Kakimoto, and T. Saitoh, "Fabrication and Transport Characteristics of Long Length Y-123 Coated Conductors Processed by IBAD and PLD," *IEEE Trans. on Appl. Supercond.* **13**, 2466 (2003).

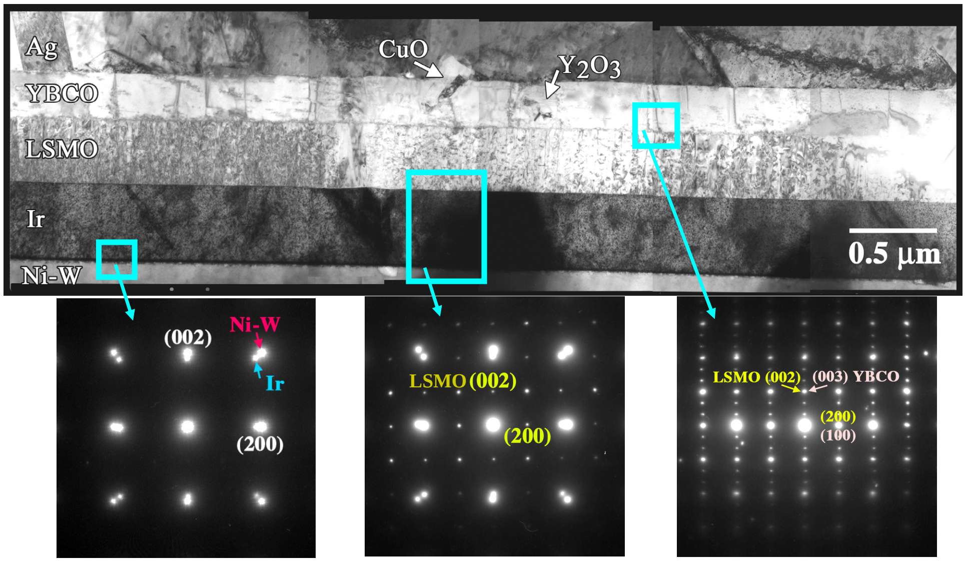

Ni-W [010] // Ir [010]   Ni-W [010] // Ir [010] // LSMO [010]   LSMO [010] // YBCO [010]

Fig. 2.27. Cross-sectional TEM bright-field image of the 200-nm-thick YBCO film on $La_{0.7}Sr_{0.3}MnO_3$/Ir buffered Ni-W tape. All the Ni-W/Ir, Ir/LSMO, LSMO/YBCO interfaces are clean. No oxide is present at the Ni-W/Ir interface. The selected area diffraction patterns taken at all the interfaces show all the layers to be oriented cube-on-cube.

3. D. T. Verebelyi et al., “Uniform Performance of Continuously Processed MOD-YBCO-Coated Conductors Using a Textured Ni-W Substrate,” *Supercond. Sci. and Technol.* **16**, L19 (2003).
4. T. Aytug et al., “Growth and Superconducting Properties of $YBa_2Cu_3O_{7-\delta}$ Films on Conductive $SrRuO_3$ and $LaNiO_3$ Multilayers for Coated Conductor Applications,” *Appl. Phys. Lett.* **76**(6), 760 (2000).
5. T. Aytug et al., “Growth and Characterization of Conductive $SrRuO_3$ and $LaNiO_3$ Multilayers on Textured Ni Tapes for High-J_c $YBa_2Cu_3O_{7-\delta}$ Coated Conductors,” *J. Mater. Res.* **16**(9), 2661 (2001).
6. T. Aytug et al., “Electrical and Magnetic Properties of Conductive Cu-Based Coated Conductors,” *Appl. Phys. Lett.* **83** (19), 3963 (2003).
7. T. Aytug et al., “An Approach for Electrical Self-Stabilization of High-Temperature Superconducting Wires for Power Applications,” *Appl. Phys. Lett.* **85**(14) 2887 (2004).

2.5 Growth of Lanthanum Manganate Buffer Layers for Coated Conductors via a Metal-Organic Decomposition Process

K. Venkataraman, E. E. Hellstrom, and M. P. Paranthaman

2.5.1 Introduction

The growth of epitaxial films of $MBa_2Cu_3O_{7-x}$ (M-123, where M = Y or a rare earth element) on metal substrates is being pursued worldwide as a means of fabricating HTS wire in long-length form for electric power applications [1–3]. This approach to develop coated-conductor HTS structures for high-current devices relies on transmitting the cube-textured epitaxy of the substrate to the M-123 film. The substrate can be a cube-textured metal (such as Ni or a Ni-base alloy) or a metal to which a cube-textured seed layer has been applied. In addition, a buffer layer is usually required to prevent constituent metal atoms in the substrate from diffusing into the M-123 film and to retard metal substrate oxidation during M-123 growth. Hence, the architecture of an M-123 coated conductor typically consists of the metal substrate, a seed layer (if one is needed), a buffer layer, a cap layer to enhance the epitaxy transmission, and the M-123 film.

Recently coated conductors that were about 8 m long and that had critical currents of more than 100A/(cm-width)$^{-1}$ have been fabricated by using the RABiTS™ process [4]. In the RABiTS™ approach, a four-layer architecture of CeO_2/YSZ/Y_2O_3/Ni/Ni–W is used to fabricate long lengths of buffered tapes by epitaxial deposition on a thermomechanically textured alloy [5]. Typically, the layers are grown via a combination of vacuum processes, such as rf magnetron sputtering, and nonvacuum chemical solution deposition (CSD) processes, such as sol-gel deposition or metal-organic deposition (MOD) [6]. A simpler three-layer RABiTS™ architecture of CeO_2/YSZ/CeO_2/Ni-W, in which the MOD is used to deposit the CeO_2 seed layer, has also been reported [7]. To reduce costs, increase throughput, and simplify and streamline the coated-conductor fabrication processes for commercial viability, it is desirable to replace the multilayer RABiTS™ architecture with a CSD-grown single buffer layer that is both a good epitaxial template for Y-123 growth and a strong diffusion barrier.

LMO has been identified as a suitable candidate for this purpose, given the low diffusivity of Ni and O through it [8] and the close lattice match of its pseudocubic lattice parameter to Y-123 and cube-textured RABiTS™ Ni–W [8]. LMO has been successfully grown by rf magnetron sputtering on bare RABiTS™ Ni-W [8], on MgO-buffered Ni alloy [5], and on $LaAlO_3$ and $SrTiO_3$ by using CSD, [9–12]. However, there has been no report of LMO growth on bare Ni alloy substrates The processes described in the literature [9–12] are not suitable for growing LMO films on bare metal substrates because they employ highly oxidizing atmospheres such as air or pure O_2. This paper reports the first successful use of an MOD process to grow an epitaxial LMO film on a bare RABiTS™ Ni-W tape.

2.5.2 Experimental Procedure

The MOD precursor solution was prepared by adding 0.454 g of La(III) acetylacetonate hydrate ($La(acac)_3.xH_2O$) and 0.352 g of Mn(III) acetylacetonate ($Mn(acac)_3.H_2O$) to 3 mL of acetic acid and stirring over a hot plate at ~70°C for about 1 min. Longer heating times resulted in rapid gelation of the solution. 1.5 mL of methanol was added slowly to the mixture to prevent gelation, and heating with stirring was continued for another 10 min. The total volume of the solution was 5 mL, with a cation concentration of 0.2 M per cation, assuming La acac has one water of crystallization. Heating was continued for about 10 min. Then, a few drops of 99% ethanolamine were added to stabilize the solution. The cation precursors were from Aldrich Co., and the solvents were from Alfa Aesar. The solution was stable for 3 to 4 days before gelation occurred. Substrates used for the study were 2×1 cm cube-textured (~99% cube-on-cube, typical (111) $\Delta\varphi$ ~7.5º, (002) $\Delta\omega$ ~5.5º) Ni-W (3 at.% W). These substrates had a c(2×2) sulfur superstructure that had been formed by vacuum-annealing the substrates at 700 to 800ºC in the presence of 5×10^{-7} to 1×10^{-6} Torr H_2S. They were preheated at ~120°C for ~1 min in an oven to remove volatile surface species. Then the precursor solution was spin-coated onto them at 2000 rpm for 30 s. The coated substrates were then fired at temperatures between 800 and 1100°C for 15 min in flowing humidified forming gas (Ar/4%H_2), then rapidly cooled to room temperature in the same ambient. Forming gas was used to prevent oxidizing the Ni-W substrate during firing. The heating ramp rate was ~500°C/min, whereas the cooling times were typically about 20 min. Samples were fired at various soak temperatures and H_2O contents in the forming gas to study the effects of the variables on the growth characteristics and quality of the fired films.

The forming gas was humidified by passing one stream of forming gas through a water bath at room temperature and by combining it with a dry stream of forming gas before it entered the furnace. Each stream was controlled by a separate flowmeter, thus allowing mixing of the streams in different proportions. The relative humidity of the wet stream, measured by a Cole-Parmer humidity meter, was ~71% at 21.8ºC, which corresponds to a partial pressure of water of ~19.6 Torr.

The films were characterized by XRD and SEM (LEO 1530 FE-SEM). A Philips XRG3100 diffractometer (Cu-K_α) was used to record θ-2θ XRD scans of the samples to provide information on the phases present in the film, their degree of texture, and thickness. A Picker 4-circle diffractometer (Cu-K_α) was used to obtain detailed epitaxy information from pole figures.

2.5.3 Results

Figure 2.28 shows the XRD scans of samples fired at 900°C in forming gas containing various water contents. LMO was observed to form when fired with $P(H_2O)$ = 2 Torr. At all higher water vapor partial pressures, MnO and La_2O_3 were observed, except for the sample fired with $P(H_2O)$ = 8 Torr, which consisted of LaO and MnO.

Figure 2.29 shows that LMO formed at $P(H_2O)$ = 1 and 2 Torr at 1100°C, but did not form with 3 Torr of H_2O or in dry forming gas. At 1100°C, La_2O_3 and MnO_2 were observed to form in dry forming gas, whereas La_2O_3 alone was formed in 3 Torr H_2O.

Figure 2.30 shows increasing intensity of the LMO (011) peak in θ-2θ XRD scans with increasing firing temperature. The lowest temperature we studied where LMO could be detected was 850°C, and it was also observed at 1100°C, the highest temperature we studied. Figures 2.31(a) and (b) are secondary electron images of the surfaces of two samples fired at 1100°C, one with 2 Torr of H_2O in the forming gas ambient [Fig. 2.31(a)], and the other with 3 Torr of H_2O [Fig. 2.31(b)]. The 2-Torr sample formed an LMO film, whereas XRD showed that the 3-Torr sample formed La_2O_3. (XRD did not show a peak for a phase that contained Mn.)

Figure 2.31(a) shows that the surface of the LMO film is homogeneous, well developed, uniform in coverage, and apparently smooth. In contrast, Fig. 2.31(b) shows a rough surface consisting of segregated islands, with no smooth, uniform film present.

Figures 2.32(a) and (b) are backscattered electron images of these same two films. Figure 2.32(a) shows the backscattered electron image of the LMO film, which appears to be uniform in elemental composition. The image in Fig. 2.32(b) shows bright (La-rich) and dark (La-deficient) regions corresponding to the separate oxides and island structure seen in Fig. 2.32(b).

The (200) LMO pole figure in Fig. 2.33 was obtained from a film made at 1100°C with 2 Torr H_2O. It indicates a cube-on-cube epitaxy of the film.

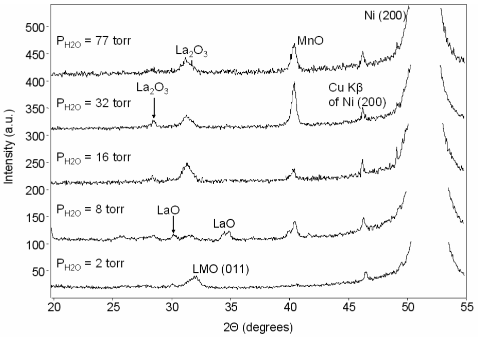

Fig. 2.28 XRD patterns after firing at 900°C with different water vapor partial pressures.

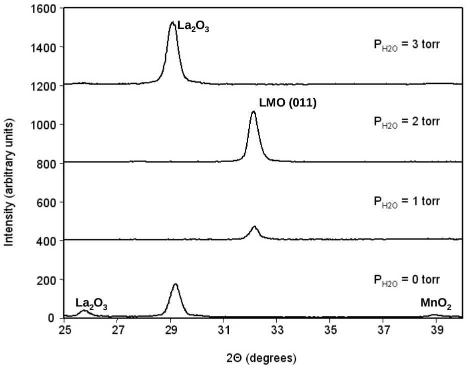

Fig. 2.29. XRD patterns of products after firing at 1100°C with various water vapor partial pressures.

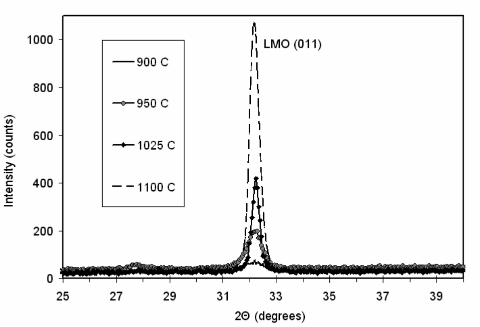

Fig. 2.30. XRD patterns of products after firing at various temperatures with 2 Torr H_2O.

2.5.4 Discussion

All of the water vapor partial pressures used in this study were selected such that the oxygen partial pressure set by the H_2:H_2O ratio in the forming gas at the reaction temperature was low enough to keep the Ni-W substrate from oxidizing. No peaks from NiO or Ni-W oxides were seen in any of the XRD patterns. The data in Figs. 2.28 and 2.29 show that water vapor partial pressure has a strong effect on the conversion of the metal-organic precursor to LMO. We found that at 1100°C, there is a narrow window (between 1 and

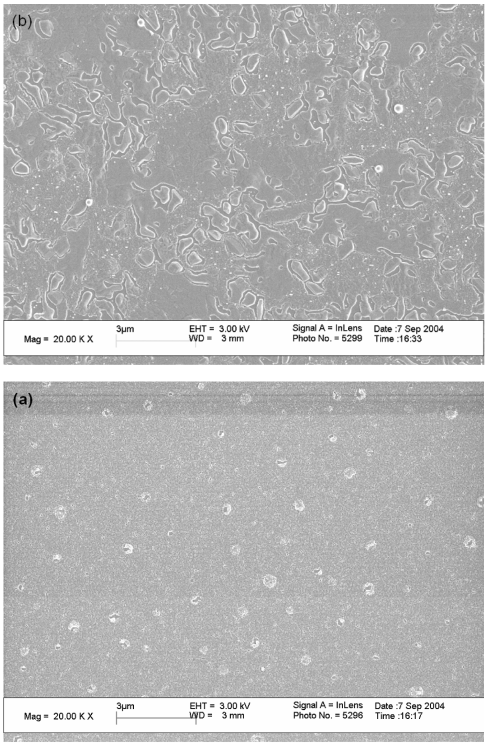
(b)
Mag = 20.00 K X
3μm
EHT = 3.00 kV
WD = 3 mm
Signal A = InLens
Photo No. = 5299
Date :7 Sep 2004
Time :16:33
(a)
Mag = 20.00 K X
3μm
EHT = 3.00 kV
WD = 3 mm
Signal A = InLens
Photo No. = 5296
Date :7 Sep 2004
Time :16:17

Fig. 2.31. Secondary electron image of the surface of the film after firing at 1100°C with (a) 2 Torr H_2O and (b) 3 Torr H_2O.

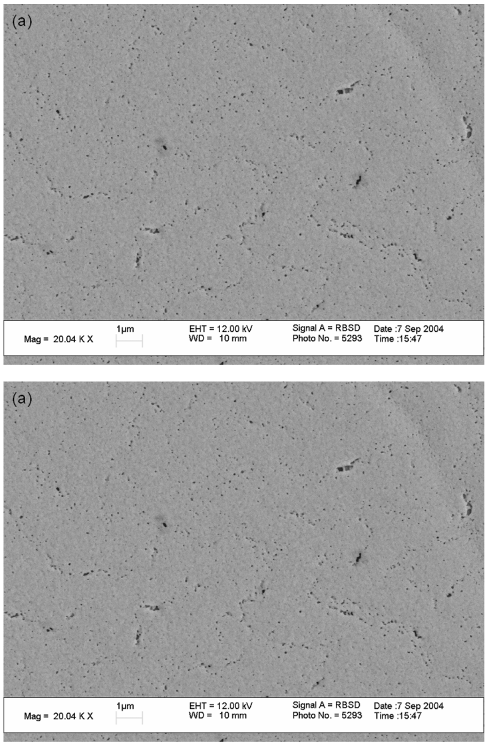
(a)
Mag = 20.04 K X
1μm
EHT = 12.00 kV
WD = 10 mm
Signal A = RBSD
Photo No. = 5293
Date :7 Sep 2004
Time :15:47
(a)
Mag = 20.04 K X
1μm
EHT = 12.00 kV
WD = 10 mm
Signal A = RBSD
Photo No. = 5293
Date :7 Sep 2004
Time :15:47

Fig. 2.32. Backscattered electron image of the surface of the film after firing at 1100°C with (a) 2 Torr H_2O and (b) 3 Torr H_2O.

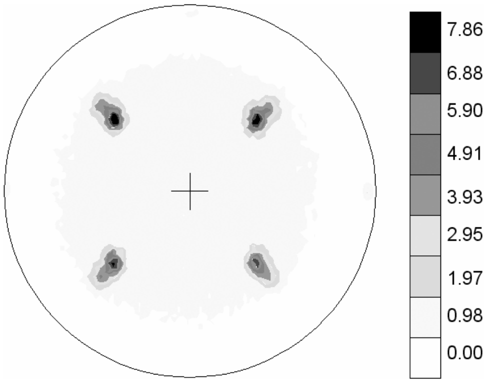

Fig. 2.33. (002) LMO pole figure showing cube-on-cube epitaxy of the LMO film. (1100°C, 2 Torr H_2O)

2 Torr H_2O) in the water vapor partial pressure at which LMO forms. This corresponds to oxygen partial pressures between 3.5×10^{-17} and 5×10^{-17} bar. La_2O_3 and MnO_2 formed with dry forming gas, whereas only La_2O_3 formed with 3 Torr H_2O. The XRD pattern for the 1100°C 3-Torr sample showed a phase that contained Mn. We have not studied this finding further.

Figure 2.30 shows that temperature has an important effect on the quality of the film. Only the (011) peak is seen in the XRD pattern, indicating the LMO is highly oriented. Because all films had similar thicknesses (~30 nm as observed from SEM images of sample cross sections), the increases in intensity represent higher degrees of crystallization, epitaxy, and grain size. Our best quality film formed at 1100°C with 2 Torr H_2O. That was the highest temperature we studied.

The LMO film grew with a (011) orientation rather than the (001) orientation of LMO films grown on similar RABiTS™ substrates with a *c*(2×2) sulfur superstructure when rf magnetron sputtering was used [8]. A report [13] indicates that LMO films grow with the (110) orientation on clean Ni surfaces. The Ni surfaces of the RABiTS™ tape sections used in the experiments described here had a *c*(2×2) sulfur superstructure, so it is not clear why the films did not grow with the (001) orientation.

2.5.5 Summary

We used an MOD precursor to deposit an epitaxial thin film of LMO on a textured, bare Ni-W alloy substrate. The LMO had a (011) orientation on the substrate. We found that LMO only formed in a narrow range of water vapor partial pressure (at 1100°C, between 1 and 2 Torr H_2O). The best film was grown at 1100°C with 2 Torr H_2O.

2.5.6 References

1. D. Larbalestier et al., "High-T_c Superconducting Materials for Electric Power Applications," *Nature* **414**(6861), 368–77 (2001).
2. Y. Iijima and K. Matsumoto, "High-Temperature-Superconductor Coated Conductors: Technical Progress in Japan," *Supercond. Sci. Technol.* **13**, 68–81 (2000).
3. D. K. Finnemore et al., "Coated Conductor Development: An Assessment," *Phys. C* **320**, 1–8 (1999).
4. D. T. Verebelyi et al., "Uniform Performance of Continuously Processed MOD-YBCO-Coated Conductors using a Textured Ni–W Substrate," *Supercond. Sci. and Technol.* **16**, L19–L22 (2003).
5. M. Paranthaman et al., "Growth of Thick $YBa_2Cu_3O_{7-\delta}$ Films Carrying a Critical Current of Over 230 A/cm on Single $LaMnO_3$-Buffered Ion-Beam-Assisted Deposition MgO Substrates," *J. Mater. Res* **18**(9), 2055–59 (2003).
6. S. Sathyamurthy et al., "Chemical Solution Deposition of Lanthanum Zirconate Buffer Layers on Biaxially Textured Ni-1.7% Fe-3% W Alloy Substrates for Coated-Conductor Fabrication," *J. Mater. Res.* **17**(6), 1543–49 (2002).
7. M. S. Bhuiyan et al., "MOD Approach for the Growth of Epitaxial CeO_2 Buffer Layers on Biaxially Textured Ni-W Substrates for YBCO Coated Conductors," *Supercond. Sci. Technol.* **16**, 1305–1309 (2003).
8. T. Aytug et al., "Single Buffer Layers of $LaMnO_3$ or $La_{0.7}Sr_{0.3}MnO_3$ for the Development of $YBa_2Cu_3O_{7-\delta}$ Coated Conductors: A Comparative Study," *J. Mater. Res* **17**(9), 2193–96 (2002).
9. D. Y. Jung and D.A. Payne, "Patterning of Rare-Earth Manganate Thin Layer Using Self-Assembled Organic Thin-Film Templates," *Bull. Korean Chem. Soc.* **20**(7), 824–26 (1999).
10. H. J. Hwang, A. Towata, and M. Awano, "Fabrication of Lanthanum Manganese Oxide Thin Films on Yttria-Stabilized Zirconia Substrates by a Chemically Modified Alkoxide Method," *J. Am. Ceram. Soc.* **10**(10), 2323–27 (2001).
11. A. D. Polli et al., "Processing Magnetoresistive Thin Films via Chemical Solution Deposition," *J. Mater. Res.* **14**(4), 1337–42 (1999).
12. Y. Shimizu and T. Murata, "Sol-Gel Synthesis of Perovskite-Type Lanthanum Manganite Thin Films and Powders using Metal Acetylacetonate and Poly(Vinyl Alcohol)," *J. Am. Ceram. Soc.* **80**(10), 2702–2704 (1997).
13. C. Cantoni et al., "Growth of Oxide Seed Layers on Ni and Other Technologically Interesting Metal Substrates: Issues Related to Formation and Control of Sulfur Superstructures for Texture Optimization," *IEEE Trans. Appl. Superconduct.* **13**(2), 2646–50 (2003).

2.6 Epitaxial Growth of Eu_3NbO_7 Buffer Layers on Biaxially Textured Ni-W Substrates

M. S. Bhuiyan, M. P. Paranthaman, D. Beach, L. Heatherly, A. Goyal, and E. A. Payzant (ORNL);
K. Salama, University of Houston, Texas

2.6.1 Introduction

As an alternative to the relatively higher cost and complexity of vacuum deposition techniques, chemical solution processing techniques have emerged as viable low-cost nonvacuum methods for producing ceramic oxide powders and films [1–3]. These processes offer many desirable aspects, such as precise control of metal oxide precursor stoichiometry and composition, ease of formation of epitaxial oxides, relatively easy scale-up of the film and possibly low cost. In the Rolling-Assisted Bi-axially Textured Substrate (RABiTS™) approach, a three-layer architecture of CeO_2/YSZ/Y_2O_3/Ni-W is used to fabricate long lengths of buffered tapes. The purpose of the buffer layers is to retard oxidation of Ni, to reduce the lattice mismatch between Ni and YBCO, and to prevent diffusion of Ni into YBCO.

We have been examining solution routes to epitaxial buffers on Ni-W substrates to simplify the multilayer buffered architecture to a single-layer buffered architecture. In recent years, various rare-earth oxides (RE_2O_3) and rare-earth zirconium oxide ($RE_2Zr_2O_7$) films have been grown epitaxially on biaxially textured Ni and Ni-W substrates by solution based methods [4–8]. A new series of single rare earth niobate (Gd_3NbO_7) buffer layers [9] has been reported for the growth of superconducting YBCO films on biaxially textured Ni-W (3 at.%) substrates. Preliminary results show that YBCO films with a critical current density of 1.1 MA/cm^2 can be grown on Gd_3NbO_7-buffered Ni-W substrates. Here we report in detail about the nucleation and growth of Eu_3NbO_7 on Ni-W substrates. Eu_3NbO_7 has a cubic pyrochlore structure with a lattice parameter of 10.672 Å (pseudocubic lattice parameter: 3.773 Å). It has a good chemical compatibility with Ni-W and good thermal stability. In this paper, we describe our successful development of the growth of Eu_3NbO_7 buffer layer on rolled Ni-W substrates by sol-gel method.

2.6.2 Experimental Details

All solution manipulations were carried out according to standard Schlenk techniques under an atmosphere of argon. Niobium ethoxide and 2-methoxyethanol (Alfa) were used as received. Europium acetate (Alfa) was purified beforehand. Europium acetate was prepared by the reaction of europium oxide (Alfa, 99.99%) with a fivefold excess of 25% acetic acid at 80°C 1 h [10]. The resulting clear solution was filtered, and the solvent was removed. The precipitate was dried at 120°C under dynamic vacuum for 16 h. A small sample was allowed to react with excess water and was then dried to constant weight at 35°C to form the well-characterized tetrahydrate. The weight gain of this sample allowed us to estimate that the degree of hydration of the europium acetate after vacuum drying is 1.5 ± 0.2.

A europium methoxyethoxide solution in 2-methoxyethanol was prepared by charging a flask with 1.234 g (3.75 mmoles) of europium acetate and 10 mL of 2-methoxyethanol. The flask was refluxed for 1 h at 130°C, and 0.398 g (1.25 mmoles) of niobium ethoxide was added. The contents were rediluted with additional 2-methoxyethanol, and the distillation/redilution cycle was repeated twice more to completely exchange the metal alkoxide ligand for the methoxyethoxide ligand. The final concentration was adjusted to produce 10 mL of a 0.50 M stock solution. The solution was spin-coated onto short (2×1 cm) cube-textured Ni-W substrates at 5000 rpm for 30 s, and the samples were heat-treated at 1050°C for 15 min in a reducing atmosphere of Ar-4% H_2. The samples were introduced into a preheated furnace kept at 1050°C after a 5-min purge with Ar-4% H_2 gas mixture at room temperature. After a 15-min heat-treatment at 1050°C, the samples were quenched to room temperature with the same atmosphere. The heating and cooling rates were in the range of 350 to 400°C/min. An individual treatment produced a Eu_3NbO_7 film that was about 20 nm thick. Multiple coatings were made to prepare thick films.

The Eu_3NbO_7 films were characterized by XRD for phase purity and texture and by high-temperature XRD for nucleation. SEM was used to determine homogeneity and microstructure. A Philips model XRG3100 diffractometer with CuKα radiation was used to record the θ–2θ XRD patterns. A Picker 4-circle diffractometer was used for texture analysis. High-temperature in situ XRD experiments were carried out in a flowing atmosphere of He-4% H_2 and heating ramp of 400°C/min on a Scintag PAD X diffractometer with an mBraun linear position-sensitive detector (PSD) covering an 8° range centered at $2\theta = 31°$. A Hitachi S-4100 field emission SEM was used for microstructural analyses of the samples.

2.6.3 Results and Discussion

For in situ high-temperature XRD, the samples were heated from room temperature to 1200°C at a heating rate of 400°C/min in a reducing atmosphere of He–4% H_2 (see Fig. 2.34). The θ–2θ XRD patterns were recorded at 400, 600, 800, 900, 1000, 1100, and 1150°C. A plot for nucleation of Eu_3NbO_7 film on

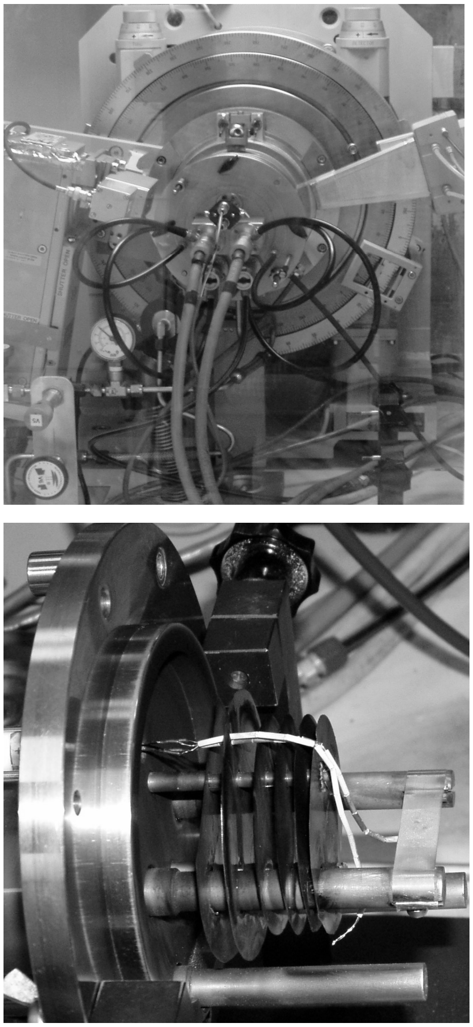

Fig. 2.34. High-temperature XRD setup with linear detector (upper right) and sample-heating strip (lower right).

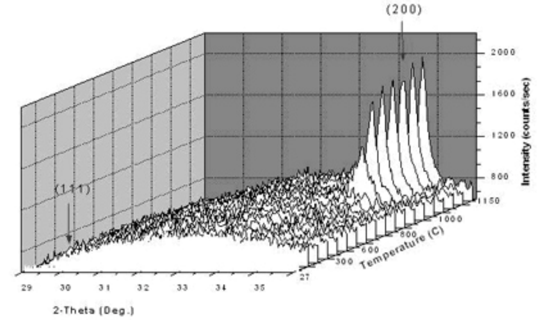

Fig. 2.35. Typical θ–2θ scan obtained for a 20-nm-thick Eu_3NbO_7 buffered Ni–W substrate heat-treated at various temperatures in a high-temperature in situ XRD. The Eu_3NbO_7 film has a preferred *c*-axis orientation and the crystallization starts around 800°C

textured Ni–W substrates is shown in Fig. 2.35, which indicates that the nucleation of the film took place around 800°C.

A typical θ–2θ XRD scan for a spin-coated Eu_3NbO_7 film on the Ni–W substrate is shown in Fig. 2.36. The intense Eu_3NbO_7 (004) peak reveals the presence of a *c*-axis-aligned film. The typical (222) pole figure in log scale for a Eu_3NbO_7 film grown on the Ni-W substrate shown in Fig. 2.37 indicates the presence of a single cube-on-cube texture. The ω (out-of-plane) and ϕ (in-plane) scans of these films on the Ni–W substrates are shown in Fig. 2.38.

The Eu_3NbO_7 film has a good out-of-plane and in-plane texture with FWHM of 6.8° and 8.21°, respectively, as compared to the Ni-W substrates values of $\Delta\omega = 5.51°$ and $\Delta\phi = 6.72°$.

The sample SEM micrograph shown in Fig. 2.39 indicate that the Eu_3NbO_7 buffer layers provide very good coverage for the Ni-W surface. Most of the Ni-W grain boundary grooves on the Ni-W surface were found to be well covered. Figure 2.39 also shows that the buffer layers are continuous and free of cracks.

These results indicate that sol-gel techniques can produce continuous, dense, and crack-free buffer layers on rolled Ni-W substrates. Efforts are being made to deposit YBCO by PLD on Eu_3NbO_7 (sol-gel)/Ni-W.

2.6.4 Summary

We have successfully developed a new chemical solution process to grow epitaxial Eu_3NbO_7 buffer layers on Ni-W (002) substrates. In-plane and out-of-plane alignments indicate that the buffer layers are sharply textured. Pole figures of buffer layers show a predominantly cube-on-cube texture. The continuous, dense, and crack-free microstructure revealed in the SEM micrographs indicate that the surfaces of the buffer layers deposited on rolled Ni-W substrates the sol-gel process are suitable for deposition of YBCO film.

2.6.5 References

1. M. W. Rupich, Y. P. Liu, and J. Ibechem, “Low-Temperature Formation of $YBa_2Cu_3O_{7-x}$ Superconducting Films from Molecular Cu-Ba-Y Precursors,” *Appl. Phys. Lett* **60**(11), 1384 (1992).
2. M. Paranthaman and D. B. Beach, “Growth of Highly Oriented $TlBa_2Ca_2Cu_3O_{9-y}$ Superconducting Films on Ag Substrates Using a Dip-Coated Barium Calcium Copper Oxice Sol-Gel Precursor,”*J. Amer. Ceram. Soc.* **78**, 2551 (1995).

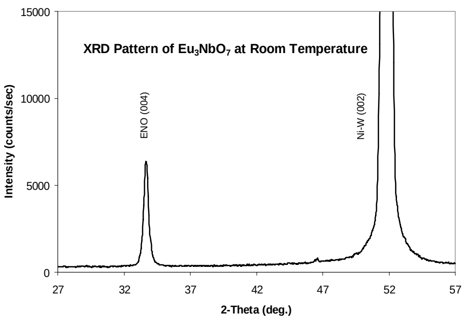

Fig. 2.36. Typical room-temperature θ-2θ scan obtained for a 20-nm-thick Eu_3NbO_7 buffered Ni-W substrate. The film has a preferred *c*-axis orientation.

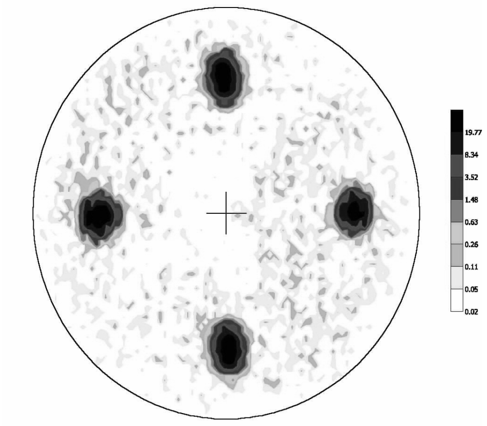

Fig. 2.37. Typical Eu_3NbO_7 (222) pole figure obtained for a 20-nm-thick film grown on the textured Ni-W substrate.

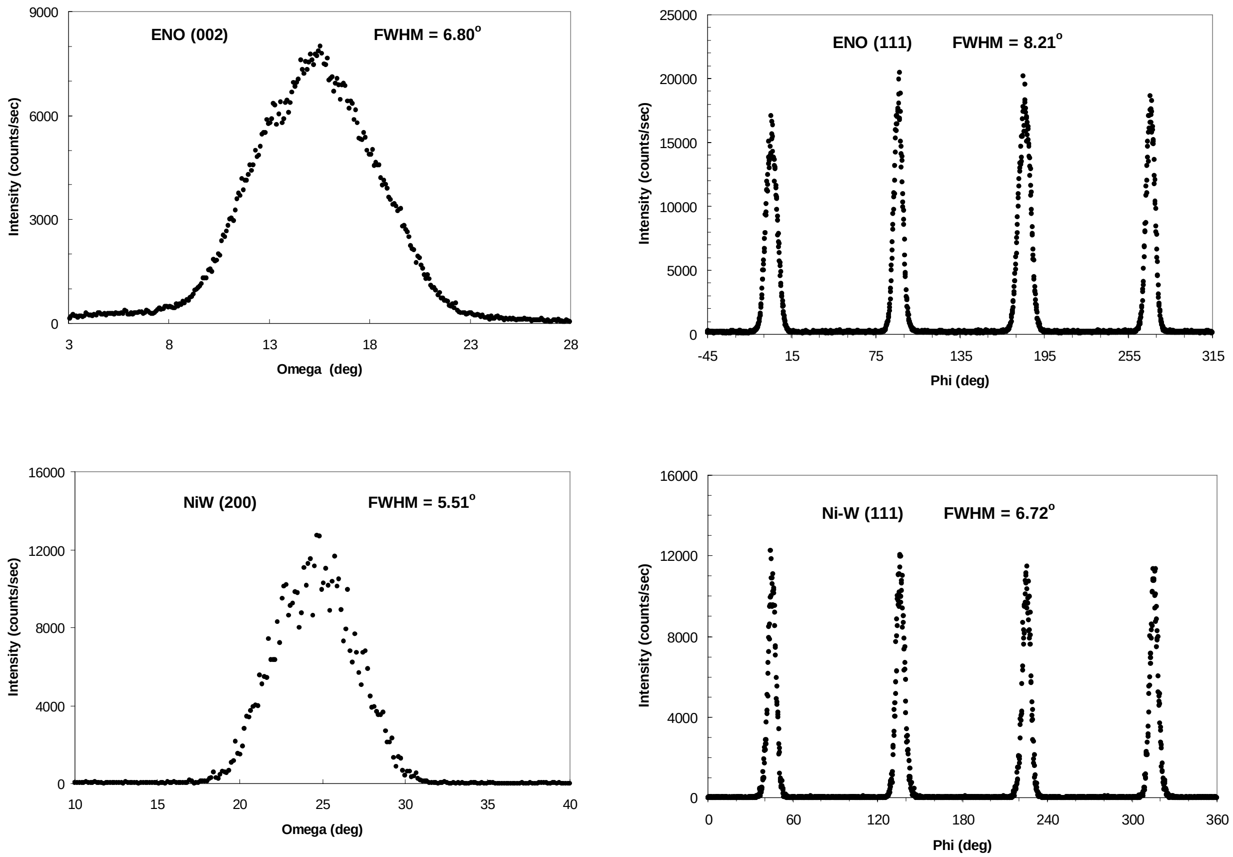

Fig. 2.38. Phi and omega scans obtained for a 20-nm-thick Eu_3NbO_7 film grown on the textured Ni-W substrate. The FWHM values for each scan are shown inside the patterns.

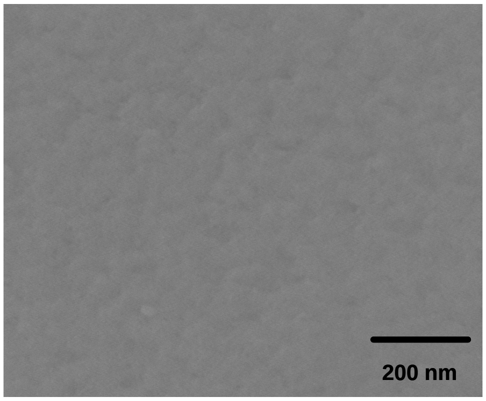

Fig. 2.39. SEM micrograph of the film surface deposited on Ni-W.

3. F. F. Lange, "Chemical Solution Routes to Single-Crystal Thin Films," *Science* **273**, 903 (1996).
4. M. Paranthaman et al., "Fabrication of Long Lengths of Epitaxial Buffer Layers on Biaxially Textured Nickel Substrates Using a Continuous Reel-to-Reel Dip-Coating Unit," *J. Amer. Ceram. Soc.* **84**(2), 273 (2001).
5. S. Sathyamurthy et al., "Chemical Solution Deposition of Lanthanum Zirconate Buffer Layers on Biaxially Textured Ni-1.7%Fe-3%W Alloy Substrates for Coated-Conductor Fabrication," *J. Mater. Res.* **17**(6), 1543 (2002).
6. T. Aytug et al., "Reel-to-Reel Continuous Chemical Solution Deposition of Epitaxial Gd_2O_3 Buffer Layers on Biaxially Textured Metal Tapes for the Fabrication of $YBa_2Cu_3O_{7-\delta}$ Coated Conductors," *J. Amer. Ceram. Soc.* **86**, 257 (2003).
7. M. S. Bhuiyan et al., "MOD Approach for the Growth of Epitaxial CeO_2 Buffer Layers on Biaxially Textured Ni–W Substrates for YBCO Coated Conductors," *Supercond. Sci. Technol.* **16**(11), 1305 (2003).
8. M. S. Bhuiyan et al., *Fall Mater. Res. Soc. Symp. Proc.* **EXS-3**, EE4.5.1 (2004).
9. M. Paranthaman et al., "Epitaxial Growth of Solution-Based Rare-Earth Niobate, $ReNbO_7$, Films on Biaxially Textured Ni-W Substrates," *J. Mater. Res.* **20**(1), 6 (2005).
10. L. Gmelin, pp. 34 in *Gmelin Handbook of Inorganic Chemistry*, eighth edition, Springer-Verlag, Berlin (1984).

2.7 Alternate Buffer Architectures for Improved YBCO Coated Conductors

M. Paranthaman, S. Sathyamurthy, and A. Goyal (ORNL); T. Kodenkandath, X. Li, W. Zhang, C. L. H. Thieme, U. Schoop, D. T. Verebelyi, and M. W. Rupich (AMSC); M. S. Bhuiyan (University of Houston)

2.7.1 Introduction

High-temperature superconductors, discovered in 1987, are moving into the development of second-generation wires or tapes. The first generation relied on BSCCO; the second generation is based on YBCO superconductors, which have the potential to be less expensive and to perform better in liquid nitrogen temperatures under applied magnetic fields. RABiTS™ has been used to fabricate high-performance YBCO coated conductors. The RABiTS™ process utilizes thermomechanical processing to obtain flexible, biaxially textured Ni-alloy substrates [1,2]. Buffer layers play a key role in transferring the texture of the metal substrate to the YBCO and prevent reaction between the substrate and the superconductor. The RABiTS™ architecture consists of a starting template of biaxially textured Ni-W (3 at.% or 5 at.%) with a 75-nm Y_2O_3 seed layer, a 75-nm YSZ barrier layer, and a 75-nm CeO_2 cap layer [2]. All the buffers are deposited by physical vapor deposition (PVD) processes. However, efforts are being made to replace these architectures with simplified architectures comprising multifunctional buffers deposited by industrially scalable methods such as chemical solution deposition (CSD). CSD offers significant cost advantages over PVD. Solution coating is amenable to the application of complex oxides. Reel-to-reel dip-coating or slot-die coating can be used to scale up the solution deposition process.

Both $La_2Zr_2O_7$ (LZO) and CeO_2 buffers have been identified as potential candidates for this study. A metal organic deposition (MOD) process has been developed to grow highly textured LZO and CeO_2 layers on biaxially textured Ni-W substrates [3,4]. Recently, 10-m lengths of RABiTS™-based YBCO coated conductors with a critical current of ~270 A/cm have been fabricated with high uniformity and reproducibility [5]. The challenge is to match the performance of American Superconductor's current PVD buffer stack with low-cost, nonvacuum solution techniques. In this paper, we report our recent success toward fabrication of all-MOD buffer YBCO tapes.

2.7.2 Experimental Procedure

Biaxially textured Ni-W (3 at.% or 5 at.%) substrates were used for this study. All the substrates were annealed under suitable H_2S atmospheres to get the desired sulfur c(2×2) superstructures at the Ni-W surface. The LZO precursor solution was prepared from lanthanum isopropoxide (Alfa, La 40% assay), zirconium n-propoxide in n-propanol (Alfa, 70%) and 2-methoxyethanol (Alfa, spectrophotometric grade). The details of the solution preparation were reported earlier [3]. A total cation concentration of about 0.5 M was used to grow LZO films with a thickness of 40 nm in a single coat. MOD was used to prepare the precursor solution for CeO_2 films. Spin coating was used to deposit both LZO and CeO_2 films with a typical speed of 2000 rpm. About 0.8-µm-thick MOD-YBCO films were deposited on MOD buffers by using American Superconductor's modified TFA process [5].

XRD was used to characterize the samples for phase purity and texture; the microstructure of both buffers and the YBCO were monitored by atomic force microscopy (AFM), and SEM. The resistivity and transport critical current density were measured by using a standard four-point probe technique. The voltage contact spacing was 0.4 cm. A 1-µV/cm criterion was used for calculation of the critical current density values. Deposition of Ag electrical contacts onto the samples was followed by an O_2 annealing in 1 atm for 30 min at 500°C.

2.7.3 Results and Discussion

A typical θ-2θ XRD pattern of a single coat 40-nm-thick LZO film on a textured Ni-W substrate is shown in Fig. 2.40. The θ-2θ scans indicate the presence of strong *c*-axis (004) aligned films. Detailed X-ray studies indicate the presence of a highly textured LZO film. To replace the e-beam Y_2O_3 seed in the RABiTS™ architecture with MOD seed, it is essential to compare the texture data of various MOD seed layers with that of e-beam Y_2O_3 seed. The texture data obtained on various seed layers grown on biaxially textured Ni-W 5 at.% substrates are shown in Table 2.4. It is very clear that the texture of MOD LZO seeds is comparable to that of e-beam Y_2O_3 seeds. Even though the texture of MOD CeO_2 is also good, we did not pursue it further. This is mainly due to the crack formation in thick CeO_2 films on textured Ni substrates. Both SEM and AFM studies indicate that LZO films are smooth, continuous, and crack-free. The typical AFM scan for 80-nm-thick LZO coated Ni-W substrate is shown in Fig. 2.41.

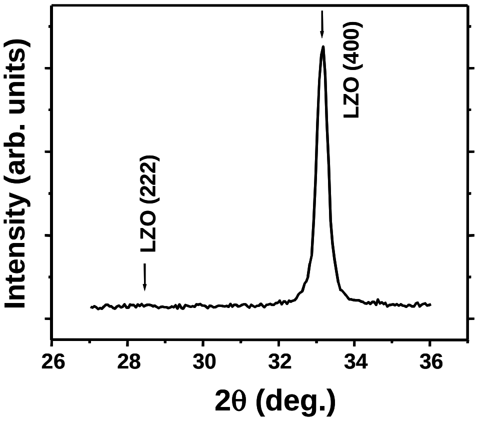

Fig. 2.40. A typical θ-2θ scan for a 40-nm-thick LZO film grown on biaxially textured Ni-W substrates by metal-organic deposition. LZO films were processed at 1100°C for 15 min in flowing Ar/H_2 4% gas atmospheres. LZO film has a preferred *c*-axis orientation.

The performance of MOD LZO seeds was tested by using magnetron rf sputtering highly textured YSZ barrier layers and CeO_2 cap layers on top of LZO layers. Results (current-volt plots) are shown in Fig. 2.42. YBCO films with a critical current density of 2.7 MA/cm^2, corresponding to a critical current of 212 A/cm-width, were obtained. This result is the first demonstration of the performance of an MOD LZO template carrying a critical current of more than 200 A. Secondary ion mass spectrometry (SIMS) analysis indicated that the properties of LZO seeds are comparable to the properties of e-beam Y_2O_3 seeds.

Multiple spin-coatings were used to grow thick LZO films. Between each coating, films were heat-treated at 1100°C for 30 min in Ar/H_2 4%. Highly textured 120-nm-thick LZO films were grown in three coatings on biaxially textured Ni-W substrates. Both MOD-CeO_2 and YBCO films were grown on MOD LZO layers. A typical θ-2θ XRD pattern of 0.8-µm-thick MOD-YBCO films grown on all-MOD buffers of CeO_2/LZO is shown in Fig. 2.43. These scans indicate the presence of a strong *c*-axis (00l) aligned YBCO films. The measured current-voltage plots obtained on all MOD YBCO coated conductors are shown in Fig. 2.44. YBCO films with a critical current density of 1.75 MA/cm^2, corresponding to

Table 2.4. Texture data on various seed layers

Sample	Full width at half maximum (degrees)			
	(002) omega Phi = 90	(002) omega Phi = 0	(111) phi	True, in-plane
Ni-W 5% (AMSC)	5.55	8.71	6.84	4.54
Y_2O_3 seed e-beam (AMSC)	4.93	7.92	6.96	5.21
LZO seed MOD (ORNL)	6.86	11.1	7.42	3.65
CeO_2 seed MOD (ORNL)	5.47	9.03	6.85	4.43
Y2O3 seed MOD (ORNL)	8.41	22.14	7.99	—

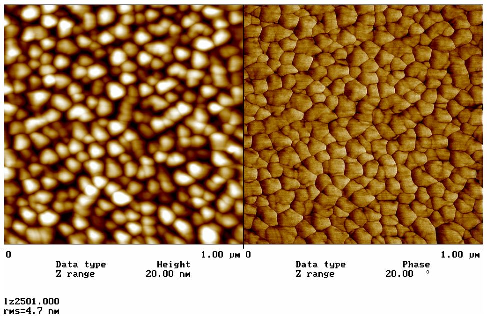

Fig. 2.41. AFM scan of the surface of an 80-nm-thick LZO film (two coats) grown on a biaxially textured Ni-W substrate. The rms surface roughness is around 4.7 nm.

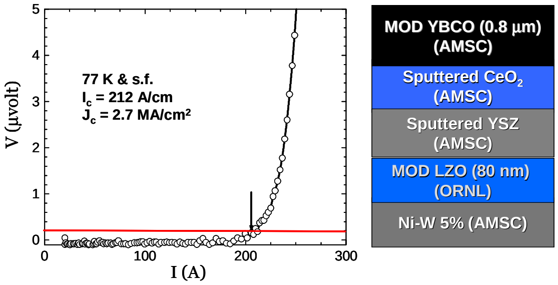

Fig. 2.42. Superconducting properties of a 0.8-µm-thick MOD-YBCO film grown on CeO_2 (sputtered)/YSZ (sputtered)/MOD-LZO (80 nm) buffered Ni-W substrates. A self-field critical current density of 2.7 MA/cm^2 at 77 K was obtained.

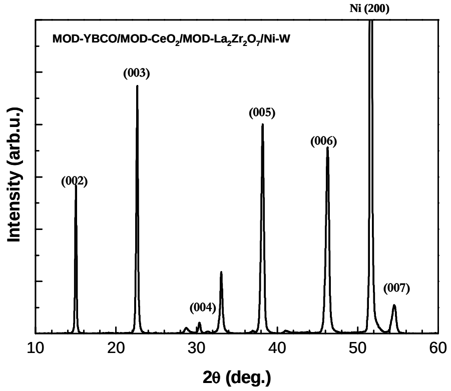

Fig. 2.43. A typical θ-2θ scan for a 0.8-µm-thick MOD-YBCO film grown on MOD-CeO_2 (60 nm)/MOD-LZO (120 nm) buffered Ni-W substrates. YBCO film has a preferred *c*-axis orientation.

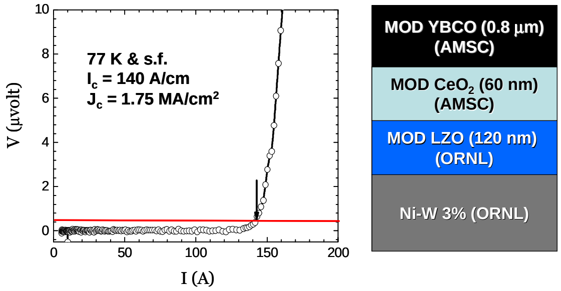

Fig. 2.44. Superconducting properties of a 0.8-µm-thick MOD-YBCO film grown on MOD-CeO_2 (60 nm)/MOD-LZO (120 nm) buffered Ni-W substrates. A self-field critical current density of 1.75 MA/cm^2 at 77 K was obtained.

a critical current of 140 A/cm-width, were achieved. This is the first demonstration of the all-MOD-based high-performance YBCO coated conductors. Efforts are being made to analyze the film, and the results will be published in the future. the all-MOD route promises to be a lower-cost process to fabricate long lengths of high-performance YBCO coated conductors.

2.7.4 Conclusions

A chemical solution deposition process has been developed to grow highly textured LZO and CeO_2 buffer layers. About 40-nm/coat LZO films were grown reproducibly on Ni-W substrates. Detailed texture data indicated that the performance of MOD LZO seeds was comparable to that of e-beam Y_2O_3 seeds. MOD-YBCO films with a critical current of 212 A/cm were grown on MOD-LZO seeds with sputtered YSZ and CeO_2 caps. In addition, MOD-YBCO films with a critical current of 140 A/cm were grown on all-MOD buffered [CeO_2 (60 nm)/LZO (120 nm)] Ni-W substrates. Efforts are being made to achieve the near-term goal of 300 A/cm on all-MOD buffers.

2.7.5 References

1. A. Goyal et al., “High Critical Current Density Superconducting Tape by Epitaxial Deposition of YBCO Thin Films on Biaxially Textured Metals,” *Appl. Phys. Lett.* **69**, 1795 (1996).
2. A. Goyal, M. Paranthaman, and U. Schoop, “The RABiTS Approach: Using Rolling-Assisted Biaxially Textured Substrates for High-Performance YBCO Superconductors,” *MRS Bulletin* **29**, 552 (2004).
3. S. Sathyamurthy et al., “Chemical Solution Deposition of Lanthanum Zirconate Buffer Layers on Biaxially Textured Ni-1.7%Fe-3%W Substrates for Coated Conductor Fabrication,” *J. Mater. Res.* **17**, 1543 (2002).
4. M. S. Bhuiyan et al., “MOD Approach for the Growth of Epitaxial CeO_2 Buffer Layers on Biaxially Textured Ni-W Substrates for YBCO Coated Conductors,” *Supercond. Sci. Tech.* **16**, 1305 (2003).
5. M. W. Rupich et al., “Metalorganic Deposition of YBCO Films for Second-Generation High-Temperature Superconductor Wires,” *MRS Bulletin* **29**, 572 (2004).

2.8 Chemical Solution Deposition of Lanthanum Zirconate Barrier Layers Applied to Low-Cost Coated Conductor Fabrication

S. Sathyamurthy, M. Paranthaman, H. Y. Zhai, S. Kang, T. Aytug, C. Cantoni, K. J. Leonard,
*E. A. Payzant, H. M. Christen, and A. Goyal (ORNL)***;** *X. Li, U. Schoop, T. Kodenkandath, and*
M. W. Rupich (AMSC)

Currently, a common RABiTS™ architecture employs a Ni-3 at.% W (Ni-W) alloy substrate with a nickel overlayer followed by a buffer layer sequence of Y_2O_3/YSZ/CeO_2. The superconductor is then deposited on the CeO_2 cap layer. A variety of deposition techniques are used for the deposition of the various layers. The Ni overlayer is deposited by dc-sputtering, the Y_2O_3 seed layer is deposited by electron beam evaporation, and the YSZ barrier layer and the CeO_2 cap layer are deposited by rf sputtering. Because of the variety of deposition techniques, scale-up of the architecture would be complex and expensive. We have reported our results with a scalable nonvacuum solution-based deposition technique for the deposition of LZO seed layers directly onto Ni-W substrates. We obtained consistent and reproducible properties and critical current densities of up to 2 MA/cm^2. We found that LZO seed layers can be consistently deposited on the Ni-W surface by the sol-gel process and that they show optimal adhesion to the substrate. This technique eliminates the need for the Ni overlayer. Recently, using sol-gel–processed LZO as a single buffer layer, we demonstrated a critical current density of 2 MA/cm^2 for a 0.2-μm YBCO layer deposited by PLD. In this report, we explore in-depth the use of sol-gel–processed LZO films as seed and barrier layers, thus simplifying the coated-conductor architecture from YBCO/CeO_2/YSZ/Y_2O_3/Ni/Ni-W to YBCO/LZO/Ni-W or YBCO/CeO_2/LZO/Ni-W. The simplified architecture will render the conductor fabrication route more scalable and cheaper. We report on the epitaxial growth and characterization of sol-gel–processed LZO buffers on Ni-W substrates, including onset of the nucleation and growth of the layers, the properties of the interface between the Ni-W substrate and the LZO layer, and the crystallinity of the surface of the LZO film. We also report on the performance of these LZO films as barrier layers during the PLD of YBCO films of various thicknesses. We also demonstrate high critical current density on YBCO processed by a trifluoroacetate-based MOD process on CeO_2-capped LZO barrier layers on Ni-W substrates.

The coating solution was prepared from alkoxides of lanthanum and zirconium. Lanthanum isopropoxide (Alfa, La 40% assay), Zirconium n-propoxide in n-propanol (Alfa, 70%), and 2-methoxyethanol (Alfa, spectrophotometric grade) were used as received. The alkoxides were handled in an argon-filled glove box, and the solution preparation was carried out under an argon atmosphere in a Schlenck-type apparatus. Stoichiometric quantities of lanthanum isopropoxide and zirconium n-propoxide were dissolved in 50 mL of 2-methoxyethanol in a 250-mL round-bottom flask. The solution was refluxed in excess 2-methoxyethanol. Based on the studies reported in the literature [1,2], we believe that lanthanum and zirconium methoxyethoxides are formed. The isopropanol formed during the exchange reaction was distilled out along with the excess 2-methoxyethanol. Solutions with a total cation concentration of 0.25 M and 1 M were used to coat thin (20-nm) and thicker (100-nm) films of LZO, respectively.

The Ni-W tapes were fabricated by cold-rolling to total deformations of greater than 98%. The details of this process have been reported earlier [3]. The Ni-W substrates, 1 cm wide and 50 μm thick, were then cleaned by reel-to-reel ultrasonication in isopropanol at a rate of 1m/h. Cleaning was followed by a recrystallization anneal by inductive heating in a reel-to-reel vacuum chamber under 3×10^{-7} Torr of H_2S and a residence time of 20 min at 1250°C to obtain the desired cube texture. The substrates, about 3 cm long and 1 cm wide, were spin-coated with LZO films at a spin speed of 2000 rpm for 30 s. The samples were then annealed at 1100°C for 15 min to 1 h.

XRD was used to characterize the phase purity and texture of the LZO layers. SEM was used for homogeneity and microstructure, and Rutherford Backscattering Spectroscopy (RBS) was used for composition and thickness analysis. A Philips XRG3100 diffractometer with Cu-K_α radiation was used to record θ-2θ XRD patterns. The texture analysis was performed with a Picker 4-circle diffractometer. The microstructural analysis of these samples was performed with a Hitachi S-4100 SEM with a field emission gun. The measurement of thickness and analysis of composition were performed by RBS; 5-MeV He^{2+} ions were used at near-normal incidence and were detected at a 160° scattering angle. With RBS, thickness could be measured to within 0.5 to 1 nm and the composition to within 5%. The nucleation and growth of LZO from the amorphous film were observed with high-temperature in situ XRD in a He-4%H_2 atmosphere on a Scintag PAD X diffractometer with an mBraun linear PSD covering an 8° range centered at a 2θ of 31°. Atomic force microscopy (AFM) and reflection high-energy electron diffraction (RHEED) were used for the analysis of the surface quality of the LZO films. The interface between the substrate and the LZO films was characterized by using a Philips CM200 TEM with a field emission gun. The performance of the LZO films as a barrier layer was evaluated in this study by depositing YBCO films by two approaches. YBCO films were deposited by PLD directly onto LZO-buffered Ni-W substrates (YBCO/LZO/Ni-W). Additionally, YBCO films were deposited by a trifluoroacetate based solution approach on LZO buffer layers with a sputtered CeO_2 cap layer (YBCO/CeO_2/LZO/Ni-W). The details of the PLD process and the trifluoroacetate process have been published elsewhere. The samples were then prepared for current density measurements by depositing silver for current and voltage leads, followed by oxygen annealing at 500°C for 1 h. A standard four-point probe technique (1-μV/cm criterion) was used to measure critical current density.

The initial thin LZO films were applied to annealed Ni-W substrates by spin-coating a 0.25 M LZO solution with a spin speed of 2000 rpm for 30 s, followed by annealing in an Ar-4%H_2 atmosphere at 1100°C for 1 h. The thickness of the films was determined by RBS analysis to be 20 nm. For a single LZO layer to perform as a good single barrier layer, a film thickness of 80 to 100 nm is required. The coating and annealing steps were repeated several times to obtain the proper thickness. The XRD patterns obtained from 1, 3, and 5 coats of LZO with intermediate annealing steps are shown in Fig. 2.45. It is

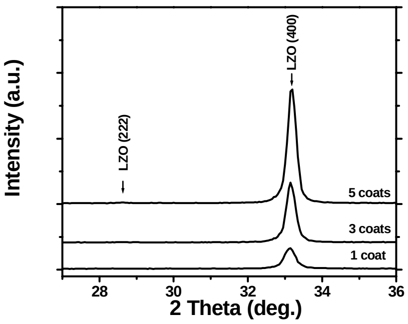

Fig. 2.45. XRD patterns of multiple coats of LZO showing proportional increase in the (004) peak intensity with the number of coats with no detectable amount of the (222) peak.

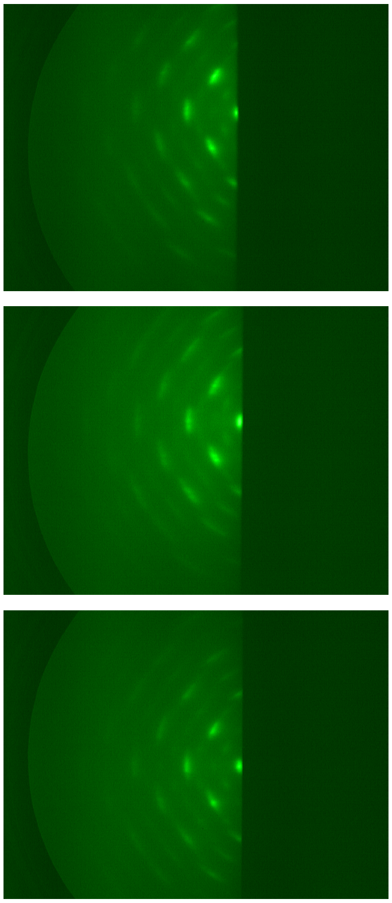

Fig. 2.46. RHEED patterns of LZO multiple coats of LZO showing good surface crystallinity of the sol-gel derived films. Top to bottom: one coat, three coats, five coats.

evident from the figure that there is a proportional increase in the intensity of the (400) peak with the number of coats while the intensity of the (222) peak remains at background levels. The in-plane and out-of-plane texture of the various layers were measured by using a Picker 4-circle goniometer. The LZO films were found to have an out-of-plane texture ($\Delta\omega$) of 6.25° and an in-plane texture ($\Delta\phi$) of 8.4°.

For epitaxial films used in multilayers, however, the bulk crystallinity and texture measured using XRD is not sufficient. It is necessary to monitor the surface texture and crystallinity. For that purpose, RHEED analysis was performed on the multiple coats of LZO. The RHEED patterns, shown in Fig. 2.46, indicate that the LZO films on samples coated one, three, and five times have good surface crystallinity and good texture.

HTXRD was used to study the nucleation and growth of the 20-nm-thick LZO films. The nucleation of LZO was studied by heating the sample from room temperature to 1200°C at a heating rate of 600°C/min in a reducing He-4% H_2 atmosphere and by monitoring the θ-2θ XRD patterns at 400, 600, 700, 750, 800, 850, 900, 1000, and 1100°C. The growth of the LZO film was studied by heating a sample up to 1100°C and collecting θ-2θ XRD data every 16 s. The nucleation characteristics of the LZO film obtained from this experiment are shown in Fig. 2.47. It is evident from the figure that the LZO nucleates at around 750°C. It was also determined from this study that the film growth is complete within the first few minutes at the process temperature. From this result, it is clear that the processing of the LZO films does not require a 1 h hold, which has been the usual hold time to fabricate LZO films, at 1100°C. Consequently, the hold time for processing these 20-nm LZO films was reduced to 15 min. The proportional increase in the (004) peak intensity with the number of coats obtained with a heat treatment with a 1 h hold time was also obtained with a 15-min hold time.

Cross-sectional TEM was used to study the interface between the Ni-W substrate and the LZO multiple-coat barrier layer. The high-resolution TEM image in Fig. 2.48 shows that the LZO film grows with a rotated cube-on-cube epitaxy of LZO[110]$(\bar{1}10)$//Ni-W[001](020) in-plane and LZO(004)//Ni-W(200) out-of-plane alignments. This is illustrated within the SAD pattern shown in Fig. 2.48(b). By using a high-resolution EDS line scan [Fig. 2.48(c)] it was determined that the interface between the LZO and the Ni-W substrates was clean. The surface roughness of the LZO film was characterized by AFM. The film was found to have an average roughness of about 5.4 nm on a 5 × 5 μm scale. Attempts are currently under way to replace the multiple-coating annealing step of LZO with a single-step process. The XRD patterns of a thin LZO film (20-nm) and a thick (100-nm) film, both processed in a single step, were compared. The 1 M coat shows an increase in (400) peak consistent with larger thickness while the (222) is at background levels. This suggests that it may be possible to process LZO in a single step. The RHEED pattern of the 100-nm LZO film shows

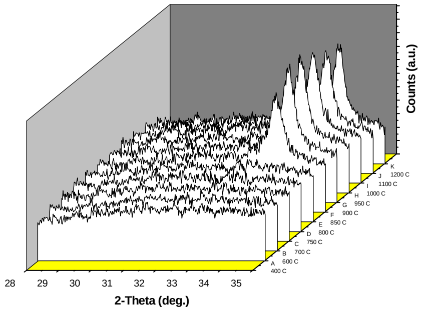

Fig. 2.47. A typical θ–2θ scan obtained for a 20-nm-thick LZO film on Ni-W substrates in a high-temperature in situ XRD showing nucleation of LZO during the heatup to the process temperature.

that the thick LZO film processed in a single step has good surface crystallinity.

The performance of the LZO buffer layers was evaluated by depositing YBCO by PLD directly onto the LZO films and by deposition of YBCO by a TFA-based MOD process on a sputtered CeO_2 cap on the LZO films. The CeO_2 cap layer was used in the latter case to prevent a reaction between the LZO layer and the TFA precursors used for YBCO deposition. The performance of a single LZO buffer layer is compared with that of the $CeO_2/YSZ/Y_2O_3$ buffer architecture in Fig. 2.49. In Fig. 2.49, the field-dependent critical current densities are given for 0.2-µm-thick YBCO films deposited by PLD on Ni-W substrates with (1) a single sol-gel buffer, (2) a three-layer buffer with a sol-gel seed layer, and (3) an all-vacuum standard three-layer buffer architecture. It is clear from this figure that the performance of the single LZO buffer layer is comparable to that of the three-layer buffer architecture. The thickness of the LZO buffer layers in this case was only about 70 nm; the buffer layer thickness is about 300 nm for the three-layer buffer architecture.

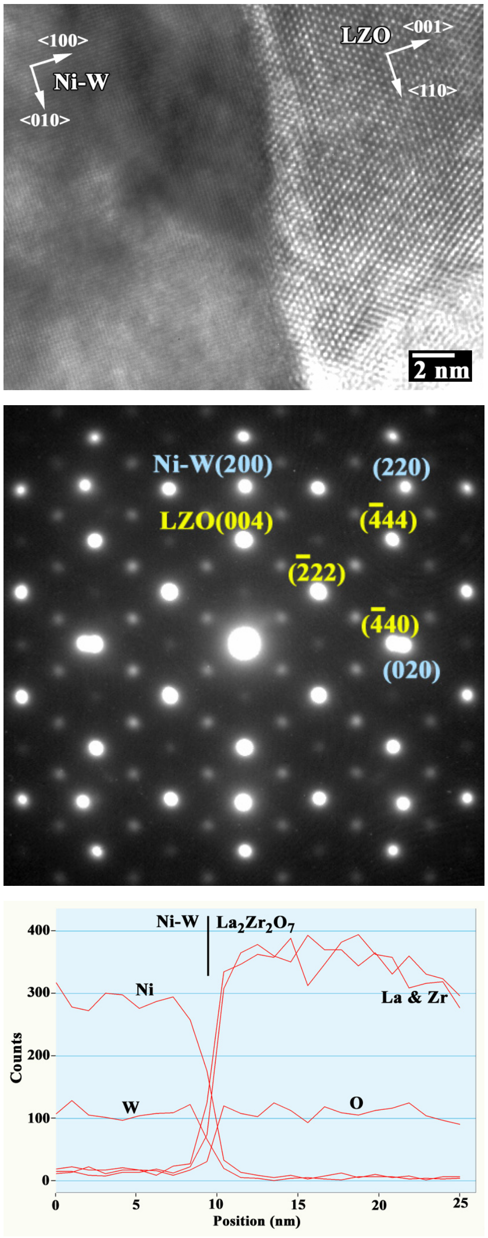

Fig. 2.48. Top: High-resolution cross-section TEM of LZO film on Ni-W substrate. Middle: SAD pattern obtained from cross-section TEM showing Ni-W[001]//LZO [110], Ni-W(010//LZO(110) orientation in the in-plane direction and Ni-W(100)// LZO(001) in the out-of-plane orientation. Bottom: EDS line-scan showing a clean interface between LZO film and Ni-W substrate.

The current-voltage characteristics of TFA based MOD YBCO on CeO_2 capped LZO barrier layers on Ni-W substrates were obtained from standard four-point probe measurements. Thus, for a 0.8-µm YBCO layer deposited on about 150 nm of buffer layers (80 to 100 nm of LZO with about 50 nm of CeO_2) a critical current density of 1.7 MA/cm^2 and an critical current of 135 A/cm have been measured. Although the critical current density is lower than that obtained on comparable TFA-based

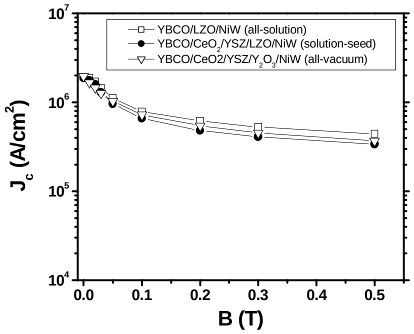

Fig. 2.49. Comparison of critical current density-B performance of solution-deposited LZO as a seed layer and as a barrier layer with a traditional all-vacuum buffered Ni-W substrate using PLD-YBCO.

YBCO films deposited on typical vacuum-deposited buffer layers, it demonstrates that both the e-beam Y_2O_3 seed layer and the sputtered YSZ barrier layer can be replaced by a sol-gel–processed LZO layer.

The properties of coated conductors processed to obtain the simplified buffer architecture of solution LZO with a CeO_2 cap have been promising. However, the measured critical current density values are still lower than that obtained from the three-layer architecture. One possible reason for this could be the presence of bulk porosity in the LZO films. For better properties, the process must be optimized to improve the density of the LZO films.

We have successfully demonstrated the use of solution-processed LZO films as barrier layers for coated-conductor fabrication. Epitaxial LZO films with a thickness of 80 to 100 nm have been deposited on Ni-W substrates by spin-coating and annealing. The films had a smooth, crack-free microstructure with very high surface crystallinity. The performance of the LZO barrier layers was evaluated by depositing YBCO on these samples by the PLD process or a TFA-based MOD process. The PLD-YBCO films, deposited directly on the LZO buffered Ni-W substrates (YBCO/LZO/Ni-W), showed critical current densities up to 2 MA/cm^2. For the MOD-YBCO, a CeO_2 cap layer was sputtered on the LZO barrier layer to avoid reaction between the LZO film and the YBCO film. Thus, using a layer sequence of YBCO/CeO_2/LZO/Ni-W, for the MOD-YBCO, a critical current density of 1.7 MA/cm^2 and a critical current of 135 A/cm were measured. These results show that the buffer layer architecture in a typical coated conductor can be simplified by using solution-processed LZO films.

2.8.1 References

1. S. D. Ramamurthy and D. A. Payne, "Structural Investigations of Prehydrolyzed Precursors Used in the Sol-Gel Processing of Lead Titanate," *J. Am. Ceram. Soc.* **73**, 2547 (1990).
2. L. F. Francis, D. A. Payne, and S. R. Wilson, "Crystal Structures of a New Lead Zinc Acetate Alkoxide, $Pb_2Zn_2(C_2H_3O_2)_4(C_3H_7O_2)_4$," *Chem. Mater.* **2**(6), 645 (1990).
3. A. Goyal et al., "Strengthened, Biaxially Textured Ni Substrate with Small Alloying Additions for Coated Conductor Applications," *Physica C* **382**(2–3), 251 (2002).

2.9 Detection of Interfacial Strain and Phase Separation in $MBa_2Cu_3O_{7-x}$ Thin Films by Raman Spectroscopy and X-Ray Diffraction Space Mapping

A. J. Kropf, C. U. Segre, Q. X. Jia (LANL), A. Goyal, B. W. Kang (ORNL), K. Venkataraman, S. Chattopadhyay, H. You, and V. A. Maroni (ANL)

2.9.1. Introduction

The growth of epitaxial films of $MBa_2Cu_3O_{7-x}$ (M-123, where M = yttrium or a rare earth element) on metal and ceramic substrates is being investigated worldwide as part of the development effort to commercially fabricate HTS wire in long-length form on textured metal substrates suitable for electric power applications [1–3]. The successful development of HTS coated conductors for commercial applications is faced with several technological hurdles, the most significant of which involve obtaining high-quality chemical and microstructural properties (and concomitant high electrical performance levels) for the M-123 films.

The current approach to the development of HTS structures for high-current, high-voltage devices relies on being able to precisely transmit a cube-textured epitaxy of the substrate to the M-123 film. The fabrication of these thin film embodiments usually also requires a buffer layer to prevent the substrate atoms from diffusing into the M-123 film. Hence, the architecture of an M-123 coated conductor typically consists of the substrate, a seed layer (if one is required), a buffer layer, one or more cap layers (to enhance the epitaxy transmission), and the M-123 film. Whereas it is desirable to have a relatively thick M-123 film (greater than a micron), most of the intervening layers (between the M-123 film and the substrate) tend to range in thickness from 10 to 200 nm. The fabrication of this multilayered epitaxial superstructure requires meticulous attention to detail at each stage of the process. In order to develop a clear understanding of these details, it is critically important to be able to measure texture, strain, and other aspects of the crystallographic architecture at each interface of the coated conductor.

The aggregate microstructure of an M-123 film profoundly influences the intergrain electrical current flow, but the intragrain superconducting properties are determined by structures and chemical states at the atomic level. The aspects of the global chemistry of an M-123 thin film, such as phase evolution and oxygenation, have been extensively investigated, but current literature on the local chemistry of M-123 films is relatively scarce. Furthermore, the interrelations between the microstructure and the local chemistry of an M-123 film also require more attention. This paper attempts to examine these interrelations through a case study of three high-quality M-123 films on single-crystal substrates and to connect those structural and chemical relationships with the observed superconducting properties of the films.

2.9.2 Experiments

2.9.2.1 Detection of Microdomains

The three specimens analyzed in this study were M-123 thin films on 5 × 10 mm single crystal $SrTiO_3$ substrates. The first film, ~140-nm-thick Eu-123 on a bare $SrTiO_3$ substrate, was deposited by PLD at Los Alamos National Laboratory (LANL) [4]. No superconducting properties were exhibited by the specimen down to a temperature of 75 K. The second film (~160 nm thick) was similarly fabricated but had a 10-nm Er-123 buffer layer between the Eu-123 layer and the $SrTiO_3$ substrate. This specimen had a critical temperature of 92.5 K and a critical current density of 2.1 MA/cm^2 at 75 K, self-field. The third specimen was a Y-123 film (~190 nm thick) deposited on a bare $SrTiO_3$ substrate by PLD at ORNL [5]. The critical temperature of the film was 86 K, with a critical current density of 5.3 MA/cm^2 at 77 K, self-field.

Microdomains of various phases in the three films were investigated by Raman micro-spectroscopy (Renishaw RM2000 Raman Microprobe) [6]. The specimens were positioned on the microprobe stage with the incident laser radiation normal to the M-123 film surface. The backscattered radiation was collected through the same optic (Leica 50×/0.55 lens). The system employed a He-Ne laser (λ = 632.8 nm) that delivered a maximum of 5 mW of incident power to the specimen surface. Raman spectra for each specimen were acquired at 100% defocus, 50% defocus, 20% defocus, and 0% defocus of the laser beam. Scans were conducted in the static grating mode with the area of the charge-coupled device array of the detector adjusted to obtain minimum noise and background levels and to interrogate the spectral frequency range between 100 and 185 cm^{-1}. At each defocus level, both the diameter and the depth of penetration of the laser beam changed. Therefore, the measurement approximates a three-dimensional scan of the specimen. The corresponding laser beam diameters were ~25 μm at 100% defocus, ~14 μm at 50% defocus, ~6 μm at 20% defocus, and between 2 and 4 μm at 0% defocus. The spectral acquisition times used were 1800, 1200, 600, and 100 s for defocus levels of 100%, 50%, 20%, and 0%, respectively. Although the Raman band shape showed some variation for the different levels of defocus, the best signal-to-noise ratios were obtained at 20% defocus and therefore formed the basis for subsequent analyses. No evidence of laser annealing effects was observed for any of the specimens as a result of the spectroscopy experiments.

2.9.2.2 Diffraction Space Mapping

Diffraction space mapping (DSM) of the three specimens was performed via XRD; synchrotron radiation was used from the Advanced Photon Source (APS) on the Materials Research Collaborative Access Team (MR-CAT) insertion device beamline equipped with an eight-circle Huber® diffractometer [7]. The energy of the radiation used was ~17 keV, corresponding to a wavelength of 0.072928 nm. The scattering experiments were conducted in reflection geometry wherein both symmetric and asymmetric reflections were scanned [8]. The average beam spot incident on the specimen surface was a 1×1.5 mm rectangle. Each specimen was centered in the goniometer and aligned for the (005) reflection of the thin M-123 film. A Si (111) crystal analyzer deployed on the detector arm made it was possible to obtain d-spacing resolution better than 0.001 nm.

The symmetric reflections (005) and (006) and the asymmetric reflections (104)/(014) of M-123 were acquired for each of the three specimens. Filters were used to attenuate the incident beam intensity when diffracted beam intensities tended to saturate the detector. The (005) and (006) reflections were obtained by ω-2θ mesh scans. The asymmetric reflections (104)/(014) were obtained in the same way, except that the specimen was tilted in the chi direction between 35^o and 38^o, in order to bring the (104)/(014) planes of the film into the Bragg reflection position. In addition to the films, a bare $SrTiO_3$ substrate was analyzed in order to isolate any effects of the substrate that might appear in the DSMs. The (200) reflection of the bare $SrTiO_3$ substrate was obtained in a manner similar to that used for the M-123 symmetric scattering experiments. Lattice parameters for the crystal structures that are referred to in this study are listed in Table 2.5.

Table 2.5. Literature values for lattice parameters of tetragonal and orthorhombic M-123 materials[a]

Materials[b]	Axis (nm)			PDF No.
	a	b	c	
Eu-123 (O)	0.384	0.390	1.171	79-1232
Eu-123 (T)	0.388	0.388	1.181	82-2303
Er-123 (O)	0.382	0.389	1.169	88-2254
Er-123 (T)	0.385	0.385	1.179	82-2308
$SrTiO_3$ (T)	0.390	0.390	0.390	86-0179
Y-123 (O)	0.382	0.388	1.168	88-2463
Y-123 (T)	0.384	0.384	1.177	88-2462

[a] Source: JCPDS-ICDD powder diffraction database.
[b] O = orthorhombic structure; T = tetragonal structure.

2.9.3 Results and Discussion

2.9.3.1 Detection of Microdomains

The global and local stoichiometries of $MBa_2Cu_3O_{7-x}$ are the same when $x = 0$ (orthorhombic) or $x = 1$ (tetragonal). However, for values of x between 0 and 1, the microstructure is characterized by the coexistence of microdomains (or "microphases") containing different types of oxygen atom arrangements in the basal Cu-O planes of the unit cells of the individual microdomains [9]. Moreover, these oxygen arrangements do not always correspond to either the purely tetragonal or purely orthorhombic case. Thus, at a microscopic level, M-123 can be considered to be a multiphase system with the relative amounts of coexisting stable and unstable microphases being determined by both the value of x and the processing history of the specimen [9,10].

The size of these microphases is generally below the detection limit of XRD and neutron diffraction techniques [10], which tend to average the d-spacings over all coexisting local structures. However, changes in the local structure due to oxygen rearrangement generate mode shifts in the corresponding Raman spectrum. Furthermore, oxygen rearrangement can cause the mode selection rules to be violated due to changes in the unit cell symmetry and coordination, giving rise to new modes that are forbidden for the ideal stoichiometry and microstructure. Hence, additional peaks may appear in the Raman spectrum. Shifting of mode frequencies, variations in band shapes, and the appearance of new modes can thus be used to discern the presence of microphases [9–12].

The four stable phases established for the $MBa_2Cu_3O_{7-x}$ system are ortho-I ($x = 0$), ortho-II ($x = 0.5$), tetragonal ($x = 1$), and the high-temperature tetragonal (T') ($0 < x < 1$) [10]. The Raman spectrum for an M-123 material of nonideal stoichiometry (which is usually the case in thin films) is a superposition of spectra of several coexisting microphases. The relative contribution from the spectrum of each microphase to the overall spectrum is determined by the abundance of each microphase and its scattering orientation with respect to the direction and polarization state of the Raman excitation beam. The latter is particularly important in determining the presence of a mixed phase in a thin film specimen, where the lack of ideal texture can be gainfully exploited to detect the coexistence of microphases. This can be accomplished by examining the bands in the Raman spectrum that occur in mutually exclusive scattering geometries for different phases. The prime example of this type of band is the Cu(2) mode of M-123. The Cu(2) mode has a frequency of ~150 cm^{-1} for the ortho-I phase, ~145 cm^{-1} for the ortho-II phase, and ~140 cm^{-1} for the tetragonal (T, T') phases [10] (i.e., there are distinct frequency differences among the three modes). Furthermore, in the case of the ortho-I phase, the Cu(2) mode is of negligible intensity in the *xx*/*yy* scattering geometry and of considerable intensity in the *zz* scattering geometry, while the opposite is true in the case of the tetragonal phases. If a scattering geometry of $z(x,x')z'$ (using Porto notation [13]) is employed, it will be parallel to the *c*-axis of the M-123 grains when that *c*-axis is normal to the substrate and perpendicular when that *c*-axis is parallel to the substrate (e.g., as for *a*-axis-oriented M-123 grains). This situation is equivalent to both *xx*/*yy* and *zz* scattering geometries (with respect to the grains) being simultaneously scanned. Because the coexisting microdomains of T, T', ortho-I, and ortho-II can exist in many possible orientations in a nonideally textured thin film, a laser beam probing a region of the thin film will produce Raman scattering from all the coexisting microdomains, giving rise to multiple Cu(2) mode bands in the acquired Raman spectrum, each band presumably assignable to a distinct microphase.

The Raman bands of the various microphases overlap due to their large widths and small frequency differences. Therefore, curve-fitting routines are required to separate the observed composite Cu(2)-mode band into component bands. Although the actual microdomain size range is not accurately known, it might be on the order of a few tens of lattice spacings, which is sufficiently within the footprint of the Raman excitation beam. In cases where a gradation of microdomain assemblages are perpendicular to the substrate surface, changes in the beam diameter, and hence depth of penetration, should change the distribution of the microdomains scanned by the laser beam. This change produces a different Cu(2) mode bandwidth and shape at each defocus level, although the observed changes may be subtle.

The curve-resolution program used was a mathematical routine of GRAMS 32 AI. Figure 2.50(a), (b), and (c) present the actual composite band, the fitted curve, and the component bands of the Y-123/STO, Eu-123/STO, and Eu-123/Er-123/STO specimens, respectively, each obtained at 20% defocus of the incident laser beam. Lorentzian functions were used to resolve the composite band into the component bands. From Fig2.50(a), (b), and (c) , it is evident that the Cu(2)-mode band envelope in the Raman spectrum of each specimen has three distinct component bands that have frequencies at ~141, ~145, and ~149 cm^{-1}. The analyses of the Cu(2) band envelopes for the three specimens are summarized in Table 2.6. The 141-cm^{-1} band can be assigned to T, T' microdomains; the 149 cm^{-1} band can be assigned to ortho-I (O-I) domains; and the 145 cm^{-1} band can be assigned to the ortho-II (O-II) phase. The range of ratios of the intensity of the T band to that of the O-I and O-II bands is nearly zero in the case of the Y-123/STO specimen and is greatest in the case of the Eu-123/Er-123/STO specimen. Also, the ratio of the intensity of the O-II band to the O-I band is greater than unity in the case of the Eu-123/STO specimen, in contrast to the other two specimens.

The most notable result of the analysis is that the specimens exhibiting superconducting properties above 70 K (i.e., Y-123/STO, Eu-123/Er-123/STO) had intensity ratios of the O-II mode to that of the O-I mode considerably less than unity, unlike in the case of the Eu-123/STO specimen, which had no observable superconducting properties down to 70 K. This finding is expected because the O-II form of M-123 films has a critical oxygen stoichiometric content of 6.5, below which the M-123 material does not exhibit superconductivity. It is thus plausible that the superconductivity in an M-123 film of nonideal oxygen stoichiometry ($0 < x < 1$) can occur if the oxygen atoms are so arranged that microdomains of separate phases exist with the major proportion of the contiguous microphases being approximately O-I in nature. The latter is true in the case of the Y-123 film on STO and the Eu-123 film on Er-123-buffered STO, but not in the case of the Eu-123 film on bare STO.

The difference in the component band intensity ratios is even more enhanced if one takes into account the texture factor of these specimens. The texture factor or the proportion of *c*-axis-oriented grains in the grain assemblages is inversely proportional to the ratio of the intensities of the O4 phonon band of M-123 to the O2+/O3- phonon band in the Raman spectra of the material [14]. From maps created of this intensity ratio as a function of position on the sample surface it was determined that the texture of the Y-123/STO specimen [Fig. 2.51(a)] was the best among the three specimens, having the most uniformly *c*-axis oriented grains. The Eu-123/STO specimen is uniformly *c*-axis oriented for just over half of the specimen but exhibits texture variation in the remainder of the specimen [Fig. 2.51(b)]. During the acquisition of the Raman spectra, care was taken to scan only the *c*-axis-oriented region for the specimen. In the case of the Eu-123/Er-123/STO specimen [Fig. 2.51(c)], the texture is uniform but with a greater presence of *a*-axis-oriented grains. However, the microstructure of each film is sensitive to the processing conditions. Therefore, no conclusions can be drawn as to the intrinsic quality of a Y-123 film when compared with a Eu-123 film.

Assuming that the microdomain distribution is uniform throughout the specimen and not dependent on the grain orientation with respect to the substrate, the greater proportion of *a*-axis-oriented grains in the Eu-123/Er-123/STO specimen, indicated by the higher value of the $I_{O4}/I_{O2+/O3-}$ in Fig. 2.51(c), should cause a greater intensity of the Cu(2) mode of the (T) domains to be detected due to its scattering geometry dependence. This is indeed observed when compared with results for the other two specimens. Specifically, the Y-123/STO specimen had a lesser proportion of *a*-axis-oriented grains [Fig. 2.51(a)], and in the case of the Eu-123/STO specimen, the proportion of *a*-axis-oriented grains in the region that was scanned by the laser was even less than that of the other two specimens [Fig. 2.51(b)]. However, unlike the Y-123 specimen, which exhibited equivalent texture, the Eu-123/STO film showed vestiges of tetragonal phases in its matrix. The difference in local oxygen content between the two Eu-123 films is even more interesting in light of the fact that they received identical deposition and annealing treatments and suggests that the underlying substrate/buffer layers may have a substantive influence on the oxygen ordering process during oxygenation. Possible causes for the differences in the proportions of T, T', O-II, and O-I microphases among the three specimens were determined by performing DSM experiments on the specimens. The experiments illuminated some of the crystallographic aspects of the specimens and their influence on observed phase-separation phenomena.

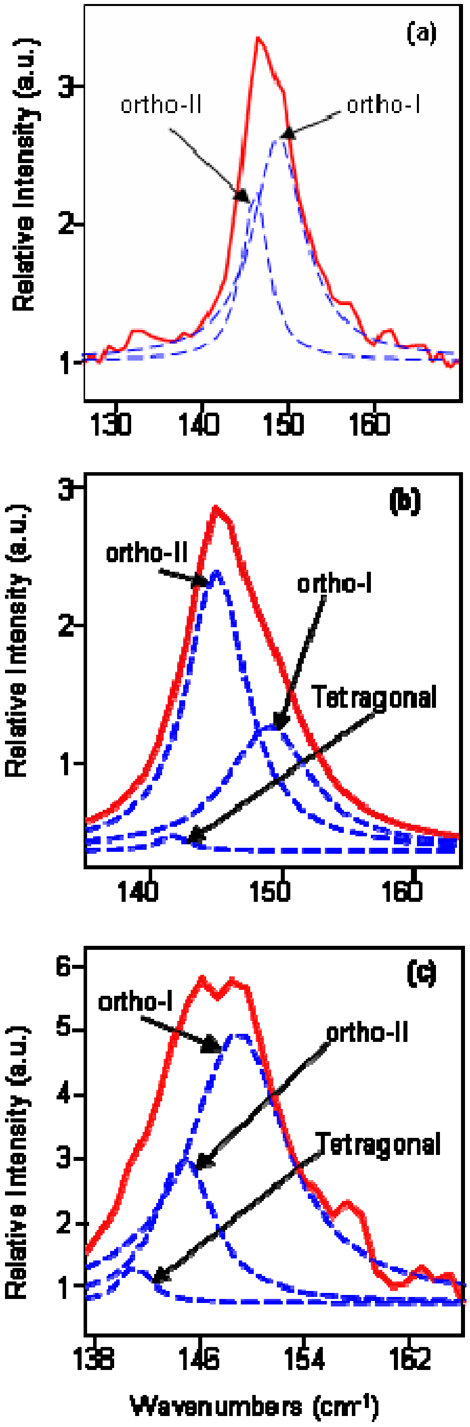

Fig. 2.50. Raman Cu(2) mode band with fitted curve and component bands of (a) Y-123/STO, (b) Eu-123/STO, and (c) Eu-123/Er-123/STO.

Table 2.6. Band-fitting results for Raman spectra of M-123/STO specimens

Sample	Band shape	Center (cm^{-1})	Relative height[a]	FWHM (cm^{-1})	Relative area[a]	Correlation coefficient	Chi^2
Y-123/STO	Lorentzian	146	71.5	4.1	43.6	0.99	1.46
		149	91.2	8.4	107.5		
Eu-123/STO	Lorentzian	142	5.3	2/9	22.3	0.99	0.52
		145	103.2	5.5	773.7		
		149	45.5	7.8	464.4		
Eu-123/Er-123/STO	Lorentzian	141	8.8	2.8	33.1	0.98	3.05
		145	34.5	5.3	244.3		
		149	65.3	9.0	724.0		

[a] The relative peak height and band width are in arbitrary units.

[b] FWHM = full width at half maximum.

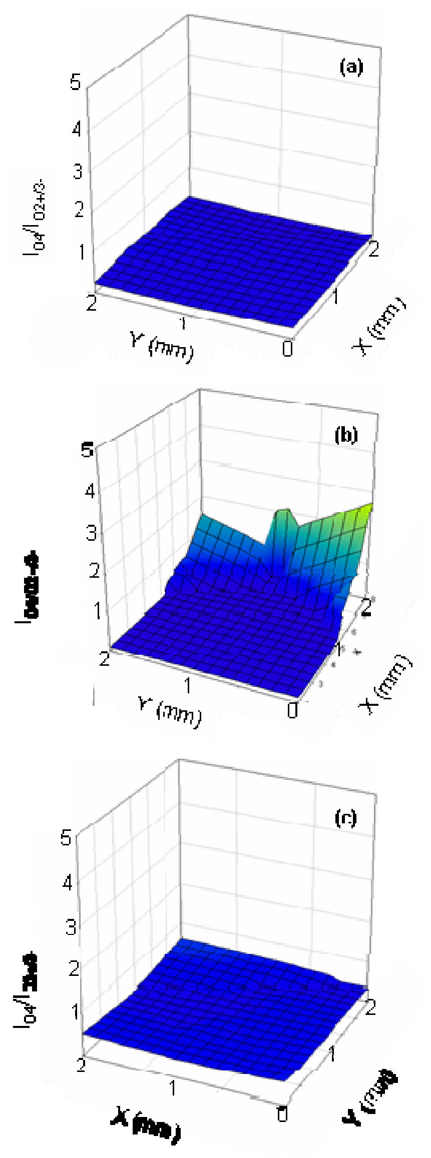

**Fig. 2.51. Texture maps:
(a) Y-123/STO, (b) Eu-123/STO,
and (c) Eu-123/Er-123/STO.**

2.9.3.2 Texture Analysis

In the DSM measurements, the out-of-plane texture of the specimens was determined by examining the spread of the intensities of the symmetric reflections of the films in the ω direction of the DSMs. Figures 2.52(a), (b), and (c) show the DSMs of the Y-123/STO, Eu-123/STO, and Eu-123/Er-123/STO specimens, respectively, obtained from the (005) reflections of the films. Figures 2.53(a), (b), and (c) show the DSMs of the Y-123/STO, Eu-123/STO, and Eu-123/Er-123/STO specimens, respectively, obtained from the (006) reflections of the films, which happen to lie close to the (200) reflection of the STO substrate. Because the (006) reflections of the film are skewed by the presence of the (200) reflections of the substrate, the (005) reflections offer more accurate depictions of the texture of the specimens. The DSM of the Y-123/STO specimen shown in Fig 2.52(a) shows that the *c*-axis orientation has a spread of about 0.35° (FWHM) about the substrate normal. Notably, the *c*-axis spread is asymmetrical, with the maximum at ~8.93°. For a *c*-axis perfectly normal to the substrate, the expected ω value is half of the 2θ value for the peak of the reflection, which corresponds to about 8.99°. The 0.06° difference between the expected and observed value is low compared to the *c*-axis spread, indicating a very high preference for the *c*-axis to be normal to the substrate. Analysis of the texture of the specimen by the Raman mapping method [Fig. 2.51(a)] corroborated this observation. The X-ray beam incident on the specimen surface samples a large region of the specimen (1.5 × 1 mm). Therefore, the DSMs provide a relatively global texture measurement, which complements the local texture quality determined by Raman micro-spectroscopy.

The DSM of the Eu-123/STO specimen [Fig. 2.52(b)] reveals that the *c*-axis spread of the specimen is about 0.18° (FWHM), which is considerably smaller than that of the Y-123/STO specimen and is consistent with the Raman mapping results for the specimen [Fig. 2.51(b)]. However, it

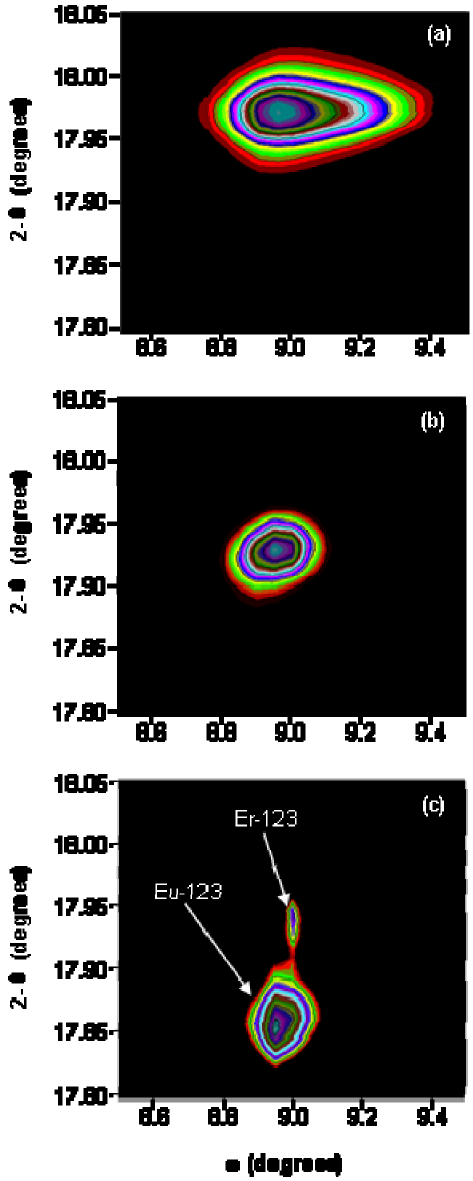

Fig. 2.52. (005) diffraction space maps: (a) Y-123/STO, (b) Eu-123/STO, and (c) Eu-123/Er-123/STO.

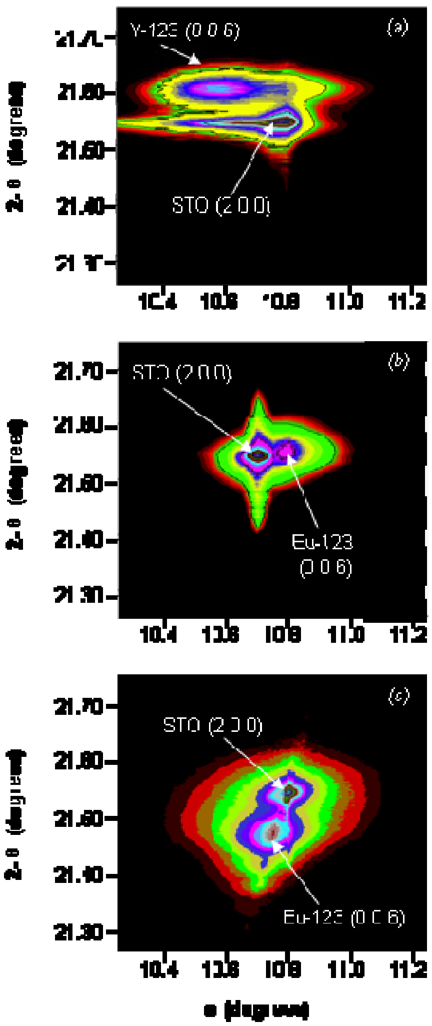

Fig. 2.53. (006) diffraction space maps: (a) Y-123/STO, (b) Eu-123/STO, and (c) Eu-123/Er-123/STO.

should be pointed out that the DSM experiment failed to detect the large change in texture (as determined via Raman spectroscopy) that this specimen exhibited toward its edges. The square region (approximately 2 × 2 mm), which was probed by the laser in the Raman spectroscopy experiments in segmented steps, was keyed to the geometric center of the specimen surface. This region corresponds closely to the rectangular region scanned by the X-ray beam in the DSM experiments. However, the DSMs indicate only a small variation in the *c*-axis tilt, which implies that the changes in texture observed in the Raman texture maps are due to the presence of distributed *a*-axis-oriented grains, rather than a wide-ranging *c*-axis tilt.

Two clear sets of reflections for the (005) scattering geometry of the Eu-123/Er-123/STO specimen are observed in Fig. 2.52(c). The less intense reflection spot corresponds to the Er-123 buffer layer (thickness ~10 nm). The larger reflection spot corresponds to the Eu-123 film (thickness ~160 nm) deposited on top of the Er-123 layer. The Er-123 layer has a minimal *c*-axis spread of about 0.06° (FWHM), as expected for such a thin buffer layer on a closely lattice-matching substrate. The Eu-123 layer has a *c*-axis spread of about 0.045° (FWHM). Hence, this film has the best texture of the three specimens analyzed based on considerations of *c*-axis orientation. However, the Raman spectroscopy results revealed that its grain texture is not as good as in the Y-123/STO film or in the high-quality regions of the Eu-123/STO specimen, implying that the proportion of *a*-axis grains in the Eu-123/Er-123/STO specimen is greater than it is in the other two specimens. This conclusion is consistent with the greater degree of phase separation shown in the specimen by Raman spectroscopy. While the DSMs provide information exclusively on *c*-axis tilt, the Raman texture map depends on both *c*-axis tilt and the presence of *a*-axis grains; hence, the effects can be separated effectively by using the DSM and Raman methods in combination.

2.9.3.3 Strain and Lattice Mismatch

As can be seen in Table 2.5, the *a*-axis and *b*-axis lattice parameters for orthorhombic and tetragonal M-123 match the lattice constant of cubic STO (0.390 nm) within 0.01 nm, but the *c*-axis parameters are considerably larger (> 1.1 nm). Despite the close match of the *a*-axis and *b*-axis lattice parameters of the M-123 films to the lattice parameter of the STO substrate, the lattice mismatch combined with the difference in thermal expansion coefficients of the film and substrate cause residual strain in the film. Due to the constraining force of the substrate on the film, the *a*-axis and *b*-axis lattice parameters are forced to match approximately the cubic lattice parameter of the STO substrate, giving rise to a pseudotetragonal distortion of the orthorhombic M-123 layer. It follows from principles of continuum mechanics that a change in the *b*-axis or *a*-axis lattice parameter should cause a concomitant change in the *c*-axis lattice parameter, such that the volume of the unit cell is preserved when strained within the elastic limit. Hence a change in the lattice parameter in the *a*-*b* plane (where the tetragonal distortion occurs) can in principle be detected by determining the *c*-axis lattice parameter from an (00*l*) reflection measured by an XRD experiment. (Because of experimental limitations, all reported experimental values of *d*-spacings in this paper are on the order of 0.001 nm in accuracy.) In Fig. 2.52(a), the peak of the (005) reflection of Y-123 appears at a 2θ value of 17.97°, which corresponds to a *d*-spacing of 0.234 nm and a *c*-lattice parameter of 1.167 nm. Fig. 2.53(a) shows the (006) reflection of the Y-123 film, which gives a *c*-lattice parameter value of 1.167 nm, in perfect agreement with the value obtained from the (005) reflection and the literature value (see Table 2.5).

As was pointed out earlier, the close match of the *c*-axis lattice parameter with the literature value suggests similarly good matches of the *a*-axis and *b*-axis lattice parameters to the literature value. This implies a lack of strain in the Y-123 film, but only if the oxygen content is ideally stoichiometric. Any variation in the oxygen content will cause a change in the lattice parameters, which can be strained by the substrate to coincide with literature values (a seemingly unlikely coincidence). To investigate that possibility, DSMs of asymmetric reflections were obtained, which provided information about the oxygen content of the specimen. The result of these asymmetric scans of the specimen revealed no abnormalities in oxygen stoichiometry (i.e., the same conclusion reached based on examinations of the Raman spectra of the specimen). It is therefore reasonable to assume that the closeness of the lattice parameters to the literature values implies a lack of residual strain in the film. The (200) reflection of the STO substrate from Fig. 2.53(a) supplies a lattice parameter value of 0.390 nm for the cubic STO material, which is in perfect agreement with the literature value (Table 2.5).

In a similar fashion, the (005) and (006) reflections of the Eu-123 film on the bare STO substrate yielded a *c*-axis lattice parameter of 1.170 nm, in close agreement with the literature value (1.171 nm, for orthorhombic Eu-123). As in the case of the Y-123 film, one can assume that this finding implies a lack of strain in the film if the oxygen content is ideally the stoichiometric value for orthorhombic Eu-123. However, as shown by the study of the film's asymmetric reflections, this is not the case. Furthermore, the Raman spectroscopy phase separation study of this specimen clearly indicates the presence of a high degree of ortho-II microdomains present in the Eu-123 film. Also, the (006) reflection of the film [Fig. 2.53(b)] has the same 2θ value as the STO substrate but is observed at a different ω value. This implies that the film is tilted with respect to the substrate [8]. The tilt is about 0.1°, as observed from Fig. 2.53(b). The c-axis lattice parameters for the Eu-123/Er-123/STO specimen obtained from the (005) and (006) reflections for the Eu-123 and Er-123 layers are 1.175 nm (which lies between the ortho-I and T phase lattice parameter values) and 1.169 nm (which approximately equals the ortho-I value), respectively [Figs. 2.51(c) and 2.52(c)]. The *c*-axis lattice parameter for the Er-123 film almost perfectly matches the literature value, but the Eu-123 *c*-axis lattice parameter deviates by as much as 0.004 nm, which is a significantly greater deviation than in the case of the other two specimens.

The *a*-axis and *b*-axis lattice parameters for Eu-123/Er-123/STO (as determined from the asymmetric scans of this specimen) are 3.843 and 3.893 nm, respectively. The *a*-axis lattice parameter is slightly higher than the literature value, and the *b*-axis lattice parameter value seems to be very close to the 3.89-nm *b*-axis lattice parameter of the Er-123 (O) buffer layer, implying an imposed compressive strain on the Eu-123 layer, which would cause an increase in the *c*-axis lattice parameter. If strain alone affected the lattice parameter, the *c*-axis lattice parameter would have increased from 1.171 to 1.172 nm. The ideal volume of the unit cell of Eu-123 based on literature values of lattice parameters is 0.1754 nm^3, but the actual volume is 0.1759 nm^3. Because strain within the elastic limit causes no change in volume, the difference between the actual and ideal volume of the unit cell can be attributed to a slight decrease in oxygen content (the unit cell volume increases inversely with oxygen content). However, it is still well within the orthorhombic domain, which is consistent with the Raman-based phase separation studies conducted on this specimen. Hence, both the slight oxygen deficiency and the lattice mismatch seem to have contributed to the strain in this specimen, the former being consistent with the fact that both *a*-axis and *c*-axis lattice parameters increase with incomplete oxygenation [15].

2.9.3.4 Orthorhombicity

A fully oxygenated M-123 specimen should be orthorhombic (O-I), with the *b*-axis lattice parameter slightly larger than the *a*-axis lattice parameter. A decrease in oxygen content reduces the length of the *b*-axis lattice parameter, with a concomitant increase in the *a*-axis and *c*-axis lattice parameters. The difference between the *a*-axis and *b*-axis lattice parameters is therefore indicative of the oxygen content of the specimen, and the expected clear splitting of the (*h*0*l*) and (0*kl*) reflections is observed in all three DSM-analyzed specimens. The DSMs using (104)/(014) reflections of the Y-123/STO, Eu-123/STO, and Eu-123/Er-123/STO specimens are shown in Fig. 2.54(a), (b), and (c), respectively. Corresponding three-dimensional versions of the DSMs shown in Fig. 2.54(c), (d), and (f). provide perspective on the relative intensities of the individual peaks. The implications of the shapes of the DSMs are discussed in a subsequent section.

The peak intensity of the (104) reflection of the Y-123 film occurs at a 2θ value of 18.06° and corresponds to a *d*-spacing of 0.232 nm, which matches the literature value of 0.232 nm [Fig. 2.54(a)]. The *c*-axis lattice parameter obtained from the symmetric reflections for the Y-123 specimen was used to obtain the *a*-axis lattice parameter in the following equation [16]:

$$1/d^2 = h^2/a^2 + k^2/b^2 + l^2/c^2. \qquad (12)$$

Equation (12) gives an *a*-axis lattice parameter of ~0.384 nm for the Y-123 film when the observed *c*-axis lattice parameter value of 1.168 nm for this specimen is used. This result deviates slightly from the literature value of 0.382 nm for the *a*-axis lattice parameter. Similarly, the (014) reflection in Fig. 2.54(a) gives a *b*-axis lattice parameter of 0.389 nm, which also deviates very slightly from the literature value of 0.388 nm. Both of these observed lattice parameters appear to be higher than the literature values reported for each of them, while the *c*-axis lattice parameter is just barely lower than the literature value. As in the case of the Eu-123/Er-123/STO specimen, this observed deviation is explained by taking into account both the change in unit cell volume due to a slight oxygen deficiency and the pseudotetragonal distortion due to strain.

The key feature is that the values of the *a*-axis and *b*-axis lattice parameters of the Y-123 film as calculated from the (104)/(014) reflections exhibit a sufficient difference, which indicates a predominantly orthorhombic Y-123 film. This finding is in conformity with the Raman-based phase separation study conducted for this specimen. However, this finding does not preclude the possible

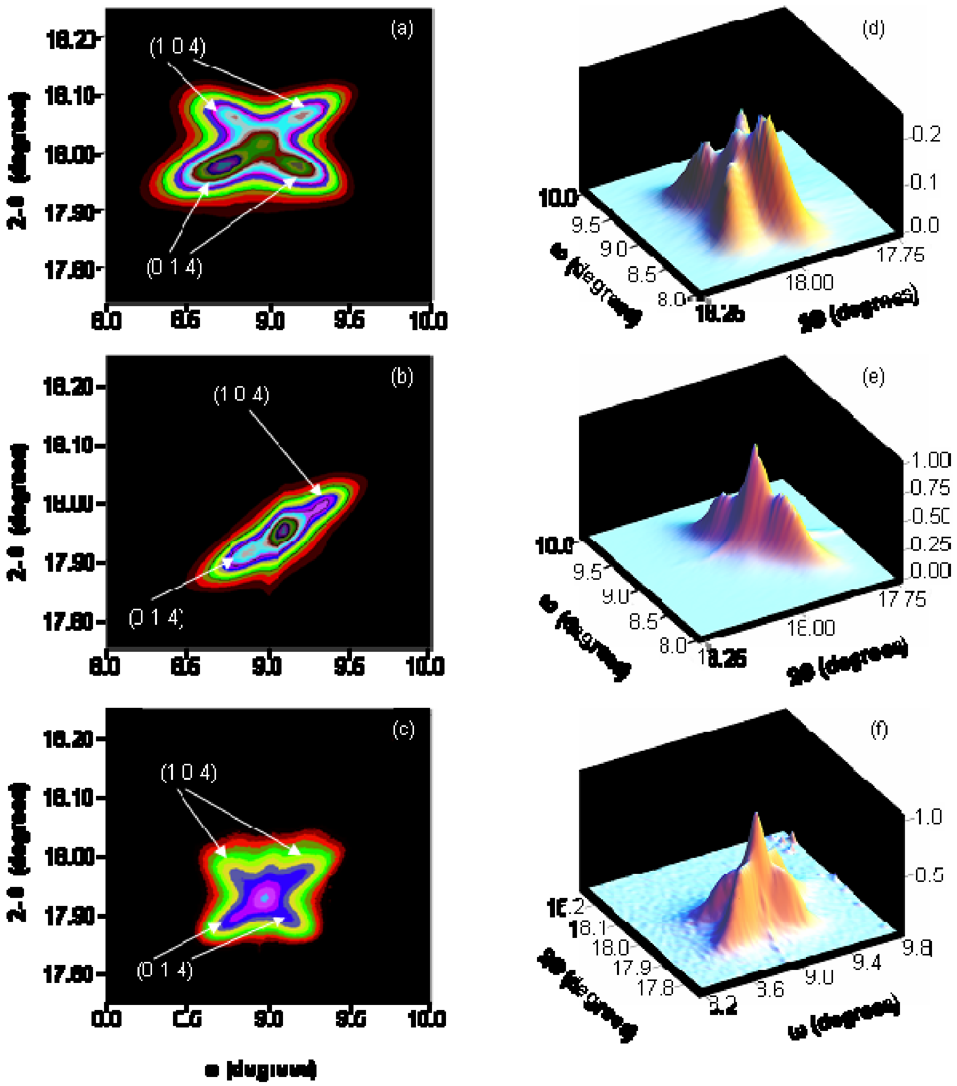

Fig. 2.54. (104)/(014) diffraction space maps: (a) Y-123/STO, (b) Eu-123/STO, and (c) Eu-123/Er-123/STO; three-dimensional (104)/(014) diffraction space maps: (d) Y-123/STO, (e) Eu-123/STO, and (f) Eu-123/Er-123/STO.

existence of tetragonal and other microdomains that were indicated in minor proportions by Raman spectroscopy. Analyses similar to that for the Y-123/STO specimen indicate that the Eu-123/STO specimen and the Eu-123/Er-123/STO specimen also exhibit sufficient divergence of *a*-axis and *b*-axis lattice parameter values for them to be orthorhombic on a global scale. These observations do not necessarily indicate uniform oxygen stoichiometry in the films, as is amply evidenced by the Raman spectroscopy phase-separation study of these specimens. The Eu-123/STO specimen exhibited a distinct excess of O-II microdomains compared with the quantity of O-I microdomains, while the opposite was true in the case of the other two specimens. It is thus not surprising that this specimen displayed no observable superconducting properties above 70 K, whereas the other two specimens did.

2.9.3.5 Crystallite Twinning

In M-123 thin films, the formation of twinned crystallites in the $(110)/(1\bar{1}0)$ direction acts as a strain-relief mechanism during the transformation of the tetragonal M-123 phases to orthorhombic phases during the film growth process [17]. As a result of the twinning geometry, twin domains nucleate and grow in four major suborientation states [17]. In asymmetric reflections of M-123 materials, these twinned domains manifest themselves in the form of two pairs of lobes, each pair having an axis roughly perpendicular to the other, in the shape of a four-leaf clover or an "X" [18]. Each arm of the X represents a twinning system, one arm in the (110) direction, the other in the (110) direction, with two lobes at the opposite ends of each arm.

Five peaks (or lobes) are observed in the DSMs of the (104)/(014) reflections of the Y-123 and Eu-123/Er-123 films, whereas in the DSM of the Eu-123/STO specimen only three peaks are observed. In Fig. 2.54(a), (b), and (c), one lobe in an arm corresponds to the (104) reflection; the other lobe in the arm corresponds to the (014) reflection arising from the twinned domain. The peak observed at the intersection of the two arms in the case of the DSM of the Y-123/STO samples is caused by the overlap of the four other lobes. However, this does not appear to be the case for the DSMs of the Eu-123 films, for which analysis of the raw data reveals that the intensity of the central peak is greater than the sum of all other "real" peaks. One possible explanation for this anomalous peak is the presence of highly mosaic microdomains whose sizes are less than the coherence length of the synchrotron radiation employed. This would cause an average value of orientation and lattice parameters to be observed as a single peak in diffraction space, which is indeed what is observed in Fig. 2.54(e) and (f). This explanation would be consistent with the Raman-based phase separation analysis, which was also based on the presence of microdomains.

The Eu-123/Er-123/STO specimen [see Fig. 2.54(c) and (f)] and Y-123/STO specimen [see Fig. 2.54(a) and (d)] display the "X" shape in their asymmetric reflections, implying they are twinned in approximately equal proportions in both the (110) and (110) directions. Consequently, they are presumed to have undergone a successful transition from the tetragonal to orthorhombic form of M-123 during the deposition/oxygenation process, with little global residual strain resulting from the transition. The phase separation study described previously indicates that the vast majority of the domains of these specimens are orthorhombic. Therefore, the detection of significant twinning in the specimens conforms to the results of the Raman-based phase separation study. One distinct feature noticeable in the asymmetric reflections of the Eu-123/STO specimen [see Fig. 2.54(b) and (e)] specimen is the lack of one arm of the "X" shape observed in the asymmetric reflections of the other specimens, implying a lack of twinning in the (110) direction. This outcome might occur because of a miscut in the STO substrate toward the (110) direction [19]. Because the twinning process takes place as a strain-relieving mechanism during the transition from the tetragonal to the orthorhombic form of M-123, the suppression of twinning in one direction in response to lattice mismatch or effects of terrace-width of the substrate could imply either a highly strained state in the film or an alternative route for strain-relief. A highly strained state would result in extreme tetragonal distortion, which implies a significantly reduced divergence of the *a*-axis and *b*-axis lattice parameters. This would cause a large reduction if not absence of orthorhombic splitting in the asymmetric reflections of the specimen. However, this is not observed. It is known from [9,10] that XRD techniques are not sensitive to local disorder of the arrangement of oxygen atoms, which is reasonable because the domain sizes involved are less than the coherence length of the incident radiation.

The formation of microdomains having different oxygen atom ordering may be a direct result of the tetragonal distortion caused by the strain imposed on the basal planes of the film by the substrate. Because oxygen atoms in the basal planes occupy the sites in the copper-oxygen chains that form the *b*-axes of the unit cells, a reduction in the length of the *b*-axes of a few hundred unit cells could force the oxygen atoms to diffuse into other vacancy sites, or to possibly form disordered unit cells, such as those of the T' and O-II phases [12]. The global oxygen content remains the same in the specimen, but there could be local variations in oxygen content that depend on the local strain fields. Strain fields have local variation due to the differences in texture, layer tilt, substrate effects, and bulk phases present. It is thus conceivable that orthorhombic phases tend to form in regions of low strain fields and that tetragonal domains tend to form in regions of high strain. The separation of phases into coexisting microdomains permits this possibility.

The possible consequence of this strain-dependent reordering of oxygen atoms is that in cases of extreme variations in the strain fields at the submicron level, bidirectional crystallite twinning might not occur due to the incomplete transformation of the tetragonal phase domains into orthorhombic ones. The combination of distinct phase separation with abundant presence of partially oxygenated (O-II) domains and the lack of bidirectional twinning is precisely what is observed in the Eu-123/STO specimen. Moreover, in the asymmetric DSMs of three specimens, the relative intensity of the central peak (which was attributed to reflections from mosaic microdomains) is the highest in the case of the Eu-123/STO sample, further buttressing the notion of large phase separation effects in this specimen. All the observations and conclusions with regard to phase separation effects and domain ordering made thus far appear to fit well with the model proposed by Khachaturyan and Morris for structural transformations in M-123 materials during the tetragonal-to-orthorhombic conversion process [20].

The excessive presence of O-II microdomains is not observed for either the Y-123/STO specimen or the Eu-123/Er-123/STO specimen. In the case of the latter, it is easily conceivable that the the buffer layer (10-nm-thick Er-123) between the substrate and the M-123 film provides sufficient strain field uniformity to minimize pseudotetragonal distortion and formation of excessive tetragonal microdomains. The Y-123/STO specimen, despite the lack of a buffer layer, exhibits a high degree of twinning and orthorhombicity. A possible explanation for this is the difference in the lattice mismatches between the Y-123 film and its substrate and between the Eu-123 film and its substrate. Also, the processing conditions for the Eu-123 and Y-123 films were different, although they were both deposited via PLD, suggesting that substrate-induced strain plays a more dynamic role during the deposition process than normally expected.

Examination of the ω-spacings of the lobes in the DSMs reveals further information about the twinning geometry. In the case of the Y-123 film, the difference in the ω positions of the lobes is 0.4°. Due to the geometry of the twinning process, the difference in angle between twin domains is either 90° or a multiple of 0.9° for Y-123 materials, assuming no local strain [17]. However, if the tetragonal phase is trapped in the orthorhombic matrix, the twin domains may differ in orientation by multiples of 0.45° [17]. The combination of the 0.4° difference and the slight local strain observed in the case of the Y-123 film imply the presence of the trapped tetragonal domains, which is consistent with the phase separation observed by Raman spectroscopy. Similar analyses on the ω-spacings of the lobes in the DSMs of the Eu-123/STO and Eu-123/Er-123/STO specimens lead to the same conclusions as in the case of Y-123/STO. Interestingly, the lattice mismatch between the film and the substrate as determined from analyses of the DSMs of all three samples seems to have little effect on the actual twinning process and concomitant strain relief. Consequently, the property of the substrate that appears to be more influential on the film growth process is the terrace structure of the vicinal substrate. This possibility was probed by analyzing a bare vicinal STO substrate via DSM of the (200) reflections.

2.9.3.6 Epitaxy

The epitaxy of the specimens in terms of the in-plane alignment of *a*-axis and *b*-axis oriented grains was determined from the DSMs of the asymmetric reflections. These were obtained by tilting the specimens in the χ-direction and rocking them in the ω-direction. The (104) and (014) reflections in an ideal M-123 crystal would occur with equal intensities at 90° intervals in ϕ. In the case of thin films of M-123, as the grain size is sufficiently small and the grain orientations are statistically distributed, the intensities of the two reflections would remain approximately equal at various values of ϕ. This would not necessarily be true for the biaxial scans used in the DSM experiments, but it is plausible in light of the relatively large region of the specimen that is scanned by the X-ray beam (1 × 1.5 mm), allowing statistical leveling of intensities. This is observed in the two Eu-123 films, where the intensities of the (104) and (014) reflections are more or less equal. In the case of the Y-123/STO film, the (014) reflections have a significantly higher intensity than the (104) reflections, implying some preferential epitaxy. The inference of preferential epitaxy is consistent with (although not necessarily substantiated by) the significantly higher critical currrent density (5.3 MA/cm^2 at 77 K, self-field) exhibited by this specimen in comparison to the Eu-123/Er-123/STO specimen, which despite having a thinner film, exhibited a critical current density of only 2.1 MA/cm^2 at 75 K, self-field. These film characteristics may be subject to differences in processing conditions, so no direct conclusions can be drawn about the intrinsic quality of Y-123 or Eu-123 films.

2.9.3.7 Substrate Effects

A bare STO substrate was analyzed by DSM to isolate the characteristics of the substrate from the DSMs involving the (006) reflections of the films. The DSM of the bare STO substrate shows Pendellosung fringes (Fig. 2.55). The presence of interference fringes indicates that there must be an overlayered interface where the *d*-spacing abruptly changes [21]. Also, the fringes indicate high crystalline quality and nearly perfect epitaxial and interface qualities for the layer [22]. The relationship between the fringe period or peak separation (θ_p) and the layer thickness (t) at a Bragg angle of θ and wavelength λ is given by the following equation [21]:

$$t = \lambda / (2\ \theta_p \cos \theta) \qquad (13)$$

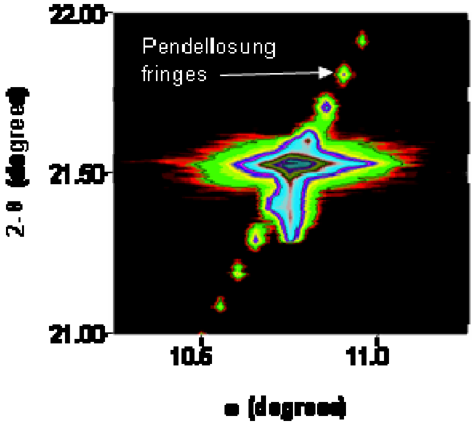

Fig. 2.55. (200) diffraction space map of STO.

From the observed fringe period of 0.055° or 9.6×10^{-4} radians, the thickness of this layer appears to be ~41 nm. It was possibly formed at the surface of the STO sample due to strain, room-temperature annealing, surface treatment, or other processes through which the lattice parameter of the STO might have been altered. It is known from AFM examinations of this STO substrate (results not reported here) that it has a stepped-surface, with a terrace-width of about four lattice constants. Perhaps it is this stepped region that has a 41-nm depth and a different composition from the bulk crystal. The steps have the important effect of inducing epitaxy in the overlying film, due to the preferrential alignment of the *b*-axis in-plane/perpendicular to the step edges and the *a*-axis in-plane along them [18]. Although these observations cannot be directly linked with the properties of the examined films, they suggest that a complete understanding of the film properties is possible only if substrate effects are taken into account and that knowledge of the properties of each substrate is essential.

2.9.4 Conclusions

The results of this study provide compelling evidence that the oxygen stoichiometry in high-quality M-123 films on single-crystal substrates can be nonuniform and can have a highly localized character. Raman spectroscopy experiments conducted on a set of such M-123 films, have provided evidence for the formation of microdomains having different oxygen atom orderings in the unit cells. The coexisting microdomains approximate a mixture of orthogonal (O-I and O-II), tetragonal (T, T'), and possibly other metastable phases. M-123 films with a major proportion of O-I domains exhibited a critical temperature above 77 K and substantial transport current. In contrast, an M-123 film with a major proportion of O-II microdomains exhibited neither. The formation of the microdomains may be the direct result of tetragonal distortion imposed on the film by the underlying substrate or buffer layer, with the degree of twinning in the M-123 film influencing the proportion of tetragonal and O-II microdomains. DSMs of symmetric reflections of the M-123 films supplied some evidence of strain in the M-123 films; DSMs of asymmetric reflections of the films offered insights into the degree of twinning in M-123 films and the associated strain reduction. The congruence of the strain/twinning/phase separation results from the Raman spectroscopy and DSM experiments supports the conjecture that strain effects can influence phase separation.

2.9.5 References

1. D. Larbalestier et al. “High-T_c Superconducting Materials for Electric Power Applications,” *Nature* **414**, 368 (2001).
2. Y. Iijima and K. Matsumoto, “High-Temperature-Superconductor Coated Conductors: Technical Progress in Japan,” *Supercond. Sci. Technol.* **13**(1), 68 (2000).
3. D. K. Finnemore et al., “Coated Conductor Development: An Assessment,” *Phys. C* **320**(1–2), 1 (1999).
4. Q. X. Jia et al., “The Role of a Superconducting Seed Layer in the Structural and Transport Properties of $EuBa_2Cu_3O_{7-x}$ Films,” *Appl. Phys. Lett.*, **83**(7), 1388 (2003).
5. B. W. Kang et al., “Comparative Study of Thickness Dependence of Critical Current Density of $YBa_2Cu_3O_{7-\gamma}$ on (100) $SrTiO_3$ and on Rolling-Assisted Biaxially Textured Substrates,” *J. Mater. Res.* **17**(7), 1750 (2002).
6. K. P. J . Williams et al., *J. Raman Spectrosc.* **25**, 131 (1994).
7. C. U. Segre et al., “The MRCAT Insertion Device Beamline at the Advanced Photon Source Synchrotron Radiation Instrumentation,” p. 419 in *Eleventh U.S. National Conference*, *American Institute of Physics*, ed. P. Pinetta et al., New York (2000).
8. R. K. Kennedy and P. A. Stampe, “Reciprocal Space Mapping of Epitaxial MgO Films on $SrTiO_3$,” *J. Cryst. Growth* **207**(3), 200 (1999).
9. M. N. Iliev, V. G. Hadjiev, and V. G. Ivanov, “Raman Spectroscopy of Local Structure and Reordering Processes in $YBa_2Cu_3O_{7-\delta}$-Type Compounds**,**” *J. Raman Spectrosc.* **27**(3–4), 333 (1996).
10. M. N. Iliev, pp. 107–119 in *Spectroscopy of Superconducting Materials*, ed. Eric Faulques, ACS Symposium Series 730, American Chemical Society, 1999.
11. M. Iliev et al., “Resonant Raman Scattering of Oxygen-Deficient $YBa_2Cu_3O_{7-\delta}$ Evidence for the Coexistence of Ortho-I, Ortho-II, and Tetragonal Microstructures,” *Phys. Rev. B* **47**(18), 12341 (1993).
12. M. N. Ilieve et al., “Raman Spectroscopy as Analytical Tool for the Local Structure of $YBa_2Cu_3O_x$ Thin Films,” *J. Alloys Compd.* **251**(1–2), 99 (1997).
13. M. Kuball, “Raman Spectroscopy of GaN, AlGaN, and AlN for Process and Growth Monitoring/Control**,**” *Surf. Interface Anal*. **31**(10) 987 (2001).
14. N. Dieckmann et al., Epitaxial Quality of *c*-Axis and *a*-Axis Oriented $YBa_2Cu_3O_7$ Films: Characterization by Raman Spectroscopy,” *Physica C* **245**(1–2), 212 (1995).
15. J. D. Budai, R. Feenstra, and L.A. Boatner, “X-Ray Study of In-Plane Epitaxy of $YBa_2Cu_3O_x$ Thin Films,” *Phys. Rev. B*, 39(16) 12355 (1999).
16. B. D. Cullity, *Elements of X-Ray Diffraction*, second ed., Addison-Wesley (1978).
17. V. K. Wadhawan, “Epitaxy and Disorientations in the Ferroelastic Superconductor “$YBa_2Cu_3O_{7-x}$,” *Phys. Rev. B* 38(13), 8936 (1988).
18. J. Brotz et al., “Anisotropic Defect Structure and Transport Properties of $YBa_2Cu_3O_{7-\delta}$ Films on Vicinal $SrTiO_3$(001),” *J. Appl. Phys.* 85(1), 635 (1999).
19. J. Brotz et al., “Controlled Modification of Interfacial Strain and Twinning in $YBa_2Cu_3O_{7-\delta}$ Films on Vicinal $SrTiO_3$ (001),” *Phys. Rev. B* 57(6), 3679 (1998).
20. A. G. Khachaturyan and J. W. Morris, “Ordering and Decomposition in the High-Temperature Superconducting Compound $YBa_2Cu_3O_x$,” *Phys. Rev. Lett.* **59**(24), 2776 (1987).
21. D. K. Bowen and B. K. Tanner, *High-Resolution X-Ray Diffractometry and Topography*, Taylor & Francis (1998).
22. J. C. P. Chang et al., “High-Resolution X-Ray Diffraction of InAlAs/InP Superlattices Grown by Gas Source Molecular Beam Epitaxy,” *Appl. Phy. Lett.* **58**, 1530 (1991).

2.10 Investigation of TiN Seed Layers for RABiTS^{TM} Architectures with Single-Crystal-Like Out-of-Plane Texture

C. Cantoni, A. Goyal, D. Budai, D. K. Christen T. A. Gapud, T. Aytug, and M. Paranthaman (ORNL); U. Schoop, X. Li, and C. Thieme (AMSC); A. K. Kim (University of Florida, Gainesville)

2.10.1 Introduction

In RABiTS™ conductors the texture of the YBCO layer is closely related to the texture of the metal substrate because it results from epitaxial deposition of superconductor and underlying buffer layers on the {001}<100> cubic textured metal. Over the years, slight improvements in the out-of-plane texture of the buffer layers as compared to that of the metal substrate have been reported, while no appreciable sharpening has been observed for the in-plane texture of films with respect to substrate. As a consequence of the usually large lattice mismatch with the substrate (> 6%), the buffer layers nucleate developing islands that then coalesce with consequent formation of a subgrain structure within each substrate grain. In this system, overgrowth of substrate grain boundaries by the buffer layer grains is highly unlikely, and the in-plane orientation of the buffer layer is predominantly determined for each island at the time of nucleation. On the other hand, a change in the out-of-plane texture of the film [tilting of the (00*l*) film planes with respect to the (00*l*) substrate planes] is possible in low- and high-misfit systems as a consequence of growth on the vicinal metal surface. Although still poorly understood, the phenomenon of tilted film growth on vicinal surfaces has been known since the beginning of semiconductor heteroepitaxy [1,2]. The origin of such *c*-axis tilt is generally twofold. In the first stage of deposition, below a critical thickness, the growth is pseudomorphic and strain energy accumulates in the film. In this system, as proposed originally by Nagai [1], the lattice constant of the film in the growth direction relaxes from the lattice constant value of the substrate (a_s) to the film value (a_f) over the length of a terrace, introducing a tilt given by

$$\Delta\psi = \tan^{-1}\left(\frac{a_s - a_f}{a_s}\tan\psi\right) , \tag{14}$$

where ψ is the miscut or vicinal angle. In this model the tilt is away from the surface normal in the case $a_f > a_s$ and toward the surface normal if $a_f < a_s$. At some critical thickness or critical island size, misfit dislocations are introduced to relieve the mismatch strain, with consequent significant changes in the structure and energy of the growing film. Misfit dislocations with a component $b_\perp$ of the Burgers vector normal to the interface can induce tilting, and, if the linear density of dislocations is just sufficient to relieve the misfit f, the film tilt will be $\Delta\psi = f\, b_\perp / b_{//}$ [2]. In an extended version of this model, Ayers et al. [3] have shown that the unequal distribution of certain misfit dislocations induced by the substrate miscut generates tilts toward the surface normal when $a_f > a_s$, opposite to the tilt direction in pseudomorphic systems. For buffer layers usually used in RABiTS™, such as CeO_2 or Y_2O_3, the observed sharpening of the (002) rocking curves is in the range of 1 to 2°. In this case, the tilt is attributed to the coherent Nagai mechanism because the film monolayer *d* spacing is smaller than that of the Ni substrate [4]. In this paper we report on an alternative seed layer, TiN ($a_f > a_s$), which consistently shows larger rocking curve sharpening than those obtained by conventional buffer layers. We also show that the deposition of two additional layers, MgO and $LaMnO_3$ (LMO), on the TiN seed offers a robust alternative buffer layer architecture that can be used on highly reactive, Cr-containing, nonmagnetic substrates.

2.10.2 Experimental

TiN films were grown by PLD from a sintered TiN target on cube-textured substrates of pure Cu, Ni-3%W, Ni-5%W, Ni-Cr-W, and Cu-48%Ni-1%Al. The deposition temperature varied depending on the substrate used and ranged between 580 and 780°C. The background gas consisted of pure N_2 at a partial pressure of 8 × 10^{-4} Torr, the wavelength of the KrF excimer laser was 248 nm, and the beam energy per laser pulse was set to 280 mJ. The laser repetition rate was 10 or 15 Hz, and the film thickness varied between 50 and 600 nm.

AFM analysis of film morphology revealed an average grain size of 20 nm for a 200-nm-thick film and a roughness of 0.4 nm measured on a 1 × 1 μm area. XRD analysis showed that the TiN films were completely (00*l*) oriented, domains with orientation other than cube-on-cube were absent, and the percentage of cube-textured material, as deduced by pole figures of the (111) reflection, was the same as for the metal substrate. The (002) rocking curves measured both in the rolling and transverse directions exhibited a considerably smaller FWHM than that of the substrate.

The buffer layer architecture was completed by in situ deposition of MgO and LMO films on the TiN films. For the deposition of the MgO layer the substrate temperature was lowered to 500°C. The N_2 was evacuated, and an O_2 flow was established with a partial pressure of 1.0 × 10^{-5} Torr. MgO was then deposited by ablating an oxide target with a repetition rate of 10 to 15 Hz. For the deposition of the LMO layer the substrate temperature was raised to 700°C and the oxygen partial pressure was increased to 1.0 × 10^{-4} Torr. The repetition rate was 10 Hz and the beam energy was kept constant for all layers. The film thickness ranged from 80 to 150 nm for MgO and 100 to 200 nm for LMO.

2.10.3 Discussion

There are two reasons for choosing MgO as second buffer layer. First, in the presence of oxygen, and at temperatures above 400°C, TiN has a high tendency to decompose into N_2 gas and TiO. This process hinders the epitaxial deposition of an oxide layer on TiN, unless the oxide to be deposited is thermodynamically more stable than TiO. MgO is one of few oxides to have a free energy of formation lower that that of TiO (ΔG^{o}_{f} [MgO] = –236; ΔG^{o}_{f} [TiO] = –203). Therefore, MgO can be deposited at temperatures and oxygen pressures low enough to avoid formation TiO on the TiN film surface.

Secondly, MgO is structurally compatible with TiN, having the same rock-salt crystal structure and a lattice constant that is only 0.5% smaller. Previous high-resolution Z-contrast scanning transmission electron microscope (Z-STEM) investigations of similar MgO/TiN bilayers have shown that the interface between these two materials is coherent and free from defects and dislocations [5]. LMO is used as cap layer for its good structural compatibility with YBCO and the ease of epitaxial growth on MgO. All samples selected for this study were scrutinized by XRD to ensure that all layers consisted of only (002) cube-on-cube oriented domains.

Figure 2.56 shows two graphs of the FWHM values for the (002) rocking curve of TiN films grown at various temperatures and with different thicknesses on Ni-3%W, Ni-5%W, Ni-Cr-W, Cu, and Cu-48%Ni-1%Al substrates. The data are plotted against the corresponding FWHM values of the substrate (002) rocking curves. In Fig. 2.57(a) the FWHMs of films and substrates are measured with azimuth parallel to the transverse direction of the tape. In Fig. 2.57(b), the azimuth is parallel to the rolling direction. In both cases the FWHM values for the TiN films are considerably smaller than the corresponding values for the substrate. The rocking curve sharpening is most evident in the transverse direction, where most of the films exhibit a FWHM ranging between one-half and one-quarter of the substrate value. Particularly impressive is the case of one of the TiN films on Cu, for which the FWHM improved by 10.4° (from a value of 13.6° in the substrate to a value of 3.2° in the film). For the same film, the corresponding FWHM values in the rolling direction were 6.3° and 2°.

Figure 2.57 shows a comparison between grain boundary maps obtained by electron backscattering Kikuchi patterns (EBKPs) on a biaxially textured Cu substrate and a TiN film deposited on the same substrate. The first map is acquired on the TiN film and highlights only grain boundaries that are larger than 3°. It is clear that with this criterion, macroscopic percolation of current is possible and that most of the material is connected by grain boundaries ≤ 3°. If the same criterion is used for the Cu substrate [Fig. 2.57(b)], the distribution of highlighted grain boundaries becomes much denser and current percolation through grain boundaries ≤ 3° is not possible. To obtain in the substrate a fraction of connected grains similar to that shown by the TiN film, we have to raise the criterion to an angle of 7°. In

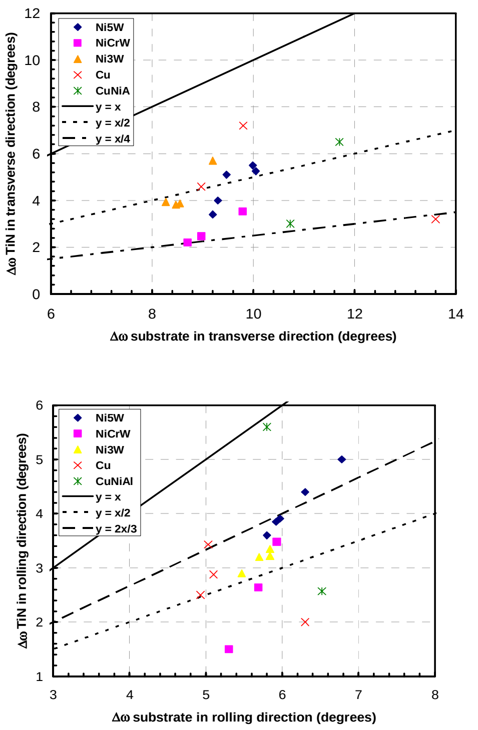

Fig. 2.56. FWHMs of the TiN (002) rocking curves vs corresponding FWHMs of the (002) substrate rocking curve for TiN films on differently textured substrates. The rocking curves are acquired in the rolling direction (lower) and in the transverse direction (upper).

other words, if buffers and the superconductor were to replicate faithfully the texture of the substrate, macroscopic current percolation would occur by transport through grain boundaries of angle ≤ 7°. The EBKP maps clearly suggest that the grain-boundary distribution has shifted toward much lower angles in the TiN film than it did the substrate. However, in these maps no distinction is made between grain boundaries obtained by tilt about the *c*-axis or an in-plane axis. At this point it is not clear whether grain boundaries formed by in-plane or out-of-plane misorientations have similar effects on the critical current density, and it has been suggested that, for grain-boundary angles of 5 to 7°, pure out-of-plane misorientations have a smaller effect on the superconducting transport properties than in-plane misorientations [6].

Comparison of XRD ϕ-scans of the (111) reflections in TiN films and metal substrates have shown that when the (111) peak FWHM is corrected for the broadening caused by the out-of-plane spread $\Delta\omega$, the resulting "true" $\Delta\phi$ [7] is the same for film and substrate. Therefore, in principle, a buffer layer architecture that uses TiN as a seed layer offers the possibility of investigating uniquely the effect of the out-of-plane texture on critical current density. However, before any speculation on the role of the out-of- plane texture can be made, the ability of the buffer layer architecture to block or sufficiently inhibit metal and oxygen diffusion and support high-critical-current YBCO films needs to be addressed. We tested the robustness of our LMO/MgO/TiN architecture by depositing the YBCO layer by a well-established high-performance industrial method such as the AMSC MOD YBCO process.

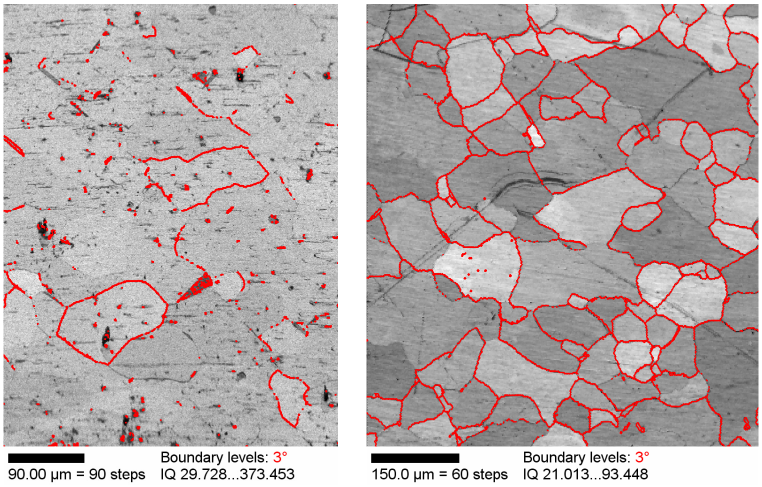

Fig. 2.57. EBKP maps showing grain boundaries larger than 3° of a TiN film on Cu (left), and the underlying Cu substrate (right).

A CeO_2 cap layer was first deposited by AMSC on our architecture for chemical compatibility with the ex situ YBCO process. Subsequently, the superconductor precursor was deposited and processed to obtain a 0.8-µm-thick YBCO film. Two different substrates were used for this experiment: Ni-5%W and a Ni-Cr-W alloy, both provided by AMSC. In particular, the Ni-Cr-W substrate contains proprietary concentrations of Cr and W that completely suppress magnetism in the resulting alloy [Ref 7; and J. R. Thompson, private communication]. For that reason, fabrication of Ni-Cr-W-based

RABiTS™ conductors is extremely interesting in view of applications that require minimization of ac losses. Unfortunately, Cr-containing alloys are extremely reactive toward oxygen, and deposition of oriented oxide buffer layers on these substrates has not been possible. TiN offers the advantage of deposition in an oxygen-free environment and can be nucleated on Ni-Cr-W once the native metal oxide layer on the surface of the alloy is removed in situ, typically by Ar^+ ion sputtering. In both cases, the YBCO was fully (00*l*) oriented and showed a considerably sharper out-of-plane texture than that of the substrate. For the YBCO on the Ni-Cr-W substrate, the rocking curves of the (005) peak showed a sharpening of 2.5° and 5.9° for the rolling and transverse directions, respectively. For the YBCO film on the Ni-5%W substrate the (005) rocking curves were 1.1° sharper in the rolling direction and 4.9° sharper in the transverse direction than the substrate values. The transport critical current density in self-field at 77 K was 1.8 MA/cm^2 for the Ni-Cr-W sample and 2 MA/cm^2 for the sample on Ni-5%W. Such a high critical current density on very reactive metal substrates is a clear indication that the buffer layers perform well as diffusion barriers and have good chemical and structural properties.

To investigate the effect of out-of-plane sharpening on critical current density, we used samples on which YBCO films were grown by PLD. The quality of PLD YBCO films is in fact much less dependent on the type of cap layer used than it is for YBCO films processed ex situ, and high-critical-current-density films are routinely deposited on perovskite buffer layers such as LMO and LSMO [8].

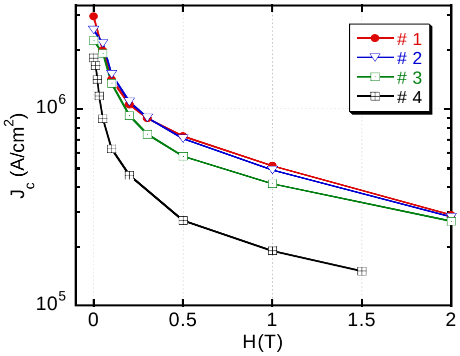

Fig. 2.58. Comparison of the J_c(H) curves for four samples having different out-of-plane texture but similar in-plane texture.

Table 2.7. Buffer layer architecture and FWHM for ω and φ scans for YBCO samples 1, 2, 3, and 4

Sample	Architecture	FWHM (degrees)		
		Δω, R	Δω, T	Δφ
1	LMO/MgO/TiN/Ni3W	3.1	4.1	7.5
2	CeO_2/LMO/MgO/TiN/Ni3W	6.3	7.5	7.9
3	LSMO/Ir/Ni3W	4.7	—	7.2
4	CeO_2/YSZ/Y_2O_3/Ni5W	6.6	5.8	6.4°

Figure 2.58 shows a comparison between critical-current-density (H) curves obtained at 77 K from 0.2-µm-thick YBCO films deposited in the same PLD conditions on RABiTS™ samples with comparable in-plane texture but significantly different out-of-plane texture. Table 2.7 shows the FWHM of YBCO Δω and Δφ scans for the four samples and their architectures. As shown by Fig. 2.58, sample 1, which has a TiN seed layer and the sharpest out-of-plane texture, has the highest self-field critical current density. Samples 3 and 4 show lower critical current densities than sample 1 at all fields. Sample 4 has the largest Δω in the rolling direction as well as the lowest critical current density. Sample 2 is perhaps the best sample to compare with sample 1. They have in fact the same architecture (except for the thin CeO_2 cap used in sample 2) and were deposited from the same YBCO PLD target. The significantly broader out-of-plane texture of sample 2 can be attributed to a broader substrate out-of-plane texture and nonoptimal deposition conditions for the LMO layer, which led to broader rocking curves for this layer than those of MgO and TiN. Interestingly, these two samples have very comparable critical current density in an applied magnetic field. Fig. 2.58 suggests that more work involving study of local grain-boundary maps in the YBCO layers is necessary to assess the role of out-of-plane texture in RABiTS™. It is conceivable that the difference in critical current density between sample 4 and sample 1 is caused by YBCO stoichiometry and reflects a difference in the intragrain critical current density of the two samples. In this case we would conclude that a sharpening of nearly 3° in the out-of-plane texture does not dramatically increase the critical current capability of RABiTS™.

2.10.4 Conclusion

We presented an alternative RABiTS architecture consisting of LMO/MgO/TiN deposited by PLD. Such architecture meets the buffer layer requirements for coated conductors and can sustain high critical current in YBCO films processed by MOD on highly reactive nonmagnetic substrates. In addition, due to a tilted epitaxy growth mechanism in the TiN seed, considerable sharpening of the out-of-plane texture occurs in YBCO films deposited on such architecture. However, our preliminary comparative results suggest that a reduction of $\Delta\omega$ from values of 6° to 7° to values of 3° to 4° does not considerably increase the critical current density at 77 K.

2.10.5 References

1. H. Nagai, "Structure of Vapor-Deposited GaxIn1-xAs Crystals," *J. Appl. Phys.* **45**, 3789 (1974).
2. G. H. Olsen and R. T. Smith, "Misorientation and Tetragonal Distortion in Heteroepitaxial Vapor-Grown III-V Structures," *Phys. Stat. Sol. A* **31**, 739 (1975).
3. J. E. Ayers, S. K. Ghandhi, and L. J. Schowalter, "Crystallographic Tilting of Heteroepitaxial Layers," *Journal of Crystal Growth* **113**, 430 (1991).
4. J. Budai et al. "X-Ray Microdiffraction Study of Growth Modes and Crystallographic Tilts in Oxide Films on Metal Substrates," *Nature Materials* **2**, 487 (2003).
5. C. Cantoni et al., "Deposition and Characterization of $YBa_2CuO_3O_{7-d}$/$LaMnO_3$/MgO/TiN Heterostructures on Cu Metal Substrates for Development of Coated Conductors," *J. Mater. Res.* **18**, 2387 (2003).
6. A. Goyal, "RABiTS-Based Strategic Research," presented at the DOE Peer Review on Superconductivity, Washington, D.C., July 2004, http://www.ornl.gov/sci/htsc/documents/pdf/fy2004/ RABiTS-Based_Strategic_Research.pdf.
7. A. Goyal, "RABiTS Substrates Research and Development," presented at the DOE Peer Review on Superconductivity, Washington, D.C. July 2003, http://www.ornl.gov/sci/htsc/documents/pdf/fy2003/ RABiTS_Substrates_R&D-Goyal.pdf.
8. T. Aytug et al. " An Approach for Electrical Self-Stabilization of High-Temperature Superconducting Wires for Power Applications" *Appl. Phys. Lett.* (in press).

2.11 Growth of YBCO Films on MgO-Based RABiTS™ Templates

M. P. Paranthaman, T. Aytug, H. Y. Zhai, L. Heatherly, A. Goyal, and D. K. Christen

2.11.1 Introduction

The RABiTS™ and IBAD approaches have been identified recently as the leading techniques to fabricate long lengths of high-performance YBCO coated conductors [1–4]. In the standard RABiTS™ approach, a three-layer architecture of CeO_2/YSZ/Y_2O_3/Ni-W is used to fabricate long lengths of YBCO coated conductors [3]. In an effort to develop a low-cost alternative buffer layer architecture, we focused our studies on identifying robust oxide buffers with both oxygen and metal diffusion barrier properties. MgO has been chosen as the potential oxygen diffusion barrier layer because the oxygen diffusivity in MgO at 800°C is 8×10^{-22} cm^2/s. In the past, we have demonstrated the epitaxial growth of MgO layers on Ag-buffered Pd/Ni substrates [5], Pd-buffered Ni substrates [5], and TiN-buffered Cu substrates [6]. LMO has also been identified as a good diffusion barrier to nickel contamination [7,8]. The pseudo-cubic lattice parameter of LMO (3.88 Å) is closely matched to YBCO; the lattice mismatch is less than 0.8%. We have also shown recently that LMO is compatible with MgO surfaces by demonstrating the growth of highly textured LMO layers on IBAD-MgO substrates [9]. As a result of these studies, MgO has been grown directly on textured Ni or Ni-3%W substrates for the first time. We have also grown LMO on MgO-buffered Ni substrates. Here we report our recent results obtained on YBCO films grown on the newly developed architecture of LMO/MgO/Ni.

2.11.2 Experimental Procedure

The MgO seed layers were grown directly on biaxially textured Ni or Ni-3%W substrates by electron beam evaporation. As-rolled Ni or Ni-W tapes were cleaned by ultrasonification in isopropanol. The tapes were then annealed in a high-vacuum system at 1200 to 1300°C in Ar/H_2(4%) and H_2S gas atmospheres to obtain the desired cube texture with a complete surface coverage of sulfur c(2×2) superstructures. The substrates used were 1 cm wide and 50 μm thick.

The biaxially textured Ni substrates were mounted on a heater in the e-beam system. After the vacuum in the chamber had reached a background pressure of 1×10^{-6} Torr at room temperature, the substrates were heated to various temperatures, ranging from 300 to 600°C. The MgO layers were deposited on the Ni substrates at an optimum temperature of 400°C. The crucibles were graphite. MgO crystals were used as the source material. The deposition rate for MgO was 0.5 nm/s at an operating pressure of 10^{-5} Torr, and the final thickness varied from 30 to 300 nm. Similarly, MgO layers were deposited by reel-to-reel e-beam evaporation on 1-cm-wide tapes of textured Ni-W substrates that were a few meters long. The deposition rates were from 0.13 to 0.27 nm/s in the presence of 5×10^{-5} Torr H_2O. The optimum deposition temperature was 400°C.

We deposited 60-nm-thick LMO buffer layers on MgO-buffered Ni substrates by rf-magnetron sputtering. The oxide sputter targets were made from single-phase LMO powders prepared by a solid-state reaction, the powders were loosely packed in a 4-in. copper tray. Typical sputter conditions consisted of 2 to 5×10^{-5} Torr of H_2O with a total pressure of 3 mTorr forming gas (Ar/H_2 4%). The water pressure is sufficient to oxidize the film to form stoichiometric LMO when grown at a substrate temperature of 650 to 750°C. The deposition rate was ~0.06 nm/s. YBCO was deposited from a stoichiometric YBCO target by PLD at 790°C in the presence of 120 mTorr oxygen; the average laser energy was 400 to 410 mJ. Deposition was followed by annealing under 550 Torr oxygen during cooldown. The typical YBCO thickness was 200 nm.

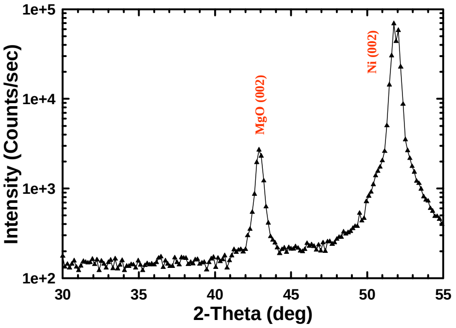

Fig. 2.59. A typical θ-2θ scan for a 30-nm-thick MgO film on textured Ni substrate. The MgO film has a preferred *c*-axis orientation.

The crystalline structure of the films was analyzed by XRD. SEM micrographs were taken with a Hitachi S-4100 field emission microscope. The thickness of both buffer layers and YBCO were determined by RBS. The films were then prepared for current density measurements by depositing silver for current and voltage leads, followed by oxygen annealing at 500°C for 1 h. The transport critical current density was measured with a standard four-point probe technique and a voltage criterion of 1 μV/cm.

2.11.3 Results and Discussion

A typical θ-2θ scan for a 30-nm-thick MgO film grown on textured Ni substrate is shown in Fig. 2.59. The scans indicate the presence of *c*-axis-aligned films. No NiO is present in the film. Detailed XRD results from ω and ϕ scans (as shown in Fig. 2.60) revealed good epitaxial texturing. The FWHM values for Ni (002) and MgO (002) are 9.6° and 4.7°, and those of Ni (111) and MgO (220) are 8.0° and 7.4°,

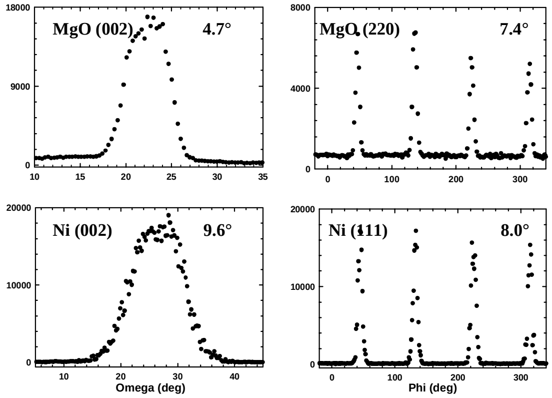

Fig. 2.60. The ω and ϕ scans obtained for a 30-nm-thick e-beam MgO film grown on textured Ni substrate. The FWHM values for each scan are shown inside the scans.

respectively. There was a significant improvement in the out-of-plane texture, possibly due to the formation of subgrains inside a Ni grain, and the MgO layers were smooth. As shown in Fig. 2.61, the MgO (220) pole figure revealed the presence of a single fourfold cube texture. Highly textured and reproducible results were obtained on the Ni or Ni-W substrates with the complete c(2×2) sulfur superstructures. SEM micrographs for both 30- and 300-nm-thick MgO seeds are shown in Fig. 2.62(a) and (b). Sample morphology of 30-nm-thick MgO layer is smooth, uniform, crack-free, and dense. MgO also has excellent coverage at grain boundaries. However, 300-nm-thick MgO layers were cracked in orthogonal regions, possibly due to either thermal expansion or lattice mismatch between Ni and MgO, causing the release of strain in MgO at higher thicknesses. Hence, it is essential to grow thin, crack-free layers of MgO. The AFM images obtained on both 60- and 300-nm-thick MgO surfaces are shown in Fig. 2.63. The surface roughness obtained on a 60-nm-thick MgO surface is 7 nm; that on 300-nm-thick MgO surface is 5.8 nm. Typical surface roughness for the Ni-W substrate is around 8 to 10 nm. A typical θ-2θ scan for a 50-nm-thick MgO film on a textured Ni-W substrate is shown in Fig. 2.64. The MgO film has a preferred *c*-axis orientation. In addition, uniform MgO (002) X-ray peak intensities at various positions in a 2-m-long Ni-W tape indicate that MgO layers can be deposited in a moving tape in the reel-to-reel system.

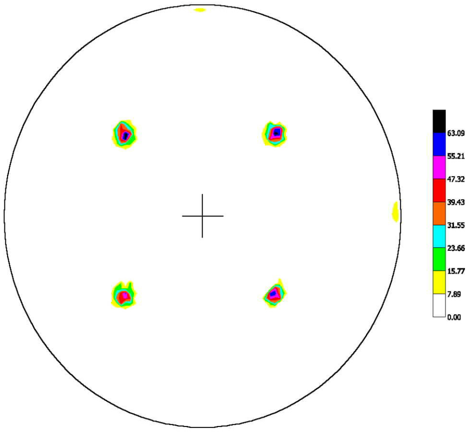

Fig. 2.61. Typical MgO (220) pole figure obtained on a 30-nm-thick e-beam MgO film grown on textured Ni substrate. Fourfold symmetry indicates the presence of cube textured MgO films.

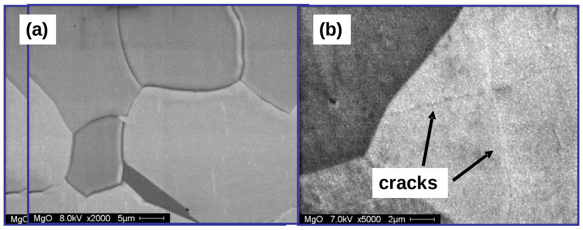

Fig. 2.62. SEM micrograph obtained on (a) crack-free 30- and (b) cracked 300-nm-thick MgO surface.

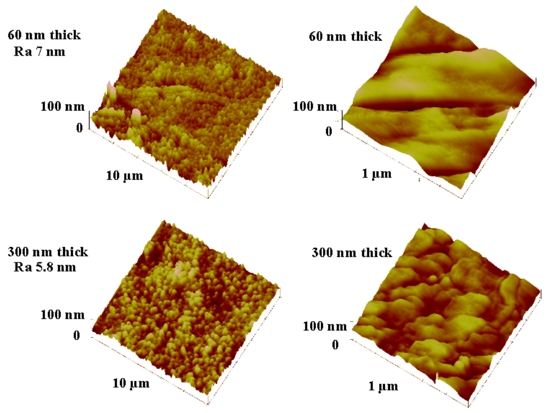

Fig. 2.63. AFM images obtained on both 60- and 300-nm-thick MgO surface.

A typical θ-2θ scan for a 60-nm-thick sputtered LMO film grown on e-beam MgO buffered Ni substrate is shown in Fig. 2.65. These scans indicate the presence of a highly *c*-axis aligned LMO film. Figure 2.66 shows detailed X-ray results obtained from ω and ϕ scans on LMO layers. It revealed very good epitaxial texturing. The FWHM values for Ni (002), MgO (002), and LMO (004) are 8.2°, 4.8°, and 5.2°, and those of Ni (111), MgO (220), and LMO (222) are 8.4°, 7.5°, and 7.2°, respectively. Highly textured 200-nm-thick PLD YBCO films were grown on LMO/MgO/Ni. The total thickness of the buffer layers was ~100 nm. The typical θ-2θ scan for a 200-nm-thick PLD YBCO film on LMO-buffered MgO/Ni is shown in Fig. 2.67. These scans indicate that the YBCO is *c*-axis aligned. In addition, very small amounts of NiO impurities were observed. A critical current density of 1×10^6 A/cm^2 at 77 K and self-field was obtained on these films (see Fig. 2.68). The critical current density at 0.5 T is about 300,000 A/cm^2. Some of the buffers on both Ni-W3% and Ni substrates delaminated during the YBCO

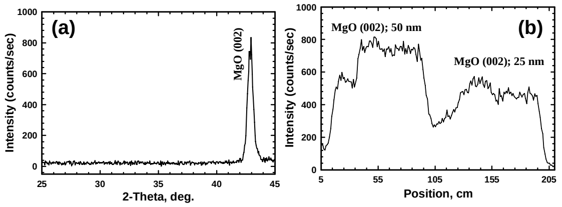

Fig. 2.64. (a) A typical θ-2θ scan for a 50-nm-thick MgO film on textured Ni-W substrate. The MgO film has a preferred *c*-axis orientation. (b) MgO (002) X-ray peak intensity at various positions in a 2-m-long Ni-W tape.

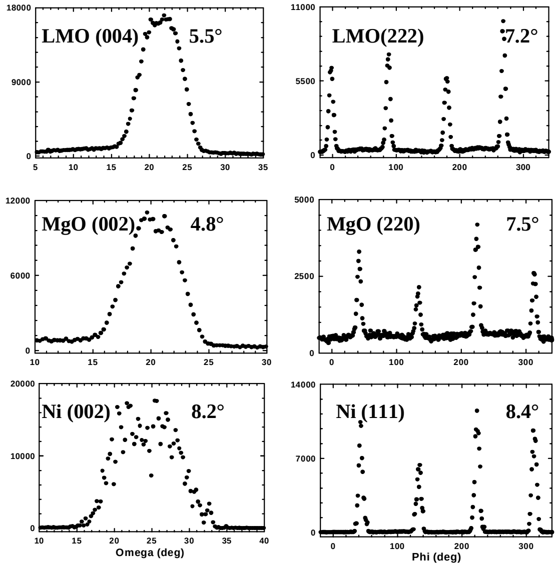

Fig. 2.66. The ω and ϕ scans obtained for a sputtered 60-nm-thick $LaMnO_3$ film on e-beam MgO buffered Ni substrate. The FWHM values for each scan are shown inside the scans.

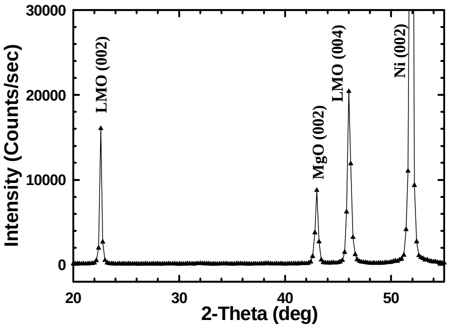

Fig. 2.65.Typical θ-2θ scan for a 60-nm-thick sputtered $LaMnO_3$ film on e-beam MgO-buffered Ni substrate. Both $LaMnO_3$ and MgO films have a preferred *c*-axis orientation.

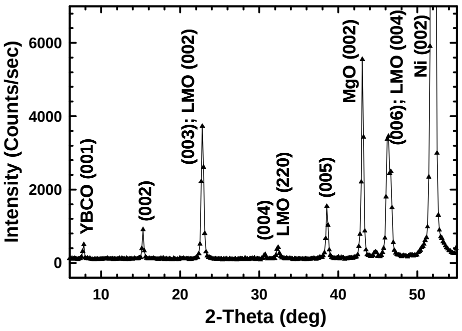

Fig. 2.67. A typical θ-2θ scan for a 200 nm thick PLD-YBCO film on sputtered $LaMnO_3$-buffered MgO/Ni substrate.

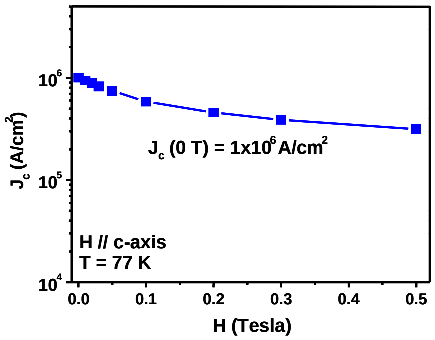

Fig. 2.68. Field dependence critical current density for a 200-nm-thick PLD-YBCO film on sputtered $LaMnO_3$-buffered MgO/Ni substrate.

growth. The main cause for the delamination is unknown at this time. Because no oxygen transport takes place through MgO layers to the substrates during the YBCO growth, the formation of a self-passivating layer of $NiWO_4$ may be limited. Recent cross-sectional TEM studies on a high-critical-current thick YBCO film based RABiTS™ have shown that the presence of $NiWO_4$ layer may be beneficial [10,11]. Efforts are being made to optimize the YBCO growth conditions and to understand the role of MgO seeds in detail.

2.11.4 Summary

In summary, we have demonstrated that MgO films can be grown epitaxially with a single cube-on-cube orientation on textured Ni substrates. The microstructure of the 30-nm-thick e-beam grown MgO films was dense, crack-free and continuous. Highly aligned LMO layers were grown on MgO-buffered Ni substrates. Our preliminary results indicate that PLD YBCO films with a critical current density of 1 MA/cm^2 can be deposited on LMO/MgO/Ni substrates.

2.11.5 References

1. A. Usoskin et al., “Large Area YBCO-Coated Stainless Steel Tapes with High Critical Currents,” *IEEE Trans on Appl. Supercond.* **13**, 2452 (2003).
2. Y. Iijima, K. Kakimoto, and T. Saitoh, “Fabrication and Transport Characteristics of Long Length Y-123 Coated Conductors Processed by IBAD and PLD,” *IEEE Trans. on Appl. Supercond.* **13**, 2466 (2003).
3. D. T. Verebelyi et al., “Uniform Performance of Continuously Processed MOD-YBCO-Coated Conductors using a Textured Ni-W Substrate,” *Supercond. Sci. and Technol.* **16**, L19 (2003).
4. J. R. Groves et al., “Improvement of IBAD MgO Template Layers on Metallic Substrates for YBCO HTS Deposition,” *IEEE Trans. on Appl. Supercond*. **13**, 2651 (2003).
5. M. Paranthaman et al., “MgO Buffer Layers on Rolled Nickel or Copper as Superconductor Substrates,” U.S. Patent No. 6,261,704 (July 17, 2001); M. Paranthaman et al., “Method of Making MgO Buffer Layers on Rolled Nickel or Copper as Superconductor Substrates,” U.S. Patent No. 6,468,591 (October 22, 2002).
6. C. Cantoni et al., “Deposition and Characterization of $YBa_2Cu_3O_{7-\delta}$/$LaMnO_3$/MgO/TiN Heterostructures on Cu Metal Substrates for Development of Coated Conductors,” *J. Mater. Res*. **18**(10), 2387 (2003).
7. M. P. Paranthaman et al., “Single Buffer Layer Technology for YBCO Coated Conductors,” *Mater. Res. Soc. Symp. Proc.*, **689**, 323 (2002).
8. T. Aytug et al., “Single Buffer Layers of $LaMnO_3$ or $La_{0.7}Sr_{0.3}MnO_3$ for the Development of $YBa_2Cu_3O_{7-\delta}$ Coated Conductors: A Comparative Study,” *J. Mater. Res*. **17**, 2193 (2002).
9. M. Paranthaman et al, “Growth of Thick $YBa_2Cu_3O_{7-\delta}$ Films Carrying a Critical Current of over 230 A/cm on Single $LaMnO_3$-Buffered Ion-Beam-Assisted Deposition MgO Substrates,” *J. Mater. Res*. **18**, 2055 (2003).
10. S. Kang et al., “High Critical Current $YBa_2Cu_3O_{7-\delta}$ Thick Films on Rolling-Assisted Biaxially Textured Substrates (RABiTS™),” *J. Mater. Res*. (in press).
11. K. J. Leonard, S. Kang, A. Goyal, K. A. Yarborough, and D. M. Kroeger, “Microstructural Characterization of Thick $YBa_2Cu_3O_{7-\delta}$ Films on Improved Rolling-Assisted Biaxially Textured Substrates,” *J. Mater. Res.* **18**, 1723 (2003).

2.12 Faster Conversion Process Produces ex situ YBCO Coated Conductors with Critical Currents Greater than 350 A/cm-Width at 77 K

R. Feenstra, A. A. Gapud, F. A. List, E. D. Specht, and D. K. Christen (ORNL); T. G. Holesinger (LANL); and D. M. Feldmann, (University of Wisconsin)

2.12.1 Introduction

Studies to enhance critical currents in YBCO coated conductors proceed in two complementary ways, as suggested by the layered geometry and accumulation-based synthesis. From an established set of growth parameters, a primary approach is to increase the YBCO layer thickness *d*, recording gains in critical current due to a larger superconductor cross section [1]. Alternatively, for a suitably large value of *d*, research may focus on increasing the critical current density by process optimization [2]. Later research may restrict itself to YBCO growth parameter adjustments or may address as well substrate-related properties or defect structure for vortex pinning. Application of the processing adjustments to films of variable thicknesses tests the general validity of the improvements and sets a framework for cyclical development. With each process iteration, distinct functional dependences of critical current or critical current density on *d* provide a touchstone for the underlying physics of layered superconductors [3], while in a practical sense provide a gauge to measure the progress.

An ex situ PVD BaF_2 process for YBCO epitaxial film growth has been adapted for coated-conductor applications since 1998 [4]. Starting from a “baseline” set of processing parameters, we found a consistent critical current for *d* in the range $0.2 \le d \le 3$ μm for YBCO coatings on both RABiTS™ and IBAD-YSZ templates [5]. Recently, efforts have focused on defining new processing parameters to enable faster conversion of the precursor into YBCO. Conversion rates limited to ~1 Å/s are inefficient for scale-up. On the other hand, 10 to 50 times faster conversion rates have been reported for a close variant of the PVD BaF_2 process, where the precursor layers were produced by metal-organic deposition (MOD) of trifluoroacetate solutions [unpublished results]. An enhanced porosity of MOD precursors has been proposed as a possible cause of the rate disparity; it enables faster diffusion of gaseous reactant (H_2O) and product (HF) species through the precursor layer. However, complete mechanistic description of the BaF_2 conversion process has not been given, leaving open questions regarding reaction pathways and the order of events. Moreover, strong similarities in the YBCO structure after conversion have been observed for either precursor type, which indicate a laminar growth mechanism, apparently mediated by transient liquid phase formation [6].

We have differentiated between conversion (chemical process) and YBCO *c*-axis epitaxial growth and have pursued alternative explanations. It is likely that the kinetics of gas exchange controls certain aspects of the laminar growth; however, other parameters, such as the reactant microstructure or transitory oxygen concentration, have remained underexposed. Opportunities exist to modify these parameters prior to the high-temperature conversion, as they do spontaneously in the course of heating [7]. Indeed, previous research suggested a connection with the precursor history and such “lineage” was thought to be a cause of residual variability in critical current density.

This report relates basic features of a newly developed fast conversion process, contrasting it with the baseline process. Implications for critical current are examined. Gains in both the rate and critical current are substantial and suggest a link. For the first time, width-normalized critical-current values that are comparable to commercial Ag-Bi-2223 multifilamentary composite wire [8] were obtained.

2.12.2 Experimental Details

The research evaporation chamber used to deposit precursor layers was described in an early publication [9]. Briefly, films of variable thickness *d* are deposited by simultaneous evaporation from electron-beam Y, BaF_2, and Cu sources. Composition is controlled is by quartz crystal monitors for the three individual evaporation rates. To avoid BaF_2 excess (within the margins of rate stability), set points are biased toward a small BaF_2 deficiency/Y excess. Expressed in ratios of the constituents, characteristic values are [Y/Ba] = 0.55 and [Ba/Cu] = 0.60. Films with this composition are referred to as "stoichiometric." As part of this work, we have also studied effects of Y_2O_3 doping on vortex pinning and thickness-dependent trends. These Y-rich films were produced by increasing the Y evaporation rate relative to the Cu and BaF_2.

During deposition, the substrates were slightly heated (to ~100°C), and small amounts of O_2 were dosed into the vacuum chamber to partially oxidize the deposit and to minimize reduction of substrate CeO_2 buffer layers. Setting an appropriate O_2 pressure requires some optimization because extraneous factors such as gettering from freshly deposited Y, chamber cleanliness, and pumping speed can affect the result. Stable precursors with the capacity to convert quickly were produced with the O_2 background pressure controlled to stationary values of 5×10^{-6} to 9×10^{-6} Torr (i.e., at an increased level relative to the idling background (2×10^{-6} Torr) or the vacuum without O_2 addition (1×10^{-6} Torr). Thickness values *d* were inferred from batch quartz crystal monitor readings, calibrated against profilometry and RBS measurements after conversion.

The RABiTS™ samples used in this study, provided by AMSC, feature a 75-µm-thick Ni-5%W deformation-textured metal template with average grain size of ~ 25 µm, and epitaxial Y_2O_3, YSZ, and CeO_2 buffer layers. Texture parameters measured on the YSZ average $\Delta\Phi$(true) = 4.8° and $\Delta\omega = 5.8°$. Reel-to-reel–produced ORNL RABiTS™ was also used. Critical-current (*d*) data for baseline-processed films were compared with fast-processed films on the AMSC template. Although a small texture difference skews the comparison somewhat, experiments confirm that conclusions regarding fast vs baseline processing hold for both templates. The ORNL RABiTS™ architecture features 50-µm-thick Ni-3%W metal tape (grain size: ~ 50 µm) coated with a Ni overlayer, and Y_2O_3, YSZ, and CeO_2 buffer layers. Average texture parameters for the YSZ are: $\Delta\Phi$(true) = 6.1° and $\Delta\omega = 5.5°$. Before being mounted in the precursor deposition chamber, the substrates were annealed in flowing N_2 gas (containing < 80 ppm O_2) to temperatures in the range 700 to 750°C for 0.5 h.

Ex situ conversion was performed in either of two annealing systems. Most of the films were processed in the standard tube furnace [9], which is equipped to operate with flowing gas mixtures at atmospheric pressure. Relatively large flow rates corresponding to a plug-flow velocity of 4 m/min were used. Helium served as the carrier gas. Improvements in the gas-handling system allow for a flexible range of water partial pressures, from dilute (calculated dew point < −30°C) to concentrated (~ 0.1 atm). The O_2 partial pressure was set at 250 ppm.

A second conversion system, equipped with in situ XRD capability and operating at reduced absolute pressures, was used to study conversion rates for films of a fixed 1-µm thickness. Details of this system were recently described by List et al. [10]. Annealing was performed in gas mixtures (Ar, O_2, H_2O) at total pressures of 0.5 to 2.5 Torr and O_2 partial pressure of 200 mTorr. Sample dimensions for the two furnace systems reflect systemic differences in out-flow capacity. This capacity is enhanced and more homogeneously distributed at subatmospheric operating pressures. Design sample dimensions for the vacuum conversion system are 3 × 1 cm. Precursor areas reduced by a factor of 10 were used for fast conversion in the standard 1-atm system. Narrow precursor strips (~2 mm wide) were deposited onto 1.5 cm long × 5 mm wide substrates through a shadow mask. XRD after the high-temperature anneal confirmed that full conversion of similarly thick precursors could be achieved in both systems by using similar annealing times.

Transport critical currents were measured by a standard four-probe technique and 1-µV/cm criterion. Measurements were made over the full YBCO width. Where current limitations prevented determination of the self-field critical current, values were extrapolated from measurements in applied magnetic fields H || c, using lower-critical-current thin films for calibration. That this procedure should lead to consistent results as a function of *d* is not obvious. However, as reported elsewhere in more detail [11], consistency is confirmed by the high degree of uniformity in the H-field dependence for variable-thickness films (made with the ex situ process), described by a power law ($J_c \propto H^{-\alpha}$) in the range 0.1 to 1 T with narrow distribution of exponents $\alpha \cong 0.6$. These observations add confidence to the robustness of observed critical-current enhancements, as they occur over a substantial H field range.

2.12.3 Fast Conversion Process

A schematic temperature-time diagram for the fast process (1-atm conversion system) is contrasted to the baseline process in Fig. 2.69. Fast conversion was achieved by heating the precursor at a rate of 130°C/min to ~780°C in gas mixtures containing 1–2% water vapor. The annealing duration was computed from a presumed growth rate and the film thickness. Following conversion, the water supply is turned off, and a drying time of 3 min began prior to cooling. Excluding the drying time, annealing durations corresponding to growth rates of 5 to 12 Å/s were found to produce complete conversion into YBCO for thickness values ranging from 0.2 to 2 µm. Electrical resistivity values at room temperature were in the range of 200 to 300 µΩ.cm.

A direct confirmation of the conversion rate is provided by the in situ XRD data of Fig. 2.70 (low-pressure system). Indicated are time-dependent, normalized peak intensities of BaF_2 (111) and YBCO (200) reflections for three 1-µm-thick films (A, B, and C) during the conversion process. Fast-conversion processing parameters were used for samples A and B. These parameters include a temperature of 780°C, water pressure of 5 mTorr, and an absolute total pressure of 0.5 Torr. Behavior typical of the baseline process is illustrated by sample C. Parameters were set according to a previous optimization study [10] to an absolute pressure of 2.5 Torr, 740°C, and 5 mTorr water pressure. A short anneal (0.5 h) at 400°C in 0.1 atm O_2 applied to samples A and C prior to ex situ conversion provides further differentiation. The anneal is not part of the standard protocol for PVD BaF_2 precursors; however, it was added here to increase the average oxidation level and/or modify the microstructure. Evidence of structural changes may be inferred from the appearance of weak BaF_2 reflections in the θ-2θ XRD spectrum. By contrast, sample B was converted directly from the as-deposited state.

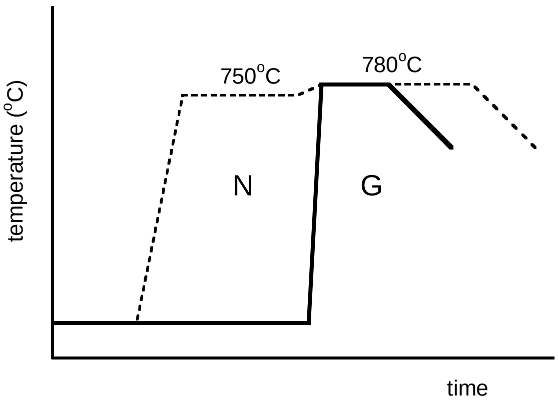

Fig. 2.69. Schematic temperature-time diagram of the "fast" conversion process (solid) and the "baseline" process (dashed) in the standard 1-atm furnace system. In the baseline process, a 0.5–1 h nucleation step (N) at reduced water supply (0.04–0.2%) precedes the main "growth" annealing step (G) at optimized water concentration of ~0.5% (relative to 1 atm). The fast process bypasses the N-step via a fast ramp and provides an increased water supply (1–2%). An oxidation step at 500°C followed by slow cooling (not shown) concludes both processes.

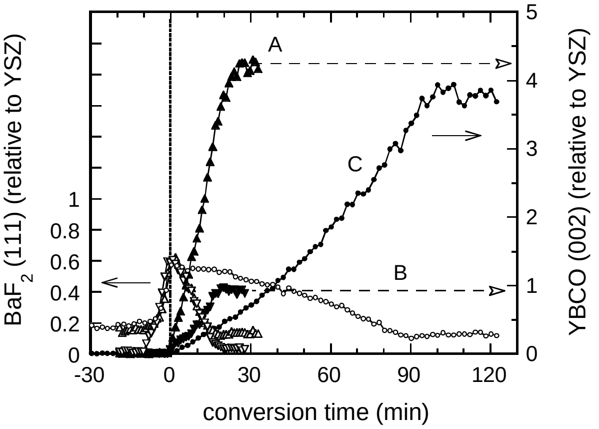

Fig. 2.70. Time-dependent variations of the peak intensities of BaF_2 (111) (open symbols, left axis) and YBCO (002) (closed symbols, right axis) reflections during fast (samples A, B) and baseline (sample C) conversion processes. The zero point of conversion time is defined as the moment that the sample temperature reaches the set point**.**

Disappearance of the BaF_2 signal and saturation of the YBCO intensity occur simultaneously and mark the moment at which conversion is complete. Thus the annealing duration for the fast sample (A) is reduced by a factor of ~4.5 compared to the slower conversion (sample C), from 90 to about 20 min. The corresponding growth rate is 7.5 Å/s. The primary cause of faster conversion for sample A stems from the imposed "aggressive" conversion parameters, featuring a higher temperature and reduced absolute pressure. Although the water supply was kept constant, the reduced total pressure increases the chemical driving force for BaF_2 decomposition by increasing the HF removal rate. For both samples the YBCO saturation level is well developed and reaches a similar intensity.

A very different picture is provided by sample B, which was converted with fast-conversion parameters but without the intermediate anneal. The BaF_2 intensity shows the same time dependence as sample A (indicating that fast conversion occurred); the *c*-axis YBCO signal remains low and levels off after about 20 min. A full XRD θ-2θ spectrum shows that this film had grown to a structure with multiple YBCO orientations, characterized by weak (00L) reflections. The critical current of the film reached merely 0.1 A at 77 K. By contrast, only (00L) reflections were measured for the properly converted film A, yielding a high critical current value of 189 A/cm-width. Modifications introduced by the intermediate anneal for sample A improved the *c*-axis epitaxial growth mechanism for the same conversion rate. This feature stands out as the primary benefit of the intermediate anneal.

Within the larger context of this research, the disparity between samples A and B qualifies as extreme. It is clear, however, that the precursor preparation history enters into the conversion process. Experimentation with inserted modification anneals was started in studies of the baseline process, where they revealed contradictory but mostly beneficial effects. In a way that is reminiscent of supersaturation in epitaxial film growth, a large chemical driving force for BaF_2 conversion seems to magnify the role of details in precursor and substrate properties. The procedural step of inserting a low-temperature anneal resembles the use of a calcination anneal for MOD BaF_2 precursors. In the latter case, however, the primary function is removal of carbon-containing residues from the solution-based deposition process, and the parameters are optimized to perform this function. The low-temperature annealing conditions selected here for PVD-BaF_2 precursors resulted from preliminary tests covering a relatively small part of parameter space. By expanding the search, we expect that further optimization is feasible. Concurrent adjustments of the ex situ conversion parameters may be needed, however, to expand the optimization matrix. All films described in the remainder of this work featured the intermediate anneal and the temperature-time profile of Fig. 2.69 for processing at 1.0 atm total pressure.

2.12.4 Relationship between YBCO Thickness and Critical Current

Values of critical current per unit width at 77 K for fast-processed YBCO on AMSC RABiTS™ are plotted as a function of *d* in Fig. 2.71. Two sets of fast-processed films are represented, indicated by the closed circles and triangles. Initial research focused on stoichiometric (slightly Ba-deficient) films. Figure 2.71 compares films produced with the fast process (closed circles) to ones produced with a baseline-process variant (open circles, labeled as "standard" process). For the fast process, starting from $I_c \cong 50$ A/cm for 0.2-μm thick films, the critical current increases approximately linearly with *d* to ~320 A/cm for a 1.34-μm-thick film. This idealized behavior contrasts with the saturation-like thickness dependence of standard-processed films. The latter behavior is illustrated more clearly by the larger dataset for baseline-processed films on the ORNL template (open diamonds). For thickness values to 3 μm, the trend is suitably described by a square root function of *d*: $I_c \propto d^{1/2}$. That is, the critical current density decreases as $1/d^{1/2}$. Other functional forms can provide equally satisfactory representations, such as the type $J_c \propto \exp(-d/d_0) + J_S$, introduced by Foltyn et al. [1] for YBCO films grown by in situ PLD. Indeed, a remarkable correspondence exists between the trends on a relative scale for this baseline ex situ BaF_2 process and in situ PLD. (Further discussions of these similarities are deferred to a future publication.)

In an attempt to further improve flux-pinning properties in the fast-processed films, we initiated a study involving the effects of Y-rich compositions. This approach was based on observations by TEM

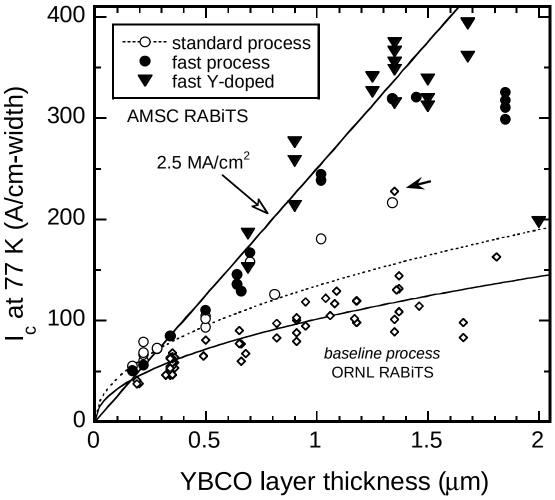

Fig. 2.71. Variation of the critical current normalized to 1-cm width with layer thickness *d* of ex situ processed YBCO coatings on RABiTS™ templates. The films were converted from PVD BaF_2 precursors. Fast-processed samples are indicated by the solid symbols. The straight line was calculated for a constant critical current density of 2.5 MA/cm^2. Curves through the baseline (standard) process data represent trend lines according to the expression $I_c = I_c(1)\ d^{1/2}$ where *d* is in μm. $I_c(1)$ = 134 A/cm for AMSC RABiTS™ (standard process) and 101 A/cm for ORNL RABiTS™ (baseline process). An exceptional film on ORNL RABiTS™ (d = 1.34 μm) is highlighted with a small arrow. [T. G. Holesinger et al., "Liquid-Mediated Growth and the Bi-Modal Microstructure of YBCO Films Made by ex situ Conversion of PVD-BaF_2 Precursors," *J. Mater. Res.*(submitted).]

that a high density of Y_2O_3 precipitates of suitably small dimensions (15–50 nm) may be incorporated as inclusions in the laminar YBCO grain structure [6]. Initial studies were performed for films of a fixed thickness of 0.7 to 0.9 μm. Variations in the Y excess ranged from 30 to 90%. Results from measurements of critical current density as a function of applied magnetic field, temperature, and field orientation are reported in a companion paper [11]. These studies revealed systematic trends due to Y addition, with self-field critical current density increasing and the magnitude of field-angle dependent critical current density variations decreasing. The data suggest a homogenized flux-pinning mechanism due to correlated defects or strain, with a multitude of orientation vectors.

The Y additions also resulted in larger critical-current values for films with $d > 0.9$ μm. A critical current greater than 350 A/cm was reached for several 30% Y-rich 1.34-μm-thick films. Best critical-current values to date are ~393 A/cm for two 50% Y-rich 1.7-μm-thick films. There is an indication that the linear $I_c(d)$ relationship may be extended by increasing the Y doping in thicker films. However, critical-current-density values for the 1.7-μm films fall slightly below the 2.5-MA/cm^2 trend line, as critical current tends to roll over for $d \geq 1.5$ μm. A clear stagnation in critical current is found for stoichiometric films between d = 1.35 μm and 1.85 μm, giving way to a sudden drop in critical current for thicker films. The 2-μm film shown in Fig. 2.71 contained 90% Y excess. The critical current continues to decrease for thicker films (not shown) to values less than that extrapolated from the baseline square root dependence, indicating that developed fast-processing conditions are not optimal for this thickness range. Within the linear regime, however, the realized gains are substantial. Maximum critical-current values are equivalent to those reported for first-generation Ag-Bi-2223 multifilamentary composite tape. Previous equivalent performance levels featured relatively thick YBCO coatings ($d \geq 3$ μm) produced by PLD on highly textured IBAD templates [12,13]. The present results show that application-grade conductors are now also available from a BaF_2 ex situ process.

According to the basic definition $I_c/w = J_c\ d$, a linear relationship between critical current per cm-width (w) and layer thickness d results if the critical current density remains constant. Because of the difficulty in sustaining a self-replicating growth process, it might be expected that strongly processing and substrate-dependent effects on critical current density render this an unlikely scenario for YBCO epitaxial films. With the fast process, however, "constant" critical-current-density values of 2.3 to 2.7 MA/cm^2 are obtained for all thickness values in the range 0.17 to 1.7 μm.

The origin of this near-ideal behavior remains under investigation. A linear $I_c(d)$ relation was obtained previously upon thinning (by ion milling) of thick ex situ YBCO coatings (0.9–2.9 μm) on ORNL RABiTS™ and IBAD-YSZ templates [14]. These baseline-processed films, however, contained "bimodal" laminar structures, with large YBCO grains near the substrate, intercalated Ba-rich secondary phases, and smaller YBCO grains near the surface [6]. A change in the growth mechanism, midway through the precursor conversion, appears inconsistent with the observed near-constant critical-current-density through thickness, perhaps pointing to compensating effects.

Preliminary results from TEM and XRD texture analysis suggest that the onset of bimodal growth (as a function of thickness) is delayed to $d > 1.3$ µm for fast-converted films. Indeed, a homogeneous, non-bimodal microstructure was observed by TEM for one of the 1.25-µm-thick Y-rich films shown in Fig. 2.71 with $I_c \cong 340$ A/cm. This film displayed a complete absence of interface reactions with the CeO_2 buffer layer. Unlike the linear $I_c(d)$ relation in the ion-milling study, the linear dependence for variable thickness, fast-processed films ($d < 1.3$ µm) could be the result of an invariant microstructure. However, additional structural trends occur.

Behavior indicative of bimodal growth was observed for one of the 1.85-µm films ($I_c \cong 320$ A/cm). Using through-thickness ion milling along with electron backscatter Kikuchi pattern (EBKP) analysis, we find that the introduction of additional grain-boundary networks in the top part of the film may be consistent with the sudden decrease in critical current for this and films of larger thickness. Future research is being directed at improving this undesirable behavior.

More generally, the EBKP imaging and cross-section TEM provide evidence of complex grain-boundary structures in the ex situ films. This finding is related to a thickness dependence in a tendency for the YBCO to completely or partially overgrow substrate grain boundaries. Films in the range of ~1 µm are especially rich in their characteristics. YBCO grain boundaries for this thickness are found to meander about the projected substrate grain-boundary plane, both through the thickness and parallel to the substrate surface. A companion paper describes these observations in more detail [15]. The role of curved and tilted grain-boundary planes on supercurrent transmission is practically uncharted territory and is being studied via newly initiated bi-crystal experiments. These hidden complexities attest to the fact that even if seemingly ideal behavior is observed, the physical mechanisms underlying current transport in YBCO coated conductors are still incompletely understood.

2.12.5 Summary

A faster conversion process of PVD BaF_2 precursors has been described with the ability to produce *c*-axis YBCO at rates up ~12 Å/s, both in a standard, 1-atm furnace and at reduced absolute pressures. A low-temperature oxidation anneal inserted as an extra processing step between precursor deposition and ex situ conversion enables application of aggressive conversion conditions. Fast-converted films exhibit a linear relationship between critical current and the YBCO layer thickness d in the range 0.2 to 1.7 µm. Enhanced vortex-pinning properties and self-field critical current density resulted from Y doping over a similar thickness range. Best critical-current values (~400 A/cm, 77 K) are equivalent to the performance of industrially produced Ag-Bi-2223 wire.

Significantly larger critical-current-density values of ~3.4 MA/cm^2 were recently reported by AMSC for 0.8-µm-thick ex situ YBCO converted over 10-m production lengths from MOD precursors on RABiTS™ tape similar to those supplied to us. [16]. Extension of these high critical-current values to the range of 1.5 to 2 µm appears feasible based on the present results, raising the prospect of conductors with a drastically improved price-to-performance ratio.

2.12.6 References

1. S. R. Foltyn et al., "Relationship Between Film Thickness and the Critical Current of YBCO Coated Conductors," *Appl. Phys. Lett.* **75**, 3692 (1999).
2. M. W. Rupich et al., "YBCO Coated Conductors by a MOD/RABiTS^{TM} Process," *IEEE Trans. Appl. Supercond.*, **13**, 2458 (2003).
3. A. Gurevich, "Thickness Dependence of Critical Currents in Thin Superconductors," (in preparation).
4. R. Feenstra, "The BaF_2 Method: A Scalable Process for YBCO Coated Conductors," presented at the DOE Wire Workshop, St. Petersburg, Fla., Jan. 29–30, 1998; R. Feenstra, D. K. Christen, and M.

Paranthaman, “Method for Making High-Critical-Current-Density YBCO Superconducting Layers on Metallic Substrates,” U.S. Patent No. 5,972,847 (1999).
5. R. Feenstra, T. G. Holesinger, and D. M. Feldmann, “Materials and Intrinsic Properties in the J_c Dependence on Thickness of ex situ YBCO Coated Conductors,” presented at the DOE Peer Review, Washington, D.C., July 23–25, 2003.
6. T. G. Holesinger et al. “Liquid Mediated Growth and the Bimodal Microstructure of YBCO Films Made by ex situ Conversion of PVD-BaF_2 precursors,” *J. Mater. Res*. (submitted).
7. W. Wong-Ng et al., “Phase Evolution of YBCO Films during the BaF_2 Process,” *Supercond. Sci. & Technol*. (accepted for publication).
8. Y. B. Huang et al., “Improving the Critical Current Density in Bi-2223 Wires via a Reduction of the Secondary Phase Content,” *IEEE Trans. Appl. Supercond*. **13**, 3038 (2003).
9. R. Feenstra et al., “Effect of Oxygen Pressure on the Synthesis of YBCO Thin Films by Post-Deposition Annealing,” *J. Appl. Phys*. **69**, 6569 (1991).
10. F. A. List et al., “Crystalline Phase Development during Vacuum Conversion of Thin Barium Fluoride Precursor Films on Metallic Substrates,” Physica C **391**, 350 (2003).
11. A. A. Gapud et al., “Temperature and Magnetic Field Dependence of Critical Currents in YBCO Coated Conductors with Processing-Induced Variations in Pinning Properties” (in press).
12. S. R. Foltyn et al., “Strongly Coupled Critical Current Density Values Achieved in YBCO Coated Conductors with Near-Single-Crystal Texture,” *Appl. Phys. Lett*. **82**, 4519 (2003).
13. A. Usoskin et al., “YBCO Coated Conductors with Extra-High Engineering Current Densities and their Implementation in Power Engineering,” presented at the Fall Meeting of the Mater. Res. Soc, December 1–4, 2003.
14. D. M. Feldmann et al., “Through-Thickness Superconducting and Normal-State Transport Properties Revealed by Thinning of Thick Film ex situ YBCO Coated Conductors,” *Appl. Phys. Lett*. **83**, 3951 (2003).
15. D. M. Feldmann et al., “Large Grains and Substrate Grain Overgrowth Resulting from Liquid-Mediated YBCO Growth in Coated Conductors” (manuscript in preparation).
16. A. P. Malozemoff, “Second Generation Wire: An Assessment,” http://www.amsuper.com (March 2004).

2.13 Low-Pressure Conversion Studies for YBCO Precursors Derived by PVD and MOD Methods

F. A. List, L. Heatherly, K. J. Leonard, D. F. Lee, and A. Goyal (ORNL); P. G. Clem and J. T. Dawley (Sandia National Laboratories)

2.13.1 Introduction

Lengths of high-performance YBCO superconducting tape have been demonstrated by a number of laboratories throughout the world. For these lengths to be suitable for large-scale applications, rapid and reliable processing is required throughout all stages of conductor fabrication. The tape from which the conductor is made consists of an epitaxial YBCO film that is deposited on biaxially textured oxide buffer layers on a flexible metallic substrate [1–3]. Deposition of YBCO is accomplished by either (a) direct methods such as pulsed laser deposition, in situ electron beam evaporation, and chemical vapor deposition or (b) precursor-based methods such as metal-organic deposition (MOD) and physical vapor deposition (PVD). For direct methods, deposition and epitaxial growth are combined into a single processing step, whereas for precursor-based methods, precursor deposition and YBCO epitaxial growth are divided into two processing steps.

The focus of this paper is on YBCO prepared by precursor-based methods. The conversion of precursor to YBCO has been studied for films deposited by both PVD [3–6] and MOD [7–9] techniques. Earlier efforts to examine the effects of processing parameters on the conversion of 0.3-μm-thick PVD precursors [10] have led to a set of processing parameters optimized for both high precursor conversion rate and high critical current density. The goals of this work are (a) to compare conversion performance of similar PVD and MOD precursors for a range of processing conditions and (b) to identify some of the factors that contribute to rapid conversion of precursor to high-critical-current-density YBCO.

2.13.2 Experimental

All precursor samples were prepared on 1-cm wide, 50-µm-thick biaxially textured Ni-3at%W substrates. The substrates were 3 cm long and buffered with epitaxial layers of Y_2O_3 (~20 nm), YSZ (~250 nm), and CeO_2 (~20 nm).

Precursors were deposited on buffered substrates by two methods—MOD and PVD. For the MOD method, precursors were prepared by spin-coating buffered substrates with a diethanolamine-stabilized solution of Ba, Y, and Cu acetates dissolved in trifluoroacetic acid [11,12]. Prior to precursor conversion, the resulting coatings were pyrolyzed in air at ~325°C for ~20 s.

For the PVD method, precursors were prepared by electron beam co-evaporation of BaF_2, metallic Y, and Cu from separate sources. Rutherford backscattering spectroscopy was used to confirm the precursor thickness and cation ratio (Y:Ba:Cu = 1:2:3).

Conversion of the precursors to YBCO was accomplished in a vacuum chamber equipped with in situ XRD. Detailed descriptions of the chamber, the conversion procedures, and the characterization procedures have been given elsewhere [10].

2.13.3 Results and Discussion

Shown in Fig. 2.72 are XRD results for a 0.3-µm-thick PVD precursor converted slowly for 90 min at 740°C.

The sample was heated in 0.5-mTorr $P(H_2O)$ and 200-mTorr $P(O_2)$ at a rate of 25°C/min to 740°C. These conversion conditions are those that were found to be optimal for high conversion rate and high critical current density for this precursor [10]. At approximately the time at which 740°C is first reached (time = 0 in Fig. 2.72), the X-ray intensity for YBCO(002) (d = 5.85 Å) begins to rise roughly linearly with respect to time. After ~25 min at 740°C, this linear rise abruptly decreases and the YBCO(002) continues to rise at a much lower rate for the remainder of the conversion time. Unlike the X-ray intensity for YBCO(002), the $BaF_2(111)$ (d = 3.58 Å) intensity develops during the initial temperature ramp, is a maximum within ~2 min after reaching 740°C, and decays to zero after ~25 min at 740°C.

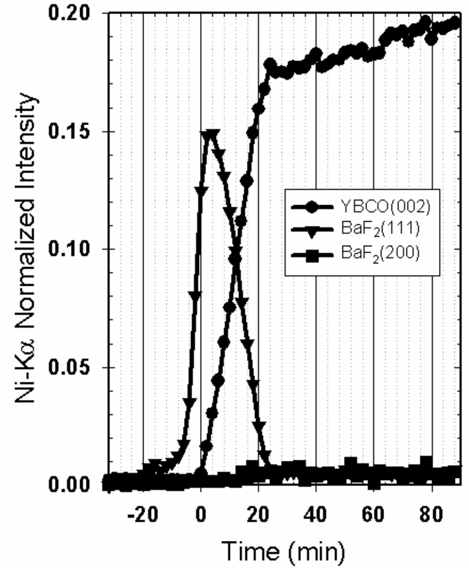

Fig. 2.72. XRD results during a slow conversion of a 0.3-µm-thick PVD precursor. $P(H_2O)$ = 0.5 mTorr, ramp rate = 25°C/min, T_{max} = 740°C, G_p = 0.20 nm/s, I_c = 37 A, J_c = 1.3 MA/cm^2.

If the intensities of YBCO(002) and $BaF_2(111)$ are assumed to be proportional to amounts of epitaxial YBCO and crystalline BaF_2, respectively, then Fig. 2.72 provides a partial X-ray timeline for the conversion of this 0.3-µm-thick stoichiometric PVD precursor. Initially during heat-up and prior to epitaxial YBCO growth, amorphous or nanocrystalline BaF_2 precursor crystallizes. When the maximum processing temperature (740°C) is reached, crystalline BaF_2 reacts and epitaxial YBCO begins to grow linearly with time. YBCO growth continues until crystalline BaF_2 is completely consumed (~25 min). The slope of the YBCO(002) intensity can be simply related to the precursor conversion rate. For this 0.3-µm-thick precursor, the conversion rate is a rather modest 0.20 nm/s. The critical current for this sample is 37.4 A, corresponding to a critical current density of 1.34 MA/cm^2.

To examine how the method of precursor deposition might affect crystalline phase development during precursor conversion, a 0.23-µm thick MOD precursor was converted slowly under conditions identical to those used for the PVD precursor sample in Fig. 2.72. Figure 2.73 shows the XRD results

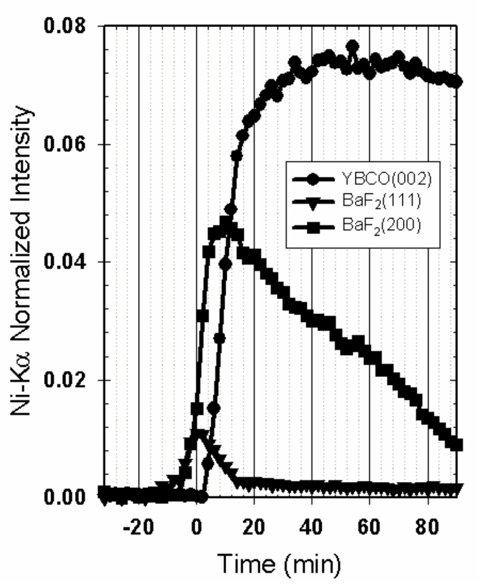

Fig. 2.73. XRD results during a slow conversion of a 0.23-μm-thick MOD precursor. $P(H_2O)$ = 0.5 mTorr, ramp rate = 25°C/min, T_{max} = 740°C, G_p = 0.20 nm/s, I_c = 17 A, J_c = 0.73 MA/cm^2.

during conversion of this MOD precursor. Although the conversion rate for the MOD precursor is equal to that of the PVD precursor (i.e., 0.20 nm/s), the crystalline development of BaF_2 is distinctly different. Rather than forming predominantly (111)-oriented BaF_2 (as is the case for the PVD precursor in Fig. 2.72), the MOD precursor appears to form mainly a (200)-oriented BaF_2 that persists after the YBCO is fully developed. X-ray pole figure analysis suggests that the BaF_2(200) is partially epitaxial in-plane with a 60% cube texture. The critical current density for this sample is 0.73 MA/cm^2.

Because of the dramatic differences in crystalline phase development observed for the PVD and MOD precursors (Figs. 2.72 and 2.73), differences in kinetics of precursor conversion might also be expected for these precursors. To explore this possibility, conversions of both precursors were conducted for conditions know to result in more rapid conversion [10]: 50 mTorr $P(H_2O)$ and a 400°C/min ramp rate. Shown in Figs. 2.74 and 2.75 are the XRD results under high-rate conversion conditions for the PVD and MOD precursors, respectively. For the high-rate PVD precursor (Fig. 2.74), the conversion rate is nearly 3 nm/s based on the development of the YBCO(103) intensity.

The YBCO is, however, randomly oriented and not epitaxial, and the critical current density is zero. For the high-rate MOD precursor (Fig. 2.75), the conversion rate is ~1.8 nm/sec and the critical current density is slightly higher than that for the low-rate conditions (~0.77 MA/cm^2). These results suggest that the maximum rate of conversion to achieve high-critical-current-density YBCO depends on both the processing conditions during conversion and the nature of the precursor prior to conversion.

The response of both PVD and MOD precursors to $P(H_2O)$ during conversion has been studied to better understand the conversion process. Figure 2.76 shows the precursor conversion rate for a range of $P(H_2O)$ for both PVD and MOD precursors. The $\sqrt{P_{H2O}}$ dependence observed for the conversion rate (solid line) is consistent with the model proposed by Solovyov et al. [13] for the precursor conversion process in which the rate limiting step is the gas-phase removal of HF.

Shown also in Fig. 2.76 are two ellipses that represent the ranges of conversion rate and $P(H_2O)$ for which PVD and MOD precursors were observed to have converted to YBCO with a critical current density of at least 0.5 MA/cm^2. For the precursors used in this study, higher rates of conversion to high-critical-current-density YBCO are possible for the MOD precursors than for the PVD precursors.

2.13.4 Conclusions

For the low-pressure conversion conditions considered here, the rate at which a precursor converts to YBCO is proportional to the square root of $P(H_2O)$ for both PVD and MOD precursors. This behavior suggests that the rate limiting step for precursor conversion is the gas-phase removal of HF. Whether high conversion rate results in high critical current density appears to depend on the nature of the precursor prior to conversion. The MOD precursors used in this study are more compatible with conversion conditions leading to high conversion rate and high critical current density than are the PVD precursors. Efforts are currently under way to identify the precursor characteristics that distinguish the conversion behavior of the PVD and MOD precursors.

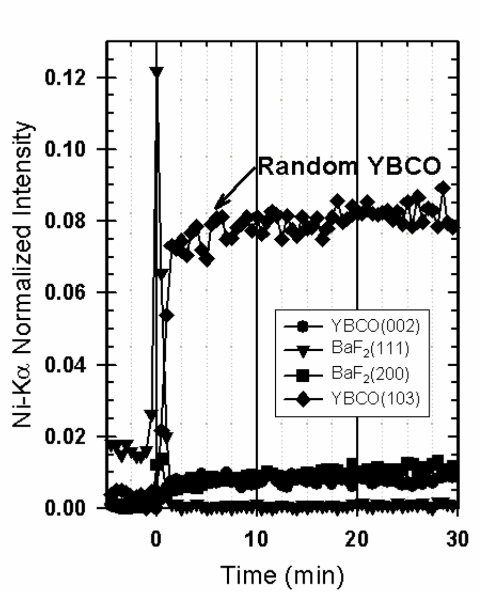

Fig. 2.74. XRD results during a fast conversion of a 0.3-nm-thick PVD precursor. $P(H_2O)$ = 50 mTorr, ramp rate = 400°C/min, T_{max} = 740°C, G_p = 3.0 nm/s, I_c = 0 A, J_c = 0 MA/cm^2.

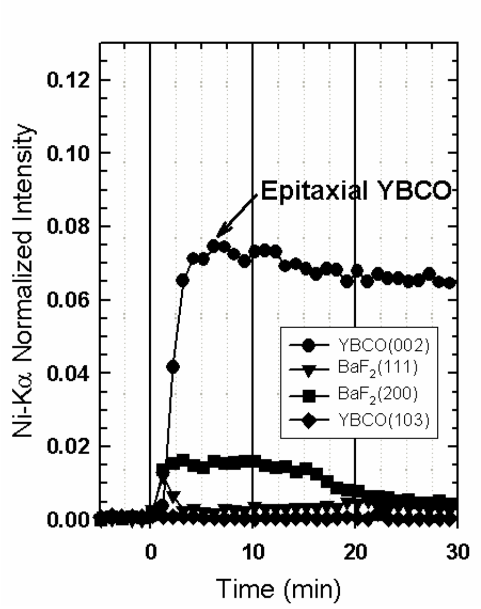

Fig. 2.75. XRD results during a fast conversion of a 0.23-nm-thick MOD precursor. $P(H_2O)$ = 50 mTorr, ramp rate = 400°C/min, T_{max} = 740°C, G_p = 1.8 nm/s, I_c = 18 A, J_c = 0.77 MA/cm^2.

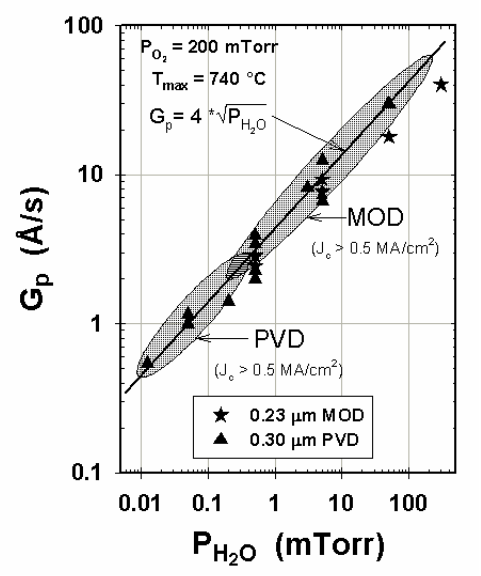

Fig. 2.76. G_p **vs** $P(H_2O)$ **for thin PVD and MOD precursors.**

2.13.5 References

1. X. D. Wu et al., "Properties of $YBa_2Cu_3O_{7-\delta}$ Thick Films on Flexible Buffered Metallic Substrates," *Appl. Phys. Lett*. **67**(16), 2397 (1995).
2. K. Hasegawa et al., p. 745 in *Advances in Superconductity IX, Proceedings of the Ninth International Symposium on Superconductivity (ISS '96)*, ed. S. Nakajima and M. Murakami, Sapporo, Japan (1996).
3. A. Goyal et al., "High Critical Current Density Superconducting Tapes by Epitaxial Deposition of $YBa_2Cu_3O_x$ Thick Films on Biaxially Textured Metals," *Appl. Phys. Lett.* **69**(12) , 1795 (1996).
4. R. Feenstra et al., "Effect of Oxygen Pressure on the Synthesis of $YBa_2Cu_3O_{7-x}$ Thin Films by Post-Deposition Annealing," *J. Appl. Phys.* **69**(9), 6569 (1991).
5. M. P. Siegal et al., "Optimization of Annealing Parameters for the Growth of Epitaxial $Ba_2YCu_3O_{7-x}$ Films on $LaAlO_3$(100)," *J. Appl. Phys.* **68**(12), 6353 (1990).
6. V. F. Solovyov, H. J. Weismann, and M. Suenaga, "Growth Rate Limiting Mechanisms of $YBa_2Cu_3O_7$ Films Manufactured by ex situ Processing," *Physica C* **353**(1–2), 14 (2001).
7. P. C. McIntyre and M. J. Cima, "Heteroepitaxial Growth of Chemically Derived ex situ $Ba_2YCu_3O_{7-x}$ thin films," *J. Mater. Res.* **9**(9), 2219 (1994).

8. P. C. McIntyre, M. J. Cima, and A. Roshko, “Epitaxial Nucleation and Growth of Chemically Derived $Ba_2YCu_3O_{7-x}$ Thin Films on (001) $SrTiO_3$,” *J. Appl. Phys.* **77**(10), 5263 (1995).
9. J. A. Smith, M. J. Cima, and N. Sonnenberg, “High Critical Current Density Thick MOD-Derived YBCO Films,” *IEEE Trans. Appl. Supercond.* **9**(2) , 1531 (1999).
10. F. A. List et al., “Crystalline Phase Development during Vacuum Conversion of Thin Barium Fluoride Precursor Films on Metallic Substrates,” *Physica C* **391**(4), 350 (2003).
11. J. T. Dawley et al., “Improving Sol-Gel $YBa_2Cu_3O_{7-\delta}$ Film Morphology using High-Boiling-Point Solvents,” *J. Mater. Res.* **17**(8), 1900 (2002).
12. J. T. Dawley et al., “Rapid Processing Method for Solution Deposited $YBa_2Cu_3O_{7-\delta}$ Thin Films,” *Physica C* **402**(1–2), 143 (2004).
13. V. F. Solovyov et al., “Ex-Situ Post-Deposition Processing for Large Area $Y_1Ba_2Cu_3O_7$ Films and Coated Tapes,” *IEEE Trans. Appl. Supercond.* **11**(1), 2939 (2001).

2.14 Growth of YBCO Films with High Critical Current at Reduced Pressures by the BaF_2 ex situ Process

J. Yoo, K. J. Leonard, H. S. Hsu, L. Heatherly, F. A. List, D. F. Lee, A. A. Gapud, P. M. Martin, S. W. Cook, M. Paranthaman, A. Goyal, and D. M. Kroeger

Significant efforts have been made for the development of superconducting coated conductors carrying high currents. Growth of thick YBCO films with high critical current density is essential for most practical applications. Although numerous parameters affect the growth and properties of ex situ YBCO, recent results have shown that the total pressure parameter influences the growth rate significantly. Through low-pressure conversion, researchers at the Massachusetts Institute of Technology have succeeded in the fast growth of 1-µm-thickYBCO with a critical current density greater than 1 MA/cm^2 on RABiTS™ with TFA. Growth rates in excess of 66.7 Å/s at 1 Torr total pressure were reported. In our previous work, at a total pressure of 0.1 atm, critical current densities greater than 2 MA/cm^2 for 0.3-µm YBCO films were achieved under low water vapor pressure (< 20 Torr) with a growth rate of 2.5 Å/s. This growth rate is five times higher than that at a total pressure of 1.5 atm.

In the present work, growth of 0.9-µm-thick YBCO films using the BaF_2 ex-situ process was investigated at reduced pressures. Samples were obtained by depositing BaF_2 precursor of desired thickness on Ni-3at%W-based RABiTS™ in our reel-to-reel e-beam co-evaporation system. XRD analyses indicated that the RABiTS™ tape has good texture with out-of-plane FWHM of roughly 5° and in-plane FWHM of roughly 7°. Samples measuring 1 × 3 cm were converted in our reduced-pressure system, shown schematically in Fig. 2.77. A pressure controller, butterfly valve, and dry pump were used in the system to control the total pressure in the chamber. Gas flow rates can be held constant independently of the chamber pressure by mass flow controllers. An oxygen sensor, pressure gauges, and a water bubbler were connected to the chamber.

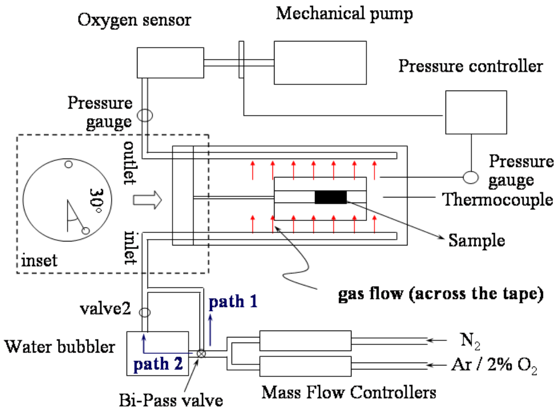

Fig. 2.77. Schematic diagram of the reduced-pressure conversion chamber.

Preliminary testing showed that processing conditions where high critical current densities were obtained for 0.3-µm films were not adequate for the growth of the thicker precursors. For example, when sample JY12_1 was processed at a P(H_2O) of ~7 Torr, wet conversion time of 60 min, conversion temperature of 740°C, total pressure of 55 Torr, P(O_2) of 150 mTorr, and a ramp-up rate of 90°C/min, the critical current was found to be zero at 77 K. The situation changed drastically when a much lower initial

$P(H_2O)$ was employed. For example, sample JY12_2 was processed at a total pressure of 50 Torr, and a $P(H_2O)$ << 7 Torr for 12 min and then at $P(H_2O)$ = 11 Torr of an additional 48 min. All other parameter remained the same. Under this set of conditions, the sample critical current density is determined to be 1.25 MA/cm^2 (I_c = 111.3 A). The beneficial effect of low initial $P(H_2O)$ was duplicated in subsequent samples. For example, sample JY12_7 was processed at an initial $P(H_2O)$ << 7 Torr for 12 min and then at a $P(H_2O)$ of 10 Torr for 48 min at a total pressure of 50 Torr, resulting in a critical current density of 1.33 MA/cm^2 (I_c = 120 A), the highest obtained in this series of samples. The magnetic field dependency (B//c) of some of these high-critical–current samples are shown in Fig. 2.78. All these samples show similar field dependency of critical current up to a measured value of 0.5 T. One sample was measured at 77 K and 65 K in high fields (Fig. 2.78 inset) and was found to possess irreversibility fields of 8.5 T at 77 K and 14 T at 65 K.

Figure 2.79 shows the resistivity vs temperature curves for samples JY12_1 and JY12_7. The room-temperature resistivity was 2350 μΩcm for sample JY12_1 and 352 μΩcm for JY12_7. As can be seen in the Fig. 2.79 inset, the resistive transition of JY12_1 film was almost completed at 90 K, but the residual resistivity still remained beyond 65 K. The higher resistivity and residual resistivity indicate that the YBCO film may have high portions of nonsuperconducting secondary phases and poor connectivity between grains. For JY12_7, the transition temperature was 92.3 K, but the transition width was roughly 2.5 K, which is thought to result from the inhomogeneity of YBCO film growth due to the narrow gas injection nozzles in the reaction chamber.

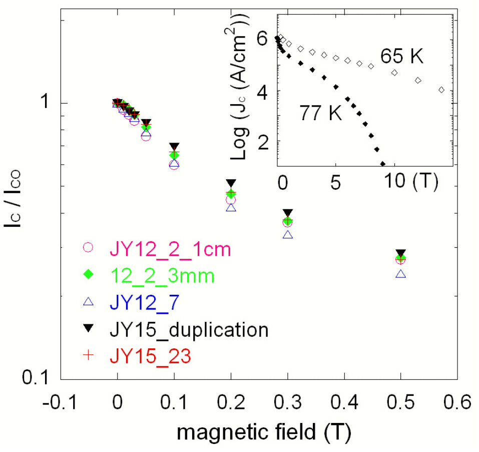

Fig. 2.78. Critical-current field dependency of several high critical-current samples processed in a similar fashion.

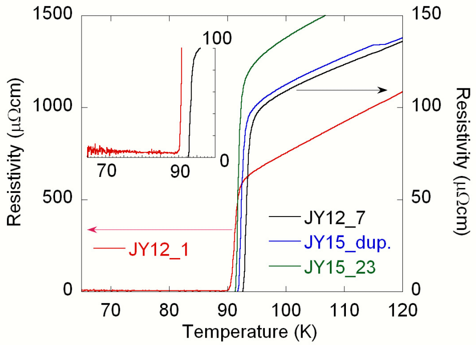

Fig. 2.79. Temperature dependence of resistivity for samples JY12_1 and JY12_7.

Figures 2.80 and 2.81 show the morphologies of the YBCO surfaces of the two samples, respectively. Surface of the JY12_1 film was found to be very nonuniform. There were many spots where large white particles were congregated, one of which is marked by “A” in Fig. 2.80(a). The large particles seem to be embedded in the YBCO film, as can be seen in the higher-magnification pictures [Figs. 2.80 (d) and (e)]. The morphology of other areas [Figs. 2.80(b) and (c)] was similar to the surface of sample JY12_7 shown in Fig. 2.81. The larger particles in area “A” were composed of Cu, Ba, and O with atomic ratios of roughly 4 to 6:1:1 to 2, as determined by EDS. We could observe the Y peaks corresponding to atomic percentages less than 3% in some spectra of the large particles. We believe that the reason for no supercurrent flow and the high residual resistivity in sample JY12_1 is that the collection of such nonsuperconducting areas led to the inability of supercurrent to percolate through the sample.

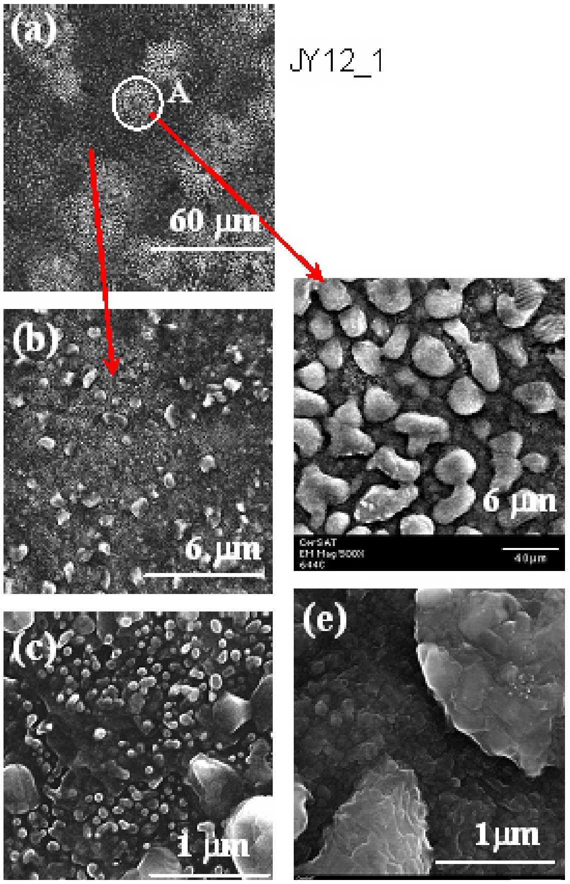

Fig. 2.80. SEM micrographs of sample JY12_1.

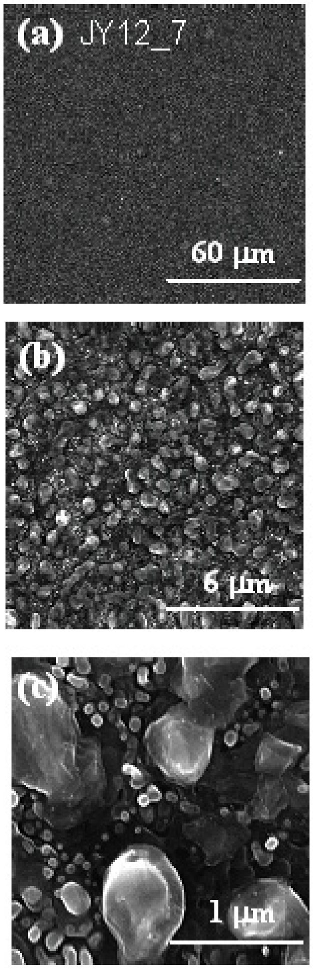

Fig. 2.81. SEM micrographs of sample JY12_7.

Figure 2.82 compares the results of the XRD θ-2θ scans and YBCO(113) pole figures of the two samples. The pole figures were plotted with a log scale. The BaF_2 peaks were observed in the θ-2θ scans, which may result from BaF_2-rich off-stoichiometry or incomplete conversion of the precursors. The intensities of YBCO(00l) peaks of sample JY12_1 were lower than those of JY12_7. This is associated with the higher portion of secondary phases in the YBCO film. In other words, the film contains a smaller amount of textured YBCO phase, which was shown in Fig. 2.80. The volume fraction of the cube texture from YBCO(113) pole figures was 97% for sample JY12_7. The FWHM values of the YBCO(113) peaks in in-plane scans and those of the YBCO(006) peaks in out-of-plane scans were 8° and 6.7°, respectively, for sample JY12_7. All these results point toward the beneficial effect of a lower initial $P(H_2O)$ during processing of thick ex situ BaF_2 precursors.

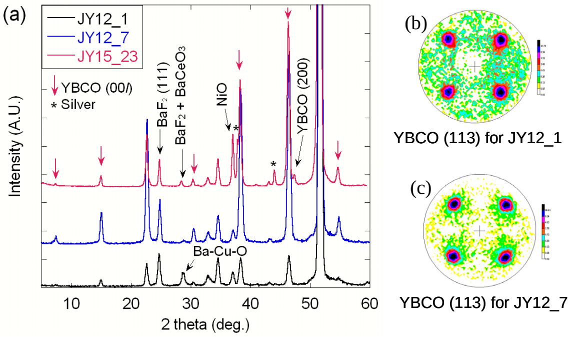

Fig. 2.82. XRD θ-2θ scans and YBCO(113) pole figures for samples JY12_1 and JY12_7.

In summary, 0,9-µm-thick BaF_2 precursors were converted at a conversion temperature of 740°C for a conversion time of 60 min under different $P(H_2O)$ conditions. The highest critical current density

(1.33 MA/cm^2) was obtained by the varying P(H_2O) from low to 10 Torr during wet conversion. We determined that a very low P(H_2O) at the initial stage of the conversion process is beneficial to the nucleation and growth of high-critical-current-density thick films. The lower water vapor condition suppresses the formation of large secondary phase particles, leading to an improvement in the YBCO film quality. It is also probable that the lower initial P(H_2O) reduces the tendency for random YBCO nucleation and growth away from the substrate-film interface. This effect may accommodate the reported longer incubation time for thick precursors and may allow epitaxial nuclei to form at the interface and subsequently grow into an epitaxial film.

2.15 Comparison of $YBa_2Cu_3O_{7-\delta}$ Precursors Made by TFA-MOD and BaF_2 ex situ Processes and their Post-Deposition Processing under Low Pressure Conditions

Y. Zhang, M. Paranthaman, R. Feenstra, T. Aytug, and D. K. Christen

MOD-TFA and e-beam co-evaporation are regarded as promising techniques for fabricating long-length, uniform, high-critical-current-density YBCO superconducting films for practical applications. Although it is generally accepted that the conversion behaviors of precursors made by MOD-TFA and by e-beam co-evaporation are basically similar, no systematic comparison study has been reported. Most previous work has been done separately on either one or the other precursor. Typical MOD-TFA and e-beam precursors were made and then annealed in the low-pressure processing system. The conditions required for the conversion of these two types of precursors are quite different. Moreover, even for the same deposition technique, recent processing studies have shown that the detailed state of the precursor is an important determining factor for both the rate of conversion and the performance of the superconducting coating. Here, precursors were compared in terms of their composition, crystallinity, surface morphology, structure, elemental chemical state, and conversion behavior. Comparative characterization and property measurement results can be used to evaluate the ex situ methods for suitability as coated conductor techniques.

Single-crystal (100) $SrTiO_3$ (STO) substrates were used for deposition by both e-beam and MOD-TFA methods in order to minimize extraneous factors that affect the quality of precursors. The e-beam precursor films were deposited at room temperature by co-evaporation of Y, BaF_2, and Cu at a deposition rate of about 1 nm/s. The oxygen pressure used during the deposition was about 5×10^{-6} Torr. The solution for making the MOD-TFA precursor was prepared by reaction of the metal acetates (Y, Ba, and Cu) with trifluoroacetic acid and refluxing the product into a glassy state. The residual was dissolved in methanol. Stoichiometric quantities of the metal acetates and trifluoroacetic acid were used. The coating was obtained by spin-coating at a speed of 2000 rpm for 30 s. The as-coated precursor was calcinated by slow heating to 400ºC in a moist oxygen atmosphere. The final film thicknesses were measured with a stylus step-profilometer. Post-deposition annealing and quenching were carried out in an induction vacuum furnace in which P(O_2) and P(H_2O) were carefully controlled and varied to different levels. Samples were heated to the desired temperatures within less than 2 min and were quenched by being quickly removed from the hot zone into the room-temperature space.

Surface morphologies of both e-beam and MOD-TFA precursors were inspected, and surface roughness was measured by AFM (Nanoscope III Multimode AFM system) in the contact mode. To analyze the crystalline phases in both the precursors and the annealed films, a Philips model XRG3100 X-ray diffractometer with Cu K_α radiation was used to record the powder θ-2θ diffraction patterns. Micrographs were taken with a JEOL JSM-840 SEM. X-ray photoelectron spectroscopy (XPS, Perkin-Elmer 5000 LS system) was used for identifying the chemical state of F, Cu, and Ba and for measuring the fluorine content in precursors and quenched samples. The Al K_α line was used with a spot size of about 0.8 mm diam. Electron binding energy was calibrated with pure Au. Prior to recording the spectra, sample surfaces were ion sputtered to remove possible contaminants. Critical-current-density values of fully converted films (~0.3 μm thick) were measured by a Quantum Design MPMS 7 superconductivity quantum interference device (SQUID) magnetometer. The magnetic fields were applied perpendicular to the film surfaces. Critical-current-density values were determined by the application of the Bean critical state model formula,

$$J_c = 30\Delta M/d \ , \tag{15}$$

where ΔM is the magnetization hysteresis (emu/cm^3) and d is the lateral size of the sample (cm).

It can be seen from the AFM micrographs in Fig. 2.83 that the surface of the e-beam BaF_2 precursor is much smoother than that of the MOD-TFA precursor. The difference in the surface roughness implies that there might also be a difference in density, which is one of the factors affecting the conversion reaction.

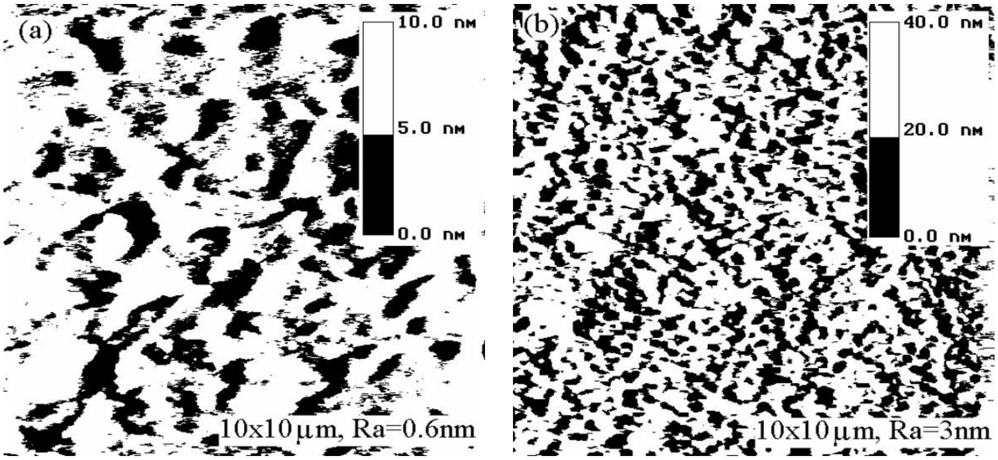

Fig. 2.83. Atomic-force microscope images of the MOD-TFA precursor (a) and the BaF_2 precursor (b).

The e-beam BaF_2 precursors were annealed at a temperature of ~740ºC with $P(O_2)$ ranging from 10 to ~200 mTorr and $P(H_2O)$ ranging from 0.5 to ~8 mTorr. Consistent with the YBCO phase diagram, when $P(O_2)$ is less than 10 mTorr, there is no YBCO conversion. For $P(O_2)$ between 10 and 200 mTorr, YBCO films can be formed and no apparent differences were observed in film orientation or properties. However, the film structure and properties are very sensitive to $P(H_2O)$ for e-beam precursors. Fully *c*-axis YBCO films can be obtained at a $P(H_2O)$ of about 1 mTorr. For $P(H_2O) > 1$ mTorr, the higher the $P(H_2O)$ the more the randomly oriented YBCO is formed together with the *c*-axis YBCO, resulting in a strong reduction in critical current density.

For the annealing of MOD-TFA precursors, the $P(O_2)$ used was between 100 and ~200 mTorr. At the same temperature of (~740°C) and $P(H_2O)$ lower than 5 mTorr, comparable to that for e-beam precursors, almost no YBCO can be formed, and high-intensity BaF_2 peaks can be seen in the XRD pattern, indicating that the conversion reaction could not complete. For a complete conversion of MOD-TFA precursors, both higher temperature (around 780°C) and higher $P(H_2O)$ (> 10 mTorr) are necessary. Fully *c*-axis YBCO can be formed at a $P(H_2O)$ of about 10 mTorr, but higher values result in the formation of more *a*/*b*-axis YBCO, which deteriorates the properties. A typical mixed-orientation YBCO film SEM image is shown in Fig. 2.84.

Shown in Fig. 2.85 are the field dependence critical-current-density results for two fully *c*-axis-oriented YBCO films produced under low-pressure conditions from e-beam and MOD-TFA precursors. At 77 K and zero field, the critical current density is 3.1 MA/cm^2 and 2.2 MA/cm^2 for the films from e-beam and MOD-TFA precursors, respectively.

Figure 2.86 shows the XRD θ-2θ scan patterns of as-deposited MOD-TFA and e-beam precursors and quenched samples. It can be seen that at as-deposited states the e-beam precursor is basically amorphous whereas the MOD-TFA precursor has developed its nanocrystalline fluorides during calcination. YBCO and BaF_2 were formed in both quenched samples; for the MOD-TFA precursor, the

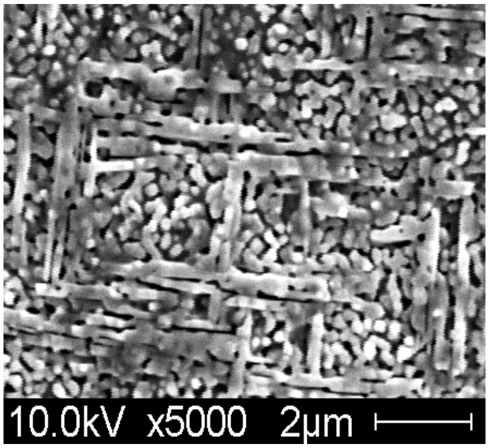

Fig. 2.84. A mixed *c*- & *a*/*b*-axis-oriented YBCO film produced from a MOD-TFA precursor annealed at 780ºC, $P(O_2) = 200$ mTorr, and $P(H_2O) = 12$ mTorr. The conversion of the MOD-TFA precursor requires higher temperature and higher $P(H_2O)$ than that of e-beam precursor.

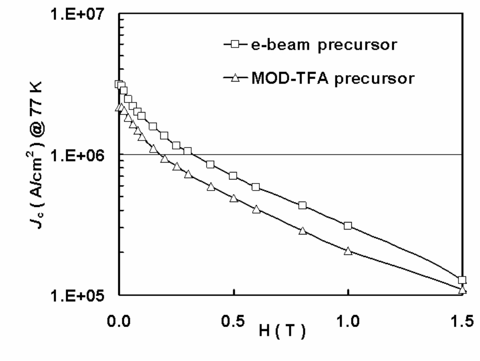

Fig. 2.85. Magnetic field dependence of critical current density at 77 K of YBCO films. One ($J_c = 3.1$ MA/cm^2, 77 K, self-field) from e-beam precursor was annealed at 730°C with $P(O_2) =$ 40 mTorr and $P(H_2O) = 0.5$ mTorr. The other ($J_c = 2.2$ MA/cm^2, 77 K, self-field) from MOD-TFA precursor was annealed at 780°C with $P(O_2) = 100$ mTorr and $P(H_2O) = 10$ mTorr.

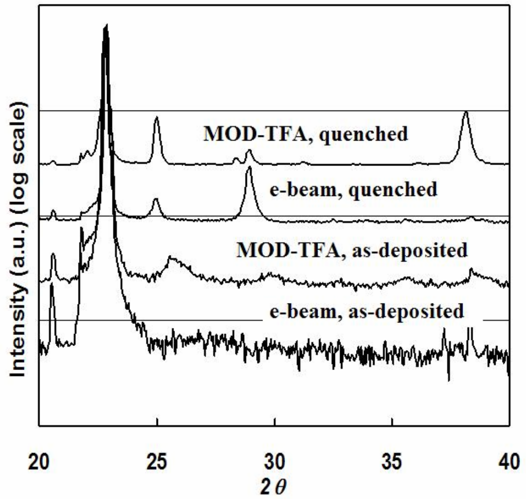

Fig. 2.86. XRD θ-2θ scan patterns of MOD-TFA and e-beam BaF_2 precursors at as-deposited and quenched states. MOD-TFA and e-beam BaF_2 precursors were quenched from 780°C /(10 mTorr H_2O, 100 mTorr O_2) and 740°C /(1 mTorr H_2O, 100 mTorr O_2), respectively, after a duration of 20 min.

BaF_2 peak position shifted to a lower angle after quenching. For the quenched MOD-TFA sample, peaks other than those of YBCO and BaF_2 are from the crystallized yttrium cuprate.

X-ray photoelectron spectroscopy (XPS) was used to analyze the chemical states of F, Cu, and Ba. The F concentration was measured for both as-deposited precursors and quenched samples. The measured concentration of F was 16.2% and 20.4%, for as-deposited e-beam and MOD-TFA precursors, respectively. That is, the fluorine content of MOD-TFA precursor was slightly higher than that of the e-beam precursor. After the quenching, the concentrations of F became 2.2% and 7.5%, respectively. As XPS is surface sensitive, the results indicate that for both precursors, fluorides at the surface have started to decompose once heated to reaction temperatures, which results in the release and loss of some F. The XPS spectra of F, Cu, and Ba shown in Fig. 2.87 suggest that the elemental chemical states are different for the two types of precursors. The electron binding energies of F, Cu, and Ba in the MOD-TFA precursor are higher than those in the e-beam precursor. Moreover, for both precursors the electron binding energies of F, Cu, and Ba shifted to lower values after high-temperature quenching. Because F is the most electronegative element, the shift is another evidence of the fluoride decomposition upon heating.

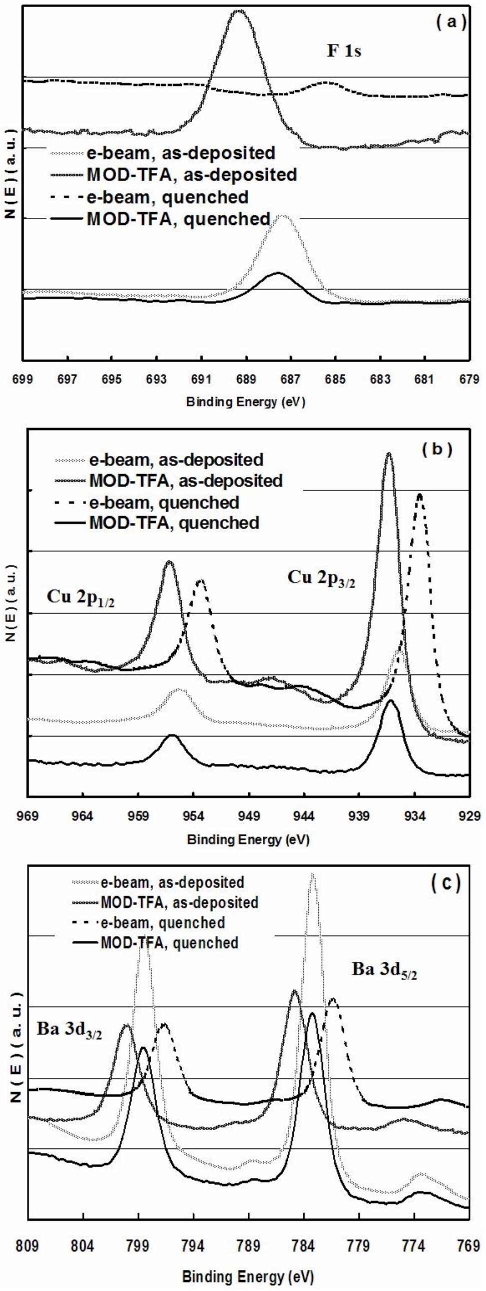

Fig. 2.87. XPS spectra for as-deposited and quenched precursors indicating the difference in chemical states of F, Cu, and Ba. (a) F 1s, (b) Cu 2p, and (c) Ba 3d.

In summary, both MOD-TFA and e-beam BaF_2 precursors on STO substrates were annealed under low-pressure conditions, yielding high-critical-current-density YBCO films. Basically, the MOD-TFA precursor requires higher temperature and higher H_2O partial pressure for conversion. YBCO film orientation is sensitive to H_2O partial pressure for both types of precursors. The comparison study shows that the surface roughness of the e-beam BaF_2 precursor is much smaller than that of MOD-TFA precursor. The as-deposited e-beam precursor is amorphous, whereas the MOD-TFA precursor contains nanocrystalline complex fluorides. The F concentration in the MOD-TFA precursor is higher than that of e-beam precursor in the as-deposited state. Upon heating a sample to reaction temperatures, the F concentration at the surface changes for both types of precursors, although surface F is more rapidly depleted for the e-beam precursor. The chemical states of F, Cu, and Ba on the surface for e-beam precursor differ from those for the MOD-TFA precursor in both the as-deposited and reaction-quenched states.

2.16 Growth of Epitaxial TiN Thin Films on Biaxially Textured NiW Substrates by rf Sputtering

J. Yoo and A. Goyal

2.16.1 Introduction

We have investigated the experimental parameters for growth of epitaxial titanium nitride (TiN) thin films directly on Ni-3 at. % W (NiW) biaxially textured substrates by using rf sputtering as a function of rf sputtering power, substrate temperature, and N_2:Ar mixture-gas ratio. The rf sputtering power, the substrate temperature, and N_2:Ar mixture-gas ratio were varied between 80 and 200 W, between 550 and 700ºC and between 0 and 0.5, respectively. For TiN films grown epitaxially, FWHM values of TiN (111) peaks in XRD ϕ-scan and that of TiN (002) in ω-scan were about 8.0º and 4.5º, respectively, which is comparable to those of NiW substrates. The crossover from (111)-oriented grains to (002)-oriented grains of TiN thin films occurred as the substrate temperature increased. Grains rotated 45º with respect to cube-on-cube orientation showed up, competing according to growth conditions due to large lattice mismatch (the lattice constant is ~4.24 Å for TiN and ~3.52 Å for Ni). Twin orientation was stronger for TiN films deposited in a mixture gas with a low N_2 content. A higher substrate temperature was essential for the epitaxial growth of TiN films in a mixture gas with a high N_2 content. Using TEM and electron diffracted reflection, we observed columnar and subgrain structure of which the <100> crystalline axis rotated around <100> of NiW tapes within 8.5º.

2.16.2 Experimental

TiN films were obtained by rf magnetron sputtering of a 2-in. TiN (99.99 % purity) target in a high-purity (99.999 %) argon and nitrogen mixture. The sputtering system was pumped down to a base pressure (typically ~3×10^{-6} Torr) before the gas mixture was introduced. A total pressure of 60 mTorr was maintained during the film growth. The target was presputtered at the deposition conditions for 30 min prior to each run. Meanwhile, the substrate was covered with a shutter. The TiN films were deposited on the sulfurized NiW metal tapes with the cube texture of preferred orientation obtained by cold rolling and heat treatment. The metal substrates were clamped down on the substrate heater, and the substrate temperature was measured at the heater by K-type thermocouples.

The experiments were designed to determine the effects of sputtering parameters on the cube-on-cube-oriented growth of TiN thin films. The N_2:Ar ratio was varied between 0 and 0.5. A film deposited in pure N_2 gas was also made and was compared with other films. The substrate temperature effects for the film growth were investigated; temperatures were varied between 550 and 780ºC with fixed different rf sputtering powers in cases in which the N_2:Ar ratio was 7, 15, and 50%. The rf power effect was varied between 80 and 200 W for conditions in which the substrate temperature was 650ºC and N_2:Ar was 15%.

Orientations of the TiN films were analyzed by XRD θ-2θ scans for out-of-plane orientation and (111) ϕ scans for in-plane texture. A Philips model XRG3100 diffractometer with Cu Ka radiation was used to record powder diffraction patterns. A Picker four-circle diffractometer was used to collect pole figures of the films with which other orientations could be verified. TEM investigation was performed for the microstructure in bulk films.

2.16.3 Results and Discussion

2.16.3.1 N_2-Ar Mixture Gas Effect

In this section we discuss influence of gas mixture on crystalline orientation of the sputtered TiN films. While total pressure and rf power were fixed at 60 mTorr and 100 W, respectively, the N_2:Ar ratio of the gas mixture was varied between 0 and 0.5. Figure 2.88 shows the XRD θ-2θ scans and (111) pole figures of the TiN films in this set of experiments. The TiN film deposited in only N_2 gas grew amorphous at a substrate temperature of 650ºC; there was no peak belonging to TiN compound. As N_2 content was reduced to 15%, the intensity of the (002) peak became higher. The thickness of TiN film deposited in a 15% gas mixture was 270 nm. It has been observed that the deposition rate during sputtering was higher when N_2 content in the Ar-N_2 mixture discharge gas was decreased. Because deposition time was 60 min for all samples, TiN films would be thicker if deposited in a gas mixture having a lower N_2 content (< 15%) mixture gas, and those deposited in a higher N_2 content would be thinner. In a lower N_2 content (< 15 %), TiN films contain {221} <–1,2,2> twin orientations [marked by an "X" in Fig. 2.88(b)], and 45º-rotated cube orientation [marked by an "X" in Fig. 2.88(c)].

2.16.3.2 Substrate Temperature Effects

TiN films were deposited at various substrate temperatures, between 550 and 780ºC in a gas mixture with N_2:Ar ratios of 7, 15, and 50%. Figure 2.89 shows texture evolution of TiN films deposited in a 15 % N_2:Ar gas mixture with respect to various substrate temperatures.

[The pole figure for 650EC is shown in Fig. 2.89(d).] TiN films seemed cube-on-cube textured, containing only a (002) peak in XRD θ-2θ scans and fourfold symmetric peaks in ϕ-scans without any indication of other crystalline orientations. This is because the (002) orientation is thermodynamically stable, corresponding to the lowest energy surface. However, we could observe non-cube-on-cube orientations in pole figures. At a substrate temperature of 550ºC, {221} <–1,2,2> twin orientations were observed clearly [see Fig. 2.89(a)]. These twin orientations gradually disappeared as the substrate temperature was increased. Textures of TiN films deposited at a substrate temperature of 600ºC contains twin and 45º-rotated cube orientations as well as cube-on-cube components, as shown in Fig. 2.89(b). Those peak intensities are very low but distinguishable from background noise. Interestingly, this texture

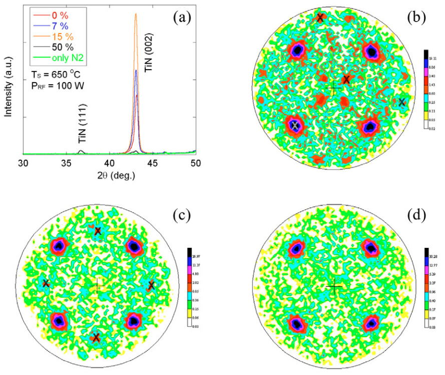

Fig. 2.88. (a) XRD θ-2θ scans for TiN films deposited at a substrate temperature of 650ºC and at an rf sputtering power of 100 W in a N_2:Ar gas mixture (0, 7, 15, 50%, and only N_2 gas). The XRD (111) pole figures are of TiN films deposited in (b) 0%, (c) %, and (d) 15% mixture gases.

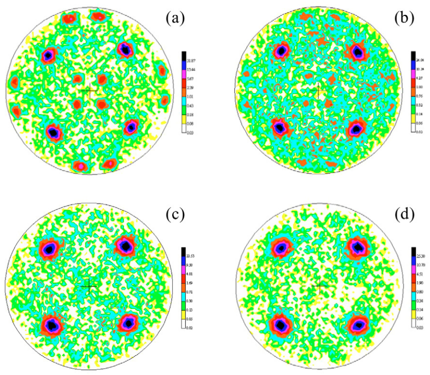

Fig. 2.89. XRD (111) pole figure of TiN films deposited at substrate temperatures of (a) 550, (b) 600, (c) 700, and (d) 780ºC in a 15% N_2:Ar gas mixture and at an rf sputtering power of 100 W.

is very similar to those of TiN films deposited at 650ºC in Ar gas [Fig. 2.88(b)]. The twin and 45º-rotated cube orientations disappeared at a substrate temperature of 650ºC, and cube-textured TiN films were obtained up to substrate temperatures of 750ºC.

When the discharge gas has a lower N_2 content, temperature conditions influence crystalline orientations of TiN films more severely. For instance, TiN films deposited in a 7% N_2:Ar gas mixture had an abrupt change of their texture (see Fig. 2.90). TiN films deposited at a substrate temperature of 600ºC had very small (111) and (002) peaks in XRD θ-2θ scan and seemed grown with random in-plane texture. Cube-on-cube orientations emerged with an increase in substrate temperature as shown in Fig. 2.90(a) (inset) and Fig. 2.88(c), competing with 45º-rotated cube texture. When the substrate temperature was increased to 700ºC, 45º-rotated cube orientation became preferred along with 45º-rotated {221} <–1,2,2> twin orientations.

For TiN films deposited in a 50% N_2:Ar gas mixture we observed similar trend of texture changes with respect to variation in the substrate temperature. At low temperature, a (111) peak was observed in an XRD θ-2θ scan; improved texture of TiN films was attained at higher temperature (780ºC), as can be seen in Fig. 2.91. We believe that the increase of substrate temperature supplied enough energy with admolecules or adatoms such that they could diffuse to cube-on-cube orientation on the TiN (002) surface with an increase in substrate temperature. However, in this case, there is an intriguing difference in texture evolution with respect to substrate temperature compared with 15% N_2:Ar and lower cases. No {221} <–1,2,2> twin orientations were observed clearly in XRD pole figures at lower growth temperatures compared with the nearly optimum substrate temperature (780ºC). It may be due to less bombardment of high-energy Ar+ or Ar particles on the surface, which induces strain energy and supplies energy for adatom mobility.

2.16.3.3 RF Power Effects

TiN films were deposited at 650ºC under the various rf sputtering powers (between 80 and 200 W) in a 15% N_2:Ar gas mixture. Figure 2.92 shows rf power effects on the texture of TiN films. As can be seen in Fig. 2.92(a), a TiN (111) peak was observed in the XRD θ-2θ scan only at a sputtering power of 200 W. It can be easily understood that (111) orientation evolved in order to lower the strain energy induced by ion bombardment. However, in pole figures, twin orientations and 45º rotated cube orientations were observed clearly. At a sputtering power of 80 W, {221} <–1,2,2> twin orientations were

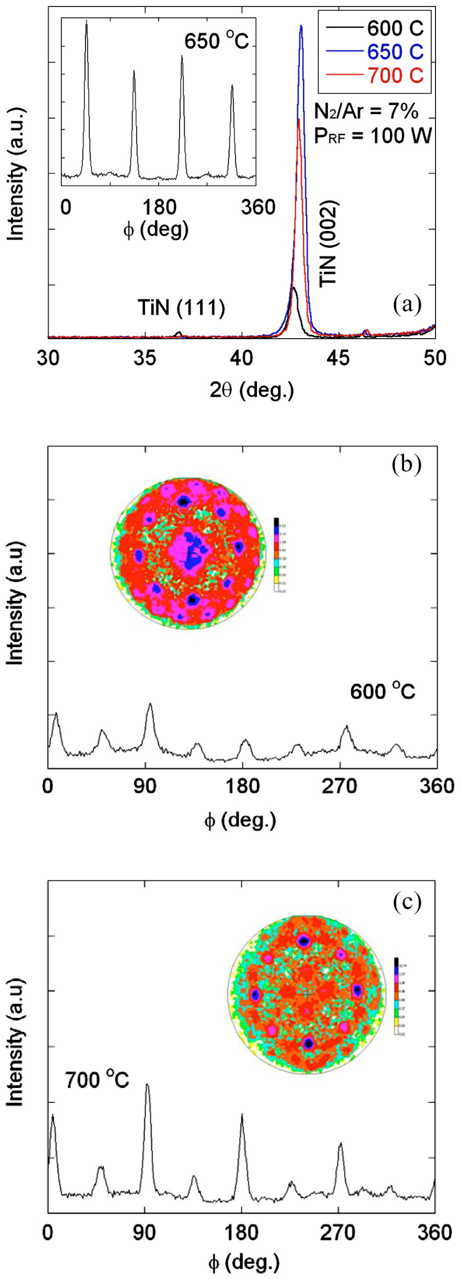

Fig. 2.90. (a) XRD θ-2θ scans for the TiN films deposited substrate temperatures of 600, 650, and 700°C in a 7% N_2: Ar gas mixture. Inset: XRD (111) ϕ-scan for TiN film deposited at a substrate temperature of 650°C. The XRD (111) ϕ-scans and pole figures are of TiN film deposited at substrate temperatures of (b) 650°C and (c) 700°C.

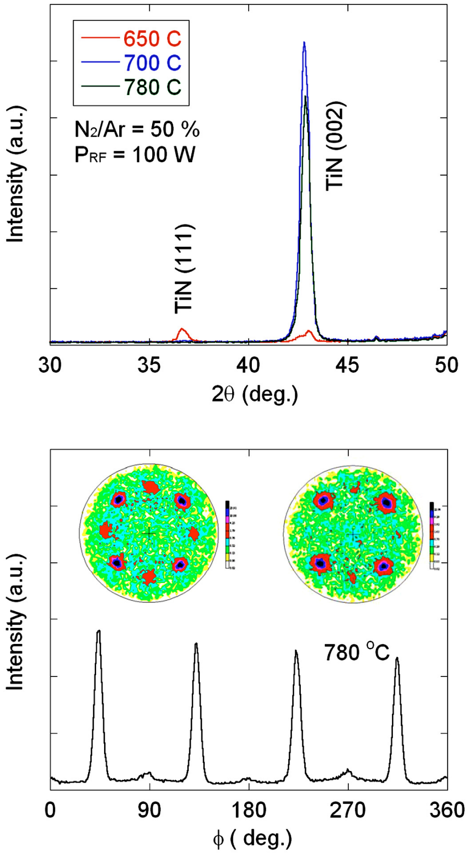

Fig. 2.91. Upper: XRD θ-2θ scans for the TiN films deposited at substrate temperatures of 650, 700, and 780°C in a 50% N_2: Ar gas mixture and an rf sputtering power of 100 W. Lower: XRD (111) ϕ-scan of TiN film deposited at a substrate temperature of 780°C. Inset: The XRD (111) pole figures of TiN films deposited at a substrate temperature of 700°C (left) and 780°C (right).

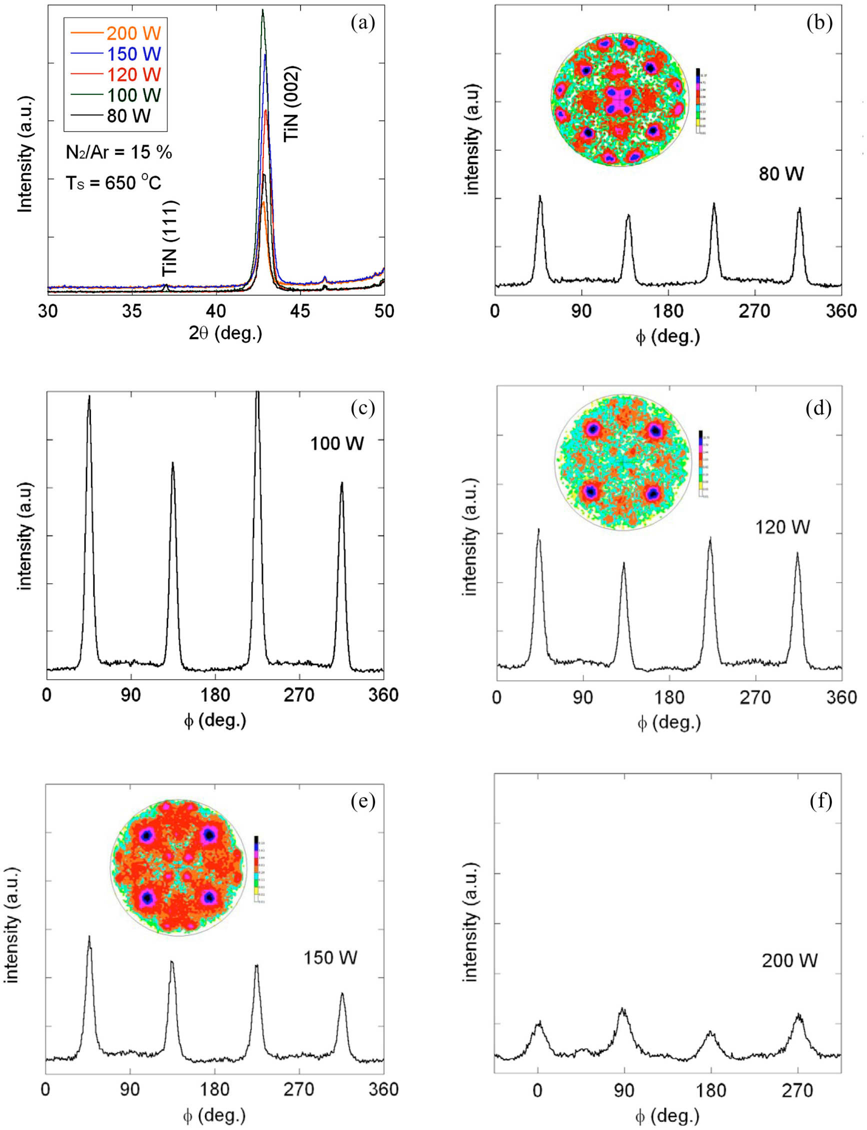

Fig. 2.92. (a) XRD θ-2θ scans for the TiN films deposited at a substrate temperature of 650ºC in a 15% N_2: Ar gas mixture and rf sputtering powers of 80, 100, 120, 150, and 200 W. XRD (111) ϕ-scan and pole figures of TiN films deposited at sputtering powers of (b) 80 W, (c) 100 W, (d) 120 W, (e) 150 W, and (f) 200 W.

observed as well as unknown orientations [marked “X” in Fig. 2.92(b). At a power of 100 W, other peaks except cube orientation disappeared, as can be seen in Figs. 2.88(d) and 2.92(c), but they were revealed again at higher sputtering powers. As rf power was increased, the texture became almost random with 45º-rotated cube orientation preferred. We think that bad texture at higher rf sputtering powers may be due to destruction by high-energy ion bombardment (e.g., by Ar+ particles). Particles with large momentum were built up by absorbing power and by a higher floating voltage between the substrate and the target. Degradation of texture by high-energy particles has been reported in thin-film growth by rf and dc sputtering methods.

Epitaxial TiN thin films were deposited directly on NiW RABiTS™ with a substrate temperature of 650ºC, an rf sputtering power of 100 W and a 15 % N_2:Ar atmosphere. For TiN films, FWHM values of TiN (111) peaks in XRD ϕ-scan and those of TiN (002) in ω-scans were about 8.0º and 4.5º, respectively. These values are comparable to those for NiW substrates; FWHM values of NiW (111) peaks and (002) are 7.5º and 5.7º, respectively.

2.16.4 Summary

The experimental parameters were investigated for growth of epitaxial TiN thin films directly on Ni-3 at. % W (NiW) biaxially textured substrates by rf sputtering as a function of rf sputtering power, substrate temperature, and the N_2:Ar ratio. The rf sputtering power, the substrate temperature, and the N_2:Ar ratio of the gas mixture were varied between 80 and 200 W, between 550 and 700ºC, and between 0 and 0.5, respectively. The best conditions for growth of epitaxial TiN by sputtering directly on NiW RABiTS™ are as follows: substrate temperature = 650ºC, rf sputtering power = 100 W, and N_2:Ar = 15%. For TiN films deposited at those conditions, FWHM values of TiN (111) peaks in XRD ϕ-scan and those of TiN (002) in ω-scans were about 8.0º and 4.5º, respectively.

2.17 Preparation of YBCO Films on CeO_2-Buffered (001) YSZ Substrates by a Non-Fluorine MOD Method

Y. Xu, A. Goyal, N. A. Rutter, D. Shi, M. Paranthaman, S. Sathyamurthy, P. M. Martin, and D. M. Kroeger

2.17.1 Introduction

Recently, the fabrication of YBCO films through the TFA-MOD approach [1,2] has become popular because high critical current density has been demonstrated on lattice-matched single-crystalline substrates [2,3,4] and on metallic substrates such as RABiTS™[5,6]. Compared with vacuum processes such as PLD, e-beam co-evaporation, sputtering, and other popular physical methods, MOD is a nonvacuum method and has such favorable features as precise composition control, high speed, low cost, and scalability for industrial production. In the MOD method, various precursors, such as acetates, citrates, oxalates, neodecanoates, trifluoroacetates, halides, acetylacetonates, and naphthenates, have been described in the literature [7–10]. The interest in fluorine-containing precursors for YBCO films began when it was noted that such solutions decompose to carbonate-free precursor films rather than films that contain substantial amounts of barium carbonate [1,2,11]. It was believed that during the YBCO phase growth in a fluorine-free MOD process, certain metal organic precursors could lead to barium carbonate as an intermediate phase due to the formation of carbon dioxide during processing of the carbon-containing precursor ligands attached to the barium ions. Usually, the ligand is removed by hydrolysis with excess water followed by precipitation of the resulting barium hydroxide. However, fatty-acid ester ligands cannot be removed by simple oxidation or hydrolysis. It is necessary to process YBCO films above 900°C to decompose the intermediate barium carbonate, which can interfere kinetically with the formation of the YBCO phase [12,13]. For these reasons, precursors that do not contain carbon are preferred. On the other hand, in the fluorine-based MOD approach, it was believed that carbon could be removed from the material at a low temperature (< 400°C) in the burnout stage in wet oxygen and that fluorine could then be removed at a higher temperature (> 700°C) in a humid and low-oxygen partial-pressure environment [1,2,3].

Our experiment shows that the formation of barium carbonate is really a processing-related intermediate product [14,15]. With novel processing parameters, no barium carbonate has been detected. In addition, fluorine-free trimethylacetate salts and proponic acid (TMAP) precursor solution is very stable and has a long shelf life (more than six months without changes being observed). Another advantage of TMAP and other fluorine-free methods is that no extra phase (such as BaF_2 in the TFA approach) in addition to YBCO has been found. The BaF_2 phase, which can be difficult to remove, has adverse effects on the electrical properties of YBCO.

In this investigation, processing parameters were optimized by employing different dwell times in a humid atmosphere during the high-temperature annealing. RBS, XRD, and SEM were employed for the detailed calibrations.

2.17.2 Experimental

Details of the procedure are reported in detail elsewhere [14,15]. Briefly, the TMAP precursor solution was prepared by dissolving trimethylacetates of Y and Cu together with barium hydroxide into proponic acid in a 1:2:3 cation ratio. Amine was added to increase the solubility and to adjust the viscosity; xylene was added to control the wetting and oxide content in the solution. The viscosity was normally adjusted in the range of 30 to 100 cp, and oxide content was about 7 to 10 wt %. The total ionic concentration was 0.5 to 1.0 mol/L. YSZ single crystals ($15 \times 3 \times 0.5$ mm^3) with (001) orientations were used as substrates. CeO_2 was sputtered onto the YSZ substrate to form a cap layer. YBCO films were prepared by spin-coating at 3000 rpm for 30 s. Multiple coatings were required for thicker films. The green films were dried at 200°C for 4 to 5 min in air on a hot plate. Each coating gave a thickness of about 100 nm. Burnout and high-temperature annealing were used to pyrolize and crystallize the films. The gel films formed on the hot plate were burned out at 400°C in humid oxygen. The high-temperature annealing was carried out at 700 to about 860°C for 1 h in a quartz tube furnace in humid atmosphere. Normally, the 180-ppm oxygen partial pressure was read by a zirconium oxygen sensor. Silver contacts of about 1-μm in thickness were sputtered onto the YBCO samples at room temperature prior to oxygen annealing. The oxygen annealing was performed at 400 to 500°C for 1 h and was followed by a cooling ramp of 2°C/min to 350°C to diffuse oxygen into the YBCO perovskite structure and to establish good contact between the Ag and the YBCO film. Transition temperature and critical current were measured by the direct four-probe transport method. Surface morphologies were observed by SEM. Thickness was determined by RBS. Texture was assessed by XRD θ-2θ scans, ω-scans, ϕ-scans, and pole figures.

2.17.3 Results

In this research, the effect of the ratio of humidified to dried atmosphere on electrical transport properties, YBCO textures, YBCO/CeO_2 interface reactions, and film morphology was investigated for the samples annealed at 740°C in 180 ppm oxygen partial pressure for 1 h. Figure 2.93 shows the variation of critical current density (at 77 K) with magnetic field and with the ratio of humidified to dried atmosphere used during the high-temperature annealing for 200-nm-thick films. The critical current density data were calculated from the thicknesses measured by RBS. The critical current density calculations were made under the assumption of fully dense YBCO films. However, porosity was observed on the top view SEM of the annealed films. The calculated critical current density varied from 0.25 MA/cm^2 for the sample held for 57 min in a humid atmosphere to 0.55 MA/cm^2 for a sample held for 30 min. In this comparison, the dew point was 35°C in the humid stage, and all the samples were kept in the same oxygen partial pressure (180 ppm) and were treated at the same total holding time at the annealing temperature (60 min). The changes of the critical current density are obvious over the range of holding time in humid furnace gas.

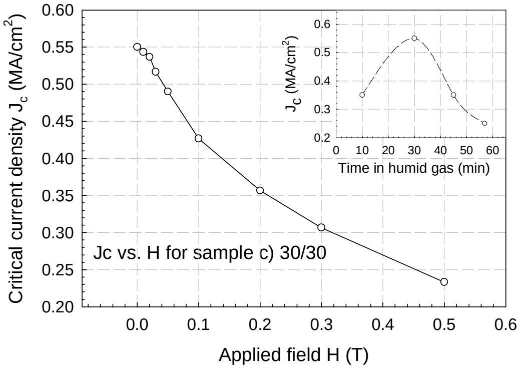

Fig. 2.93. Transition critical current density with different humidity-to-dry ratio values and with magnetic field for samples annealed at 740°C in 180-ppm oxygen pressure for 30 min wet and 30 min dry.

The other electrical properties of the film varied in a similar manner with the change in the ratio of humidified to dried atmosphere. Transition widths (ΔT_c) decreased and zero resistance critical temperatures [T_c (0)] and resistivity ratios (ρ_{285}/ρ_{100}) increased for a ratio close to 1 (30/30). The critical current densities, transition temperatures (Fig. 2.94), and resistivity ratios (ratio of the measured sample resistance at 285 K to that at 100 K) for samples annealed at 740°C under several different humid-to-dry ratios are summarized in Table 2.8.

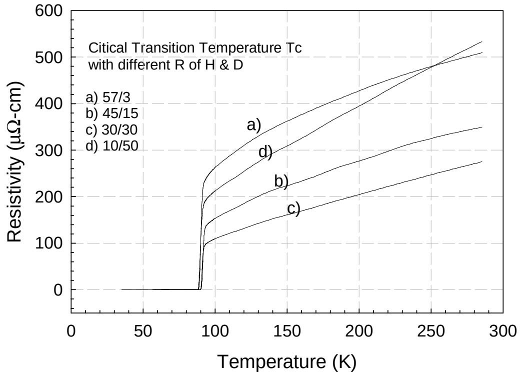

Fig. 2.94. Four-probe-method critical transition temperature for samples annealed at 740°C in 180-ppm oxygen pressure with different humidity-to-dry ratio values.

The θ-2θ XRD patterns of films annealed under different conditions and a detailed indexed θ-2θ scan for the sample annealed 30 min wet and 30 min dry are shown in Figs. 2.95 and 2.96, respectively. The diffraction patterns for different ratios did not change dramatically except for the differences in intensity. The films produced under all conditions in Fig. 2.95 showed very sharp and intense (00*l*) YBCO reflections. The (002) YSZ peaks, peaks from buffer layer CeO_2 (002), and peaks from (110) and (002) reflections associated with the reaction product $BaCeO_3$ are shown in Fig. 2.96.

Table 2.8. Processing parameters and electrical properties of YBCO films derived from TMAP approach

Sample	P (O_2) (ppm)	Dew point (°C)	T_{ann} (°C)	Humid:dry ratio (min:min)	$T_c(0)$ (K)	ΔT_c (°C)	J_c (MA/cm^2)	YBCO (005) FWHM (°)	ρ_{285}/ρ_{100}
(a)	180	35	740	57:3	88.75	2.53	0.25	1.31	1.93
(b)	180	35	740	45:15	90.17	2.43	0.35	1.18	2.28
(c)	180	35	740	30:30	90.18	1.62	0.55	1.73	2.51
(d)	180	35	740	10:50	88.33	2.98	0.35	1.68	2.51

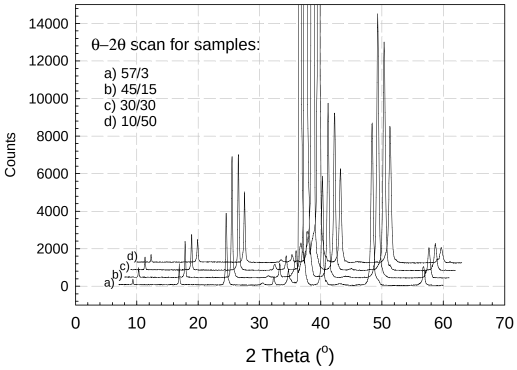

Fig. 2.95. The θ-2θ XRD patterns of films annealed at 740°C in 180-ppm oxygen pressure with different humid-to-dry ratio values.

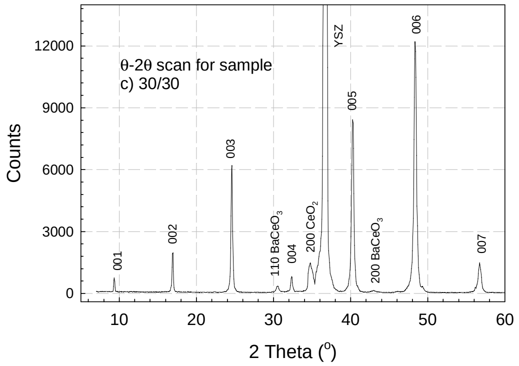

Fig. 2.96. The X-ray θ-2θ scan pattern for a sample annealed at 740°C in 180-ppm oxygen pressure for 30 min wet and 30 min dry.

The textures of YBCO layer were investigated by ω-scans, ϕ-scans, and pole figures (Figs. 2.97, 2.98, and 2.99, respectively). The FWHM data of YBCO (005) ω-scans (Fig. 2.97) were collected and tabulated in Table 2.8. Under the experimental conditions, all of these FWHM values are less than 2°,

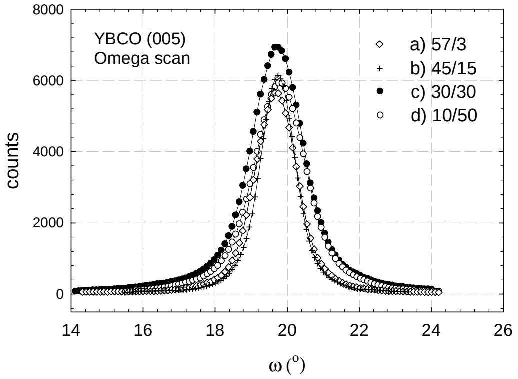

Fig. 2.97. The X-ray ω-scans of the YBCO (005) plane for samples annealed at 740°C in 180-ppm oxygen pressure with different humid-to-dry ratio values.

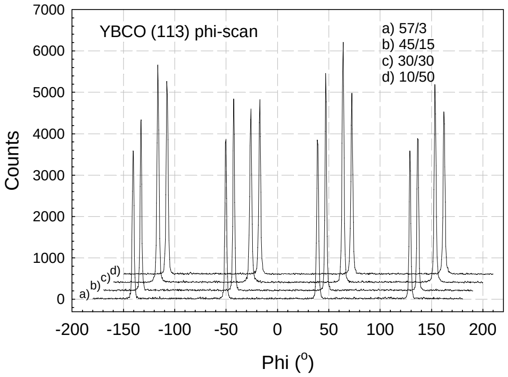

Fig. 2.98. The X-ray ϕ-scans of YBCO (113) plane for samples annealed at 740°C in 180-ppm oxygen pressure with different humid-to-dry ratio values.

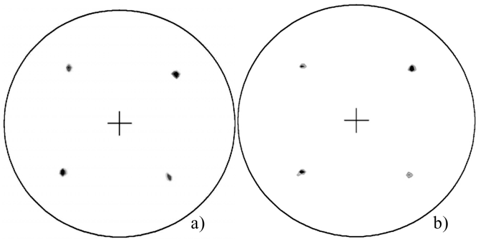

Fig. 2.99. Pole figures of YBCO (113) plane for films annealed at 740°C in 180-ppm oxygen pressure with different humid-to-dry ratio values: (a) 57:3, and (b) 30:30.

demonstrating good out-of-plane *c*-axis-oriented textures. Peaks 90° apart in the YBCO (113) ϕ-scans shown in Fig. 2.98 demonstrate good in-plane texture for samples annealed under different humid-to-dry ratios Pole figures were measured for each of the samples to check for misoriented grains. The results are essentially the same, except for differences in the intensities, as shown in Fig. 2.99 for samples annealed under ratios of 30:30 and 57:3.

A stronger dependence on the humid-to-dry ratio was observed in the RBS image in Fig. 2.100. No clear YBCO-CeO_2 boundary can be detected for any of the samples. The element Ba is seen at a greater depth in the samples annealed for shorter times in a humid atmosphere. An average thickness of approximately 200 nm based on Ba content and assuming fully dense YBCO was estimated from the RBS data. This suggests that the film structure is close to a single planar array of grains. Due to the overlapping of the buffer layer and substrate peaks, it is difficult to get an accurate assessment of the stoichiometry.

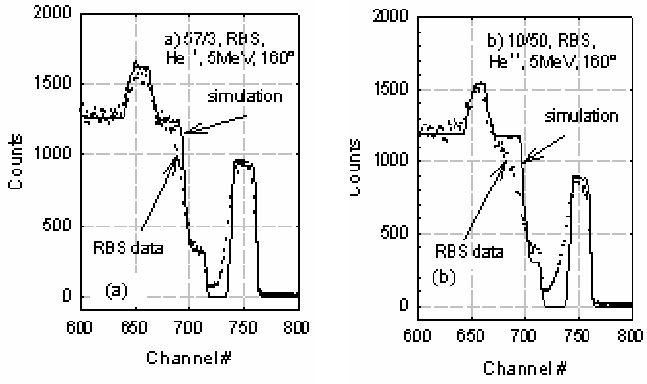

Fig. 2.100. RBS spectra of a thin film of YBCO on YSZ buffered with CeO_2. Each spectrum was acquired with 5-MeV He^{++} and a backscatter angle of 160°; the humid-to-dry ratio values are (a) 57:3 and (b) 10:50.

The SEM top view micrographs in Fig. 2.101 show the effect of the humid-to-dry ratio during high-temperature annealing on morphology for 200-nm-thick films. The grains grow as large interconnected platelets that lie parallel to the surface. Smaller grains with spherical morphology decorate the surface of the platelets [clearly visible in Figs. 2.101(a) and (b)]. These features seem to be associated with the longer time spent in a humid atmosphere. These grains are noticeably absent when the film is heated in a dry atmosphere for a longer time. For example, the samples treated in 30:30 and 10:50 ratios (Figs. 2.101(c) and (d)]. Other features,

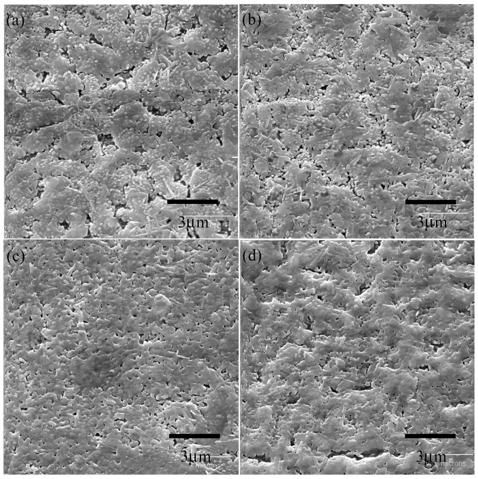

Fig. 2.101. SEM micrograph of 200 nm-thick TMAP-derived films annealed at 740°C in 180-ppm oxygen pressure with different humid-to-dry ratio values: (a) 57:3, (b) 45:15, (c) 30:30, and (d) 50:10.

such as pores, large voids [especially for high humid-to-dry values, see Fig. 2.101(a)], and irregularly shaped surface segregates are observed. Surface roughness in the 30-min-wet, 30-min-dry sample appeared to be finer than the roughness of samples processed in other conditions. Surface roughness increases when wet and dry times are not similar, especially for a longer time held in humid gas. The connectivity of the grains also degraded with increased holding time in humid gas during the high-temperature annealing. The average grain size is estimated to be 2 to 3 μm, which is comparable to those found in bulk materials.

Different heat treatment times have also been investigated. Lengthening the duration of the high-temperature hold beyond 60 min had a negative effect on the morphology of films annealed at 740°C in 180-ppm oxygen.

2.17.4 Discussion

We observed a marked degradation in transition temperature when YBCO films were annealed in a humid atmosphere for more than 45 min or for less than 30 min, as shown in Table 2.8. Samples (b) and (c) have almost the same $T\mathrm{c}(0)$ value; however, the transition width, ΔT_c, tends to broad with humid-to-dry ratios away from 1. For the samples annealed in a dry atmosphere for longer than 30 min, the normal-state section of the ρ vs T curves shows straight lines that would intersect the axis near to the origin. Also, the ratio of ρ_{285}/ρ_{100} tends to be constant (2.51), which is comparable with the data reported by R. Feenstra et al. [16], even though the longer holding time resulted in higher values of resistivity, both at 285 K and 100 K compared with that of sample (c) (30:30). This result has been observed routinely in other sets of samples. However, lengthening the holding time in a humid atmosphere during high-temperature annealing resulted in a curvature of the R-T line in the normal state and higher values at both 285 K and 100 K. High critical-current densities are associated with high transition-temperatures and low transition widths.

Extensive reaction between YBCO films and the CeO_2 buffer layer were shown in both XRD results and RBS data. In Figs. 2.95 and 2.96, the (110) and (200) peaks from the reaction product $BaCeO_3$, which are the same as those reported in the TFA approach [17], can be identified for all of the samples studied. The RBS data [Figs. 2.100(a) and (b)] show that the element Ba diffused deeply into the lower layers during the high-temperature annealing; Ba was identified more deeply in the samples held for a longer time in a dry atmosphere. It seems that the dry atmosphere promotes the faster diffusion or reaction between the CeO_2 buffer layer and the YBCO film. As the thickness (nominal thickness) of the YBCO films were identified by the depth of the barium atoms and as the reaction product $BaCeO_3$ cannot be viewed as superconductor, so the effective thickness of the YBCO layer is smaller than the values estimated from RBS data. Normally, the buffer-layer CeO_2 had a thickness of about 50 nm, and no CeO_2 layer can be identified in the RBS spectra for all of the samples in this research. Hence the actual critical current density of the superconducting layer will be somewhat higher than the values listed in Table 2.8.

The differences in the textures of the various samples, reflected by ω-scans (Fig. 2.97), ϕ-scans (Fig. 2.98), and pole figures (Fig. 2.99), are minor, indicating that the annealing times in wet and dry atmospheres has essentially no effect on the crystallographic alignment of the YBCO grains. This is consistent with the grain orientations being determined by the nucleation process, which occurs during the early stages of annealing. SEM top-view micrographs revealed that voids and pores are present around grain boundaries and that lengthening the holding time in humid gas resulted in large size voids and bad connectivity between grains. The charging in the grain boundaries during SEM measurements

[Figs. 2.101(a) and (b)] indicates poor conductivity in these regions. One possible reason is that water vapor degraded the YBCO films after their formation. For the sample annealed at 740°C for 30 min wet and 30 min dry, the grains were well developed and the grain boundaries are not so evident [Fig. 2.101(c)]. But for sample (b) (45:15), grain boundaries are more obvious [Fig. 2.101(b)] and the film in these regions is not very dense, as is the case to an even greater extent for sample (a) [Fig. 2.101(a)]. Thus it is obvious that YBCO reacts with humid gas and degrades the electrical properties of the YBCO. Another consideration is the stability of the YBCO phase. The phase diagram proposed by Feenstra et al. [18] is shown in Fig. 2.102. In our study, the TMAP-derived films were produced by annealing under Po(O)$_2$ and temperature conditions (1.8×10^{-4} atm at 740°C) near the CuO and Cu_2O transition line. There was no evidence of the volatilization of any of the components from the films during the burnout or high-temperature annealing. Therefore, the overall Y:Ba:Cu ratio in the films is believed to be very close to 1:2:3. Surface segregates such as small particles were observed to cover a large fraction of the film surface [Figs. 2.101(a) and (b)] as the holding time in humid gas was increased, suggesting that they may be produced by a reaction between water vapor and the YBCO phase at high temperature. These small particles, which are a slightly copper-rich YBCO phase, are believed to indicate the beginning of composition segregations or YBCO decomposition. Formation of the smaller particles may be a consequence of the chemical inhomogeneities that formed during holding in humid gas at an elevated temperature, resulting in a deviation of local YBCO composition from the ideal ratio. Water vapor may have the effect of accelerating the decomposition process.

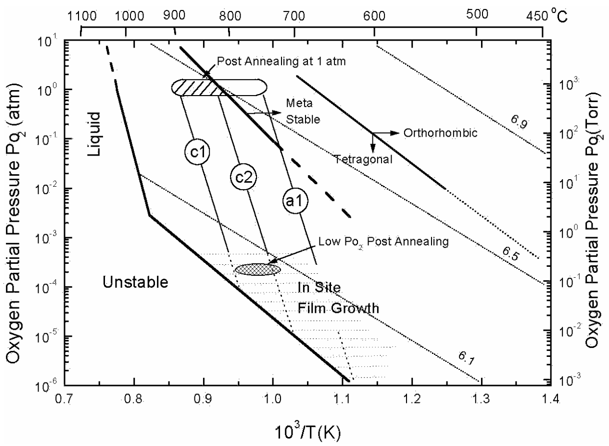

Fig. 2.102. Diagram of the oxygen partial pressure vs temperature for $YBa_2Cu_3O_{7-x}$ material. [Adapted from R. Feenstra et al., *J. Appl. Phys.* 69(9), 6569 (1991).]

Some small pores (about 100 to 300 nm diam) such as those in Fig. 2.101(c) on the TMAP-derived thin films may be a consequence of the pores present in the burnout intermediate films prior to crystallization of the YBCO. These small pores formed by the evaporation of organic precursors could not be removed totally by optimizing the processing parameters and can be viewed as “intrinsic defects.”

Rough surface morphologies of the YBCO films were observed routinely on samples annealed for short times in humid gas at elevated temperatures, as shown in Fig. 2.101(d). Due to the experimental arrangement, the time it takes for the humid furnace gas to become completely dry after the inlet gas is switched to dry is delayed by about 10 min. Therefore, for sample (d), the total time exposed to water vapor at high temperature was probably about 20 min, not enough for the full development of the YBCO phase.

The observed decrease in critical current density and critical transition temperature with extension of the time in humid gas at high temperature is consistent with the idea that the current is limited by bad connectivity and the weak links at grain boundaries. Other factors, such as porosity and small-particle precipitates, will contribute to the low current density also.

The reaction between the YBCO film and the CeO_2 buffer layer is another reason that the critical current density for sample (c) (0.55 MA/cm^2), treated at a humid:dry ratio of 30:30, is not as high as those achieved by the same process on LAO and STO substrates (over 1 MA/cm^2) [19]. Other factors, such as phase development and surface roughness, should be taken into account as well when considering the low current density for the samples treated under different conditions.

2.17.5 Summary

A new fluorine-free TMAP approach was used for this study. Superconducting YBCO films with thickness of 200 nm, $Tc(0)$ greater than 90 K, and a critical current density (77K, zero field) of 5.5×10^5A/cm^2 were prepared by the TMAP metalorganic deposition process. Varying the humid-to-dry ratio during high-temperature annealing from 57:3 to 10:50 had a strong effect on the SEM top-view morphologies and electrical properties of the resulting films, though not on the crystallographic texture. The highest critical temperature and critical current density were observed in film annealed at 740°C in an oxygen partial pressure of about 180 ppm with 30:30 ratio. RBS data shows significant reaction of samples under any of the experimental conditions in this research such that no remaining CeO_2 buffer layer can be detected. Degradation of the properties and surface smoothness was observed as the ratio differed from 30:30 during high-temperature annealing. The humid atmosphere seems to have the trend of accelerating the decomposition of YBCO film annealed under conditions near the instability line proposed by Feenstra et al. Although there are minor intensity differences for YBCO films in X-ray measurements, it is not reasonable to associate these differences with differences in the electrical properties. The reaction between YBCO and CeO_2, the poor connections companioned with voids and pores in grain boundaries, and the difference between the “nominal thickness” from RBS data and the “real thickness” are the reasons that the critical current densities are less than 1 MA/cm^2. In all of the measurements and tests on the samples processed with this novel procedure, no data show any sign of the formation of an intermediate phase of $BaCO_3$.

2.17.6 References

1. A. Gupta et al., “Superconducting Oxide Films with High Transition Temperature Prepared from Metal Trifluoroacetate Precursors,” *Appl. Phys. Lett.* **52**(24), 2077 (1988).
2. P. C. Mclntyre, M. J. Cima, and M. F. Ng, “Metalorganic Deposition of High-J_c $Ba_2YCu_3O_{7-x}$ Thin Films from Trifluoroacetate Precursors onto (100) $SrTiO_3$” *J. Appl. Phys.* **68**(8), 4183 (1990).
3. J. A. Smith, M. J. Cima, and N. Sonnenberg, “High Critical Current Density Thick MOD-Derived YBCO Films,” *IEEE Transactions on Applied Superconductivity* **9**(2), 1531 (1999).
4. Y.-A. Jee et al., “Texture Development and Superconducting Properties of $YBa_2Cu_3O_x$ Thin Films Prepared by a Solution Process in Low Oxygen Partial Pressure,” *Supercond. Sci. Technol.* **14**(5), 285 (2001).
5. A. Goyal et al., “High Critical Current Density Superconducting Tapes by Epitaxial Deposition of $YBa_2Cu_3O_x$ Thick Films on Biaxially Textured Metals,” *Appl. Phys. Lett.* **69**(12), 1795 (1996). A. Goyal et al., U.S. Patents 5,739,086; 5,741,377; 5,846,912; and 5,898,020.
6. T. Araki et al., “Firing Condition for Entire Reactions of Fluorides with Water Vapor in Metalorganic Deposition Method using Trifluoroacetate,” *Physica C* **357-360**, 991 (2001).
7. C. E. Rice, R. B. Van Dover, and G. J. Fisanick, “Preparation of Superconducting Thin Films of $Ba_2YCu_3O_7$ by a Novel Spin-on Pyrolysis Technique,” *Appl. Phys. Lett.* **51**(22), 1842 (1987).
8. M. E. Gross et al., “Versatile New Metalorganic Process for Preparing Superconducting Thin Films,” *Appl. Phys. Lett.* **52**(2), 160 (1988).
9. A. H. Hamdi et al., “Formation of Thin-Film High T_c Superconductors by Metalorganic Deposition,” *Appl. Phys. Lett.* **51**(25), 2152 (1987).
10. P.-Y. Chu and R. C. Buchanan, “Reactive Liquid Phase Sintering of Solution-Derived $YBa_2Cu_3O_{7-x}$ Superconducting Thin Films: Part I. Ambient and Precursor Effects on BaO-CuO Liquid Phase Formation,” *J. Mater. Res.* **8**(9), 2134 (1993).
11. A. Gupta et al., p. 265 in *Chemistry of High-Temperature Superconductors II*, ed. D. L. Nelson and T. F. George, American Chemical Society, Washington, D.C. (1988).
12. S. Hirano, T. Hayashi, and M. Miuram, *J. Am. Ceram. Soc.* **73**(4), 885 (1990).
13. F. Parmigiani, G. Chiarello, and N. Ripamonti, “Preparation of $Ba_2YCu_3O_{7-\delta}$ Thin Films with Preferred Orientation through an Organometallic Route,” *Physical Review B* **36**(13), 7148 (1987).

14. Y. Xu et al., “Deposition of Epitaxial YBCO Thin Film on Single Domain YBCO Substrate for the Development of RF Components,” *IEEE Trans. Appl. Supercond.* **11**(1), 2865 (2001).
15. D. Shi et al., “Epitaxial Growth of $YBa_2Cu_3O_x$ Film on Single-Domain YBCO Substrate for rf Component Development,” *Physica C* **354**, 71 (2001).
16. V. F. Solovyov et al., “Thick $YBa_2Cu_3O_7$ Films by Post Annealing of the Precursor by High Rate e-Beam Deposition on $SrTiO_3$ Substrates,” *Physica C* **309**, 269 (1998).
17. A. P. Malozemoff et al., “Low-Cost YBCO Coated Conductor Technology,” *Supercond. Sci. Technol.* **13**(5), 473 (2000).
18. R. Feenstra et al., “Effect of Oxygen Pressure on the Synthesis of $YBa_2Cu_3O_{7-x}$ Thin Films by Post-Deposition Annealing,” *J. Appl. Phys.* **69**(9), 6569 (1991).
19. Y. Xu et al., “Fabrication of High J_c $YBa_2Cu_3O_{7-\delta}$ Films using a Fluorine Free Sol Gel Approach,” *J Mat. Res*. (accepted).

2.18 Non-Fluorine-Based Bulk Solution Techniques to Grow Superconducting $YBa_2Cu_3O_{7-\delta}$ Films—A Review

M. P. Paranthaman

2.18.1 Introduction

Major advances have been made in the last 14 years in the area of HTS research, resulting in increasing use of HTS materials in commercial and precommercial applications. HTS conductors are expected to be useful for numerous electric power applications, including underground transmission cables, oil-free transformers, high-efficiency motors, compact generators, and superconducting magnetic energy storage systems for smoothing voltage fluctuations in the power grid. Research on second-generation YBCO-based conductors is now being intensively carried out in the world. Recently, the U.S. Department of Energy conducted a Coated Conductor Technology Development Roadmap Workshop in St. Petersburg, Florida. This roadmap identified specific near-term activities that are needed to advance techniques for continuous processing of high-quality, low-cost coated conductors that will lead to industrial-scale commercial manufacturing [1]. The activities specified in the roadmap are focused on achieving the following vision. “Low-cost, high-performance YBCO Coated Conductors will be available in 2005 in kilometer lengths. For applications in liquid nitrogen, the wire cost will be less than \$50/kA-m, while for applications requiring cooling to temperatures of 20–60 K the cost will be less than \$ 30/kA-m. By 2010 the cost-performance ratio will have improved by at least a factor of four”. One of the important critical needs that came out of this workshop was to develop alternative nonvacuum processes for fast, reliable and economic deposition of YBCO. The traditional in situ process, in which PLD of oxide or coevaporation of Y, Ba, and Cu metals under appropriate oxygen atmospheres could be used to fabricate YBCO films. However, it may be difficult to scale up these processes to produce low-cost conductors. This is mainly due to the initial high-cost investment (e.g., laser, large vacuum chambers with pumping system). The control of substrate temperature during deposition is also difficult. To circumvent this problem, ex situ precursor processes can be used. Chemical solution epitaxy has emerged as a viable, low-cost, nonvacuum process for fabricating long lengths of YBCO coated conductors. In these processes, YBCO precursors can be deposited at room temperature and later post-annealed in a controlled-atmosphere furnace. The advantages of the ex situ processes are the separation of the deposition and post-annealing steps and a wider processing window by combining temperature and oxygen partial pressures. The dependence of oxygen partial pressure and the YBCO process temperatures is shown in Fig. 2.103 [2]. Also, the precursor stoichiometry and dopant concentration can be easily controlled, and the post-annealing step can be a batch process. The growth rate of YBCO generally varies from 1 to 3 Å/s. This could be a rate-limiting step in these processes. However, it is possible to overcome these limitations by suitably modifying the furnace designs to process large quantities of wires (hence, a large area) in a single step. The following are the most commonly used bulk solution techniques to fabricate YBCO coated conductors:

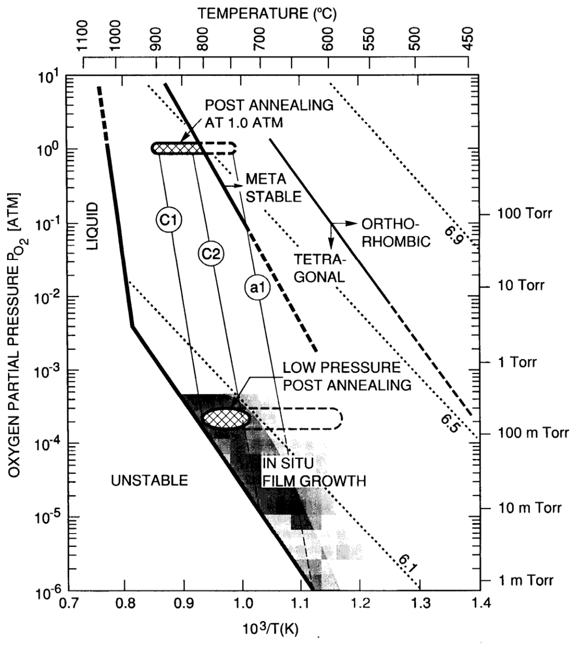

Fig. 2.103. Oxygen partial pressure vs temperature diagram showing liquid-phase boundaries, stability of YBCO, tetragonal-to-orthorhombic transition line, and lines of constant oxygen stoichiometry of $YBa_2Cu_3O_{7-x}$. The *c*-axis–aligned YBCO films are obtained between the c1 and c2 boundary lines; *c*- and *a*-axis–aligned YBCO films, between the c2 and a1 boundary lines. Experimental and extrapolated ranges are indicated by solid and dashed lines, respectively. [Adapted from R. Feenstra et al., *J. Appl. Phys.* 69, 6569 (1991).]

- sol-gel processing
  - sol-gel alkoxide approach
  - metal-organic decomposition (MOD)
- electrodeposition
- electrophoresis
- spray (aerosol) pyrolysis techniques
- chemical vapor deposition
  - combustion chemical vapor deposition (CCVD)
  - metal-organic chemical vapor deposition (MOCVD)
- powder suspension techniques
- liquid-phase epitaxy (LPE)

Each film deposition process will have some maximum rate, beyond which defects or other problems such as supplying source material or removing by-products may become limiting. The properties of YBCO films will depend critically upon the microstructures that develop during the nucleation and growth of the films. These microstructures depend on the substrate properties, the particular deposition technique, the processing conditions, and the film thickness. In this review, we report the recent achievements in growing YBCO films by using non-fluorine-containing solution precursors. In addition, the recent developments in the buffer layer work at ORNL are also highlighted.

2.18.2 Sol-Gel Processing

The most commonly used chemical solution deposition techniques may be grouped into three categories: (1) sol-gel processes that use 2-methoxyethanol as a reactant and solvent; (2) hybrid processes that use chelating agents such as acetylacetonate or diethanolamine to reduce alkoxide reactivity, and (3) metal-organic decomposition techniques that use, for example, high-molecular-weight precursors and water-insensitive carboxylates and 2-ethyl-hexanoates. The sol-gel precursor route has been used to grow both oxide buffer layers and superconductors because of the ease of formation of epitaxial oxides at relatively low temperatures, control over the polymeric viscous gel formation, and the relatively easy scale-up of film thickness.

Sol-gel processing is a wet chemical route to synthesis of a colloidal suspension of solid particles or clusters in a liquid (sol) and subsequently to formation of a dual-phase material of a solid skeleton filled with a solvent (wet gel) through sol-gel transition (gelation). When the solvent is removed, the wet gel converts to a xerogel through ambient pressure drying or an aerogel through supercritical drying. The sol-gel process involves synthesis of a polymerizable solution (often referred to as sol) by mixing or reacting metal alkoxides and metal-organic salts in a common solvent. Alkoxides are referred to as “M(OR)n,” where M is a metal, n is the valency of the metal, and R is an alkyl group. The most common solvent used in this process is 2-methoxyethanol. The complete hydrolysis of the sol will form a rigid gel that can be heat-treated to powders. Partial hydrolysis of the sol will produce a polymeric, viscous gel that can be deposited on substrates and heat-treated to crystallize. The polymeric network can be important for microstructure and phase development. The reactivity of alkoxide ligands with water is the driving force for the sol-gel process. This reaction must be controlled in order to promote the desired gelation, and the starting metal alkoxides must undergo complete ligand exchange to form methoxyethoxide ligands. The ligand exchange can be described easily by the following equation:

$$M(OR)_n + n\,R'OH = M(OR')_n + n\,ROH \tag{16}$$

Due to the bidentate nature of the methoxyethoxide ligand, which ties up vacant coordination sites, it slows the rate of hydrolysis and thus more readily allows the formation of a gel rather than precipitate. In addition, the bidentate nature of the methoxyethoxide ligand allows the more facile formation of mixed-metal alkoxide complexes. The complete gelation process can be summarized by the following equations. Hydrolysis of alkoxides:

$$M(OR)_n + H_2O = M(OR)_{n-1}(OH) + ROH \tag{17}$$

Condensation:

$$M(OR)_{n-1}(OH) + M(OR)_n = M_2O(OR)_{2n-2} + ROH \tag{18}$$

$$M(OR)_{n-1}(OH) + M(OR)_{n-1}(OH) = M_2O(OR)_{2n-2} \tag{19}$$

The primary advantage of sol-gel processing over conventional ceramic processing is that the polymeric network formation of the metal-organic complexes leads to intimate mixing of the amorphous preceramic oxides, thus allowing a dramatic reduction in reaction temperatures and time.

Thin (~100-nm), uniform, and crack-free films can be readily formed on various materials by spin, dip, or spray coating; thick films can be obtained by applying multiple coatings. Spin coating involves the acceleration of a liquid puddle on a rotating substrate. The coating material is deposited in the center of the substrate either manually or by a robotic arm. The physics behind spin coating involves a balance between centrifugal forces, which are controlled by spin speed, and viscous forces, which are determined by solvent viscosity. The spin-coating technique consists of three basic stages: (1) the polymer is dispensed onto the substrate, (2) the polymer is spread across the substrate (by spinning at approximately500 rpm), and (3) the substrate is then spun at a higher speed (2000–4000 rpm). Some of the variable process parameters involved in spin coating are solution viscosity, solid content, angular speed, and spin time. The film-forming process is primarily driven by two independent parameters: viscosity and spin speed. A range of film thickness can be easily obtained by spin coating. For thicker films, high material viscosity, low spin speed, and a short spin time are needed. However, these parameters can affect the uniformity of the coat. In order to scale up these techniques, a dip-coating process has to be developed. The dip-coated tapes could be processed in a batch or in a continuous mode. The advantage of the dip-coating process is its ability to coat large areas, complex shapes, and double-sided tapes. Furthermore, material utilization is almost 100 %. Solution-derived films crack with increasing thickness due to the high-volume shrinkage as organics are removed during the heat-treatment process. Restricting the film thickness to a critical film thickness prevents cracking, and thicker films may be achieved by multiple coating and heat-treatment procedures. In the dip-coating process, the substrate is usually withdrawn vertically from the coating bath at a constant speed. The film thickness is directly proportional to the withdrawal velocity. The inner layer of the coating solution moves upward with the substrate, while the outer layer is returned to the bath. The viscosity and surface tension of the coating liquid control the film thickness to a lesser extent. A schematic diagram of the reel-to-reel continuous dip-coating unit is shown in Fig. 2.104. The sol-gel alkoxide and MOD approaches to grow YBCO films are discussed in Sects. 2.18.2.1 and 2.18.2.2, respectively. In the sol-gel alkoxide approach, the recent developments in the solution buffer layer work at ORNL are described in Sect. 2.18.2.1.1.

2.18.2.1. Sol Gel Alkoxide Approach

2.18.2.1.1 Buffer Layers

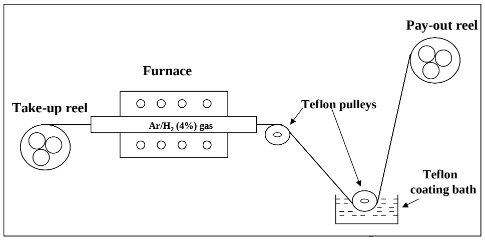

Fig. 2.104. Schematic diagram of reel-to-reel continuous dip-coating unit.

Chemical solution epitaxy has emerged as a viable, low-cost, nonvacuum process for fabricating long lengths of YBCO coated conductors [3–11]. RABiTS™ is an ideal starting template for this solution process [12–14]. For a film to function as an effective buffer, it is also essential to grow dense and crack-free films. To develop the solution process, buffer layers such as $REAlO_3$ (rare-earth aluminate; RE = La,Nd) and $BaZrO_3$, were initially grown epitaxially on $SrTiO_3$ (100) single-crystal substrates from sol-gel alkoxide precursors [8,11]. The $REAlO_3$ buffers grown on biaxially textured Ni (100)<001> substrates had a good out-of-plane texture but had two in-plane textures [15–17]. Following this work, single cube-on-cube epitaxy of various RE_2O_3 (RE=Gd, Yb, and Eu) and $RE_2Zr_2O_7$ (rare-earth zirconates; RE = La,Nd) buffers were grown directly on textured Ni substrates by spin coating [18–21]. To scale up this technique, a dip-coating process was developed. As seen from the Fig. 2.104, both ends of the annealed nickel tape were electrically spot-welded to nickel leaders mounted on two reels. The take-up reel was driven continuously by a stepper motor, and the pay-out reel was tensioned by a variable torque motor. The travel speed of the tape could be varied up to 100 m/h. The reel-to-reel system has the capability of processing up to several meters of buffered tape.

The dip-coating process was used to grow epitaxial buffers of Eu_2O_3, Gd_2O_3, and $La_2Zr_2O_7$ (LZO) on both Ni and Ni-W (3 at. %) (strengthened and substrate with reduced magnetism) substrates. A 2-methoxyethanol solution of europium methoxyethoxide/acetate, gadolinium methoxyethoxide/acetate, or lanthanum zirconium methoxyethoxide was used for the dip-coating process. The details of the solution preparations were reported earlier [18–21]. The concentration of the coating solution was typically 0.25–0.5 M. The Ni and Ni-W tapes from the pay-out reel were withdrawn from the coating bath at a constant speed of 1 to 10 m/h. The tapes were coated on both sides. The dip-coated tapes were then annealed in the furnace, which had been preheated to 1000–1100°C. The flow rate of Ar/H_2 (4%) gas purging the furnace was 2–4 L/min. The heat-treatment times typically varied from 10 min to 1 h in the hot zone. After heat treatment, the tapes were spooled on the take-up reel. The details of the optimized coating speed and annealing speed are reported elsewhere [22–24]. Detailed X-ray studies indicated that single-cube-texture Eu_2O_3, Gd_2O_3, and LZO buffers were produced. The typical thicknesses of these buffers were 20 to 60 nm. The dip-coated seed layers were carbon-free, smooth, continuous, and crack-free. The typical microstructure of 20-nm-thick Gd_2O_3 on Ni-W substrate is shown in Fig. 2.105.

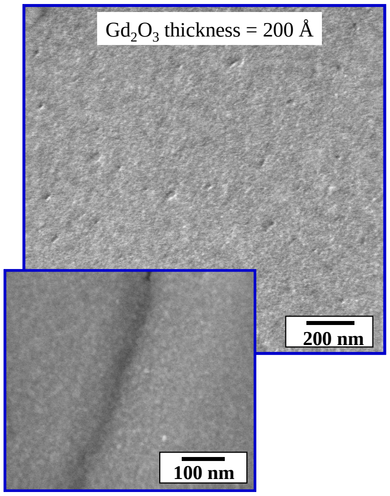

Fig. 2.105. The typical microstructure of 20-nm-thick Gd_2O_3 seed layer on Ni-W substrate.

As shown in Fig. 2.106, the AFM scan indicated the surface roughness of the Gd_2O_3 seed layer on Ni-W tape to be 3.2 nm. This proves that smooth buffers can be produced using the solution process. In addition, the substrate grain boundary is also completely covered by the Gd_2O_3 layer. Seed layers in 1- to 2-m lengths of Eu_2O_3, Gd_2O_3, and LZO were produced. Attempts to grow YBCO films directly on the dip-coated buffer layers by PLD resulted in YBCO films with poor properties. Therefore, sol-gel chemistry for CeO_2 cap layers was also developed. On all solution buffers [(CeO_2 cap/Eu_2O_3 (five coats)/Ni) or (LZO (four coats)/Ni-W)], the highest critical current density obtained to date is 2×10^5 A/cm^2 at 77 K and self-field [25]. On either short or long tapes, both YSZ barrier layers and CeO_2 cap layers were deposited by rf magnetron sputtering at 780°C in 10 mTorr of

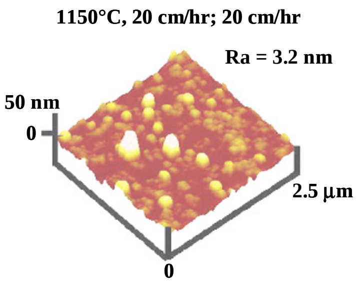

Fig. 2.106. AFM scan of the 20-nm-thick Gd_2O_3 seed layer on Ni-W substrate.

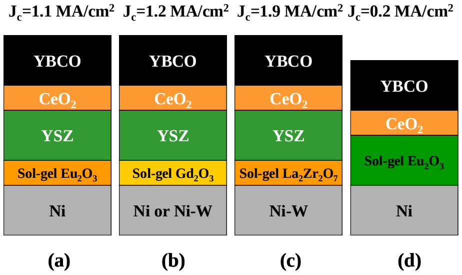

Fig. 2.107. The various architectures developed by using solution seed layers.

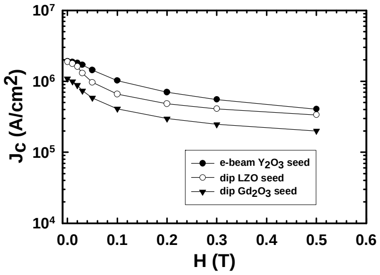

Fig. 2.108. The field dependence of critical current density for YBCO films grown on various seed layers. The architecture is YBCO/CeO_2/YSZ/dip-coated(or e-beam) seed layer/Ni-W.

Ar/H_2 (4%) gas. The plasma power was 75 W at 13.56 MHz. Ex situ YBCO precursors were deposited on CeO_2-buffered YSZ/dip-coated seed/Ni or Ni-W tapes by e-beam coevaporation of yttrium, copper, and BaF_2 in a reel-to-reel configuration. The tapes were post-annealed in wet oxygen atmospheres. The details are reported by Lee et al [26]. On fully buffered short tapes, YBCO films were also grown by PLD at 780°C and a $P(O_2)$ of 120 mTorr. The transport property measurements of the YBCO films grown on these dip-coated seed layers are shown in Fig. 2.107. The field dependence of the critical current density for YBCO films deposited on Gd_2O_3 and LZO seed layers with sputtered YSZ and CeO_2 cap layers is shown in Fig. 2.108. YBCO films deposited on e-beam Y_2O_3 seed layers are also compared. A high critical current density of 1.9 MA/cm^2 at 77 K and self-field was obtained on both Y_2O_3 and LZO seed layers. The performance of the solution seed layers approached that of the vacuum seed layers.

Very recently, on 0.8-m Gd_2O_3 seeded ORNL RABiTS™ sample, YBCO films with end-to-end critical current densities of 625 KA/cm^2 were produced by the reel-to-reel BaF_2 precursor approach [26]. The average critical current density is 750 KA/cm^2 with the standard deviation of only 10.5%. The critical-current-density data on the 0.8-m solution seed is shown in Fig. 2.109. This demonstrates that high-critical-current-density YBCO films can be grown on the solution seed layers in lengths and promises a route for producing long lengths of YBCO coated conductors by both vacuum and nonvacuum buffer layer technologies.

2.18.2.1.2 YBCO films

Highly oriented superconducting YBCO films were prepared by Rupich et al. [5] on (100) $LaAlO_3$ (LAO) and (100) yttria-stabilized zirconium oxide (YSZ) single-crystal substrates by sequential heat treatment in flowing Ar (< 2 ppm oxygen) and oxidation of Y-Ba-Cu alkoxide precursor films at 730ºC. The precursor solution was prepared from a pyridine solution of Y-methoxyethoxide, Ba-methoxyethoxide, and $(CuO)_n$ in 2-methoxyethanol at room temperature. The YBCO films processed at 730ºC showed metallic behavior in the normal state and a sharp resistive superconducting transition with transition temperature (zero) at 89.5 K. Critical current densities of 2×10^5 A/cm^2 at 77 K and self-field were obtained with YBCO films on YSZ substrates. The Cu-alkoxide precursors are generally insoluble in alcohol. However, Paranthaman et al. [7] have dissolved Cu-methoxide precursors in solvents like triethanolamine or diethanolamine in their alkoxide approach and have grown highly aligned superconducting

Masuda et al. [28,29] have grown superconducting YBCO films with a transition temperature of 85 K on polycrystalline YSZ substrates by using all alkoxide precursors at 920ºC in pure O_2. The YBCO precursor solutions were prepared by dissolving copper acetate in di-methyl formamide (DMF) solvent and mixing the copper solution with an alcohol solution in which yttrium-isopropoxide and Ba-ethoxides

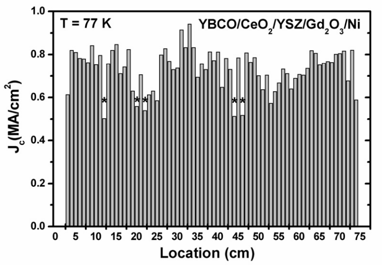

Fig. 2.109. Critical-current-density data on the 0.8-m solution seed ORNL RABiTS™.

were dissolved. Films with a thickness of about 10 µm were produced by dip-coating the sols kept at temperatures of 60 to 80ºC and a viscosity of 5×10^{-3} to 1×10^{-2} Pascal.second (Pa.s). Highly oriented YBCO and $YBa_2Cu_4O_8$ (Y-124) films were fabricated by Katayama et al. [30,31] on Ag substrates. A Cu-methoxide solution was obtained by dissolving Cu-methoxide in 2-methoxyethanol and ethylenediamine to form a coordination compound of $Cu(OCH_3)_2(en)_2$. Y-isopropoxide solution was prepared by dissolving Y-isopropoxide in 2-methoxy-ethanol and ethyl acetoacetate to form a chelate compound of $Y(O\text{-}iC_3H_7)_2(EAA)$. The modified Cu alkoxide was partially hydrolyzed with equimolar water and was mixed with Y and Ba alkoxide solutions to prepare a heterometallic alkoxide solution. Superconducting YBCO films were produced by dip-coating the YBCO precursor solution onto polycrystalline Nb-doped STO substrates and heat-treating up to 870ºC in oxygen [32]. The precursor solution was based on Y-acetate, Ba-alcoholate in 2-methoxy-ethanol, and Cu-butyrate in an alcoholic solvent. Niobium, used as a dopant in STO, inhibited the formation of oxides containing Cu-Ti and Ba-Ti, yielding better superconducting properties than for films deposited on undoped STO substrates. However the YBCO films grown on those substrates had much lower transition temperatures. The summary of the growth of YBCO films using sol-gel alkoxide approach is shown in Table 2.9.

2.18.2.2 Metal-Organic Decomposition (MOD) Approach

In the MOD approach, various metal-organic precursors such as citrates, oxalates, neodecanoates, trifluoroacetates, halides, acetates, acetylacetonates, and naphthenates have been described in the literature. During the $YBa_2Cu_3O_7$ growth, it is possible that certain metalorganic precursors can lead to barium carbonate as the intermediate phases due to the formation of carbon dioxide during processing of the carbon-containing precursor ligands attached to the barium ions. Usually, the ligand is removed by hydrolysis with excess water followed by precipitation of the resulting barium hydroxide. However, fatty-acid ester ligands cannot be removed by simple oxidation or hydrolysis. It is necessary to process YBCO films above 900°C to decompose the intermediate barium carbonate, which can interfere kinetically with the formation of the YBCO phase. For these reasons, non-carbon-containing precursors are preferred. The TFA approach is the most popular one where high-current-density YBCO films have been reproducibly grown on RABiTS™. It is also possible to process non-fluorine-containing precursors under reduced pressures to avoid the $BaCO_3$ formation as the intermediate phase.

The trifluoroacetate approach was originally developed by Gupta et al. [33] to grow high-quality YBCO films. McIntyre et al. [6] later perfected the TFA process. Superconducting YBCO films with a critical current density of 1 to 5×10^6 A/cm^2 were grown on single-crystal STO or LAO substrates by various groups [6,25,34–40]. $NdBa_2Cu_3O_7$ films with a transition temperature of 89 K have also been prepared by the TFA approach on single-crystal STO substrates at 800°C and a $p(O_2)$ of 3×10^{-4} atm [40]. The disadvantage of this approach is that HF forms during the YBCO film growth. The rate of HF removal determines the growth rate of YBCO; the YBCO growth rate is typically 1 to 3 Å/s. Also, processing of thicker films takes longer, and the burn-out step is slow. Li et al [39] have processed YBCO films of 1.2 µm with a critical current density of 2.5 MA/cm^2 on 20-nm CeO_2-buffered YSZ single-crystal substrates in three coats. In addition, they have also demonstrated the growth of YBCO films with a critical current density of 1.7 MA/cm^2 on CeO_2(sputtered)/YSZ(sputtered)/solution Gd_2O_3/Ni substrates. $TlBa_2Ca_2Cu_3O_{9-y}$ films on Ag substrates. Similarly, Monde et al. [27] have prepared a YBCO precursor solution by dissolving yttrium butoxide, barium methoxide and copper methoxide in triethanolamine-methanol solution. However they obtained only a transition temperature of 56 K for YBCO films grown on polycrystalline YSZ substrates. In this demonstration, both seed layers and the superconductors were grown by a solution process. It is also possible to modify the furnace design to post-anneal long lengths of

Table 2.9. Summary of the growth of YBCO films

YBCO precursors	Substrate	Process conditions	Physical properties	References
Alkoxide approach				
Y-methoxyethoxide; Ba-methoxyethoxide; $(CuO)_n$ in 2 MeEtOH	YSZ xtal	730°C; 2 ppm O_2	$T_c = 89.5$ K $J_c = 2 \times 10^5$ MA/cm^2 (77 K)	5
Y-butoxide; Ba-methoxide; Cu-methoxide in triethanolamine and methanol	YSZ poly	800°C; air	$T_c = 56$ K	27
Y-isopropoxide; Ba-ethoxide; Cu-acetate in DMF	YSZ poly	920°C; O_2	$T_c = 85$ K	28, 29
Y-isopropoxide; Ba-alkoxide; Cu-methoxide in 2 MeEtOH/ethylenediamine	Ag	800°C	Y-124 phase	30, 31
Y-acetate/Ba-alcoholate in 2 MeEtOH; Cu-butyrate	Nb-STO poly	870°C	low T_c Nb-STO inhibits Cu-Ti; Ba-Ti formation	32
MOD approach				
Y-acetate; Ba-acetate; and Cu-acetate in trifluoroacetic acid/methanol	LAO or STO xtals	725–800°C; 100–300 ppm O_2	$T_c = 91$ K $J_c = 1–4 \times 10^6$ A/cm^2 thickness 0.4µm (77 K)	6, 25, 34–39
YBCO TFA	Nb-STO/Ni	Three coats	$J_c = 1.3 \times 10^6$ A/cm^2	38
$NdBa_2Cu_3O_7$ TFA precursors	STO xtal	800°C; $P(O_2)$ 3×10^{-4} atm	Nd123 phase $T_c = 89$ K	40
YI_3, BaI_2, and CuI in acetonitrile/Ethanol (or NH_4I/DMF/2-MeEtOH)	STO xtal	800–830°C 300 ppm O_2	$T_c = 90$ K $J_c = 1.3 \times 10^5$ A/cm^2	41, 42
Y-trimethylacetate $Ba(OH)_2$; Cu-trimethylacetate in propionic acid/amine solvent	STO xtal	800°C	$T_c = 90$ K $J_c = 1 \times 10^5$ A/cm^2	43
Yb-acac; Ba-neodecanoate, and Cu 2-ethylhexanoate in toluene/pyridine/propionic acid	STO xtal	730–770°C 100 ppm O_2	Yb-123 $T_c = 87$ K $J_c = 6.4 \times 10^5$ A/cm^2	45
YBCO acac precursors	STO xtal		J_c $1–5 \times 10^5$ A/cm^2	46–48
YBCO naphthenate precursors	LAO & STO	Low $P(O_2)$	$J_c = 1.2 \times 10^6$ A/cm^2	53, 55
Electrodeposition				
Y, Ba, and Cu hydroxides deposited in nitrate solutions	Ag	–1.4V (vs SCE)		64
Y, Ba, and Cu nitrates in dimethy sulfoxide	Ni MgO YSZ xtal	Post-annealed	$T_c = 74$ K (on Ni) $T_c = 78$ K (on MgO) $T_c = 91$ K (on YSZ) $J_c = 360$ A/cm^2 (77 K)	65, 66
Y, Ba, and Cu perchlorates in TBAP and acetonitrile	Ag		$T_c = 88$ K	67–69
Y, Ba, and Cu hydroxides deposited in nitrate solutions		Post-annealed in O_2	$T_c = 88$ K	70
Spray pyrolysis technique				
Y, Ba, and Cu nitrate solutions	Various substrates	Substrate at 200–400°C and heat-treated at 600–900°C	Low J_c; film 2–5 µm	71–79
Y, Ba, and Cu nitrate solutions	MgO xtalAl_2O_3 poly	Post-annealed at 750°C	$T_c > 80$ K; film1–10 µm $J_c = 10^3–10^4$ A/cm^2(77 K)	73
Y, Ba, and Cu nitrate solutions		Post-annealed in a fluorine atmosphere		80

thick and wider tape in a batch mode. Very recently Clem et al. [38] have demonstrated the growth of YBCO films with a critical current density of 1.3 MA/cm^2 at 77 K on all-solution Nb-doped STO buffered Ni substrates in short lengths. This demonstration is the first step toward the fabrication of low-cost YBCO coated conductors.

Similar to fluoride precursors, solution-based metal iodide precursor routes have been developed [41,42]. Stoichiometric mixtures of YI_3, BaI_2, and CuI are dissolved in either acetonitrile/ethanol solutions or ammonium iodide/dimethylformamide/2-methoxy-ethanol solutions. The fact that BaI_2 can be decomposed without the use of water during YBCO film growth makes this approach very interesting. This process eliminates the formation of highly reactive HI vapors. YBCO films with a transition temperature of 90 K and a critical current density of 1.3×10^5 A/cm^2 have been grown on STO single-crystal substrates. The films were processed at 800 to 830°C in 300-ppm oxygen. The temperature dependence of the resistivity for YBCO film on STO substrate is shown in Fig. 2.110. The surface morphology of the YBCO film produced by the iodide process is shown in Fig. 2.111. Enhanced plate-like grains with size of 1 to 3 μm and a less-porous microstructure are obtained. It may be possible to use the chloride precursors in the form of dichloroacetic acid or trichloroacetic acid to grow YBCO films.

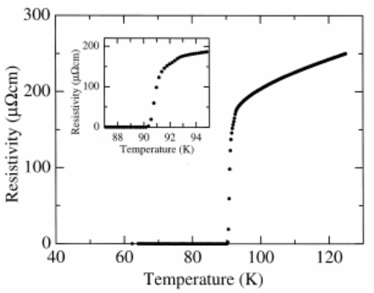

Fig. 2.110. Temperature dependence of resistivity for YBCO film on STO (100) single-crystal substrates grown from iodide precursors.

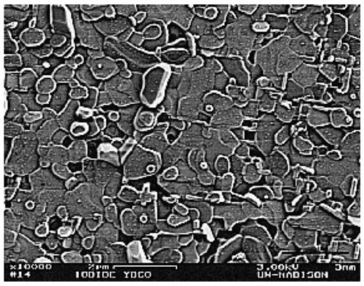

Fig. 2.111. Scanning electron micrograph of YBCO film on STO (100) single-crystal substrates grown from iodide precursors.

Recently, Shi et al. [43] have developed a nonfluorine solution route to grow YBCO films on LAO single crystals. In this method, stoichiometric yttrium trimethylacetate, barium hydroxide, and copper trimethylacetate powders were dissolved in a mixture of propionic acid/amine solvent. The YBCO films had a transition temperature of 90 K and a transport critical current density of 1×10^5 A/cm^2 at 77 K. This precursor approach was originally developed by Chu et al. [44]. Matsubara et al. [45] have used ytterbium acetylacetonate, barium neodecanoate, and copper (II) 2-ethylhexanoate in a mixture of solvents containing toluene/pyridine/propionic acid to prepare epitaxial $YbBa_2Cu_3O_{7-y}$ films on STO single-crystal substrates. In this method, the YbBCO films were processed at 730 to 770°C and 100-ppm oxygen. The highest transition temperature obtained was 87.2 K. The measured transport critical current density was 6.4×10^5 A/cm^2 at 77 K and self-field. The magnetic field dependence critical current density of $YbBa_2Cu_3O_{7-y}$ is shown in Fig. 2.112. Even though the critical current density is little bit low, it is extremely promising to use this precursor route for growing superconducting films on substrates developed by the RABiTS™, IBAD, and ISD processes. In the literature, various acetylacetonate (acac) precursor approaches have been described in detail [46–52]. The highest critical current density obtained on YBCO films grown by using the acac approach is on the order of 10^5 A/cm^2 at 77 K.

Highly *c*-axis-aligned superconducting $REBa_2Cu_3O_{7-\delta}$ (RE = rare earth) films were prepared on STO and LAO single crystal substrates by using the corresponding metal naphthenates in toluene solution [53–62]. In this approach, YBCO films with a critical current density of 1.2×10^6 A/cm^2 were produced. The summary of the growth of YBCO films by MOD routes is shown in Table 2.9. Ottosson et al. [63] have deposited superconducting YBCO films by chemical vapor deposition of the halide precursors YCl_3, BaI_2, and CuCl as metal sources in the presence of O_2/H_2O gas mixtures. The as-grown films had a transition temperature of 40 K, and the transition temperature was increased to 70 K upon post-annealing in O_2 at 475°C

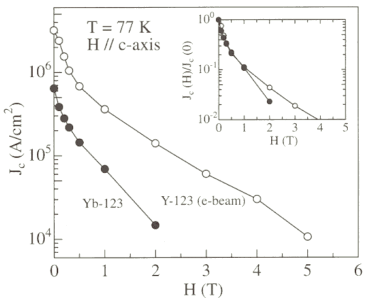

Fig. 2.112. Magnetic field dependence of the transport J_c of $YbBa_2Cu_3O_{7-y}$ film deposited by solution process (solid circle) compared with YBCO film deposited by ex situ BaF_2 process (open circle) on STO (100) single-crystal substrates. Inset: the magnetic field dependence of normalized J_c, $J_c(H)/J_c(0)$.

2.18.3 Electrochemical Deposition

Electrochemical deposition involves reduction of metallic ions from aqueous, inorganic, and fused salt electrolytes. The reduction process [M^{n+} (solution) + $ne^- \rightarrow$ M (lattice)] can be accomplished by the electrodeposition process, in which n electrons are supplied by an external power supply or by electroless (autocatalytic) deposition process in which a reducing agent in the solution is the electron source (there is no external power supply). Thin films of hydroxide precursors of YBCO have been electrodeposited from aqueous solution at a potentiostatic voltage of –1.4 V [vs a Standard Calomel Electrode (SCE)] onto a Ag electrode by Monk et al. [64]. The compositions of the films were tailored by adjusting the deposition voltage and by varying the relative amounts of precursor solutes in solution. The aqueous solution contained 0.0125 mol dm^{-3} of $Y(NO_3)_3$, 0.150 mol dm^{-3} of $Ba(NO_3)_2$, and 0.025 mol dm^{-3} of $Cu(NO_3)_2$. No further annealing of these hydroxide precursors was reported. Bhattacharya et al. [65,66] electrodeposited YBCO precursors from an electrolyte solution consisting of nitrate salts of Y(III), Ba(II), and Cu(II) dissolved in an organic solvent (dimethyl sulfoxide). Nominal deposition potentials ranged from –2.5 to –4 V (vs an Ag/AgNO$_3$ reference electrode). The post-annealed electrodeposited films show a reproducible transition temperature (zero) of 74 K on Ni, 78 K on MgO, and 91 K on (100) YSZ substrate. The critical current density obtained for YBCO films on YSZ substrate is 4000 A/cm^2 at 4 K and self-field and 360 A/cm^2 at 77 K and self-field. YBCO films with a transition temperature of 88 K were deposited on Ag substrates by electrodeposition of metal perchlorate salts, tetrabutylammonium perchlorate (TBAP) and acetonitrile [67–69]. Abolmaali et al. [70] have deposited YBCO hydroxide precursors from metal nitrate salts in isopropanol and post-annealed in oxygen. The YBCO films grown from a single simultaneous deposition had a transition temperature of 79 K and 88 K for films grown from several successive depositions. In the literature, no information was found related to a suitable buffer coating over a metal substrate; however, it is possible that this technique may work on any suitably textured substrate followed by post-annealing in low $P(O_2)$. The summary of the growth of YBCO films by electrodeposition is shown in Table 2.9.

2.18.4 Spray (Aerosol) Pyrolysis Techniques

In this technique, aqueous solutions of $Y(NO_3)_3.5H_2O$, $Ba(NO_3)_2$, and $Cu(NO_3)_2.3H_2O$ in stoichiometric amounts are prepared from high-purity nitrates and deionized water [71–79]. The aqueous solution was sprayed onto a heated substrate (maintained at a temperature in the range of 200 to 400°C. Typical thicknesses of the as-deposited samples vary from 2 to 5 μm. The films were then heat-treated in various partial pressures of O_2 and in temperatures ranging from 600 to 900°C. Most of the groups obtained very low critical current densities. Jergel et al. [73] obtained YBCO films of 1 to 10 μm thickness with a transition temperature > 80 K and a critical current density of 10^3 to 10^4 A/cm^2 at 77 K and self-field. To use this technique, it is necessary to develop suitable buffer layers and to process YBCO films at temperatures around 750°C. It is also essential to avoid the formation of $BaCO_3$ as the intermediate phase. To circumvent this problem, Suenaga et al. [80] have post-annealed spray pyrolyzed films in a fluorine atmosphere to form BaF_2 as the intermediate phase. The summary of the growth of YBCO films by spray pyrolysis technique is shown in Table 2.9.

2.18.5. Conclusions

A detailed review of the summary of the various bulk solution techniques to grow superconducting YBCO films has led to the following conclusions.

- It is essential to develop an alternative low-cost solution approach to grow both buffers and superconductors to fabricate low-cost YBCO coated conductors.
- Solution seed layers such as Gd_2O_3, $La_2Zr_2O_7$ provide good templates on which to grow high-current-density YBCO films. The performance of the solution seed layers approached that of the vacuum seed layers.
- YBCO tapes 0.8 m long and carrying an end-to-end critical current density of 625 KA/cm^2 were produced by combining both nonvacuum and vacuum buffer layer technologies.
- YBCO films with a critical current density of 2×10^5 A/cm^2 were produced from sol-gel alkoxide precursors.
- Very high current density ($J_c > 4 \times 10^6$ A/cm^2) YBCO films have been fabricated by using the TFA precursor approach. The TFA process has become the most popular nonvacuum route to YBCO so far. HF evolution during the film growth could limit the YBCO growth rate.
- Iodide precursors are promising, mainly because the method that employs them does not need any water during processing. YBCO films with a transition temperature of 90 K and a critical current density of 1.3×10^5 A/cm^2 have been obtained by using iodide precursors.
- Nonfluorine solution precursor routes have been developed to deposit YBCO and YbBCO films with a critical current density of up to 6.4×10^5 A/cm^2. This is another promising route.
- Naphthenate precursors in toluene have been used to grow YBCO films with a critical current density of 1.2×10^6 A/cm^2. Naphthenate precursors are only available in Japan. This could be a limiting factor for widespread application of this method.
- Electrodeposition and spray pyrolysis have resulted in low critical current densities so far.

2.18.6 References

1. Energetics, Inc., *Coated Conductor Technology Development Roadmap: Priority Research & Development Activities Leading to Economical Commercial Manufacturing*, Sponsored by U.S. Department of Energy, Superconductivity for Electric Systems Program, Energetics, Inc., Columbia, Md. (August 2001).
2. R. Feenstra et al., “Effect of Oxygen Pressure on the Synthesis of $YBa_2Cu_3O_{7-x}$ Thin Films by Post-Deposition Annealing,” *J. Appl. Phys.* **69**, 6569 (1991).
3. C. J. Brinker and G. W. Scherer, *Sol-Gel Science: The Physics and Chemistry of Sol-Gel Processing*, Academic Press, San Diego, Calif., (1990).
4. C. J. Brinker et al., “Review of Sol-Gel Thin Film Formation,” *J. Non-Cryst. Solids* **147&148**, 424 (1992).
5. M. W. Rupich, Y. P. Liu, and J. Ibechem, “Low-Temperature Formation of $YBa_2Cu_3O_{7-x}$ Superconducting Films from Molecular Cu-Ba-Y Precursors,” *Appl. Phys. Lett.* **60**, 1384 (1992).
6. P. C. McIntyre et al., “Effect of Growth-Conditions on the Properties and Morphology of Chemical Derived Epitaxial Thin Films of $YBa_2Cu_3O_{7-x}$ on (001) $LaAlO_3$,” *J. Appl. Phys.* **71**, 1868 (1992).
7. M. Paranthaman and D. B. Beach, “Growth of Highly Oriented $TlBa_2Ca_2Cu_3O_{9-y}$ Superconducting Films on Ag Substrates using a Dip-Coated Barium Calcium Copper Oxide Sol-Gel Precursor,” *J. Am. Ceram. Soc.* **78**, 2551 (1995).
8. M. Paranthaman et al., “Epitaxial Growth of $BaZrO_3$ Films on Single Crystal Oxide Substrates using Sol-Gel Alkoxide Precursors,” *Mater. Res. Bull.* **32**, 1697 (1997).

9. F. F. Lange, “Chemical Solution Routes to Single-Crystal Thin Films,” *Science* **273**, 903 (1996).
10. R. W. Schwartz, “Chemical Solution Deposition of Perovskite Thin Films,” *Chem. Mater.* **9**, 2325 (1997).
11. S. S. Shoup et al., Sol-Gel Synthesis of $LaAlO_3$: Epitaxial Growth of $LaAlO_3$ Thin Films on $SrTiO_3$ (100),” *J. Mater. Res.* **12**, 1017 (1997).
12. A. Goyal et al., “High Critical Current Density Superconducting Tapes by Epitaxial Deposition of $YBa_2Cu_3O_{7-x}$ Thick Films on Biaxially Textured Metals,” *Appl. Phys. Lett.* **69**, 1795 (1996).
13. D. P. Norton et al., “Epitaxial $YBa_2Cu_3O_7$ on Biaxially Textured Nickel (001): An Approach to Superconducting Tapes with High Critical Current Density,” *Science* **274**, 755 (1996).
14. M. Paranthaman et al., “Growth of Biaxially Textured Buffer Layers on Rolled Ni Substrates by Electron Beam Evaporation,” *Physica C* **275**, 266 (1997).
15. S. S. Shoup et al., “Epitaxial Thin Film Growth of Lanthanum and Neodymium Aluminate Films on Roll-Textured Nickel using a Sol-Gel Method,” *J. Am. Ceram. Soc.* **81**, 3019 (1998).
16. D. B. Beach et al., “Sol-Gel Synthesis of Rare Earth Aluminate Films as Buffer Layers for High T_c Superconducting Films,” *Mater. Res. Soc. Symp. Proc.* **495**, 263 (1998).
17. M. Paranthaman et al., “Growth of Textured Buffer Layers and Superconductors on Rolled-Ni Substrates using Sol-Gel Alkoxide Precursors,” p. 185 in *Symp. VI-Science and Engg. Of HTC Superconducitivity*, Proc. of the 9th CIMTEC-World Ceramics Congress and Form on New Materials, ed. P. Vincenzini, Tehna, Srl. (1999).
18. T. G. Chirayil et al., “Epitaxial Growth of Yb_2O_3 Buffer Layers on Biaxially Textured-Ni (100) Substrates by Sol-Gel Process,” *Mater. Res. Soc. Symp. Proc.* **574**, 51 (1999).
19. T. G. Chirayil et al., “Epitaxial Growth of $La_2Zr_2O_7$ Thin Films on Rolled-Ni Substrates by Sol-Gel Process for High T_c Superconducting Tapes,” *Physica C* **336**, 63 2000.
20. J. S. Morrell et al., “Epitaxial Growth of Gadolinium Oxide on Roll-Textured Nickel using a Solution Growth Technique,” *J. Mater. Res.* **15**, 621 (2000).
21. M. Paranthaman et al., “Demonstration of High Current Density YBCO Coated Conductors on RE_2O_3-Buffered Ni Substrates with Two New Alternative Architectures,” p. 879 in *Advances in Cryogenic Eng. Mater.*, Vol. 46, Ed. U. Balachandran et al., Kluwer Academic/Plenum, New York (2000).
22. M. P. Paranthaman et al., “Fabrication of Long Lengths of Epitaxial Buffer Layers on Biaxially Textured Nickel Substrates using a Continuous Reel-to-Reel Dip-Coating Unit,” *J. Am. Ceram. Soc.* **84**, 273 (2001).
23. S. Sathyamurthy et al., “Chemical Solution Deposition of Lanthanum Zirconate Buffer Layers on Biaxially Textured Ni-3at%W Alloy Substrates for Coated-Conductor Fabrication,” *J. Mater. Res.* (submitted).
24. T. Aytug et al., “Continuous Reel-to-Reel Chemical Solution Deposition of Epitaxial Gd_2O_3 Buffer Layers on Biaxially Textured Ni-(3 at% W-1.7 at% Fe) Alloy and Ni Substrates for the Fabrication of High-J_c $YBa_2Cu_3O_{7-\delta}$ Coated Conductors,” *J. Am. Ceram. Soc.* (submitted).
25. M. Paranthaman et al., “Fabrication of Long Lengths of YBCO Coated Conductors using a Continuous Reel-to-Reel Dip-Coating Unit,” *IEEE Trans. on Appl. Supercond.* **11**, 3146 (2001).
26. D. F. Lee et al., “Reel-to-Reel Processing of YBCO Coated Conductors using a BaF_2 Process,” pp. 149–77 in *Second-Generation HTS Conductors*, ed. A. Goyal, Kluwer Academic Publishers (2004).
27. T. Monde, H. Kozuka, and S. Sakka, “Superconducting Oxide Thin Films Prepared by Sol-Gel Technique using Metal Alkoxides,” *Chem. Lett.* **2**, 287 (1988).
28. Y. Masuda et al., “Preparation of $YBa_2Cu_3O_{7-x}$ Superconductive Film using Sol-Gel Method,” *Jpn. J. Appl. Phys.* **30**, 1390 (1991).
29. Y. Masuda et al., “Preparation of $YBa_2Cu_3O_{7-x}$ Superconducting Films through the Sol-Gel Method using Metal Alkoxides as Starting Materials,” *J. Mater. Res.* **7**(4), 819 (1992).
30. S. Katayama and M. Sekine, p. 897 in *Better Ceramics Through Chemistry IV*, ed. B. J. J. Zelinski et al., Material Research Society, Pittsburgh, Pa. (1990).

31. S. Katayama et al., “Highly Oriented $YBa_2Cu_4O_8$ Films Fabricated at Atmospheric Pressure by the Sol-Gel Method using Metal Alkoxide,” *Appl. Phys. Lett.* **60**, 118 (1992).
32. E. Benavidez et al., “Chemical Method to Prepare $YBa_2Cu_3O_{7-x}$ Films by Dipping onto $SrTi(Nb)O_3$ Ceramics,” *Mater. Chem. and Phys.* **62**, 9 (2000).
33. A. Gupta et al., “Preparation of Superconducting Oxide Films from Metal Trifluoroacetate Solution Precursors,” p. 265 in *Chemistry of High-Temperature Superconductors II, ACS Symp. Series 377*, ed. D. L. Nelson, and T. F. George, American Chemical Society, Washington, D.C. (1988).
34. S. Sathyamurthy and K. Salama, “Processing of $Y_1Ba_2Cu_3O_x$ Films by Solution Techniques using Metal-Organic Decomposition,” *J. of Supercond.* **11**, 545 (1998).
35. K. Yamagiwa et al., “Epitaxial Growth of $REBa_2Cu_3O_{7-y}$ Films on Various Substrates by Chemical Solution Deposition, *J. Crystal Growth* **229**, 353 (2001).
36. J. T. Dawley et al., “High J_c $YBa_2Cu_3O_{7-\delta}$ Films via Rapid, Low pO_2 Pyrolysis,” *J. Mater. Res.* **16**, 13 (2001).
37. J. T. Dawley et al., “Thick Sol-Gel Derived $YBa_2Cu_3O_{7-\delta}$ Films,” *IEEE Trans. on Appl. Supercond.* **11**, 2873 (2001).
38. P. Clem et al., “Solution Deposition of YBCO Coated Conductors,” DOE Superconductivity Annual Peer Review Meeting Presentations, Washington D.C., August 1–3 (2001).
39. Q. Li et al., “Progress in Solution-Based YBCO Coated Conductor,” *Physica C* **357–360**, 987 (2001).
40. T. Honjo et al., “Preparations of $REBa_2Cu_3O_{7-y}$ Films Grown by Metal Trifluoroacetate Precursors,” *Physica C* **357–360**, 999 (2001).
41. R. H. Baney, D. F. Bergstrom, and B. H. Justice, “Metal Iodides: Novel Solution Precursors to Cuprate Superconductors,” *Chem. Mater.* **4**, 984 (1992).
42. I. Matsubara et al., “Preparation of Textured YBCO Films using All-Iodide Precursors,” *Physica C* **319**, 127 (1999).
43. D. Shi et al., “Deposition and Interface Structures of YBCO Thin Films via a Non-Fluorine Sol-Gel Route,” *Physica C* (in press).
44. P.-Y. Chu and R. C. Buchanan, “Reactive Liquid Phase Sintering of Solution-Derived $YBa_2Cu_3O_{7-\delta}$ Superconducting Thin Films: Part I. Ambient and Precursor Effects on BaO-CuO Liquid Phase Formation,” *J. Mater. Res.* **8**, 2134 (1993).
45. I. Matsubara et al., “Preparation of Epitaxial $YbBa_2Cu_3O_{7-\delta}$ on $SrTiO_3$ Single Crystal Substrates using a Solution Process,” *Jpn. J. Appl. Phys.* **38**, L727 (1999).
46. G. Risse et al., “Textured YBCO-Film Formation by Sol-Gel Process and Post-Annealing,” *J. of European Ceram. Soc.* **19**, 125 (1999).
47. T. Manabe et al., “Preparation of High-J_c $YBa_2Cu_3O_{7-\delta}$ Films on STO (100) Substrates by the Dipping-Pyrolysis Process at 750°C,” *Jpn. J. Appl. Phys.* **30**, L1641 (1991).
48. T. Manabe et al., “Carbon Dioxide Controlled Annealing Method for Preparation of $YBa_2Cu_3O_{7-\delta}$ Films by Dipping-Pyrolysis Process,” *Physica C* **276**, 160 (1997).
49. S. R. Breeze and S. N. Wang, “The Preparation of YBCO Epitaxial Superconducting Films by a Chemical Solution Deposition Process,” *J. Mater. Sci.* **34**, 1099 (1999).
50. M. Nagano and M. Greenblatt, “High Temperature Superconducting Films by Sol-Gel Preparation,” *Solid State Commun.* **67**, 595 (1988).
51. C. E. Rice, R. B. van Dover, and G. J. Fisanick, “Preparation of Superconducting Thin Films of $YBa_2Cu_3O_{7-\delta}$ by a Novel Spin-on Pyrolysis Technique,” *Appl. Phys. Lett.* **51**, 1842 (1987).
52. A. A. Hussain and M. Sayer, “Chemical Fabrication of Superconducting Y-Ba-Cu Oxide Films, *J. of Supercond.* **5**, 11 (1992).
53. X. L. Ma et al., “Characterization of $YbBa_2Cu_3O_{7-\delta}$ Superconducting Thin Films Prepared by Chemical Solution Deposition of STO (001) and LAO (001) Substrates,” *Phys. Stat. Sol.* (a) **173**, 441 (1999).
54. K. Yamagiwa and I. Hirabayashi, “Structural and Superconducting Properties of Biaxially Aligned Yb123 Films Prepared by Chemical Solution Deposition,” *Physica C* **30**, 12 (1998).

55. K. Yamagiwa and I. Hirabayashi, “Orientation Behavior of $REBa_2Cu_3O_{7-y}$ (RE=Rare Earth and Y) Films Prepared by Chemical Solution Deposition,” *Jpn. J. Appl. Phys.* **39**, 452 (2000).
56. T. Kumagai et al., “Critical Current Densities at 77 K in $YBa_2Cu_3O_{7-\delta}$/Ag Films Prepared by Dipping-Pyrolysis Process,” *Jpn. J. Appl. Phys.* **32**, L1602 (1993).
57. H. Hiei et al., “YBCO Thin Films on Multilayers Prepared by All-Chemical Solution Deposition Processing,” *Physica C* **357–360**, 942 (2001).
58. J. Shibata et al., “Effects of the Initial Heat-Treatment Conditions on Microstructures of $YbBa_2Cu_3O_{7-\delta}$ Superconducting Final Films Deposited on STO (001) Substrates by the Dipping-Pyrolysis Process,” *Jpn. J. Appl. Phys.* **38**, 5050 (1999).
59. H. Kanaya et al., “Microwave Characteristics of YBaCuO Coplanar Waveguide Resonators Fabricated by the Sol-Gel Process on Polycrystalline MgO,” *Jpn. J. Appl. Phys.* **36**, 6311 (1997).
60. H. Yokota and J. S. Abell, “Preparation of YBCO Films on YSZ and Silver Substrates by the Dipping Pyrolysis Process,” *Physica C* **235–240**, 629 (1994).
61. Y. Shiohara and N. Hobara, “R&D of Coated Conductors in Japan,” *Physica C* **341–348**, 2521 (2000).
62. Y. Iijima and K. Matsumoto, “High-Temperature-Superconductor Coated Conductors: Technical Progress in Japan,” *Supercond. Sci. Technol.* **13**, 68 (2000).
63. M. Ottosson et al., “Chemical Vapor Deposition of the Superconducting $YBa_2Cu_3O_{7-x}$ Phase using Halides as Metal Sources,” *Appl. Phys. Lett.* **54**, 2476 (1989).
64. P. M. S. Monk, R. Janes, and R. D. Partridge, “Electrochemical Deposition of the Hydroxide Precursors to $YBa_2Cu_3O_{7-\delta}$ and Related Phases,” *J. Mater. Chem.* **8**, 1779 (1998).
65. R. N. Battacharya et al., “YBaCuO Superconductor Thin Films via an Electrodeposition Process,” *J. Electrochem. Soc.* **138**, 1643 (1991).
66. R. N. Bhattacharya et al., “YBaCuO and TlBaCaCuO Superconductor Thin Films via an Electrodeposition Process,” *J. Electrochem. Soc.* **139**, 67 (1992).
67. J. M. Rosamilia and B. Miller, “Electrochemical Behavior of Several Metal Ion Solutions at $YBa_2Cu_3O_7$ and CuO Electrodes,” *J. Electrochem. Soc.* **135**, 3030 (1988).
68. J. M. Rosamilia and B. Miller, “Electrodeposition on Cuprate-Based Superconductors in Nonaqueous Media,” *J. Electrochem. Soc.* **136**, 1053 (1989).
69. H. D. Rubin et al., “Properties of Metal-$YBa_2Cu_3O_7$ Composites Formed by Electrodeposition from Nonaqueous Solutions onto the Superconductor,” *Appl. Phys. Lett.* **54**, 2151 (1989).
70. S. B. Abolmaalli and J. B. Talbot, “Synthesis of Superconductive Thin Films of YBCO by a Nonaqueous Electrodeposition Process,” *J. Electrochem. Soc.* **140**, 443 (1993).
71. J. J. Chu et al., “Epitaxial Growth of High Tc Superconducting Y-Ba-Cu-O Thin Films on (001) MgO by a Chemical Spray Pyrolysis Method,” *J. Appl. Phys.* **64**, 2523 (1988).
72. A. Derraa and M. Sayer, “Superconducting Y-Ba-Cu-O Thin Films by Spray Pyrolysis,” *J. Appl. Phys.* **68**, 1401 (1990).
73. M. Jergel et al., “Thin YBCO Films Prepared by Low-Temperature Spray Pyrolysis,” *Supercond. Sci. Technol.* **5**, 225 (1992).
74. T. T. Kodas, E. M. Engler, and V. Y. Lee, “Generation of Thick $YBa_2Cu_3O_7$ Films by Aerosol Deposition,” *Appl. Phys. Lett.* **54**, 1923 (1989).
75. M. Jergel, “Synthesis of High-Tc Superconducting Films by Deposition from Aerosol,” *Supercond. Sci. Technol.* **8**, 67 (1995).
76. Y. S. Chung, K. H. Auh, and D. N. Hill, “Effects of Solution Parameters on the Deposition of YBCO Phase Prepared by Aerosol Feed Method in a Cold Plasma Reactor,” *Mater. Lett.* **27**, 201 (1996).
77. V. Lovchinov et al., “Preparation of YBCO Superconducting Films by Spray Deposition and MTG Processing,” *Mater. Lett.* **24**, 267 (1995).
78. M. Kawai et al., “Formation of Y-Ba-Cu-O Superconducting Film by a Spray Pyrolysis Method,” *Jpn. J. Appl. Phys.* **26**, L1740 (1987).
79. M. L. Kullberg et al., “A Sol-Gel Method for Preparing Oriented $YBa_2Cu_3O_{7-\delta}$ Films on Silver Substrates,” *Supercond. Sci. Technol.* **4**, 337 (1991).

80. M. Suenaga, DOE Superconductivity Annual Peer Review Meeting Presentations, Washington, D.C., August 1–3, 2001.

2.19 Epitaxial Growth of Solution-Based Rare Earth Niobate, RE_3NbO_7 Films on Biaxially Textured Ni-W Substrates

M. Paranthaman, S. Sathyamurthy, H. Y. Zhai, A. Goyal and M. S. Bhuiyan (ORNL); and K. Salama (University of Houston)

2.19.1 Introduction

Chemical solution deposition has emerged as a viable, low-cost, nonvacuum process for fabricating long lengths of YBCO coated conductors. RABiTS™ starting templates are ideal for this process [1]. Solution deposition of buffer layers offers potential cost advantage relative to PVD. The main objective of this work is to research and develop faster, potentially lower-cost, and simpler RABiTS™ architectures as alternatives to the standard PVD-grown three-layer architecture of YBCO/CeO_2/YSZ/Y_2O_3/Ni-W [2]. The challenge is to match the high quality of currently used PVD buffer stacks with solution buffers in long lengths and preferably at lower cost. For a film to function as an effective buffer, it must be dense and crack-free. Buffer layers such as $REAlO_3$ (rare-earth aluminate; RE = La, Nd) [3,4], $NdGaO_3$ [5], and $BaZrO_3$ [6] have been initially grown epitaxially on $SrTiO_3$ (100) single-crystal substrates from sol-gel alkoxide precursors. The $REAlO_3$ buffers grown on biaxially textured Ni (100) <001> substrates had a good out-of-plane texture but had two in-plane textures [7]. Following this work, chemical solution deposition was used to grow single cube-on-cube epitaxy of various RE_2O_3 (RE = Gd, Yb, and Eu) [8–11], $SrTiO_3$ [12], and $RE_2Zr_2O_7$ (rare-earth zirconates; RE = La, Gd) [13–17] buffers directly on textured Ni or Ni-W substrates. YBCO films with a critical current density of 2 MA/cm^2 were grown on single LZO buffered Ni-W substrates by pulsed laser deposition. However, MOD YBCO films grown directly on LZO-buffered Ni-W substrates yielded poor-quality films, mainly because $BaZrO_3$ formed at the buffer-superconductor interface. Hence, there is a need to cap LZO buffers with CeO_2 cap layers. By using sputtered CeO_2 cap layers on LZO buffered Ni-W substrates, YBCO films with a critical current of 135 A/cm have been achieved [16]. We have also developed a MOD precursor route to make textured CeO_2 films [18].

To develop a single buffer layer that is compatible with MOD YBCO process, there is a need to search for new innovative buffers. Dawley et al. [19] have shown that Nb-doped $SrTiO_3$ cap layers are compatible with the MOD YBCO process. Hence, we started exploring rare earth niobium oxides as the potential candidates. As per the phase diagram of the Y_2O_3-Nb_2O_5 system, $YNbO_4$ and Y_3NbO_7 (pyrochlore: $Y_2(YNb)O_7$) phases are known to exist. Both phases may be used as the buffer layers. In the present work, we have studied the Y_3NbO_7 system. Y_3NbO_7 is a cubic pyrochlore with a lattice parameter of 5.2499 Å (pseudo cubic lattice parameter: 3.713 Å). Similarly, RE_3NbO_7 (RE = Rare Earth) phases are also known to exist in the literature. RE_3NbO_7 films have been grown by both the sol-gel alkoxide precursor route and by MOD. Here, we report our successful demonstration of the growth of single epitaxial RE_3NbO_7 (RE = Y, Eu, and Gd) solution buffer on strengthened and textured Ni-W (3 at. %) substrates.

2.19.2 Experimental

The starting reagents were weighed in an argon-filled, inert-atmosphere glove box, and the solution preparation was carried out under argon, with a standard Schlenk-type apparatus. Yttrium (III) isopropoxide (Alfa, 92–95%), niobium ethoxide (Alfa, 99.999%), and 2-methoxyethanol (Alfa, spectrophotometric grade) were used without further purification. For preparing Eu_3NbO_7 and Gd_3NbO_7, europium (III) acetate (Alfa, 99.9%) and gadolinium (III) acetate (Alfa, 99.9%) were used after purification. The Y_3NbO_7 precursor solution with 0.4 M total cation concentration was prepared by refluxing stoichiometric quantities of yttrium isopropoxide and niobium ethoxide in 2-methoxyethanol.

The Y_3NbO_7 precursor solution was then spin-coated onto short (2 × 1 cm) coupons of cube-textured Ni-W substrates at 5000 rpm for 30 s; followed by heat treatment at the optimum temperature of 1100°C for 15 min in a flowing reducing atmosphere of Ar-4%H_2. The tapes were introduced into a preheated furnace kept at 1100°C after a 5-min purge with an Ar-4%H_2 gas mixture at room temperature. After 15 min of heat treatment at 1100°C, the tapes were quenched to room temperature in the same atmosphere. Similarly, Eu_3NbO_7 and Gd_3NbO_7 films on textured Ni-W substrates were prepared at optimum temperatures of 1050°C/15 min and 1100°C/15 min, respectively. About 20-nm-thick RE_3NbO_7 films were produced in a single coat. Multiple coatings were made to prepare thick films. On the Gd_3NbO_7-buffered Ni-W tape, YBCO films were deposited by PLD at 780°C in 120mTorr oxygen with average laser energy of 200 mJ. XRD was used to characterize the samples for phase purity and texture, and the microstructure of both RE_3NbO_7 (RE = Y,Eu,Gd) and YBCO were monitored by SEM. A standard four-point probe technique was used to measure the resistivity and transport critical current density. The voltage contact spacing was 0.4 cm. A 1-μV/cm criterion was used to calculate critical-current-density values. Electrical contacts of Ag were deposited onto the samples by dc sputtering followed by an O_2 annealing in 1 atm for 30 min at 500°C.

A typical θ-2θ XRD pattern of a single coat RE_3NbO_7 (RE = Y,Eu,Gd) film on a textured Ni-W substrate is shown in Fig. 2.113. These scans indicate the presence of strong *c*-axis (200) aligned films.

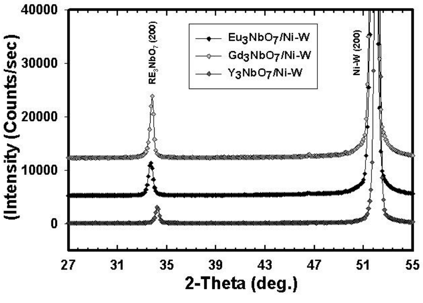

Fig. 2.113. A typical θ-2θ scan for a 20-nm-thick RE_3NbO_7 (RE = Y, Gd, Eu) film grown on biaxially textured Ni-W substrates by MOD. RE_3NbO_7 film has a preferred *c*-axis orientation.

Similar results were obtained for three coats of Gd_3NbO_7 and Eu_3NbO_7 films on Ni-W substrates. Thickness of the film is estimated to be 20 nm/coat. The ω and ϕ scans for a 20-nm-thick Gd_3NbO_7 film on a textured Ni-W substrate are shown in Fig. 2.114. The FWHM values for Gd_3NbO_7 (002) and Ni-W (002) were 7.15° and 5.51°, respectively. Similarly, the FWHM values for Gd_3NbO_7 (111) and Ni-W (111) were 8.0° and 6.72°, respectively. The (111) X-ray pole figures for 20-nm-thick RE_3NbO_7 (RE = Y,Eu,Gd) buffers on Ni-W substrate are shown in Fig. 2.115. The presence of a fourfold symmetry indicates the presence of a single cube-textured RE_3NbO_7 film. As shown in Fig. 2.116, crack-free RE_3NbO_7 (RE = Y,Eu,Gd) buffers were produced.

As shown in Fig. 2.117, the θ-2θ XRD pattern of a YBCO film on Gd_3NbO_7-buffered Ni-W substrate indicated the presence of a strong (200) reflection of YBCO films. The transport properties for the YBCO film grown on Gd_3NbO_7 (three coats) buffered Ni-W substrate is shown in Fig. 2.118. A zero-field critical current density of more than 1.1×10^6 A/cm^2 at 77 K and self-field was obtained. Efforts are being made to grow MOD YBCO films directly on RE_3NbO_7 buffers. The ferroelectric properties of epitaxial rare earth niobates on various technical substrates such as Si, $SrTiO_3$ may also be measured in the future.

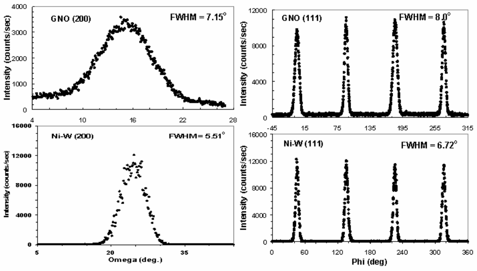

Fig. 2.114.The ω and ϕ scans for a 20-nm-thick Gd_3NbO_7 film grown on biaxially textured Ni-W substrates by MOD. The FWHM values for each scan are shown inside the scans.

2.19.3 Summary

In summary, epitaxial RE_3NbO_7 (RE = Y,Gd,Eu) films have been deposited on textured Ni-W substrates by chemical solution deposition. Gd_3NbO_7 films have been used as a single buffer layer for deposition of YBCO by PLD on these metal substrates. Critical current densities greater than 1.1 MA/cm^2 have been measured for the Ni-W substrates. The present invention offers promise to long-

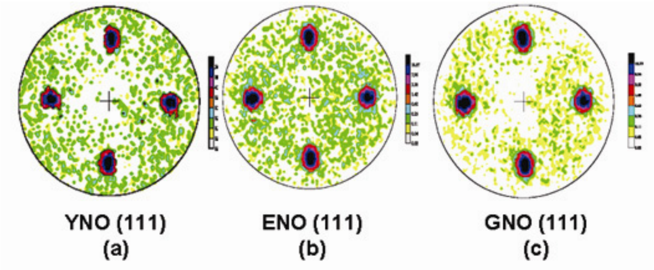

Fig. 2.115. The (111) pole figure for 20-nm-thick (a) Y_3NbO_7, (b) Eu_3NbO_7, and (c) Gd_3NbO_7.

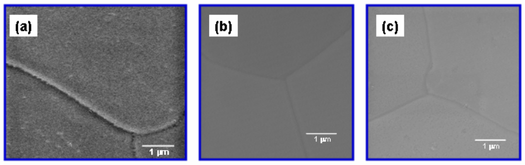

Fig 2.116. SEM micrograph for a 20-nm-thick (a) Y_3NbO_7, (b) Eu_3NbO_7, and (c) Gd_3NbO_7 film surface.

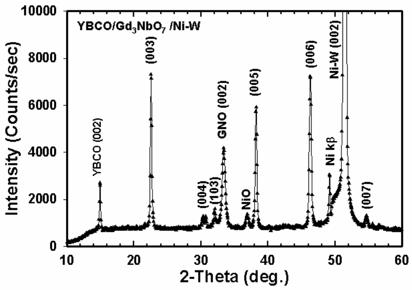

Fig. 2.117. A typical θ-2θ scan for a 200-nm-thick YBCO film grown on three coats of 60-nm-thick Gd_3NbO_7 buffered Ni-W substrates by PLD. YBCO film has a preferred *c*-axis orientation. Small amounts of NiO impurities and polycrystalline YBCO peaks were also identified.

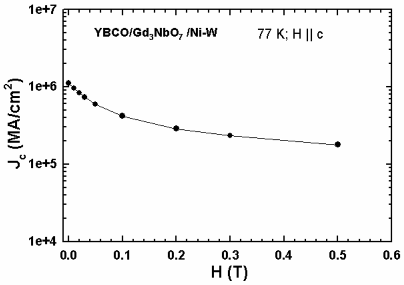

Fig. 2.118. Superconducting properties of a 200-nm-thick YBCO film grown on Gd_3NbO_7 buffered Ni-W substrates by PLD. A self-field critical current density of 1.1 MA/cm^2 at 77 K was obtained.

length coated-conductor fabrication by using a single buffer layer processed by a scaleable solution deposition route.

2.19.4 References

1. A. Goyal et al., “High Critical Current Density Superconducting Tapes by Epitaxial Deposition of $YBa_2Cu_3O_x$ Thick Films on Biaxially Textured Metals,” *Appl. Phys. Lett*. **69**, 1795 (1996).
2. D. T. Verebelyi et al., “Uniform Performance of Continuously Processed MOD-YBCO-Coated Conductors using a Textured Ni–W Substrate,” *Supercond. Sci. Tech.* **16**(5), L19 (2003).
3. S. S. Shoup et al., “Sol-Gel Synthesis of $LaAlO_3$; Epitaxial Growth of $LaAlO_3$ Thin Films on $SrTiO_3$ (100),” *J. Mater. Res*. **12**(4), 1017 (1997).
4. M. W. Rupich et al., “Growth and Characterization of Oxide Buffer Layers for YBCO Coated Conductors,” *IEEE Trans. on Appl. Supercond*. **9**(2), 1527 (1999).
5. C. Y. Yang et al., “Microstructure of a High J_c, Laser-Ablated $YBa_2Cu_3O_{7-\delta}$/Sol-Gel Deposited $NdGaO_3$ Buffer Layer/(001) $SrTiO_3$ Multilayer Structure,” *Physica C* **331**(1), 73 (2000).
6. M. Paranthaman et al., “Epitaxial Growth of $BaZrO_3$ Films on Single Crystal Oxide Substrates using Sol-Gel Alkoxide Precursors,” *Materials Research Bulletin* **32**(12), 1697 (1997).
7. S. S. Shoup et al., “Epitaxial Thin Film Growth of Lanthanum and Neodymium Aluminate Films on Roll-Textured Nickel Using a Sol-Gel Method,” *J. Amer. Ceram. Soc.* **81**(11), 3019 (1998).
8. J. S. Morrell et al.“Epitaxial Growth of Gadolinium Oxide on Roll-Textured Nickel using a Solution Growth Technique,” *J. Mater. Res.* **15**(3), 621 (2000).

9. M. Paranthaman et al., “Fabrication of Long Lengths of YBCO Coated Conductors using a Continuous Reel-to-Reel Dip-Coating Unit,” *IEEE Trans. on Appl. Supercond*. **11**(1), 3146 (2001).
10. T. G. Chirayil et al., *Mat. Res. Soc. Symp. Proc.*, **574**, 51–56 (1999).
11. Y. Akin et al., “Engineered Oxide Thin Films as 100% Lattice Match Buffer Layers for YBCO Coated Conductors,” *Solid-State Electronics* **47**(12), 2171 (2003).
12. S. Sathyamurthy and K. Salama, “Application of Metal-Organic Decomposition Techniques for the Deposition of Buffer Layers and Y123 for Coated-Conductor Fabrication,” *Physica C* **329**(1), 58 (2000).
13. M. Paranthaman et al., “Fabrication of Long Lengths of Epitaxial Buffer Layers on Biaxially Textured Nickel Substrates Using a Continuous Reel-to-Reel Dip-Coating Unit,” *J. Amer. Ceram. Soc*. **84**(2), 273 (2001).
14. T.G. Chirayil et al., “Epitaxial Growth of $La_2Zr_2O_7$ Thin Films on Rolled Ni-Substrates by Sol–Gel Process for High T_c Superconducting Tapes,” *Physica C* **336**(1–2), 63 (2000).
15. S. Sathyamurthy et al., “Lanthanum Zirconate: A Single Buffer Layer Processed by Solution Deposition for Coated Conductor Fabrication,” *J. Mater. Res*. **17**(9), 2181 (2002).
16. M. P. Paranthaman et al., “Bulk Solution Techniques to Fabricate High J_c YBCO Coated Conductors,” *Physica C* **378-381**(2), 1009 (2002).
17. S. Sathyamurthy et al., “Chemical Solution Deposition of Lanthanum Zirconate Barrier Layers Applied to Low-Cost Coated-Conductor Fabrication,” *J. Mater. Res*. **19**(7), 2117 (2004).
18. M. S. Bhuiyan et al., “MOD Approach for the Growth of Epitaxial CeO_2 Buffer Layers on Biaxially Textured Ni–W Substrates for YBCO Coated Conductors,” *Supercond. Sci. and Tech*. **16**(11), 1305 (2003).
19. J. T. Dawley, R. J. Ong, and P. G. Clem, “Chemical Solution Deposition of (100)-Oriented $SrTiO_3$ Buffer Layers on Ni Substrates,” *J. Mater. Res*. **17**(7), 1678 (2002).

2.20 Pulsed Electron Deposition of YBCO Precursors

H. M. Christen, D. F. Lee, F. A. List, and S. W. Cook

2.20.1 Introduction

Pulsed electron deposition (PED), an ablation-based film growth technique similar to pulsed-laser deposition (PLD) but based on much simpler equipment, is a comparatively new method for the fabrication of superconducting tapes. In this work, we show how this approach can be applied to the deposition of fluoride-based precursors. Last year’s work explored both in situ YBCO growth and ex situ precursor studies. The results showed serious difficulties for the in situ growth. Hence, that work led us to focus on room-temperature precursor deposition, for which we implemented apparatus. The main hurdles of the approach (composition control, growth rate variations, and source performance) were overcome, leading to PED being applicable as a routine precursor-deposition method.

2.20.2 Growth Apparatus and Precursor Targets

Figure 2.119 shows a schematic drawing of the PED apparatus. A photograph of the system is given in Fig. 2.120. The tape to be coated travels between

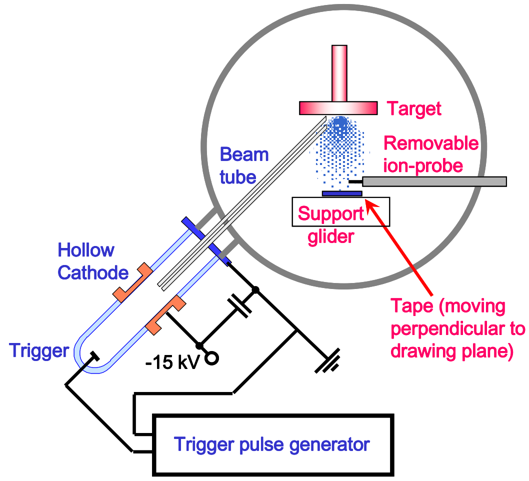

Fig. 2.119. Schematic representation of the pulsed electron deposition apparatus.

the two reels in a reciprocating action; multiple passes are performed for a full deposition, with the tape traveling at a fixed speed of 0.15 cm/s.

Figure 2.121 shows the spatial distribution of ablated material in the plane of the traveling substrate. The plot shows a calculated profile given as a product of a Gaussian variation in the horizontal direction and a Gaussian variation in the vertical direction, with the parameters determined from a least-square fit to 15 datapoints obtained by profilometry. The width of the profile is a function of the target-to-substrate distance, which must be chosen as a compromise between two opposite constraints: a short target-to-substrate distance yields a higher collection efficiency of the ablated material but also a larger thickness nonuniformity. For a tape traveling through a 5-cm-long deposition zone, as schematically indicated in Fig. 2.121(a), the resulting thickness profile across a 1-cm-wide tape is shown in Fig. 2.121(b).

According to the profile in Fig. 2.121(a), 25% of the deposited material is deposited onto the tape. Actual experiments (thickness measurements on long tapes and weighing the target before and after the deposition) showed that only 10% of the material is collected in a typical process. This indicates that the actual profile is broader than the assumed Gaussian or that some of the material is not collected on the substrate. Finally, after resurfacing of the target as required due to uneven target wear, a total of 5% of the target material is actually deposited onto the substrate. While this seems low, it represents a significant improvement over simple evaporation processes. Multiple tape passes through the deposition zone would obviously increase the collection efficiency.

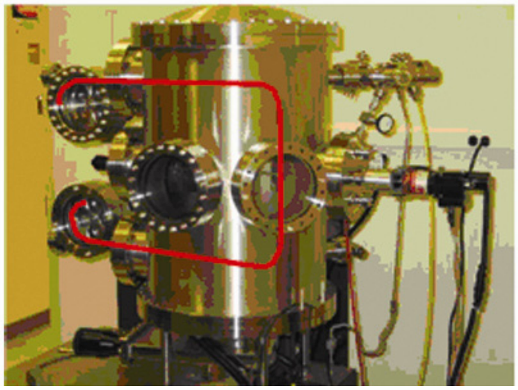

Fig. 2.120. Photograph of the PED reel-to-reel deposition system. The target manipulator is seen on the right, the supply and pick-up reels on the left. The red line shows the travel path of the tape.

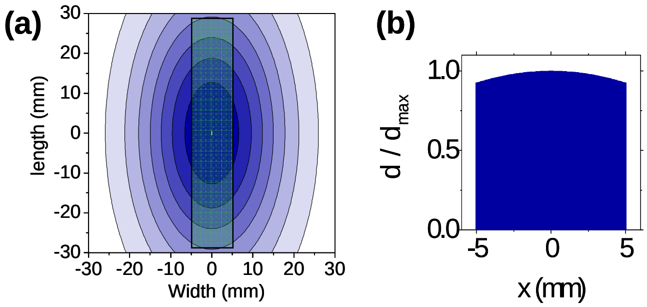

Fig. 2.121. (a) Spatial variation of the deposited material, determined from profilometry and a fit to Gaussian profiles. (b) Lateral thickness profile resulting from the deposition onto a tape moving vertically through a rectangular deposition zone as illustrated in (a).

Long-term source stability tests showed that repeated firing (> 500,000 pulses) in oxygen led to missing pulses (i.e., triggered pulses that resulted in no discharge to the target). However, when operating in nitrogen, the source performs satisfactorily, with more than 9 million pulses fired without error to date. All experiments were performed with a source voltage of 16 kV and a repetition rate of 10 Hz.

The targets used for this study were made by ball-milling the desired ratios of powders of YF_3, BaF_2, and CuO, pressing 1-in. pellets at 8000 lb, and sintering for several hours in air at 800°C.

2.20.3 Composition Control

An initial series of experiments was performed in which a target with Y:Ba:Cu-ratio of 1:2:3 was used and films were deposited at different pressures. The chemical composition of the deposits was then analyzed by inductively coupled plasma-mass spectroscopy (ICP-MS). As is seen in Fig. 2.122, the correct ratio of Ba:Y = 2 is achieved at a pressure of about 11 mTorr; however, at that pressure the deposit is Cu-deficient. The correct Cu-stoichiometry is obtained at 6 mTorr. Therefore, the correct stoichiometry cannot be obtained from a stoichiometric $(YF_3) + (BaF_2)_2 + (CuO)_3$ target. For all further experiments, the targets were therefore prepared with an off-stoichiometric Y:Ba:Cu ratio.

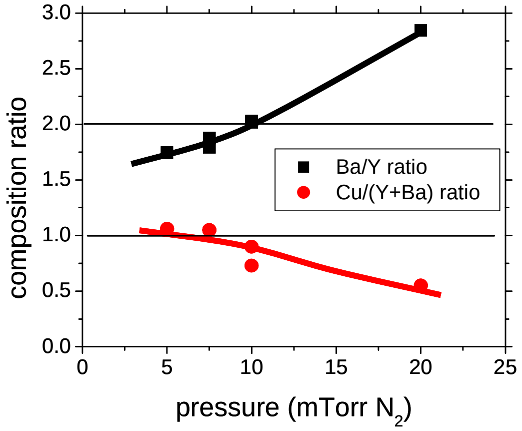

Fig. 2.122. Composition (determined by ICP-MS) for films deposited at various background pressures and using a target of composition $(YF_3)(BaF_2)_2(CuO)_3$.

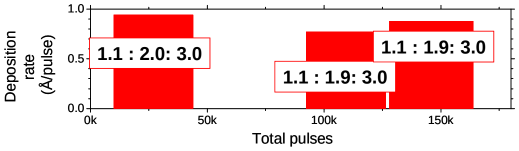

Fig. 2.123. Composition of the deposited material as a function of process time. Three samples were deposited at different times while the source was running continuously, and the composition for all was measured by ICP-MS. Target composition was Y:Ba:Cu = 1:1.8:3. Also shown is the growth rate as function of time. Target was mounted on a copper plate.

Most important for the deposition of precursors onto long tapes is the stability of the process with process time. To verify that the composition of the ablated material does not change with time, we performed an experiment in which individual samples were introduced at different times during a long run (170,000 pulses). The deposit was then analyzed by ICP-MS. Figure 2.123 shows the corresponding result. A target of composition Y:Ba:Cu = 1:1.8:3 was used, resulting in slightly Y-rich and Ba-deficient films as desired. As can be seen in Fig. 2.124, the composition remains fairly constant. Additionally, in this experiments where the target was mounted on a copper plate, the growth rate varied only little during the 170,000 pulses. (See below for a more thorough treatment of growth rate variations with time).

2.20.4 Ion-Probe-Based Diagnostics

The deposition of precursors onto long lengths of tapes requires long-time operation of equipment with many of the parameters held constant. It is therefore of great importance to have a method that allows the operator a quick verification of the essential growth process, without having to insert and remove a sample. Ion probes have been used previously in PLD, as they probe directly the flux of ions from the target toward the substrate. In Fig. 2.125, the insert shows the schematic of the ion probe circuit used here. As indicated in Fig. 2.119, the probe can be inserted and removed during a growth run and is located close to the substrate for a measurement. Electronic noise dominates the signal during the first 3 to 4 µs. A positive signal then corresponds to positive ions being collected at the negatively charged exposed probe. The area under the curve is therefore proportional to the ionic charge arriving at the substrate, and for a ionization rate that can be assumed to be constant during an experiment, this signal is proportional to the deposition rate.

For in situ monitoring during a growth experiments where chamber pressure and target-substrate distance are held constant, it is sufficient to keep track of the peak voltage rather than the integrated signal. In Fig. 2.126, the deposition rate is compared to that peak voltage. To obtain this data, the source was operated continuously for 12 h, during which the growth rate gradually decreased (see below). At different times, a sample was placed in the deposition zone and removed again after 40,000 to 60,000 pulses. The ion probe signal was measured before and after the deposition onto the sample, and the value used for the abscissa is the average of those two voltages.

The data in Fig. 2.126 clearly demonstrate that the ion probe is a useful tool for the determination of the growth rate during a long experiment.

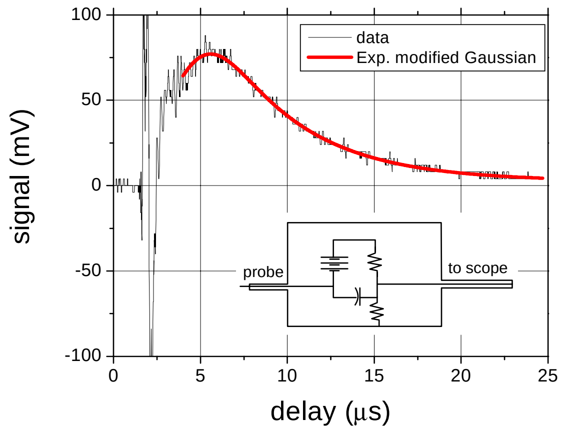

Fig. 2.124. The typical trace (voltage as function of time, with the PED trigger signal defining the zero of time) can be fitted well with an exponentially modified Gaussian. Inset shows the circuit diagram of the ion probe used for plume diagnostics.

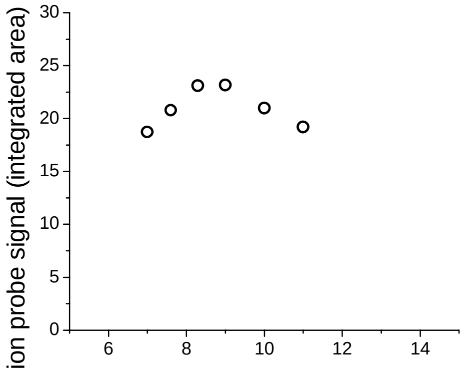

Fig. 2.125. Integrated area of ion probe traces (from least-square fits to a exponentially modified Gaussian curve) as a function of chamber pressure. The highest ion current is achieved at ≈ 9 mTorr.

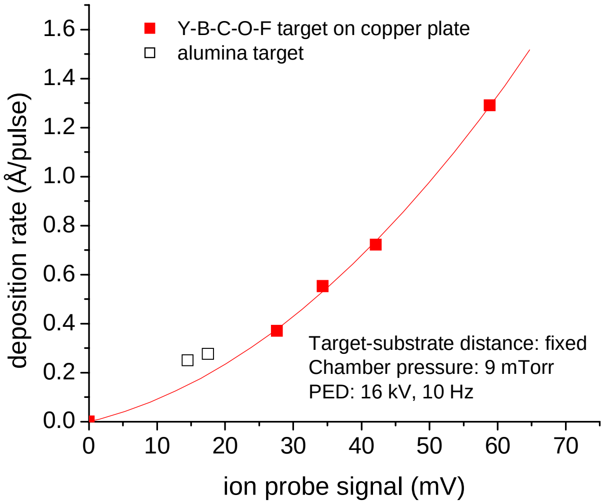

Fig. 2.126. Correlation between deposition rate and ion probe peak signal for two types of targets. Data points taken at various times during a 12-h run, during which the growth rate gradually decreased. Each data point was obtained by depositing 40,000 to 60,000 shots onto a sample and measuring its thickness.

2.20.5 Target Wear and Growth-Rate Reduction

A challenging issue in PED is the observed decrease of deposition rate during prolonged runs. Due to target wear, a similar decrease is occasionally observed in PLD; however, under some conditions the effects seen in PED are much more severe.

One possible reason for a decrease in deposition rate is a potential change in source performance with time. To test that hypothesis, two identical targets were mounted in the chamber, and we first ablated from the first one until a visual decrease in plume intensity was observed. The targets were then exchanged in situ, and ablation proceeded from the second target. It was immediately observed that the plume intensity returned to the initial value, and source performance can thus be ruled out as a cause of deposition rate reduction.

Both thermal and electrical changes are possible reasons for a deterioration of the target surface that leads to a reduction in the ablation rate. The target is subject to large electrical fields, which may result in microstructure changes and strong thermal stresses. In fact, the target temperature may reach several hundred degrees Celsius during the deposition.

A series of experiments was performed with the target mounted in different ways. Figure 2.127 shows the various configurations. In a first experiment (A), the target was deliberately isolated thermally and electrically by placing an alumina disc between the target and its mount. Silver paste was used for all connections. As seen in Fig. 2.128, mounting the target on the alumina disc led to a very quick decrease in the deposition rate. Interestingly, replacing the alumina disc with a copper plate barely changed this

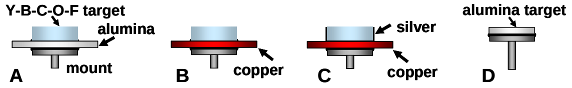

Fig. 2.127. Various target mounting approaches used for the study of growth rate deterioration. A, B, and C are examples for precursor deposition. D is used to compare with a strongly insulating target.

behavior (B). However, when silver paste was painted onto the sides of the target, the deposition rate remained high for a much longer time. This behavior was confirmed in a second experiment, in which the ion probe was used to monitor the plume intensity during an even longer run (Fig. 2.129). In a fourth configuration, ablation took place from an alumina target. The deposition rate was low in this case for the entire experiment.

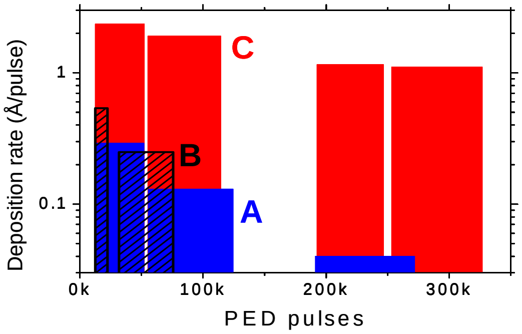

Fig. 2.128. Growth rate as function of process time for the various target-mounting approaches. The width of each rectangle corresponds to the time over which the growth rate is averaged.

These results allow us to speculate that electrical surface conductivity (from the place where the electron pulse impinges toward the edge of the target) is a very important factor in the ablation mechanism. Removing the current path (from the edge of the target to ground) does not initially change the plume intensity (blue and red symbols in Fig. 2.129) but results in a very quick deterioration of the ablation process. This indicates electric-field-induced changes in the target. SEM analysis and energy-dispersive X-ray diffraction (EDX)-mapping across the target did not show any clear differences between well-grounded and other targets, however.

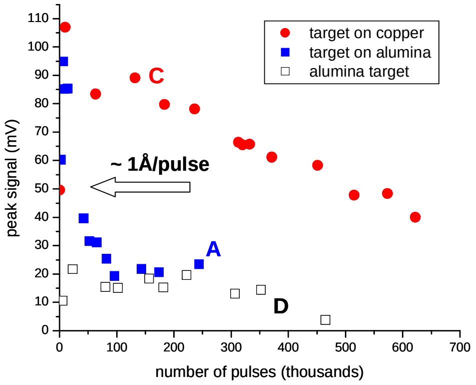

Fig. 2.129. Ion probe peak voltage as function of process time for the various target mounting approaches.

2.20.6 Summary and Conclusions

This series of experiments has shown that PED can be a reliable approach for the deposition of fluorine-based precursors. In fact, the originally encountered problems associated with compositional control and growth rate variations can all be addressed by comparatively simple methods. Furthermore, temporarily inserting an ion probe between the substrate and the target yields a quick measurement of the deposition rate and thus represents a valid process control approach.

2.21 An Approach for Electrical Self-Stabilization of HTS Wires for Power Applications

T. Aytug and J. R. Thompson (ORNL and the University of Tennessee) M. Paranthaman, H. Y. Zhai, A. A. Gapud, K. J. Leonard, and D. K Christen (ORNL)

For effective implementation of coated conductors, it is necessary to electrically and thermally stabilize the HTS coating by means of a parallel electrical conductor capable of shunting the current away from the HTS layer in the event of a local transient to the dissipative state, possibly caused by a thermal spike, a microcrack in the superconductor layer, or a current surge beyond the superconductor’s critical current. Otherwise, because of the extremely high current density carried by the superconductor layer (~10^6 A/cm^2), such an event would immediately damage an electrically isolated superconducting coating due to the extreme level of local Joule heating.

From an applications perspective, the optimum engineering current density (current per unit total cross-sectional area) is achieved by using the metal tape as both substrate and stabilizer. Such a configuration requires electrical connectivity between the HTS layer and the underlying metal substrate by using an intermediate conductive buffer layer structure. On the other hand, if the substrate tape has high resistivity (> 10 μΩ-cm at 77 K) or the buffer layers are insulating, an additional high-conductivity metal stabilizer layer (e.g., Cu or Ag) must be added onto the HTS coating. Presently, all precommercial approaches to coated conductors use low-conductivity Ni-alloy tapes and insulating buffer layers so that an additional layer of copper is laminated onto the superconductor. An envisioned HTS wire architecture would involve the combined use of a strong, high-conductivity Cu-alloy tape substrate and a conductive buffer layer, thereby eliminating the need for additional stabilizing layers. This achievement would not only yield substantial improvement in the engineering critical current density; it would also provide benefits in reduced material cost, absence of substrate ferromagnetism, and increased thermal conductivity when compared with Ni-alloys.

In our previous investigations on the development of conductive buffer layers directly on pure Cu or Ni surfaces, electrical connectivity proved to be a major challenge, mainly because of the poor oxidation resistance and high reactivity/diffusivity of Cu or Ni. A discontinuous insulating oxide layer (i.e., Cu_2O or NiO) usually forms at the metal-substrate interface, either during the growth of conductive buffer layers or after the processing of YBCO films. In this study, we have addressed these issues by using several unique properties of the *fcc* metal Ir as a base buffer, followed by a single buffer layer of $La_{0.7}Sr_{0.3}MnO_3$ (LSMO). This buffer layer combination improves oxidation resistance of the substrate and effectively blocks diffusion of the substrate species into the HTS layer. Iridium is identified as having excellent oxidation and corrosion resistance among platinum group metals, and low oxygen diffusivity. Moreover, its native oxide, IrO_2, under conditions of stability, is characterized by metallic conductivity (bulk resistivity, ρ ~30–100 μΩ-cm) and chemical inertness. These properties make Ir a unique candidate for a conductive interface. LSMO was selected for its electrical conductivity and structural/chemical compatibility with YBCO. In this initial work, we have used Ni-alloy substrates for a proof-of-principle assessment of the feasibility of LSMO/Ir as a conductive buffer interface.

Magnetron sputtering systems with rf and dc sources were used to deposit LSMO and Ir thin films, respectively, on biaxially textured Ni-3at%W (Ni-W) substrates. For Ir film growth, sputtering gas of Ar + 4%H_2 and substrate temperatures in the range of 550 to 650°C were used. Subsequent LSMO deposition was conducted at 625 to 700°C in a mixture of forming gas and 5×10^{-5} Torr of H_2O. For both films, sputter-gas pressure was around 10 mTorr. Film thicknesses were varied from 50 to 500 nm for Ir and 40 to 300 nm for LSMO. YBCO films with thickness in the range of 200 to 1500 nm were grown by PLD; a KrF excimer laser system operated at an energy density of ≈ 2 J/cm^2 was used. Samples were characterized for crystal structure, phase, and texture by XRD. Cross-section examinations of the samples were conducted by a high-resolution TEM equipped with an EDS unit. A standard four-probe technique was used to evaluate the electrical properties, including the temperature-dependent resistivity of the conductive buffer layers, superconducting transition temperature, critical current density, and current-voltage characteristics of the composite structure. Values of critical current density were assigned at a 1-μV/cm criterion.

A typical XRD spectrum for a 1-µm-thick YBCO film deposited on LSMO/Ir/Ni-W is shown in Fig. 2.130. All diffraction peaks are (00*l*) type reflections, indicating *c*-axis growth for each layer. After 1-µm-thick YBCO deposition, there is no evidence of peaks from unwanted insulating NiO or other reactants. This is a significant observation because our previous studies of conductive buffer layers on Ni-based templates always showed some NiO formation at the substrate–buffer-layer interface, even after growth of only 0.2-µm-thick YBCO. It is apparent that this buffer structure effectively blocks diffusion of oxygen inward as well as Ni outward. Further support for this assertion comes from the high-resolution TEM image in Fig. 2.131, showing a cross-sectional view of a 0.2-µm-thick YBCO/LSMO/Ir/Ni-W sample. To clearly identify the interfaces, the sample was tilted away from the [010] Ni-W zone axis along the (001) direction. All interfaces are clean and homogeneous with no intermediate reaction zones

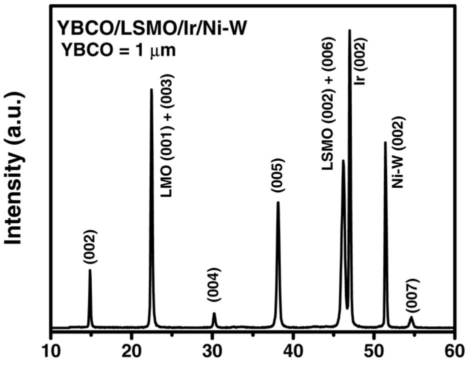

Fig. 2.130. X-ray diffraction θ-2θ pattern of a 1-μm YBCO film on conductive LSMO(40 nm)/Ir(400 nm) buffered, biaxially textured Ni-W substrate.

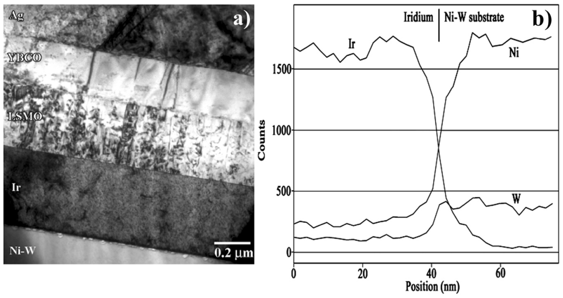

Fig. 2.131. (a) Cross-section TEM bright-field image of the 0.2-μm-thick YBCO/LSMO/Ir/ Ni(W) composite structure showing well-defined interfaces between the layers. (b) High-resolution EDS line scan across the Ir/Ni-W boundary showing undetectable oxygen levels and sharp drop of Ni signal at the interface.

or phases present between the individual layers. More importantly, an EDS line scan (using an electron probe approximately 1.5 nm in diameter) across the boundary between the Ir buffer and Ni-W substrate [Fig. 2.131(b)] confirmed the absence of oxygen within the Ir, Ni-W, or at the interface. Sharp changes of the Ir, Ni, and W signals at the interface also verify that there is no significant intermixing. While Ir has an equiaxed grain structure, both YBCO and LSMO exhibit *c*-axis columnar growth, typical for perovskites, with no secondary phases or porosity. Some porosity is visible at the Ir and Ni-W boundary, although diffraction analysis confirmed that the interface is atomically coherent, and there was no indication of reaction phases that could have been pulled out during the sample preparation. Possibly, the pores result from strain induced by either lattice mismatch or the large difference in thermal expansion coefficient between the Ir layer and the substrate.

The XRD and TEM observations are consistent with measurements of the temperature-dependent resistivity, ρ_{net}-*T* (Fig. 2.132). Here ρ_{net} is calculated from the thickness of the entire structure, assuming a negligible interfacial contact resistance (i.e., $<10^{-8}$ Ω-cm^2). For direct comparison, data for bare Ni-W substrate are also included. The metallic $\rho_{\rm net}$-*T* behavior of the as-deposited conductive LSMO/Ir/Ni-W is indistinguishable from the same structure after deposition of a thick (0.7-µm) YBCO layer. This observation indicates excellent electrical coupling between YBCO-LSMO-Ir-(Ni-W). Presence of a native metal oxide layer at the substrate-buffer interface would likely decouple the HTS layer, which in turn would increase the calculated $\rho_{\rm net}$ of the YBCO/LSMO/Ir/Ni-W by nearly a factor of 300 times the present value. The comparable transition temperature values, in the range of 88 to 89 K for both the 0.2- and 0.7-µm-thick YBCO films, further point to the effectiveness of Ir layers as diffusion barriers to Ni and W because growing thicker films requires longer time at elevated temperatures in the presence of an oxygen ambient. The slightly lower net normal-state resistivity for the Ir coated architectures as compared with that of the Ni-W substrate, along with the sharp decrease observed in $\rho_{\rm net}$ at lower

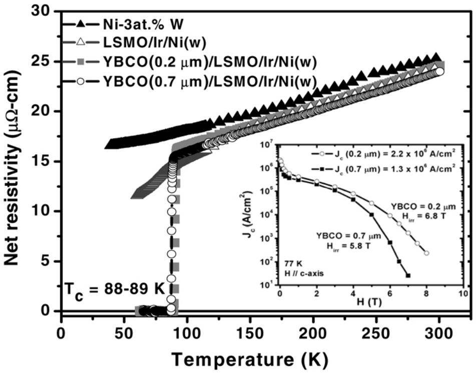

Fig. 2.132. Temperature-dependent net resistivity measurements for 0.2 and 0.7-μm thick YBCO samples grown on conductive LSMO/Ir/Ni-W substrates. For comparison, data for LSMO/Ir/Ni-W and biaxially textured Ni-W substrate is also included. Inset shows the field-dependent transport critical current densities at 77 K for the same YBCO films.

temperatures (< 100 K), is associated with the much lower resistivity [ρ (300 K) = 4.8 μΩ-cm] and larger resistivity ratio of Ir [ρ(273 K)/ρ(77 K) ≈ 7], compared with Ni-W. The inset of Fig. 2.132 shows the transport critical current density at 77 K for the same YBCO films as a function of magnetic field, applied parallel to *c*-axis. Self-field critical-current-density values of 2.2×10^6 A/cm^2 and 1.3×10^6 A/cm^2 were obtained for the 0.2- and 0.7-μm YBCO coatings, respectively. These high critical-current-density values result from the presence of only low-angle grain-to-grain alignments, along with an overall a high-quality YBCO coating, free of cation contamination. However, the decrease of critical current density with increasing YBCO thickness is probably associated with degradation in the microstructure and crystalline orientation of PLD films, as is well documented.

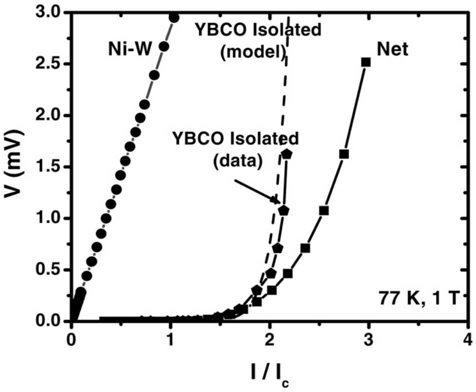

Fig. 2.133. The *I-V* curves obtained from the 0.2-μm-thick YBCO on conductive LSMO/Ir/Ni-W in a field of 1 Tesla and for the bare Ni-W substrate. The figure includes also a model curve with power law *n*=15 and the curve derived for the isolated YBCO film from the actual measurement.

To evaluate the stability provided by the conductive buffer interface, we measured current vs voltage characteristics of YBCO/LSMO/Ir/Ni-W. Tests were conducted on 0.2-μm-thick YBCO films at an applied field of 1 Tesla due to the limitations of our current source. In Fig. 2.133 are displayed three current-voltage curves: for the Ni-W tape only; for a typical isolated HTS coating at 77 K, for 1 Tesla having a power law relation $V \propto (I/I_c)^{15}$; and for the actual sample. The data from the sample agree well with the expected current-voltage curve for the net, combined ideal case of a nonlinear HTS layer and ohmic LSMO/Ir/Ni-W. That is, for an envisioned current surge with $I > I_c$, the total current is partitioned ideally between the YBCO and the substrate (i.e. $I_{tot} = I_{Sub} + I_{HTS}$) via the conductive interface. As a check, we are able to recover the current-voltage behavior of an isolated HTS film by subtracting the expected current through the substrate from the total measured current. The result of this exercise, labeled "model" in Fig. 2.133, is in reasonable agreement with the curve generated from the expected power law relation. Although for the present case of a thin YBCO coating in a magnetic field, electrical stability to an overcurrent of ~3 I_c is provided, the ρ_{net} value of ~15 μΩ-cm is not sufficiently low to provide necessary stabilization for a practical, high-current conductor. As an example, for a YBCO film carrying 100 A/cm-width (a practical current level), in the event of a transient loss of superconductivity, the dissipated heat flux would be ~32 W/cm^2, which is above the critical heat flux of ~10 W/cm^2 for boiling liquid nitrogen. Nevertheless, the present results establish a proof of principle for a conductive buffer stack on a metal substrate and provide motivation for the development of a fully conductive Cu-based RABiTS™, where the metal substrate conductivity is sufficient to provide stabilization. Research is in progress on both the development of textured copper-based substrates and implementation of the Ir-based architecture, which promises high electrical conduction to the substrate combined with an excellent barrier to both oxygen and cation diffusion.

2.22 Characterization of Suitable Buffer Layers on Cu and Cu-Alloy Metal Substrates for Development of Coated Conductors

C. Cantoni, D. K. Christen, E. D. Specht, M. Varela, J. R. Thompson, A. Goyal, Y. Xu, and S. J. Pennycook

We investigated several issues associated with the development of buffer and superconducting layers directly on Cu substrates, including poor Cu oxidation resistance, high Cu thermal expansion, and surface sulphur-mediated buffer layer epitaxy.

The fast Cu oxidation is due to the very high diffusivity of Cu ions through CuO/Cu_2O, and the consequent inability of the native metal oxide to be self-protective (at YBCO processing conditions). This poses stringent requirements on the buffer layers to be used on Cu. Such layers need to block cation and oxygen diffusion more efficiently than the Y_2O_3/YSZ/CeO_2 buffer combination on Ni-W alloy, for which self-passivation of the native oxide at the buffer-substrate interface does occur.

Another concern related to the use of Cu-RABiTS™ is the large strain imposed by the substrate on the YBCO film during cooldown. In fact, the thermal expansion coefficient of Cu can be estimated as $18 \times 10^{-6}\ K^{-1}$ in the temperature region of interest (the same quantity for Ni is $16 \times 10^{-6}\ K^{-1}$). On the sole basis of the difference between Cu and YBCO thermal expansion ($a_{YBCO} = 12 \times 10^{-6}\ K^{-1}$), a residual strain of ~0.45 % in the YBCO film can be calculated. This value is very close to the failure limit of 0.5% for compressive strain, as experimentally derived by bending tests of coated conductors.

Although an ordered sulphur superstructure is necessary on the Cu surface (just as for Ni) to nucleate and grow many cubic oxides, such superstructure cannot be formed on Cu by controlling sulphur adsorption as is done for Ni and Ni alloys. Therefore, the choice of possible buffer layers on Cu is limited to materials that can be grown on a clean *fcc* metal surface.

Among the possible oxides used today in coated-conductor technologies, MgO is certainly a good candidate as a barrier layer for oxygen in buffer layer architectures intended for Cu. Previous ^{18}O transport studies indicate that the oxygen diffusion coefficient of MgO at 800ºC is roughly $10^{-20}\ cm^2/s$, nearly 13 orders of magnitude smaller than that of YSZ at the same temperature. Although MgO is known to grow on clean *fcc* metal surfaces, this layer alone is not a suitable buffer layer due to rapid Cu diffusion. For this reason a seed layer of TiN was introduced as a Cu diffusion barrier between MgO and the metal substrate. TiN is one of the most widely investigated barrier materials in Cu metallization for integrated circuit technology and is structurally compatible with MgO, having the same rock-salt crystal structure and a lattice mismatch of only 0.5%. Further, we found that TiN could be easily grown epitaxially on Cu without the need for a sulphur template. We deposited LMO as a cap layer on MgO for good lattice match and chemical compatibility with YBCO. LMO was selected among other perovskites ($SrTiO_3$, $SrRuO_3$) because of the wide window of deposition conditions for single-oriented (100) films on MgO.

The Cu substrates used for this study include Cu (001) single crystals, Cu (001) epitaxial films deposited on (001) MgO or (001) $SrTiO_3$ (STO) single crystals, {100}<100> textured Cu tapes, and {100}<100> textured Cu-48%Ni-1%Al tapes. All the oxide buffer layers were grown in an ultra high vacuum PLD chamber equipped with a load lock for loading samples and targets, a reflection high-energy electron diffraction (RHEED) system, a residual gas analyzer, and a Kaufman-type ion source for sputter-cleaning. The laser used for ablating target materials was a KrF excimer laser with a power of 150 W and a wavelength of 248 nm. The laser fluence varied between 4 and 5 J/cm^2, and the repetition rate between 10 and 20 Hz.

Fully (100)-oriented, epitaxial TiN films were grown on a TiN target in a nitrogen background pressure of 3.0 to 10×10^{-5} Torr and a substrate temperature of 580°C. The film nucleation and growth were monitored by RHEED, and a cube-on-cube epitaxial relationship was observed between the Cu substrate and TiN film. After a nearly 200-nm-thick TiN film was grown, the nitrogen was pumped out, the substrate temperature was increased to 600°C, and oxygen was introduced in the chamber with a partial pressure of 0.8 to 1.0×10^{-5} Torr for the growth of the MgO layer. In that range of oxygen pressure, the TiN RHEED pattern exhibited spots in addition to those typical of a clean (001) surface. Figure 2.134 shows the RHEED pattern produced by a clean TiN surface and that of a TiN film when exposed to the oxygen pressure and temperature indicated above. The latter suggests the presence of a 6 × 6 superstructure, likely formed by oxygen adatoms bonded on film surface lattice sites. The superstructure was stable at the deposition condition employed for the MgO buffer layer, and fully (001) oriented MgO films could be grown on the surface. Thermodynamic data of free energy of formation for MgO and TiO, indicate higher stability of the former oxide than for the latter. The formation of MgO is thus favored over the formation of TiO, and the O adatoms initially present on the TiN surface at the time the MgO

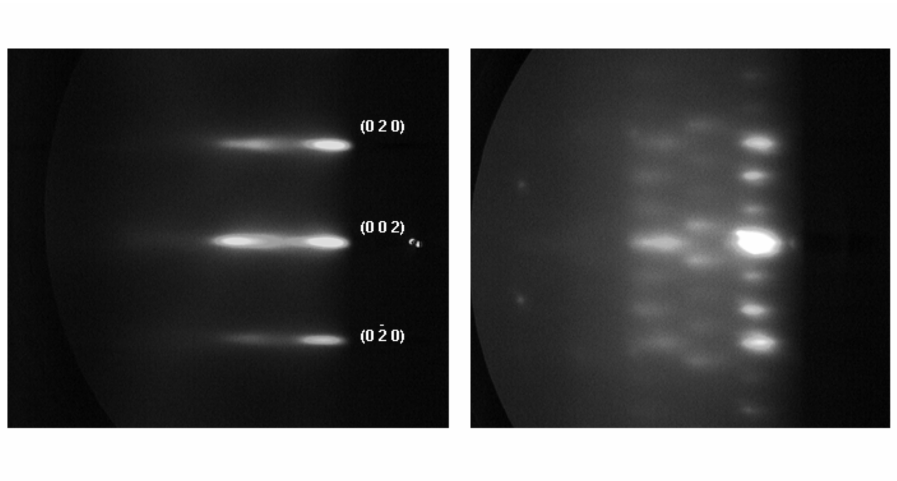

Fig. 2.134. RHEED patterns of an epitaxial TiN film on (001) Cu (left) as deposited in a vacuum background and when exposed to an oxygen partial pressure of 8 × 10^{-6} Torr at a temperature of 600° (right).

deposition starts are likely incorporated in the growing MgO film. Once a 100-nm-thick MgO film was grown, an additional LMO cap layer was deposited in situ at a temperature of 620°C and an H_2O partial pressure of 5 to 8 mTorr.

Figure 2.135 shows the critical current density of a YBCO film grown by PLD on a buffered Cu (001) epitaxial film on MgO single crystal. The critical current was measured by electrical transport as a function of the applied magnetic field at 77 K. The thickness of the laser-ablated YBCO film (180 nm) was measured by RBS, and the corresponding critical current density in self-field was 3.5 MA/cm^2. That value is comparable with those obtained on YBCO films deposited directly on single-crystal STO substrates. The behavior of critical current density in field and the value of irreversibility field (H_{irr} = 7 T) are also typical of YBCO films on STO or LAO single crystals.

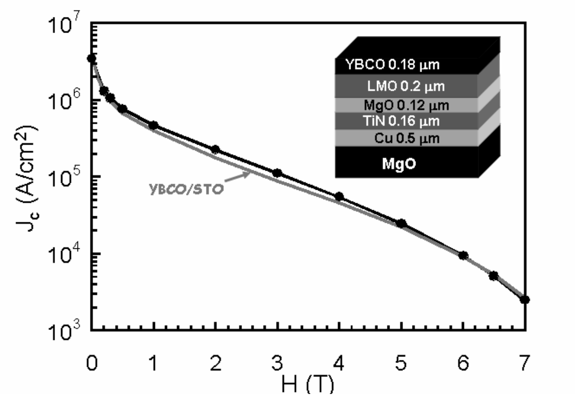

Fig. 2.135. Critical current density vs applied magnetic field for a YBCO film deposited on LMO/MgO/TiN/Cu/MgO(crystal) (black line and dots), and a typical YBCO films deposited on single crystal STO (gray line).

Figure 2.136 shows a low-magnification Z-contrast STEM image of the multilayered structure LMO/MgO/TiN grown on the Cu film on MgO single crystal after deposition of the YBCO top film. All the interfaces appear clean and there is no evidence of reactions or interdiffusion between the different layers. Further, oxygen presence at the Cu/TiN interface was not detected from in situ electron energy loss spectroscopy measurements.

To estimate the actual residual strain induced by the Cu substrate in the superconductor, we deposited the same buffer layer architecture and YBCO film described above on a 1.5-mm-thick Cu crystal. The Cu crystal was nearly a single crystal with a FWHM of 0.28° for the (001) rocking curve, and a [001]-tilt of 1°. The critical current density was derived in this case by measuring the sample magnetic moment hysteresis in a SQUID magnetometer as a function of temperature and field. The observed sharp transition temperature transition and the high critical-current-density value at low temperature (J_c [5 K] = 1.42 × 10^7 A/cm^2) were indicative of absence of weak-links. The critical-current-density value at 77 K and low magnetic field was 1 MA/cm^2. We used high-resolution XRD to measure the lattice parameters of the layers composing the heterostructure. By using (002) and (111) type reflections, we calculated a lattice distortion of $(a\text{-}c)/a$ = -1.31% in the TiN film and 0.04% for MgO. The YBCO lattice constants were evaluated by using (005), (006), and (113) reflections, and the residual strain was estimated to be ε_{zz} = 0.25%. This value is significantly lower than the 0.45% calculated on the basis of differences in thermal expansion, and closer to the residual strain measured on the 50-μm-thick Ni-3%W substrate (0.08%). This result indicates that strain is released by introduction of dislocations within the buffer layers or at their interfaces. An example of this mechanism is illustrated in Fig. 2.137, which shows a high-magnification Z-contrast STEM image of the interface between MgO and LMO. The large lattice mismatch between the two oxides (7.3%) is accommodated in the early stages of film nucleation with the introduction of disorder and misfit dislocations in the very first atomic planes of LMO, leading to virtually unstrained growth of the rest of the film. Another strain-relief mechanism that can occur when stiff and brittle films are deposited on soft and ductile metals is the insertion (and motion) of dislocations in the underlying metal substrate rather than the film.

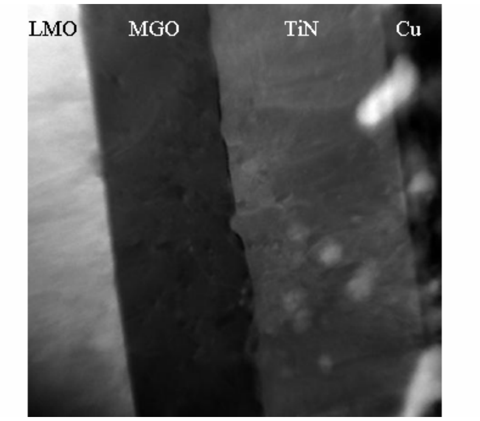

Fig. 2.136. STEM image of a YBCO/LMO/MgO/TiN/Cu multilayer structure on MgO single crystal acquired with high-angle annular dark field detector. This technique provides direct compositional contrast, and the heavier elements appear brighter.

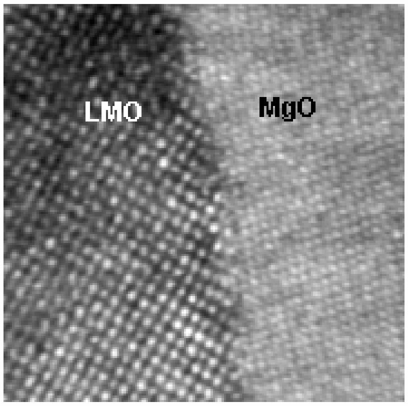

Fig. 2.137. High-resolution STEM micrograph of the LMO/MgO interface.

To complete our study we grew the LMO/MgO/TiN buffer layer heterostructure and the YBCO film on 99.99% pure Cu tapes that were thermomechanically processed to obtain a biaxial texture with XRD FWHMs of 6° and 5° for the in-plane and out-of-plane alignment. In this case, the magnetically determined critical current density at 77 K and low magnetic field was 0.7 MA/cm^2, corresponding to a transport critical current density of nearly 1.5 MA/cm^2. Although this is a very encouraging value, it is not consistent with the optimal degree of texture of the buffered substrate, which, according to previous studies on the dependence of transport critical current density on grain boundary distribution in coated conductors, should correspond to 2.5 MA/cm^2. These samples also showed a lower transition temperature (T_c = 88.5 K) than typical YBCO films on coated conductors, which suggests the possibility of chemical contamination of the YBCO film by outward Cu diffusion. SEM measurements were consistent with this hypothesis and in particular showed sparse Cu_2O outgrowths in the form of big particles and, sometimes, straight lines aligned with the substrate rolling direction. We attributed the formation of these outgrowths to oxidation that occurs during the YBCO deposition on the unprotected back side and edges of the substrate, and that propagates toward the front. Outgrowths form preferentially in correspondence to defects, such as pin holes or scratches, introduced on the substrate surface during the rolling process. EDX measurements performed before and after subsequent high-temperature vacuum anneals on TiN/Cu bilayers deposited on 7° STO bicrystals indicated no detectable Cu diffusion through the TiN grain boundary. This experiment suggests that the occurrence of the Cu_2O outgrowths is not related to the presence of a low-angle grain boundary in the textured substrate. No such Cu_2O eruptions were in fact observed along the Cu substrate grain boundaries, whose traces are still visible through the YBCO film.

One of the possible ways to avoid oxidation from the back side is to alloy Cu with a more oxidation-resistant metal. We investigated the performance of nonmagnetic Cu-48%Ni with 1–1.5% Al using the same buffer layer architecture used on pure Cu and a 0.3-μm-thick YBCO film grown by PLD. The small percentage of Al in the substrate is very effective in passivating the CuNi alloy, which otherwise can oxidize nearly as fast as pure Cu. Passivation occurs by formation of a thin Al_2O_3 surface layer at extremely low oxygen partial pressure. The layer is very desirable for protecting the back side but is not a suitable template for well-oriented buffer or superconducting layers. Therefore, the Al_2O_3 layer that had formed on the substrate front surface during the texturing anneal was removed by ion sputtering prior to the deposition of the seed layer. Although the TiN deposition occurs without introduction of oxygen in the deposition chamber, the Al present in the substrate can readily diffuse up to the surface at temperatures greater than 400°C and oxidizes in the presence of residual background oxygen, thus corrupting the buffer layer epitaxy. This problem was avoided by depositing an initial 100-Å-thick TiN layer at 400 °C. The cube epitaxial growth, which does not normally occur at such low temperature, was achieved by locally increasing the energy of the impinging species with a 400- to 500-eV Ar^+ ion beam.

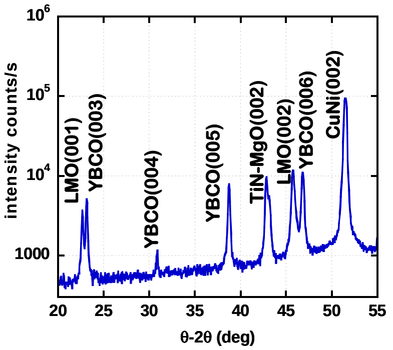

Fig. 2.138. θ–2θ XRD scan of a YBCO/LMO/MgO/TIN/CuNiAl sample.

The rest of the TiN film and the subsequent buffer layers were deposited at the conditions used for pure Cu substrates. Figure 2.138 shows the XRD θ-2θ pattern acquired on a YBCO/LMO/MgO/TiN/

CuNiAl sample that showed a transport critical current density of 2 MA/cm^2. Only YBCO and substrate peaks are present, and there is no evidence of unwanted oxide peaks. Four-circle diffractometer measurements revealed optimal alignment of the YBCO film with a FWHM of 2.8° for the out-of-plane texture (in the rolling direction) and 6.5° for the in-plane texture.

In conclusion, we have shown that a multilayered structure consisting of LMO/MgO/TiN acts as a good diffusion barrier and structural template for the deposition of high-critical-current-density YBCO film on pure Cu and Cu alloy substrates. Each of the three buffer layers has a unique property that is essential to suppress Cu oxidation, keep the interfaces clean, and accommodate strain. TiN is a barrier to outward Cu diffusion. MgO is a barrier to inward oxygen diffusion and is stable enough thermodynamically to be grown on TiN. LMO provides structural compatibility with the YBCO lattice.

2.23 Electrical and Magnetic Properties of Conductive Cu-Based Coated Conductors

T. Aytug, M. Paranthaman, A. Goyal, N. Rutter, H. Y. Zhai, A. A. Gapud, and D. K Christen (ORNL); J. R. Thompson and A. O. Ijaduola (University of Tennessee)

For the effective implementation of coated conductors at cryogenic temperatures (~30–77 K), stabilization against thermal runaway will be required in the event of an overcurrent situation (exceeding critical current of the HTS coating). In general, a coated conductor architecture involves epitaxial fabrication of a thin layer (1–2 µm) of HTS film (usually YBCO) on biaxially textured buffer layers deposited on a thick (50-µm) flexible metal substrate (Ni or dilute Ni-alloys). Thus, additional stabilization by electrical connection to a good conductor is required for insulating buffer layers and resistive Ni-alloy substrates (> 10 µΩ-cm at 77 K). A solution is to electrically shunt the HTS layer, either by an intermediate conductive buffer layer to a low-resistive metal substrate (i.e., Ni or Cu) or by depositing a stabilizing metallic cap layer (i.e., Cu or Ag) onto the HTS coating. While a conductive buffer provides an effective solution only when the substrate material is highly conductive, it is the most desirable approach from an applications perspective since it would yield the optimum engineering current density (critical current per unit total cross-sectional area). Coupling the HTS layer adequately to a pure Ni or Cu tape through a conductive-buffer layer also provides an overall less complicated structure with reduced resistance and an increased thermal conductivity, providing more efficient heat transfer to either a coolant bath or through the thermal diffusivity of the system.

To date, many reports on using the RABiTS™ technique for coated conductor fabrication have utilized high-purity Ni (99.99%) and strengthened Ni-alloy as the base, textured material. However, the ferromagnetism of pure Ni and Ni-alloy hinders their use in applications requiring time-varying (ac) currents due to hysteretic energy losses. On the other hand, Cu is a lower-cost, lower-resistivity and nonmagnetic alternative for the production of long RABiTS™-based coated conductor tapes. Recently, we have demonstrated the growth of electrically well-coupled YBCO films on conductive $SrRuO_3/LaNiO_3$ bilayer and $La_{0.7}Sr_{0.3}MnO_3$ (LSMO) single-layer buffer structures deposited on biaxially textured Ni tapes. Although recent progress has been made in the development of nonconductive, protective buffer architecture, there have been no reports on the development of conductive buffer layers on pure Cu substrates for coated conductor applications. Because of its electrical conductivity, thermal stability, and structural compatibility with YBCO; we have investigated the viability of LSMO as a conductive buffer interface on biaxially textured Cu substrates. Here, we demonstrate the fabrication of electrically connected high-critical-current ($> 2 \times 10^6$ A/cm^2 at 77 K) YBCO coatings on Cu tapes. The electrical, superconducting, and magnetic (hysteretic loss) properties of these short prototype conductors are reported.

Cube-textured [{100}(100)] Cu substrates of 50-μm thickness were obtained from randomly oriented, high-purity (99.99%) Cu bars by cold-rolling, followed by an anneal in vacuum at 800°C for 1 h. To minimize Cu diffusion and to reduce the oxidation rate of the substrate, first a protective Ni overlayer (1.6 μm) was deposited by dc-magnetron sputtering at a temperature of 600°C in a reducing atmosphere of forming gas (96%Ar + 4%H_2). Subsequent growth of the LSMO buffer was conducted by rf-magnetron sputtering in a mixture of forming gas and 2×10^{-5} Torr of H_2O, with the substrate temperature at 550 to 625°C. These conditions have solved the slight Sr contamination that we have observed in earlier work of LSMO on Ni. The YBCO films were grown at 780°C in 120 mTorr of O_2 by PLD) by using a KrF excimer laser system operated at an energy density of ≈2 J/cm^2. For these research samples, typical thicknesses of the LSMO and the YBCO films were 300 and 200 nm, respectively. The crystallographic orientation and texture of the films were characterized by XRD. A standard four-probe technique was used to evaluate the electrical properties, including the temperature-dependent resistivity of the conductive buffer layers, superconducting transition temperature, critical current density, and current-voltage characteristics of the composite structure. Critical-current-density values were assigned at a 1-μV/cm criterion. The magnetic properties of the samples were measured in a SQUID-based magnetometer at a temperature of 95 K, in fields up to 800 Oe applied parallel to the tape plane.

Figure 2.139 shows the critical current density performance of a YBCO film deposited on an LSMO/Ni/Cu substrate as a function of magnetic field measured at the boiling and near-triple-point temperatures of liquid nitrogen with the field applied parallel to *c*-axis. The sample has a transition temperature greater than 90 K, indicating YBCO free of cation contamination. At 77 K, the zero-field transport critical current density is 2.3×10^6 A/cm^2, and the irreversibility field is high, near 7 T. At 65 K, the critical current density is 4.8×10^6 A/cm^2 and remains around 1×10^6 A/cm^2 at 3 T, which is highly desirable for applications such as motors, generators and energy storage requiring field strengths of several Tesla. The high critical-current-density values could be obtained primarily due to the excellent texture, with low-angle grain-to-grain correlations dominating the entire sample and an overall high degree of in-plane (Δϕ) and out-of-plane (Δω) alignment. In fact, the measured XRD FWHM widths Δϕ and Δω of the average total ensemble of grains are sharp; 7° and 6.5° for YBCO, 6° and 5° for underlying Cu substrate, respectively. It is clear from the inset of Fig. 2.139, which shows the

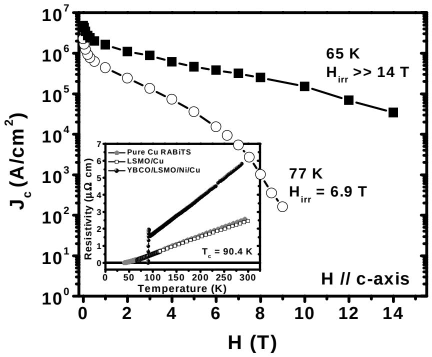

Fig. 2.139. Magnetic field dependence of critical-current-density curves measured at 65 and 77 K, for a YBCO film on the conducting buffer structure of LSMO/Ni/Cu. The inset shows the temperature-dependent net resistivity of the same YBCO sample, as well as the data for LSMO/Cu and for a pure biaxially textured Cu substrate.

temperature-dependent four-point resistivity measurements, that there is excellent electrical coupling between the Cu substrate and the LSMO layer, as evidenced by the similar ρ_{net}-T behaviors. However, after the YBCO deposition, ρ_{net}-T characteristics of the sample deviates from the ideal behavior, indicating somewhat degraded metallic connectivity, most likely resulting from the presence of discontinuous NiO regions (detected from the XRD analysis) at the LSMO-Ni interface. In fact, our model calculations showed that the observed increase in ρ_{net} at the superconducting transition can be associated with a significant interfacial contact resistance between the YBCO film and the Cu substrate. On the other hand, complete isolation of YBCO from the substrate would yield a ρ_{net} (calculated for the entire structure) that is 2×10^4 times higher than the present value of ρ (2 $\mu\Omega$-cm) at the transition regime. The observed value is low enough to provide significant stabilization for the current levels of the present structure.

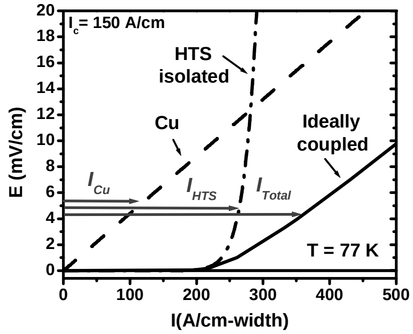

Fig. 2.140. Ideal current vs electric field characteristics for a model conductor architecture. Data for Cu, electrically isolated HTS, and the same HTS layer electrically connected to the underlying Cu substrate are compared. Arrows indicate the current sharing among layers for a specific electric field criterion.

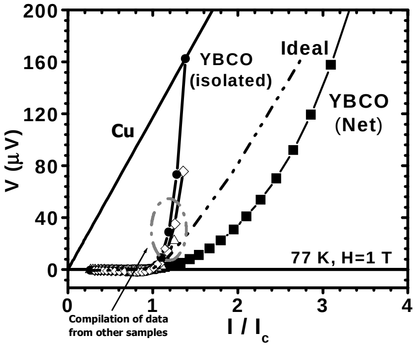

Fig. 2.141. The *I-V* curves obtained from the actual sample in a field of 1 Tesla. The figure includes curves for Cu, isolated YBCO films, and data from the YBCO/LSMO/Ni/Cu sample. The dashed line displays the response if there were a complete electrical coupling.

Next we compare in Fig. 2.140 the current-voltage characteristics at 77 K of a model, ideally coupled conductor architecture (HTS + conductive buffer + substrate) with experimental results from the actual sample in Fig. 2.141. Figure 2.140 (model) plots current vs electric field (voltage/distance between voltage taps) curves for the Cu tape only, for the isolated HTS coating with a critical current of 150 A/cm-width (practical level of operating current), and for the combined ideal case, in which the HTS layer and Cu are electrically connected through an intermediate conductive buffer layer. The interfacial contact resistance is assumed to be negligible (i.e., $<10^{-8}$ Ω-cm^2).The typical nonlinear I-E behavior for the isolated HTS layer has a power law relation $E \propto (I/I_c)^n$. For $I > I_c$, the ideal case exhibits a near-linear differential ohmic behavior, with slope determined by the metal tape resistivity. Then, for an envisioned transient with $I > I_c$, the total current through the conductor partitions between the HTS layer and the metal tape, greatly reducing the power excursion in the entire structure. The current-voltage curves obtained from our actual sample are displayed in Fig. 2.141. While the scales are quantitatively different, qualitatively we observe similar characteristic compared to the model conductor, although the interfacial resistivity is nonnegligible, as noted above. In order to check the stabilization provided by the metal tape and to push the current to levels greater than the critical current, we recorded the data at 1 Tesla and compared that with the data compiled from three other isolated YBCO films having similar power-law behaviors. While the results exhibit similar current-voltage characteristics for bare Cu and isolated HTS film (compared with Fig. 2.140), data obtained from the actual sample do not agree quantitatively with the ideal behavior (dashed curve). This may be explained by the inhomogeneous electrical coupling and current transfer between the YBCO and the Cu substrate, possibly due to the formation of a discontinuous NiO layer at the interface. Nevertheless, were there a complete isolation, the superconductor would have been destroyed at current levels,

$I = 3 \times I_c$ (see Fig. 2.141). Currently, we are trying to improve the electrical coupling and implement a detection mechanism that will monitor voltage across the metal tape.

To determine the potential ferromagnetic ac loss due to the Ni diffusion barrier, we measured the hysteretic magnetic properties of a fully formed coated conductor at 95 K, just above the superconductive transition temperature. For these Ni materials, the loss properties change little below 95 K. The quasistatic studies were performed on a sample of mass 9.6 g, with the dc magnetic field oriented parallel to the plane of the tape. This configuration approximates the self-field on the substrate due to current flow in a tape and minimizes demagnetization effects. After cooling to 95 K in zero applied field, the hysteretic magnetization loop was measured by sweeping the field from $+H_{max}$ to $-H_{max}$ to $+H_{max}$ in small steps. A numerical integration of the area inside the loop $M(H)$ provides $W = \oint M(H)d(H)$, the ferromagnetic energy loss per cycle, with maximum magnetic field (H_{max}). The measurements were repeated as a function of H_{max} up to 800 Oe, since the ferromagnetic loss increases with ac field amplitude, which is proportional to the peak ac current. The resulting ferromagnetic loss (W) per cycle per gram of tape is shown in Fig. 2.142 as a function of H_{max}. The inset of this figure shows the magnetization of the sample for several field excursions. At $H_{max} = \pm 800$ Oe, the loss has nearly saturated at approximately 180 erg/g of tape per cycle. The calculated maximum hysteretic ac ferromagnetic loss at 60 Hz for a 50-μm-thick, 1 m × 1cm tape would be 5.5 mW, compared with 43 mW for the biaxially textured all-Ni RABiTS™ and 8.4 mW for a magnetically reduced Ni–5at%W tape. These ferromagnetic losses of 5 to 9 mW correspond to modest additions (10–20%) to the energy losses expected in an HTS coating of achievable YBCO-based conductors. As an example, for an envisioned coated conductor architecture operating at $I_0 = I_c$ of 200 A/cm-width, applying the Norris theory, which is shown to provide a good estimate of ac loss for YBCO-based conductors, the power loss per meter per cycle is, $L_c = (\mu_o / 2\pi)I_o^2 = 480$ mW at 60 Hz. For more realistic operation at $I_o = I_c/2$, in which case the loss is smaller by a factor of 17, the superconductive hysteretic loss component yields a value of $L_c \sim 28$ mW. Obviously, further reducing the total energy loss would be possible by either reducing the thickness of Ni or completely replacing the Ni film with a functional nonmagnetic metal layer. Similarly, the hysteretic loss in HTS can also be decreased by producing conductors with higher critical current that can operate at smaller I_o/I_c, or possibly by geometrical optimization such as subdividing the tape into noninteracting conductors.

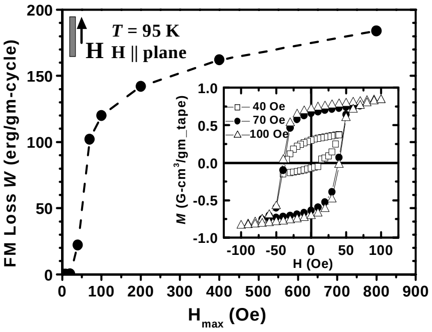

Fig. 2.142. Ferromagnetic hysteretic loss, *W*, due to the Ni layer in YBCO/LSMO/Ni/Cu. First, *W* increases rapidly with H_{max}, then saturates. The inset shows the magnetization loops for the same sample at $T = 95$ K, for various H_{max} excursions, where the field is applied parallel to the plane of the tape.

This work shows the development of a conductive coated conductor architecture on biaxially textured Cu tapes having a layer sequence of YBCO/LSMO/Ni/Cu. A self-field critical current density (77 K) value exceeding 2×10^6 A/cm^2 was achieved, and electrical characterization suggests good electrical coupling between the YBCO and the Cu substrate. Assessment of the magnetic loss associated with the Ni overlayer shows that it should be small compared with the hysteretic loss in an operational superconductive coating. Although these initial studies were conducted on pure copper, the ultimate implementation will require strengthened tape. In principle, this can be achieved by appropriate alloying and precipitation hardening, which will also retain high electrical conductivity of the tape.

2.24 Simultaneous Inductive Determination of Grain And Intergrain Critical Current Densities of YBCO Coated Conductors

A. Palau, T. Puig, and X. Obradors (Institut de Ciència de Materials de Barcelona); E. Pardo, C. Navau, and A. Sanchez (Universitat Autònoma de Barcelona); A. Usoskin and H. C. Freyhardt (Zentrum fur Funktion Wekstoffe, Göttingen); L. Fernández and B. Holzapfel (IFW Dresden); R. Feenstra (ORNL)

Magneto-optic flux imaging and transport measurements have demonstrated that the supercurrent flow in coated conductors is of a percolative nature through a network of low-angle grain boundaries. As a result, for certain magnetic field histories, complex flux patterns of currents circulating within the grains and currents crossing grain boundaries may arise. Some attempts have been made to develop noninvasive experimental methodologies to determine the intergrain critical current density associated with the grain boundary network, J_c^{GB}, and the intragrain critical current density, J_c^G. Here we present an inductive methodology that is suitable for calculating J_c^{GB} and J_c^G of a single conductor from a set of hysteresis loops. This method is based on the anomalous behavior of the hysteresis loops in coated conductors and reflects the effect of superimposed fields in the grain boundaries from circulating currents within the grains.

A number of high-quality IBAD and RABiTS™ coated conductors from different laboratories have been analyzed. A YBCO–IBAD sample, IBAD-a, is a 1-µm-thick YBCO film grown by a high-rate PLD process, on an IBAD–YSZ/Ni–Cr stainless steel substrate. Additionally, two RABiTS™ samples have also been analyzed: RABiTS™-a is an 800-nm YBCO film deposited by PLD on a YSZ/CeO_2 /Ni–0.1%Mn tape, and RABiTS™-b is a 1-µm -thick YBCO film grown by a BaF_2 ex situ process that uses evaporated precursors on a CeO_2/YSZ/Y_2O_3/Ni/Ni–3%W tape. Zero-field cooled magnetic measurements were carried out with a standard SQUID magnetometer equipped with a 5.5-T superconducting coil on samples of 5 × 5 mm^2. Subtraction of the substrate magnetic signal was required in all cases.

The right-hand side inset of Fig. 2.143 shows a typical hysteresis loop for RABiTS™-b after substrate subtraction for a maximum applied field (H_m=5000 Oe at 5 K). The hysteresis loop appears to be anomalous with a maximum on the reverse branch of the magnetization at an applied field of $H_a \cong 2300$ Oe, instead of at $H_a \cong 0$ as expected for an epitaxial film on single-crystal substrate (see also the result for a 230-nm thin film in the inset of Fig. 2.143). A maximum in the reverse magnetization at $H_a > 0$ has been observed earlier ascribed to granularity effects and was explained by the same mechanism as that of the hysteretic behavior of critical current density in transport measurements. As the magnetic field is ramped up, flux enters the material and gets pinned into the grains. Subsequent decrease of the magnetic field results in a reverse magnetic field component through the grain boundaries due to the flux lines trapped in the superconducting grains. Thus, the local magnetic field at the grain boundary, $H_{\mathrm{loc}}^{\mathrm{GB}}$, results from the vectorial sum of the applied magnetic field, H_a, and the return field coming from each grain that contributes at the boundary, H_{return} (see upper left-hand side inset of Fig. 2.143), $H_{\mathrm{loc}}^{\mathrm{GB}}=H_a-H_{\mathrm{return}}$. In this work, $H_{\mathrm{loc}}^{\mathrm{GB}}$ has been considered to be uniform over the sample because the contribution of the self-magnetic field arising from the percolating intergrain critical current density can be neglected in thin-film materials, as it has been evidenced by critical-state model calculations for this particular

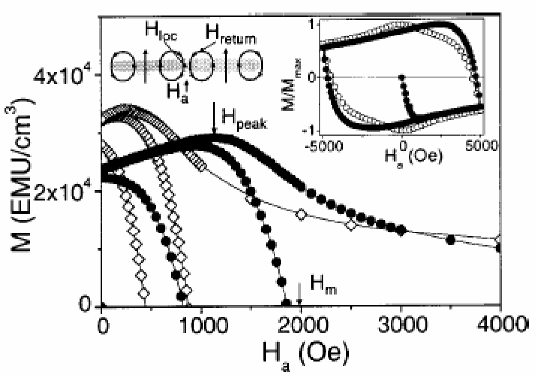

• RABiTS™-b for H_m = 1000, 2000, and 3000 Oe.

◊ IBAD-a for H_m = 600, 1000, and 5000 Oe.

Fig. 2.143. Magnetic hysteresis loops at 50 K. Left inset: schematic of magnetic fields at a grain boundary. Right inset: *M*(*H*) curve at 5 K for H_m = 5000 Oe for RABiTS™-b (•) and YBCO film (◊).

geometry. Therefore, when $H_{\mathrm{loc}}^{\mathrm{GB}}=0$, the magnetization peaks and $H_{\mathrm{peak}}\sim H_{\mathrm{return}}$. Magnetization measurements are then a very powerful method to infer the granularity effects of coated conductors.

Figure 2.143 shows hysteresis loops at different H_m for IBAD-a and RABiTS™-b at 50 K. It is confirmed that both types of coated conductor samples display the maximum in the reverse magnetization at $H_a>0$. How-ever, the magnetization of both samples peaks at different H_{peak}, and this peak evolves differently with increasing H_m. The inset of Fig. 2.144 shows H_{peak} as a function of H_m for the three samples analyzed, IBAD-a, RABiTS™-a, and RABiTS™-b at 50 K. Clearly, H_{peak} increases for low values of H_m and then it saturates. The values of both the saturation field, H_m^{sat}, and the peak saturation field, $H_{\mathrm{peak}}^{\mathrm{sat}}$, are characteristic of each type of coated conductor.

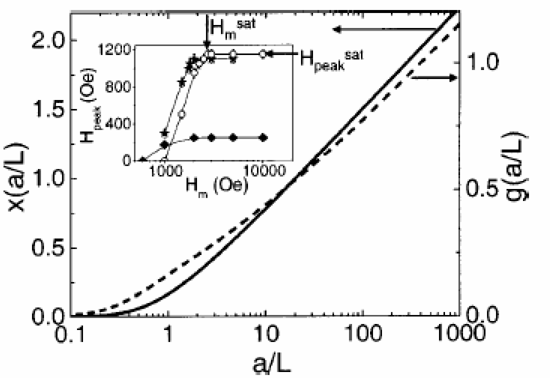

Fig. 2.144. Numerically calculated dimensionless factors *g* and *x* as a function of *a*/*L*. Inset: H_{peak} as a function of H_m at 50 K for IBAD-a (♦)RABiTS™-a (★), and RABiTS™-b (○). Also indicated are the $H_{\mathrm{sat}}^{\mathrm{peak}}$ and H_{sat}^{m} values for the RABiTS™-b sample.

The relation $H_{\mathrm{peak}}\sim H_{\mathrm{return}}$ establishes that (i) $H_{\mathrm{peak}}^{\mathrm{sat}}$ is reached when the grain magnetization saturates; thus $H_{\mathrm{peak}}^{\mathrm{sat}}(T)\sim H_{\mathrm{return}}^{\max}(T)$, and (ii) H_m^{sat} is a measure of the magnetic field required to saturate the grains (i.e., $H_m^{\mathrm{sat}}(T)\sim 2H_G^*(T)$, where H_G^* is the full penetration field of the grains). Therefore, by using the experimental values, $H_{\mathrm{peak}}^{\mathrm{sat}}(T)$ and $H_m^{\mathrm{sat}}(T)$, we will be able to determine the grain critical current density, J_c^G, and the grain size if the relations $J_c^G(H_{\mathrm{return}})$ and $J_c^G(H_G^*)$ are known.

We have calculated the return field for saturated cylinders with constant critical current density (Bean critical-state model), assuming that two isolated adjacent grains (zero separation) contribute to the return field at the grain boundary. Calculations have been derived for cylinders of different aspect ratios, *a*/*L* (*a*=cylinder radius and *L*=cylinder thickness), to emulate the grains composing IBAD and RABiTS™ coated conductors. Using a numerical simulation based on energy minimization in the Bean critical-state model, we have then also determined the full penetration field for isolated cylindrical grains of different aspect ratios. The two equations obtained are

$$J_c^{\,G}=\frac{10}{4\pi}\frac{H_{return}^{\max}}{xL}\sim\frac{10}{4\pi}\frac{H_{peak}^{sat}}{xL}, \tag{20}$$

$$J_c^{\,G}=\frac{10}{4\pi}\frac{H_G^*}{na}\sim\frac{10}{4\pi}\frac{H_m^{sat}}{2na}, \tag{21}$$

where *x* and *n* are numerically calculated dimensionless factors depending on the ratio *a*/*L*. These equations, derived for isolated cylindrical grains, do not need to be corrected for any component of the intergranular self-field for thin-film samples. Therefore, combining Eqs. (20) and (21) we obtain the relation, $(H_{\mathrm{peak}}^{\mathrm{sat}}/H_m^{\mathrm{sat}})=(x/2n)/(a/L)=g(a/L)$, which can be used to estimate the average grain size by means of the function $g(a/L)$ shown in Fig. 2.144, and the experimental value $H_{\mathrm{peak}}^{\mathrm{sat}}/H_m^{\mathrm{sat}}$. For all IBAD and RABiTS samples analyzed the grain size obtained is indeed temperature independent (see the upper inset of Fig. 2.145). The average grain radius, *a*, obtained for IBAD-a sample is ~1.7 μm, while the RABiTS™-a and RABiTS™-b samples gave average grain radius of ~20 and ~12 μm, respectively. The obtained grain radius, *a*, for both IBAD and RABiTS™ coated conductors are consistent with the structural grains determined by TEM and electron backscattered diffraction.

The determination of the aspect ratio *a*/*L* enables us to estimate J_c^G using the $x(a/L)$ dependence shown in Fig. 2.144 and Eq. (20). Results are presented in Fig. 2.145 (open symbols). Values for J_c^G are

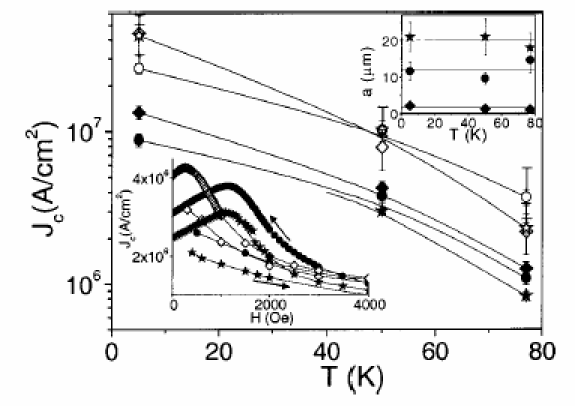

Fig. 2.145. Temperature dependence of J_c^{GB} (closed symbols) and J_c^G (open symbols) for IBAD-a (♦), RABiTS™-a (★), and RABiTS™-b (•). Lower inset: magnetic field dependence and hysteretic behavior of $J_c^{GB}(H)$ IBAD-a (♦), RABiTS™-a (★), and RABiTS™-b (•) at 50 K and H_m = 5000 Oe. Upper inset: temperature dependence of the average train radius obtained for three samples: IBAD-a with ‹a› = 1.7 μm, (♦), RABiTS™-a with ‹a› = 20 μm (★), and RABiTS™-b with ‹a› = 12 μm (•).

in the expected range of YBCO thin films. However, RABiTS™-b sample, grown by the BaF_2 ex situ process, displays a slightly less sensitive temperature dependence than the other samples grown by PLD. This feature deserves further investigation because it could indicate that different pinning mechanisms are relevant in these films.

Positive errors bars have been introduced in the J_c^G values in order to consider that J_c^G has been calculated at $H_{\mathrm{peak}}^{\mathrm{sat}}$, where we have determined H_{return} from the grains. The decrease in J_c from H_a=0 to $H_{\mathrm{peak}}^{\mathrm{sat}}$ has been estimated from results of thin films.

On the other hand, the hysteresis loop measurements for $H_m > 2H_S^*$, where H_S^* is the full penetration field of the sample, allow us to determine the percolating intergrain critical current density, J_c^{GB}. The total measured magnetic moment, $m \sim m^{GB}$, where m^{GB} is the magnetic moment of the intergranular part, because the magnetic moment of the grains is $m^G < 10^{-2}$–10^{-3} m in all the samples. This indicates that the large current loops of the intergrain percolating currents generate a larger magnetic moment than the grain current loops associated with J_c^G. Thus, it can be considered that the measured magnetic moments of the $m(H)$ cycles solely correspond to the magnetic moment of the intergranular component, though strongly influenced by the return field of the grains. Then, the temperature dependence of J_c^{GB} at $H_{\mathrm{loc}}^{GB}\sim 0$ can be calculated from the equation, $J_c^{GB}=(30m/R_sV_s)$, where m is the value of the magnetic moment at the peak, and R_s and V_s are the total sample radius and volume, respectively. Results are shown in Fig. 2.145 (closed symbols) for the three samples. The $J_c^{GB}(T)$ values for the IBAD and RABiTS™ samples are just two to four times smaller than the corresponding $J_c^G(T)$, indicating that these coated conductors are of very high quality.

Finally, by applying the same equation, $J_c^{GB}=(30m/R_sV_s)$, to both the initial and reverse branches of the $m(H)$ curve, we have determined the magnetic field dependence of J_c^{GB} and the associated hysteretic behavior responsible for the anomalous hysteresis loops (see lower inset of Fig. 2.145). Therefore, we encounter now by inductive magnetic measurements, the hysteretic behavior of $J_c^{GB}(H)$ reported earlier from transport measurements.

In conclusion, we have demonstrated that solely from magnetic hysteresis loops measured at different maximum applied magnetic fields, we are able to determine simultaneously the grain and intergrain critical current densities of IBAD and RABiTS™ coated conductors. The simplicity of the method paves the way to a full investigation of the relationship between granularity and vortex pinning effects. This inductive contactless methodology is based on the anomalous behavior of the hysteresis loops of high-critical-current granular materials, induced by the return field from the grains into the grain boundaries. Numerical calculations determining the return field and full penetration field of saturated finite grains in the Bean critical-state model have been required in order to properly quantify the grain critical current and give relevant evidence for grain size structure of both types of conductors.

2.25 Magnetism and Ferromagnetic Loss in Ni-W Textured Substrates for Coated Conductors

A. O. Ijaduola, J. R. Thompson (University of Tennessee), A. Goyal (ORNL), C. Thieme (AMSC), and K. Marken (OST)

2.25.1 Introduction

High-temperature superconductors are fascinating materials with great fundamental interest and significant technological potential, one of which is the development of tapes and cables for low-loss conduction of high-density electric currents. However, problems arising from the "weak-link" intergrain current transport have led to the development of different methods for their fabrication. The RABiTS™ [1–3], IBAD [4–7] and the ISD [8,9] methods are the most recent methods being used to create a substrate on which a highly textured HTS with low angle grain boundaries can conduct large intergrain currents. The Ni-W alloys studied in this work are well suited as the base material for RABiTS™ applications.

Nickel, which is more amenable to the thermomechanical processing that produces biaxial texturing, was initially used for RABiTS™ conductors. However, its ferromagnetism, with a Curie temperature of 627 K and a saturation magnetization of 57.5 emu/g at $T = 0$, is considered undesirable. Moreover, its use in ac applications can lead to high hysteretic losses that add to the usual ac losses in the superconductor. Consequently, suitable alloys with reduced ferromagnetism need to be developed. In earlier work, we investigated certain magnetic properties of a series of Ni-Cr materials that were biaxially textured.[10]. This present work deals more extensively with the Ni-W alloy series, highlighting their magnetic properties. The Ni-W materials are particularly interesting and desirable because they facilitate the subsequent deposition of epitaxial buffer layers by the presence of a thin nickel tungstate surface layer, which inhibits oxidation and interdiffusion. These advantages, together with greatly increased strength, have led at least two commercial manufacturers to adopt Ni-W materials for use in production of prototype coated conductors.

2.25.2 Experimental Details

$Ni_{1-x}W_x$ materials with nominal compositions $x = 0, 3, 5, 6$, and 9 at. % W were used. The alloys were formed by either vacuum-melting or powder metallurgy methods. The starting alloys were then subjected to thermomechanical processing (a series of rolling deformations and heat treatment) to produce the desired {100}<100> biaxial texturing. In the final step, the alloys were recrystallized by annealing at temperatures near 1000°C for the vacuum-cast materials and 1300°C for the powder metallurgy alloys; the maximum temperature is limited by the need to avoid secondary recrystallization, which destroys the desired biaxial texturing.

For the magnetic studies, a sample of tape, with typical dimensions of 3 to 3.5 mm × 3.5 to 4 mm and thickness of 50 to 75 μm, was mounted in a SQUID-based magnetometer, either a Quantum Design model MPMS-7 or a model XL with ac capabilities. The tape was vertical with the magnetic field applied parallel to the sample's surface in order to minimize demagnetizing effects. Temperatures ranged from 5 K to 375 K in fields up to 50 kOe. We measured both the isothermal mass magnetization $M(H)$ at different fixed temperatures and $M(T)$ in fixed field. For the ferromagnetic loss studies, we measured one complete loop of the dc magnetization $M(H)$, starting from field $+H_{\max}$ and sweeping to field $-H_{\max}$, then back to field $+H_{\max}$. This process was repeated at progressively higher field amplitudes $H_{\max}$ in the range 5 to 800 Oe. For example, in a 100-Oe cycle, ($H_{\max} = 100$ Oe) the sample was first "exercised" by applying a magnetic field $H = +100$ Oe, –100 Oe, +100 Oe and –100 Oe, which simulates several cycles of ac field in an application and establishes the steady state ferromagnetic response. Then the loop $M(H)$ (in units of G cm^3/g) was measured, sweeping the field in small increments from +100 Oe to –100 Oe and back to + 100 Oe. In any conductor configuration, the field excursion $H_{\max}$ will increase with the amplitude of the ac current, with a geometry-dependent proportionality [11]. Measurements of ferromagnetic loss were done at $T = 50$ K and 77 K.

In some cases, the ac magnetization was measured to determine whether the ferromagnetic loss per cycle depended on frequency. Frequencies ranged from 2.5 to 600 Hz, with ac field amplitudes h_{ac} up to 6.8 Oe-peak. In one case, a bias dc field was applied parallel to the ac field to assess its influence. For the deformation studies, we used a common bending strain of 0.4% for all the deformed samples. The formula

$$bending\ \ strain = \frac{thickness\ of\ \ sample}{diameter\ of\ \ mandrel} \tag{22}$$

was used to determine the appropriate mandrel to deform each of the samples. A sample was wrapped around the mandrel and then flattened to complete a half cycle of deformation; when reverse wrapped and again flattened, the tape completed one complete deformation cycle. The objective of this bending study was to simulate the work hardening that might be encountered during handling or fabrication of electrical equipment. Finally, the effect of temperature cycling was investigated for one sample, by dipping it in liquid nitrogen, warming it to room temperature, and then immersing it again. This thermal cycle was repeated eight times, after which the ferromagnetic loss was remeasured in a 400-Oe cycle at 77 K.

2.25.3 Results and Discussion

For an overall perspective, Fig. 2.146 shows the mass magnetization *M* plotted versus applied field *H* for all samples studied. The measurements were done at *T* = 5 K in fields *H* up to 10 kOe; in order to obtain the saturation magnetization M_{sat}; these measurements were done at 5 K. The values of M_{sat} steadily decrease with the addition of tungsten. This is clearly seen in Fig. 2.147, a plot of M_{sat} vs W-content *x*. The figure reveals a variation with *x* that is very nearly linear, similar to that observed in Ni-Cr alloys.[10,12] A linear extrapolation to $M_{sat} = 0$ intersects at critical W concentration $x_c = 9.55 \pm 0.40$ at.%. Long ago, this alloy system was studied by Marian [13] and subsequently reported in [14] and in a data compilation still later [15]. The data of Marian are shown in Fig. 2.147 as well.

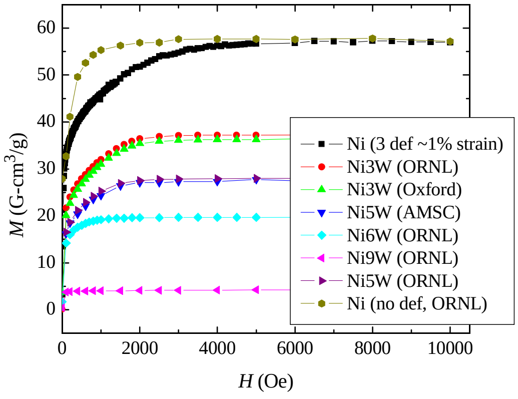

Fig. 1 of AOI et al

Fig. 2.146. Magnetization *M* vs applied magnetic field *H* for all samples studied. Measurements were done at *T* = 5 K.

We determined the Curie temperature for several alloys from temperature-dependent measurements of *M*(*T*). The analysis was based on the relation that the spontaneous magnetization varies with temperature as $M \propto (T_c - T)^{\beta}$ with β = 1/3 for a 3D Heisenberg magnet.[16]. In approximating the spontaneous magnetization by the bulk signal, we ignore all data very close to T_c due to the influence of the applied field. The process is illustrated in Fig. 2.148, which shows M^3 plotted against *T* for two alloys, Ni-5at%W and Ni-6at%W. The substantial region of linearity shows that the "critical point" relation given above describes the system rather well. The Curie temperature was obtained by a linear extrapolation to $M^3 = 0$. The resulting values of T_c are presented in Fig. 2.149 as a function of W-concentration *x*. Again, the values of Marian [13] are included for comparison. As with the saturation magnetization M_{sat}, we observe a nearly linear decrease with *x*; a linear extrapolation to $T_c = 0$ gives a value for the critical concentration $x_c = 9.75 \pm 0.40$ at. %, which is consistent within experimental error with the result from M_{sat}. This implies, perhaps more fundamentally, that M_{sat} and the Curie temperature are proportional in these Ni-W (and Ni-Cr) alloys. Table 2.10 lists these two parameters for the present samples.

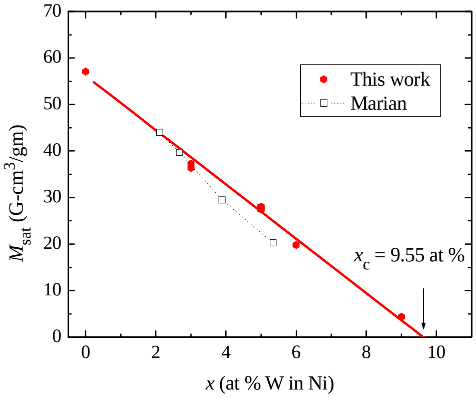

Fig. 2 of AOI et al

Fig. 2.147. Variation of saturation magnetization of Ni$_{1-x}$W$_x$ alloys with W-content *x*, including values obtained here and those reported by Marian [V. Marian, *Ann. Phys. Ser.* 11**(7), 459 (1937)].** The line is a linear dependence fitted to the present data extrapolated to the critical concentration x_c.

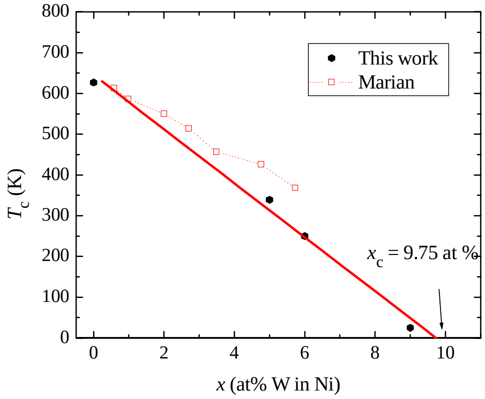

Fig. 4 of AOI et al

Fig. 2.149. Dependence of Curie temperature of Ni$_{1-x}$W$_x$ alloys on W-content *x*, with present results and those of Marian [V. Marian, *Ann. Phys. Ser.* 11(7), 459 (1937)]. The straight line extrapolates to the critical concentration x_c.

Table 2.10. Magnetic properties of Ni-W alloys

Material	M_{sat} (G-cm^3/g)	T_c (K)
Nickel	57.06	627
Ni-3at%W	36.4–37.3	>420
Ni-5at%W	27.4–28.0	339
Ni-6at%W	19.8	250
Ni-9at%W	4.36	25

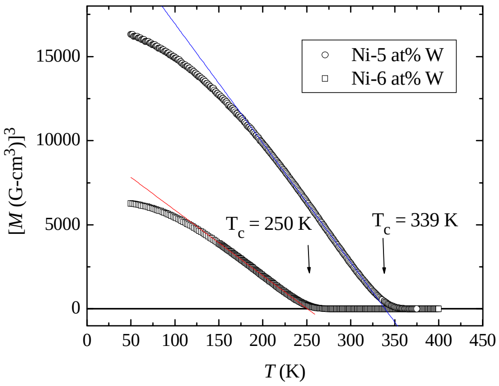

Fig. 3 of AOI et al

Fig. 2.148. A plot of *M*^{3} vs temperature *T* for Ni-5at%W and Ni-6at%W. Straight lines show the extrapolation to *M* = 0 used to define Curie temperature.

Next, we consider the hysteretic energy loss in these ferromagnetic Ni materials. To illustrate some essential features, we show in Fig. 2.150 several plots of magnetization *M* vs *H* for a rather lossy sample of electroplated Ni, at *T* = 120 K. Included are curves for cycles with H_{max} = 100, 200, 400 and 800 Oe. Qualitatively, it is clear that the area inside the loop increases as the field excursion increases, and then saturates when the material becomes reversible in sufficiently large fields. This is the general behavior for all materials studied. To obtain the hysteretic energy loss per cycle *W*, we numerically integrate each *M*(*H*) loop to obtain its area. Many of these results are collected in Fig. 2.151, a plot of loss *W* vs field excursion H_{max}. The general behavior of these soft ferromagnetic materials (coercive fields of a few Oe) is similar, with a roughly linear variation at low field amplitudes H_{max}, followed by saturation at higher field amplitudes. As the temperature decreases, the loss *W* increases as might be expected, but only slightly between 77 and 50 K.

To better visualize some trends, we show in Fig. 2.152 the maximum ferromagnetic energy loss per cycle *W* for each alloy as biaxially textured (no bending deformation), at *T* = 77 K. In particular, the histogram contains values of loss measured in 400-Oe cycles, with the materials listed in order of increasing W content. Two qualitative trends can

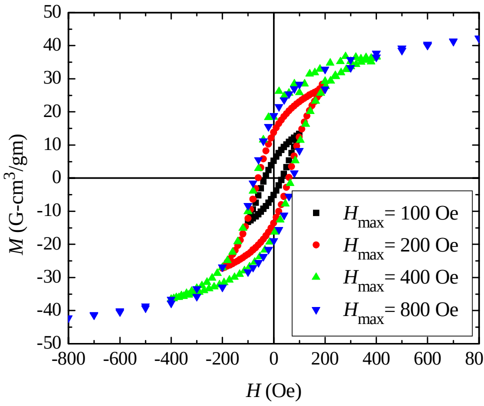

Fig. 5 of AOI et al

Fig. 2.150. The magnetization *M* vs *H* for lossy, electroplated Ni at a temperature of 120 K. The plot illustrates that the ferromagnetic Loss, $W = \int MdH$ = loop area, increases with H_{max}.

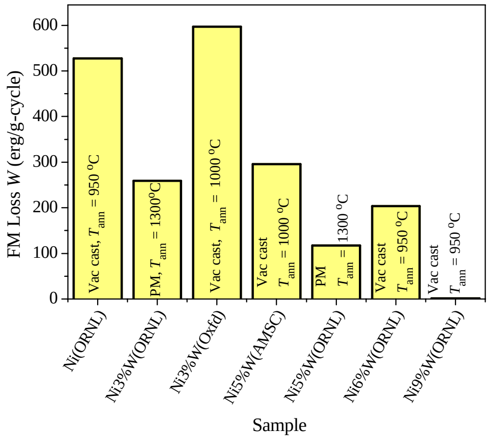

Fig. 7 of AOI et al

Fig. 2.151. Hysteretic loss per cycle *W* as a function of field excursion H_{max}, for undeformed Ni, Ni-6at%W and Ni-5at%W samples (prepared by vacuum casting (AMSC, ORNL, and Oxford) or powder metallurgy methods (ORNL). Loss increases roughly linearly with H_{max}, then saturates. Also, loss increases somewhat as *T* decreases.

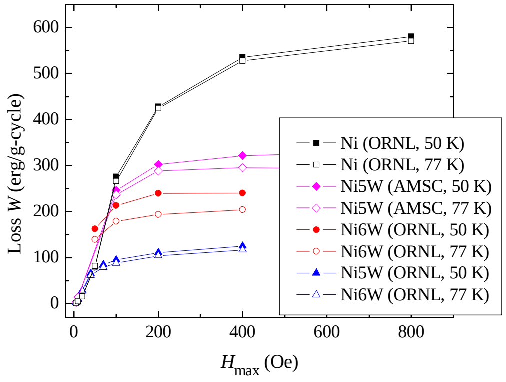

Fig. 6 of AOI et al

Fig. 2.152. Histogram showing maximum hysteretic loss *W* of samples studied. Ni-9at%W has an almost negligible loss. Alloys with same atomic composition have different values of ferromagnetic losses due to different methods of preparation. In particular, alloys annealed at higher temperatures have lower ferromagnetic losses. T_{ann}. = annealing temperature; PM = powder metallurgy; Vac cast = vacuum cast.

be discerned. First, the loss *W* generally decreases when tungsten is added. This is hardly surprising because Ni-W at these compositions forms a solid solution (no precipitates or inclusions that could pin domain walls) and, as shown in Fig. 2.147, the saturation magnetization M_{sat} decreases approximately linearly with W content. The Ni-9at%W has negligible loss, as expected from the critical concentration of W in Ni. The loss depends both on intrinsic material properties, such as M_{sat}, and on extrinsic features, such as the density of defects that pin domain walls. We also observe that the ferromagnetic loss is lower for the powder metallurgy materials compared with vacuum-cast materials with similar compositions. Interestingly, the Ni- 5at% W powder metallurgy material has even lower loss that the vacuum-cast 6 at% W alloy. This second observation most likely originates from the higher annealing temperatures (~1300°C) that could be used with the PM-based alloys (without inducing unwanted secondary recrystallization), compared with the lower (~1000°C) temperatures used for these vacuum cast materials. Qualitatively, this should lead to a lower density of dislocations and related structural defects. Indeed, dislocations are reported to be the primary pins that impede domain wall motion in Ni [17], and one may expect similar effects in these dilute Ni-W alloys. Grain boundaries also act as pin domain walls, but the present materials are all strongly textured with small angle grain boundaries and the mean grain sizes are similar; this implies that the differences between materials arise mostly from other features. Overall, the method of preparation of the alloy plays a prominent role in determining its hysteretic losses.

To assess the impact of deformation on the ferromagnetic loss per cycle, we used pure Ni, Ni-3at%W and Ni-5at%W. Each of these samples was deformed controllably by applying 0.4% bending strain, as described earlier. Figure 2.153 shows how the loss W increases with the number of half-cycles of bend, for Ni-3at%W and Ni-5at%W materials. This figure shows the maximal ferromagnetic loss per cycle, as observed in field cycles with $H_{\max}$ = 400 Oe. For all alloys, the hysteretic loss increased with number of cycles of deformation, with the biggest jump in loss coming from the first half-step of deformation. A bending strain of 0.4 % lies near the limit tolerated by the superconductive coating in fully fabricated materials [18,19].

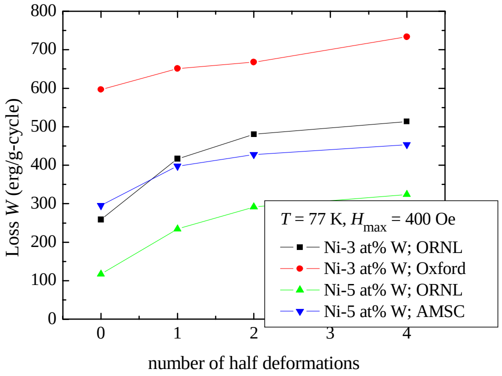

Fig. 8 of AOI et al

Fig. 2.153. Hysteretic loss per cycle for Ni-3at%W and Ni-5at%W as a function of number of half-cycles of deformation. Loss increases with number of cycles of deformation (0.4% bending strain)**.**

A check was made for adverse effects of temperature cycling, using a vacuum cast Ni-5at%W sample as biaxially textured. Eight thermal cycles of T = 300 K to 77 K to 300 K changed the ferromagnetic loss only slightly, from W = 295 to 302 erg/g-cycle. From this, we can say that ferromagnetic loss is essentially unaffected by temperature cycling.

In ac magnetic measurements, a small oscillatory magnetic field is applied, and the induced sample moment is time-dependent, unlike the dc measurements, where the sample moment is constant during the measurement time. Such measurements can be very sensitive to small changes in $M(H)$. The ac susceptibility, $\chi = \mathrm{d}M/\mathrm{d}H$ is the (local) slope of the $M(H)$ curve and it is frequently the quantity of interest in ac magnetometry. More generally, however, a measurement of an ac magnetic moment yields two quantities: the magnitude of the moment $|m|$ and its phase shift φ, relative to the drive signal. Alternatively, one can consider the in-phase or real component m' and an out-of-phase, or imaginary, component m''. For ferromagnets, an irreversible domain wall movement appears as a finite dissipative component m''. Values for the ferromagnetic loss were obtained from the expression

$$W = \pi \times h_{ac} \times M'' , \tag{23}$$

where M'' is the out-of-phase mass magnetization and h_{ac} is the amplitude of the applied ac field [20]. The SQUID magnetometer provides an ac field up to 6.8 Oe, and its frequency range is from 0.001 to 1000 Hz. Comparing experimental values for loss W from ac and dc measurements gave good agreement between the two methods, although this could only be done for small fields, up to 6.8 Oe.

We used this ac capability to investigate the relationship between the ferromagnetic loss per cycle and the frequency of the applied field. This is important because of potential applications for coated conductors in specialized electrical equipment (e.g., airborne generators and devices with operating frequencies above the usual 50 to 60 Hz of the power grid). As seen in Fig. 2.155, the loss per cycle W was found to be independent of the ac field frequency. The figure shows results for vacuum-cast Ni-5at%W at 77 K subjected to field amplitudes h_{ac} = 4 and 6.8 Oe, for frequencies f up to 600 Hz. Here, there was no dc bias field and the sample had no bending deformation. The significant increase in loss with h_{ac} = 6.8 Oe compared with that at h_{ac} = 4 Oe occurs when the field amplitude h_{ac} or $H_{\max}$ is comparable with the coercive field H_c. Another potential loss mechanism is from eddy currents, which gives a nominally frequency-dependent but amplitude-independent loss. However, we estimate the skin

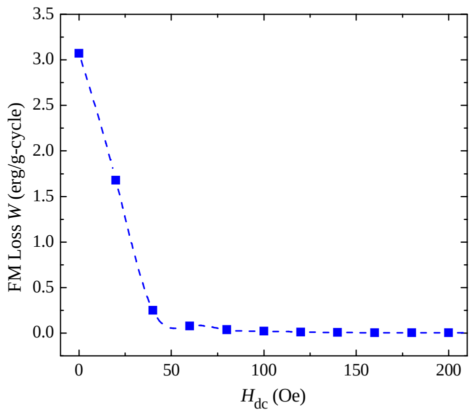

Fig. 10 of AOI et al

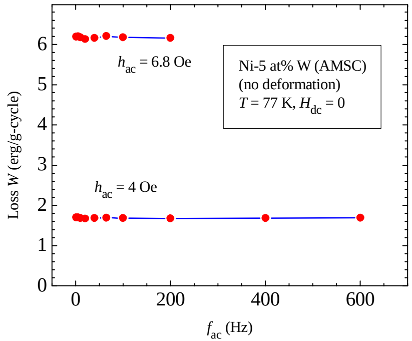

Fig. 9 of AOI et al

Fig. 2.154. Hysteretic loss for undeformed Ni-5at%W vs dc bias field at temperature of 77 K and a fixed ac field of 5 Oe. Loss decrease drastically when alloy is magnetized into reversibility by dc bias field.

Fig. 2.155. Ferromagnetic loss as a function of applied ac frequency for two different fixed values of ac field. Loss per cycle is independent of frequency in the range shown.

depth of this alloy to be several millimeters, much larger than the sample thickness, meaning that eddy losses should be small relative to the ferromagnetic loss, as observed.

Finally, we investigated the effect of a dc bias field, H_{dc} on the ferromagnetic loss W for a fixed ac field amplitude and frequency. Figure 2.154 shows the result obtained for an undeformed Ni-5at%W at h_{ac} of 5 Oe and temperature of 77 K. The loss decreased rapidly as the bias field H_{dc} increased and reduced W to nearly zero for a dc field of ~50 Oe. This is readily understood as a consequence of the fact that a dc field can magnetize the sample into its region of magnetic reversibility (and eventually saturation). For the lossy electroplated Ni in Fig. 2.146, this region corresponds to dc fields > ~400 Oe; it occurs at lower fields for the more reversible biaxially textured and annealed Ni-W alloys.

2.25.4 Conclusions

In summary, both the saturation magnetization M_{sat} and Curie temperature T_c decrease linearly with W-content x in $Ni_{1-x}W_x$ alloys (with x = 0, 3, 5, 6, and 9 at. % W), with a critical concentration $x_c \approx 9.6$ at. % W. Generally, the ferromagnetic hysteretic loss decreases as the concentration of W rises. The loss increases with magnetic field excursion H_{max}, at first almost linearly and then saturating at larger H_{max}. The loss is stable with temperature cycling. When subjected to bending deformation, (0.4 % bend strain), the materials gave higher levels of ferromagnetic loss. This is due to the effects of pinning of domain walls by induced defects. From ac studies, we found that ferromagnetic loss is independent of the ac frequency applied and that it decreases drastically when the alloy is biased into its reversible regime by a collinear dc bias field.

2.25.5 References

1. A. Goyal et al., "High Critical Current Density Superconducting Tapes by Epitaxial Deposition of $YBa_2Cu_3O_x$ Thick Films on Biaxially Textured Metals," *Appl. Phys. Lett.* **69**, 1795 (1996).
2. A. Goyal et al., US patents: 5,739,086; 5,741, 377; 5,898,020; and 5,958,599.
3. A. Goyal et al. "Using RABiTS to Fabricate High-Temperature Superconducting Wire," *J. Metals* **51**, 19 (1999).
4. Y. Iijima et al., "In-Plane Aligned $YBa_2Cu_3O_{7-x}$ Thin Films Deposited on Polycrystalline Metallic Substrates," *Appl. Phys. Lett.* **60**, 769 (1992).

5. Y. Iijima et al., “Structural and Transport Properties of Biaxially Aligned $YBa_2Cu_3O_{7-x}$ Films on Polycrystalline Ni-Based Alloy with Ion-Beam-Modified Buffer Layers,” *J. Appl. Phys.* **74**, 1905 (1993).
6. R. P. Reade et al., “Laser Deposition of Biaxially Textured Yttria-Stabilized Zirconia Buffer Layers on Polycrystalline Metallic Alloys for High Critical Current Y-Ba-Cu-O Thin Films,” *Appl. Phys. Lett.* **61**(18), 2231 (1993).
7. X. D. Wu et al., “Properties of $YBa_2Cu_3O_{7-\gamma}$ Thick Films on Flexible Buffered Metallic Substrates,” *Appl. Phys. Lett*. **67**, 2397 (1995).
8. K. Hasegawa et al., “Biaxially Aligned YBCO Film Tapes Fabricated by All Pulsed Laser Deposition,” *Appl. Supercond*. **4**, 487 (1996).
9. M. Fukutomi et al., “Deposition of in-Plane Aligned $YBa_2Cu_3O_y/Y_2O_3$ Stabilized ZrO_2 Thin Films on Both Sides of Metallic Tape Substrates,” *Physica C* **231**, 113 (1994).
10. J. R. Thompson et al. “Ni–Cr Textured Substrates with Reduced Ferromagnetism for Coated Conductor Applications,” *Physica C* **370**(3), 169 (2002).
11. R. C. Duckworth et al., “Transport ac Loss Studies of YBCO Coated Conductors with Nickel Alloy Substrates,” *Supercond. Sci. Technol.* **16**, 1294 (2003).
12. M. J. Besnus, Y., Gottehrer, and G. Munshy, “Magnetic Properties of NiCr Alloys,” *Phys. Stat. Sol. B* **49**(2), 597 (1972).
13. V. Marian, “Curie Points of Ferromagnetism and Absolute Saturation of Some Alloys of Nickel,” *Ann. Phys. Paris* 11, **7** 459 (1937).
14. R. P. Bozorth, ed., p. 325 in *Ferromagnetism*, IEEE Press, Piscatawa, N.J. (1978).
15. M. Shiga, ed., p. 563 in *Landolt-Boernstein New Series Group III, Magnetic Properties of Metals*, vol. 19, Springer-Verlag, Berlin (1989).
16. N. W. Ashcroft and N. D. Mermin, p. 699 in *Solid State Physics*, Holt, Rinehart and Winston, New York (1976).
17. V. A. Demkin, “Coercive Force and Electrical Resistivity of Polycrystalline Nickel after Low-Temperature Ultrasonic Fatigue,” *Phys. Stat. Sol. (a)* **128** 375 (1991).
18. C. Park et al., “Bend Strain Tolerance of Critical Currents for $YBa_2Cu_3O_7$ Films Deposited on Rolled-Textured (001)Ni,” *Appl Phys. Lett*. 73, 1904 (1998).
19. C. L. H. Thieme et al., “Axial Strain Dependence at 77 K of the Critical Current of Thick YBaCuO Films on Ni-Alloy Substrates with IBAD Buffer Layers,” *IEEE Trans. Appl. Supercond*. **9**, 1494 (1999).
20. J. R. Clem and A. Sanchez, “Hysteretic ac Losses and Susceptibility of Thin Superconducting Disks,” *Phys. Rev. B* **50**(13) (1994) 9355.

2.26 Improvement of In-Field Transport Critical Currents in (Y_2BaCuO_5/$YBa_2Cu_3O_{7-x}$)xN Multilayer Films on Ni-Based Textured Substrates

A. A. Gapud, A. Goyal, S. Kang, L. Heatherly, and D. K. Christen (ORNL); T. J. Haugan, P. N. Barnes, and T. A. Campbell (Air Force Research Laboratory, Wright-Patterson Air Force Base)

2.26.1 Introduction

In the endeavor to enhance flux pinning in $YBa_2Cu_3O_{7-\delta}$ (YBCO) films of coated conductors for real-world industrial applications, two recent developments in particular have played a great role. First, the old issue of weak links caused by high-angle grain boundaries has been circumvented by reproducibly fabricating highly textured YBCO films, for example those grown on RABiTS^{TM} [1,2]. Second, there has been a great deal of effort towards in situ introduction of pinning sites in YBCO films, in which useful defects are produced as the film is grown, as opposed to ex situ methods requiring an additional step such as irradiation by energetic particles. Some examples of this involve the introduction of nanoparticles of $BaZrO_3$ [3] into the superconducting bulk, propagation of linear defects by growing a film on a substrate dusted with nanoparticles [4], and using different combinations of rare-earth components in place of the Y in 123 compounds [5,6].

Previously, growth of (211/123)xN multilayer films was shown to increase critical current density (77 K,~1–2 T) of YBCO by 200 to 300% when deposited on single-crystal substrates [7,8]. The composite (211/123)xN films are a superlattice type structure of alternating layers of 123 and Y_2BaCuO_5 (211) “pseudo-layers” containing discontinuous 211 nanoparticles that deposit by the island growth mode. The 211 nanoparticle size is as small as ~8 nm with area number density estimated as $> 4 \times 10^{11}$ particles/cm^2 [8]. The resulting structure is essentially a layered nanoparticulate dispersion of nonsuperconducting 211 nanoparticles inside a 123 matrix.

This paper reports on the extension of the (211/123)xN multilayering process to YBCO films on RABiTS™. Details of critical-current-density enhancement as a function of temperature, applied magnetic field, and orientation with respect to this field are reported.

2.26.2 Experimental

Buffered Ni and $Ni_{0.97}W_{0.03}$ substrates were prepared at ORNL. The as-rolled tapes were annealed at 1250°C for 20 min in a vacuum chamber containing 3×10^{-7} Torr of H_2S, which produced the primary texture and a sulfur superstructure on the surface of the alloy. After it was annealed, the tape was rewound to its starting position, and a seed layer of Y_2O_3 was deposited in the same chamber by a reactive electron beam evaporation method. For this deposition yttrium metal was evaporated in the presence of 5×10^{-5} Torr H_2O. The tape was then transferred to another chamber, and the YSZ and CeO_2 layers were deposited by an rf magnetron sputtering process. YSZ and CeO_2 targets were sputtered in the presence of 3 and 8×10^{-5} Torr H_2O, respectively. The resulting buffer layer architecture was a 25-nm-thick cap layer of CeO_2, a 200-nm-thick intermediate layer of YSZ, and a 30-nm-thick seed layer of Y_2O_3. At the Air Force Research Laboratory, alternating 211/123 layers were applied in situ by PLD on buffered Ni tape; the processes were described in detail elsewhere [7,8]. The samples in this study had a thickness of 0.3 µm.

PLD was used to prepare 0.2-µm-thick control samples at ORNL. All transport measurements were conducted at ORNL by a standard four-probe method in which applied current was pulsed to minimize joule heating. Current-terminal contact resistances to the sample were also minimized, on the order of 10 µΩ, by applying the leads onto annealed, sputtered-silver pads topped with indium. Current was averaged over opposite directions to subtract any thermal-voltage offset. A criterion of 1 µV/cm was used to determine critical current density from the voltage-current curves. Measurements were performed in fields up to 9 T, in liquid-helium-cooled cryostats in which the samples were cooled in helium vapor with very good temperature stability (within 10 mK).

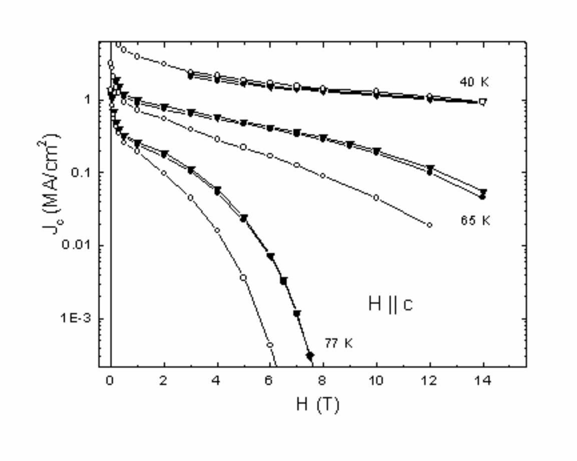

Fig. 2.156. Critical current density of two films with 211 nanoparticles (filled symbols) compared to PLD film without (open symbols), in applied field *H* || *c* at the temperatures shown. Enhancement in critical current density is seen only at the two higher temperatures.

2.26.3 Results and Discussion

The field dependence of critical current density at three different temperatures is shown in Fig. 2.156 for a field oriented along the *c*-axis. As with the results on single crystals, the critical current density of the film with and without the nanoparticles overlap at the lowest fields. However, the in-field performance of the film is significantly improved. At 5 T, the critical current density is higher by a factor of more than 8 at 77 K and more than two at 65 K. At 2 T, the increase is twofold at 77 K and a factor of 1.5 at 65 K. The increase, however, stops at 40 K. Thus the enhancement provided by this process may only be effective at liquid nitrogen temperatures and would be best suited for moderate field applications in this particular regime.

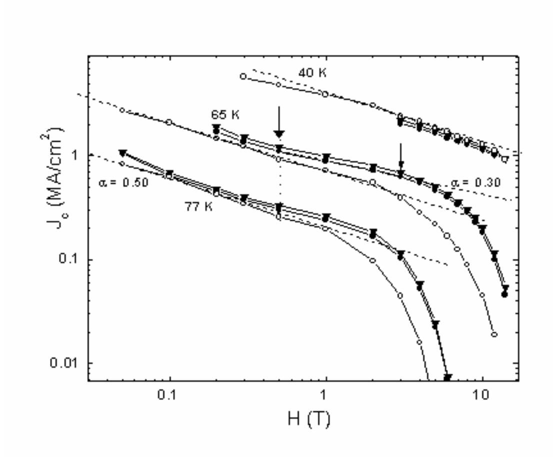

Fig. 2.157. Log-log plot of two films with 211 nanoparticles compared to PLD film without in applied field *H* || *c* at the temperatures shown, indicating the estimates of α (dotted lines) for the power-law regime between 0.1 and 1 T where $J_c \sim H^{-\alpha}$.

Improvement of critical current density in field is also indicated by the "flatness" of $J_c(H)$, which is quantified by the scaling exponent α in the so-called collective flux pinning regime [9], where $J_c(H) \sim H^{\alpha}$. For the film without a 211 phase, we find α ~0.5, as shown in Fig. 2.157. For the multilayered film, the field dependence transitions to power law past a temperature-independent field, marked in the plot by the large arrow, at about 0.5 T, where α is as low as 0.3. (The dependence then falls off rapidly as H_{irr} takes effect at intermediate fields.) This is reminiscent of the effect of matching fields in irradiated film with columnar defects, in which a temperature-independent kink is clearly seen in $J_c(H)$ at a matching field *H*. In fact, just recently, in these multilayered films, Civale et al. have found strong evidence of a matching field of ~2.5 T at 77 K along the *ab* direction [10]. Because of this, it may not be unreasonable to find a matching phenomenon along the *c* direction as well. If one were to assume the area density of pinning sites to be similar to that of the nanoparticles (4×10^{11}/cm^2), the matching field would be 8 T. Figure 2.157 suggests something closer to 3 T, indicated by the smaller arrow, although this could be due to the significant effect of H_{irr} in this regime; thus the actual matching field may not be clear. It is for this reason that the effect is diminished for the case of T = 77 K. For T = 40 K, it is expected that the effect is also diminished, and for the limited number of data points available (due to maximum system current available), there is no clear sign of matching-field effects.

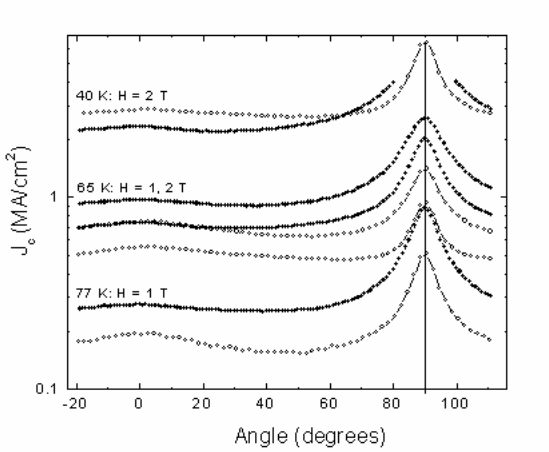

Fig. 2.158. Critical current density vs angle between the applied magnetic field and *c* direction, at 1 T for 77 K, at 1 T and 2 T for 65 K, and at 2 T for 40 K. Solid circles are with nanoparticles; open circles are without. For 65 K, the higher curve in the pair corresponds to 1 T; the lower one to 2 T.

Previously, the exponent α has been theoretically predicted [11,12] to have values 0.5 or 0.63, where *no* correlated pinning is assumed in the models. The α value obtained for our unmodified film is consistent with this. The fact that the multilayered films show a smaller α value, albeit for a limited range of fields, suggests highly correlated flux pinning, which would be consistent with extended structures seen on TEM for multilayer films on single crystals [8].

Of particular interest is the dependence of critical current density on the angle θ between the *c* axis and the applied field, shown in Fig. 2.158. At a field of 1 T, along *c* axis there is enhancement at the two higher temperatures over all orientations. Again, in the case of 40 K the effect has diminished, consistent with $J_c(H)$ data (see Fig. 2.156). Most striking is the enhancement for fields along *ab* for all three temperatures, implying that this particular effect has weak temperature dependence, if any. In fact, for T = 65 K and 77 K, the relative increase in $J_c(H \parallel ab)$ for all three curves is about the same, by a factor between 1.8 and 2.1. These observations are also consistent with the Civale et al. report of matching field effect along *ab* for 2.5 T, 77 K due to the spacing of the nanoparticle layers when viewed along the *ab* direction.

Because of the strong enhancement of critical current density for $H \parallel ab$ compared with $H \parallel c$ for the multilayered samples, the variation in critical current density with respect to θ is significantly affected by the multilayering. If one were to quantify $J_c(\theta)$ nonuniformity by defining $\beta \equiv J_c(H\parallel ab)/J_c(H\parallel c)$, then β for 77 K, 1 T increases by about 20%, from 2.6 to 3.1. For 65 K, β increases by about 40% from 1.9 to 2.7 for H = 1 T, while at 2 T the increase is from 1.7 to 2.7, a slightly higher increase of about 60%.

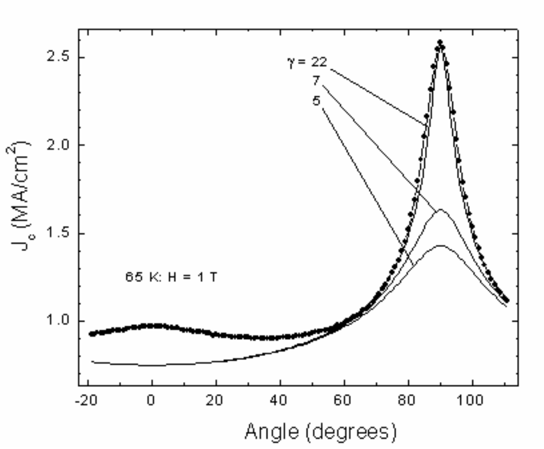

Fig. 2.159. Attempt to fit mass-anisotropy curve to data at 65 K, 1 T, using $J_c[H\varepsilon(\theta)] = J_c[1\ \mathrm{T}*\varepsilon(\theta)]^{-0.5}$.

Another indication that correlated pinning is a greater factor than random pinning, point-like pinning is the comparison with angular dependence as predicted by using the treatment of Blatter [9] and recently applied by Civale et al. [13], where the point flux pinning angular dependence is given by $J_c(\theta) = J_c[H\varepsilon(\theta)]$, and where we have the anisotropic effective mass function $\varepsilon(\theta) = [\cos^2\theta + \gamma^{-2}\sin^2\theta]^{1/2}$, $\gamma^{-2} = m_{ab}/m_c$. In this case, effects of correlated defects would manifest as additional pinning for aligned fields, such as for ion tracks or the well-known intrinsic pinning for fields parallel to the *ab* planes. Unlike the success of Civale et al. in applying this model to PLD films [10,13], our attempts to fit the data to this theoretical curve by using the α values have not been successful, as shown in Fig. 2.159 for a multilayered film at T = 65 K and 1 T, where we have assumed, based on Fig. 2.157, that the critical current density reasonably follows the power law, $\sim H^{-0.5}$ at H = 1 T. Because of the shallow peak in critical current density for θ ~0°, the mass anisotropy description fails, indicating that the additional pinning in this direction is correlated. Moreover, even with the highest reasonable γ, the elevated values of $J_c\ (H \parallel ab)$ could not be due to random pinning. This would be consistent with evidence of matching effects in this direction. Interestingly, if this peak were to be due only due to mass anisotropy, then any field matching effect would be equivalent to a mass anisotropy of about 22, as shown.

Mass anisotropy scaling also fails to predict the anisotropy β of the curve $J_c(\theta)$ because of the strong $J_c\ (H \parallel ab)$. As was previously shown in our recent study at moderate fields [14], one can first assume that $J_c(H)$ follows the power law, $\sim H^{\alpha}$ at H = 1 T. Then for H = 1 T , γ = 5, and α = 0.5, the prediction for $\beta = J_c[H\varepsilon(90°)]/J_c[H\varepsilon(0°)] = \gamma^{\alpha} = 2.24$, which is much lower than 2.7 at 65 K and 3.1 at 77 K for the multilayered films.

It should also be noted from Fig. 2.158 that even without multilayering the YBCO film already shows significant structure along *c* and fails to fit the curve predicted by mass anisotropy scaling. In fact, the poor fit is very similar to that shown in Fig. 2.159 for the multilayered film, implying that there was already some correlated pinning along *c* and along *ab*. However, the angular-dependent variation in critical current density is less than that predicted by mass anisotropy: for 65 K, β is less than 1.9. It is possible that the island or columnar growth from our PLD processing already encouraged correlated pinning along the thickness of the *c*-oriented film, and the multilayering further enhanced this effect by superimposing another correlated pinning mechanism. Any correlated pinning along *ab* may have been further enhanced by the even stronger matching-field effect of the nanoparticle layering along *ab*, thus elevating β.

The introduction of 211 nanoparticles into PLD YBCO films has been shown to enhance flux pinning at temperatures above 40 K, for fields up to 2 T. There is further evidence of correlated field matching along both *c* and *ab*, but most especially along *ab* where angular dependence shows the greatest enhancement in critical current density, by about a factor of two.

2.26.4 References

1. A. Goyal et al., “High Critical Current Density Superconducting Tapes by Epitaxial Deposition of $YBa_2Cu_3O_x$ Thick Films on Biaxially Textured Metals,” *Appl. Phys. Lett*. **69**(12), 1795 (1996).
2. A. Goyal et al., U.S. Patents 5,739,086; 5,741,377; 5,846,912; and 5,898,020.
3. J. L. MacManus-Driscoll et al., “Strongly Enhanced Current Densities in Superconducting Coated Conductors of $YBa_2Cu_3O_{7-x}$ + $BaZrO_3$,” *Nature Materials* **3**(7), 439 (2004).
4. Kaname Matsumoto et al., “Enhancement of Critical Current Density of YBCO Films by Introduction of Artificial Pinning Centers due to the Distributed Nano-Scaled Y_2O_3 Islands on Substrates,” *Physica C* **412-414,** 1267 (2004), plus references therein.
5. J. L. MacManus-Driscoll et al., “Systematic Enhancement of in-Field Critical Current Density with Rare-Earth Ion Size Variance in Superconducting Rare-Earth Barium Cuprate Films,” *Appl. Phys. Lett.* **84**, 5329 (2004)
6. C. Cai et al., “Magnetotransport and Flux Pinning Characteristics in $RBa_2Cu_3O_{7-\delta}$ (R = Gd,Eu,Nd) and $(Gd_{1/3}Eu_{1/3}Nd_{1/3})Ba_2Cu_3O_{7-\delta}$ High-T_c Superconducting Thin Films on $SrTiO_3$(100),” *Phys. Rev. B* **69**, 104531 (2004).
7. T. Haugan et al., “Island Growth of Y_2BaCuO_5 Nanoparticles in $(211_{\sim 1.5\ nm}/123_{\sim 10\ nm})\times N$ Composite Multilayer Structures to Enhance Flux Pinning of $YBa_2Cu_3O_{7-\delta}$ Films,” *J. Mat. Res*. **18,** 2618 (2003).
8. T. Haugan et al., “Addition of Nanoparticle Dispersions to Enhance Flux Pinning of the $YBa_2Cu_3O_{7-x}$ Superconductor,” *Nature* **430**, 867 (2004).
9. G. Blatter et al., “Vortices in High-temperature Superconductors,” *Rev. Mod. Phys*. **66**, 1125 (1994).
10. L. Civale and J. Driscoll, unpublished, presented at the DOE Peer Review, Washington D.C., July 23–25, 2003; available on line at http://www.energetics.com/supercon04.html.
11. Y. N. Ovchinnikov and B. I. Ivlev, “Pinning in Layered Inhomogeneous Superconductors,” *Phys. Rev. B* **43**, 8024 (1991).
12. D. R. Nelson and V. M. Vinokur, “Boson Localization and Correlated Pinning of Superconducting Vortex Arrays,” *Phys. Rev. B* **48**, 13060 (1993).
13. L. Civale et al., “Angular-Dependent Vortex Pinning Mechanisms in $YBa_2Cu_3O_7$ Coated Conductors and Thin Films,” *Appl. Phys. Lett.* **84**, 2121 (2004).
14. A. A. Gapud, R. Feenstra, D. K. Christen, J. R. Thompson, and T. G. Holesinger, “Temperature and Magnetic Field Dependence of Critical Currents in YBCO Coated Conductors with Processing-Induced Variations in Pinning Properties,” submitted to *IEEE Trans. Appl. Supercond,* presented at Applied Superconductivity Conference, Jacksonville, Fla. Oct. 3–8, 2004.

2.27 Modeling Current Flow in Granular Superconductors and Implications for Potential Applications

N. A. Rutter and A. Goyal

2.27.1 Introduction

A coated conductor fabricated by the RABiTS™ route consists of a metallic substrate, one or more buffer layers, and a high-temperature superconducting layer such as YBCO [1,2]. The metallic tape, which is usually Ni-based, is cold-rolled and recrystallized to induce the cube texture {001}<100> [3]. If the tape is a Ni-alloy, it may be coated with a layer of pure Ni [4]. The substrate may also be annealed in a sulfur-containing environment to produce a surface onto which oxide layers may be grown epitaxially

[5]. Buffer layers such as Y_2O_3, YSZ and CeO_2 are deposited, maintaining the cube texture of the underlying grains [6]. The superconductor is then deposited such that it grows biaxially, with the crystallographic *c*-axis perpendicular to the tape and with the *a* and *b* axes aligned with the rolling and transverse directions of the tape. Electron backscatter measurements have demonstrated that the crystallographic orientations of the superconducting grains are indeed determined by those in the underlying layers [7]. Hence the superconducting film is made up of a network of grains that have crystallographic orientations that are within a few degrees of {001}<100>.

The critical current density (J_c) of such a superconducting grain network is likely to be limited by dissipation at the low-angle grain boundaries, which generally have less current-carrying capability than the grains [8]. (In this chapter, the uppercase symbol J is used to represent macroscopic current densities of samples; the lowercase symbol j is used to represent the microscopic current densities in individual grains and boundaries.) Current flow in polycrystalline coated conductors therefore relies on the transfer of current across the grain boundaries. Thus when model current flow is attempted, the physical structure of the superconducting film may be represented as a two-dimensional network of grains, each being oriented close to {001}<100>. The current that is able to flow between any two neighboring grains depends upon the relative misorientation of the grains and the surface area of the common interface.

2.27.2 Coated Conductor Models

A number of models that study current percolation in networks of low-angle grain boundaries have been developed [9–14]. The factors studied in such models include grain size, sample dimensions, extent of grain misorientation, and grain shape.

2.27.2.1 Grain Shape

In most models the conductor consists of a regular array of equally sized, identically shaped grains. The models of Specht et al. [10] and Rutter et al. [11,12] use an array of hexagons; Nakamura et al. [13] use squares. The only model in which the grains are not identically shaped is that of Holzapfel et al. [14]. This model is unlike the others in that the grain structure used is one that has been measured by electron backscatter diffraction (EBSD) rather than being simulated.

Each of these methods of modeling the structure has various advantages and disadvantages. The square-grain structure is the simplest to model, but its main limitation is that each grain has only four neighbors, whereas in real tapes the number of neighbors is around six. The other problem with the square-based model is that the length of the shortest grain boundary path across the width of the sample is exactly equal to the tape width. In a real tape, this is unlikely to be true. Thus the critical current (which is proportional to the length of the grain boundary path across which dissipation occurs) is likely to be underestimated by the square model.

The use of a hexagonal model addresses these issues. The number of nearest neighbors is six, and the shortest boundary path length is increased in excess of the tape width. One of the main problems of the hexagonal grain model is that one of two distinctive orientations, which are shown in Fig. 2.160, must be chosen.

Both existing models [10,11] placed the hexagons in the orientation shown in Fig. 2.160(a), relative to the tape length and width directions. The minimum boundary path length (marked in bold) is now approximately a factor of 4/3 greater than the tape width. In the arrangement shown in Fig. 2.160(b), this minimum length is just 2/√3 times the width. Also, it is clear from the figure that the number of grains along the length of the tape and the number across the width are not as easily defined as for the square grains. Although both cases would be well described as a 4 × 4 array of hexagons, the aspect ratios of the samples are quite different.

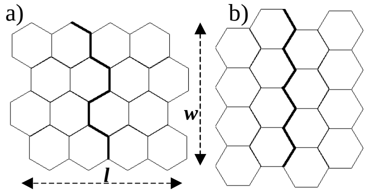

Fig. 2.160. Different ways in which a 4×4 array of hexagonal grains can be arranged. In (a) the minimum grain boundary path across the conductor width is 4w/3, whereas in (b), the value is 2w/√3.

The Holzapfel model [14] has grains with more irregular shapes. In this case the structure is that of a real tape measured by EBSD. The resolution of the grain edges is determined by the size of the square pixels in the array. This model is more realistic in that the grains have a range of shapes and sizes and have differing numbers of nearest neighbors.

2.27.2.2 Grain Boundary Misorientation

The first attempt to study critical currents in coated conductors by percolation modeling [10] used a bimodal distribution of boundary currents, assigning values of 0 or 1 randomly to the grain boundaries, rendering a given fraction, *f*, conducting and the remainder, (1-*f*), nonconducting. Subsequent models have attempted to assign critical currents to the boundaries based on grain misorientation. Holzapfel was able to use the true orientations of the grain as measured by EBSD to determine the boundary misorientation. An alternative is to use a gaussian distribution to assign grain orientations [13] before calculating the boundary misorientations. This effectively simulates a conductor for which the grains are misoriented about one axis (for example, only in-plane rotations). However, the result is a grain boundary misorientation distribution (GBMD) which is not quite accurate. The GBMD produced by this approach will always give a peak at 0°, indicating that that is the most common grain boundary angle. If a three-dimensional orientation is assigned to each of the grains [11], the GBMD instead indicates no 0° boundaries and a peak at an angle of a few degrees. The latter approach produces results similar to EBSD measurements [12], but the former would be a good approximation if the out-of-plane texture of a tape was very good.

2.27.2.3 The Relationship Between Misorientation Angle and Critical Current Density

After the misorientation angles of all boundaries in a model sample have been determined, the next step is to associate this angle (θ) with a critical current density. The relationship was first investigated by making measurements on bicrystal grain boundaries [15,16]. Because most data exist for zero applied field and at a temperature of 77 K, this is the situation that is usually considered in modeling. This relationship between j_c and θ [17–20] is not precisely known, and thus there have been various different attempts at quantifying it. It is most generally expressed as

$$
\begin{aligned}
j_c(\theta) &= j_c' \exp\left(\frac{-(\theta-\beta)}{\alpha}\right) \text{ for } \theta > \beta \\
j_c(\theta) &= j_c' \text{ for } \theta < \beta
\end{aligned}
\qquad (24)
$$

where j_c' is the value measured for single crystals.

Equation (24) therefore suggests that there is a plateau region for very small angles where there is no decrease in j_c, followed by an exponential decrease with increasing angle. It is believed that this “plateau region” is simply a region in which the measured properties are determined by the properties of the grain [12,19] and that the grain boundary properties probably continue to improve all the way to 0°. It has been noted that twin boundaries, which are present within the granular regions, are effectively 1.8° boundaries [21], and thus it is assumed that when a measurement on a bicrystal boundary has a misorientation angle less than 1.8°, the critical current will be limited by the grains.

Whether or not the plateau is included, there is still some variation in the values quoted for the factor α. Tables 2.11 and 2.12 show some values estimated from bicrystal measurements and the values used in percolation models. Figure 2.161 shows this relationship schematically. The straight line portion represents the properties of grain boundaries with misorientation angle θ; a

Table 2.11. A summary of the values of α for measurements on [001] tilt boundaries in thin film YBCO in self-field at 77 K

Author	α (°)
Ivanov [17]	4.4
Heinig [18]	3.8
Verebelyi [19]	3.2
Holzapfel [14]	2.4

plateau is shown representing cases where the grains have the same j_c as (a) 4° boundaries [14] or (b) 1.8° boundaries [21].

Table 2.12. Values of α and β used in percolation models

Author	α (°)	β (°)
Rutter [11,12]	3.4	0
Holzapfel [14]	2.4	2.4
Nakamura* [13]	3.0	3.0

*not stated explicitly – estimated from text and figure 3

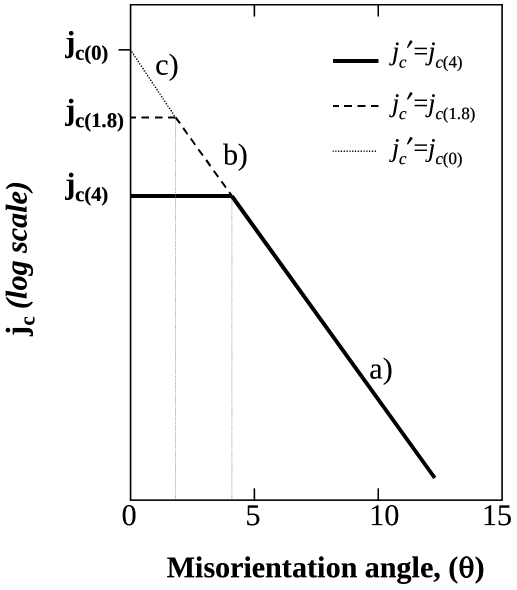

Fig. 2.161. Schematic showing the relationship between critical current and boundary angle, with plateaus at (a) 4° and (b) 1.8° due to granular dissipation.

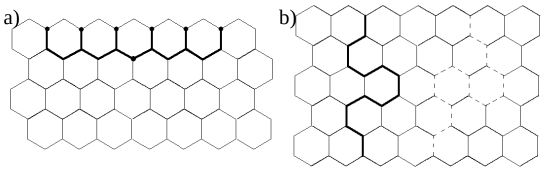

Fig. 2.162. (a) Illustration of the algorithm for finding the minimum current sum across the tape width. Six alternative paths from the top of the conductor to a point at the bottom of the top row are shown in bold. (b) A path across the conductor which will be considered (bold) and one which will not (dotted line).

2.27.2.4 Algorithms to Calculate the Critical Current

When the grain structure has been determined and the critical currents of the grain boundaries assigned, the calculation of the critical current depends upon the solution of a network problem. Consider a path along the grain boundaries that traverses the width of the sample. The maximum current that can cross this path is equal to the sum of the critical currents of the grain boundary segments that comprise the path. When all such paths are considered, the weakest is the one that limits the amount of current that can flow along the sample length. If that path can be found and the sum of the boundary currents comprising the path is calculated, the critical current of the sample is known. This method is based on a property of networks known as the “maximum-flow/minimum-cut theorem,” proved by Ford and Fulkerson [22]. In physical terms, when the critical current of a sample is reached, the limiting path of grain boundaries will be where dissipation occurs and, in the presence of a magnetic field, the path will act as a flux flow channel [23,24].

One inexact algorithm that has been utilized to calculate the minimum boundary sum for hexagonal grains [11,12] is the following. The minimum path across the conductor width along the grain boundaries is sought. The width is comprised of a number of rows of grains as shown in Fig. 2.162(a). Several possible routes from the top of the sample to the point at the bottom of row 1 are indicated in bold. The route involving the lowest critical current sum from the top of the conductor to this point is likely to be one of the paths marked in bold, and an assumption is made that any other paths will be longer. The minimum sums to all points along this first row are found. Subsequently, the minimum sums to all points along the bottom of the r^{th} row can be calculated by considering paths from the $(r-1)^{th}$ row. This algorithm does not consider paths such as the one shown by the dotted line in Fig. 2.162(b), although it does analyze the type of path shown in bold. Analysis of such modeled hexagonal structures has indicated that the paths that are not analyzed are rarely part of the limiting path [12], and thus the algorithm is often accurate. The main advantage of this method is that it does not require that all the grain boundary critical currents be stored in the computer’s memory at the same time.

The method used by Holzapfel et al. [14] produces an exact solution. It describes each square in the array as a "room" and each boundary as a "door." A unit of current is represented by a "mouse," which attempts to walk from one end of the conductor to the other by passing through the doors according to a rule, such as always keeping the walls on the right hand side. When a mouse gets to the end, the capacity of each door for carrying further mice is reduced by one. When a mouse fails to reach the other end of the tape, the critical current has been reached. Using this method the current is quantized and, if the ratio of the highest possible boundary critical current to the lowest is to be sufficiently high (~10^4), then the number of mice that must travel through the sample will be very high, and the calculation will be time-consuming for large networks.

There are a number of ways in which this method may be made more efficient. The first is to close permanently any door that a single mouse goes through in both directions to prevent further mice from going down dead ends. An alternative is to use mice that can carry different amounts of current, with the large-capacity mice going through the network first, followed by smaller-capacity mice.

The mouse-walk method is based upon the Ford-Fulkerson algorithm of flow-augmenting paths [25–27]. This algorithm finds a path through the network along which the capacity has not yet been reached (a flow-augmenting path). The flow (current) is then increased by the maximum amount that can flow along that path (δ), and the remaining capacity of each boundary along the path is reduced by δ. When no more flow-augmenting paths remain, the maximum flow has been reached and the critical current has been calculated.

2.27.3. Development of a New Model

The main limitation of most existing models is that they use unrealistic grain shapes (i.e., hexagons or squares). The Holzapfel model [14] calculates a critical current in a more realistic grain network but is limited by the need to perform the EBSD measurement. The aim is therefore to develop a model that combines the type of grain structure in the Holzapfel model with flexibility of conductor scale and crystallographic orientation.

2.27.3.1 Simulation of a 2-D Grain Network

Grain structure simulation is carried out by the Monte-Carlo Potts method [28] developed as a grain growth model by Anderson et al. [29–31]. The method has been used recently by a number of authors [32–35] to generate both two- and three-dimensional grain structures. For the purposes of a coated conductor model, we use a two-dimensional array of square pixels. Initially, each pixel is attributed a unique index number or letter, which identifies it as a grain and hence at the start of the simulation, the sample consists of a large number of small, square grains. The algorithm used to simulate grain growth begins by randomly selecting an individual pixel. The overall "energy" associated with that pixel is determined based on the number of near neighbors (of the eight linked by edges or vertices) in different grains. The algorithm then evaluates the effect on the energy of changing the index number of the pixel such that it is in the same grain as one of its four nearest neighbors (linked by edges). If this energy change is favorable (negative) or neutral (zero), then the change is made with probability (P) equal to 1. If however, the energy change would be positive, then the change is made with a probability given by Eq. (25):

$$P = \exp\left(\frac{-\Delta G}{kT}\right) \tag{25}$$

where ΔG is the difference between the number of neighboring pixels in different grains before and after the change is made. The factor kT is a thermodynamic variable and has been set equal to 1 for the purposes of this model.

An example of this process is shown in Fig. 2.163. The grain structure starts out as shown in (a) with the center pixel selected. It has an "energy" of 5 (five out of eight neighbors that share an edge or vertex are in other grains). It will then be provisionally assigned the index of one of the four neighbors with

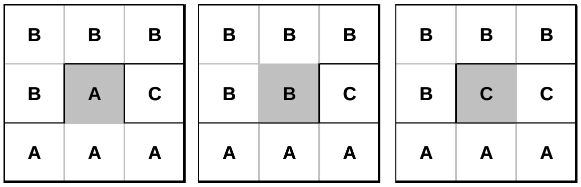

a) E=5 b) E=4 c) E=7

Fig. 2.163. The center pixel has an energy of (a) 5, (b) 4, or (c) 7, depending on which grain it is in.

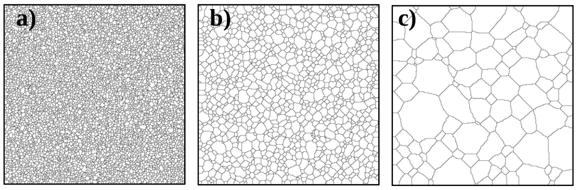

Fig. 2.164. Grain structures generated by the model on a 300 × 300 pixel grid with MCS numbers of (a) 10, (b) 100, and (c) 1000.

which it shares an edge, and the consequences of making the change are evaluated. The trivial case is that it “changes” to grain A, and the structure is maintained with no effect on the overall energy. Alternatively, it could attempt to change to B which would result in the situation shown in Fig. 2.163(b). The new energy for this pixel would be 4 units, and as this is favorable, the change would be confirmed. The remaining alternative is to attempt to become a C grain, resulting in the structure shown in Fig. 2.163(c). As this energy change is positive (+2 units), the change will occur with a probability of exp(-2). When the number of attempted pixel index changes equals the total number of pixels in the lattice, one time period of grain growth, known as a Monte Carlo Step has occurred. Grain growth progresses to produce structures such as those shown in Fig. 2.164 for a 300 × 300 pixel lattice. Once a physical grain structure has been established, the crystallographic orientation of each grain is assigned. This assignment is carried out randomly based on a typical X-ray gaussian distribution as is the case in other simulations. In order to simplify the model slightly, only a single grain misorientation (i.e. in-plane) is considered here, rather than the three-dimensional misorientation used elsewhere [11,12]. Except where stated otherwise, a FWHM of 10° is used.

2.27.3.2. Defining Sample Parameters

A modeled sample, which carries current along its length, is composed of P_l pixels along its length and P_w pixels across its width. There are an average of N_l grains in the length direction and N_w grains across the width. Each grain is, on average, composed of p_l pixels in the length direction and p_w in the width direction. This is shown in Fig. 2.165. Hence, $N_l \times p_l = P_l$ and $N_w \times p_w = P_w$; thus so for equiaxed grains, $p_l = p_w = p$.

The average grain size is determined by calculating the total numbers of “vertical” grain boundary segments, v, and “horizontal” boundary segments, h, in the sample.

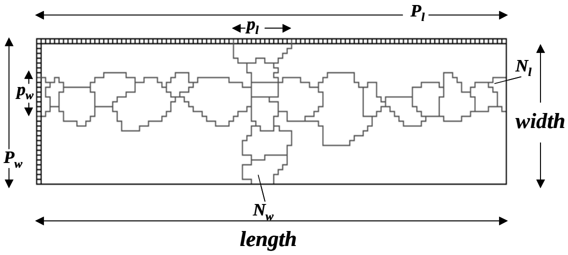

Fig. 2.165. Definition of the total number of pixels (P), the average number of pixels per grain (p), and the number of grains in the width (N_w) and length (N_l) directions.

$$p_l = \frac{(P_l - 1)(P_w - 1)}{v} \tag{26}$$

$$p_w = \frac{(P_l - 1)(P_w - 1)}{h} \tag{27}$$

The (P-1) term arises from the fact that the sample edge boundaries are not counted when summing the grain boundaries. This method is essentially equivalent to using a linear intercept method in the two perpendicular sample directions.

2.27.3.3 Calculating the Critical Current

The relationship between grain boundary angle and j_c was discussed earlier [see Eq. (1)]. Values of $\alpha = 2.4°$ and $\beta = 1.8°$ will be used in the initial calculations. Hence all grain boundaries for which $\theta \le 1.8°$ will be indistinguishable from the grains. Results will be normalized by dividing the calculated critical current density (J) by the single crystal value j_c'.

Once the network of grain boundaries, each with an assigned critical current, has been established, one needs to calculate the maximum current that may flow through such a network. One requires an algorithm that determines the path of grain boundaries across the width of the conductor whose critical current sum is the minimum of all such possible paths.

$$J_c = \frac{1}{w} \sum_{\min} \left(j_c \cdot l \right) \tag{28}$$

As noted previously, several algorithms may be used, some of which are approximations and others exact solutions. A solution was sought that would be both exact and efficient to reduce calculation time.

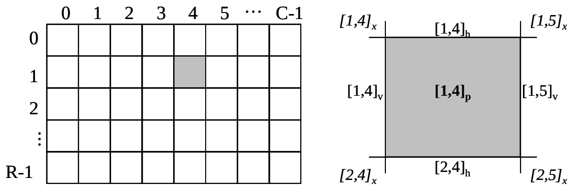

Fig. 2.166. Indexing of cells, edges and vertices in the square pixel model for a conductor C columns long and R rows wide.

The pixel grid consists of R rows and C columns as shown in Fig. 2.166 and is indexed as follows. Pixels are indexed $[r,c]_p$ with r running from 0 to (R–1) and c from 0 to (C–1). A horizontal boundary with the index $[r,c]_h$ forms the upper edge of pixel $[r,c]_p$. A vertical boundary with the index $[r,c]_v$ forms the left edge of pixel $[r,c]$. A vertex with the index $[r,c]_x$ is located at the upper left corner of pixel $[r,c]_p$.

Each pixel boundary has already been assigned a critical current. Hence values of $[r,c]_h$ are filled from $r = 1$ to $R–1$ and $c = 0$ to $C–1$ and values of $[r,c]_v$ are filled from $r = 0$ to $R–1$ and $c = 1$ to $C–1$. The calculation is performed by finding minimum values of paths to the vertices, and thus initial values of the vertices must be assigned as follows :

$$\begin{aligned} [r,c]_x &= 0 && \text{for } r = 0 \\ [r,c]_x &= \infty && \text{for all other } r \end{aligned} \tag{29}$$

The problem is to find the ‘shortest’ route from the vertices in row 0 to those in row R, where shortest means having the lowest critical current sum. The calculation is carried out in two stages, as follows.

Consider a vertex $[1,c]_x$. One route from the top of the sample to it is along vertical boundary $[0,c]_v$. The critical current sum along this path is equal to the sum of the value stored at $[0,c]_x$ and the value of $[0,c]_v$. If this sum is lower (which must be the case here since $[1,c]_x = \infty$), then the new value replaces the old one.

Step 1:

$$[r,c]_{x(\mathrm{new})} = \min \{ [r,c]_{x(\mathrm{old})} , [r–1,c]_x + [r–1,c\text{-}1]_v \} \qquad (c=1 \rightarrow C\text{-}1) \tag{30}$$

where min { a , b } represents the lower of values a and b.

When this calculation is performed with c ranging from 1 to C, the vertex values in row 1 are now critical current sums between there and the top of the conductor. However, they may not be the minimum values. Lower-sum paths may exist that include the horizontal boundaries in row 1. Thus the following calculations are performed for the vertices in row 1.

Step 2:

$$[r,c]_{x(\mathrm{new})} = \min \{ [r,c]_{x(\mathrm{old})} , [r,c\text{-}1]_x + [r,c+1]_h \} \qquad (c=1 \rightarrow C\text{-}1) \tag{31}$$

Step 3:

$$[r,c]_{x(\text{new})} = \min \{ [r,c]_{x(\text{old})} , [r,c+1]_x + [r,c]_h \} \quad (c=C\text{-}1 \rightarrow 1) \tag{32}$$

The 3 steps are carried out in sequence along each row of the array from top to bottom, and when this has been completed, the values of the vertices along row *R* represent critical current sums for possible routes across the sample width, but these are not necessarily the lowest J_c paths. The algorithm can be made to produce an exact solution by continuing as follows.

$$[r,c]_{x(\text{new})} = \min \{ [r,c]_{x(\text{old})} , [r+1,c]_x + [r,c]_v \} \quad (c=1 \rightarrow C\text{-}1) \tag{33}$$

In Step 4, Eq. (33) is followed by steps 2 and 3, first in the $(R-1)^{th}$ row, then in each subsequent row up to row 1. Steps 1–3 are then repeated from the top of the sample to the bottom.

If these steps leave the values at all the vertices in the grid unchanged, then the solution found in the initial stage (steps 1–3 only) was exact and the lowest value along row *R* is the critical current. Otherwise, this scan along the rows of vertices is repeated up to the top of the sample (steps 4, 2, 3) and back to the bottom (steps 1, 2, 3) until no changes are made to the vertex values.

This method was used for a number of model structures alongside the “mouse-walk” algorithm [14] and the Ford-Fulkerson algorithm [25–27] to ensure that the results were identical. The time taken to solve a 600 × 600 pixel array with grain sizes of 5 × 5 pixels completely is approximately 80 s, of which the initial scan of the grid (steps 1, 2, 3) is completed within the first 10 s. The answer produced by just the single downward scan is on average an overestimate of approximately 10 to 15%. This algorithm as coded is many times faster than the Ford-Fulkerson method. As the values of all grain boundaries are held in memory at the same time, the limitations of the hardware used to carry out the calculation restrict the size of network used to around 400,000 pixels.

2.27.4. Modeling Results

2.27.4.1 Features of the Model

First we will examine the nature of the grain structures produced by the Anderson grain growth model. One Monte-Carlo Step is defined as attempting $P_l \times P_w$ grain transitions, and this is the basic time unit for growth. Growth is symmetrical in the vertical and horizontal directions, and so p_l and p_w will be equal. When the Monte Carlo Step = 0, the grains are all composed of a single pixel ($p = p_l = p_w = 1$). The dependence of *p*, the average grain size expressed in pixels, as the Monte Carlo Step is increased is shown in Fig. 2.167. The structures from which the grain sizes were calculated were generated on a 600 × 600 square pixel lattice. The model replicates the result found by Burke [36] such that the grain size is proportional to the square root of the growth time, which is represented by the Monte Carlo Step number. The resulting grain size for a given Monte Carlo Step value is not dependent upon the sample size or shape (as long as there remain several grains across both width and length).

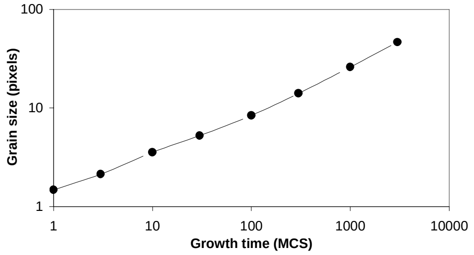

Fig. 2.167. Plot showing grain growth rate in the Anderson model. Grain size is the average linear dimension.

The fact that there are grains of different sizes for cases other than $p = 1$ is an important feature of the model. Figure 2.168(a) shows the linear grain size distribution functions for average grain sizes of 1.9 and 4.7 pixels; Fig. 2.168(b) shows a normalized plot, in which the grain size is divided by the average. These plots demonstrate that the peak in the distribution is just below the mean grain size, and only approximately 1% of grains have a linear dimension greater than three times the average. This distribution has been noted to correspond closely with that measured in real materials [33].

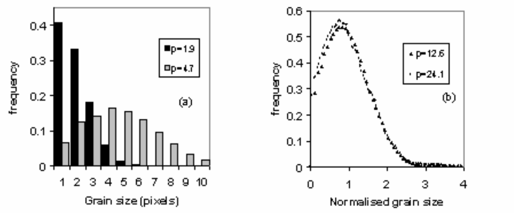

Figure 2.168. (a) Histogram showing the distribution of absolute grain sizes for MCS = 3 (p = 1.9) and MCS = 30 (p = 4.7) and (b) the normalized distribution which for high values of p lie on a single curve.

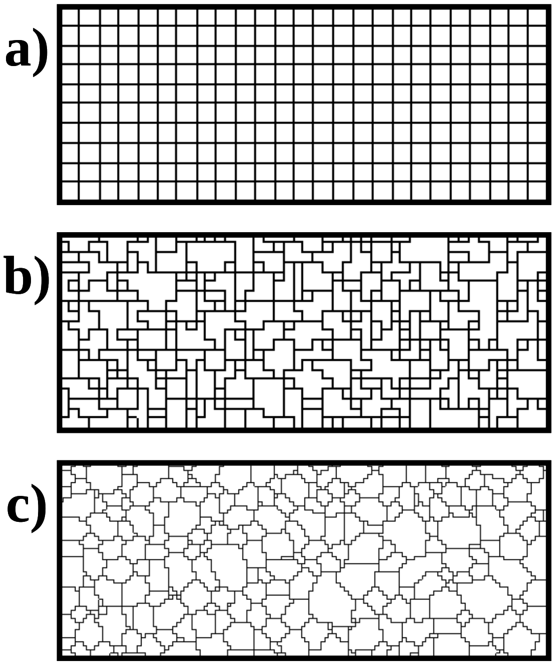

Fig. 2.169. Modeled samples for which N_l = 25 and N_w = 10. (a) p = 1 generates the simple square model, (b) p = 2 produces irregular grains, but highly pixelated, and (c) p = 5, with more realistic grain shapes.

In order to discover the essential differences between this percolation model and previous models, samples containing N_l grains along the length and N_w grains across the width are considered. In the simplest case, no Monte Carlo steps are carried out, and the grain structure consists of square grains, each 1 pixel by 1 pixel in size. This situation is then identical to the Nakamura model [13]. We compare it with samples that still have $N_l \times N_w$ grains, but the grains are irregularly shaped and have $p > 1$.

Figure 2.169 shows three such modeled samples, for which N_l = 25 and N_w = 10. The simplest case is that p = 1 where the grains are regular, identical squares (Fig. 2.169(a)]. Figure 2.169(b) shows a structure for which p = 2. Although the grain structure is still not realistic, it does at least have a range of grain sizes and there are two other differences that may be important for percolation. The average number of neighbors with which each grain shares a boundary is greater than four, and the minimum grain boundary path length connecting the upper and lower edges of the sample is now somewhat greater than the sample width. In figure 2.169(c), for which p = 5, it is evident that a much more realistic grain structure exists than in the previous cases, even though the pixel resolution is still apparent.

The critical current densities of samples such as those illustrated in Fig. 2.169 have been calculated so that the differences between the square-grain model and one with more realistic grains can be understood. Samples with N_l = 200 and N_w = 20 have been considered with the value of p varying from 1 to 10 in order to study the effect upon J_c. Additionally, the p = 1 and p = 5 models are compared for samples of fixed width over a range of lengths.

Figure 2.170(a) shows results of simulations of 100 samples for each value of p. It demonstrates that the square pixel model (p = 1) produces a significantly different result with a much lower average critical current. The reason for this is associated with the fact that the value of J_c is directly proportional to the length of the path that limits the current. In the case of square grains, this path is likely to be a straight line across the sample width. However, when the grains are irregular, this path is likely to be more circuitous, leading to higher values for J_c. Increasing p above around 5 has little effect. The p = 1 and p = 5 models are compared over a range of sample lengths in Fig. 2.170(b). This illustrates again the lower values of J_c produced by the simple square model.

2.27.4.2 Sample Dimensions

Although the three parameters of tape length, tape width, and average grain size may each be independently varied, the grain network is best described in a dimensionless manner, describing the sample in terms of the number of grains along the length and the number of grain across the width. In

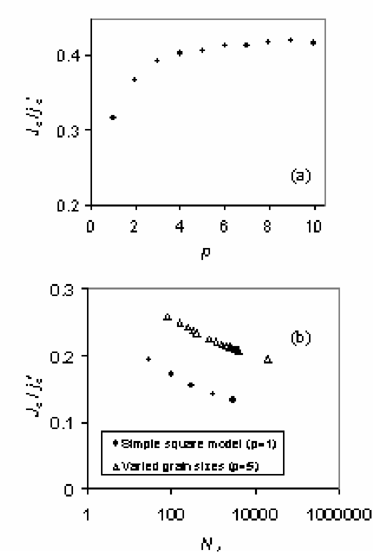

Fig. 2.170. (a) The dependence of the calculated sample critical current density on the value of *p* (N_l = 200, N_w = 20) and (b) comparison of p=1 and p=5 for various conductor lengths (N_w=40).

terms of the critical current density of a network, the solutions to a 10-cm-long, 1-cm-wide tape with 100-μm grains is identical to a 1 cm × 1 mm tape with 10-μm grains. We can vary the grain size for a sample of fixed dimensions, which is equivalent to varying the sample area (maintaining the aspect ratio) while holding the grain size constant.

We will first consider a square sample of dimensions $(10\text{ mm})^2$. The grains are isotropic and the average linear grain size is 5 pixels. The average number of grains in each dimension is varied from 5 up to 120. This sample is compared with a sample that is 30 mm long and 3 mm wide in which N_w ranges from 4 to 60. Thus in both cases the range of grain sizes examined is approximately 25to 250 μm. The calculated critical current densities are shown in Fig. 2.171, demonstrating that grain size has little or no effect for the square conductor but is important for tapes that are longer than they are wide.

The critical current of the tape that has an aspect ratio of 10 falls rather significantly as the size of the grains become a significant fraction of the tape width. For a conductor with this shape and size, the grain size would have to be around 50 μm or smaller to avoid any significant reduction in J_c. The difference in behavior between the two conductor shapes is important to consider when designing an experiment to verify the proposition that smaller grains are favorable for coated conductors. To see a reduction in J_c, one would need to ensure that the length (which corresponds to the distance between the voltage contacts in a four-point measurement) was significantly greater than the tape width. This often not the case for measurements made on small-scale samples.

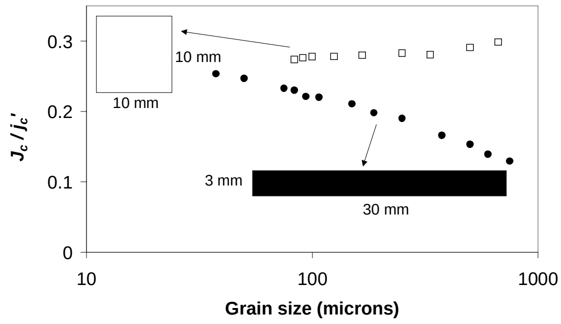

Fig. 2.171. Dependence of calculated critical current density on grain size for two different conductor shapes, a 10 × 10 mm square and a 3 × 30 mm rectangle (*p* = 5).

Previous grain-boundary network models that use square or hexagonal grains have predicted that the sample width must contain at least 50 to 100 grains to avoid “percolative pinch-off” [6,10]. It has also been observed that there is an approximately logarithmic decrease in J_c as the sample length is increased [13]. These ideas have been investigated here by using the more realistic grain shape model.

It has been proposed [12] that for a given sample width, there is the following relationship between J_c and conductor length:

$$J_c \propto \left(\frac{1}{l}\right)^{\frac{1}{m}} . \qquad (34)$$

This expression arises from a Weibull analysis [37], and *m* represents the Weibull modulus among a set of tape sections.

Calculations have been carried out over a range of widths and lengths for $p = 1$ (the square-grain model) and $p = 5$ (irregular grain model). A plot of log J_c vs log $(1/N_l)$ for both cases is shown in Fig. 2.172. It turns out that the gradients of the lines in these plots varies with and is approximately equal

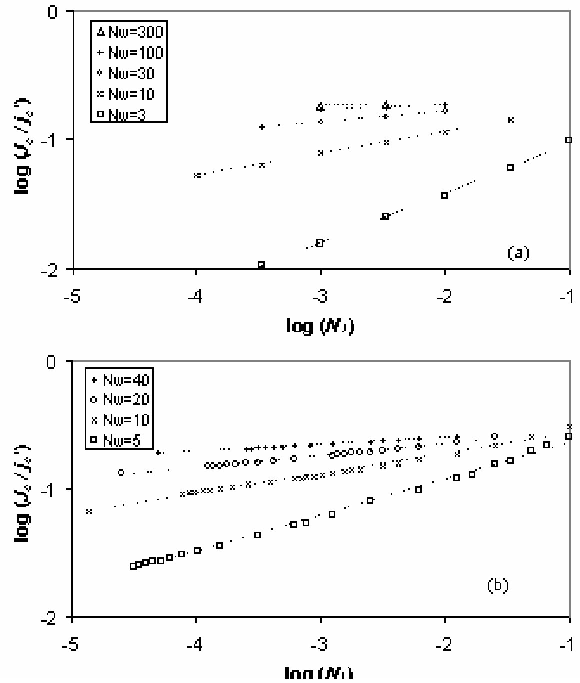

Fig. 2.172. Log-log plots of critical current density vs length for various conductor widths for a FWHM of 10° with (a) *p* = 1 and (b) *p* = 5.

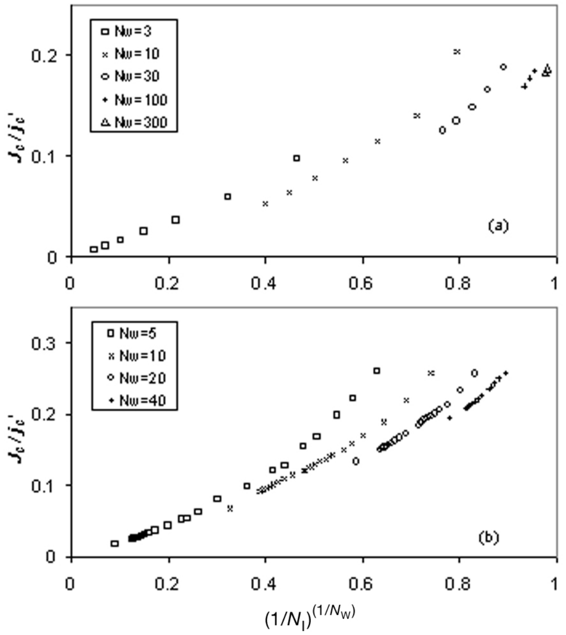

Fig. 2.173. Plots demonstrating the relationship between critical current density and sample width and length for a FWHM of 10° with (a) *p* = 1 and *p* = 5.

to the conductor width. Hence the following relationship between tape width and length is proposed to approximate J_c over limited ranges:

$$J_c \approx \left(\frac{1}{N_l}\right)^{\frac{1}{N_w}} . \qquad (35)$$

Figure 2.173 shows the data from Fig. 2.172 replotted in terms of Eq. (12) for $p = 1$ and $p = 5$. The plot indicates a series of lines for different widths rather than a single straight line, although the values do lie along a single line for tapes that are highly aspected ($l >> w$).

These two figures demonstrate how the critical current is reduced as the tape length increases, and that this dependence becomes stronger as the tape width narrows. An alternative way of looking at it is that the current is reduced as the width decreases and that this dependence becomes more significant for long tapes. Figure 2.173 demonstrates that Eq. (12) is most accurate in predicting the width and length dependence of tapes when the grain size is a small fraction of the sample dimensions and the tape is highly aspected. Fortunately, this is the case for most practical coated conductors.

2.27.4.3 Crystallographic Texture and Intragranular Dissipation

Another advantage of the model is that it can be adapted to study the effect of intragranular dissipation. Because each grain in the model is made up of a number of small square pixels, it is possible to assign critical-current values to the boundaries between the intragranular regions in order to simulate the intragranular J_c. The effect of the intragranular regions will be considered together with the effect of changing the FWHM of the grain orientations because the effects of the two parameters are closely interrelated. For example, if the grains were able to carry the same amount of current as 1.8° grain boundaries, which may occur due to the existence of twins, it is evident that intragranular dissipation in a sample would be significant if all grains are aligned to within a few degrees. If however the sample has a large FWHM, the effect of the grains is likely to be less significant, with most dissipation occurring at the grain boundaries, most of which will have a lower j_c.

It is useful to define a parameter that describes the current-carrying capability of the granular regions in a similar way to that of the boundaries. Instead of using absolute values of j_c, we will instead define the “equivalent angle” of the grains, ε, such that grains that carry the same amount of current as 2° grain boundaries are described as $\varepsilon = 2°$ grains. We will assume that all the grains within a sample have the same j_c and that this value is independent of the orientations of the grains.

The effect of varying the FWHM of the distribution of grain orientations has been modeled for samples with different intragranular critical currents. Figure 2.174 shows how J_c varies with FWHM when the grains carry the same j_c as 0°, 1.8°, and 4° boundaries. Also shown (by the dotted line) is the situation in which the grains are not considered and hence effectively can carry an infinite amount of current. In the case in which the grains have $\varepsilon = 0°$ and the FWHM is very low, we can draw two conclusions. As the critical current decreases with increasing FWHM, this must be a regime in which grain boundaries affect J_c. Also as J_c is lower than would be the case if the grains could carry infinite current (the dotted line), then there must also be some intragranular dissipation. Hence for high j_c grains, when the FWHM is low, dissipation is both intra- and intergranular. If the FWHM is above 5° however, this sample has the same critical current as it would if the grain j_c were infinite. Therefore, there must be no intragranular dissipation for a FWHM above 5°, and sample J_c is only limited by the grain boundaries.

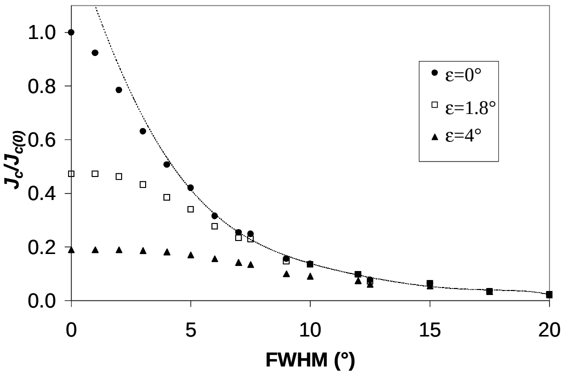

Fig. 2.174. Graph showing how the critical current is reduced as the FWHM increases, and how it depends on the current carried by the grains. The broken line shows the critical-current-density values if intragranular dissipation is not considered.

For the situation in which $\varepsilon = 4°$, the grains in the sample can only carry the same amount of current as a 4° grain boundary. Figure 2.174 shows that up until approximately 3°, J_c does not fall with increasing FWHM. Hence in this regime, the critical current of the sample must be limited only by dissipation within the grains. At higher FWHM values (between 5° up to around 20°), J_c changes with FWHM and is below the value that would be achieved with perfect grains and hence is in the mixed regime with some dissipation within grains and some at grain boundaries. Above around 20°, J_c is determined only by the grain boundaries.

Figure 2.175 shows in a three-dimensional plot how J_c varies with both FWHM (a factor which affects the current-carrying ability of the grain boundaries) and ε (a measure of the current-carrying capability of the grains). Depending upon where samples produced by a particular coated conductor process lie on the plotted surface, one may determine whether it is more important to concentrate on the quality of the grains, the boundaries, or both, to best improve the critical current. For example, process A produces a sample that is very well textured with a FWHM of just 2° but has rather poor grains, which behave like 4° grain boundaries ($\varepsilon = 4°$). Process B gives a FWHM of 8° but has better grains, which are able to carry the same currents as 2° boundaries. Figure 2.176 indicates that these samples will carry similar critical currents. It also shows that in order to improve sample A, it is of little use trying to improve the texture further or to dope the boundaries with calcium because doing so would have little effect on the overall J_c. Instead, one needs to improve the quality of the grains. Conversely for sample B, concentrating on the grain boundaries is more important.

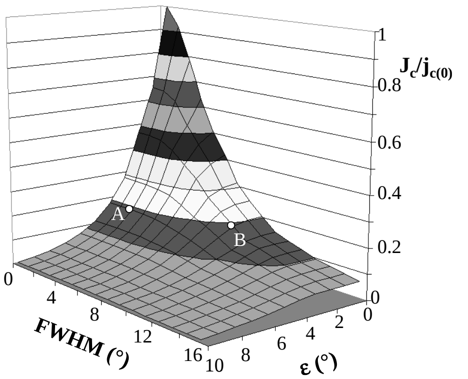

Fig. 2.175. The effect of the FWHM and the intra-granular critical current density (represented by ε, the equivalent angle) on critical current density as predicted by the model. Points A and B are possible samples discussed in the text.

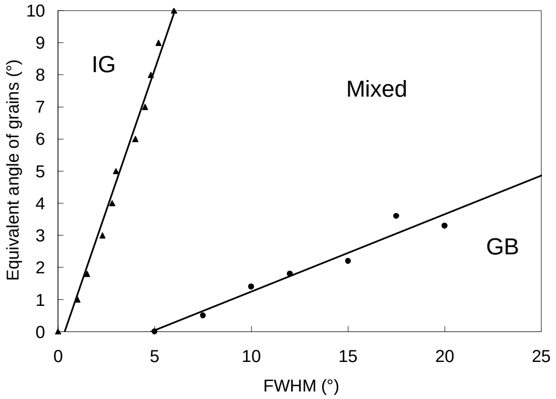

Fig. 2.176. Graph showing regimes of dominance of grain boundary dissipation (GB), intragranular dissipation (IG) and the combination of the two (mixed). Lines are plotted for changes of 1% in critical current density.

From the data plotted in Figs. 2.174 and 2.175, it is possible to produce a schematic phase diagram indicating the regions in which dissipation is entirely intragranular, or entirely intergranular or a combination of both. To calculate the points comprising the boundaries in Fig. 2.176, one considers in turn given values of ε. The transition between the intragranular region and the mixed region is determined by increasing the FWHM from zero until a fall in J_c is observed. The FWHM is then increased further until the point at which J_c is indistinguishable from that in a sample with perfect grains. This marks the transition to the regime of grain-boundary dissipation only. This has been done for values of ε up to 10°.

Figure 2.176 indicates that most coated conductors are probably in the mixed zone but closer to the grain-boundary regime (i.e. most dissipation occurs along grain boundaries, but grains also have some effect). For example, if we assume that the quality of grains is limited to ε=1.8° by the presence of twin boundaries, then only conductors in which the FWHM is higher than 12° have no significant granular dissipation. The figure also shows that very sharply aligned (almost single-crystalline) samples have to be achieved before the regime of exclusively intragranular dissipation is reached. Textures with FWHM values of 5 to 6° are currently being reported in RABiTS™ tapes [38].

The mechanism of dissipation will have important consequences for the effect of the sample dimensions. Percolation modeling generally considers samples in which dissipation occurs only at grain boundaries (i.e., in the grain-boundary zone). If a sample were in the mixed zone, it is likely that the length and width dependences would be lessened, and ultimately for samples in the intragranular zone, J_c should be totally independent of the sample dimensions.

2.27.5 References

1. D. P. Norton et al., "Epitaxial $YBa_2Cu_3O_7$ on Biaxially Textured Nickel (001): An Approach to Superconducting Tapes with High Critical Current Density," *Science* **274**(5288), 755 (1996).
2. *A. Goyal et al.*, "High Critical Current Density Superconducting Tapes by Epitaxial Deposition of $YBa_2Cu_3O_x$ Thick Films on Biaxially Textured Metals," *Appl. Phys. Lett.* ***69**, 1795 (1996).*
3. A. Goyal et al., "Conductors with Controlled Grain Boundaries: An Approach to the Next Generation, High Temperature Superconducting Wire," *J. Mater. Res.* **12**(11), 2924 (1997).
4. N. A. Rutter et al., "Ni Overlayers on Biaxially Textured Ni-Alloy and Cu Substrates by DC Sputtering," *Superconductor Science & Technology* **17**(3), 527–31 (2004).
5. C. Cantoni et al., "Quantification and Control of the Sulfur *c*(2 × 2) Superstructure on $\{100\}_2$, and $SrTiO_3$ Seed Layer Texture," *J. Mater. Res.* **17**(10), 2549 (2002).

6. A. Goyal et al., “Recent Progress in the Fabrication of High-J_c Tapes by Epitaxial Deposition of YBCO on RABiTS,” *Physica C* **357**(2), 903 (2001).
7. A. Goyal et al., “Texture Formation and Grain Boundary Networks in Rolling Assisted Biaxially Textured Substrates and in Epitaxial YBCO Films on Such Substrates,” *Micron* **30,** 463 (1999).
8. D. M. Feldmann et al., “Influence of Nickel Substrate Grain Structure on $YBa_2Cu_3O_{7-x}$ Supercurrent Connectivity in Deformation-Textured Coated Conductors,” *Appl. Phys. Lett.* **77**(18), 2906 (2000).
9. B. Zeimetz, B. A. Glowacki, and J. E. Evetts, “Application of Percolation Theory to Current Transfer in Granular Superconductors,” *European Physical Journal B* **29**, 359 (2002).
10. E. D. Specht, A. Goyal, and D. M. Kroeger, “Scaling of Percolative Current Flow to Long Lengths in Biaxially Textured Conductors,” *Supercond. Sci. Technol.* **13,** 592 (2000).
11. N. A Rutter, B. A. Glowacki, and J. E. Evetts, “Percolation Modelling for Highly Aligned Polycrystalline Superconducting Tapes,” *Supercond. Sci. & Technol*. **13,** L25 (2000).
12. N.A. Rutter, “Microstructural Development and Superconducting Parameters of the $YBa_2Cu_3O_{7-\delta}$ Coated Conductor,” Ph.D. Thesis, University of Cambridge, Cambridge, U.K., ftp://dmg-stairs.msm.cam.ac.uk/pub/theses/ (2001).
13. Y. Nakamura, T. Izumi, and Y. Shiohara, “Percolation Analysis of the Effect of Tape Length on the Critical Current Density of 123 Coated Conductors,” *Phys. C* **371,** 275 (2002).
14. B. Holzapfel et al., “Grain Boundary Networks in Y123 Coated Conductors: Formation, Properties, and Simulation,” *IEEE. Trans. Appl. Supercond.* **11**(1), 3872 (2001).
15. D. Dimos et al., “Orientation Dependence of Grain-Boundary Critical Currents in $YBa_2Cu_3O_{7-delta}$ Bicrystals,” *Phys. Rev. Lett.* **61**(2), 219 (1988).
16. D. Dimos, P. Chaudhari, and J. Mannhart, “Superconducting Transport Properties of Grain Boundaries in $YBa_2Cu_3O_7$ Bicrystals,” *Phys. Rev. B* **41**(7), 4038 (1990).
17. Z. G. Ivanov et al., “Weak links and dc SQUIDS on Artificial Nonsymmetric Grain Boundaries in $YBa_2Cu_3O_{7-\delta}$,” *Appl. Phys. Lett.* **59** (23), 3030 (1991).
18. N. F. Heinig et al., “Evidence for Channel Conduction in Low Misorientation Angle [001] Tilt $YBa_2Cu_3O_{7-x}$ Bicrystal Films,” *Appl. Phys. Lett.* **69**(4), 577 (1996).
19. D. T. Verebelyi et al., “Low Angle Grain Boundary Transport in $YBa_2Cu_3O_{7-\delta}$ Coated Conductors,” *Appl. Phys. Lett* **76**(13), 1755 (2000).
20. K. E. Gray, M. B. Field, and D. J. Miller, “Explanation of Low Critical Currents in Flat, Bulk versus Meandering, Thin-Film [001] Tilt Bicrystal Grain Boundaries in $YBa_2Cu_3O_7$,” *Phys. Rev. B.* **58**(14), 9543 (1998).
21. D. T. Verebelyi et al., “Critical Current Density of $YBa_2Cu_3O_{7-\delta}$ Low-Angle Grain Boundaries in Self-Field,” *Appl. Phys. Lett.* **78**(14), 2031 (2001).
22. L. R. Ford, and D. R. Fulkerson, *Naval Research Logistics Quarterly*, **4**(1), 47 (1957).
23. N. A. Rutter and B.A. Glowacki, “Modelling the *V-I* Characteristic of Coated Conductors,” *Supercond. Sci. Technol*. **14**(9), 680 (2001).
24. J. E. Evetts et al., “Current Percolation and the *V-I* Transition in $YBa_2Cu_3O_7$ Bicrystals and Granular Coated Conductors,” *Supercond. Sci. Technol*. **12** (12), 1050 (1999).
25. L. R. Ford, Jr., and D. R. Fulkerson, “Maximal Flow through a Network,” *Canadian Journal of Mathematics* **8**, 399 (1956).
26. L. R. Ford, Jr., and D. R. Fulkerson, “A Simple Algorithm for Finding Maximal Network Flows and an Application to the Hitchcock Problem,” *Canadian Journal of Mathematics* **9,** 210 (1957).
27. L. R. Ford, Jr., and D. R. Fulkerson, *Flows in Networks*, Princeton University Press, Princeton, N.J. (1962).
28. R. B. Potts, *Proceedings of the Cambridge Philosophical Society* **48**(106) (1952).
29. M. P. Anderson, *Simulation of Grain Growth in Two and Three Dimensions*, Risø National Laboratory, Roskilde, Denmark (1988).
30. M. P. Anderson et al., “Computer Simulation of Grain Growth—I. Kinetics,” *Act. Metall*. **32**(5), 783 (1984).

31. D. J. Srolovitz et al., “Computer Simulation of Grain Growth—II. Grain Size Distribution, Topology, and Local Dynamics,” *Act. Metall.* **32**(5), 793 (1984).
32. E. A. Holm, C.C. Battaile, “The Computer Simulation of Microstructural Evolution,” *Journal of Materials* **53**(9), 200 (2001).
33. K. Mehnert and P. Klimanek, “Monte Carlo Simulation of Grain Growth in Textured Metals,” *Scripta Materialia* **35**(6), 699 (1996).
34. M. Morhac and E. Morhacova, “Monte Carlo Simulation Algorithms of Grain Growth in Polycrystalline Materials,” *Cryst. Res. Technol*. **35**(1), 117 (2000).
35. P. Blikstein, A. P. Tschiptschin, “Monte Carlo Simulation of Grain Growth,” *Materials Research* **2**(3), 133 (1999).
36. J. E. Burke, *Trans. Am. Inst. Min. Engrs* **180**, 73 (1949).
37. W. Weibull, “A Statistical Distribution Function of Wide Applicability,” *J. Appl. Mech.* **18**, 293, (1951).
38. A. Goyal et al., Florida Wire Workshop, January 2003.

3. Summary of Technology Partnership Activities

3.1 Background

Oak Ridge National Laboratory (ORNL) is a key participant in the U.S. Department of Energy's (DOE's) national effort on electric power applications of high-temperature superconductivity (HTS). ORNL has formed effective teams that combine the resources of the Laboratory with the entrepreneurial drive of private companies. New technology partnership mechanisms, a feature of the ORNL Superconducting Technology Program for Electric Power Systems since its inception in 1988, have resulted in 42 superconductivity "pilot center" cooperative agreements and 10 cooperative research and development agreements (CRADAs). Eight cooperative agreements and two interagency agreements were active during FY 2004. In addition, licensing agreements, joint inventions, and joint publications with the private industry partners have ensured that there *is* technology transfer throughout the program.

Technology partnering on Laboratory-industry teams can occur in several ways. In the ORNL program, the cooperative development level of technology partnering is emphasized: joint Laboratory-industry teams work on problems that (1) require combined resources and expertise and (2) have a clear objective of precompetitive research and technology development. For the project to succeed, each partner depends on the success of the other. Most of the cooperative projects with private industry and the Laboratory precompetitive research and development (R&D) projects involve developing key technology in which commercialization of the results is expected to occur after a minimum of 3 to 5 years.

3.2 Relationship to the DOE Mission

The ORNL program mission is that of its program sponsor, DOE's Office of Electricity Delivery and Energy Reliability Superconductivity Program: to develop the technology base necessary for industry to proceed to commercialization of electric energy applications of HTS. HTS will enable new energy-efficient motors, transformers, and transmission lines and will also provide electric power equipment manufacturers with strategic technology for global competitiveness. Electric utilities can defer acquisition of new transmission rights-of-way with successful introduction of superconducting cables. System stability and protection will be enhanced with the introduction of fault-current limiters. Distributed utility systems in the future, which will include distributed generation systems, will benefit from the small size and light weight of the next generation of electric power equipment. In addition, oil-free power transformers and cables will provide a cost-effective, more environmentally friendly option for the utility sector.

3.3 Funding

DOE funding for the ORNL program and a summary of funds-out cooperative agreements in 2004 are shown in Table 3.1. Funds-out to industry, universities, and other federal agencies (e.g., the National Institute of Standards and Technology) was more than $3 million in FY 2004.

3.4 Technology Partnership Approach

An interdisciplinary approach uses many of the resources available at ORNL to meet the program goals for joint Laboratory-industry development of HTS technology for electric power applications. The superconductivity agreement mechanism interlinks R&D projects with industry and universities that optimize utilization of facilities, expertise, and program resources for the benefit of all participants. This program also coordinates the ORNL activities with the other national laboratories, government agencies, university centers, and industry groups.

Cooperative agreements ensure that technology development is industry-driven. The ORNL Office of Technology Transfer and Economic Development and patent counsel work together to place these agreements. Where appropriate, these efforts are coordinated with projects within ORNL that are funded by the DOE Office of Science as well as Work for Others and ORNL Laboratory Director's R&D Fund projects.

Effective funds-out to industry is used to supplement industry cost share. In FY 2004, $3 million in funds-out to industry and universities was provided through cooperative agreements and subcontracts. To keep industry involved from the start of the program and to ensure commercialization potential, all of these technology-partnering mechanisms are augmented by CRADAs, user agreements, and licensing activities.

Responsiveness to American industry has high priority in this program. An ORNL ad hoc technical review committee, consisting of a project manager, a scientific coordinator, a manager for conductor development, and a manager for applications development, reviews all inquiries from industry and recommends projects for possible funding. This review ensures that (1) the proposed work fits the program mission, (2) the work is collaborative, (3) there is legitimate commercial interest, and (4) the work is feasible. Substantial private-sector cost share is required on cooperative agreements.

ORNL provides support to the DOE Headquarters (DOE-HQ) Superconductivity Program for Electric Power Systems by identifying, guiding, and monitoring R&D at ORNL and ORNL subcontractor sites and by performing coordination, analysis, and planning of activities related to the national program.

ORNL works with the other program laboratories to address such issues as communication among program participants, workshop and meeting implementation, planned competitive solicitations and superconductivity agreements, and coordination of technical and economic assessments. ORNL leads the Superconductivity Partnerships with Industry Technical Review Committee and manages the Cryogenics Initiative subcontracts on behalf of all the program stakeholders.

3.5 Program Inventions

A summary of the new invention disclosures for FY 2004 is shown in Table 3.2. Patents issued in FY 2004 are shown in Table 3.3, and all patents issued since 1994 are shown in Table 3.4.

Table 3.1. Superconductivity Program summary of cooperative agreements as of September 30, 2004

Participant	Approved term	Type^a	Total agreement cost share ($K) By DOE To ORNL	To Industry	By industry	Technology Area
American Superconductor	4/5/01–4/4/05	C	2,400	0	2,400	HTS conductors for electric power applications; Wire Development Group; and YBCO wires
General Electric Company	8/2/02–7/31/05	C	650	0	650	Design and development of a 100-MVA HTS generator
MicroCoating Technologies	5/15/03–5/14/05	C	200	0	100	Demonstration of high current density YBCO films on CCVD buffers; effort stopped August 2003
NIST-Gaithersburg	12/1/00–12/31/04	IAG	0	860	860	YBCO phase diagram support
NIST-Boulder	3/98–2/29/07	IAG	0	1,297	1,297	Electromechanical properties for superconductor applications
Oxford Instruments	1/94–12/31/2004	C	1450	0	1675	Develop technology for dip-coated BSCCO-2212 wire and RABiTS™
Southwire Company	2/1/97–9/30/2005	FO	12066	500	12631	Develop HTS cable technology
SuperPower, Inc.	10/8/02–9/30/06	C	500	0	500	Produce high current density YBCO coated conductors
SuperPower, Inc.	07/01/04–02/28/07	C	850	0	850	Matrix fault current limiter SPI
Waukesha Electric Systems	6/15/97–9/30/2005	FO	3197	250	2556.4	HTS transformer
Total Active Agreements			21,213	2,907	23,519.4	
Total Completed Agreements			17,374	6,535.6	22,496.7	
TOTALS			38,587	9,442.6	46,0616.1	

[a] NFE = no-funds-exchange; FO = funds-out; FI = funds-in; IAG = interagency agreement; and C = CRADA.
**DOE to LANL

Table 3.2. Invention disclosures during FY 2004

ID No.	Subject	Submitted by
1336	Novel Oxide Buffers for Superconductors and Other Electronic Devices	M. Paranthaman, S. Sathyamurthy, and S. Bhuiyan
1358	Fabrication of High-J_c YBCO Thick Films via Solution Processing	A. Goyal and Y. Xu
1362	Fabrication of Solution-Derived Epitaxial Films	A. Goyal
1399	Modified Buffer Stack for Epitaxial Superconductors on RABiTS™	A. Goyal, D. F. Lee, E. D. Specht, L. Heatherly, and F. A. List
1401	Simplified Buffer Stack for RABiTS™	L. Heatherly, F. A. List, D. F. Lee, A. Goyal, T. Aytug, M. Paranthaman, C. Cantoni, and R. Feenstra
1449	Method to Form Self-Aligned Nano-Dots and Nano-Rods within the Superconductor to Enhance Properties	A. Goyal and S. Kang
1457	Novel Functional Buffer Layers for YBCO Coated Conductors (CRADA ORNL00-0577)	M. Paranthaman and A. Goyal (ORNL); U. Schoop, C. Thieme, D. Verebelyi, and M. W. Rupich (AMSC)
1461	Chemical Solution Deposition Method to Fabricate Highly Aligned IBAD-MgO Templates	M. Paranthaman (ORNL); S. Sathyamurthy and T. Aytug (UT); P. Arendt, L. Stan, and S. Foltyn (LANL)

Table 3.3. Patents issued in FY 2004

Patent No./ID No.	Date Issued	Title
6,635,097 B2/316.4	Oct. 21, 2003	Biaxially Textured Articles Formed by Powder Metallurgy
6,645,313 B2/1697-X	Nov. 11, 2003	Powder-in-Tube and Thick-Film Methods of Fabricating High Temperature Superconductors having Enhanced Biaxial Texture
6,663,976 B2/649.2	Dec. 16, 2003	Laminate Articles on Biaxially Textured Metal Substrates
6,700,297 B2	March 2, 2004	Superconducting PM Undiffused Machines with Stationary Superconducting Coils
6,716,795 B2/726.2	Apr. 6, 2004	Buffer Architecture for Biaxially Textured Structures and Method of Fabricating Same
6,740,421 B1/1205	May 25, 2004	Rolling Process for Producing Biaxially Textured Substrates
6,764,770 B2/1047	July 20, 2004	Buffer Layers and Articles for Electronic Devices
6,784,139 B1/375	August 31, 2004	Conductive and Robust Nitride Buffer Layers on Biaxially Textured Substrates
6,790,253 B2/316.13	September 14, 2004	Biaxially Textured Articles Formed by Powder Metallurgy
6,797,030/316.12	September 28, 2004	Biaxially Textured Articles Formed by Powder Metallurgy

Table 3.4. Cumulative listing of patents

Patent No./ID No.	Date Issued	Title
5,357,756 (1185-X)	October 25, 1994	Bipolar Pulse Field for Magnetic Refrigeration
5,395,821 (1039-X)	March 7, 1995	Method of Producing Pb-Stabilized Superconductor Precursors and Method of Producing Superconductor Articles Therefrom
5,525,583 (1471-X)	June 11, 1996	Superconducting Magnetic Coil (with AMSC)
5,546,261	August 13, 1996	Hermetically Sealed Superconducting Magnet Motor
5,646,097	July 8, 1997	Method of Fabricating a (1223) Tl-Ba-Ca-Cu-O Superconductor
5,739,086 (1640-X)	April 14, 1998	Structures Having Enhanced Biaxial Texture and Method of Fabricating Same
5,741,377 (1640-X)	April 21, 1998	Structures Having Enhanced Biaxial Texture and Method of Fabricating Same
5,830,828 (1193-X)	November 3, 1998	Process for Fabricating Continuous lengths of Superconductor
5,846,912 (1512-X)	December 8, 1998	Method for Preparation of Textured $YBa_2Cu_3O_x$ Superconductor
5,898,020 (1640-X)	April 27, 1999	Structures having Enhanced Biaxial Texture and Method of Fabricating Same
5,958,599 (1640-X)	September 28, 1999	Structures Having Enhanced Biaxial Texture
5,964,966	October 12, 1999	Method of Forming Biaxially Textured Alloy Substrates and Devices Thereon
5,968,877 (18-19)	October 19, 1999	High Tc YBCO Superconductor Deposited on Biaxially Textured Ni Substrate
5,972,847 (458)	October 26, 1999	Method for Making High-Critical-Current-Density $YBa_2Cu_3O_7$ Superconducting Layers on Metallic Substrates.
6,055,446 (1193)	April 25, 2000	Continuous Lengths of Oxide Superconductors
6,077,344 (223)	June 20, 2000	Sol-Gel Deposition of Buffer Layers on Biaxially Textured Metal Substances
6,106,615 (368)	August 22, 2000	Method of Forming Biaxially Textured Alloy Substrates and Devices Thereon
6,114,287 (534) (HTSPC-023)	September 5, 2000	Method of Deforming a Biaxially Textured Buffer Layer on a Textured Metallic Substrate and Articles Therefrom
6,150,034 (467)	November 21, 2000	Buffer Layers on Rolled Nickel, or Copper as Superconductor Substrates
6,156,376 (467)	December 5, 2000	Buffer Layers on Metal Surfaces having Biaxial Texture as Superconductor Substrates
6,159,610 (467)	December 12, 2000	Buffer Layers on Metal Surfaces having Biaxial Texture as Superconductor Substrates
6,180,570 B1 (312)	January 30, 2001	Biaxially Textured Articles Formed by Plastic Deformation
6,256,521 B1 (1784, new 148)	July 3, 2001	Preferentially Oriented, High Temperature Superconductors by Seeding and a Method for their Preparation
6,261,704 B1 (218)	July 17, 2001	MGO Buffer Layers on Rolled Nickel or Copper as Superconductor Substrates
6,270,908 B1 (734)	August 7, 2001	Rare Earth Zirconium Oxide Buffer Layers on Metal Substrates
6,286,194 B (1193)	September 11, 2001	Apparatus for Fabricating Continuous Lengths of Superconductor
6,296,701 B1 (296)	October 2, 2001	Method of Depositing An Electrically Conductive Oxide Film on a Textured Metallic Substrate and Articles Formed Therefrom
6,331,199 B1	December 18, 2001	Biaxially Textured Articles Formed by Powder Metallurgy
6,375,768 B1 (312)	April 23, 2002	Method for Making Biaxially Textured Articles by Plastic Deformation
6,385,835 B1	May 14, 2002	Apparatus for Fabricating Continuous Lengths of Superconductor

Table 3.4 (continued)

Patent No./ID No.	Date Issued	Title
6,399,154 B1 (734)	June 4, 2002	Laminate Article
6,440,211 B1 (649)	August 27, 2002	Method of Depositing Buffer Layers on Biaxially Textured Metal Substrates
6,447,714 B1 (316)	September 10, 2002	Method for Forming Biaxially Textured Articles by Powder Metallurgy
6,451,450 B1 (749)	September 17, 2002	Method of Depositing a Protective Layer over a Biaxially Textured Alloy Substrate and Composition Therefrom
6,468,591 (218)	October 22, 2002	Method for making MgO buffer layers on rolled nickel or copper as superconductor substrates
6,486,100 B1	November 26, 2002	Method for Preparing Preferentially Oriented, High Temperature Superconductors Using Solution Reagents
6,555,256 B1	April 29, 2003	Method of Depositing an Electrically Conductive Oxide Film on a Textured Metallic Substrate and Articles Formed Therefrom
6,599,346 B2 (316.3)	July 29, 2003	Biaxially Textured Articles Formed by Powder Metallurgy
6,602,313 B2 (316.2)	August 5, 2003	Biaxially Textured Articles Formed by Powder Metallurgy
6,607,839 B2 (316.9)	August 19, 2003	Biaxially Textured Articles Formed by Powder Metallurgy
6,610,413 (316.5)	August 26, 2003	Biaxially Textured Articles Formed by Powder Metallurgy
6,610,414 (316.11)	August 26, 2003	Biaxially Textured Articles Formed by Powder Metallurgy
6,617,283 B2 (889)	September 9, 2003	Method of Depositing an Electrically Conductive Oxide Buffer Layer on a Textured Substrate and Articles Formed Therefrom
6,635,097 B2 (316.4)	October 21, 2003	Biaxially Textured Articles Formed by Powder Metallurgy
6,645,313 B2 (1697-X)	November 11, 2003	Powder-in-Tube and Thick-Film Methods of Fabricating High Temperature Superconductors having Enhanced Biaxial Texture
6,663,976 B2 (649.2)	December 16, 2003	Laminate Articles on Biaxially Textured Metal Substrates
6,700,297 B2	March 2, 2004	Superconducting PM Undiffused Machines with Stationary Superconducting Coils
6,716,795 B2 (726.2)	April 6, 2004	Buffer Architecture for Biaxially Textured Structures and Method of Fabricating Same
6,740,421 B1 (1205)	May 25, 2004	Rolling Process for Producing Biaxially Textured Substrates
6,764,770 B2 (1047)	July 20, 2004	Buffer Layers and Articles for Electronic Devices
6,784,139 B1 (375)	August 31, 2004	Conductive and Robust Nitride Buffer Layers on Biaxially Textured Substrates
6,790,253 B2 (316.13)	September 14, 2004	Biaxially Textured Articles Formed by Powder Metallurgy
6,797,030 (316.12)	September 28, 2004	Biaxially Textured Articles Formed by Powder Metallurgy

4. Events, Honors, and Awards

4.1 Mike Gouge Named Editorial Board Member for the *Journal of Superconductivity: Incorporating Novel Magnetism*

Mike Gouge, leader of the Applied Superconductivity Group in the Fusion Energy Division and applications team leader in the ORNL Superconductivity Program, was named as a new editorial board member of the *Journal of Superconductivity: Incorporating Novel Magnetism*, beginning in January 2005. Typically, board members serve three to five years. Mike will specifically help secure article submissions in the area of applied superconductivity.

The *Journal of Superconductivity: Incorporating Novel Magnetism* is in its fifteenth year of publication. Its scope includes novel magnetic phenomena. In addition to regular submission articles, proceedings of topical conferences within the subject matter of the journal, as well as an occasional invited review article, are published in it. The journal publishes six issues annually with over 1000 pages of text.

4.2 ORNL Showcases Superconducting Wire Technology at "Superconductivity Day on the Hill"

The Coalition for the Commercial Application of Superconductors (CCAS) sponsored a Superconductivity Day on the Hill on February 26, 2004, in the Rayburn House Office Building (Fig. 4.1). Congressmen Markey and Olver (both D-MA) visited and spoke, and Congressman McNulty (D-NY) spent a long time examining the exhibits. A substantial number of legislative directors, assistants, and staff from multiple committees also heard CCAS President John Howe's presentations, entered into significant discussions, and picked up literature. ORNL's Dave Hill and Bob Hawsey attended the exhibition. ORNL displayed a length of second-generation RABiTS™-based superconducting wire and provided information to a number of the attendees.

Office of Electric Transmission and Distribution
Improving the way electricity is delivered to you
Ni Alloy Applications
ATI Wah Chang

Fig. 4.1. Attendees at the Superconductivity Day on the Hill, sponsored by the Coalition for the Commercial Application of Superconductors, February 26, 2004.

4.3 Goyal Co-Edits Book on High-Temperature Superconductivity

Amit Goyal, of ORNL's Metals and Ceramics Division, co-edited *Fabrication of Long-Length and Bulk High Temperature Superconductors* (The American Ceramic Society, Ceramic Transactions, Vol. 149, 2004). Other co-editors include Ruling Meng of the University of Texas, Houston; Kaname Matsumoto of Kyoto University, Japan; Herbert Freyhardt of University of Guttingen, Germany; and Winnie Wong-Ng of the National Institute of Standards and Technology, Gaithersburg, Maryland.

The book, a summary of developments in HTS research, is divided into three sections: "Coated Conductors"; "BSCCO-Based Conductors, MgB_2 , and Other HTS Materials"; and "Control of

Microstructure.” Papers include topics such as long-length flexible wires and tapes, melt-textured YBCO materials, processing of HTS materials, the current status and potential for YBCO-based coated conductors, BSCCO-based conductors, and MgB_2-based wires.

4.4 ORNL’s Superconductivity Project Inventors named Patent Award Recipients at May 25 Ceremony

The ORNL superconductivity project was cited in FY 2004 for significant patents awarded in 2003. ORNL senior scientist Amit Goyal and ORNL retirees Don Kroeger and Bob Williams were the only ORNL inventors named as Patent Award Recipients at the May 25, 2004 “Key Contributor and Patent Awards Ceremony” sponsored by the ORNL Technology Transfer and Economic Development Directorate. The award was for the U.S. patent, “Biaxially Textured Articles Formed by Powder Metallurgy.” The patent describes powder metallurgical methods to make alloys for the textured template used for RABiTS™-based high-temperature superconducting wires. The patent has been licensed to American Superconductor Corporation.

4.5 ORNL Superconductivity Researchers Partnered with North Carolina S&T State University to win $1.4 million NSF Grant

ORNL was notified in May 2004 that its Historically Black Colleges and Universities (HBCU) partner university, North Carolina A&T State University, has been awarded a $1.4 million National Science Foundation grant. For this, Professor Dhananjay Kumar, an ORNL joint faculty member with North Carolina A&T State University, along with ORNL staff members David Christen, Steve Pennycook and Jianxin Zhong, will develop a science and education program in the areas of nanostructured magnetic and HTS materials. Dr. Christen is a team leader in the OE-funded superconductivity project at ORNL as well as a principal investigator for research funded by the DOE Office of Basic Energy Sciences into the physical properties of high-temperature superconductors.

4.6 Paranthaman named an Associate Editor of the Journal of the American Ceramic Society

ORNL’s Parans Paranthaman was named an associate editor of the *Journal of the American Ceramic Society*. Dr. Paranthaman is a senior research staff member funded by DOE-OE/Superconductivity Program for Electric Power. For more than three-quarters of a century, the *Journal of the American Ceramic Society* has been the premier forum and archive used by scientists, engineers, and students to learn about original research in ceramics. Since HTS materials are ceramics, the journal is an important forum for dissemination of results of original research in the field of HTS. Every month the journal publishes more than 40 papers that have been rigorously reviewed by an international team of renowned ceramists. The papers describe research concerning traditional and advanced ceramic materials and composites, fabrication processes, applications, and instrumentation. Invited feature papers by recognized authorities who review scientific developments in particular fields of research are published frequently. The journal is published 12 times each year. It includes approximately 3600 editorial pages.

4.7 ORNL participates in Superconducting Cable Kick-off Event on Capitol Hill

ORNL participated along with industrial partner Southwire Company in a superconducting cable project “kick-off” event on June 2, 2004. The event was organized by the three cable companies and their superconducting wire suppliers, who were awarded cost-shared demonstration projects in the United States. ORNL’s partner, Southwire Company (and their joint venture partner *nkt cables* of Denmark), will be developing and installing a 200-m-long three phase HTS cable at an American Electric Power substation in Columbus, Ohio. The cable has the highest rated current of any of the three new projects announced on June 2.

4.8 ORNL Team Leader Co-Edits an issue in *MRS Bulletin*

Parans Paranthaman of ORNL's Chemical Sciences Division co-edited a special issue in the area of "High-Performance YBCO-coated Superconductor Wires" in the August 2004 issue of *MRS Bulletin* (Fig. 4.2). The issue provides an overview of the current status of the R&D in the area of HTS wires in the world. Parans has also co-written an article on RABiTS™ with Amit Goyal of ORNL and Urs Schoop of American Superconductor Corp. More details may be found on the *MRS Bulletin* website: http://www.mrs.org/publications/bulletin/2004/aug/

MRS Bulletin ranked second among 159 materials science journals and first among 67 applied physics journals in the Institute for Scientific Information® Journal Citation Reports® (JCR) impact factor ratings, 1999 Science Edition.

MRS
BULLETIN
Serving the International Materials Research Community
A Publication of the Materials Research Society
August 2004, Volume 29, No. 8
High-Performance YBCO-Coated Superconductor Wires

Fig. 4.2. *MRS Bulletin* special issue, August 2004.

4.9 Amit Goyal named to Executive Editorial Board for the *Encyclopedia of Superconductivity*

Amit Goyal was invited to join the executive editorial board (comprised of only four members internationally) for creation of a comprehensive *Encyclopedia of Superconductivity*, to be published by John Wiley & Sons. It will have three volumes:

Vol.1: *Superconductivity Basic Aspects and Theory*
Vol.2: *Materials Development*
Vol.3: *Superconductivity Applications*

Key functions of the executive editorial board are to (1) appoint an international advisory editorial board, (2) formulate the table of contents outlining what the volumes will consist of, and (3) invite appropriate contributors worldwide to provide their input.

4.10 Day of Science—November 17, 2003

The ORNL Superconductivity Program participated in the Lab's "Day of Science," in which approximately 500 undergraduate science, math, engineering, and technology students from selected HBCUs and core universities were invited to a "Day of Science" at ORNL (Fig. 4.3). The purpose of the event is to increase the number of minority students that apply and are chosen for the Laboratory's summer or semester undergraduate research programs. The main attraction of the Day of Science is an ORNL science exhibition, in which research divisions present displays that showcase their major research initiatives and "their most personable scientists and engineers."

Fig. 4.3. Parans Paranthaman with students at the 2003 ORNL Day of Science.

4.11 The 2004 Summer Intern Program

The ORNL Superconductivity Program hosted several interns with its Summer Intern Program in 2004, which represents a variety of DOE educational programs (see Table 4.1 and Figs. 4.4–4.7).

Table 4.1. 2004 Summer Intern Program information

Name	Institution	DOE program	ORNL mentor
Prof. Dhanajay Kumar Julius Steed II Tony Davis Jeffrey Jordon	North Carolina A&T University	Faculty and Student Teams	Dave Christen
Jennifer Williams (teacher)	Carter High School (Knoxville, Tenn.)	Laboratory Science Teacher Professional Development	Patrick Martin
Erin Stewart	Indiana University of Pennsylvania	Science Undergraduate Laboratory Internships	Parans Paranthaman
Nicolas Cunningham	Middle Tennessee State University	Research Alliance for Minorities	Patrick Martin
Alex Thorn	Princeton University	Higher Education Research Experiences at ORNL	Mike Gouge
Kartik Venkataraman	University of Wisconsin-Madison	Visiting Researcher	Parans Paranthaman

Fig. 4.4. Summer interns from North Carolina A&T University with mentors (left to right) Jeffery Jordan, Julius Steed, Jim Thompson (UT-ORNL), Dave Christen (ORNL), Professor Dhanajay Kumar, and Tony Davis.

Fig. 4.5. Interns Jennifer Williams, a teacher from Carter High School in Knoxville, and Nicolas Cunningham, from Middle Tennessee State University, with ORNL mentor Patrick Martin (right).

Fig. 4.6. Interns Erin Stuart, from Indiana University of Pennsylvania, and Nicolas Cunningham, from Middle Tennessee State University, with ORNL mentor, Patrick Martin (center).

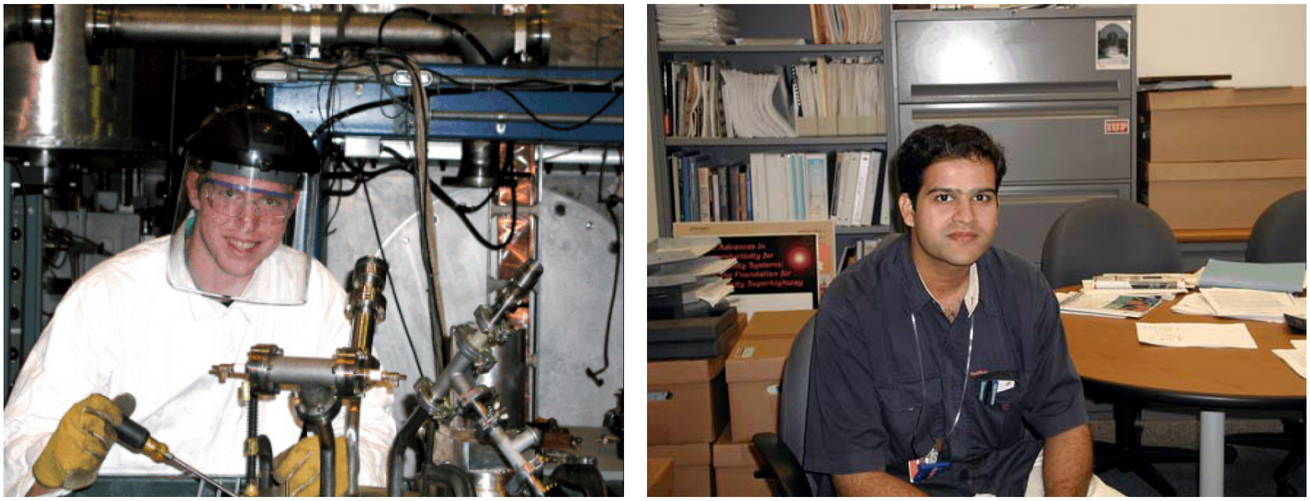

Fig. 4.7. Alex Thorn (left), intern from Princeton University. Kartik Venkataraman, visiting researcher from the University of Wisconsin.

5. FY 2004 Presentations/Publications

Aytug, T., M. Paranthaman, H. Y. Zhai, A. A. Gapud, K. J. Leonard, P. M. Martin, A. Goyal, J. R. Thompson, and D. K. Christen, “An Approach for Electrical Self-Stabilization of High-Temperature Superconducting Wires for Power Applications,” *Appl. Phys. Lett*. **85** (14), 2887–89 (2004), and *Virtual Journal of Applications of Superconductivity* **7** (8) (2004).

Aytug, T., M. Paranthaman, H. Y. Zhai, K. J. Leonard, A. A. Gapud, J. R. Thompson, P. M. Martin, A. Goyal, and D. K. Christen, “Iridium: An Oxygen Diffusion Barrier and a Conductive Seed Layer for RABiTS-Based Coated Conductors,” submitted to the 2004 Applied Superconductivity Conference, Jacksonville, Fla., October 3–8, 2004, to be published in June 2005 issue of *IEEE Transactions on Applied Superconductivity*.

Aytug, T., M. Paranthaman, H. Y. Zhai, K. J. Leonard, A. A. Gapud, P. M. Martin, C. Cantoni, R. Feenstra, A. Goyal, and D. K. Christen, “A New Conductive Buffer Layer Architecture for Electrical Self-Stabilization of YBCO Coated Conductors,” abstract submitted to the 2005 Spring Meeting of the Materials Research Society, San Francisco, Calif., March 28–April 1, 2005.

Aytug, T., M. Paranthaman, J. R. Thompson, A. Goyal, N. Rutter, H. Y. Zhai, A. A. Gapud, A. O. Ijaduola, and D. K. Christen, “Electrical and Magnetic Properties of Conductive Cu-Based Coated Conductors,” *Appl. Phys. Lett.* **83** (19) 3963–65 (2003).

Bhattacharya, R., P. Spagnol, D. Lee, and D. K. Christen, “Epitaxial Growth of Metal and Superconductor Oxide Films,” 204th Meeting of the Electrochemical Society, Orlando, Fla., October 12–17, 2003.

Bhuiyan, M. S., M. Paranthaman, D. Beach, L. Heatherly, A. Goyal, and E. A. Payzant, “Epitaxial Growth of Eu_3NbO_7 Buffer Layers on Biaxially Textured Ni-W Substrates,” submitted to Proceedings of Annual Meeting of the American Ceramic Society Meeting, April 2004, Indianapolis Ind., to be published in *Ceramic Transactions*, Vol. 160.

Bhuiyan, M. S., M. Paranthaman, S. Sathyamurthy, A. Goyal, and K. Salama, “Growth of Rare Earth Niobate Based Pyrochlores on Textured Ni-W Substrates with Ionic Radii Dependency,” paper submitted to *J. Mater. Research*.

Bhuiyan, M. S., M. Paranthaman, S. Sathyamurthy, D. F. Lee, S. Kang, A. Goyal, and K. Salama, “Study of Chemically Deposited Buffer Layers for YBCO Coated Conductors,” abstract submitted to the 2005 Spring Meeting of the Materials Research Society, San Francisco, Calif., March 28–April 1, 2005.

Bhuiyan, M. S., M. Paranthaman, S. Sathyamurthy, T. Aytug, S. Kang, D. F. Lee, A. Goyal, E. A. Payzant, and K. Salama, “Growth of Epitaxial Y_2O_3 Film on Biaxially Textured Ni-W Substrates,” *Mat. Res. Soc. Symp. Proc.* Vol. EXS-3, 2004 (Frontiers in Superconducting Materials—New Materials and Applications Symposium).

Bugoslavsky, Y., Y. Miyoshi, G. K. Perkins, A. D. Caplin, L. F. Cohen, H.-Y. Zhai, H. M. Christen, A. V. Pogrebnyakov, X. X. Xi, and O. V. Dolgov, “Superconducting Gap Structure and Pinning in Disordered MgB_2 Films,” *Supercond. Sci. Technol.* **17**, S350–54 (2004).

Cantoni, C., A. Goyal, J. D. Budai, A. A. Gapud, M. Feldmann, N. Nelson, K. J. Leonard, M. Paranthaman, and D. K. Christen, “Isolating the Effect of the Out-of-Plane Misorientation on J_c in RABiTS through *c*-Axis Tilted Epitaxial Growth of TiN Seed Layers,” abstract submitted to the 2005 Spring Meeting of the Materials Research Society, San Francisco, Calif., March 28–April 1, 2005.

Cantoni, C., A. Goyal, U. Schoop, X. Li, M. W. Rupich, C. Thieme, A. A. Gapud, T. Aytug, M. Paranthaman, K. Kim, J. D. Budai, and D. K. Christen, "Investigation of TiN Seed Layers for RABiTS Architectures with a Single-Crystal-Like Out-of-Plane Texture," submitted to the 2004 Applied Superconductivity Conference, Jacksonville, Fla., October 3–8, 2004, to be published in June 2005 issue of *IEEE Transactions on Applied Superconductivity*.

Cantoni, C., D. K. Christen, E. D. Specht, M. Varela, J. R. Thompson, A. Goyal, C. Thieme, Y. Xu, and S. J. Pennycook, "Characterization of Suitable Buffer Layers on Cu and Cu-Alloy Metal Substrates for Development of Coated Conductors," *Supercond. Sci. Technol.* **17** (5) S341–44 (2004).

Cantoni, C., D. T. Verebelyi, E. D. Specht, J. D. Budai, and D. K. Christen, "Anisotropic, Non-Monotonic Behavior of Superconducting Critical Current in Thin YBCO Films on Vicinal $SrTiO_3$ Surfaces," paper submitted to *Phys. Rev. B.*

Cheggour, N., J. W. Ekin, C. C. Clickner, D. T. Verebelyi, C. L. H. Thieme, R. Feenstra, and A. Goyal, "Reversible Axial-Strain Effect and Extended Strain Limits in Y-Ba-Cu-O Coatings on Deformation-Textured Substrates," *Appl. Phys. Lett.* **83** (20) 4223–25 (2003).

Christen, D. K., "Pumping Up for Wire Applications," *Nature* **3** (7), 421–22 (2004).

Demko, J. A., J. W. Lue, M. J. Gouge, P. W. Fisher, D. Lindsay, and M. Roden,, "Analysis of a Liquid Nitrogen-Cooled Tri-Axial HTS Cable System," *Advances in Cryogenic Engineering* **49A**, 913 (2004).

Demko, J. A., J. W. Lue, R. C. Duckworth, M. A. Young, M. J. Gouge, D. Lindsay, J. Tolbert, M. Roden, D. Willen, and C. Traeholt, "Testing of a 1.5-m Single Phase Short Sample Cable Made with Copper Laminated HTS Tapes at ORNL," submitted to the 2004 Applied Superconductivity Conference, Jacksonville, Fla., October 3–8, 2004, to be published in June 2005 issue of *IEEE Transactions on Applied Superconductivity*.

Emergo, R. L. S., J. Z. Wu, T. Aytug, and D. K. Christen, "Thickness Dependence of Superconducting Critical Current Density in Vicinal $YBa_2Cu_3O_{7-\delta}$ Thick Films," *Appl. Phys. Lett.* **85** (4) 618–20 (2004).

Feenstra, R., A. A. Gapud, D. K. Christen, T. Aytug, E. D. Specht, D. M. Feldmann, D. C. Larbalestier, T. G. Holesinger, A. Palau, T. Puig, and X. Obradors, "Thickness Dependent Current Transport in YBCO Coated Conductors," abstract to 2004 American Physical Society March Meeting, Montreal, Canada, March 22–26, 2004.

Feenstra, R., A. A. Gapud, E. D. Specht, C. Cantoni, A. Ijaduola, J. R. Thompson, D. K. Christen, T. G. Holesinger, D. M. Feldman, D. C. Larbalestier, A. Palau, T. Puig, and X. Obradors, "Development of high-I_c ex situ YBCO Coated Conductors: Trends in Thickness Dependence, Grain Boundary Networks, and Vortex Pinning," abstract submitted to the 2005 Spring Meeting of the Materials Research Society, San Francisco, Calif., March 28–April 1, 2005.

Feldmann, D. M., D. C. Larbalestier, R. Feenstra, A. A. Gapud, J. D. Budai, T. G. Holesinger, and P. N. Arendt, "Through-Thickness Superconducting and Normal-State Transport Properties Revealed by Thinning of Thick Film ex situ $YBa_2Cu_3O_{7-x}$ Coated Conductors," *Appl. Phys. Lett.* **83** (19) 3951–53 (2003).

Fisher, P. W. , M. J. Cole, J. A. Demko, M. J. Gouge, D. T. Lindsay, J. W. Lue, A. L. Qualls, M. L. Roden, and J. C. Tolbert, "Tri-axial Cable Terminations for 1.3- and 3-kA HTS Cables," *Advances in Cryogenic Engineering* **49A**, 892 (2004).

Gapud, A. A., J. R. Thompson, D. K. Christen, H. J. Kim, R. Feenstra, and D. M. Feldmann, "Intra-Inter-Granular Critical Currents of Coated Conductors from Field-Hystseretic Transport J_c," abstract submitted to the March Meeting of American Physical Society, Montreal, Canada, March 22–26, 2004.

Gapud, A. A., R. Feenstra, A. Goyal, C. Cantoni, T. Aytug, M. Paranthaman, S. Kang, K. J. Leonard, T. G. Holesinger, M. Varela del Arco, D. K. Christen, D. Kumar, and J. R. Thompson, "Enhancement of Flux Pinning in YBCO Coated Conductors via Processing-Induced Nanostructures," abstract submitted to the 2005 Spring Meeting of the Materials Research Society, San Francisco, Calif., March 28–April 1, 2005.

Gonzalez, J. C., N. Mestres, T. Puig, J. Gazquez, F. Sandiumenge, X. Obradors, A. Usoskin, C. Jooss, H. C. Freyhardt, and R. Feenstra, "Biaxial Texture Analysis of $YBa_2Cu_3O_7$-Coated Conductors by Micro-Raman Spectroscopy, *Phys. Rev. B* **70**, 094525 (2004), and *Virtual Journal of Applications of Superconductivity* **7** (7) (2004).

Gouge, M. J., "Cryogenic Cooling Technology for HTS Electric Machinery," Panel Session on Advances in Superconducting Machinery, sponsored by the Electric Machinery Committee, Synchronous Machinery Subcommittee. 2004 IEEE Summer Power Meeting, Denver, Colo., June 6–10, 2004.

Gouge, M. J., "Cryogenic Cooling Technology for HTS Electric Machinery," talk presented at IEEE PES Meeting, Denver, Colo., June 6–10, 2004.

Gouge, M. J., D. T. Lindsay, J. A. Demko, R. C. Duckworth, A. R. Ellis, P. W. Fisher, D. R. James, J. W. Lue, M. L. Roden, I. Sauers, J. C. Tolbert, C. Traeholt, and D. Willen, "Tests of Tri-Axial HTS Cables," submitted to the 2004 Applied Superconductivity Conference, Jacksonville, Fla.), October 3–8, 2004, to be published in June 2005 issue of *IEEE Transactions on Applied Superconductivity*.

Gouge, M. J., J. W. Lue, J. A. Demko, R. C. Duckworth, P. W. Fisher, M. Daumling, D. T. Lindsay, M. L. Roden, and J. C. Tolbert, "Testing of a 1.25-m HTS Cable Made from YBCO Tapes," *Advances in Cryogenic Engineering*, **49A**, 885 (2004).

Goyal, A., S. Kang, A. Gapud, K. Leonard, M. Paranthaman, D. F. Lee, F. A. List, L. Heatherly, S. Cook, and D. K. Christen (ORNL); T. Haugan, T. A. Campbell, P. Barnes (AFRL), "Enhancement of Flux-Pinning in Epitaxial ReBaCuO Films on RABiTS," abstract submitted to Applied Superconductivity Conference, Jacksonville, Fla., October 3–8, 2004.

Goyal, Amit, M. Parans Paranthaman, and U. Schoop, "The RABiTS Approach: Using Rolling-Assisted Biaxially Textured Substrates for High-Performance YBCO Superconductors," *MRS Bulletin* **29**(8), 552 (August 2004).

Grabovickic, R., D. R. James, I. Sauers, A. R. Ellis, P. C. Irwin, K. Weeber, L. Li, and A. D. Gadre, "Measurements of Temperature Dependence of Partial Discharge in Air Gaps between Insultated Bi-Sr-Ca-Cu-O Tapes," submitted to the 2004 Applied Superconductivity Conference, Jacksonville, Fla., October 3–8, 2004, to be published in June 2005 issue of *IEEE Transactions on Applied Superconductivity*.

Grabovickic, R., D. R. James, I. Sauers, A. R. Ellis, P. C. Irwin, K. Weeber, L. Li, and A. D. Gadre, "Partial Discharge and Pulsed Aging of Insulation between Bi-Sr-Ca-Cu-O Tapes at Room Temperature," abstract to Conference on Electrical Insulation and Dielectric Phenomena (CEIDP), Boulder, Colo., October 17–20, 2004.

Ijaduola, A. O., J. R. Thompson, A. Goyal, C. L. H. Thieme, and K. Marken "Magnetism and Ferromagnetic Loss in Ni-W Textured Substrates for Coated Conductors," *Physica C* **403**, 163–71 (2004).

Ijaduola, A. O., J. R. Thompson, A. Goyal, C. L. Thieme, and K. Marken, "Magnetism and Ferromagnetic Loss in Ni-W Textured Substrates for Coated Conductors," abstract to March Meeting of American Physical Society, Montreal, Canada, March 22–26, 2004.

James, D. R., and I. Sauers, "Electrical Insulation Materials for Superconducting Coil Applications," talk presented at IEEE PES Meeting, Denver, Colo., June 6–10, 2004.

James, D. R., and I. Sauers, "Electrical Insulation Materials for Superconducting Coil Application," Panel Session on Advances in Superconducting Machinery, sponsored by the Electric Machinery Committee, Synchronous Machinery Subcommittee. 2004 IEEE Summer Power Meeting, Denver, Colo., June 6–10, 2004.

James, D. R., I. Sauers, A. R. Ellis, and M. O. Pace, "Effect of Solid Condensation Layers on PD Onset Voltages In Voids in Epoxy," abstract to Conference on Electrical Insulation and Dielectric Phenomena (CEIDP), Boulder, Colo., October 17–20, 2004.

James, D. R., I. Sauers, A. R. Ellis, M. O. Pace, and D. J. Deschenes, "Effect of Gas Pressure on Partial Discharge in Voids in Epoxy," pp. 628–32 in *2003 Annual Report, Conference on Electrical Insulation and Dielectric Phenomena*, Oct. 19–22, 2003, Albuquerque, N.M., IEEE Pub. No. 03CH37471 (2003).

Kim, K., Y. W. Kwon, D. P. Norton, D. K. Christen, J. D. Budai, B. C. Sales, M. F. Chisholm, C. Cantoni, and K. Marken, "Epitaxial (La,Sr)TiO_3 as a Conductive Buffer for High Temperature Superconducting Coated Conductors," *Solid State Electronics* **47** (12), 2177–81 (2003).

Lee, D. F., K. J. Leonard, L. Heatherly, Jr., J. Yoo, F. A. List, N. Rutter, A. S. Cook, S. Sathyamurthy, M. Paranthaman, P. M. Martin, A. Goyal, and D. M. Kroeger, "Reel-to-Reel ex situ Conversion of High Critical Current Density Electron-Beam Co-Evaporated BaF_2 Precursor on RABiTS," *Supercond. Sci. Technol.* **17,** 386–94 (2004).

Leonard, K. J., A. Goyal, S. Kang, K. A. Yarborough, and D. M. Kroeger, "Identification of a Self-Limiting Reaction Layer in Ni-3at%W Rolling-Assisted Biaxially Textured Substrates," *Supercond. Sci. Technol*. **17,** 1295–1302 (2004).

List, F. A., L. Heatherly, D. F. Lee, K. J. Leonard, and A. Goyal, "Oxidation of Carbon on Nickel-Based Metallic Substrates: Implications for HTS Coated Conductors," paper submitted to *J. Mater. Research*.

List, F. A., P. G. Clem, L. Heatherly, J. T. Dawley, K. J. Leonard, D. F. Lee, and A. Goyal, "Low-Pressure Conversion Studies for YBCO Precursors Derived by PVD and MOD Methods," submitted to the 2004 Applied Superconductivity Conference, Jacksonville, Fla., October 3–8, 2004, to be published in June 2005 issue of *IEEE Transactions on Applied Superconductivity*.

Lue, J. W., J. A. Demko, P. W. Fisher, R. C. Duckworth, M. J. Gouge, J. C. Tolbert, M. L. Roden, and D. T. Lindsay, "Tests of 5-m Long Triaxial HTS Cables," *Advances in Cryogenic Engineering* **49A**, 877 (2004).

Lue, J. W., R. C. Duckworth, and M. J. Gouge, "Over-Current Testing of HTS Tapes," submitted to the 2004 Applied Superconductivity Conference, Jacksonville, Fla., October 3–8, 2004, to be published in June 2005 issue of *IEEE Transactions on Applied Superconductivity*.

McConnell, B. W., "Applications of High Temperature Superconductors to Direct Current Electric Power Transmission and Distribution," submitted to the 2004 Applied Superconductivity Conference, Jacksonville, Fla., October 3–8, 2004, to be published in June 2005 issue of *IEEE Transactions on Applied Superconductivity*.

Mehta, S. P., S. W. Schwenterly, and C. T. Reis, "Assembly and Test of 5/10 MVA HTS Transformer," talk presented at IEEE PES Meeting, Denver, Colo., June 6–10, 2004.

Palau, A., T. Puig, X. Obradors, E. Pardo, C. Navau, A. Sanchez, A. Usoskin, H. C. Freyhardt, L. Fernandez, B. Holzapfel, and R. Feenstra, "Simultaneous Inductive Determination of Grain and Intergrain Critical Current Densities of $YBa_2Cu_3O_{7-x}$ Coated Conductors," *Appl. Phys. Lett.* . **84** (2), 230–32 (2004).

Palau, A., T. Puig, X. Obradors, A. Usoskin, H. Freyhardt, L. Fernandez, B. Holzapfel, R. Feenstra, A. Sanchez, and E. Pardo, "Magnetic Granularity Analysis of YBCO Coated Conductors," *Physica C* **408–410**, 866–68 (2004).

Paranthaman, M. P., M. S. Bhuiyan, S. Sathyamurthy, H. Y. Zhai, A. Goyal, and K. Salama, "Epitaxial Growth of Solution Based Rare Earth Niobate, RE_3NbO_7 Films on Biaxially Textured Ni-W Substrates, submitted to *J. Mater. Res*.

Paranthaman, M. P., S. Sathyamurthy, M. S. Bhuiyan, A. Goyal, T. Kodenkandath, X. Li, W. Zhang, C. L. H. Thieme, U. Schoop, D. T. Verebelyi, and M. W. Rupich, "Improved YBCO Coated Conductors Using Alternate Buffer Architectures," submitted to the 2004 Applied Superconductivity Conference, Jacksonville, Fla., October 3–8, 2004, to be published in June 2005 issue of *IEEE Transactions on Applied Superconductivity*.

Paranthaman, M. P., S. Sathyamurthy, M. S. Bhuiyan, A. Goyal, T. Kodenkandath, X. Li, W. Zhang, C. L. H. Thieme, U. Schoop, D. T. Verebelyi, M. W. Rupich, "Chemical Solution Deposition of Functional Buffers for YBCO Coated Conductors," abstract submitted to the 2005 Spring Meeting of the Materials Research Society, San Francisco, Calif., March 28–April 1, 2005.

Paranthaman, M. P., T. Aytug, H.Y. Zhai, A. A. Gapud, P. M. Martin, K. J. Leonard, A. Goyal, and D. K. Christen, "Perovskite Type Buffers for YBCO Coated Conductors," submitted to Proceedings of Annual Meeting of the American Ceramic Society Meeting, April 2004, Indianapolis, Ind., to be published in *Ceramic Transactions*, Vol. 160.

Paranthaman, M. P., and T. Izumi (also guest editors), "High-Performance YBCO-Coated Superconductor Wires," *MRS Bulletin* **29** (8), 533 (2004).

Purnell, A. J., L. F. Cohen, H.-Y. Zhai, H. M. Christen, M. P. Paranthaman, D. H. Lowndes, L. Hao, and J. C. Gallop, "Nonlinear Microwave Response to an MgB_2 Thin Film," *Supercond. Sci. Technol.* **17**, 681–84 (2004).

Rane, J., H. Efstathiadis, H. Bakhru, F. Ramos, P. Haldar, M. S. Bhuiyan, A. Goyal, and M. Paranthaman, "Chemical and Microstructural Evaluation of Europium Niobate Buffer Layers for YBCO Coated Conductors," abstract submitted to the 2005 Spring Meeting of the Materials Research Society, San Francisco, Calif., March 28–April 1, 2005.

Rupich, M. W., U. Schoop, C. Thieme, D. T. Verebelyi, W. Zhang, X. Li, T. Kodenkandath, N. Nguyen, E. Siegal, L. Civale, T. Holesinger, A. Goyal, and M. Paranthaman, "Second Generation HTS Wire Based on RABiTS™ Substrates and MOD YBCO," submitted to the 2004 Applied Superconductivity Conference, Jacksonville, Fla., October 3–8, 2004, to be published in June 2005 issue of *IEEE Transactions on Applied Superconductivity*.

Rutter, N. A., A. Goyal, C. E. Vallet, F. A. List, D. F. Lee., L. Heatherly, and D. M. Kroeger, "Ni Overlayers on Biaxially Textured Ni-Alloy and Cu Substrates by DC Sputtering," *Supercond. Sci. Technol.* **17**, 527–31 (2004).

Sathyamurthy, S., K. J. Leonard, and M. P. Paranthaman, "Solution-Based Approaches to Enhance Flux-Pinning in YBCO for Low-Cost Coated Conductor Fabrication," abstract submitted to the 2005 Spring Meeting of the Materials Research Society, San Francisco, Calif., March 28–April 1, 2005.

Sathyamurthy, S., M. Paranthaman, H. Y. Zhai, S. Kang, T. Aytug, C. Cantoni, K. J. Leonard, E. A. Payzant, H. M. Christten, and A. Goyal, "Chemical Solution Deposition of Lanthanum Zirconate Barrier Layers Applied to Low-Cost Coated-Conductor Fabrication," *J. Mater. Res.* **19** (7), 2117–23 (2004).

Sathyamurthy, S., M. Paranthaman, M. S. Bhuiyan, E. A. Payzant, D. F. Lee, and A. Goyal, "Solution Deposition Approach to High J_c Coated Conductor Fabrication," submitted to the 2004 Applied Superconductivity Conference, Jacksonville, Fla., October 3–8, 2004, to be published in June 2005 issue of *IEEE Transactions on Applied Superconductivity*.

Sauers, I., M. O. Pace, D. R. James, and A. R. Ellis, "Energy Dissipation by Partial Discharge in Cryogenic Cables," pp. 624–27 in *2003 Annual Report, Conference on Electrical Insulation and Dielectric Phenomena*, Oct. 19—22, 2003, Albuquerque, N.M., IEEE Pub. No. 03CH37471 (2003).

Sauers, I., M. O. Pace, D. R. James, and A. R. Ellis, "Partial Discharge and Energy Dissipation in Voids in Epoxy at Cryogenic Temperature," abstract to Conference on Electrical Insulation and Dielectric Phenomena (CEIDP), Boulder, Colo., October 17–20, 2004.

Schwenterly, S. W., M. J. Cole, J. A. Demko, E. F. Pleva, and D. W. Hazelton, "Design and Operating Performance of Cryocooled Helium Thermosiphon Loops for HTS Transformers," *Advances in Cryogenic Engineering* **49A**, 839 (2004).

Thompson, J. R., J. G. Ossandon, L. Krusin-Elbaum, K. D. Sorge, and J. L. Ullmann, "Pinning Action of Correlated Disorder Against Equilibrium Properties of $HgBa_2Ca_2Cu_3O_x$: a Delicate Balance," abstract to March Meeting of American Physical Society, Montreal, Canada, March 22–26, 2004.

Thompson, J. R., and D. K. Christen, "Coated Conductors: A Developing Application of High Temperature Superconductivity," in *Superconductivity: Physics and Applications*. ed. K. Fossheim and A. Sudbo, John Wiley & Sons, Inc., London (2004).

Thompson, J. R., H. J. Kim, C. Cantoni, D. K. Christen, R. Feenstra, and D. T. Verebelyi, "Self-Organized Current Transport through Low Angle Grain Boundaries in $YBa_2Cu_3O_{7-\delta}$ Thin Films, Studied Magnetometrically," *Phys. Rev. B* **69** (10) 104509 (2004).

Venkataraman, K., A. J. Kropf, C. U. Segre, Q. X. Jia, A. Goyal, B. W. Kang, S. Chattopadhyay, H. You, and V. A. Maroni, "Detection of interfacial strain and phase separation in $MBa_2Cu_3O_{7-x}$ Thin Films using Raman Spectroscopy and X-ray Diffraction Space Mapping," *Physica C* **402**, 1–16 (2004).

Venkataraman, K., D. F. Lee, K. Leonard, L. Heatherly, S. Cook, M. Paranthaman, M. Mika, and V. A. Maroni, "Reel-to-Reel X-Ray Diffraction and Raman Microscopy Analysis of Differentially Heat-Treated Y-BaF_2-Cu Precursor Films on Meter-Length RABiTS," *Supercond. Sci. Technol.* **17,** 739–49 (2004).

Venkataraman, K., E. E. Hellstrom, and M. Paranthaman, "Growth of Lanthanum Manganate Buffer Layers for Coated Conductors via a Metal-Organic Decomposition Process," submitted to the 2004 Applied Superconductivity Conference, Jacksonville, Fla., October 3–8, 2004, to be published in June 2005 issue of *IEEE Transactions on Applied Superconductivity*.

Xi, X., X., A. V. Pogrebnyakov, X. H. Zeng, J. M. Redwing, S. Y. Xu, Qi Li, Z.-K. Liu, J. Lettieri, V. Vaithyanathan, D. G. Schlom, H. M. Christen, H.-Y. Zhai, and A. Goyal, "Progress in the Deposition of MgB_2 Thin Films," *Supercond. Sci. Technol.* **17**, S196–S201 (2004).

Xie, Y. Y., J. Z. Wu, S. H. Yun, R. Emergo, R. Aga, and D. K. Christen, "Magnetic Flux Pinning Enhancement in $HgBa_2CaCu_2O_{6+*}$ Films on Vicinal Substrates," *Appl. Phys. Lett.* **85** (1), 70–72 (2004).

Xu, Y., A. Goyal, J. Lian, N. A. Rutter, D. Shi, S. Sathyamurthy, M. Paranthaman, L. Wang, P. M. Martin, and D. M. Kroeger, "Preparation of YBCO Films on CeO_2-Buffered (001) YSZ Substrates by a Non-Fluorine MOD Method," *J. Am. Ceram. Soc*. **87** (9), 1669–76 (2004).

Yoo, J., A. Goyal, and K. J. Leonard, "Growth of Epitaxial TiN Films on Biaxially Textured Metal Substrates by Sputtering," paper submitted to *J. Mater. Research*.

Yoo, J., K. J. Leonard, D. F. Lee, H. S. Hsu, L. Heatherly, F. A. List, N. A. Rutter, A. Goyal, M. Paranthaman, and D. M. Kroeger, "Effects of Conversion Parameters on the Transport Properties of YBCO Films in the BaF_2 ex situ Process," *J. Mater. Res* **19** (4), 1281–89 (2004).

Yoo, J., K. J. Leonard, H. S. Hsu, L. Heatherly, F. A. List, D. F. Lee, A. A. Gapud, P. M. Martin, S. Cook, M. Paranthaman, A. Goyal, and D. M. Kroeger, "The Growth of YBCO Films with High Critical Current at Reduced Pressures using the BaF_2 ex situ Process," *Supercond. Sci. Technol.* **17**, 1209–14 (2004).

Young, M. A., J. A. Demko, R. C. Duckworth, J. W. Lue, M. J. Gouge, and M. O. Pace, "Burn-Out Tests of 1st and 2nd Generation HTS Tapes in Liquid Nitrogen Bath Cooling," *Advances in Cryogenic Engineering Materials* **50B**, 860 (2004).

Young, M. A., M. J. Gouge, M. O. Pace, J. A. Demko, R. C. Duckworth, J. W. Lue, and A. Fathy, "An Investigation of the Current Distribution in The Triaxial Cable and Its Operational Impacts on a Power System," submitted to the 2004 Applied Superconductivity Conference, Jacksonville, Fla., October 3–8, 2004, to be published in June 2005 issue of *IEEE Transactions on Applied Superconductivity*.

Zhai, H. Y., H. M. Christen, M. P. Paranthaman, C. Cantoni, L. Zhang, C. W. White, D. K. Christen, and D. H. Lowndes, "Progress and Perspectives in Magnesium Diboride Films," pp. 207–36 in *Studies of High Temperature Superconductors (Advances in Research and Applications) Layered Cuprates and More on Magnesium Diboride*, Vol. 44, ed. A. Narlikar, Nova Sci. Publ., New York (2003).

Zhang, Y., R. Feenstra, J. R. Thompson, A. A. Gapud, T. Aytug, P. M. Martin, and D. K. Christen, "High Critical Current Density $YBa_2Cu_3O_{7-*}$ Thin Films Fabricated by ex situ Processing at Low Pressures," *Supercond. Sci. Technol*. **17**, 1154–59 (2004).

Zhang, Y., R. Feenstra, J. R. Thompson, A. A. Gapud, T. Aytug, P. M. Martin, and D. K. Christen, "High Critical Current Density $YBa_2Cu_3O_{7-*}$ Thin Films Fabricated by ex situ Processing at Low Pressures," paper submitted to *Supercond. Sci. Technol*.

INTERNAL DISTRIBUTION

1. D. B. Beach
2. E. E. Bloom
3. M. V. Buchanan
4. D. K. Christen
5. J. F. Cooke
6. L. M. Dickens
7. M. J. Gouge
8. A. Goyal

9–18. R. A. Hawsey

19. D. J. Hill
20. J. Johnson, OTIC
21. W. Koncinski
22. S. L. Milora
23. C. Narula
24. M. Paranthaman
25. C. Porto
26. R. B. Shelton

EXTERNAL DISTRIBUTION

27. N. Aversa, Consultant, Waukesha Electric Systems, 400 S. Prairie Ave., Waukesha, WI 53186-5937
28. P. N. Barnes, Air Force Research Laboratory, AFRL/PRPG, 2645 Fifth Street, WPAFB, OH 45433-7919
29. R. Bhattacharya, National Renewable Energy Laboratory, 1617 Cole Blvd., Golden, CO 80401
30. J. W. Bray, Physicist/Program Manager, General Electric Corporate Research and Development, P.O. Box 8, Schenectady, NY 12301
31. L. Castelloni, Metal Oxide Technologies Inc., 8807 Emmott Rd., Suite 100, Houston, TX 77040
32. H. S. Chhabra,OE-2, U.S. Department of Energy, 6H-034/FORS, 1000 Independence Ave., S.W., Washington, DC 20585
33. P. G. Clem, Sandia National Laboratories, MS 1411, P.O. Box 5800, Albuquerque, NM 87185-1405
34. G. Crabtree, Argonne National Laboratory, ET/212, 9700 South Cass Ave., Argonne, IL 60439-4838
35. S. J. Dale, Florida Adv Power Lab, Florida State University, 2000 Levy Ave., Bldg. A, Tallahassee, FL 32310
36. J. G. Daley, OE-2, U.S. Department of Energy, 6H-034/FORS, 1000 Independence Ave., S.W., Washington, DC 20585
37. J. Ekin, National Institute of Standards and Technology, 325 Broadway, Boulder, CO 80303
38. S. Fleshler, American Superconductor Corporation, Two Technology Dr., Westborough MA 01581
39. H. Harshavardhan, Neocera, 10000 Virginia Manor Rd., Beltsville, MD 20705
40. X. Huang, General Electric Corporate Research and Development, EP-113, P. O. Box 8, Schenectady, NY 12301
41. K. Kolevar, OE-1, U.S. Department of Energy, 1000 Independence Ave., S.W., Washington, DC 20085
42. L. Kovalsky, SuperPower, Inc., 450 Duane Avenue, Schenectady, NY 12305
43. V. Kruse, Southwire Company, P. O. Box 1000, Carrollton, GA 30119
44. D. C. Larbalestier, University of Wisconsin–Madison, Applied Superconductivity Center, 1500 Engineering Drive, Madison, WI 53706-1687

45. W. C. Lin, U.S. Department of Energy, Office of Assistant Manager for Energy Research and Development, Oak Ridge Field Office, P.O. Box 2008, Oak Ridge, TN 37831-6269
46. D. Lindsay, Ultera-Southwire Company, P. O. Box 1000, Carrollton, GA 30119
47. A. P. Malozemoff, American Superconductor Corporation, Two Technology Dr., Westborough MA 01581
48. K. R. Marken, Jr., Oxford Superconducting Technology, P.O. Box 429, Carteret, NJ 07008-0429
49. S. P. Mehta, Waukesha Electric Systems, 400 S. Prairie Ave., Waukesha, WI 53186-5937
50. C. E. Oberly, WL/POOX-2, Aerospace Power Div., Wright Laboratory, 2645 Fifth St., WPAFB OH 45433-6563
51. P. N. Overholt, OE-2, U.S. Department of Energy, 1000 Independence Avenue, S.W., Washington, DC 20585
52. S. M. Parker, Oxford Superconducting Technology, P.O. Box 429, Carteret, NJ 07008- 0429
53. W. P. Parks, Jr., OE-1, U.S. Department of Energy, 1000 Independence Avenue, S.W., Washington, DC 20585
54. P. Pellegrino, SuperPower, Inc., 450 Duane Avenue, Schenectady, NY 12305
55. D. E. Peterson, Los Alamos National Laboratory, Superconductivity Technology Center, P.O. Box 1663, MS K763, Los Alamos, NM 87545
56. E. Pleva, Waukesha Electric Systems, 400 S. Prairie Ave., Waukesha, WI 53186-5937
57. C. Reis, SuperPower, Inc., 450 Duane Avenue, Schenectady, NY 12305
58. M. W. Rupich, American Superconductor Corporation, Two Technology Drive, Westborough, MA 01581
59. R. F. Schiferl, Rockwell Automation Power Systems, 26391 Curtiss Wright Pkwy, Suite 102, Richmond Heights, OH 44143
60. V. Selvamanickam, SuperPower, Inc., 450 Duane Avenue, Schenectady, NY 12305
61. M. Suenaga, Brookhaven National Laboratory, Bldg. 480, P. O. Box 5000, Upton, NY 11973-5000
62. K. Weeber, GE Electronic and Photonic Systems Technologies, 1 Research Circle, Bldg EP, Rm 111c, Niskayuna, NY 12309
63. W. Wong-Ng, National Institute of Standards and Technology, Ceramics Division, Building 223, A-256 Materials, Gaithersburg, MD 20899
64. G. Yurek, American Superconductor Corporation, Two Technology Drive, Westborough, MA 01581